PHD

The simulation of shunt compensated power transmission systems and their associated distance protection equipment.

Elnour, Mohamed A. H. Abu

Award date:
1980

Awarding institution:
University of Bath

The simulation of shunt compensated power transmission systems and their associated distance protection equipment.

by

Mohamed A. H. Abu Elnour

B.Sc. (Engg.), M.Sc. (Engg.)

Thesis submitted for the degree of Doctor of Philosophy

of

The University of Bath

1980

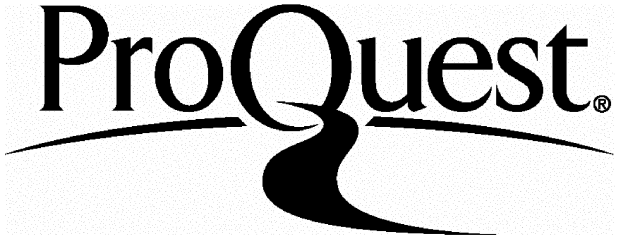

TO

MY PARENTS

MY WIFE AND MY SON 'TAMIR'

SUMMARY

In this thesis a thorough investigation of 4-reactor shunt compensated systems under unbalanced fault-transient conditions has been carried out. Mathematical models for incorporating 4-reactor compensators into single and multi-section feeder systems, together with the technique used to simulate reactor saturation, are developed. The techniques are very general, are applicable to transposed and untransposed multi-conductor lines of any configuration, and can take into account the frequency dependence of system parameters. Using these techniques computer programs are developed to study :

a - Effect of shunt-compensation on primary system response.

b - System and reactor overvoltages.

c - The probability of reactor saturation and its effect on primary system wave forms and hence on the performance of distance protection.

d - Effect of shunt-compensation on the performance of distance protection.

ACKNOWLEDGEMENTS

The work presented in this thesis was carried out under the supervision of Dr. A. T. Johns, B.Sc., Ph.D., C. Eng., M. I. E. E., of the school of Electrical Engineering, University of Bath, whose constant encouragement and guidance are gratefully acknowledged.

The author is grateful to the University of Bath for the provision of research studentship and wishes to thank Professor J. F. Eastham for his encouragement.

Sincere thanks are due to Dr. R. K. Aggarwal for his co-operation.

Thanks are also due to the staff of the University of Bath Computer Centre, in particular Messrs M. Gill and D. Davies for their co-operation.

Finally the author wishes to express his sincere gratitude and thanks to the Egyptian Government for the continuous help and encouragement received.

LIST OF CONTENTS

			Page No
Chapter (1)	:	Introduction	1
Chapter (2)	:	Development of methods to simulate shunt compensated single-section feeder systems.	17
Chapter (3)	:	Development of methods to simulate practical multi-section feeder systems.	37
Chapter (4)	:	Simulation of saturation effects in 4- reactor compensated systems.	53
Chapter (5)	:	Parameters of systems studied.	70
Chapter (6)	:	Digital evaluation of primary system wave forms.	81
Chapter (7)	:	Digital evaluation of fault-induced over-voltages.	95
Chapter (8)	:	Digital simulation of saturation effects in 4-reactor compensated systems.	104
Chapter (9)	:	Digital evaluation of distance relay performance.	114
Chapter (10)	:	Conclusions and future work.	147
Appendix (A1.1)	:	Transmission line parameters for fault-transient studies.	158
Appendix (A1.2)	:	Evaluation of phase and neutral reactances of the 4-reactor scheme.	166
Appendix (A2)	:	Solution of travelling wave phenomena in polyphase systems.	169
Appendix (A3)	:	Fault simulation for a multi-conductor 3-phase system.	181
Appendix (A4)	:	Evaluation of transmission line charts.	189
Appendix (A5)	:	Digital simulation of relay mixing circuits.	192
Appendix (A6)	:	Evaluation of protective relay parameters.	202
Appendix (A7)	:	Evaluation of measurement accuracy of relays applied to 3-reactor compensated systems.	204
Appendix (A8)	:	Published work.	
References	:		206

LIST OF SYMBOLS

PPS , ZPS	=	Positive and zero phase sequences.
B_{c1} , B_{c0}	=	PPS and ZPS line capacitive susceptances.
X_{c1} , X_{c0}	=	$1/B_{c1}$, $1/B_{c0}$.
B_{ch} , B_{cg}	=	Phase-phase and phase-ground capacitive susceptances.
X_{ch} , X_{cg}	=	$1/B_{ch}$, $1/B_{cg}$.
X_{cn}	=	Capacitive reactance of grounded leg of 4-branched, Y equivalent circuit.
XP , X_n	=	Phase and neutral reactances of a 4-legged reactor.
X_1 , X_0	=	PPS and ZPS reactances of reactor arrangements.
$X_{\ell h}$, $X_{\ell g}$	=	Phase-phase and phase-ground reactances of 6-reactor scheme.
$B_{\ell h}$ ℓg	=	$1/X_{\ell h}$, $1/X_{\ell g}$.
B_{L1} , B_{LO}	=	PPS and ZPS inductive susceptances of reactor schemes.
h_1 , h_0	=	PPS and ZPS degrees of shunt compensation.
Q_{SR}	=	Shunt reactor rating.
SE , RE	=	Sending and receiving ends.
$\bar{V}$, $\bar{I}$	=	Voltage and current transform.
SR_1 , SR_2	=	Two-port transfer matrices of SE and RE reactors.
U , 0	=	Unit and zero matrices.
X	=	Distance of fault.
ℓ	=	Length of feeder under consideration.
A_{T1},B_{T1},C_{T1},D_{T1}	=	Matrices defining the system up to point of fault.
A_{T2},B_{T2},C_{T2},D_{T2}	=	Matrices defining the system beyond point of fault.
Z_{SR1},Z_{SR2}	=	Impedance matrices of SE and RE reactors.
Y_{SR1},Y_{SR2}	=	Admittance matrices of SE and RE reactors.
S.S	=	Steady-state.
$\bar{V}_{SS}$,$\bar{I}_{SS}$	=	Transform of S.S. voltages and currents at the SE.
$\bar{V}_{RS}$,$\bar{I}_{RS}$	=	Transform of S.S. voltages and currents at the RE.
$\bar{V}_{fs}$,$\bar{I}_{fs}$	=	Transform of S.S. voltages and currents at point of fault.

$\bar{V}_{ff}$, $\bar{E}_{ff}$	=	Transform of superimposed voltages at point of fault.
$\bar{V}_{sf}$, $\bar{I}_{sf}$	=	Transform of superimposed voltages and currents at the S.E.
$\bar{V}_{Rf}$, $\bar{I}_{Rf}$	=	Transform of superimposed voltages and currents at the R.E.
$\bar{I}_{fsf}$, $\bar{I}_{fRf}$	=	Transform of superimposed currents at point of fault.
Z_f , R_f	=	Fault impedance and resistance matrices.
Z_{SS} , Z_{RS}	=	Impedance matrices of main sources at the S.E. and R.E.
SCL , I_{Sc}	=	Short circuit level and current.
S.S.C.L. , R.S.C.L.	=	SCL at the S.E. and R.E.
Z_1 , Z_0	=	PPS and ZPS impedances of main sources.
Z_{SSO}/Z_{SS1} , Z_{RSO}/Z_{RS1}	=	ZPS/PPS impedance ratio of S.E. and R.E. main sources.
Q_S , Q_R	=	X/R ratio of S.E. and R.E. main sources.
$\ell_1, \ell_2, \ell_3 \cdots \ell_n$	=	Line length of feeder having n-sections.
ℓ_m	=	Length of line model under consideration.
$A_{21}, B_{21}, C_{21}, D_{21}$	=	Matrices defining the multi-section feeder system up to point of fault (including S.E. main source).
Z_{SM} , Z_{SSM}	=	Modified (3,3) and (6,6) S.E. source impedance matrices due to the near-S.E. line sections.
Z_{RM} , Z_{RSM}	=	Modified (3,3) and (6,6) R.E. source impedance matrices due to the near-R.E. line section.
γ	=	Propagation constant matrix.
Z,Y	=	Series impedance and shunt admittance matrices per unit length.
S	=	Voltage eignvector matrix.
Z_c , Y_c	=	Surge impedance and admittance matrices.
A_1, B_1, C_1, D_1	=	Constants of first section of a transposed line.
A_2, B_2, C_2, D_2	=	Constants of second section of a transposed line.
A_3, B_3, C_3, D_3	=	Constants of third section of a transposed line.
CN, CN´, CP, CP´	=	Transposition constant matrices.
t	=	Transpose of a matrix.
$\psi(t)$	=	Time variation of flux linkage of any of the 4-reactors.
ψ_{ss}	=	S.S. peak flux linkage of phase-reactors.

ω_0	=	System nominal angular frequency.
ω	=	Angular frequency.
V_m , V_{mn}	=	Peak voltage across phase and neutral reactors.
Δt	=	Time interval between samples of voltage or current.
$v(t)$	=	Time variation of voltage across reactors.
L_1 , L_2	=	Initial and final slopes of a non-linear reactor.
L_s	=	Saturation shunt inductance.
V_{sat}	=	Voltage source for simulating reactor saturation.
V_n , L_n	=	Voltage across and inductance of linear neutral reactor.
T_s	=	Time at which saturation occurs.
$\bar{V}_X$	=	Transform of voltage-earth of neutral point 'X'.
$\bar{I}_X$	=	Transform of current of non-linear neutral reactor.
X_0	=	WL_s.
K, K_1, K_2	=	Constants.
$\bar{V}_S$, $\bar{I}_S$	=	Transform of voltages due to saturation - at S.E.
$\bar{V}_R$, $\bar{I}_R$	=	Transform of voltages due to saturation - at R.E.
$\bar{V}_{SE}$, $\bar{I}_{SE}$	=	Transform of overall system voltages and currents at the S.E. with S.E. neutral reactor in saturation.
TOB	=	Observation time.
α	=	Frequency shift constant.
FT	=	Fault inception time.
NS	=	Number of frequency samples.
Z_{L1} , Z_{LO}	=	PPS and ZPS impedances of line under consideration.
θ	=	Line angle.
ϕT	=	The mho characteristic argument.
Z_r	=	Current replica impedance.
S_1 , S_2	=	General form of relaying signals.
C.T., V.T.	=	Current and voltage transformers.
V_L , I_L	=	Relaying voltage and current at the secondaries of V.T. and C.T. respectively.
V_P	=	Sound-phase polarising voltage.

V_a, V_b, V_c	=	Voltages of phases a,b,c respectively at V.T. secondaries.
I_a, I_b, I_c	=	Currents of phases a,b,c respectively at C.T secondaries.
k	=	Residual compensating factor.
$I_{res.}$	=	Residual current at C.T. secondaries.
KP_e	=	Sound-phase polarising voltage constant.
$v(t)$, $i(t)$	=	Time variation of voltages and currents at secondaries of V.T. and C.T. respectively.
R_T , L_T	=	Referred resistance and inductance of transformer reactor.
R_P , C_P	=	Component resistance and capacitance for polarising phase-shift circuit.
N	=	Secondary to primary turns ratio of transformer reactor.
$v_s(t)$	=	Time variation of sound-phase voltage input to polarising circuit.
$v_0(t)$	=	Time variation of output voltage of transformer-reactor or polarising circuit.
$A_{34}, B_{34}, C_{34}, D_{34}$	=	Matrices defining the multi-section feeder system beyond point of fault (including R.E. main source).

CHAPTER 1 INTRODUCTION

1.1 Literature Review and State of Knowledge

Due to the enormous growth of electrical power systems in both size and complexity, much effort has been made to enable an accurate simulation of power system transients and hence proper system design and development of system protective schemes to be achieved.

The response of a transmission system following any sudden change in operating conditions such as fault initiation or switching operation may generally be classified as follows:[1,5]

1 - An initial surge-period in which travelling wave effects predominate.
2 - A final steady-state period during which system voltages and currents are periodic.
3 - A dynamic or temporary period - a transient period linking (1) and (2).

On modern EHV systems, control of surge-period overvoltages allows relatively low insulation levels to be adopted. It is therefore important to predict the temporary-period overvoltages so that the probability of insulation failure can be maintained at an acceptably low value. This is usually done through the study of transient phenomena using a realistic model for a typical power system where some form of simulation is to be adopted.

For many years investigations have been made using analogue models of the actual systems. These models called "simulators" or "Transient Network Analysers" (T.N.A.s), usually consist of a scaled down analogue in which transmission lines are represented by a large number of lumped-parameter π or T sections[2,3]. Although it has always been a powerful tool for transient simulation, the T.N.A. is not convenient to simulate the distributed nature of line parameters[2,3]. Besides, in a line model with a finite number of sections, it is not possible to cover the infinite frequency response bandwidth and hence a rather approximate response is unavoidable[4].

An obvious alternative to study power system transients is the use of digital techniques. Based on travelling wave phenomena, a number of methods are available to solve the system equations (1.1) and (1.2):

$$dV/dx = -Z \cdot I \qquad \ldots\ldots \quad 1.1$$

$$dI/dx = -Y \cdot V \qquad \ldots\ldots \quad 1.2$$

The equations may be solved using the laplace transform[6,7,11]. Applied to system equations for the phase voltages the method produces a number of interdependent second order differential equations for voltage in terms of distance. These are separated by transforming the voltages into independent modes which travel on the line without interaction. Once the modal waves are known, the phase voltages are evaluated by adding the forward and backward modal waves and using the inverse of the modal transformation.

An alternative form of the laplace method was employed by Dommel[8] and assumes lossless or distortionless propagation.

A third method is based on the well known lattice-diagram technique described by Bewley[9] and was used in much of the earlier work[10] for computer simulation of travelling waves in power systems. Again, the method is based on the assumption of lossless or distortionless propagation. The calculations are performed in terms of the voltage wave increments which travel on the line and the behaviour of these travelling waves at points of discontinuities is determined by reflection and refraction coefficients. Whereas for single phase calculations these coefficients are calculated from the individual line surge impedances, for 3-phase studies they are replaced by surge impedance matrices and in this way the mutual effects between phases are taken into account. Line surge impedance matrix is evaluated at the transient predominant frequency or if this is not known, at a frequency based on the travel time of the line being subjected to transient.

Most power lines have small losses, and for transmission involving only the lines themselves, the line distributed parameters can be considered nearly constant over a wide range of frequency. In such a case, the digital simulation techniques just mentioned, among others, may give results in close agreement with actual system response.

For transmission involving the earth, however, line resistance and inductance vary significantly with frequency, and therefore it follows that a lossless or distortionless model is not a satisfactory

representation of this type of propagation if extreme accuracy is required.

In such cases, Fourier transform (FT) techniques have been very effectively utilised. Fundamentally, the method requires the calculation of system response to be performed over a wide range of frequency and the inverse Fourier transform is used to obtain the response in the time domain. The theory of natural modes in multi-conductor power lines was formulated by Wedephol[12] and then effectively used in conjunction with the Fourier transform techniques for predicting the behaviour of such lines under energisation and de-energisation conditions[13]. Similar work has been done by Hedman[14] and a theory of modal analysis used in a frequency-domain program was presented. The study of transients due to switching operations[15] and the effects of frequency dependence of transmission line parameters have also been reported[16].

Again, it has to be emphasised that accurately simulating power system transients can serve two main purposes:

1 - To examine the effect of primary system wave forms on protective relays and the possibility of improving them if they prove inadequate.
2 - To predict system overvoltages according to which economical insulation levels are determined.

It has always been known that the main switching overvoltages are due to line energisation and de-energisation. In practice, however, it has been found possible to restrict these overvoltages to below 1.5pu,

especially in EHV systems. This reduction has been achieved by various control methods such as single or multiple pre-insertion resistors, opening resistors, synchronised circuit breaker pole closure etc.. When switching overvoltages are so reduced, overvoltages due to fault initiation may become the limiting factor. Because[17] 90% or more of the faults that occur in a practical system are single-line-to-ground faults, transient overvoltages of the order of 2 pu may be experienced by the sound phases and it follows that accurate simulation of system transients due to initiation of such faults, becomes of considerable importance. The problem of fault surges was brought into sharper focus when Kimbark[18] and Legate used the T.N.A. to study the phenomena on a single circuit line. In addition, they presented a lattice diagram approach for a theoretical study of the problem with certain approximations. Later, analogue computer studies of the problem have been made[19,22]. In their study, however, Clericic et al[22] have emphasised the importance of overvoltages due to fault initiation and fault clearing in determining system insulation level when switching overvoltages are controlled by using modern circuit breakers. They have given consideration to the sequence of events when a line-earth fault occurs, i.e. fault initiation, fault clearing, and reclosing operation. In such a case, the overvoltages generated on the sound phases of the same line can cause the fault to develop from a single-phase into a multi-phase or even can cause faults on other lines on the system. During fault clearing, the risks have been shown as the loss of another line in the network in addition to the faulted line. For the reclosing operation, the risk has been defined as the possibility of insulation failure of the

line being switched due to overvoltages. The authors have concluded emphasising the importance of choosing the best accurate simulation technique suitable for fault-surge predictions.

In the above reviewed studies, so far, lines were assumed to be ideally transposed, uncompensated, with frequency invarient parameters. Boonyubol et al[20], however, have made use of the laplace transform method to evaluate fault-transient overvoltages. Furthermore, a more accurate and realistic simulation of fault-surges on single and double-circuit uncompensated lines, using the modified Fourier transform technique has been presented[17,21].

The continuous increase in transmission voltages over long distances has emphasised the importance in EHV systems of the excessive line reactive power and the associated means to control them so that a reasonably constant voltage along the line can be maintained. Especially in the case of initial systems or long a.c. lines energised through relatively weak sources, the adoption of shunt reactors to compensate a portion of the line charging MVAR is an indispensable method for excessive voltage and reactive power control. Reactive VARs are both generated and absorbed throughout a power system. Lightly loaded lines or cables are net generators of VARs owing to their shunt capacitances, whereas, loads, transformers or heavily loaded lines and cables are major consumers of VARs through their series inductive reactances. Uncontrolled flow of VARs in a system can produce unacceptable voltage levels and the advantages of controlling VAR flow for increased transmission capability and utilisation of equipment has always been appreciated.

EHV reactors have been widely used for reactive power control on long transmission lines. Ferranti-effect is well known and shunt reactors are used to counteract this phenomena, especially at the far end of unloaded or lightly loaded lines[5,23-27].

Following load rejection, power frequency overvoltages that occur on long lines may be aggravated by low system short-circuit level, high excitation when transmitting full load and by the absence of loads along the line. The simultaneous occurrence of single-line-to-earth fault can increase the overvoltage still further[26]. Again, these overvoltages can be effectively counteracted by permanently connected EHV reactors. Results of a series of field tests compared to predictions obtained by T.N.A. and digital studies for EHV systems, have also shown the increasing effectiveness of EHV reactors in reducing switching surges[28-30]. The reason for surge-reduction is primarily the lower power frequency overvoltage at the far end of a line owing to the use of shunt reactors. The reactor at the far end of a line offers a finite impedance which tends to reduce the reflection coefficient, thus contributing to surge reduction. However, this effect has been reported to be very small. In addition, some researchers have found that in some cases, shunt reactors are effective in controlling transient component of switching overvoltages[31-33]. It is a normal practice to use both permanent reactors and switched reactors connected to the tertiaries of step-down transformers[34]. The former control the reactive power flow under normal operating conditions, while the latter are switched on to the system to compensate for the excessive capacitive currents in conditions such as lightly loaded or unloaded long lines.

An alternative way of doing this is to use non-linear reactors which provide less inductive compensation during normal operating conditions and still provide the required compensation during steady-state open-ended line conditions[5]. These reactors, among other reactor arrangements are dealt with in more detail in Chapter 2.

A transmission system comprising short lines, especially encountered in the U.K., is often very stiff at the generator ends (busbars) because there are a number of infeeding lines from other sources connected to the busbar. Because transmission is usually over short distances, both line reactance and capacitance are relatively small (in fact line capacitance can often be neglected) so that a generator can operate at a reasonably low load angle in order to push appropriate amounts of power over the line. This means that the problem of generator instability due to disturbances is reduced. Due to the stiffness of the busbar, even if a line goes out due to a fault, successful autoreclosure of the three circuit-breakers is accomplished without loss of stability or any serious disruption (also the presence of a second circuit helps to maintain stability).

On long lines, however, where sources of generation are often remotely located from the load (especially in case of hydro-power stations), the system at the generation end is very weak. In fact, in most cases, there are just one or two machines connected to the busbar and the feeder is of radial type. In such cases, the problem of maintaining stability becomes that much greater. Double circuit lines are not very economical to use because of the very long transmission distances involved. Thus, because there is only a single-circuit line, 3-phase

autoreclosure schemes are not very practical because in the majority of cases the closing of the breakers is not fast enough to maintain system transient stability. Due to the fact that the majority of faults on EHV a.c. systems are single-line-to-earth faults (mainly due to lightning) and of transitory nature, single-pole autoreclosure was found to greatly improve system transient stability[35-47] provided that such faults could be successfully cleared.

However, opening the circuit breakers on the ends of the faulted line conductor does not assume fault clearing. The isolated conductor is still capacitively and inductively coupled to the other healthy conductors which are still energised at normal voltage and carry a load current. This coupling has two main effects[36,37]:

1 - Before fault arc extinction, it feeds current to the fault and maintains the arc.
2 - After the fault current becomes zero (as it does twice/cycle), the coupling causes a recovery voltage across the arc path.

Extinction of the secondary arc depends on many factors, the most important of which are[36,37]:

a - Magnitude of the secondary arc current.
b - The magnitude of and the rate of rise of steady-state recovery voltage.

On long lines, however, because of the high system voltage and the high capacitive coupling (which is considered to be the most important)[37],

both secondary arc current and recovery voltage are that much higher so that some means of neutralising the capacitive coupling has to be employed.

Knudson[36] and Kimbark[37] have developed a method to help secondary arc extinction by using a 4-legged reactor scheme. Economically the scheme is highly justified since EHV reactors have to be used for reactive power control and the cost of the additional neutral-reactor required for secondary arc suppression is a small fraction of the cost of the main reactors.

The introduction of the 4-reactor scheme has paved the way for many researchers for further investigations[35,38-44] and is used by the author throughout the present investigation.

Neutralisation of capacitive coupling has been suggested by the addition of a capacitor, connected across the terminals of each breaker pole, proportional to the particular line being switched[39]. Field tests and hybrid computer programs using lumped parameter, 500 kV line model, have been performed to simulate single-pole switching and to evaluate the dead time required for arc extinction[48].

Relating both the residual arc current and the steady-state recovery voltage to the positive and zero degrees of shunt compensation (h_1, h_0), Kimbark[49] has produced very useful sets of families of curves that can be suited to any line construction. Residual arc current, steady-state recovery voltage and natural frequency of transient recovery voltage

have been considered and the loci of each of them has been plotted in a rectangular coordinates h_0 versus h_1. The charts help the researcher to know the correct degree of shunt compensation (h_0) that corresponds to the desired degree of compensation (h_1) for corresponding values of secondary arc current and steady-state recovery voltage.

Kimbark has extended his work by developing the reactor arrangement necessary to neutralise capacitive coupling in a double-circuit line[50]. Furthermore, he has considered the elimination of the effect of inductive coupling which was neglected in his previous analysis[37].

Recently, some papers concerning the use of shunt reactors for the purpose of secondary arc extinction have been presented. The first, based on earlier concepts developed by Knudson[36] and Kimbark[37], examines the influence of single-phase switching on long EHV lines and system design[51]. The authors examine the effect of various factors such as the ohmic value of the neutral reactor, pre-fault loading, source reactance, fault location and line transposition, on the secondary arc using mainly the T.N.A.. It has been shown that leaving inductive coupling uncompensated can generate a substantial voltage on the isolated phase which sufficiently contributes to secondary arc current and transient and sustained overvoltages.

The second paper, also based on the same concepts[36,37], has presented a modified 4-reactor scheme for secondary arc suppression[52].

Simply, the scheme provides four switches, two between the outer phase reactors and the neutral and two between the same reactors and the ground. When a single-line-to-ground fault occurs on one of the line conductors, two of these switches are closed yielding a different 4-reactor arrangement. The authors used a simple computer program, in which the line is represented by a number of cascaded π-sections, to compute secondary arc current and both steady-state and transient recovery voltages for different 4-reactor arrangements.

As mentioned previously, when EHV long lines are subjected to internal or external disturbances (such as switching operations, lightning surges and faults) abnormal voltages and currents of different frequencies are produced. It is not of course directly possible to prevent the occurrence of these disturbances, but their subsequent effects can be limited with proper system design and adequate protective devices. For a design engineer to achieve this, a realistic and accurate knowledge of the transient behaviour of the system under consideration is therefore essential.

Faults on modern EHV transmission systems have to be cleared as soon as possible to avoid excessive damage. Furthermore, fast fault clearance is essential to maintain system stability, to prevent any possible hazard to people and to prevent the escalation of single-line-to-ground faults to multi-phase-to-ground faults. For these reasons many studies currently focus on very high speed distance protection utilising minicomputers or microprocessors operated on the on-line mode. Extensive

work in this field, however, does not give a clear indication of the true viability of many digital protective schemes from a practical point of view[53]. From a measurement point of view, the nature of the problem is completely different when making the transition from the conventional protective schemes to those in which measurements are to be made from signals derived from a power system during a relatively short period of time following fault inception. With many conventional relays, the very noisy period following a fault is effectively ignored, and measurements commence after a delay without any loss of accuracy[53,54]. Here it is unnecessary to have a very precise knowledge of the response derived from faulted systems and a simulation based on lumped line parameters will often yield an adequate indication of performance in power systems.

However, the same is not true when very high speed measurements are considered because the waveforms from which measurements must be made can include very significant travelling wave components in both faulted and healthy phases. The design, testing and development of protective schemes therefore requires the knowledge of the precise nature of primary system wave forms immediately derived after fault initiation.

Precise primary system response is very difficult to achieve by field tests or analogue techniques and hence the recent trend is to use modern digital techniques.

On this respect, Benarjee[56] has digitally simulated power system transients due to both shunt and series faults on uncompensated 3-phase transmission line using the fast Fourier transform technique.

Digital simulation of EHV short power lines under unbalanced fault conditions for protection purposes has also been presented by Johns and Aggarwal[54,57]. Methods have also been developed to give a more accurate model of synchronous sources to be combined with generator/transformer and distributed-frequency variant transmission line interconnection[58].

1.2 Outline of the Present Investigation

In this thesis frequency-domain methods of fault-transient analysis for shunt-compensated systems, using 4-reactor schemes, are developed. The methods are suitable for studying practical shunt-compensated systems subjected to single-line-to-ground, 2 line-to-ground and line-to-line faults.

The main objectives behind the present work are:-

1 - To develop mathematical and digital modelling techniques suitable for simulating practical 4-reactor shunt compensated systems.
2 - To develop mathematical and digital techniques suitable for modelling shunt reactor saturation.

In this respect, it has to be emphasised that saturation of the neutral reactor is particularly critical. This is due to the fact that due to saturation, neutral reactance is effectively reduced and its tuning with line capacitance is no longer maintained. Therefore it follows that due to saturation, secondary arc suppression becomes more difficult.

3 - To use these techniques in the study of:

a - The effects of shunt compensation on primary system wave forms.

b - Fault induced system and reactor overvoltages.

Again, neutral-reactor overvoltages are particularly important. If, due to severe overvoltages, the surge diverter protecting it is short-circuited, the neutral reactor is effectively eliminated. Hence single-pole autoreclosure may not be successful.

c - The effects of reactor saturation on primary system wave forms.

4 - To use the techniques to study the performance of modern high speed distance protective relays.

The methods developed to incorporate 4-reactor schemes into simple single-section feeder systems are presented in Chapter 2. In the same chapter, a brief review of shunt compensation schemes is presented.

In Chapter 3, simulation techniques for studying practical multi-section feeder systems are developed. Also the analysis of the main source network models and the transposition scheme developed by the author are described.

The techniques developed to simulate reactor saturation in a frequency-domain program are presented in Chapter 4.

In Chapter 5, the configuration of systems studied is detailed. This covers line construction, line parameters, source parameters, line charts and the 4-reactor scheme parameters.

Digital computer results are presented in Chapters 6-9. In Chapter 6 digital examination of the difference of primary system responses for both compensated and uncompensated (single and multi-section feeder) systems is presented.

The problem of system and reactor overvoltages is studied in Chapter 7. Findings in relation to reactor saturation and its likely effects on system response are presented in Chapter 8. In Chapter 9, digital studies of the performance of cross-polarised mho-relay applied to compensated and uncompensated (single and 3-section feeder) systems is prescribed.

General conclusions and suggestions for future work are presented in Chapter 10.

CHAPTER 2 DEVELOPMENT OF METHODS TO SIMULATE SHUNT COMPENSATED SINGLE-SECTION FEEDER SYSTEMS

2.1 Introduction

For the purpose of reactive power compensation in EHV long transmission systems, one or two banks of Y-connected shunt reactors with solidly earthed neutral are commonly employed. The size of the reactors is expressed in terms of their MVAR at rated voltage, their per-phase reactance, or their degree of shunt compensation[50].

In single-circuit transmission lines, however, where single-pole autoreclosure is desirable, shunt reactors have been used to serve a second purpose, i.e. the suppression of secondary arc. Neutralisation of shunt capacitive coupling between phases makes single-pole switching feasible on longer lines[50]. By proper connection of EHV reactors used to wholly or partially compensate the normal line charging current, these reactors can be made to serve the additional purpose of ground fault suppression at a moderate additional cost[36,37].

A brief review of the existing shunt compensation schemes is presented in section 2.2. Possible reactor arrangements to serve the above mentioned purposes are examined in section 2.3.1.

The 4-legged reactor scheme is dealt with in more detail and its parameters, i.e. the phase reactance, the neutral reactance and each reactor rating are evaluated in section 2.3.2.

Developed mathematical techniques to incorporate the 4-reactor scheme under steady-state and transient-fault conditions are presented in section 2.4.

2.2 Review of The Existing Shunt Compensation Schemes

Beside forming a vital link between remote generating units and load centres, EHV lines have the advantages of large load capacity, reduced transmission losses (better efficiency) and better voltage regulation. There are two main problems, however, in transmitting large amounts of power over long a.c. lines; system instability and overvoltages.

The problem of overvoltages becomes particularly evident at EHV and UHV levels[59,60] due to the fact that capacitive charging MVARs of lines and cables is approximately proportional to the square of system voltage and directly proportional to line length. Capacitive current of EHV systems is mainly compensated for a number of reasons[5,24,30-31, 33, 61, 62, 77, 79]:

1 - To improve stability of transmission.
2 - To reduce power frequency and transient system overvoltages.
3 - To prevent self excitation of generators when connecting open-circuited lines.

A variety of shunt-reactor schemes exist which may be classified as follows:

a - Linear reactors[63,77].

b - Externally controlled reactors[62,66,67].

c - Self-saturated reactors[64,65,68,69,73-75,76].

Each of the above schemes has its own particular characteristics and none of them is usually a 'best buy' for a specific problem on technical grounds alone. EHV reactors are connected to systems either directly or via the secondary or the tertiary windings of intermediate transformers. Although EHV reactors may be either 3-phase or single-phase units, so far only single-phase units have been used at 500 kV level and above[62].

In case of very long lines, the above mentioned schemes may be used in conjunction with series capacitance. The former compensates for part of line capacitance while the latter compensates for part of its series reactance. In such a case, total reactive and capacitive power compensation has to be avoided for stability considerations[63]. A 60% inductance and capacitance compensation may be the best compromise although under light load conditions 100% shunt compensation is required.

Externally controlled reactors may include:[62,66-68,69]

1 - D.C. controlled reactors (transductors).

2 - Thyristor-controlled shunt reactors[67].

The first transductor introduced on the British grid system was in 1967[66] and comprised a 30 MVAR transductor and three 20 MVAR capacitor banks. The device enabled reactive power variation from 30 MVAR

lagging to 60 MVAR leading, since the transductor reactive power was continuously variable and capacitor banks were switched in and out automatically as required. A major advantage is, due to its static nature, transductors cannot lose synchronism with the system even under fault conditions. They can maintain a good average level of voltage but not suitable to deal with fast fluctuating loads due to their relatively slow response. Another disadvantage of transductors is, as with any saturable reactor, the generation of harmonics. Thyristor-controlled reactors can also achieve a continuous, relatively fast (0.01 s)[68] control of reactive power generation on a large scale. Such schemes are particularly applicable for suppression of voltage fluctuations caused by severe loads and are commercially associated with ASEA[67].

Harmonic generation in system voltage is possible (in the event of incorrect point-on-wave switching relative to system fundamental) and therefore their compensation is required.

Self-saturated reactors were developed by the late E. Friedlander[70], first for suppressing voltage fluctuations due to disturbing loads (arc furnaces in particular) and then for reactive power control on EHV transmission systems.

In these reactors, lower order harmonic currents are internally eliminated so that only harmonics of the order $4n \pm 1$ can appear under steady-state conditions (n = number of limbs). Ideal reactive power control is achieved by using the reactor together with a series slope correcting capacitance[70,71] and a parallel capacitor (to provide the leading VAR range).

Static compensators are commercially associated with the G.E.C. and may use one of the following saturable reactors:

1 - The Quin reactor[64,70,72].
2 - The Twin-Tripler reactor[64,65,70,73].
3 - The Treble-Tripler reactor[64,65,73,74].

A detailed study of the twin and treble-tripler arrangements is presented in references (68) and (75) respectively.

2.3 Choice of Shunt Reactors For Secondary Arc Suppression

2.3.1 Possible reactor arrangements

Secondary arcs are maintained by two types of coupling, namely, the shunt capacitive coupling and the longitudinal coupling from mutual inductance and resistance, between the disconnected, faulted conductor and the energised, unfaulted conductors. In his analysis, Kimbark[37,50] however, assumes that capacitive coupling is more important and has neglected the longitudinal coupling. According to such assumption, possible reactor schemes used for reactive power compensation and ground fault suppression are given in Fig. 2.1. Before comparing these arrangements, it is useful if the shunt capacitances of the line are considered. Their equivalent circuits are shown in Fig.2.2. The interphase capacitances of Fig.2.2a are designated $(Bc_1-Bc_0)/3$ while the capacitances between each phase and ground is Bc_0. These values can be evaluated as follows:

Replacing $(Bc_1 - Bc_0)/3$ and Bc_0 respectively by B_{ch} and B_{cg}, to get the PPS impedance 'Xc_1' of Fig. 2.2a , apply a set of PPS voltages to the 3-phases. The current at point 'a' is given by:

$$Ia_1 = I_1 + I_2 + I_3$$

$$= (Va_1 - Vc_1)/X_{ch} + (Va_1 - Vb_1)/X_{ch} + Va_1/X_{cg}$$

where $X_{cg} = \frac{1}{B_{cg}}$, $Xch = \frac{1}{B_{ch}}$

$$\therefore \quad Ia_1 = Va_1\left(\frac{1}{X_{cg}} + \frac{1 - h + 1 - h^2}{X_{ch}}\right)$$

$$Ia_1 = Va_1\left(\frac{1}{X_{cg}} + \frac{3}{X_{ch}}\right)$$

or $$Xc_1 = 1/(1/X_{cg} + 3/X_{ch})$$

or $$Xc_1 = \frac{X_{cg} \cdot X_{ch}}{X_{ch} + 3X_{cg}} \qquad \ldots\ldots 2.1$$

From equation 2.1 the PPS susceptance can be obtained as :

$$Bc_1 = \frac{1}{Xc_1} = B_{cg} + 3B_{ch} \qquad \ldots\ldots 2.2$$

In a similar way, the ZPS impedance and susceptance of Fig. 2.2a can be obtained by applying a set of ZPS voltages to the 3-phases.

$$Xc_0 = X_{cg}$$
$$Bc_0 = B_{cg} \qquad \ldots\ldots 2.3$$

From equations 2.1 - 2.3 it follows that;

$$Bc_1 = Bc_0 + 3B_{ch}$$

$$\therefore \quad B_{ch} = 1/3\ (Bc_1 - Bc_0) \qquad \ldots\ldots 2.4$$

$$\text{and} \quad B_{cg} = Bc_0$$

Equation 2.4 proves the correctness of the susceptances shown in Fig. 2.2a.

The most common equivalent circuit of Fig. 2.2a can always be replaced by Fig. 2.2b, by transforming the Δ-connected capacitances (B_{ch}) into their Y equivalent.

The PPS and the ZPS impedances of Fig. 2.2c are Z_1 and Z_0,

$$Z_1 = Xc_1$$

$$Z_0 = Xc_1 + 3Xcn \qquad \ldots\ldots 2.5$$

From which the neutral reactance and susceptance are:

$$X_{cn} = 1/3\ (Z_0 - Z_1)$$

$$\text{and} \quad B_{cn} = \frac{3\ Z_0\ Z_1}{Z_1 - Z_0} \qquad \ldots\ldots 2.6$$

Now it is obvious that the shunt reactor schemes of Fig. 2.1, a-c are analogous to the equivalent capacitance circuits of Fig. 2.2 a-c respectively. Figs. 2.1c and 2.1d are similar and the analysis

applied to one of them, applies to the other. For the schemes of Figs. 2.1a, b and d(1), the total MVAR rating of the group of shunt reactors is the same, equals that required for shunt compensation under normal conditions. For the 4-reactor scheme, the phase reactors have the same total rating as that of Fig. 2.1a, b, d(1). The neutral reactor carries no current under steady-state conditions. It is energised only during a line-to-ground fault and its rating is only a small fraction of the three main reactor ratings.[36,37] According to Kimbark[37] and Knudson[36], from economical and technical viewpoints, schemes of Figs. 2.1c, d, are the most economical. Since the scheme of Fig. 2.1c is the one simulated throughout this work, it will now be considered in detail.

2.3.2 The 4-legged reactor parameters

2.3.2.1 Reactor phase and neutral reactances

Referring to Fig. 2.1c, the PPS and ZPS impedances are calculated as mentioned previously by applying respectively a set of PPS and ZPS voltages to the 3-phases. Therefore, it follows that:

For Fig. 2.1c

$$\begin{aligned} X_1 &= XP \\ X_0 &= XP + 3Xn \end{aligned} \qquad \ldots\ldots 2.7$$

Similarly for Fig. 2.1a

$$\begin{aligned} X_1 &= X_{\ell g}\ X_{\ell h}/X_{\ell h} + 3X_{\ell g} \\ X_0 &= X_{\ell g} \end{aligned} \qquad \ldots\ldots 2.8$$

For the two circuits of Fig (2.1.a) and (2.1.c) to be equal, the corresponding quantities of equations 2-7 and 2-8 should be equal, i.e $X_1 + 3X_n = X_{\ell g}$ 2.9.a

and $X_1 = (X_{\ell g} \cdot X_{\ell h})/(X_{\ell h} + 3X_{\ell g})$ 2.9.b

Now, for reactive power compensation,

$$BL_1 = h_1 \cdot Bc_1 \qquad .....2.10$$

and for total elimination of interphase capacitive coupling;

$$BL_0 = h_0 \cdot Bc_0 \qquad ....2.11$$

using equations 2.9 - 2.11, it is shown in Appendix (A1.2) that the phase and neutral reactances of the 4-reactor scheme are given by;

$$X_n = \frac{h_1 Bc_1 - h_0 Bc_0}{3 . h_1 Bc_1 . h_0 Bc_0} \quad ...a \qquad ..... 2.12$$

$$X_p = \frac{1}{h_1 Bc_1} \quad ... b$$

Therefore equation 2.12 gives the phase and neutral reactances of the 4-legged reactor scheme of Fig. (2.1.c) in terms of the line 'PPS' and 'ZPS' susceptances Bc_1 and Bc_0 respectively and the 'PPS' and 'ZPS' degrees of shunt compensation (h_1) and (h_0). It has to be emphasized here that the neutral reactance of the 4-legged reactor scheme derived in Appendix A1 (equation A1·23) is only true if $B_{\ell h} = B_{ch}$ or if:

$$h_0 = 1 + \frac{Bc_1}{Bc_0} (h_1 - 1) \qquad .....2.13$$

However equation (2.12.a) is a more general form which has been used throughout the present work. The shunt capacitances of a transmission line are usually described as shown above by the equivalent circuits of Fig (2.2) and in particular by the more common circuit of Fig (2.2.a). An alternative way is to describe line capacitances by its shunt admittance matrix given

by equation (5.2). For a balanced line (as the transposed line simulated here), there are only two different values of capacitances (or admittances). As clearly seen from equation 5.2 the elements in the main diagonal have one value and the off-diagonal elements have another value.

Therefore, it now remains to relate the line admittance matrix (equation 5.2) to the line capacitances mesh circuit of Fig (2.2.a).

Calling the diagonal terms of a balanced line shunt admittance matrix 'Y_s' and the off-diagonal terms 'Y_m', it can be proved by applying a set of balanced voltages and currents to the circuit of Fig (2.2.a) that:

$$Y_s = Y_{cg} + 2Y_{ch}$$
$$Y_m = -Y_{ch} \qquad \text{.....2.14}$$

From which

$$Y_{cg} = Y_s + 2Y_m$$
$$Y_{ch} = -Y_m \qquad \text{.....2.15}$$

Therefore, in a digital computer program, Y_{cg} and Y_{ch} are calculated from the line shunt admittance matrix, the 'PPS ' and the 'ZPS ' susceptances Bc_1 and Bc_0 are evaluated from equations 2.2 and 2.3 respectively, and then equations 2.12 are used with the desired degrees of shunt compensation (h_1, h_0) to determine the phase and neutral reactances of the 4-reactor scheme.

A quality factor 'Q ' has to be chosen for both phase and neutral reactor banks.

2.3.2.2 Reactor Rating

From the basic line parameters evaluated in Appendix A1.1, Y_s

and Y_m can be used to solve equation 2.15 and hence Bc_1 and Bc_0 can be known from equations 2.2 and 2.3.

Assuming that two 4-reactor schemes are to be used for reactive power compensation over the whole line length, one at each end, the MVAR rating of each reactor is:

$$Q_{SR} = V^2/X_1$$

or $$Q_{SR} = V^2 . h_1 Bc_1 . \ell/2 \qquad .....2.16$$

Totally compensating line charging current, equation 2.16 becomes;

$$Q_{SR} = V^2 . Bc_1 . \ell/2 \qquad .....2.17$$

2.4 Mathematical Treatment of 4-reactor Compensated Systems

In this section, methods suitable for simulating 4-reactor shunt compensated single-feeder systems under steady-state and fault-transient conditions are developed. The system examined comprises a single-circuit, 3-phase, 500 kV transmission line of the horizontal construction detailed in Chapter (5) (together with other line data). The method of calculating the basic parameters of multi-conductor lines, i.e. the (Z) and (Y) matrics, has been developed for the purpose of digital simulation by Galloway etal[55]. It takes into account conductor geometry, conductor self parameters and earth return path. An outline of the method is presented in Appendix (A1.1).

The line model is fed from both ends from main source models which are described in Chapter (3). Two 4-legged reactor schemes are required, one situated at each line end. Each

scheme compensates for half of the positive phase sequence charging current of the line. Methods of evaluating reactor parameters were described in section (3) of this Chapter and the parameters that have been used throughout this analysis are presented in Chapter (5).

The analysis developed in this section is based on the theory of natural modes as developed by Wedephol[12,13] for application to multi-conductor lines. A description of the theory is presented in Appendix (A2).

At power frequency, line parameters are calculated by considering each mode of propagation, the multi-port equations representing each element in the system are formulated and voltages and currents at points of interest are then evaluated.

Fault transient analysis is based on the same theory. Line parameters are calculated, and by considering each mode of propagation at any given frequency, the multi-port equations describing the part of the system before and beyond the fault point are formulated. These equations are then combined with the source-side network equations to yield a final two 2-port equations and the fault is simulated[53,54,56] by a suddenly applied voltage of appropriate magnitude and polarity.

The frequency spectrum of voltages and currents of interest is converted to time domain using the inverse Fourier transform[88-91], and the overall system response is the sum of the prefault (steady-state) response plus the response due to fault. This is achieved by applying the principle of superposition.

2.4.1 Steady-state Analysis

Under steady-state conditions, the system is represented by the 3-wire diagram and its block equivalent of Fig (2.3).

From the Fig. we have:

$$\begin{bmatrix} \bar{V}_S \\ \bar{I}_S \end{bmatrix} = \begin{bmatrix} SR_1 \end{bmatrix} \begin{bmatrix} \bar{V}_{S1} \\ \bar{I}_{S1} \end{bmatrix} \qquad \text{.....2.18}$$

Where:

$\bar{V}_S$, $\bar{I}_S$, $\bar{Y}_S$, $\bar{I}_S$, are the transforms of the respective voltages and currents shown in Fig (2.3).

SR_1 = The two port matrix representing the near-sending end shunt reactor. It is evaluated as follows:

From Fig (2.3.a) we have

$$\bar{V}_{Sa} = \bar{I}_{a1} \cdot Z_1 + (\bar{I}_{a1} + \bar{I}_{b1} + \bar{I}_{c1})\, Zn$$

V_{Sb} and V_{Sc} are calculated in a similar way so that:

$$\begin{bmatrix} \bar{V}_{Sa} \\ \bar{V}_{Sb} \\ \bar{V}_{Sc} \end{bmatrix} = \begin{bmatrix} \bar{V}_{Sa1} \\ \bar{V}_{Sb1} \\ \bar{V}_{Sc1} \end{bmatrix} = \begin{bmatrix} Z_1+Z_n & Z_n & Z_n \\ Z_n & Z_1+Z_n & Z_n \\ Z_n & Z_n & Z_1+Z_n \end{bmatrix} \begin{bmatrix} \bar{I}_{a1} \\ \bar{I}_{b1} \\ \bar{I}_{c1} \end{bmatrix} \qquad \text{...2.19}$$

or $$\begin{bmatrix} \bar{V}_S \end{bmatrix} = \begin{bmatrix} \bar{V}_{S1} \end{bmatrix} = \begin{bmatrix} Z_{SR} \end{bmatrix} \begin{bmatrix} \bar{I}_1 \end{bmatrix} \qquad \text{...2.19}$$

Where Z_1 and Z_n are

$$Z_1 = R_1 + J\, X_1$$

$$Z_n = R_n + J\, X_n$$

X_1 and X_n have been evaluated in section (3) and a quality factor of 250 has been used to get both Z_1 and Z_n. From equation 2.19 the currents through the phase reactors are:

$$\bar{I}_1 = \begin{bmatrix} Z_{SR1} \end{bmatrix}^{-1} \begin{bmatrix} \bar{V}_S \end{bmatrix} = \begin{bmatrix} Z_{SR1} \end{bmatrix}^{-1} \begin{bmatrix} \bar{V}_{S1} \end{bmatrix}$$

and if $Y_{SR1} = \begin{bmatrix} Z_{SR1} \end{bmatrix}^{-1}$

$$\bar{I}_1 = \begin{bmatrix} Y_{SR1} \end{bmatrix} \begin{bmatrix} \bar{V}_S \end{bmatrix} = \begin{bmatrix} Y_{SR1} \end{bmatrix} \begin{bmatrix} \bar{V}_{S1} \end{bmatrix}$$

but $$\begin{bmatrix} \bar{I}_S \end{bmatrix} = \begin{bmatrix} \bar{I}_1 \end{bmatrix} + \begin{bmatrix} \bar{I}_{S1} \end{bmatrix}$$

substituting $\bar{I}_1$ in the above equation

$\therefore \quad (\bar{I}_S) = (\bar{Y}_{SR1}) \quad (\bar{V}_S) + \bar{I}_{S1}$

$\therefore$ voltage and current transforms input to the sending-end reactor are related to the corresponding output quantities by:

$$\begin{bmatrix} \bar{V}_S \\ \bar{I}_S \end{bmatrix} = \left[\begin{array}{c|c} U & O \\ \hline Y_{SR1} & U \end{array}\right] \begin{bmatrix} \bar{V}_{S1} \\ \bar{I}_{S1} \end{bmatrix} \qquad \ldots.2.21.a$$

Y_{SR1} = sending-end reactor admittance matrix

$= (Z_{SR1})^{-1}$

Also from Fig (2.3)

$$\begin{bmatrix} \bar{V}_{S1} \\ \bar{I}_{S1} \end{bmatrix} = \begin{bmatrix} A & B \\ C & D \end{bmatrix} \begin{bmatrix} \bar{V}_{R1} \\ \bar{I}_{R1} \end{bmatrix}$$

and

$$\begin{bmatrix} \bar{V}_{R1} \\ \bar{I}_{R1} \end{bmatrix} = \begin{bmatrix} U & O \\ Y_{SR2} & U \end{bmatrix} \begin{bmatrix} \bar{V}_R \\ \bar{I}_R \end{bmatrix}$$

where

A,B,C,D = transmission line constants,[54] as described in Appendix (A2).

(Y_{SR2}) = receiving-end shunt reactor admittance matrix

$= (Z_{SR2})^{-1}$

Since each reactor compensates for half of line charging current

$\therefore \qquad (Z_{SR1}) = (Z_{SR2})$

$(Y_{SR1}) = (Y_{SR2})$

It follows that equation 2.21.a becomes

$$\left[\begin{array}{c} \bar{V}_S \\ \hline \bar{I}_S \end{array}\right] = \left[\begin{array}{c|c} U & O \\ \hline Y_{SR1} & U \end{array}\right] \left[\begin{array}{c|c} A & B \\ \hline C & D \end{array}\right] \left[\begin{array}{c|c} U & O \\ \hline Y_{SR2} & U \end{array}\right] \left[\begin{array}{c} \bar{V}_R \\ \hline \bar{I}_R \end{array}\right]$$

or $$\left[\begin{array}{c} \bar{V}_S \\ \hline \bar{I}_S \end{array}\right] \left[\begin{array}{c|c} A_T & B_T \\ \hline C_T & D_T \end{array}\right] \left[\begin{array}{c} \bar{V}_R \\ \hline \bar{I}_R \end{array}\right] \qquad \ldots.2.21.b$$

where

$$\left[\begin{array}{c|c} A_T & B_T \\ \hline C_T & D_T \end{array}\right] = \left[\begin{array}{c|c} U & O \\ \hline Y_{SR1} & U \end{array}\right] \left[\begin{array}{c|c} A & B \\ \hline C & D \end{array}\right] \left[\begin{array}{c|c} U & O \\ \hline Y_{SR2} & U \end{array}\right] \qquad \ldots.2.21.c$$

The procedure followed to derive equation 2.21 above, assumes that the line is homogeneous. However, due to transposition, this is not the case but each transposed section is dealt with separately as a homogeneous section and then the multi-port equations for the 3-transposition sections are combined to yield a single two-port equation for the whole line.

Under steady-state conditions, three quantities are required, namely, sending end current, receiving end current and the voltage at the point of fault (f) before the fault occurs. These three quantities are obtained from equation 2.21.b (by adding the letter 'S' to the subscript of each variable to distinguish them from fault quantities).

$$\bar{I}_{SS} = C_T.\bar{V}_{RS} + D_T\bar{I}_{RS}$$
$$\bar{V}_{SS} = A_T.\bar{V}_{RS} + B_T.\bar{I}_{RS}$$

and it follows that:

$$\bar{I}_{SS} = (C_T - D_T.B_T^{-1}.A_T)\bar{V}_{RS} + D_TB_T^{-1}.\bar{V}_{SS}$$
$$\bar{I}_{RS} = B_T^{-1}\,\bar{V}_{SS} - B_T^{-1}\,A_T\,.\,\bar{V}_{RS} \qquad .....2.22.a$$

Assuming that the fault will occur at a distance 'X' from the sending end, the line constant matrix given by equation 2.21.c can be split into two matrices. These matrices correspond to line lengths (X) and (ℓ- X) respectively so that:

$$\left[\begin{array}{c|c} A & B \\ \hline C & D \end{array}\right] = \left[\begin{array}{c|c} A_1 & B_1 \\ \hline C_1 & D_1 \end{array}\right] \left[\begin{array}{c|c} A_2 & B_2 \\ \hline C_2 & D_2 \end{array}\right]$$

steady state voltages and currents at the point of fault are related to voltages and currents at the receiving-end as follows:

$$\left[\begin{array}{c} \bar{V}_{fS} \\ \hline \bar{I}_{fS} \end{array}\right] = \left[\begin{array}{c|c} A_{T2} & B_{T2} \\ \hline C_{T2} & D_{T2} \end{array}\right] \left[\begin{array}{c} \bar{V}_{RS} \\ \hline \bar{I}_{RS} \end{array}\right]$$

Using the above equation in conjunction with equation 2.22.a, we get:

$$\bar{V}_{fS} = (A_{T2} - B_{T2}.B_T^{-1}.A_T)\bar{V}_{RS} + B_{T2}B_T^{-1}\,\bar{V}_{SS} \quad .....2.22.b$$

where

$\bar{V}_{fS}$ = steady-state voltage transform at the point of fault before the fault occurs.

and

$$\left[\begin{array}{c|c} A_{T2} & B_{T2} \\ \hline C_{T2} & D_{T2} \end{array}\right] = \left[\begin{array}{c|c} A_2 & B_2 \\ \hline C_2 & D_2 \end{array}\right] \left[\begin{array}{c|c} U & 0 \\ \hline y_{SR2} & U \end{array}\right] \quad .....2.22.c$$

In actual fact the steady state quantities $\bar{I}_{SS}$, $\bar{I}_{RS}$ and $\bar{V}_{fS}$ may be considered in phasor form and converted directly to the time domain without the need to go through the inverse fourier transform.

2.4.2 Fault-Transient Analysis

Fig (2.4) shows the faulted compensated system in which the fault is simulated by a suddenly applied voltage source at the point of fault. It has been shown in reference (54), that this voltage source is equal in magnitude and opposite in polarity to the prefault voltage of the faulted phase, at the point of fault.

Methods of simulating unsymmetrical shunt faults, i.e. single-phase-earth, phase-to-phase, and double-phase-to-earth faults are dealt with in detail in Appendix (A3).

From Fig. (2.4) two main equations exist:

$$\left[\begin{array}{c} \bar{E}_{ff} \\ \hline -\bar{I}_{fSf} \end{array}\right] = \left[\begin{array}{c|c} A_{T1} & B_{T1} \\ \hline C_{T1} & D_{T1} \end{array}\right] \left[\begin{array}{c} \bar{V}_{Sf} \\ \hline -I_{Sf} \end{array}\right] \quad .....2.23.a$$

and

$$\left[\begin{array}{c} \bar{E}_{ff} \\ \bar{I}_{fRf} \end{array}\right] = \left[\begin{array}{c|c} A_{T2} & B_{T2} \\ \hline C_{T2} & D_{T2} \end{array}\right] \left[\begin{array}{c} \bar{V}_{Rf} \\ \hline \bar{I}_{Rf} \end{array}\right] \quad .....2.23.b$$

where, $\bar{E}_{ff}$, $\bar{I}_{fSf}$, $\bar{V}_{Sf}$, $\bar{I}_{Sf}$, $\bar{V}_{Rf}$, and $\bar{I}_{Rf}$ are the transforms of the respective voltages and currents shown in Fig (2.4).

$$\begin{bmatrix} A_{T1} & B_{T1} \\ C_{T1} & D_{T1} \end{bmatrix} = \begin{bmatrix} A_1 & B_1 \\ C_1 & B_1 \end{bmatrix} \begin{bmatrix} U & O \\ Y_{SR1} & U \end{bmatrix} \quad \ldots\ldots$$

2.23.c

$$\begin{bmatrix} A_{T2} & B_{T2} \\ C_{T2} & D_{T2} \end{bmatrix} = \begin{bmatrix} A_2 & B_2 \\ C_2 & D_2 \end{bmatrix} \begin{bmatrix} U & O \\ Y_{SR2} & U \end{bmatrix} \quad \ldots\ldots$$

The before-fault matrices A_1, B_1, C_1, D_1, and the beyond-fault po int matrices A_2, B_2, C_2, D_2, are evaluated by substituting 'X' and $(\ell - x)$ respectively; instead of 'ℓ' in equation A2.37.

Line transposition is taken into account by using the matrices described in Chapter (3).

Applying the superposition principle, $\bar{V}_{ff}$ is the only voltage source in the circuit of Fig (2.4).

$$\therefore \quad \begin{aligned} \bar{V}_{Sf} &= -(Z_{SS})\ \bar{I}_{Sf} \\ \bar{V}_{Rf} &= (Z_{RS})\ \bar{I}_{Rf} \end{aligned} \qquad \ldots\ldots 2.23.d$$

where Z_{SS} and Z_{RS} are the sending-and receiving-ends source impedance matrices respectively.

From equation 2.23.b, we have:

$$\bar{E}_{ff} = A_{T2}.\bar{V}_{Rf} + B_{T2}\ \bar{I}_{Rf}$$

substituting the value of $\bar{I}_{Rf} = Z_{RS}^{-1}.V_{Rf}$ from equation 2.23.d

$$\therefore \quad \bar{E}_{ff} = (A_{T2} + B_{T2}.Z_{RS}^{-1})\ \bar{V}_{Rf} \qquad \ldots\ldots 2.24.a$$

similarly from 2.23.b

$$\bar{I}_{fRf} = C_{T2}.\bar{V}_{Rf} + D_{T2}.\bar{I}_{Rf}$$

substituting for $\bar{I}_{Rf}$ from equation 2.23.d

$$\therefore \quad \bar{I}_{fRf} = (C_{T2} + D_{T2}.Z_{RS}^{-1})\ \bar{V}_{Rf} \qquad \ldots\ldots 2.24.b$$

From equation 2.24.a

$$\bar{V}_{Rf} = (A_{T2} + B_{T2}.Z_{RS}^{-1})^{-1}\bar{E}_{ff} \quad \text{, substituting in 2.24.b}$$

$$\therefore \quad \bar{I}_{fRf} = (C_{T2} + D_{T2}.Z_{RS}^{-1})(A_{T2} + B_{T2}.Z_{RS}^{-1})^{-1}.\bar{E}_{ff} \quad .....2.25.a$$

similarly; if the same proceedure is followed using equations 2.23.a,d, we get:

$$\bar{I}_{fSf} = -(C_{T1} + D_{T1}\, Z_{SS}^{-1})(A_{T1} + B_{T1}.Z_{SS}^{-1})^{-1}.\bar{E}_{ff} \quad ...2.25.b$$

subtracting 2.25.a from 2.25.b we get:

$$(\bar{I}_{fSf} - \bar{I}_{fRf}) = -\left[(C_{T1} + D_{T1}\, Z_{SS}^{-1})(A_{T1} + B_{T1}\, Z_{SS}^{-1})^{-1} + (C_{T2} + D_{T2}\, Z_{RS}^{-1})X (A_{T2} + B_{T2}.Z_{RS}^{-1})^{-1}\right]\bar{E}_{ff}$$

$$.....2.26.a$$

For a general earth fault:

$$\bar{E}_{ff} = \bar{V}_{ff} + Z_f\,(\bar{I}_{fSf} - \bar{I}_{fRf}) \quad .....2.26.b$$

From equation 2.26.a, we have:

$$\bar{E}_{ff} = -\left[(C_{T1} + D_{T1}\, Z_{SS}^{-1})(A_{T1} + B_{T1}\, Z_{SS}^{-1})^{-1} + (C_{T2} + D_{T2}\, Z_{RS}^{-1})(A_{T2} + B_{T2}\, Z_{RS}^{-1})^{-1}\right]^{-1} X(\bar{I}_{fSf} - \bar{I}_{fRf})$$

$$.....2.26.c$$

and from 2.26.b, we have:

$$\bar{V}_{ff} = \bar{E}_{ff} - Z_f\,(\bar{I}_{fSf} - \bar{I}_{fRf})$$

substituting the value of $\bar{E}_{ff}$ from 2.26.c:

$$\bar{V}_{ff} = -\left[\left[(C_{T1} + D_{T1}.Z_{SS}^{-1})(A_{T1} + B_{T1}.Z_{SS}^{-1})^{-1} + (C_{T2} + D_{T2}.Z_{RS}^{-1})(A_{T2}+B_{T2}.Z_{RS}^{-1})^{-1}\right] + Z_f\right](\bar{I}_{fSf}-\bar{I}_{fRf})$$

$$.....2.27$$

Equation 2.27 relates the superimposed voltages $\bar{V}_{ff}$ to the fault current $(\bar{I}_{fSf}-\bar{I}_{fRf})$. In the case of faulted phase (s), no difficulty[54] exists in evaluating $\bar{V}_{ff}$.

Assuming a single-line-to earth fault on phase 'a', $\bar{V}_{ffa}$ is the Fourier transform of a suddenly applied voltage of the form:

$$V_{ffa} = - V_{fsa}.\sin(wot + \beta).h(t) \qquad .....2.28$$

Where:

V_{fsa} = peak of the fault point prefault voltage

β = phase displacement between the prefault voltage of phase 'a' and the reference voltage.

$h(t)$ = a unit-step function.

Equation 2.27 may be rewritten in the form:

$$\begin{bmatrix} \bar{V}_{ffa} \\ \bar{V}_{ffb} \\ \bar{V}_{ffc} \end{bmatrix} = \begin{bmatrix} Z_{f11} & Z_{f12} & Z_{f13} \\ Z_{f21} & Z_{f22} & Z_{f23} \\ Z_{f31} & Z_{f32} & Z_{f33} \end{bmatrix} \begin{bmatrix} \bar{I}_{fa} \\ \bar{I}_{fb} \\ \bar{I}_{fc} \end{bmatrix} \qquad ...2.29$$

where $\bar{I}_{fa}=I_{fSfa}-\bar{I}_{fRfa}, I_{fb}=\bar{I}_{fSfb}-\bar{I}_{fRfb}, I_{fc}=\bar{I}_{fSfc}-\bar{I}_{fRfc}$

For an a-earth fault, $I_{fb} = I_{fc} = 0$, and equation 2.29 yields

$$\begin{bmatrix} \bar{V}_{ffa} \\ \bar{V}_{ffb} \\ \bar{V}_{ffc} \end{bmatrix} = \begin{bmatrix} Z_{f11} \\ Z_{f21} \\ Z_{f31} \end{bmatrix} \begin{bmatrix} \bar{I}_{fa} \end{bmatrix} \qquad ...2.30$$

From equation 2.30, the superimposed voltages for the healthy phasescan therefore be determined.

2.4.3 Superimposed voltages and currents at the relaying points

Voltages and currents at the sending and receiving end busbars are obtained by using equations 2.23, so that,

$$\bar{V}_{Sf} = (B_{T1}.D_{T1}^{-1}Z_{SS}^{-1} + U)^{-1}(A_{T1}-B_{T1}.D_{T1}^{-1}.C_{T1})(\bar{E}_{ff})$$

$$\bar{I}_{Sf} = -(Z_{SS})^{-1}(V_{Sf}) \qquad ...2.31$$

and

$$\bar{V}_{Rf} = (B_{T2}.D_{T2}^{-1}.Z_{RS}^{-1} + U)^{-1}(A_{T2}-B_{T2}.D_{T2}^{-1}.C_{T2})(\bar{E}_{ff})$$

$$\bar{I}_{Rf} = (Z_{RS})^{-1}(\bar{V}_{Rf}) \qquad ....2.32$$

The overall system response is obtained by converting the voltage

and current transforms given by equations 2.31 - 2.32 to time domain and adding to it the prefault steady-state response determined in section 2.4.1.

i.e.

$$\bar{V}_S = \bar{V}_{SS} + \bar{V}_{Sf}$$
$$\bar{I}_S = \bar{I}_{SS} + \bar{I}_{Sf} \qquad \ldots\ldots 2.33$$

$$\bar{V}_R = \bar{V}_{RS} + \bar{V}_{Rf}$$
$$\bar{I}_R = \bar{I}_{RS} + \bar{I}_{Rf} \qquad \ldots\ldots 2.34$$

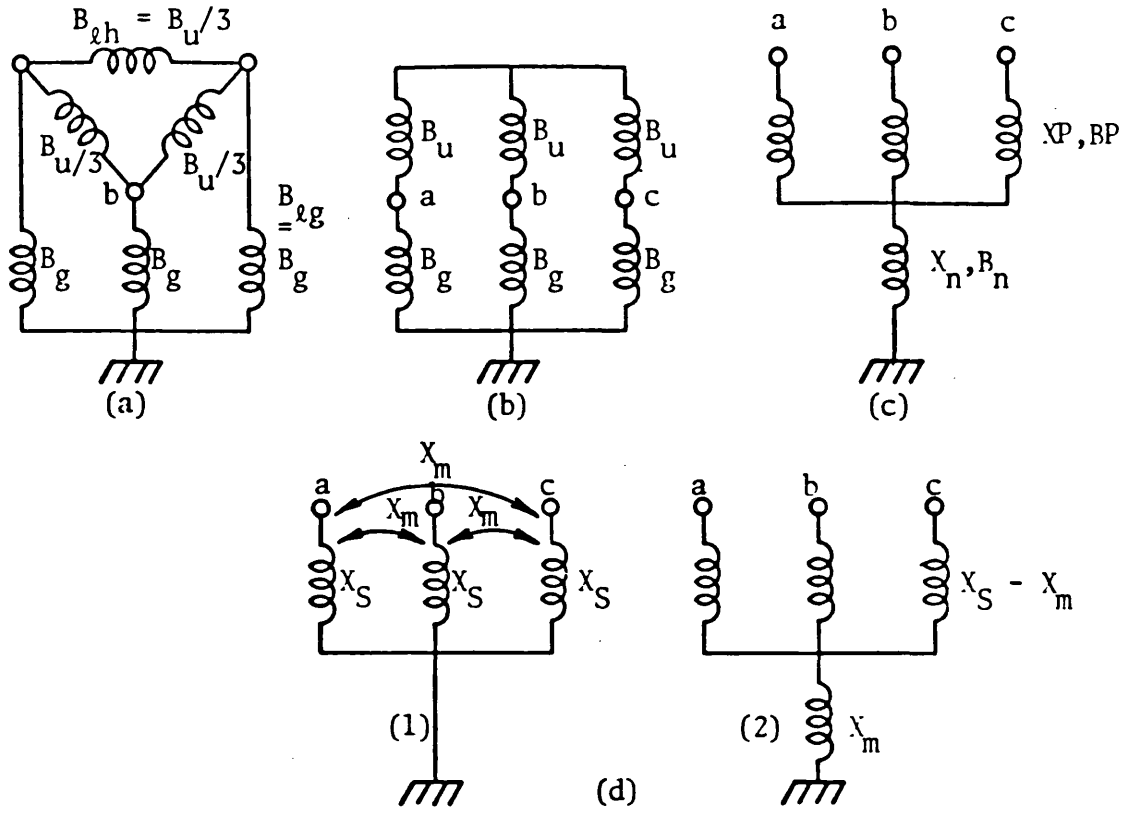

Fig 2.1

Possible shunt reactor arrangements for reactive power compensation and fault arc suppression.

$$B_u = BL_1 - BL_0$$

- (a),(b) = 6-reactor schemes
- (d.1) = (d.2).

(c),(d.2) = 4-reactor schemes.

c = single phase units.
d.2 = 3-phase units.

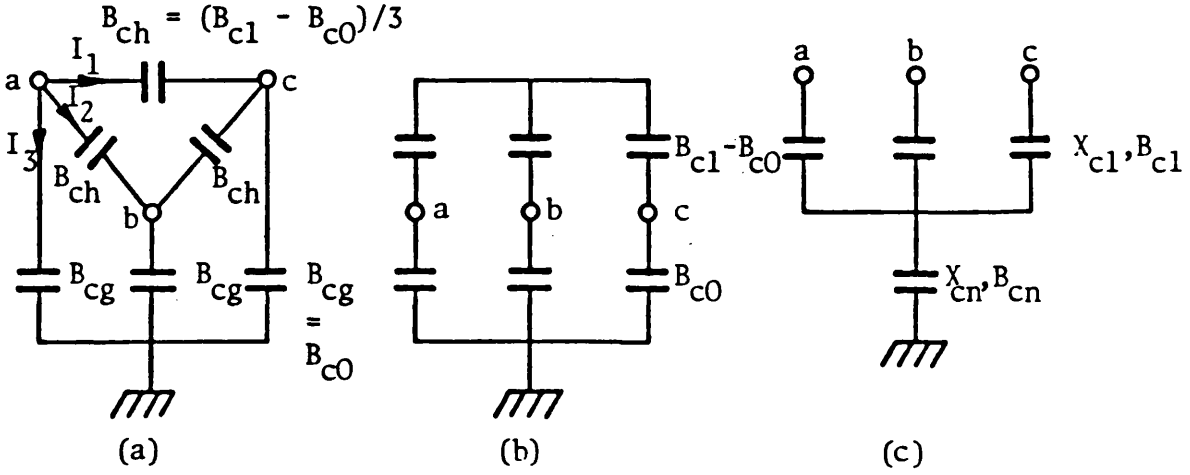

Fig 2.2

Equivalent circuits of the shunt capacitances of a 3-phase transmission line.

- (a),(b) = 6-capacitor schemes

(c) = 4-capacitor schemes.

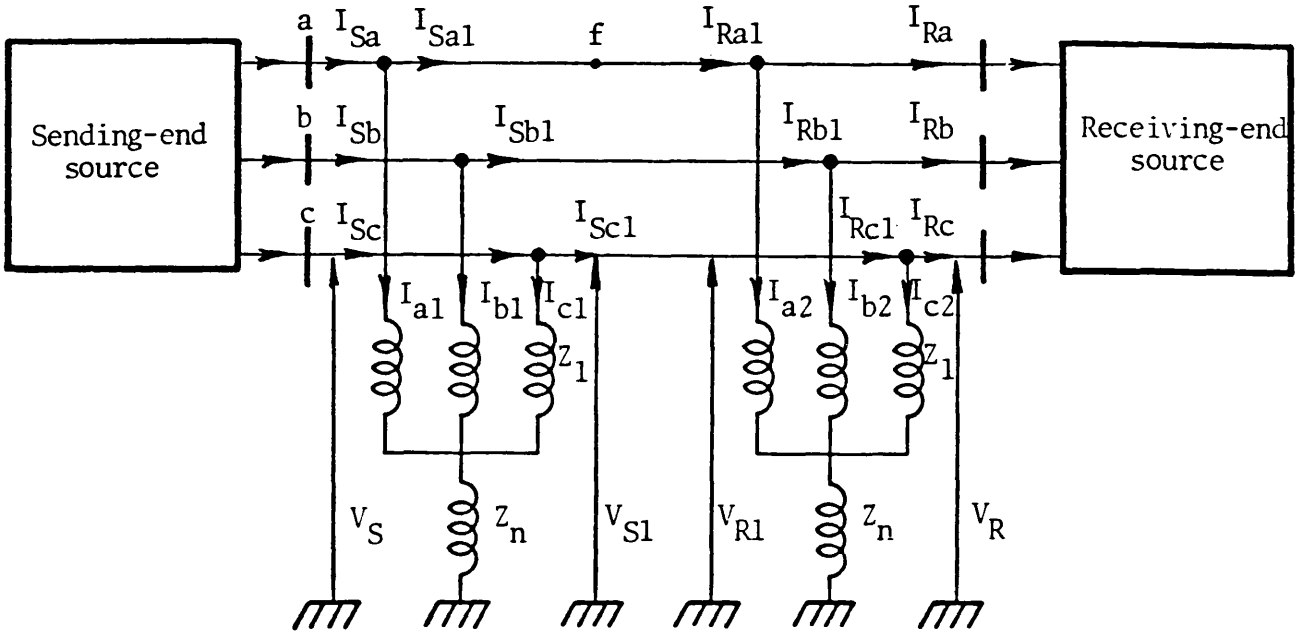

(a)

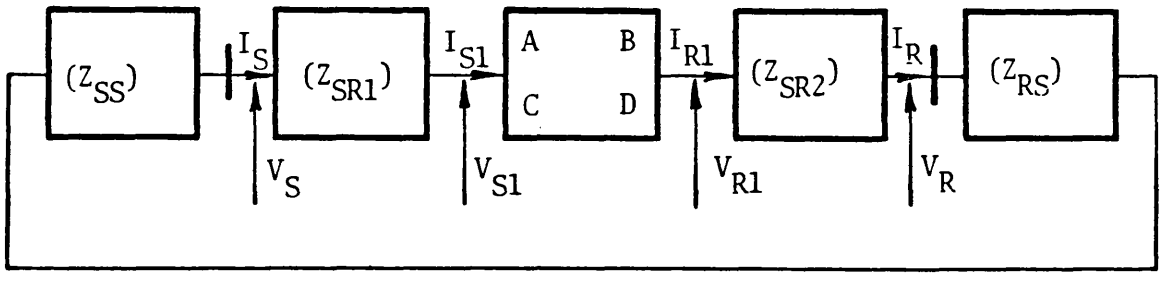

(b)

Fig 2.3

Single-section feeder, 4-reactor compensated system fed from main sources.

a - 3-wire diagram.

b - Steady-state block diagram.

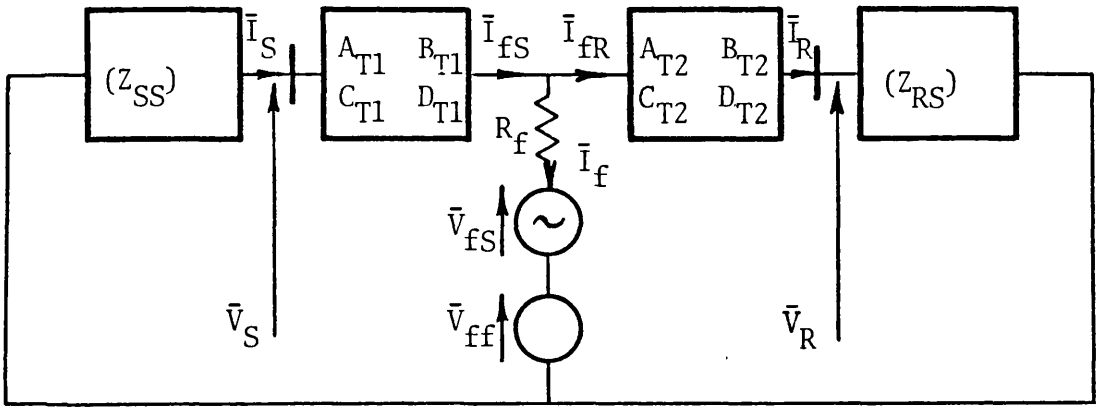

Fig 2.4

Faulted single-section, 4-reactor compensated system.

$$\bar{V}_S = \bar{V}_{SS} + \bar{V}_{Sf} \quad , \quad \bar{V}_R = \bar{V}_{RS} + \bar{V}_{Rf}$$
$$\bar{I}_S = \bar{I}_{SS} + \bar{I}_{Sf} \quad , \quad \bar{I}_R = \bar{I}_{RS} + \bar{I}_{Rf}$$
$$\bar{I}_{fS} = \bar{I}_{fSS} + \bar{I}_{fSf} \quad , \quad \bar{I}_{fR} = \bar{I}_{fRS} + \bar{I}_{fRf}$$
$$\bar{I}_f = \bar{I}_{fS} - \bar{I}_{fR}$$

CHAPTER 3 DEVELOPMENT OF METHODS TO SIMULATE PRACTICAL MULTI-SECTION FEEDER SYSTEMS

3.1 Introduction

In power system transient analysis, it is a common practice to assume that the line under consideration is energised either from infinite-busbar or lumped parameter sources. For accurate and realistic evaluation of system transient behaviour, however, it is necessary to take into account source-side network models. Several authors[13,54] have indicated that, in fact, there is no limit to the complexity of the source-side network terminating in a busbar from which a transmission line is energised. For example, several infeeds originating at remote points in the system may terminate at the busbar. These points may, in turn, be fed from other localised or remote generation sources. In order to evaluate the transient response of such a system, the input impedance of the network on both the source side and line side is required at the busbar considered.

Travelling wave distortion of system response at the point of interest has been shown to be considerably affected when source-side networks are considered under fault[54] and switching[13]- transient conditions.

It is not always necessary, however, to take into account the entire network source configuration, since, computationally, this may not be economical. In some cases, it is not even necessary to consider the entire source-side network, since transit times to the distant points of such networks and back may exceed the observation time chosen and hence would be of no direct relevance to the study.

This Chapter therefore is mainly devoted to develop methods suitable for simulating compensated multi-section feeder systems so that the effect of the complexity of source-side networks on system response can be examined.

Simulation of the main source model, based on system short-circuit level, is outlined in section (2). A very general line transposition scheme suitable for digital simulation has been developed by the author and is presented in section (4). In section (3), the methods developed for modelling 4-reactor, shunt compensated multi-section feeder systems are presented.

3.2 Analysis of Main Source Network Models

For the purpose of confirming the digital simulation presented in this thesis, a general source model based upon arbitrarily defined short-circuit levels at the terminating busbars has been used.[13-54] The model can further be modified to incorporate a lumped capacitance to represent any stray capacitance of the busbar to earth plus the capacitance of voltage transformers for metering or relaying purposes. This capacitance has been neglected in the course of the work here presented, because it complicates the process of verifying the simulation as a whole.[54] The basic source model is shown in Fig (3.1) and the source inpedance matrix can be calculated as follows:

$$E_{sa} = I_{sa} \cdot Z_{s1} + (I_{sa} + I_{sb} + I_{sc}) Z_{sn} + V_{sa}$$

$$\text{i.e.} \quad E_{sa} = I_{sa} (Z_{s1} + Z_{sn}) + I_{sb} \cdot Z_{sn} + I_{sc} \cdot Z_{sn} + V_{sa}$$

similarly

$$E_{sb} = I_{sa} \cdot Z_{sn} + I_{sb} (Z_{s1} + Z_{sn}) + I_{sc} \cdot Z_{sn} + V_{sb}$$

$$E_{sc} = I_{sa} \cdot Z_{sn} \quad I_{sb} \cdot Z_{sn} + I_{sc} (Z_{s1} + Z_{sn}) + V_{sc}$$

In matrix form:

$$\begin{bmatrix} E_{sa} \\ E_{sb} \\ E_{sc} \end{bmatrix} = \begin{bmatrix} Z_{s1}+Z_{sn} & Z_{sn} & Z_{sn} \\ Z_{sn} & Z_{s1}+Z_{sn} & Z_{sn} \\ Z_{sn} & Z_{sn} & Z_{s1}+Z_{sn} \end{bmatrix} \begin{bmatrix} I_{sa} \\ I_{sb} \\ I_{sc} \end{bmatrix} + \begin{bmatrix} V_{sa} \\ V_{sb} \\ V_{sc} \end{bmatrix}$$

In a more general form to suit a (6.6) matrix simulation, we have:

$$\left[\begin{array}{c} E_{sa} \\ E_{sb} \\ E_{sc} \\ \hline I_{sa} \\ I_{sb} \\ I_{sc} \end{array}\right] = \left[\begin{array}{ccc:ccc} 1 & 0 & 0 & Z_{s1}+Z_{sn} & Z_{sn} & Z_{sn} \\ 0 & 1 & 0 & Z_{sn} & Z_{s1}+Z_{sn} & Z_{sn} \\ 0 & 0 & 1 & Z_{sn} & Z_{sn} & Z_{s1}+Z_{sn} \\ \hline 0 & 0 & 0 & 1 & 0 & 0 \\ 0 & 0 & 0 & 0 & 1 & 0 \\ 0 & 0 & 0 & 0 & 0 & 1 \end{array}\right] \left[\begin{array}{c} V_{sa} \\ V_{sb} \\ V_{sc} \\ \hline I_{sa} \\ I_{sb} \\ I_{sc} \end{array}\right] \quad \ldots\ldots 3.1.a$$

equation 3.1.a is a more detailed one which may take the form:

$$\left[\begin{array}{c} E_s \\ \hline I_s \end{array}\right] = \left[\begin{array}{c:c} U & Z_{ss} \\ \hline 0 & U \end{array}\right] \left[\begin{array}{c} V_s \\ \hline I_s \end{array}\right] \quad \ldots\ldots 3.1.b$$

where

Z_{ss} = the source impedance matrix according to Fig (3.1) of diagonal elements = $Z_{s1} + Z_{sn}$ and off-diagonal elements of Z_{sn}. These elements are calculated as follows:

$$S\ C\ L = \sqrt{3}\,|V_L| \cdot |I_{SC}| = \frac{\sqrt{3}|V_L{}^2|}{\sqrt{3}|\cdot Z_{s1}|}$$

or $Z_{s1} = |V_L|^2 / (SCL)$ 3.2.a

But $Z_{s1} = R_{s1} + JX_{s1}$ 3.2.b

Defining the X/R ratio of the sending-end and receiving-end sources, the two elements of equation 3.2.b can be defined. This ratio may take[53] any value between 30 - 100.

The neutral source impedance Z_{sn} is calculated by producing both the PPS and ZPS impedances Z_1 and Z_0 for the circuit of Fig (3.1), where:

$$Z_1 = Z_{s1}$$

$$Z_0 = Z_{s1} + 3Z_{sn}$$

$$\therefore \quad Z_0 = Z_1 + 3Z_{sn}$$

$$\text{and} \quad Z_{sn} = (Z_0 - Z_1)/3$$

$$\text{or} \quad Z_{sn} = Z_{s1}\left[(Z_0/Z_1) - 1\right]/3 \qquad \ldots\ldots 3.2.c$$

The zero phase sequence / positive phase sequence impedance ratio (Z_0/Z_1) is among other source parameters an input data to the computer programs developed in this thesis. These parameters are presented in Chapter (5).

All the studies presented are for double-end fed systems, hence, equations 3.1, 3.2 may be used to formulate source impedance matrices at the sending and receiving ends of the line.

3.3 Modelling of multi-section Feeder Systems

In practice, several infeeds may terminate at the switching-station busbar to which a transmission line is connected. In order to examine the transient response of such a network, the input inpedance of the network on both the source side and the line-model side will be required at the busbar under consideration. The modal equations presented by wedepohl [12,13] and others, provide a means of evaluating the line-model examined input impedance matrix. On the source side, the equivalent impedance matrix will be made up of a contribution of input impedances of various infeeds connected to the switching-station busbar under consideration. The individual source infeeds can be represented as a distributed parameter network and thus treated exactly in the same way as the line-model studied and the 'ABCD' constants of the source side infeeds are derived from its propagation properties. At the remote end of these infeeds, there may be a localised source of generation and this can be taken into consideration in the analysis by the lumped parameter method of source simulation given by equations 3.1, 3.2.

The multi-section feeder system considered in the course of the present analysis is of the type shown in Fig (3.2.b). For the purpose of comparison, the figure also shows a single-section feeder system comprising a transmission line model (ℓ_m) provided with two 4-reactor schemes and fed from both ends by the main sources, Fig 3.2.a.

The 3-section feeder system assumes two infeeds from each side of the line considered (ℓ_m), i.e. two feeders connected to the line model receiving-end busbar(RB), and another two infeeds connected to its sending-end busbar. Both infeeds are terminated with the main source models. Each feeder of the system of Fig (3.2.b) is compensated by two 4-reactor schemes and each feeder of the two systems is regularly transposed through three equal intervals.

By assuming $\ell_1 = \ell_2 = \ell_3 = \ell_4 = 0$, the multi-section feeder system of Fig (3.2.b) yields the single-section system of Fig (3.2.a). A very general mathematical technique has been developed to simulate any type of fault that may occur on any of the feeders of Fig (3.2.b). The method is based on the fact that when a fault occurs, source-side networks and main-source models, represented by their impedance matrices Z_{SS} and Z_{SR}, have to be taken into account. The methods developed have enabled considering source-side networks by simply modifying the main source impedance matrices.

To get the input source impedances, consider a fault that occurs on the line model 'ℓ_m'. In this case, the developed method suggests that the sending-end source is made-up of a combination of the two feeders ℓ_1 and ℓ_2 and the simple source represented by the impedance matrix Z_{SS}. similarly, the receiving-end source is a combination of line sections ℓ_3 and ℓ_4 and the receiving-end source represented by its impedance matrix

Z_{SR}. Both the receiving-end and sending-end input impedance matrices can be evaluated if Fig (3.3) is considered.

Assuming that:

$$\begin{bmatrix} A_1 & B_1 \\ C_1 & D_1 \end{bmatrix}, \begin{bmatrix} A_2 & B_2 \\ C_2 & D_2 \end{bmatrix} \quad \ldots\ldots 3.3$$

are the constant matrices of lines ℓ_1 and ℓ_2. The matrices account for each respective line and its shunt compensation in the way described in Chapter (2).

The response of the system due to fault is obtained by simulating the fault by a suddenly applied voltage source (of certain magnitude and polarity) at the point of fault and other sources in the system are short-circuited. Under these conditions the sending-end input impedance matrix is obtained by looking from the fault point to the sending-end source combining line sections ℓ_1 and ℓ_2 with source impedance matrix Z_{SS}.

From Fig (3.3) it follows that:

$$\left[\begin{array}{c|c} A_{21} & B_{21} \\ \hline C_{21} & D_{21} \end{array}\right] = \left[\begin{array}{c|c} A_2 & B_2 \\ \hline C_2 & C_2 \end{array}\right] \left[\begin{array}{c|c} A_1 & B_1 \\ \hline C_1 & C_1 \end{array}\right] \left[\begin{array}{c|c} U & Z_{SS} \\ \hline O & U \end{array}\right] \ldots 3.4$$

and from Fig (3.3.a), we have:

$$\left[\begin{array}{c} V_2 \\ \hline I_2 \end{array}\right] = \left[\begin{array}{c|c} A_{21} & B_{21} \\ \hline C_{21} & D_{21} \end{array}\right] \left[\begin{array}{c} E_s \\ \hline I_s \end{array}\right] \quad \ldots\ldots 3.5$$

where E_s in the above equation = 0

From equation 3.5, we have:

$$\begin{bmatrix} V_2 \end{bmatrix} = \begin{bmatrix} B_{21} \end{bmatrix} \begin{bmatrix} I_s \end{bmatrix},$$

and

$$\begin{bmatrix} I_2 \end{bmatrix} = \begin{bmatrix} D_{21} \end{bmatrix} \begin{bmatrix} I_s \end{bmatrix}, \text{ i.e. } \begin{bmatrix} I_s \end{bmatrix} = \begin{bmatrix} D_{21} \end{bmatrix}^{-1} \begin{bmatrix} I_2 \end{bmatrix}$$

$$\therefore \quad \begin{bmatrix} V_2 \end{bmatrix} = \begin{bmatrix} B_{21} \end{bmatrix} \begin{bmatrix} D_{21} \end{bmatrix}^{-1} \begin{bmatrix} I_2 \end{bmatrix} \quad \ldots\ldots 3.6$$

Examination of equation 3.6 shows that the term $B_{21}.D_{21}^{-1}$ represents the new modified sending-end source impedance matrix (Z_{SM}) that accounts

for line infeeds ℓ_1 and ℓ_2. The modified (6.6) matrix will be:

$$\left[Z_{SSM}\right] = \left[\begin{array}{c|c} U & Z_{SM} \\ \hline 0 & U \end{array}\right] \qquad \ldots\ldots 3.7$$

The same procedure is followed to get the receiving-end modified source impedance matrix that accounts for line infeeds ℓ_3 and ℓ_4. Refering to Fig (3.3.b), we have:

$$\left[\begin{array}{c} V_3 \\ \hline I_3 \end{array}\right] = \left[\begin{array}{c|c} A_{34} & B_{34} \\ \hline C_{34} & D_{34} \end{array}\right] \left[\begin{array}{c} E_R \\ \hline I_R \end{array}\right] \qquad \ldots\ldots 3.8$$

where

$$\left[\begin{array}{c|c} A_{34} & B_{34} \\ \hline C_{34} & D_{34} \end{array}\right] = \left[\begin{array}{c|c} A_3 & B_3 \\ \hline C_3 & D_3 \end{array}\right] \left[\begin{array}{c|c} A_4 & B_4 \\ \hline C_4 & D_4 \end{array}\right] \left[\begin{array}{c|c} U & Z_{RS} \\ \hline 0 & U \end{array}\right] \qquad \ldots\ldots 3.9$$

The line constant matrices in the RHS of equation 3.9 account for line sections ℓ_3 and ℓ_4 together with their respective shunt reactors in a way similar to that presented in Chapter (2).

With $E_R = 0$, in equation 3.8, we get:

$$\left[V_3\right] = \left[B_{34}\right]\left[I_R\right] \quad \text{and} \quad \left[I_3\right] = \left[D_{34}\right]\left[I_R\right]$$

$$\therefore \quad \left[I_R\right] = \left[D_{34}\right]^{-1}\left[I_3\right]$$

and

$$\left[V_3\right] = \left[B_{34}\right]\left[D_{34}\right]^{-1}\left[I_3\right] \qquad \ldots\ldots 3.10$$

From equation 3.10, it is obvious that the modified receiving-end source impedance matrix that accounts for line sections ℓ_3 and ℓ_4 is $(Z_{RM}) = (B_{34})\ (D_{34})^{-1}$. The modified receiving-end (6.6) source impedance matrix is:

$$\left[Z_{RSM}\right] = \left[\begin{array}{c|c} U & Z_{RM} \\ \hline 0 & U \end{array}\right] \qquad \ldots\ldots 3.11$$

Equations 3.7, 3.11 are to be used together with the matrices describing the compensated line model 'ℓ_m' for transient fault studies on the middle

line section.

Equations similar to 3.7 and 3.11 can be formulated to represent the sending-end and receiving-end source network models when faults occur on any of the feeders ℓ_1, ℓ_2, ℓ_3, and ℓ_4.

A very general and very efficient computer program has been developed to deal with faults in both single and three-section feeder, 4-reactor compensated systems.

3.4 Line Transposition Scheme

When the conductors of a three-phase power line are not spaced equilaterally, the flux linkage and inductance of each phase are not the same. A different inductance in each phase results in an unbalanced circuit and in induced voltages in other adjacent power and communication lines even if the phase currents are balanced.[80] The unbalance is further aggravated by the unequal phase-to-phase and phase-to-earth capacitances. These undesirable characteristics can be overcome by exchanging the positions of the conductors at regular intervals along the line so that each conductor occupies the original position of every other conductor over an equal distance. Such an exchange of conductor positions is commonly known as transposition.

A complete transposition-cycle of the horizontal construction of the line examined is shown in Fig (3.4). Phase conductors are designated a,b,c, and the positions occupied are numbered 1,2,3. Transposition results in the conductors having the same average inductances and capacitances over one complete cycle.

Modern power lines are not necessarily transposed at regular intervals,

although they may be interchanged in positions at switching stations for the purpose of balancing more closely line inductances and capacitances.

In many situations, line transposition is assumed by averaging the diagonal and off-diagonal terms of the basic impedance and admittance matrices, thus taking into account the balancing effect of transposition. While this may be accurate enough for steady-state analysis of power systems, it fails to produce adequately the effect of discrete transposition on the electromagnetic transient, i.e. the reflection and conversion of the propagating modes due to the discontinuity of the surge impedance matrix at the transposition points.

Therefore, modelling of a discrete rather than continuous transpositions is mandatory when dealing with transients on transmission systems.[85]

Transposition of the transmission line studied has been simulated in a computer program and for a better understanding of the simulation Fig (3.4) and the following proceedures are considered:
According to Fig (3.4), voltages V_{a1}, V_{b1}, V_{c1} and currents I_{a1}, I_{b1} I_{c1}, are the transmission line sending-end quantities. The line length 'ℓ' is transposed through 3 equal sections of length $\ell/3$.

$A_1\ B_1\ C_1\ D_1$ = Constants of first line section

$A_2\ B_2\ C_2\ D_2$ = Constants of second line section

$A_3\ B_3\ C_3\ D_3$ = Constants of third line section

voltages and currents along the line are related by the following equations:

$$\begin{bmatrix} V_{R1} \\ I_{R1} \end{bmatrix} = \begin{bmatrix} A_1 & B_1 \\ C_1 & D_1 \end{bmatrix} \begin{bmatrix} V_{R2} \\ I_{R2} \end{bmatrix}, \quad \begin{bmatrix} V_{R2} \\ I_{R2} \end{bmatrix} = \begin{bmatrix} A_2 & B_2 \\ C_2 & D_2 \end{bmatrix} \begin{bmatrix} V_{R3} \\ I_{R3} \end{bmatrix}, \quad \begin{bmatrix} V_{R3} \\ I_{R3} \end{bmatrix} = \begin{bmatrix} A_3 & B_3 \\ C_3 & D_3 \end{bmatrix} \begin{bmatrix} V_{R4} \\ I_{R4} \end{bmatrix}$$

where, ... 3.12

each element of any of the RHS constant matrices of equation 3.12 is a (3.3) matrix.

The sending-end and receiving-end voltages and currents are related to each other as follows:

$$\begin{bmatrix} V_{R1} \\ I_{R1} \end{bmatrix} = \begin{bmatrix} A_1 & B_1 \\ C_1 & D_1 \end{bmatrix} \begin{bmatrix} A_2 & B_2 \\ C_2 & D_2 \end{bmatrix} \begin{bmatrix} A_3 & B_3 \\ C_3 & D_3 \end{bmatrix} \begin{bmatrix} V_{R4} \\ I_{R4} \end{bmatrix} \quad \ldots\ldots 3.13$$

The 'A B C D' constants of each of the 3-transposed line sections are defined as given below.

3.4.1 Constant Matrices for the 3-transposed Sections

a For first section

According to the conductor positions of Fig (3.4), the first line section constants, i.e. A_1, B_1, C_1, D_1 are:

$$A_1 = \begin{bmatrix} A_{11} & A_{12} & A_{13} \\ A_{21} & A_{22} & A_{23} \\ A_{31} & A_{32} & A_{33} \end{bmatrix}, \quad B_1 = \begin{bmatrix} B_{11} & B_{12} & B_{13} \\ B_{21} & B_{22} & B_{23} \\ B_{31} & B_{32} & B_{33} \end{bmatrix}, \quad C_1 = \begin{bmatrix} C_{11} & C_{12} & C_{13} \\ C_{21} & C_{22} & C_{23} \\ C_{31} & C_{32} & C_{33} \end{bmatrix},$$

$$D_1 = \begin{bmatrix} D_{11} & D_{12} & D_{13} \\ D_{21} & D_{22} & D_{23} \\ D_{31} & D_{32} & D_{33} \end{bmatrix} \quad \ldots\ldots 3.14$$

Thus

$$\begin{bmatrix} A_1 & B_1 \\ C_1 & D_1 \end{bmatrix} = \left[\begin{array}{ccc:ccc} A_{11} & A_{12} & A_{13} & B_{11} & B_{12} & B_{13} \\ A_{21} & A_{22} & A_{23} & B_{21} & B_{22} & B_{23} \\ A_{31} & A_{32} & A_{33} & B_{31} & B_{32} & B_{33} \\ \hdashline C_{11} & C_{12} & C_{13} & D_{11} & D_{12} & D_{13} \\ C_{21} & C_{22} & C_{23} & D_{21} & D_{22} & D_{23} \\ C_{31} & C_{32} & C_{33} & D_{31} & D_{32} & D_{33} \end{array}\right] \quad \ldots\ldots 3.15$$

where

$$A_1 = S.\cosh.(\gamma.\ell/3).S^{-1}$$
$$B_1 = S.\sinh.(\gamma.\ell/3)S^{-1}.Z_c$$
$$C_1 = Y_c.S.\sinh(\gamma.\ell/3).S^{-1} \quad \text{..... 3.16}$$
$$D_1 = Y_c.S.\cosh(\gamma.\ell/3).S.^{-1}Z_c$$

$$\gamma = \begin{bmatrix} \gamma_1 & 0 & 0 \\ 0 & \gamma_2 & 0 \\ 0 & 0 & \gamma_3 \end{bmatrix} \quad \text{..... 3.17}$$

$$Z_c = S.\gamma^{-1}.S^{-1}.Z$$
$$Y_c = Z_c^{-1}$$

All the variables in equations 3.16, 3.17 are explained in more detail in the modal analysis of the system studied considered in Appendix (A2).

It is clear from Fig 3.4 (a) that phases a,b,and c take the positions 1,2,3 respectively during the first transposition section. This may also be observed from equation (3.15) if any row or column of any of the sub-matrices A_1, B_1, C_1 and D_1 is considered. For example, the elements of the first row of submatrix A_1 show that the second suffix of the respective elements corresponds to the position of the respective phases.

b For second section

From equation 3.12,

$$\begin{bmatrix} V_{R1} \\ I_{R1} \end{bmatrix} = \begin{bmatrix} A_1 & B_1 \\ C_i & D_1 \end{bmatrix} \begin{bmatrix} V_{R2} \\ I_{R2} \end{bmatrix} \text{ where;}$$

$$\begin{bmatrix} V_{R1} \end{bmatrix} = \begin{bmatrix} V_{Ra1} \\ V_{Rb1} \\ V_{Rc1} \end{bmatrix}, \begin{bmatrix} I_{R1} \end{bmatrix} = \begin{bmatrix} I_{Ra1} \\ I_{Rb1} \\ I_{Rc1} \end{bmatrix}, \begin{bmatrix} V_{R2} \end{bmatrix} = \begin{bmatrix} V_{Ra2} \\ V_{Rb2} \\ V_{Rc2} \end{bmatrix}, \begin{bmatrix} I_{R2} \end{bmatrix} = \begin{bmatrix} I_{Ra2} \\ I_{Rb2} \\ I_{Rc2} \end{bmatrix}$$

For section 2:

$$\begin{bmatrix} V_{R2} \\ I_{R2} \end{bmatrix} = \begin{bmatrix} A_2 & B_2 \\ C_2 & D_2 \end{bmatrix} \begin{bmatrix} V_{R3} \\ I_{R3} \end{bmatrix}, \text{ where:}$$

$$V_{R3} = \begin{bmatrix} V_{Ra3} \\ V_{Rb3} \\ V_{Rc3} \end{bmatrix}, \begin{bmatrix} I_{R3} \end{bmatrix} = \begin{bmatrix} I_{Ra3} \\ I_{Rb3} \\ I_{Rc3} \end{bmatrix}$$

It is now required to define A_2, B_2, C_2 and D_2 which will correspond to the transposition of section 2 as shown in Fig (3.4.a). The equation defining the second section may be obtained in terms of the first section constant matrices as follows:

$$\begin{bmatrix} V_{Rc2} \\ V_{Ra2} \\ V_{Rb2} \\ I_{Rc2} \\ I_{Ra2} \\ I_{Rb2} \end{bmatrix} = \begin{bmatrix} A_1 & B_1 \\ C_1 & D_1 \end{bmatrix} \begin{bmatrix} V_{Rc3} \\ V_{Ra3} \\ V_{Rb3} \\ I_{Rc3} \\ I_{Ra3} \\ I_{Rb3} \end{bmatrix} \quad \ldots\ldots 3.18$$

on the other hand, if:

$$\begin{bmatrix} V_{Ra2} \\ V_{Rb2} \\ V_{Rc2} \end{bmatrix} = \begin{bmatrix} CN \end{bmatrix} \begin{bmatrix} V_{Rc2} \\ V_{Ra2} \\ V_{Rb2} \end{bmatrix}, \begin{bmatrix} V_{Ra3} \\ V_{Rb3} \\ V_{Rc3} \end{bmatrix} = \begin{bmatrix} CN \end{bmatrix} \begin{bmatrix} V_{Rc3} \\ V_{Ra3} \\ V_{Rb3} \end{bmatrix} \quad \ldots\ldots 3.19$$

and

$$\begin{bmatrix} I_{Ra2} \\ I_{Rb2} \\ I_{Rc2} \end{bmatrix} = \begin{bmatrix} CN \end{bmatrix} \begin{bmatrix} I_{Rc2} \\ I_{Ra2} \\ I_{Rb2} \end{bmatrix}, \begin{bmatrix} I_{Ra3} \\ I_{Rb3} \\ I_{Rc3} \end{bmatrix} = \begin{bmatrix} CN \end{bmatrix} \begin{bmatrix} I_{Rc3} \\ I_{Ra3} \\ I_{Rb3} \end{bmatrix} \quad \ldots\ldots 3.20$$

where,

$$CN = \begin{bmatrix} 0 & 0 & 1 \\ 1 & 0 & 0 \\ 0 & 1 & 0 \end{bmatrix} \quad \ldots\ldots 3.21$$

From equation 3.18 - 3.21, we have:

$$\begin{bmatrix} V_{R2} \\ I_{R2} \end{bmatrix} = \begin{bmatrix} CN\,A_1 \cdot CN^{-1} & CN.B_1 \cdot CN^{-1} \\ CN\,C_1 \cdot CN^{-1} & CN.D_1 \cdot CN^{-1} \end{bmatrix} \begin{bmatrix} V_{R3} \\ I_{R3} \end{bmatrix}$$

and therefore it follows that:

$$A_2 = [CN][A_1][CN]^{-1} \quad , \quad C_2 = [CN].[C_1] \cdot [CN]^{-1}$$
$$B_2 = [CN][B_1][CN]^{-1} \quad D_2 = [CN].[D_1] \cdot [CN]^{-1} \qquad \ldots\ldots 3.22$$

or

$$A_2 = [CN].[A_1].[CN]^t \quad , \quad C_2 = [CN][C_1][CN]^t$$
$$B_2 = [CN][B_1][CN]^t \quad , \quad D_2 = [CN][D_1][CN]^t \qquad \ldots\ldots 3.23$$

where ,

$$CN^{-1} = CN^t = \begin{bmatrix} 0 & 1 & 0 \\ 0 & 0 & 1 \\ 1 & 0 & 0 \end{bmatrix} \qquad \ldots\ldots 3.24$$

Hence, A_2 , B_2 , C_2 and D_2 can be obtained respectively from A_1 B_1 C_1 and D_1 ,even without performing the matrix multiplication in equations 3.22 - 3.23, by just reshuffling the elements in matrices A_1 B_1 C_1 and D_1 as shown below.

If positions 1, 2, 3 are occupied by conductors 3, 1, 2 respectively (in the second section), a matrix CP is:

$$CP = [\,3 \;\; 1 \;\; 2\,] \qquad \ldots\ldots 3.25$$

and

$$A_2(I,J) = A_1(CP(I), CP(J))$$
$$B_2(I,J) = B_1(CP(I), CP(J)) \qquad \ldots\ldots 3.26$$
$$C_2(I,J) = C_1(CP(I), CP(J))$$
$$D_2(I,J) = D_1(CP(I), CP(J)) \qquad \ldots\ldots 3.26$$

using either equations 3.22, 3.23 or equation 3.26 the matrix representing the second line section is:

$$A_2 = \begin{bmatrix} A_{33} & A_{31} & A_{32} \\ A_{13} & A_{11} & A_{12} \\ A_{23} & A_{21} & A_{22} \end{bmatrix}, \quad B_2 = \begin{bmatrix} B_{33} & B_{31} & B_{32} \\ B_{13} & B_{11} & B_{12} \\ B_{23} & B_{21} & B_{22} \end{bmatrix} \qquad \ldots\ldots 3.27$$

$$C_2 = \begin{bmatrix} C_{33} & C_{31} & C_{32} \\ C_{13} & C_{11} & C_{12} \\ C_{23} & C_{21} & C_{22} \end{bmatrix}, \quad D_2 = \begin{bmatrix} D_{33} & D_{31} & D_{32} \\ D_{13} & D_{11} & D_{12} \\ D_{23} & D_{21} & D_{22} \end{bmatrix} \qquad \ldots\ldots 3.27$$

c For third section

From equation 3.12 we have:

$$\begin{bmatrix} V_{R3} \\ I_{R3} \end{bmatrix} = \begin{bmatrix} A_3 & B_3 \\ C_3 & D_3 \end{bmatrix} \begin{bmatrix} V_{R4} \\ I_{R4} \end{bmatrix}$$

applying equation 3.23 we get:

$$A_3 = [C\acute{N}][A_1][C\acute{N}]^t \quad , \quad C_3 = [C\acute{N}][C_1][C\acute{N}]^t$$
$$B_3 = [C\acute{N}][B_1][C\acute{N}]^t \quad , \quad D_3 = [C\acute{N}][D_1][C\acute{N}]^t \qquad \ldots\ldots 3.28$$

where,

$$C\acute{N} = \begin{bmatrix} 0 & 1 & 0 \\ 0 & 0 & 1 \\ 1 & 0 & 0 \end{bmatrix}, \quad C\acute{N}^t = \begin{bmatrix} 0 & 0 & 1 \\ 1 & 0 & 0 \\ 0 & 1 & 0 \end{bmatrix} \qquad \ldots\ldots 3.29$$

If equation 3.26 is used to get the matrices for the third line section, equation 3.25 will be:

$$C\acute{P} = [\,2 \quad 3 \quad 1\,] \qquad \ldots\ldots 3.30$$

using either equation 3.28 or equations 3.25 - 3.30, the third line section matrices are given by equation 3.31:

$$\begin{bmatrix} A_3 & B_3 \\ \hline C_3 & D_3 \end{bmatrix} = \left[\begin{array}{ccc:ccc} A_{22} & A_{23} & A_{21} & B_{22} & B_{23} & B_{21} \\ A_{32} & A_{33} & A_{31} & B_{32} & B_{33} & B_{31} \\ A_{12} & A_{13} & A_{11} & B_{12} & B_{13} & B_{11} \\ \hline C_{22} & C_{23} & C_{21} & D_{22} & D_{23} & D_{21} \\ C_{32} & C_{33} & C_{31} & D_{32} & D_{33} & D_{31} \\ C_{12} & C_{13} & C_{11} & D_{12} & D_{13} & D_{11} \end{array}\right] \qquad \ldots\ldots 3.31$$

3.4.2 Two-port Transfer matrices for the 3-Transposed Sections

A fault separates the network into two parts. If each line section consists of homogeneous conductors, e.g. symmetrical or nontransposed lines, the

two port equations similar to that given by equations 2.25 may be used with constants A_{T1}, B_{T1}, C_{T1} and D_{T1} calculated by replacing '$\ell/3$' in equation (3.16) by 'x' (the distance to the fault from the sending-end). Similarly, constants A_{T2}, B_{T2}, C_{T2} and D_{T2} are calculated by replacing '$\ell/3$' by 'ℓ-x'.

If each line section, however, consists of nonhomogenous conductors such as the case of transposition or conductors having different characteristics, their terminal voltages and currents can not be related by equation 2.25. However, they may be related to each other by a set of cascaded connected quadripoles, each representing a homogeneous sub-section of the line.

To illustrate this point, let us consider the case of a transposed line with a fault at a distance $\ell/3 < x < 2\ell/3$ as shown in Fig (3.5), other cases can be similarly treated.

For each homogeneous section, two-port transfer matrix may be used as shown in Fig (3.5.b). For the part of the line before the fault, the two quadripoles representing the two homogeneous sections can be represented by an equivalent quadripole:

$$\begin{bmatrix} \bar{V}_{sf} \\ \bar{I}_{sf} \end{bmatrix} = \left[\begin{array}{c|c} a_1 & b_1 \\ \hline c_1 & d_1 \end{array}\right] \left[\begin{array}{c|c} a_2 & b_2 \\ \hline c_2 & d_2 \end{array}\right] \begin{bmatrix} \bar{E}_{ff} \\ \bar{I}_{fsf} \end{bmatrix} = \left[\begin{array}{c|c} A_1 & B_1 \\ \hline C_1 & D_1 \end{array}\right] \begin{bmatrix} \bar{E}_{ff} \\ \bar{I}_{fsf} \end{bmatrix} \quad \ldots\ldots 3.32$$

where a_1, b_1, c_1, d_1 are the constants of the first section calculated from equation 3.16.

a_2, b_2, c_2 and d_2 are the constants of section (2) before the fault. They are calculated using equations 3.22 - 3.26 and first section constants are calculated by replacing $\ell/3$ in equation 3.16 by $(x - \ell/3)$.

Similarly:

$$\begin{bmatrix} \bar{E}_{ff} \\ \hline \bar{I}_{fRf} \end{bmatrix} = \left[\begin{array}{c|c} a_3 & b_3 \\ \hline c_3 & d_3 \end{array}\right] \left[\begin{array}{c|c} a_4 & b_4 \\ \hline c_3 & d_3 \end{array}\right] \begin{bmatrix} \bar{V}_{Rf} \\ \hline \bar{I}_{Rf} \end{bmatrix} = \left[\begin{array}{c|c} A_2 & B_2 \\ \hline C_2 & D_2 \end{array}\right] \begin{bmatrix} \bar{V}_{Rf} \\ \hline \bar{I}_{Rf} \end{bmatrix} \quad \ldots\ldots 3.33$$

where: a_3, b_3, c_3, d_3 are the constants of section (2) beyond the fault point. They are calculated from equations 3.22 - 3.26 if constants of the first section are evaluated from equation 3.16 by replacing '$\ell/3$' by '$(2\ell/3)-x$'.

Constants a_4, b_4, c_4 and d_4 are the constants of section (3) and are directly calculated from equations 3.28 - 3.30.

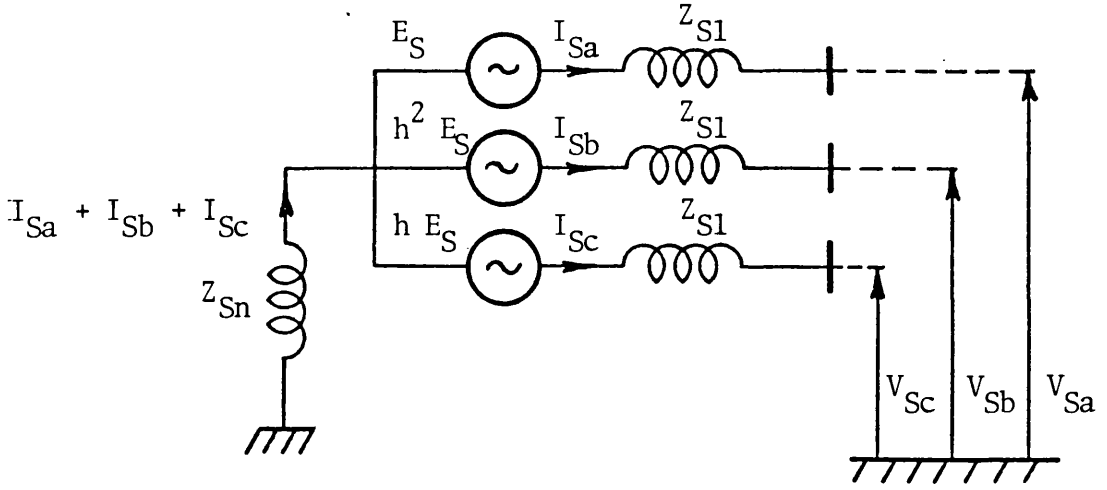

Fig 3.1

Main source network model.

Z_{S1} = PPS impedance.

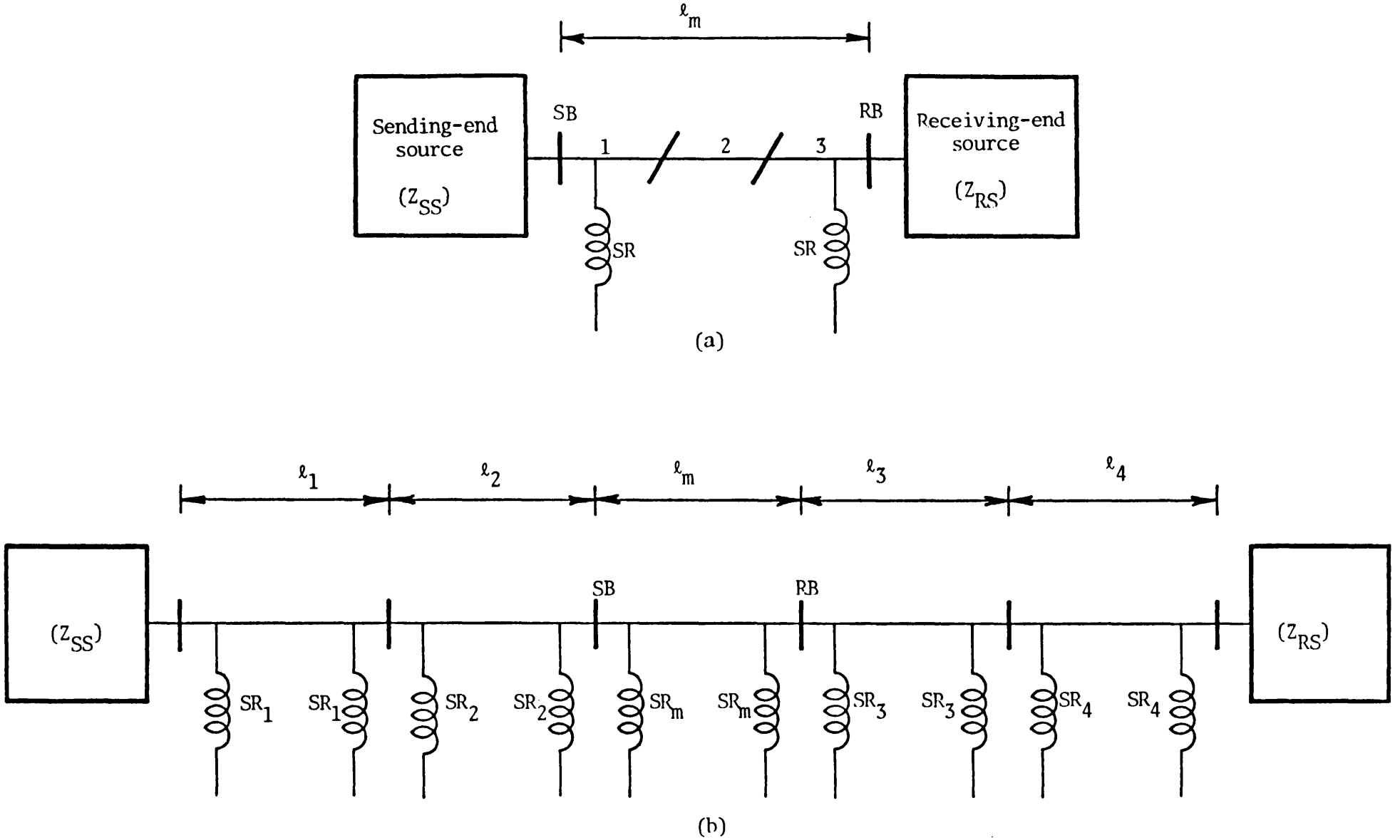

$SR, SR_1, SR_2, SR_m, SR_3, SR_4$ = shunt reactor schemes for the respective feeders.
SB,RB = sending and receiving end busbars of line under sonsideration.

Fig 3.2

Schematic diagram of the shunt-compensated systems studied.
a- single-section feeder system.
b- multi-section feeder system.

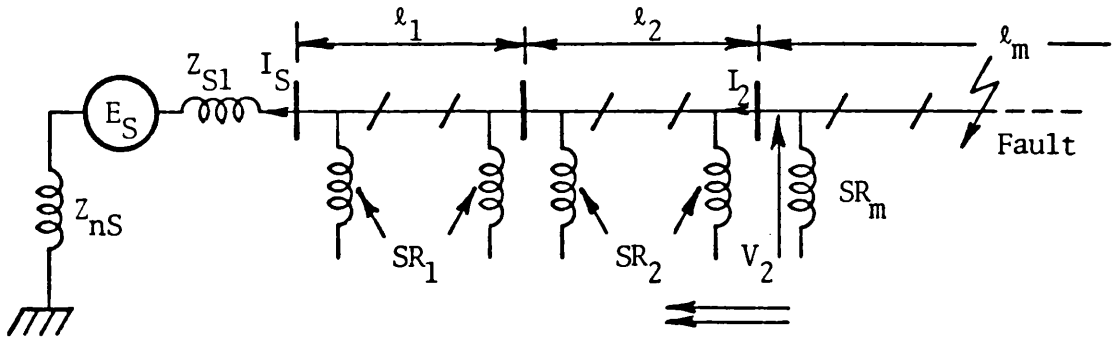

(a)

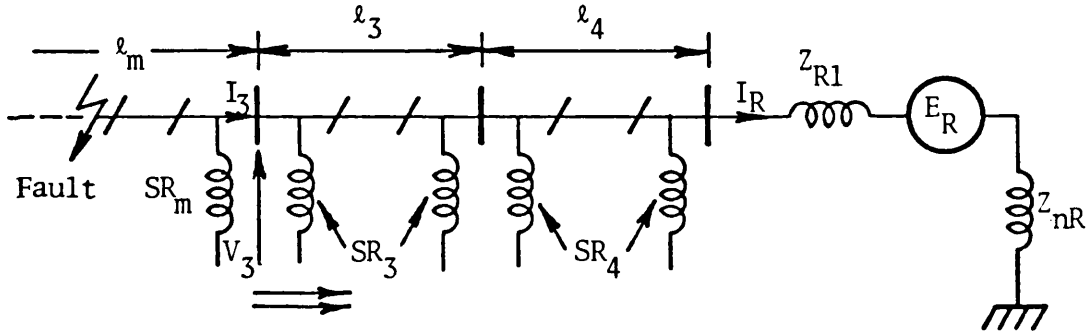

(b)

Fig 3.3

Single-line diagram of faulted multi-section feeder system.

a - Sending-end source side network.

b - Receiving-end source side network.

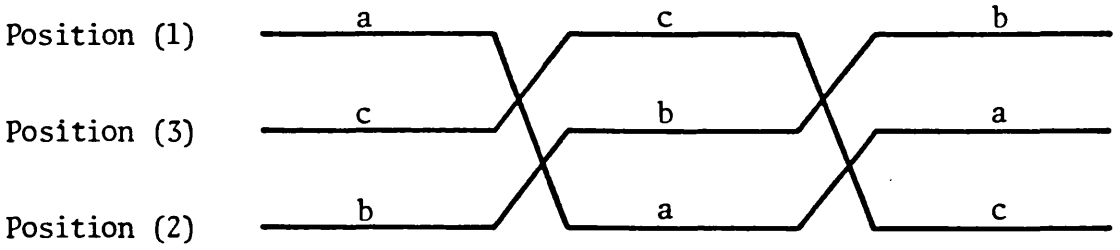

(a)

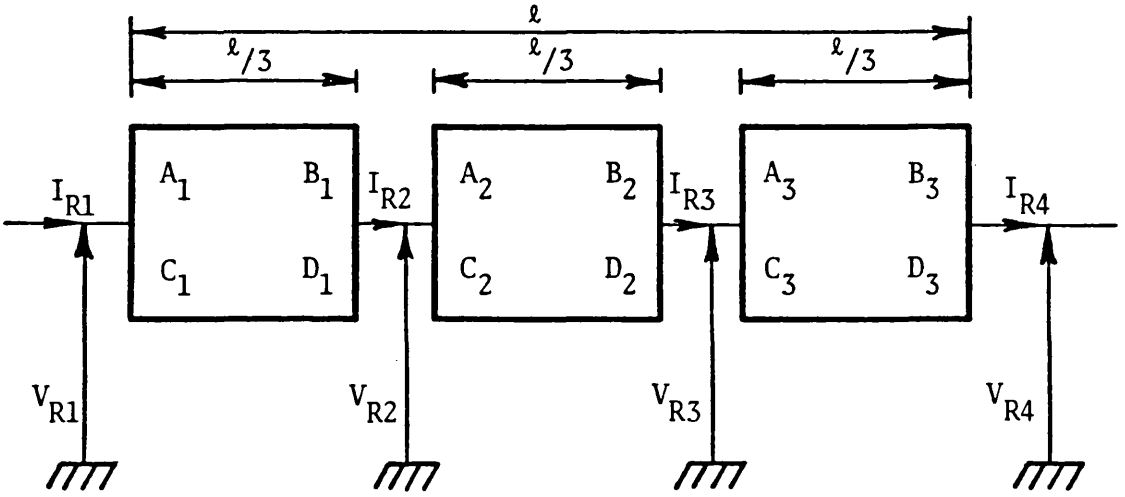

(b)

Fig 3.4

Line-transposition scheme.
a- Complete transposition cycle.
b- Block diagram of transposed sections.

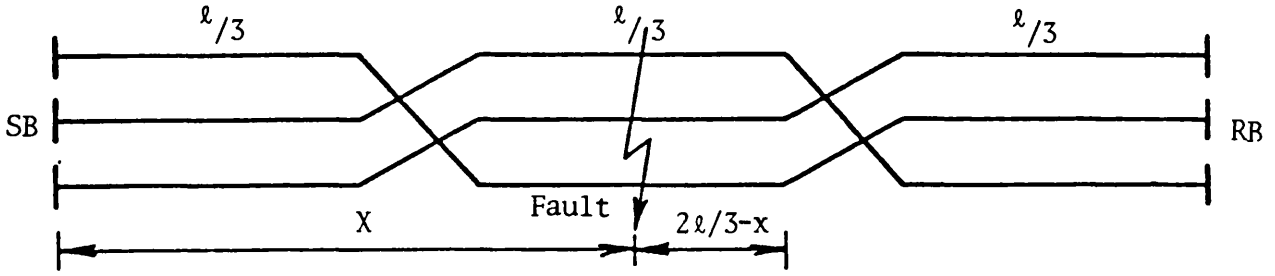

(a)

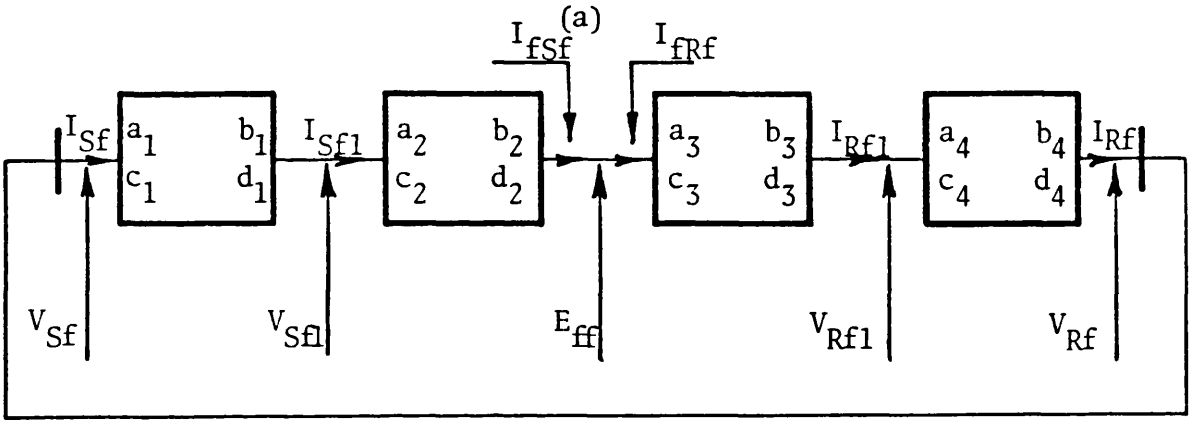

(b)

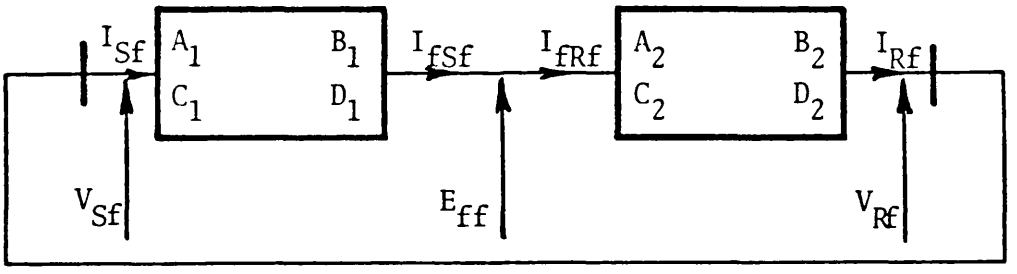

(c)

Fig 3.5

Transfer matrices of a transposed line.

CHAPTER 4 SIMULATION OF SATURATION EFFECTS IN 4-REACTOR CONPENSATED SYSTEMS

4.1 Introduction

The four-legged reactor model used in the present investigation as described in Chapter (3) assumes no saturation effects, ie., an ideal linear reactor. However, a "linear" shunt reactor does saturate to some extent, the degree of saturation being dependent on the reactor design.

Saturation of the reactor limbs will affect system response in two ways:

1. Saturation of any of the phase reactors will effectively change the system reactive power compensation.

2. Saturation of the neutral reactor effectively reduces its reactance which is no longer tuned with line interphase capacitances, hence fault arc suppression becomes extremely difficult.

In this Chapter therefore, the probability of reactor saturation is dealt with through a general mathematical treatment of the problem. Analytical and numerical evaluation of flux linkages of the 4-reactor limbs is presented in section (2). The technique developed to simulate reactor saturation is presented in section (3). In section (4) methods developed to evaluate superimposed voltages and currents at any point in the system due to saturation are presented.

These methods are used first to examine digitally, whether or not the phase or the neutral reactors are going to saturate. The judgement is based on the available information[23,34] concerning the knee point

voltage, saturation currents, and flux linkages of both the neutral and phase reactors. The methods are then used to digitally examine the effect of saturation on the primary system wave forms at the relaying points.

All digital computer results concerning reactor saturation are presented in Chapter (8), and reactor computed parameters are presented in Chapter (5).

4.2 Evaluation of Reactor Flux Linkages

4.2.1 Analytical Treatment

According to Fig (2.3), the two-port equation 2.21.a, relating sending-end shunt reactor input voltages and currents to its corresponding output quantities are:

$$\begin{bmatrix} \bar{V}_S \\ \hline \bar{I}_S \end{bmatrix} = \left[\begin{array}{cc} U & 0 \\ \hline Y_{SR1} & U \end{array}\right] \begin{bmatrix} \bar{V}_{S1} \\ \hline \bar{I}_{S1} \end{bmatrix} \qquad \ldots\ldots 4.1$$

where Y_{SR1} is given by

$$Y_{SR1} = \frac{1}{Z_1(Z_1+3Z_n)} \begin{bmatrix} Z_1+2Z_n & -Z_n & -Z_n \\ -Z_n & Z_1+2Z_n & -Z_n \\ -Z_n & -Z_n & Z_1+2Z_n \end{bmatrix} \qquad \ldots\ldots 4.2$$

From equation 4.1

$$\bar{I}_S = Y_{SR1}\,\bar{V}_{S1} + \bar{I}_{S1}$$

$$\bar{I}_S - \bar{I}_{S1} = \bar{I} = Y_{SR1}\,\bar{V}_{S1} = Y_{SR1}\,\bar{V}_S$$

where $\bar{I} = \bar{I}_a, \bar{I}_b, \bar{I}_c$; the currents through the main reactors connected to phases a, b and c respectively.

The current in the neutral is given by

$$\bar{I}_n = \bar{I}_a + \bar{I}_b + \bar{I}_c$$

$$\bar{I}_n = \Sigma Y_{SR1} \bar{V}_S$$

In terms of the shunt reactor admittance matrix Y_{SR1}, given by equation 4.2, the neutral current $\bar{I}_n$ is

$$\bar{I}_n = \frac{(\bar{V}_{Sa} + \bar{V}_{Sb} + \bar{V}_{Sc})}{Z_1 + 3Z_n} \qquad \ldots\ldots 4.3.a$$

and the voltages across the neutral reactor $\bar{V}_n$ is:

$$\bar{V}_n = Z_n \cdot \bar{I}_n = Z_n \frac{(\bar{V}_{Sa} + \bar{V}_{Sb} + \bar{V}_{Sc})}{Z_1 + 3Z_n} \qquad \ldots\ldots 4.3.b$$

The voltages across the phase-reactors are therefore given by:

$$\begin{aligned} \bar{V}_{a1} &= \bar{V}_{Sa} - \bar{V}_n \\ \bar{V}_{b1} &= \bar{V}_{Sb} - \bar{V}_n \\ \bar{V}_{c1} &= \bar{V}_{Sc} - \bar{V}_n \end{aligned} \qquad \ldots\ldots 4.4$$

Under steady-state balanced conditions, both neutral reactor current and voltage yield to zero and thus in equation 4.4, the main reactor voltages are the same as that of line conductors. The knowledge of the 4-reactor voltages, now enables the evaluation of their flux linkages.

Generally, the applied voltage 'v' across an inductor produces a current 'i' and a flux linkage 'ψ', then,

$$v(t) = + \frac{d\psi(t)}{dt} + R.i(t)$$

since the quality factors of practical EHV reactors are generally high [34] (between 250 - 350), the resistance drop in the above equation can be neglected, so that

$$v(t) = + \frac{d\psi(t)}{dt} \qquad \ldots\ldots 4.5$$

and the flux linkage can be obtained from equation 4.5 as:

$$\psi(t) = \psi(0) + \int_0^t v(t)\, dt \qquad \ldots\ldots 4.6$$

where t = 0 is the time at which the voltage across the reactor changes from the steady-state to the transient conditions, i.e. the wave forms

are as shown in Fig 4·1 .
Now at t = 0, we have

$$\psi(t) = \psi(0) = \psi_{ss} \cdot \cos\alpha \qquad \ldots\ldots 4.7.a$$

Also from equation 4.5 it follows that

$$V_m = \psi_{ss} \cdot \omega_0 \qquad \ldots\ldots 4.7.b$$

∴ equation 4.6 becomes

$$\underline{\psi(t)} = \psi_{ss} \cos\alpha + \int_0^t v(t)\, dt$$

Dividing by ψ_{ss}

$$\therefore \frac{\psi(t)}{\psi_{ss}} = \cos\alpha + \frac{1}{\psi_{ss}} \int_0^t v(t)\, dt$$

substituting the value of ψ_{ss} from equation 4.7.b in the above equation, we get:

$$\frac{\psi(t)}{\psi_{ss}} = \cos\alpha + \frac{\omega_0}{V_m} \int_0^t v(t)\, dt \qquad \ldots\ldots 4.8$$

Thus equation 4.8 can be used to evaluate the reactor flux linkages swing "$\frac{\psi(t)}{\psi_{ss}}$" numerically as outlined below.

4.2.2 Numerical Integration Method

Using the well known trapizoidal rule of numerical integration, equation 4.8 can be rewritten in the form

$$\frac{\psi(t)}{\psi_{ss}} = \cos\alpha + \frac{\omega_0}{V_m} \int_0^{n\Delta T} v(t)\, dt$$

or

$$\frac{\psi(t)}{\psi_{ss}} = \cos\alpha + \frac{\omega_0}{V_m} \cdot \frac{\Delta T}{2} \left[V_0 + 2V_1 + 2V_2 + \ldots + 2V_{n-1} + \ldots + V_n\right] \qquad \ldots\ldots 4.9$$

Equation 4.9 gives the swing of flux linkages of the phase and neutral reactors as follows:

4.2.2.1 For the Phase-reactors

The flux linkage swing of the a-phase reactor is derived and that of other phase-reactors are derived in a similar way.

The a-phase reactor voltage in phasor form is:

$$Va_1 = Va_R + JVa_{Im}$$

and

$$\alpha_a = \tan^{-1} Va_{Im}/Va_R$$

$$\therefore \quad \frac{\psi a(0)}{\psi_{ss}} = \cos\alpha$$

$$\frac{\psi a(\Delta T)}{\psi_{ss}} = \frac{\psi a(0)}{\psi_{ss}} + \frac{\omega_0}{V_m} \cdot \Delta T \frac{(V_{a0} + V_{a1})}{2}$$

$$\frac{\psi a(2\Delta T)}{\psi_{ss}} = \frac{\psi a(\Delta T)}{\psi_{ss}} + \frac{\omega_0}{V_m} \cdot \Delta T \frac{(V_{a1}+V_{a2})}{2} \qquad \ldots\ldots 4.10$$

$$\vdots$$

$$\frac{\psi a(n\Delta T)}{\psi_{ss}} = \frac{\psi a((n-1)\Delta T)}{\psi_{ss}} + \frac{\omega_0}{V_m} \cdot \Delta T \frac{(Va_{(n-1)} + Va_{(n)})}{2}$$

4.2.2.2 For the neutral reactor

Under steady-state balanced conditions, the neutral reactor voltage 'V_n' is zero. Therefore, trying to apply equation (4.9) can lead to computational problems (such as the division by the neutral reactor steady-state voltage which is zero). Accordingly, it has been decided to evaluate the neutral reactor flux linkage swing in terms of the steady-state peak flux linkage 'ψ_{ss}' of the phase-reactors.

It follows that, for the neutral reactor, equation (4.9) becomes:

$$\frac{\psi n(0)}{\psi_{ss}} = \frac{V_{mn}}{V_m} \cdot \cos\alpha n$$

$$\frac{\psi n(\Delta T)}{\psi_{ss}} = \frac{\psi n(0)}{\psi_{ss}} + \frac{\omega_0}{V_m} \cdot \Delta T \frac{(V_{n0}+V_{n1})}{2}$$

$$\vdots \qquad \ldots\ldots 4.11$$

$$\frac{\psi n(n\Delta T)}{\psi_{ss}} = \frac{\psi n((n-1)\Delta T)}{\psi_{ss}} + \frac{\omega_0}{V_m} \cdot \Delta T \frac{(V_{n(n-1)}+V_{n(n)})}{2}$$

Knowing the knee-point voltages of the 4-reactor limbs,[34] the reactor phase and neutral reactances, their saturation current and flux linkages can be evaluated. Equations 4.10, 4.11, then are used and the possibility

of saturation can be examined (Chapter (8)).

4.3 Modelling of Reactor Saturation

In this section, the method developed to simulate neutral reactor saturation is presented. Saturation of phase-reactors can be dealt with in the same way.

The "linear" neutral reactor model has been made representative of a non linear reactor by connecting another linear reactor branch in parallel with it. The non linear reactor characteristic may be therefore represented by the piece wise approximation shown in Fig (4.2.a). The ratio of the final to initial slope of the characteristic (L_2/L_1) has been assumed[75] = 0.10. The initial slope of the characteristic of Fig (4.2.a) is the inductance of the neutral linear reactor previously evaluated and tabulated in Table 5.3. Assuming a slope ratio of '10' therefore enables the evaluation of the final slope L_2 as = $L_1/10.0$.

Before saturation takes place, switch 'sw' of Fig (4.2.b) is opened and the voltage across it (V_{sw}) is the pre-saturation voltage, i.e. the voltage across the "linear" neutral reactor 'L_1'. At the time 'T_s' when saturation is assumed to occur, switch 'sw' is closed so that the voltage across it 'V_{sw}' drops to zero and the saturating inductance L_s is switched into the circuit. The final slope inductance L_2 is therefore:

$$L_2 = \frac{L_1 \cdot L_s}{L_1 + L_s} \qquad \ldots\ldots 4.12$$

and $L_s = L_1.L_2 / L_1 - L_2$

$\therefore$ according to Fig (4.2.b),

1 - before saturation, switch 'sw' open

$I_n \leq I_s$

$L_2 = L_1 = L_n$, see Table 5.3

$V_{sw} = V_{sat} = V_n$

2 - At the time of saturation, switch 'sw' closes

$I_n > I_s$

$L_2 = \frac{L_1 \cdot L_s}{L_1 + L_s}$, L_1 , L_2 , L_s = incremental inductances.

$V_{sw} = V_{sat} = 0$

The non linear operation of closing and opening switch (sw) is represented by a voltage source as shown in Fig (4.2.b). Before saturation, this voltage source 'V_{sat}' is equal in magnitude and of the same polarity as the voltage across the neutral reactor at any instant of time. When saturation takes place 'L_s' has to be switched into the circuit, i.e. switch 'sw' closes, ie. the voltage source 'V_{sat}' drops to zero.

Therefore the computational process requires the knowledge of the voltage across the neutral reactor from time zero until the end of observation time.

To get the response of the system under transient-fault conditions with the neutral reactor in the saturation region, three component responses have to be considered:

1. The normal prefault steady-state response, Chapter (3).
2. The system response due to fault as previously evaluated in Chapter(3)
3. The system response due to the application of the saturation voltage source 'V_{sat}'.

The overall system response is therefore evaluated as the sum of the three above mentioned component responses and is obtained by applying the principle of superposition previously used for fault analysis in Chapter (3).

The pre-saturation neutral reactor voltage 'V_n' is therefore first

evaluated in frequency domain, converted to time domain using the inverse modified Fourier transform[88-91] and then converted again to frequency domain using the modified Fourier transform to allow for saturation simulation in frequency domain. For saturation purpose, the only additional input data to the computer program are the slope ratio L_2/L_1 (= 0.1) and the saturation time 'T_s'.

Analytical treatment of the integrated 3-section system under fault-transient and saturation conditions is dealt with in the next section.

4.4 Methods Developed for the evaluation of super-imposed Voltage and Current Components due to Saturation

In the computer program, reactor saturation has been simulated according to the following:

1. Saturation time 'T_s' has been fixed as input data and in this way the simulation technique has been very much simplified. Naturally saturation should be simulated to occur when the current of the reactor under consideration exceeds its saturation level given in Table 5.3.

2. The neutral reactor adjacent to the sending-end busbar only has been considered as far as saturation is concerned. However, the technique used to simulate saturation is very general and may be used to simulate saturation of any main or neutral reactor that may work in the saturation region under any transient fault conditions, see Tables 5.3, 8.1.

3. The system simulated is the 3-section-double-end fed system. For simplicity, only one line section is shown in Fig (4.3). All three line sections are of the same configuration, transposition schemes, and have the same degrees of shunt compensation (h_1, h_0).

4. Simulation of sending-end reactor saturation has been based on the following analysis:

Refering to Fig (4.3), the following two-port equations may be easily derived.

$$\begin{bmatrix} \bar{V}_s \\ \bar{I}_1 \end{bmatrix} = \begin{bmatrix} A_1 & B_1 \\ C_1 & D_1 \end{bmatrix} \begin{bmatrix} \bar{V}_f \\ \bar{I}_f \end{bmatrix} \qquad \ldots\ldots 4.13$$

where

$\bar{V}_s$, $\bar{I}_1$ = the frequency domain output sending-end superimposed voltages and currents - due to saturation - respectively.

$\bar{V}_f$, $\bar{I}_f$ = the frequency domain fault point super imposed voltages and currents - due to saturation - respectively.

A_1, B_1, C_1, D_1 = constant matrix representing line section or subsections before the fault point.

The fault point network is represented by the two-port transfer matrix given in equation 4.15 as follows:

$$\bar{V}_{fa} = \bar{I}_{fa}.R_{fa} \;,\; \bar{V}_{fb}=\bar{I}_{fb}.R_{fb} \;,\; \bar{V}_{fc} = \bar{I}_{fc}.R_{fc}$$

$$\text{ie.} \begin{bmatrix} \bar{V}_{fa} \\ \bar{V}_{fb} \\ \bar{V}_{fc} \end{bmatrix} = \begin{bmatrix} R_{fa} & 0 & 0 \\ 0 & R_{fb} & 0 \\ 0 & 0 & R_{fc} \end{bmatrix} \begin{bmatrix} \bar{I}_{fa} \\ \bar{I}_{fb} \\ \bar{I}_{fc} \end{bmatrix} \qquad \ldots\ldots 4.14.a$$

where $R_{fa} = R_{fb} = R_{fc} = R_f$.

From equation 4.14.a, we have;

$$(\bar{I}_f) = (R_f)^{-1} (\bar{V}_f) = \begin{bmatrix} 1/R_f & 0 & 0 \\ 0 & 1/R_f & 0 \\ 0 & 0 & 1/R_f \end{bmatrix} \begin{bmatrix} V_{fa} \\ V_{fb} \\ V_{fc} \end{bmatrix} \qquad \ldots\ldots 4.14.b$$

But from Fig 4.3 we have:

$$\begin{aligned} \bar{I}_{a2} &= \bar{I}_{fa} + \bar{I}_{a3} \\ \bar{I}_{b2} &= \bar{I}_{fb} + \bar{I}_{b3} \\ \bar{I}_{c2} &= \bar{I}_{fc} + \bar{I}_{c3} \end{aligned} \quad \text{or} \begin{bmatrix} \bar{I}_{a2} \\ \bar{I}_{b2} \\ \bar{I}_{c2} \end{bmatrix} = \begin{bmatrix} \bar{I}_{fa} \\ \bar{I}_{fb} \\ \bar{I}_{fc} \end{bmatrix} + \begin{bmatrix} \bar{I}_{a3} \\ \bar{I}_{b3} \\ \bar{I}_{c3} \end{bmatrix}$$

Substituting $\bar{I}_f$ as given by equation 4.14.b

$$\therefore \begin{bmatrix} \bar{I}_{a2} \\ \bar{I}_{b2} \\ \bar{I}_{c2} \end{bmatrix} = \begin{bmatrix} 1/R_f & 0 & 0 \\ 0 & 1/R_f & 0 \\ 0 & 0 & 1/R_f \end{bmatrix} \begin{bmatrix} \bar{V}_a \\ \bar{V}_b \\ \bar{V}_c \end{bmatrix} + \begin{bmatrix} \bar{I}_{a3} \\ \bar{I}_{b3} \\ \bar{I}_{c3} \end{bmatrix}$$

$\therefore$ The fault point network transfer matrix is

$$\begin{bmatrix} \bar{V}_{fa} \\ \bar{V}_{fb} \\ \bar{V}_{fc} \\ \hline \bar{I}_{a2} \\ \bar{I}_{b2} \\ \bar{I}_{c2} \end{bmatrix} = \left[\begin{array}{ccc:ccc} 1 & 0 & 0 & 0 & 0 & 0 \\ 0 & 1 & 0 & 0 & 0 & 0 \\ 0 & 0 & 1 & 0 & 0 & 0 \\ \hline 1/R_f & 0 & 0 & 1 & 0 & 0 \\ 0 & 1/R_f & 0 & 0 & 1 & 0 \\ 0 & 0 & 1/R_f & 0 & 0 & 1 \end{array}\right] \begin{bmatrix} \bar{V}_{fa} \\ \bar{V}_{fb} \\ \bar{V}_{fc} \\ \hline \bar{I}_{a3} \\ \bar{I}_{b3} \\ \bar{I}_{c3} \end{bmatrix}$$

or $$\left[\begin{array}{c} \bar{V}_f \\ \hline \bar{I}_2 \end{array}\right] = \left[\begin{array}{c:c} U & 0 \\ \hline Y_f & U \end{array}\right] \left[\begin{array}{c} \bar{V}_f \\ \hline \bar{I}_3 \end{array}\right] \qquad \ldots\ldots 4.15$$

Where $\bar{V}_f$, $\bar{I}_2$ are the transforms of the fault point network input voltage and current components due to saturation.

$\bar{I}_3$ = the transform of the fault point network output current component due to saturation.

Y_f = fault conductance matrix whose elements have been evaluated in Appendix (A3) for different types of faults.

From the computer results presented in Chapter (6), it was found that 'R_f' has nearly no effect on the wave forms of interest if it is below 20 Ω. Therefore assuming $R_f = 10$, i.e. $Y_f = 0.1$ through the present analysis will reasonably represent a solid fault and in the same time computational stability is maintained.

Equations 4.14 and 4.15 are combined to give:

$$\begin{bmatrix} \bar{V}_s \\ \bar{I}_1 \end{bmatrix} = \begin{bmatrix} A_1 & B_1 \\ C_1 & D_1 \end{bmatrix} \begin{bmatrix} U & 0 \\ Y_f & U \end{bmatrix} \begin{bmatrix} \bar{V}_f \\ \bar{I}_3 \end{bmatrix} \qquad \ldots\ldots 4.16$$

The two-port transfer matrix representing the network beyond the fault point up to the receiving-end busbar is:

$$\begin{bmatrix} \bar{V}_f \\ \bar{I}_3 \end{bmatrix} = \begin{bmatrix} \acute{A} & \acute{B} \\ \acute{C} & \acute{D} \end{bmatrix} \begin{bmatrix} U & 0 \\ Y_{SR2} & U \end{bmatrix} \begin{bmatrix} \bar{V}_R \\ \bar{I}_R \end{bmatrix} \qquad \ldots\ldots 4.17.a$$

where

$\acute{A}$, $\acute{B}$, $\acute{C}$, $\acute{D}$ = Constant matrices representing the line section or subsections beyond fault point. The non homogeneous situation resulting from line transposition is overcome in the same way as previously dealt with in Chapter (3).

Y_{SR2} is the receiving-end shunt reactor admittance matrix. Its 9 elements are evaluated in the same way as for linear reactors, Chapter (2).

$\bar{V}_R$, $\bar{I}_R$ = frequency domain voltage and current superimposed components due to saturation (at the receiving-end).

Receiving-end busbar is related to its source by the following matrix:

$$\left[\begin{array}{c} \bar{V}_R \\ \hline \bar{I}_R \end{array}\right] = \left[\begin{array}{c|c} U & Z_{Rs} \\ \hline 0 & U \end{array}\right] \left[\begin{array}{c} \bar{E}_{Rs} \\ \hline \bar{I}_R \end{array}\right]$$

where Z_{Rs} is the main - source impedance matrix previously derived in Chapter (3).

$\bar{E}_{Rs}$ = the frequency domain receiving-end source e.m.f. Since this analysis is concerned with voltage and current components due to saturation, all voltage sources are short circuited (superposition) except that representing saturation 'V_{sat}'.

$$\therefore \begin{bmatrix} \bar{V}_R \\ \bar{I}_R \end{bmatrix} = \begin{bmatrix} U & Z_{Rs} \\ 0 & U \end{bmatrix} \begin{bmatrix} 0 \\ \bar{I}_R \end{bmatrix} \qquad \ldots\ldots 4.17.b$$

combining equation 4.16 and 4.17, we get:

$$\therefore \begin{bmatrix} \bar{V}_s \\ \bar{I}_1 \end{bmatrix} = \begin{bmatrix} A_1 & B_1 \\ C_1 & D_1 \end{bmatrix} \begin{bmatrix} U & 0 \\ Y_f & U \end{bmatrix} \begin{bmatrix} \acute{A} & \acute{B} \\ \acute{C} & \acute{D} \end{bmatrix} \begin{bmatrix} U & 0 \\ Y_{SR2} & U \end{bmatrix} \begin{bmatrix} U & Z_{Rs} \\ 0 & U \end{bmatrix} \begin{bmatrix} 0 \\ \bar{I}_R \end{bmatrix}$$

or

$$\begin{bmatrix} \bar{V}_s \\ \bar{I}_1 \end{bmatrix} = \begin{bmatrix} A_2 & B_2 \\ C_2 & D_2 \end{bmatrix} \begin{bmatrix} 0 \\ \bar{I}_R \end{bmatrix} \qquad \ldots\ldots 4.18$$

From equation 4.18

$$\bar{V}_s = B_2 \bar{I}_R$$

$$\bar{I}_1 = D_2 \bar{I}_R$$

$$\therefore \bar{I}_R = D_2^{-1} \bar{I}_1$$

$$\text{and } \bar{V}_s = B_2 D_2^{-1} \bar{I}_1 \qquad \ldots\ldots 4.19$$

Now back to Fig (4.3), the transfer matrix representing the sending-end source is:

$$\begin{bmatrix} \bar{V}_s \\ -\bar{I}_s \end{bmatrix} = \begin{bmatrix} U & Z_{ss} \\ 0 & U \end{bmatrix} \begin{bmatrix} 0 \\ -\bar{I}_s \end{bmatrix} \qquad \ldots\ldots 4.20$$

From equation 4.20 we have

$$\bar{V}_s = -Z_{ss} \bar{I}_s \qquad \ldots\ldots 4.21$$

Equations 4.19, 4.21 are the two basic equations used to solve and simulate saturation of sending-end neutral reactor.

These equations may be rewritten as

$$\bar{V}_s = Z_1 \bar{I}_1$$

$$\bar{V}_s = Z_2 \bar{I}_s \qquad \ldots\ldots 4.22$$

where $Z_1 = B_2 D_2^{-1}$

$$Z_2 = -Z_{ss}$$

From equation 4.22 we have:

$$\bar{I}_1 = Z_1^{-1}\ \bar{V}_s$$
$$\bar{I}_s = Z_2^{-1}\ \bar{V}_s$$

$$\therefore \quad \bar{I} = \bar{I}_s - \bar{I}_1 = \left[Z_2^{-1} - Z_1^{-1}\right]\ \bar{V}_s$$
$$\text{or} \qquad \bar{V}_s = \left[Z_2^{-1} - Z_1^{-1}\right]^{-1}\ \bar{I}$$

Let us call:

$$\left[Z_2^{-1} - Z_1^{-1}\right] = [YY] \text{ and } \left[Z_2^{-1} - Z_1^{-1}\right]^{-1} = [ZZ]$$

where $(YY) = \begin{bmatrix} YY_{11} & YY_{12} & YY_{13} \\ YY_{21} & YY_{22} & YY_{23} \\ YY_{31} & YY_{32} & YY_{33} \end{bmatrix}$ and $(ZZ) = \begin{bmatrix} ZZ_{11} & ZZ_{12} & ZZ_{13} \\ ZZ_{21} & ZZ_{22} & ZZ_{23} \\ ZZ_{31} & ZZ_{32} & ZZ_{33} \end{bmatrix}$

$$\therefore \quad \bar{I} = YY \,.\, \bar{V}_s$$
$$\text{or} \quad \bar{V}_s = ZZ \,.\, \bar{I} \qquad \ldots\ldots 4.23$$

From Fig 4.3 we have:

$$\bar{V}_{sa} = \bar{I}_a \,.\, X_1 + \bar{V}_{xa}$$
$$\bar{V}_{sb} = \bar{I}_b \,.\, X_1 + \bar{V}_{xb}$$
$$\bar{V}_{sc} = \bar{I}_c \,.\, X_1 + \bar{V}_{xc}$$

where $\bar{V}_{xa} = \bar{V}_{xb} = \bar{V}_{xc} = \bar{V}_x$

= the neutral point-to-earth voltage transform.

$\bar{I}_a$, $\bar{I}_b$, $\bar{I}_c$ are the transforms of phase-reactor currents

X_1 = phase-reactors reactances as given in Table 5.1

In matrix form:

$$\begin{bmatrix} \bar{V}_{sa} \\ \bar{V}_{sb} \\ \bar{V}_{sc} \end{bmatrix} = \begin{bmatrix} \bar{V}_{xa} \\ \bar{V}_{xb} \\ \bar{V}_{xc} \end{bmatrix} + X_1 \begin{bmatrix} 1 & 0 & 0 \\ 0 & 1 & 0 \\ 0 & 0 & 1 \end{bmatrix} \begin{bmatrix} \bar{I}_a \\ \bar{I}_b \\ \bar{I}_c \end{bmatrix} \qquad \ldots\ldots$$

$$\text{or} \begin{bmatrix} \bar{V}_s \end{bmatrix} = \begin{bmatrix} \bar{V}_x \end{bmatrix} + X_1 \begin{bmatrix} U \end{bmatrix} \begin{bmatrix} \bar{I} \end{bmatrix} \qquad \ldots\ldots 4.24$$

From equation 4.24:

$$[\bar{V}_x] = [\bar{V}_s] - X_1 [U][\bar{I}]$$

substituting $\bar{V}_s$ as given in equation 4.23, we get:

$$\begin{bmatrix} \bar{V}_{xa} \\ \bar{V}_{xb} \\ \bar{V}_{xc} \end{bmatrix} = \begin{bmatrix} ZZ_{11} & ZZ_{12} & ZZ_{13} \\ ZZ_{21} & ZZ_{22} & ZZ_{23} \\ ZZ_{31} & ZZ_{32} & ZZ_{33} \end{bmatrix} \begin{bmatrix} \bar{I}_a \\ \bar{I}_b \\ \bar{I}_c \end{bmatrix} - X_1 \begin{bmatrix} 1 & 0 & 0 \\ 0 & 1 & 0 \\ 0 & 0 & 1 \end{bmatrix} \begin{bmatrix} \bar{I}_a \\ \bar{I}_b \\ \bar{I}_c \end{bmatrix} \quad \ldots\ldots \quad 4.25.a$$

or $\left[\bar{V}_x\right] = (ZZ)(\bar{I}) - X_1 (U)(\bar{I})$ .....

From equation 4.25.a we have:

$$\bar{V}_x = (ZZ - X_1 \cdot U)\, \bar{I}$$

or

$$\bar{I} = (ZZ - X_1 \cdot U)^{-1} \cdot \bar{V}_x$$

call $(ZZ - X_1 U)^{-1} = (Y_2)$

$$= \begin{bmatrix} Y_{11} & Y_{12} & Y_{13} \\ Y_{21} & Y_{22} & Y_{23} \\ Y_{31} & Y_{32} & Y_{33} \end{bmatrix}$$

$$\therefore \quad \bar{I} = Y_2 \cdot \bar{V}_x \qquad \ldots\ldots 4.25.b$$

Now, the neutral reactor current transform can be obtained as the sum of

$$\bar{I}_a + \bar{I}_b + \bar{I}_c$$

$$\therefore \quad \bar{I}_x = \bar{I}_a + \bar{I}_b + \bar{I}_c$$

$$\bar{I}_x = \Sigma\, Y_2 \cdot \bar{V}_x = (Y_{11} + Y_{12} + Y_{13} + Y_{21} + Y_{22} + Y_{23} + Y_{31} + Y_{32} + Y_{33})\, \bar{V}_x$$

$$\therefore \quad \bar{I}_x = Y_s \bar{V}_x \qquad \ldots\ldots 4.26$$

where, $Y_s = (Y_{11} + Y_{12} + Y_{13} + \ldots + Y_{33})$

But as may be seen from Fig 4.3

$$\bar{I}_x = \bar{I}_{x1} + \bar{I}_{x2} \qquad \ldots\ldots 4.27.a$$

and $\bar{V}_x = \bar{I}_{x2} \cdot X_n \qquad \ldots\ldots 4.27.b$

$$\bar{V}_x = \bar{I}_{x1} \cdot \bar{X}_o + \bar{V}_{sat} \qquad \ldots\ldots 4.27.c$$

Equating equations 4.27 a, b we have:

$$\bar{I}_{x2}\ X_n = \bar{I}_{x1}\ X_o + \bar{V}_{sat}$$

substituting the value of $\bar{I}_{x1} = \bar{I}_x - \bar{I}_{x2}$ from 4.27.a

$$\therefore \quad \bar{I}_{x2}.X_n = (\bar{I}_x - \bar{I}_{x2})\ X_o + \bar{V}_{sat}$$

$$\therefore \quad \bar{I}_{x2}\ (X_n + X_o) = \bar{I}_x.X_o + \bar{V}_{sat}$$

$$\therefore \quad \bar{V}_{sat} = \bar{I}_{x2}\ (X_n + X_o) - \bar{I}_x \cdot X_o$$

But from 4.27.b, $\bar{I}_{x2} = \bar{V}_x/X_n$

$$\therefore \quad \bar{V}_{sat} = \frac{\bar{V}_x}{X_n}\ (X_n + X_o) - \bar{I}_x \cdot X_o$$

substituting for $\bar{I}_x$ from equation 4.26:

$$\therefore \quad \bar{V}_{sat} = \frac{\bar{V}_x}{X_n}\ (X_n + X_o) - Y_s \cdot \bar{V}_x \cdot X_o$$

$$= \bar{V}_x\ \frac{(X_n + X_o - Y_s\ X_o)}{X_n}$$

$$= \bar{V}_x\ \frac{(X_n + X_o - Ys\ X_n\ X_o)}{X_n}$$

or

$$\bar{V}_{sat} = K_1 \cdot \bar{V}_x \qquad \text{..... 4.28.a}$$

where

$$K_1 = (X_n + X_o - Y_s\ X_n\ X_o) \qquad \text{..... 4.28.b}$$

and

$$\bar{V}_x = \bar{V}_{sat} / K_1 = K_2 \cdot \bar{V}_{sat} \qquad \text{..... 4.28.c}$$

Back now to equation 4.24:

$$\left[\bar{V}_s\right] = \left[\bar{V}_x\right] + X_1 \left[U\right]\left[\bar{I}\right]$$

and substituting $\bar{I} = Y_2\ \bar{V}_x$ from equation 4.25.b yields:

$$\left[\bar{V}_s\right] = \left[\bar{V}_x\right] + X_1 \left[U\right]\left[Y_2\right]\left[\bar{V}_x\right]$$

Finally substitute $\bar{V}_x = K_2 \cdot \bar{V}_{sat}$ from equation 4.28.c yields:

$$\left[\bar{V}_s\right] = \left[U + X_1\ U\ Y_2\right] \quad \left[K_2 \cdot V_{sat}\right] \qquad \text{..... 4.29}$$

or

$$\begin{bmatrix} V_{sa} \\ V_{sb} \\ V_{sc} \end{bmatrix} = \left[\begin{bmatrix} 1 & 0 & 0 \\ 0 & 1 & 0 \\ 0 & 0 & 1 \end{bmatrix} + X_1 \begin{bmatrix} 1 & 0 & 0 \\ 0 & 1 & 0 \\ 0 & 0 & 1 \end{bmatrix} \begin{bmatrix} Y_{11} & Y_{12} & Y_{13} \\ Y_{21} & Y_{22} & Y_{23} \\ Y_{31} & Y_{32} & Y_{33} \end{bmatrix}\right] \begin{bmatrix} K_2.V_{sat} \\ K_2.V_{sat} \\ K_2.V_{sat} \end{bmatrix}$$

where

$\bar{V}_s$ = Transforms of the super imposed sending-end voltages due to saturation.

Y_2 is a (3,3) admittance matrix given by equation 4.25.b

$$Y_2 = \left[ZZ - X_1 U \right]^{-1} = \left\{ \left[Z_2^{-1} - Z_1^{-1} \right]^{-1} - X_1 U \right]^{-1}$$

$$K_2 = {}^{1}/\left[X_n + X_o - Y_s X_n X_o \right]$$

X_o may be obtained using equation 4.12 as:

$$X_o = \frac{X_n \cdot X_{n2}}{X_n - X_{n2}}$$

where X_n/X_{n2} is the assumed B/H characteristic slope ratio (10.0).

$\bar{V}_{sat}$ = the transform of the voltage source which is equal to the voltage across the neutral reactor before saturation and then drops to zero when saturation occurs.

To get the superimposed sending-end current components, equation 4.22 applies:

$$\bar{I}_s = Z_2^{-1} \cdot \bar{V}_s = - Z_{ss}^{-1} \bar{V}_s$$

$$\therefore \bar{I}_s = - Z_{ss}^{-1} \left[U + X_1 U Y_2 \right] \left[K_2 \bar{V}_{sat} \right] \quad \ldots\ldots 4.30$$

Equations 4.29, 4.30 enable the evaluation of the transform of sending-end voltage and current superimposed components due to saturation. In a similar way voltage and current components due to saturation can be obtained at any point on the system. It has to be mentioned that throughout the foregoing analysis, as well as in Fig (4.3), a single section model has been assumed. However, the 3-section feeder system can be simulated, by simply modifying Z_{SS} and Z_{RS} to Z_{SM} and Z_{RM} as previously explained in Chapter (3). Accordingly Z_{SS}, Z_{RS} have to be replaced by Z_{SM} and Z_{RM} respectively in the above analysis.

The overall system response is obtained by superposition and it is made up of:

$$\bar{V}_{SE} = \bar{V}_{SS} + \bar{V}_{Sf} + \bar{V}_{S}$$
$$\bar{I}_{SE} = \bar{I}_{SS} + \bar{I}_{Sf} + \bar{I}_{S} \quad \ldots\ldots 4.31$$

where

$\bar{V}_{SS}$, $\bar{V}_{Sf}$, $\bar{V}_{S}$ are the transforms of sending-end voltage components under steady-state condition, due to fault and due to saturation respectively.

$\bar{I}_{SS}$, $\bar{I}_{Sf}$, $\bar{I}_{S}$ are the transforms of sending-end current components under steady-state condition, due to fault and due to saturation respectively. Time variation of system overall response is obtained using the inverse Fourier transform. System response under fault-transient and saturation conditions is dealt with in Chapter (8).

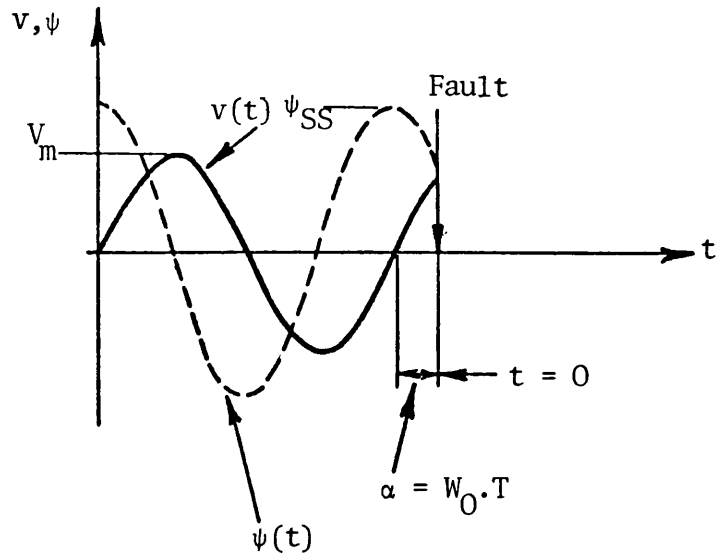

Fig 4.1

Reactor voltage and flux-linkage wave-forms.

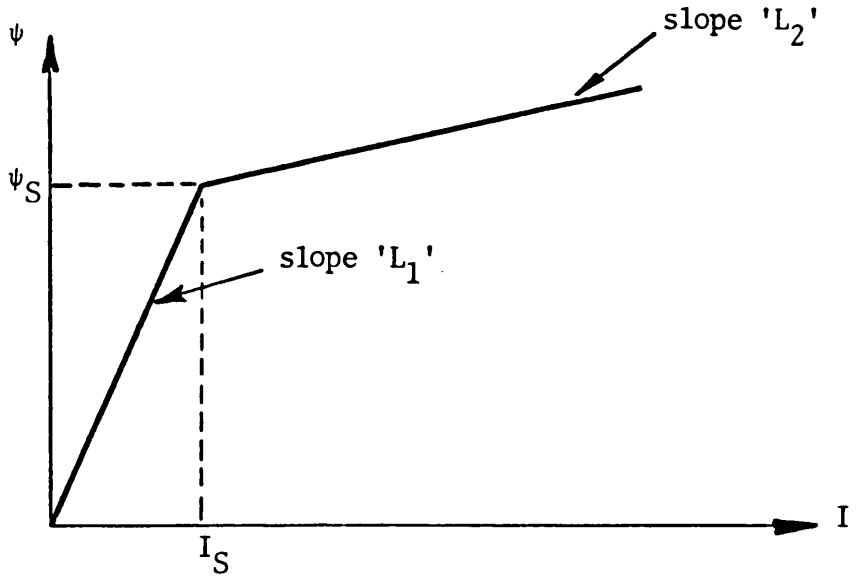

(a)

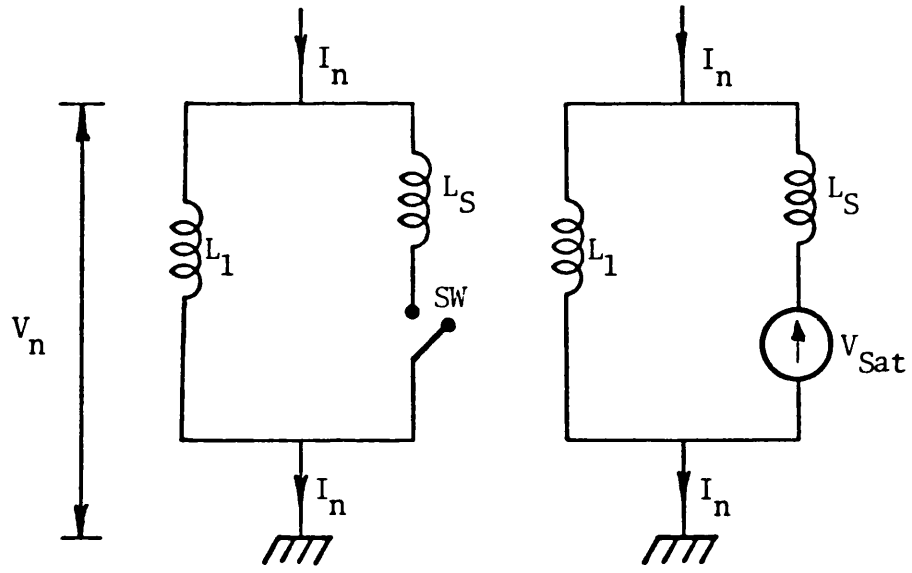

(b)

Fig 4.2

Simulation of neutral reactor saturation.
a - Piece-wise approximate ψ/I characteristic.
b - Saturation modelling circuit.

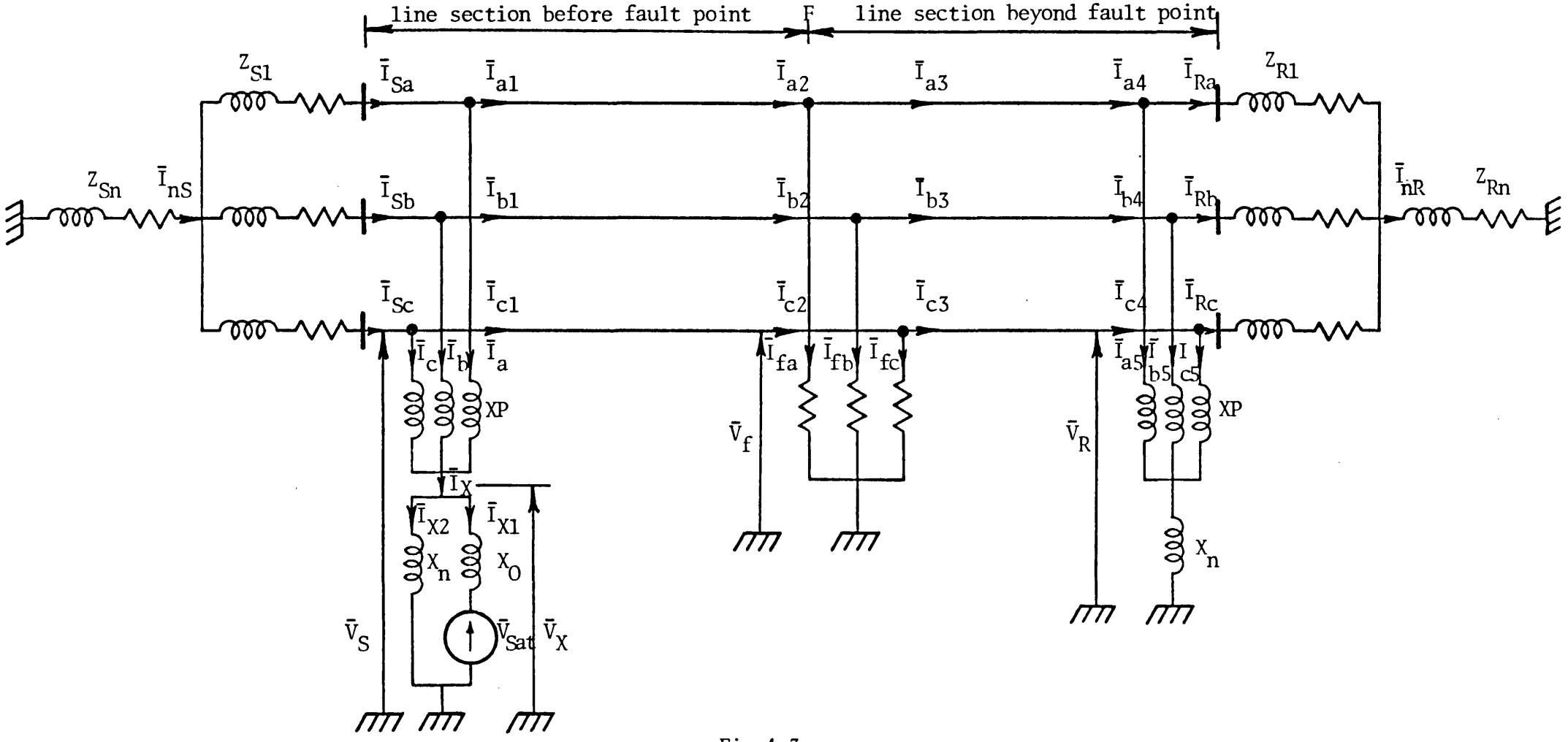

Fig 4.3

3-wire diagram fo double-end fed system under fault transient and reactor saturation conditions.

CHAPTER 5 PARAMETERS OF SYSTEMS STUDIED

5.1 Introduction

The computational results presented in Chapters 6 — 9 are for two different systems, i.e. single-section and 3-section feeder systems. Both systems comprise 500 kV, single-circuit transmission line (s) fed at its remote-ends by the main sources described in Chapter 3. Each line-section is regularly transposed through three equal intervals using the scheme developed in Chapter 3 and may be uncompensated or shunt-compensated by the 4-reactor scheme (described in Chapter 2) located at each line end.

In this Chapter the parameters of transmission line (s), shunt reactors, main sources and that used in the Fourier transform routine are presented. Also the parameters of protective relays applied to systems considered are given.

5.2 Transmission Line Parameters

5.2.1 Line construction

Line sections are of the horizontal construction shown in Fig. 5.1 and the data are as follows:

1 - Phase conductors are 2 x 84/19/0.35 cm S.C.A. with 0.45 m bundle spacing.

2 - Earth wires are 7/0.35 cm A.W..

3 - Earth resistivity = 100 Ω·m.

4 - Conductor resistance = 0.03387 Ω/km. (at power frequency)

5 - Earth wire resistance = 1.882 Ω/km. (at power frequency)

6 - Conductor reactance = 0.007865 Ω/km.(at power frequency)

7 - Earth wire reactance = 0.388 Ω/km. (at power frequency)

8 - Conductor overall radius = 9.1 cm.

9 - Earth wire overall radius = 0.64 cm.

10 - For the two systems considered, line lengths are:

a - for the single-section feeder system ℓ = 300 km;

b - for the 3-section feeder system line lengths are 400, 300 and 100 km from the sending-end to the receiving-end respectively.

5.2.2 Computed basic parameters

These are the per-unit length impedance and admittance matrices, propagation constant matrix and the line surge impedance and admittance matrices. These parameters are evaluated[55] in Appendix A1. Velocities of different modal components are also here presented. At power frequency these parameters are:

Impedance Matrix (Z):

$$(Z) = \begin{bmatrix} 0.054 + J0.45 & 0.02 + J.11 & 0.02 + J0.15 \\ 0.02 + J0.11 & 0.054 + J0.45 & 0.02 + J0.15 \\ 0.02 + J0.15 & 0.02 + J0.15 & 0.045 + J0.45 \end{bmatrix} .10^{-3} \ \Omega/m \quad \ldots\ldots 5.1$$

Admittance Matrix (Y):

$$(Y) = \begin{bmatrix} J0.33 & -J0.02 & -J0.06 \\ -J0.02 & J0.33 & -J0.06 \\ -J0.06 & -J0.06 & J0.33 \end{bmatrix} .10^{-8} \text{ } \mho/m \quad \ldots\ldots \quad 5.2$$

From equations 5.1, 5.2 the propagation constant matrix 'γ' are:[12,13]

$$(\gamma) = \begin{bmatrix} 0.085 + J1.32 & 0.06 + J1.08 & 0.06 + J1.08 \end{bmatrix}_{\text{diag.}} .10^{-6} \quad \ldots\ldots \quad 5.3$$

and

The surge impedance matrix 'Z_0' as evaluated in Appendix A2 is:

$$(Z_0) = \begin{bmatrix} 378.0 - J22.0 & 89.33 - J6.67 & 89.33 - J6.69 \\ 89.33 - J6.67 & 378.0 - J22.0 & 89.33 - J6.69 \\ 89.33 - J6.67 & 89.33 - J6.67 & 378.0 - J22.0 \end{bmatrix} \Omega \quad \ldots\ldots \quad 5.4$$

and

The corresponding symmetrical surge admittance matrix 'Y_0' is:

$$(Y_0) = \begin{bmatrix} 2.9 + J0.16 & -0.56 - J0.02 & -0.56 - J0.02 \\ -0.56 - J0.02 & 2.9 + J0.16 & -0.56 - J0.02 \\ -0.56 - J0.02 & -0.56 - J0.02 & 2.9 + J0.16 \end{bmatrix} \mho \quad \ldots\ldots \quad 5.5$$

The computed, different modes, velocity of propagation 'V' matrix is given by equation 5.6:[55,80]

$$\begin{aligned} &\text{For earth mode: } V_1 = 2.38 \times 10^5 \text{ km/s} \\ &\text{For aerial modes: } V_2 = V_3 = 2.92 \times 10^5 \text{ km/s} \end{aligned} \quad \ldots\ldots \quad 5.6$$

5.2.3 Transmission line charts

In spite of the fact that secondary arc phenomena is out of the scope of this present work, some of the charts developed by Kimbark[49] have to be plotted for the line model examined. These charts will ensure that the correct values of the closely related degrees of shunt compensation (h_1, h_0) are chosen to secure nearly zero secondary arc current and steady-state recovery voltage.

The method of evaluating these charts as developed by Kimbark[49] is briefly described in Appendix (A4).

5.2.3.1 Steady-state recovery voltage

From equation 5.2, line capacitance ratio 'k' is:

$$k = C_0/C_1 = \frac{0.236}{0.372} \simeq 0.63 \qquad \ldots\ldots 5.7$$

The steady-state recovery voltage family of curves are plotted in Fig. 5.2 and the degrees of shunt compensation associated to each value of per unit recovery voltage are shown in Table 5.1.

5.2.3.2 Secondary arc current

Plotted as a function of the degrees of shunt compensation (h_1,h_0) the loci of constant values of secondary arc current are shown in Fig. 5.3. Each number of points constituting one of the straight lines of Fig. 5.3 are calculated as described in Appendix A5 and are presented, for the family of straight lines, in Table 5.2.

Recovery Voltage (V_{rpu})	3	2	1	.9	.8	.7	.6	.5	.4	.3	.2	.1	0	-.1	-.2	-.3	-.4	-.5	-.6	-.7	-.8	-.9	-1	-2	-3
PPS degree of shunt compensation (h_1)	ZPS degree of shunt compensation (h_0)																								
0	6.6	8.9	- ∞	-43.4	-19.6	-11.7	-7.7	-5.4	-3.8	-2.6	-1.8	-1.1	-.6	-.15	-.21	.51	.77	1.0	1.2	1.4	1.5	1.7	1.8	2.6	3.0
0.25	5.2	7.0	- ∞	-32.3	-14.5	- 8.5	-5.6	-3.8	-2.6	-1.7	-1.1	- .6	-.2	.14	.41	.63	.83	1.0	1.15	1.3	1.4	1.5	1.6	2.2	2.5
0.5	3.8	5.0	- ∞	-21.2	- 9.3	- 5.4	-3.4	-2.2	-1.4	- .8	- .4	- .1	.21	.42	.60	.76	.89	1.0	1.1	1.2	1.26	1.33	1.4	1.8	2.0
0.75	2.4	3.5	- ∞	-10.1	- 4.2	- 2.2	-1.2	- .6	- .2	.1	.31	.47	.6	.71	.80	.88	.94	1.0	1.05	1.1	1.13	1.17	1.2	1.4	1.5
1.0	1.0	1.0	- ∞	1.0	1.0	1.0	1.0	1.0	1.0	1.0	1.0	1.0	1.0	1.0	1.0	1.0	1.0	1.0	1.0	1.0	1.0	1.0	1.0	1.0	1.0
1.25	-.4	-1.5	- ∞	12.1	6.2	4.2	3.2	2.6	2.2	1.9	1.7	1.5	1.4	1.3	1.2	1.12	1.06	1.0	.95	.91	.87	.83	0.8	.60	.50

Table 5.1

Steady-state recovery voltage as a function of h_1 , h_0.

I_{rpu}	.35	.3	.25	.2	.15	.1	.05	0	-.05	-.1	-.15	-.2	-.25	-.3	-.35
h_1	ZPS degree of shunt compensation (h_0)														
0	-2.25	-2.02	-1.78	-1.54	-1.3	-1.06	-.83	-.6	-.35	-.11	0.127	.365	.603	.841	1.08
0.25	-1.86	-1.62	-1.38	-1.14	-.90	-.67	-.43	-.19	.048	.29	.524	.762	1.0	1.24	1.48
0.5	-1.46	-1.22	-.98	-.75	-.51	-.27	-.03	0.21	.44	.68	0.92	1.16	1.4	1.64	1.87
0.75	-1.06	-.83	-.59	-.35	-.11	0.13	0.37	0.6	.84	1.08	1.32	1.56	1.79	2.03	2.27
1.0	-.67	-.43	-.19	0.05	0.29	0.52	0.76	1.0	1.24	1.48	1.71	1.95	2.19	2.43	2.67
1.25	-.27	-.03	0.21	0.44	0.68	0.92	1.16	1.4	1.64	1.87	2.11	2.35	2.59	2.83	3.06

Table 5.2 Residual arc current as a function of h_1 , h_0

V_{rpu} & I_{rpu}	h_1	h_0	X_1 (Ω)	X_n (Ω)	X_n/X_1	L_1 (H)	L_n (H)	I_{ms} (A)	I_{ns} (A)
0	0.5	0.21	3536.7	1076.8	0.304	11.26	3.43	207.72	203.6
0	0.75	0.60	2357.8	757.2	0.321	7.5	2.41	311.4	289.6
0	1.0	1.0	1768.35	336.48	0.19	5.63	1.07	415.55	651.45
0	1.25	1.4	1414.7	189.82	0.134	4.5	0.6	519.48	1154.8

Table 5.3 Parameters of the 4-reactor scheme applied to 300 km line.

- V_{rpu} , I_{rpu} = perunit values of recovery voltage and secondary arc current.
- I_{ms} , I_{ns} = saturation currents of phase and neutral reactors.

From table 5.3, saturation flux linkages of phase and neutral reactors are:

$$\psi_{ms} = 3.34 \times 10^3 \quad \text{W.T.}$$
$$\psi_{ns} = 698.35 \quad \text{W.T.} \qquad \ldots\ldots 5.9$$

5.3 Shunt-Reactor Parameters[23,34]

In this section, the calculated reactor parameters are presented. These include reactor rating, phase and neutral reactances, knee-point voltages and saturation currents and flux linkages.

Knee-point[34] voltage of phase-reactors = $1.8 \times \frac{500\sqrt{2}}{\sqrt{3}} = 734.85$ kV

Knee-point[34] voltage of the neutral reactor = $155\sqrt{2} = 219.2$ kV

For a 300 km line and 100% reactive power compensation, the 3-phase MVAR rating of the reactor is:

$$Q_{SR} = 141.38 \text{ MVAR} \qquad \ldots\ldots 5.8$$

A 'Q ' factor of 250 was assumed for neutral and phase reactors.

Equations 2.12 were used to calculate Xn, X_1 and they are tabulated together with other reactor parameters for different degrees of shunt compensation in Table 5.3. The parameters shown in the table are for one, 300 km line reactor.

5.4 Main Source Parameters[54]

Sources short-circuit levels = 5 - 35 GVA

Sources X/R ratio (Q factor) = 30 - 100

Sources (Z_0/Z_1) = 0.25 - 2.5

5.5 Fourier Transform Parameters[88-91]

Observation time 'TOB' = 32 - 128 ms

Frequency shift constant 'α' = 250 - 62.5

For TOB = 32 ms α = 250

For TOB = 64 ms α = 125

For TOB = 128 ms α = 62.5

Number of samples 'NS' = 256 or 512

For 256 samples, truncation frequencies are:

Truncation Frequency 'Ω' : TOB = 32 ms, Ω = 4.0 k Hz

TOB = 64 ms, Ω = 2.0 k Hz

TOB = 128 ms, Ω = 1.0 k Hz

5.6 Protective Relay Parameters

In the present analysis, zone (1) relays with a setting of 80% are considered and the characteristics are arranged so that the diameter of the nominal mho circle has an argument which is 10^{o} less than that of the line positive phase sequence impedance.

Typically[57], the nominal C.T. ratios are 1/1200 and the V.T. ratios are 110/500 x 10^3, for a 500 kV system.

Responses have been obtained for a level of sound-phase polarisation equal to 10% of the sound phase voltage or voltages[57], and the comparator has a setting voltage of 0.1 V.

From equation (5.1) we have:

$$Z_1 = (0.034 + J0.31)\ 10^{-3}\ \Omega/m$$
$$Z_0 = (0.094 + J0.73)\ 10^{-3}\ \Omega/m \qquad \ldots\ldots 5.10$$

According to the relay specifications mentioned above, the impedance of the line protected is:

$$|ZL_1| = 0.8 \times 300 \times 0.312 = 74.88\ \Omega \qquad \ldots\ldots 5.11a$$

and the line angle 'θ' is

$$\theta = \tan^{-1} 0.31/0.034$$
$$\theta = 83.74^{o} \qquad \ldots\ldots 5.11b$$

and the mho characteristic argument is

$$\phi T = 73.74^{o} \qquad \ldots\ldots 5.11c$$

The mho characterstic of the relay is shown in Fig. 5.4, from which:

$$|Z_r| = 76.0\ \Omega \qquad \ldots\ldots 5.11d$$

Using equation (A6.2.C), with N = 1,

$$\therefore \quad |\acute{Z}_r| = \frac{110}{500 \times 10^3} \times 1200 \times 76.0 = 20.064\ \Omega \qquad \ldots\ldots \text{5.12a}$$

and from equation (A6.1.C),

$$|\acute{Z}_r| = \frac{Xm}{\sqrt{1+\cot^2 \phi T}} \quad \text{or} \quad Xm = |\acute{Z}_r| \cdot \sqrt{1+\cot^2 \phi T}$$

$$\therefore \quad Xm = 20.064 \sqrt{1+\cot^2 73.74^{o}}$$

$$\text{i.e} \quad Xm = 20.9\ \Omega \qquad \ldots\ldots \text{5.12b}$$

$$\therefore \quad Lm = \frac{Xm}{W_0} = \frac{20.9}{314.2} = 66.52\ \text{mH} \qquad \ldots\ldots \text{5.12c}$$

But $R_b = N^2\ Xm \tan \phi T = 20.9 \times \tan 73.74$

$$\therefore \quad R_b = 71.663\ \Omega \qquad \ldots\ldots \text{5.12d}$$

For a-e fault, the signal S_1 of equation (A5.2) is

$$S_1 = (Ia + K.I\ res).Z_r$$

where K is the residual compensating factor which is given by

$$K = \frac{1}{3} \left| Z\ L_0 / ZL_1 - 1 \right|, \quad \text{and}$$

$$\frac{ZL_0}{ZL_1} = \frac{0.094 + J0.73}{0.034 + J0.31} = \frac{(0.094 + J0.73)\ (0.034 - J0.31)}{(0.034 + J0.31)\ (.034 - J0.31)}$$

$$\therefore \quad \frac{ZL_0}{ZL_1} = 2.36 - J0.044$$

$$|ZL_0/ZL_1| = 2.36$$

$$\therefore \quad K = \frac{1}{3}(2.36 - 1) = 1.36/3$$

$$\text{or} \quad K = 0.4533 \qquad \ldots\ldots \quad 5.13$$

The parameters evaluated in this section, i.e. θ, ϕ T, Z_r, R_b, K, etc., together with the parameters of the polarising phase-shift circuit (RP = 3.18 k Ω, CP = 1 μ F), have been used as input data to the computer programs developed to evaluate the transactor and the polarising component voltages, and hence signals S_1 and S_2. The digital evaluation of these signals is based on the step-by-step technique described in Appendix A5 utilising equations A5.12 and A5.21.

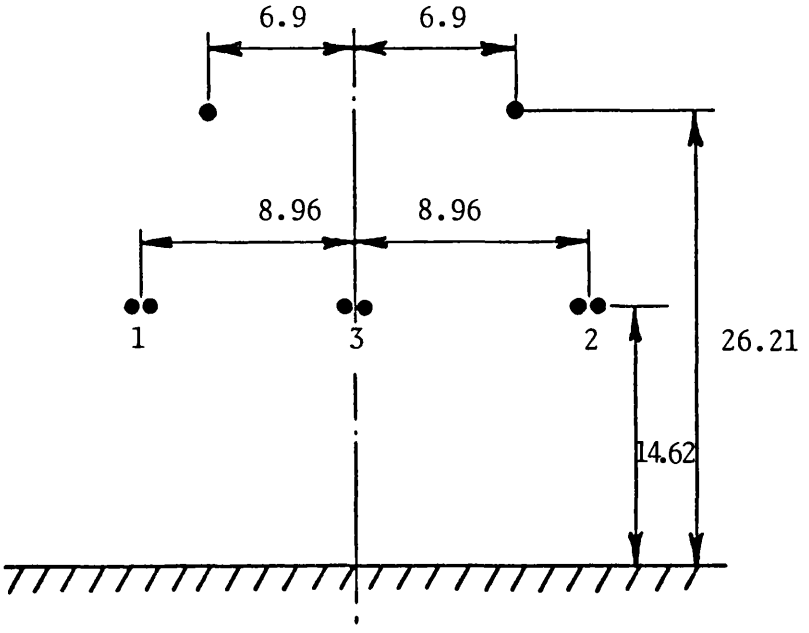

Fig 5.1

Transmission line construction.
- Distances are in meters.

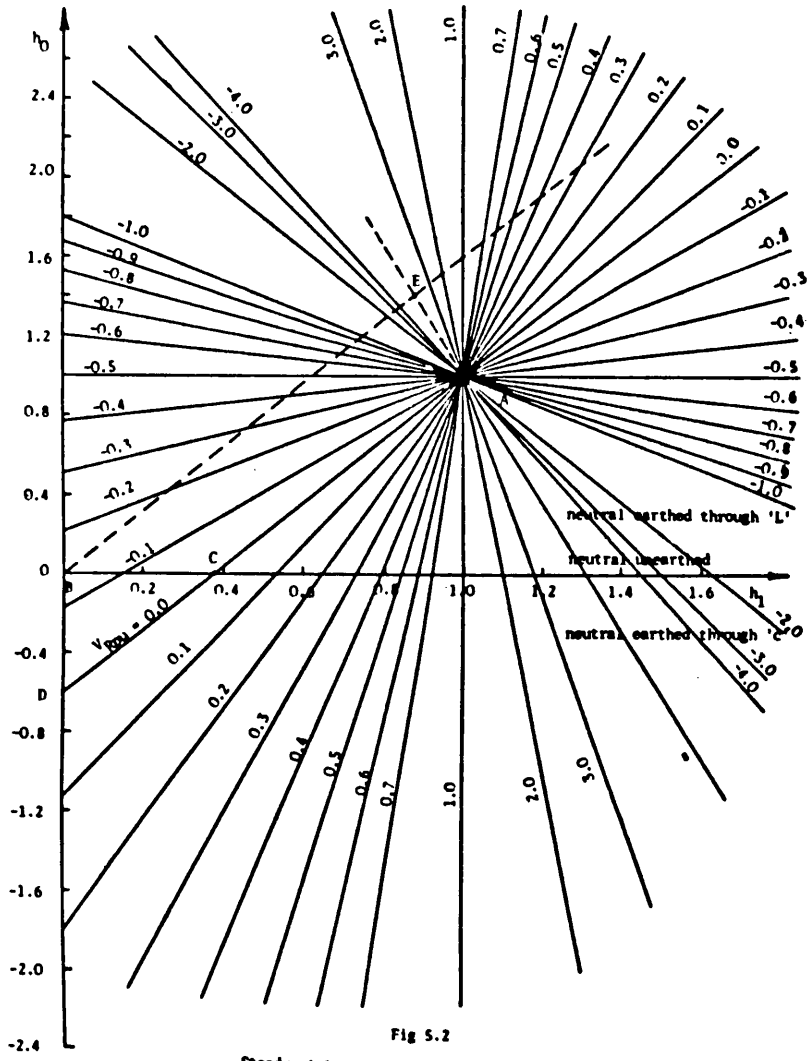

Fig 5.2

Steady-state recovery voltage chart.
- $K = c_0/c_1 = 0.63$

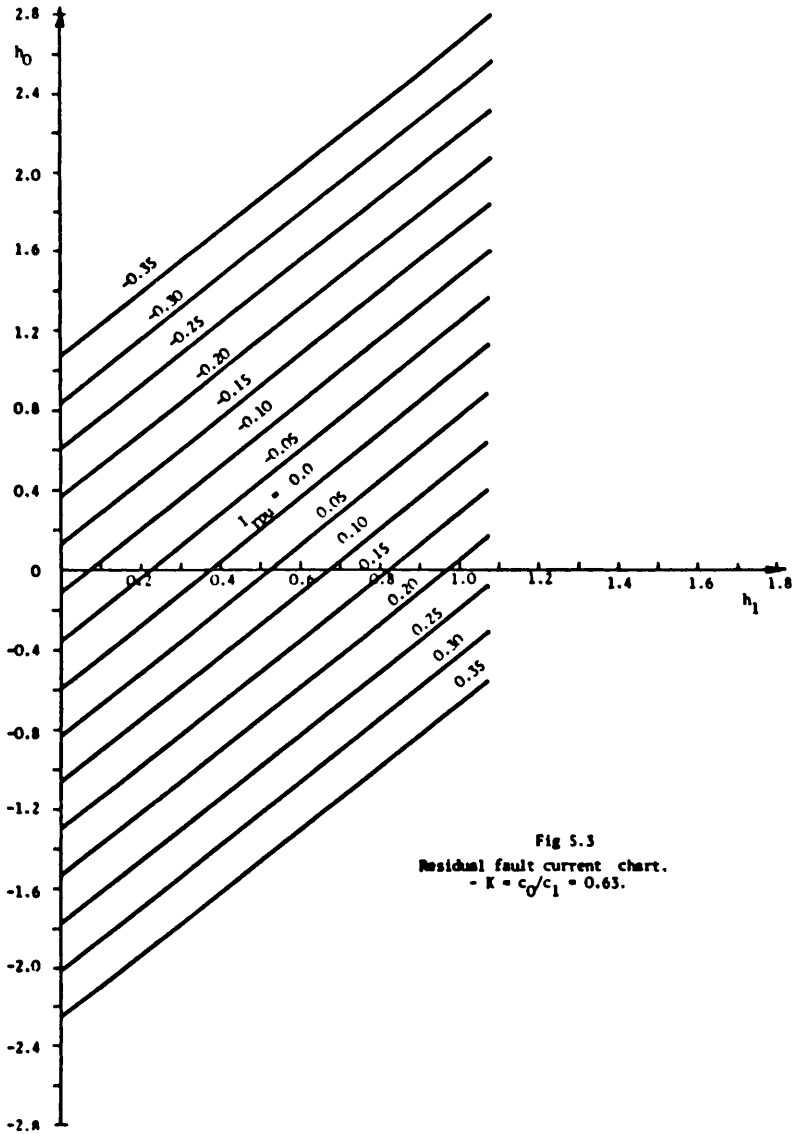

Fig 5.3

Residual fault current chart.
- $K = c_0/c_1 = 0.63$.

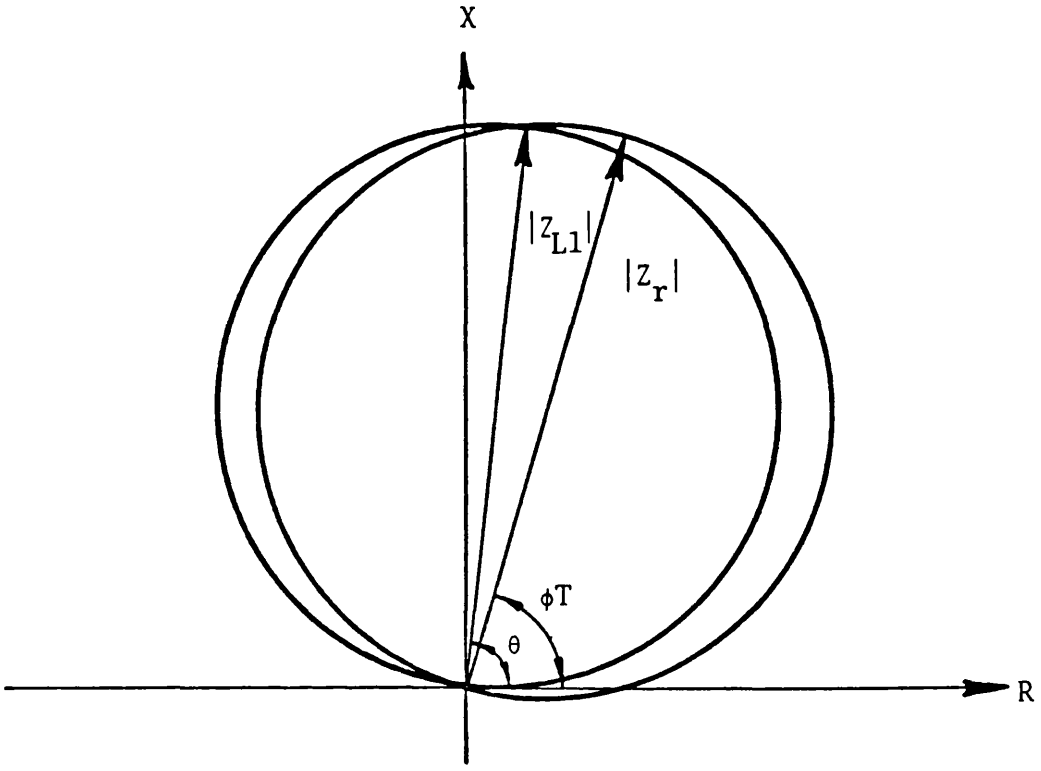

Fig 5.4

mho characteristic of the relay protecting 80% of a 500 kv, 300 km line model.

CHAPTER 6 DIGITAL EVALUATION OF PRIMARY SYSTEM WAVE FORMS

6.1 Introduction

In this chapter the mathematical models of the two basic system configurations considered, as developed in Chapters 2 and 3, are used to obtain primary system response. In the first system (single-section feeder system) faults are initiated and primary voltage and current wave forms at the relaying points (particularly at the sending-end busbar) are computed. In the 3-section feeder system , faults on the middle line-section are initiated and the response, particularly at the sending-end busbar of that section, is evaluated. In this way the differences between the responses of the two systems can be examined. The parameters of different system elements as used in the digital computer program were described in Chapter 5 and faults were simulated as described in Appendix A3.

It has been shown[53,54] that various factors such as fault position, fault time, source parameters, prefault loading, type of fault ... etc. can considerably affect travelling wave distortion in the wave forms associated with faults in uncompensated single-section feeder systems. Since such distortion affects system fault induced overvoltages (Chapter 7) and the performance of system protective relays (Chapter 9), it was felt necessary to consider the effect of the above mentioned factors in this present analysis.

6.2 Response of Single-Section Feeder Systems

6.2.1 Effect of fault position

Figs. 6.1 - 6.3 show sending-end wave forms for a solid a-e fault at the sending-end, the mid-point and the receiving-end of the line respectively. The system is assumed to be under steady-state conditions before the disturbance and the fault occurs when the pre-fault a-e voltage 'Va' is at its positive peak.

For a close-up fault (Fig. 6.1) it is expected that the a-e sending-end voltage drops to zero at the moment of fault inception. However, as may be seen from Fig. 6.1a, the a-e voltage drops to zero but not at the same time as the fault takes place (FT = 5ms). Instead, some time delay (≃.125ms) is observed in the occurrence of such change and this is due to the time delay inherent to the modified Fourier transform technique. From Fig. 6.1b the faulted-phase current 'Ia' appears to reach a peak value of about 57.5 kA. In fact the correctness of this figure can be roughly checked by the knowledge of system peak voltage (408.25 kV), and the sending-end source positive phase sequence impedance Zs_1, (≃ 7.14Ω). Currents in the sound phases are also disturbed because of the mutual electromagnetic and electrostatic coupling between phases. As the fault position advances along the line away from the observation point, travelling-wave phenomena becomes more prominent and this can be seen by comparing the wave forms of Fig. 6.2 to that of Fig. 6.3. Both diagrams confirm the fact that[53,54] earth mode dominates the faulted phase wave forms

while aerial modes dominate the wave forms of healthy phases. Fig. 6.2a clearly shows that initially, the transit time from the fault to the sending-end is about 1.25 ms, which is obviously correct for an earth mode to travel from the mid-point of the line to the sending-end and back to the fault point with an effective velocity of about 2.4×10^5 km/s (see equation 5.6). The corresponding time for a fault at the receiving-end (Fig. 6.3a) is about 2.6 ms.

As transit time increases, the apparent frequency of the superimposed travelling-wave components decreases and it follows that these components are damped relatively slower for more distant faults (Figs. 6.2, 6.3). The different velocities of propagation of the earth and the dominant aerial modes are obvious from the frequency of occurrence of the ripples on the sound phase voltages of Figs. 6.1 - 6.3. The faulted phase currents 'Ia' of Figs. 6.2b and 6.3b can be seen to reach about 5 and 3.2 kA respectively. Again, the correctness of these currents can be roughly checked from the knowledge of the peak phase voltage ($\simeq$408 kV), the sending-end source impedance Zs_1($\simeq$7.14Ω) and the line self and mutual impedances ($\simeq$ .45 and 0.11 Ω / km respectively). Due to coupling, the sound phase currents of Figs. 6.2b - 6.3b are also affected and the same travelling-wave principle is applied to both faulted and healthy-phase currents.

6.2.2 Effect of fault inception time

Faults at an instant of time corresponding to the peak voltage of the faulted phase produce maximum travelling-wave distortion[53,54,48]

as shown in Figs. 6.1 - 6.3. Faults at an instant of time corresponding to zero faulted phase voltage-to-earth, however, produce maximum offset of the wave forms particularly the currents. In such cases, travelling-wave distortion is significantly reduced because there is not that large or sudden voltage change at the point of fault. This can be observed from Fig. 6.4 for a solid a-e fault under the same conditions as that of Fig. 6.2 except that the fault occurs when Va = 0 (FT = 10 ms). The Fig. clearly shows that travelling-wave phenomena are relatively insignificant and the very well known offset nature of the currents is produced.

6.2.3 Effect of source parameters

The results presented so far assume two large source capacities, 35 GVA each at both line ends respectively. However, in practice, this is rarely, if ever, the case and hence, assuming a low capacity source at one end and a large capacity source at the other end may reveal the effect source capacities have on the wave forms at the observation point. This may be shown from Fig. 6.5 for a solid a-e fault under the same fault conditions as that of Fig. 6.2 except that the capacity of the sending-end source is reduced from 35 to 5 GVA.

Comparing the two Figs. clearly shows that a low source capacity at the observation point significantly increases the distortion of the wave forms, particularly the voltages. This finding can be explained in terms of travelling-wave reflections as affected by the terminating

networks. For example, in an open-ended line, the terminating impedance is nearly infinity and all the incident waves are reflected, i.e. a reflection factor of nearly unity is obtained in this case. The extreme case is a short-circuited line at the terminating busbar, i.e. nearly zero terminating impedance and the reflected waves[18] will be of the same magnitudes but of opposite sign to the incident waves.

In other words, a low source capacity (high source impedance) near the observation point forms a major point of electrical discontinuity from which high frequency components are easily reflected - Fig. 6.5. The opposite is true when the source capacity near the observation point is large - Fig. 6.2.

It has also been found that, for earth faults, the magnitude of travelling-wave components is significantly affected by the magnitude of the zero-sequence source impedance zs_0. In the above mentioned results, the ratio (zs_0/zs_1) was assumed to be unity. However, other values were assumed (typically $(zs_0/zs_1) = 0.25 - 2.5$) and the results obtained indicated that for lower (zs_0/zs_1), the magnitude of the superimposed travelling-wave components is relatively low. This again can be explained by the effect the sending-end source has on the reflections of the incident waves. In other words, for an earth fault, the dominant earth-mode component of the voltage wave is more readily absorbed by the source if its zero-sequence impedance is low.

6.2.4 Effect of prefault loading

In case of uncompensated long lines, line capacitance can no longer be neglected. Due to the relatively high capacitance of long lines, the voltage at any point along an uncompensated line becomes dependent on line loading. The voltage rise at an open end of uncompensated long line is a good example.

Even if 75% of line capacitance is compensated by shunt reactors, the uncompensated line capacitance can still affect the wave forms at the sending-end of a prefault loaded line. This can be seen from Fig. 6.6 for a solid a-e mid point fault, under the same conditions as that of Fig. 6.2 except that a prefault loading corresponding to a load angle 'δ' = 30^{o} is assumed. Both voltage and current wave forms are relatively more distorted in case of a prefault loaded line - Fig. 6.6. Due to coupling, the wave forms of the healthy phases are also affected.

Other remarks concerning travelling-wave content of healthy and faulted phases voltage and current wave forms (applied to Fig. 6.2) also apply to Fig. 6.6.

6.2.5 Effect of type of fault

So far an earth fault involving phase 'a' and the ground has been considered. However, system response under other shunt asymmetrical faults (2-line-to-earth, line-to-line and earth faults involving other phases, 'b', 'c') has been computed.

Figs. 6.7-6.8 show an earth fault involving phases 'a, b' and a solid a-b fault respectively. For both faults, line prefault loading corresponds to a load angle $\delta = +30^{o}$ and faults occur when Vab is at its positive peak.

Other fault conditions are similar to that of Fig. 6.6. Apparently, earth-mode voltage and current components dominate the faulted phases (a,b) of Fig. 6.7, while aerial modes dominate the healthy phase wave forms. Again, this may be observed from the more frequent, slower attenuated and the less frequent, more rapid attenuated travelling-waves in the healthy phase and the faulted phases respectively. For the pure phase fault of Fig. 6.8, a very remarkable difference can be observed. The Fig. shows that these faults produce more wave distortion, which, due to the dominant aerial modes (in the waves of all phases), takes relatively longer time to disappear.

Fig. 6.9 shows the wave forms when a solid 'b-e' fault is initiated under the same conditions as that of Fig. 6.2. A comparison of the two responses clearly indicates that the system responds in a predictable way when subjected to different single line to ground faults.

6.2.6 Effect of degrees of shunt compensation

As one of the primary objectives of this work is to examine the effect of shunt compensation on primary system response, different degrees of shunt compensation (h_1, h_0) have been chosen and system responses were computed. The positive degrees of compensation used are (h_1 = 0, .25, 0.5, .75, 1.0, 1.25) and the corresponding zero-sequence degrees of

compensation that theoretically produce zero secondary arc currents and steady-state recovery voltage (excluding the uncompensated case) are respectively(h_0 = 0, -0.19, 0.21, 0.6, 1.0, 1.4)as may be seen from table 5.3.

Digital computer results showed that, in general, the patterns of primary system wave forms are hardly affected by the degrees of shunt compensation over the whole range (h_1 = 0 - 1.25). For example, Figs. 6.10 and 6.11 show the wave forms for an uncompensated system (h_1 = h_0 = 0) and that of an over-compensated system (h_1 = 1.25, h_0 = 1.4). A comparison of these two Figs. with that of Fig. 6.5, (h_1 = .75, h_0 = .6) confirms the above mentioned facts, i.e. no significant change in the profile of system wave forms when h_1 increased from zero to 1.25. However, the magnitudes of the currents of Figs. 6.10, 6.5 and 6.11 are affected, being less for higher degrees of compensation (h_1). Both the prefault and post-fault currents are reduced with the increase of h_1 and this can be particularly seen from the sound phase currents since the faulted phase current is very high by comparison with the prefault line charging current.

6.2.7 Primary response at other relaying points

To examine the effect of the above mentioned factors on the receiving-end voltage and current wave forms, a similar series of studies have been carried out and some of the computed results are here presented. The effect of fault position and inception time is shown in Figs. 6.12 and 6.13 respectively. Figs. 6.14 and 6.15 respectively show the

effect of prefault loading and source capacities while the effect of degrees of shunt compensation on the receiving-end wave forms is shown in Fig. 6.16 - 6.18. The discussion concerning the effect of these factors as explained in sections 6.2.1 - 6.2.6 above, also apply to the wave forms of Figs. 6.12 - 6.18.

6.3 Response of 3-Section Feeder Systems

In this section, a series of studies similar to that presented in section 6.2 have been carried out mainly to determine any differences between the responses of single-section and 3-section feeder systems. In addition, the influence of the various factors (described in section 6.2) on the response of 3-section feeder systems is considered.

6.3.1 Effect of fault position

As previously mentioned in section 6.2.1, as the point of fault becomes more distant from the observation point, travelling-wave phenomena can easily be recognised and the occurrence of the ripples in the wave forms, particularly the voltages, becomes less frequent due to the larger transit times involved. This can be observed from the wave forms of Fig. 6.19 for a solid a-e fault at the mid-point of the middle line section of the 3-section feeder system. Fault conditions are typically the same as that of Fig. 6.2.

Comparison of the two responses of Figs. 6.2 and 6.19 reveals that there is a very remarkable difference between the two responses. The voltage wave forms can be seen to differ significantly and, most importantly, the wave forms associated with the fault on the 3-section feeder system are very considerably more distorted than is the case for the single-section feeder system. The reason for this is that travelling-waves of current set up in the 3-section feeder successively propagate from the fault through the observation point along the 400 km line towards the sources at that remote end of the system and are partially reflected back through the observation point producing relatively high levels of travelling-wave distortion. It follows that transit times between the point of fault and the observation point are relatively higher for the case of Fig. 6.19 than that for the fault of Fig. 6.2. This means that the apparent frequency of travelling-wave components is relatively lower in 3-section feeder than is the case for 1-section feeder. But system damping is much higher at higher frequency which means that travelling-wave distortion is damped much more slowly in 3-section feeder systems - Fig. 6.19. Other remarks applied to Fig. 6.2 apply also to Fig.6.19.

6.3.2 Effect of fault inception time

The effect of fault instant is shown in Fig. 6.20 for a mid-point, solid a-e fault in the middle-section of the 3-section feeder system. The fault occurs when the prefault a-e voltage is zero. Other fault conditions are the same as that of Fig. 6.4. Although such fault instants produce minimum travelling-wave distortion, a marked difference can still be observed between the responses of single and

3-section feeder systems of Figs. 6.4 and 6.20 respectively. The faulted phase voltage of Fig. 6.20 in particular is shown to be different to that of Fig. 6.4.

6.3.3 Effect of source parameters

The studies of section 6.2.3 indicated that lower capacities and higher (zs_0/zs_1) ratio of the source near the observation point significantly increase travelling-wave distortion. This has also been found to be the case for a 3-section system and the effect of source capacity can be observed by comparing Fig. 6.21 to Fig. 6.19. The two responses are under the same fault conditions except that in the former, sending-end source capacity is 5 GVA. Apparently the voltage and current wave forms of Fig. 6.21 are relatively more distorted. Furthermore, comparing the response of Fig. 6.21 to that under the same fault conditions in single-section feeder (Fig. 6.5) will reveal the difference between the two responses. It can be seen that the frequency of travelling-wave components of Fig. 6.21 is much lower due to the longer travelling distances involved. Also the Fig. shows that these components are damped much more slowly relative to that of Fig. 6.5.

The same remarks concerning the effect of (zs_0/zs_1) discussed in section 6.2.3, also apply to the 3-section feeder case.

6.3.4 Effect of prefault loading

Fig 6.22 shows the wave forms at the sending-end of the middle line

section when a solid, a-e, mid-point fault occurs under the same conditions as that of Fig. 6.19, except that in the former case the line is prefault loaded, $\delta = +30^{o}$. It can be observed from Fig. 6.22 that travelling-wave distortion remarkably increased with line loading. This finding further confirms the fact that in long lines the voltage at any point depends on line loading.

The difference between responses of single and 3-section feeder systems can be seen from Figs. 6.6 and 6.22 respectively. In the latter case, Fig. 6.22 indicates that due to the long travelling distances involved, the response of 3-section feeder system is relatively more distorted.

6.3.5 Effect of type of fault

Figs. 6.23 and 6.24 show the wave forms at the sending-end of the middle line section for a solid 'b-c-e' and 'b-c' faults respectively. The 'b-c-e' fault occurs under the same conditions as that of Fig. 6.19 while the 'b-c' fault occurs under the same conditions as that of Fig. 6.21. As previously explained, Fig. 6.23 clearly shows that, for faults involving the earth, earth mode dominates the faulted phases wave forms while aerial modes dominate the wave forms of the healthy phase. Fig. 6.24 on the other hand shows that due to the dominant aerial modes in the wave forms of all phases, travelling-wave phenomena persist considerably longer than is the case for faults involving the earth - Fig. 6.23. Again, because of the longer transmission distances involved, the wave forms of Figs. 6.23 and 6.24, particularly the faulted-phases wave forms, are relatively

more distorted and more slowly attenuated compared to the respective wave forms of Figs. 6.7 and 6.8.

6.3.6 Effect of degrees of shunt compensation

In section 6.2.6, it was found that the degrees of shunt compensation do not affect the response of a single-section feeder system. In 3-section feeder systems, however, the degrees of compensation were found to slightly affect primary system response. This can be observed by referring to Figs. 6.25, 6.21 and 6.26 where the positive phase sequence degree of compensation h_1 = .25, .75 and 1.25 respectively. The faulted phase voltage in particular obviously becomes more distorted as the degree of shunt compensation increases. Again, the difference between the responses of the single and 3-section feeder systems can be observed by comparing Figs. 6.21 and 6.26 to Figs. 6.5 and 6.11 respectively.

6.3.7 Primary response at other relaying points

The primary system wave forms presented so far have been computed at the sending-end of the middle line section. A similar set of results were obtained and the effect of the factors described in sections 6.3.1 - 6.3.6 on the receiving-end wave forms of that line section was examined. Some of these results are presented in this section where the remarks applied to Figs. 6.19 - 6.26 also apply to the corresponding Figs. presented below.

The effect of fault location and fault instant is shown in Figs. 6.27 and 6.28 respectively. Fault conditions are similar to that of Figs. 6.19 and 6.20 respectively. The effect of source capacities and prefault loading is shown in Figs. 6.29 and 6.30, where faults occur under conditions similar to that of Figs. 6.21 and 6.22 respectively.

The receiving-end wave forms for 'b-c-e' and 'b-c' faults are shown in Figs. 6.31 and 6.32. Fault conditions are typically the same as that of Figs. 6.23 and 6.24 respectively. The effect of different degrees of shunt compensation under the same fault conditions as that of Figs. 6.25 and 6.26 is shown in Figs. 6.33 and 6.34 respectively.

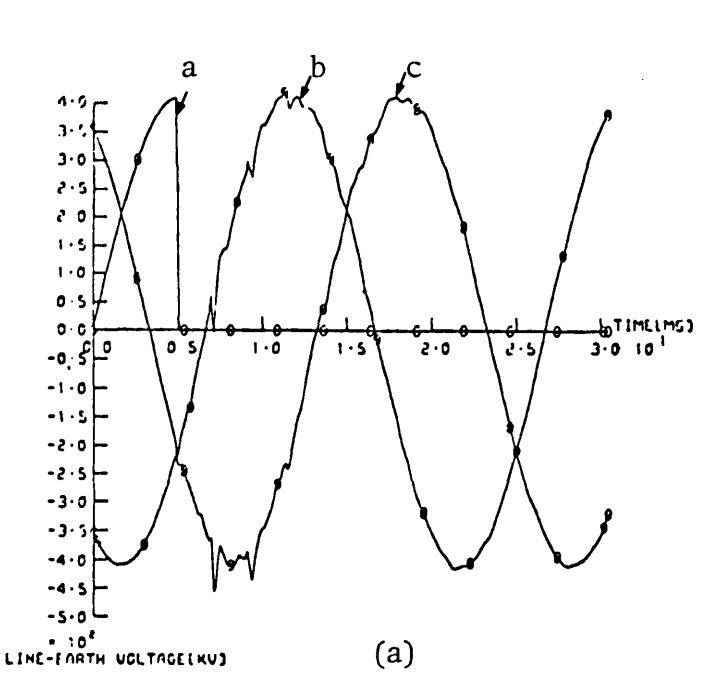

(a)

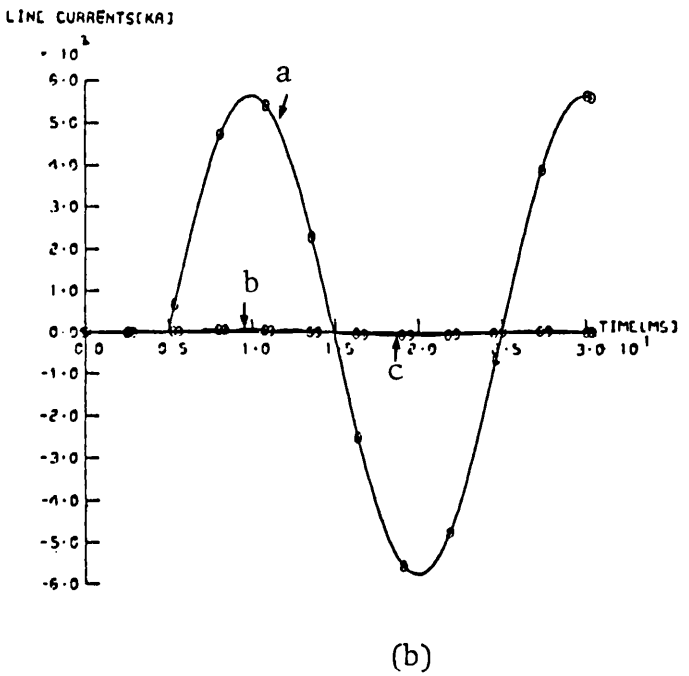

(b)

Fig 6.1

Voltage and current wave-forms at the S.E. of the single-section feeder system examined.

- Solid 'a-E' fault.

$X = 0$, FT = 5 ms, $V_S/V_R = 0^o$

$Z_{SSO}/Z_{SS1} = Z_{RSO}/Z_{RS1} = 1.0$

S.S.C.L. = R.S.C.L. = 35 GVA

$Q_S = Q_R = 100.0$

$h_1 = 0.75$, $h_0 = 0.6$

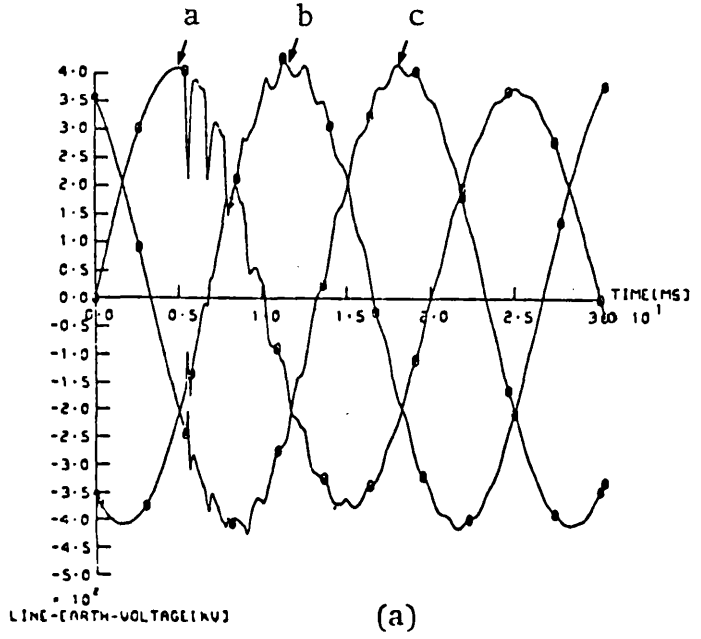

(a)

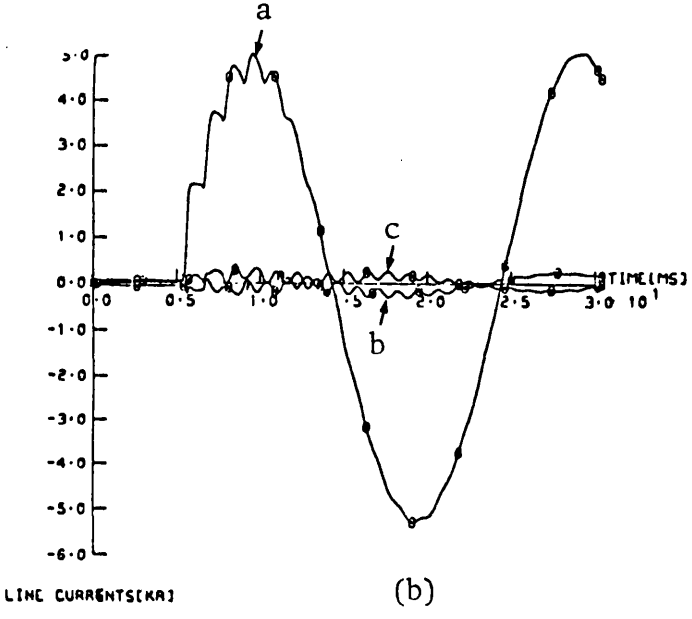

(b)

Fig 6.2

Voltage and current wave-forms at the S.E. of the single-section feeder system examined.

- Solid 'a-E' fault.
- $X = \ell/2$ (150 km).
- Other fault conditions are similar to that of Fig 6.1.

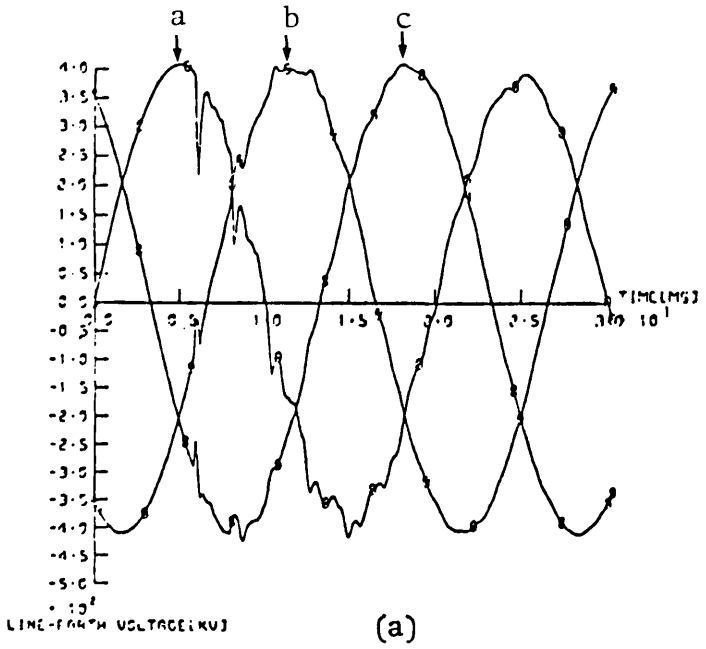

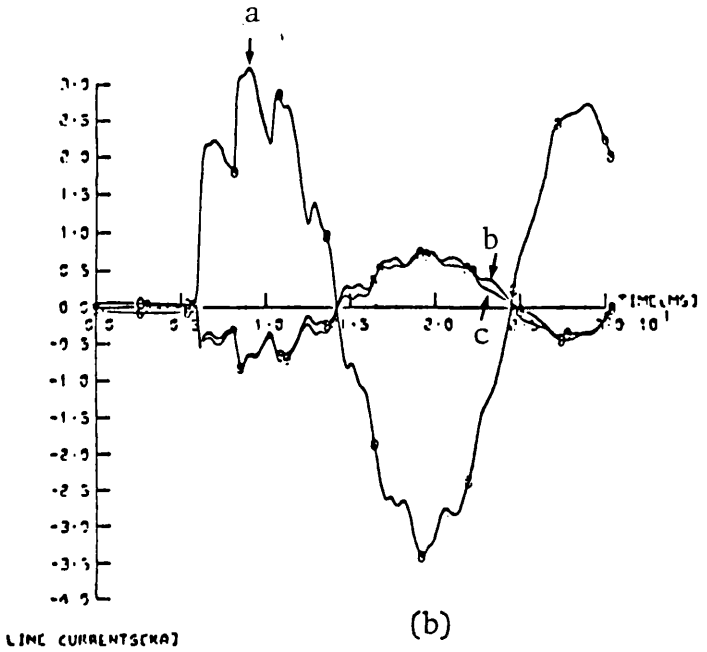

Fig 6.3

Voltage and current wave-forms at the S.E. of the single-section feeder system examined.

- Solid 'a-E' fault
- X = ℓ (300 km)
- Other fault conditions are similar to that of Fig 6.1.

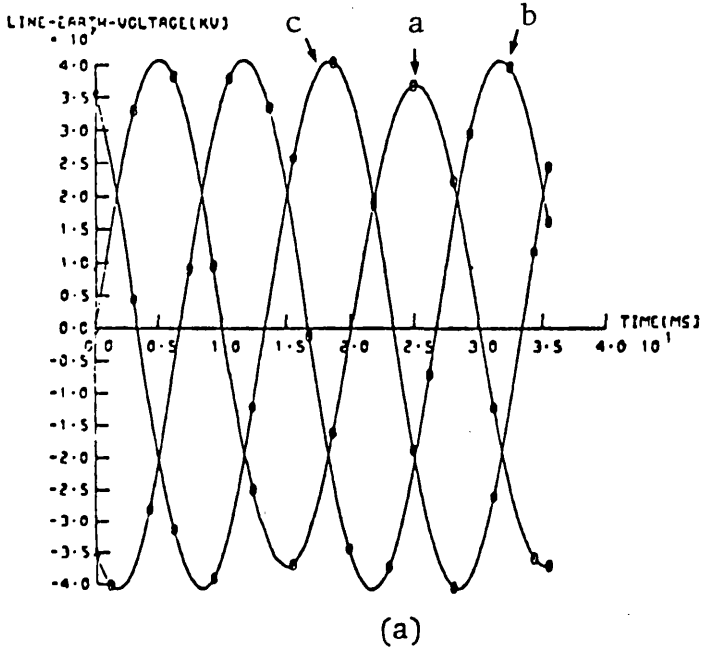

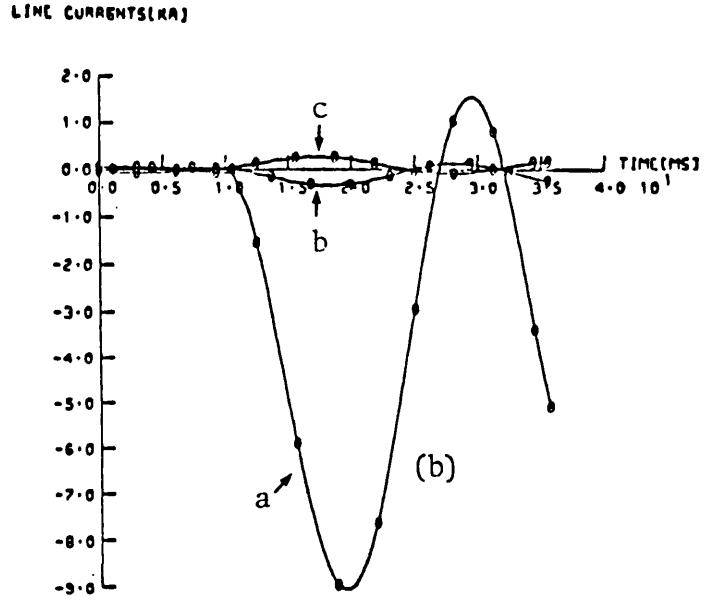

Fig 6.4

Voltage and current wave-forms at the S.E. of the single-section feeder system examined.

- Solid 'a-E' fault
- FT = 10.0 ms
- Other fault conditions are similar to that of Fig 6.2.

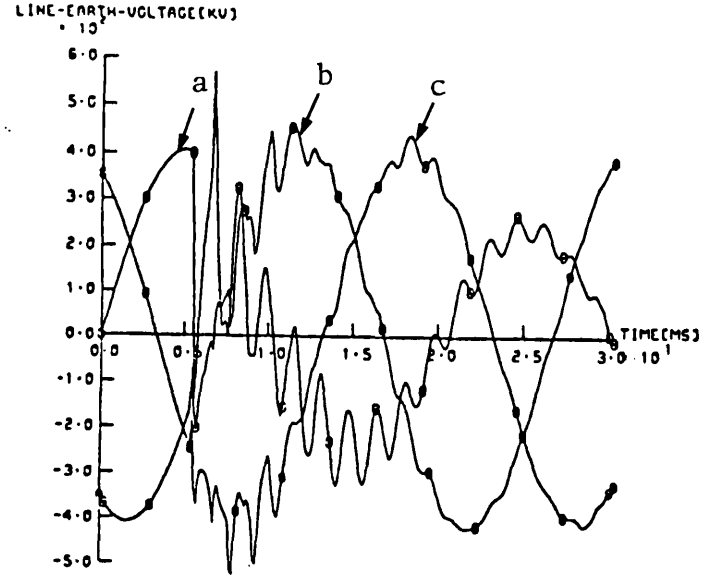

(a)

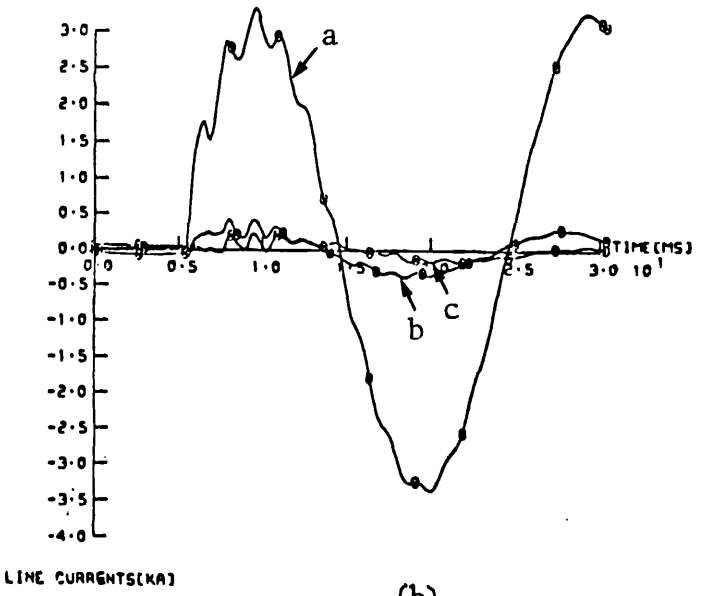

(b)

Fig 6.5

Voltage and current waveforms at the S.E. of the single-section feeder system examined.

- Solid 'a-E' fault.
- S.S.C.L. = 5 GVA
- Other fault conditions are similar to that of Fig 6.2

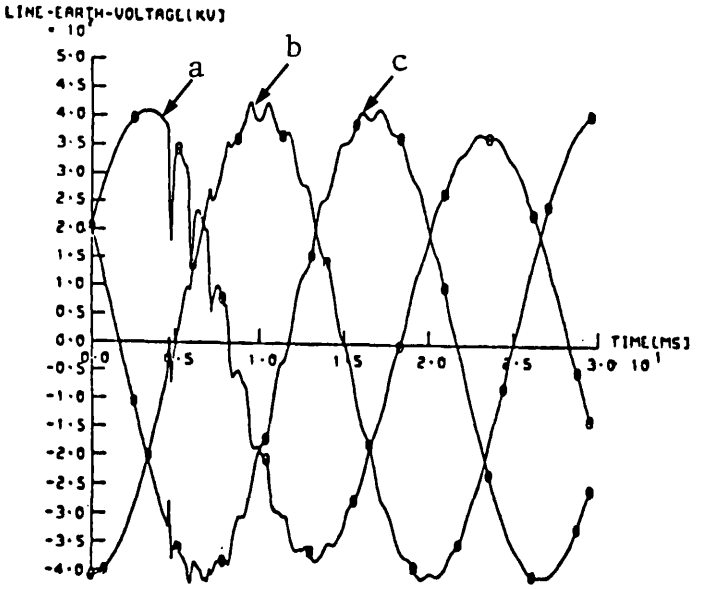

(a)

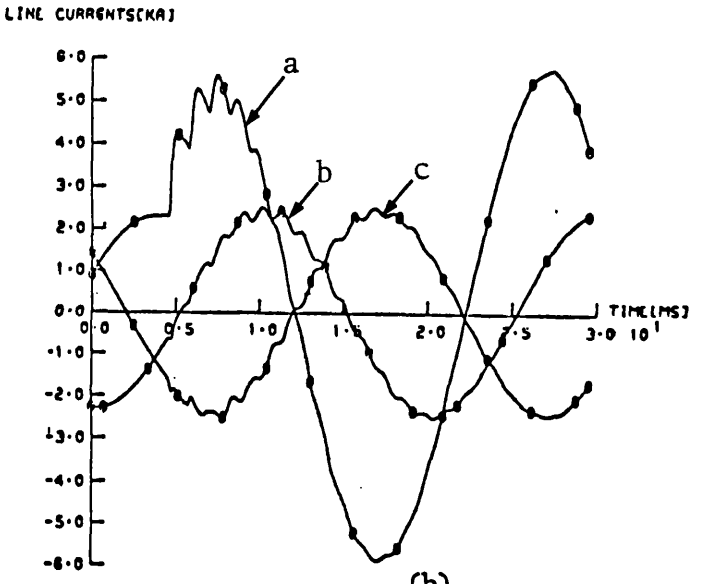

(b)

Fig 6.6

Voltage and current waveforms at the S.E. of the single-section feeder system examined.

- Solid a-E fault.
- $V_S/V_R = \underline{|30^o}$
- FT = 4.167 ms
- Other fault conditions are similar to that of Fig 6.2.

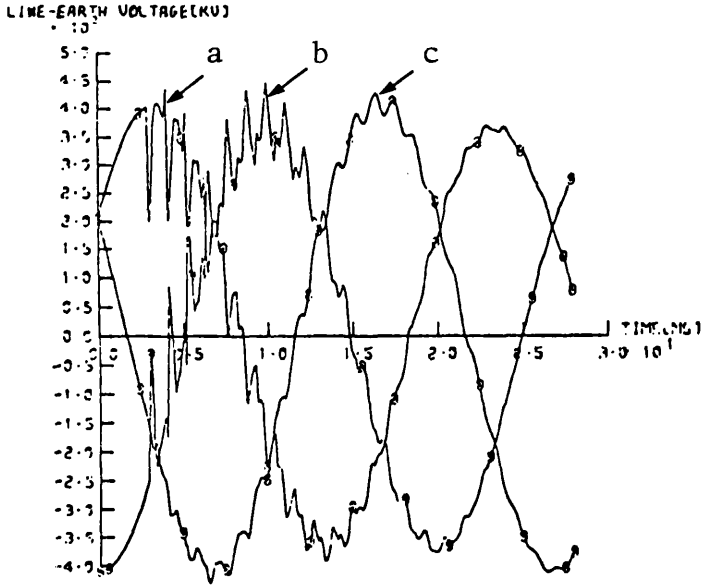

(a)

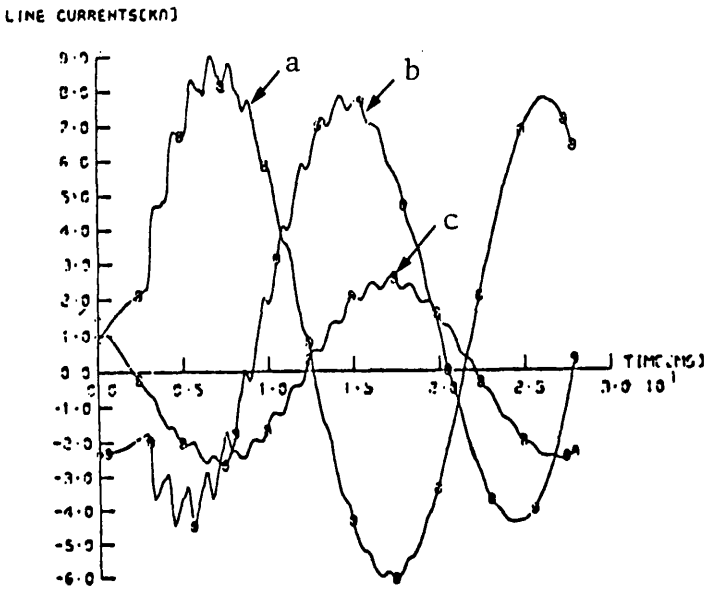

(b)

Fig 6.7

Voltage and current waveforms at the S.E. of the single-section feeder system examined.

- Solid 'a-b-E' fault
- $V_S/V_R = \angle 30^o$
- FT = 2.5 ms
- Other fault conditions are similar to that of Fig 6.2.

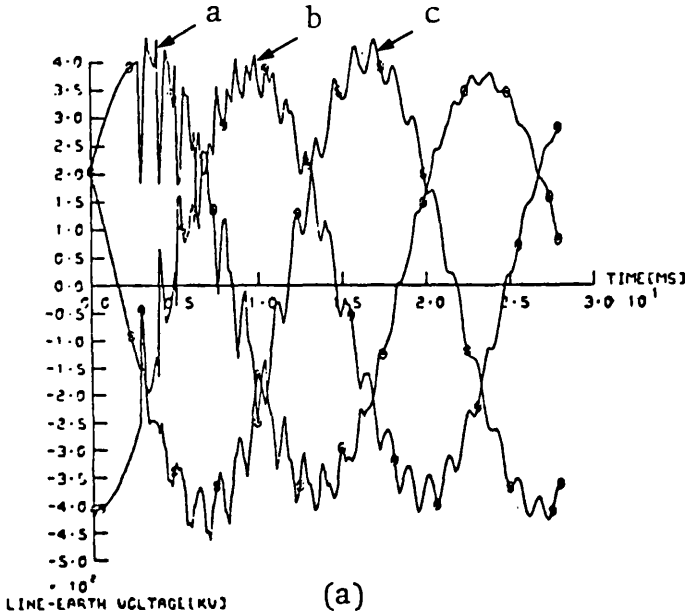

(a)

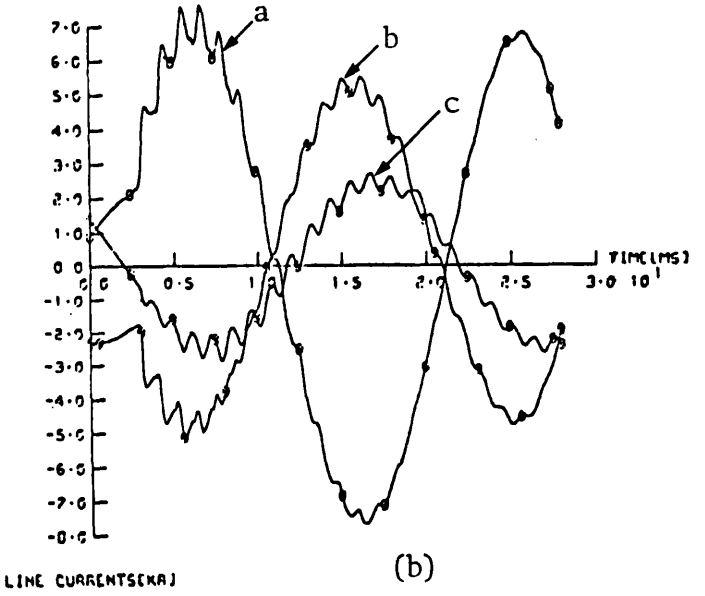

(b)

Fig 6.8

Voltage and current waveforms at the S.E. of the single-section feeder system examined.

- Solid 'a-b' fault
- Other fault conditions are similar to that of Fig 6.7.

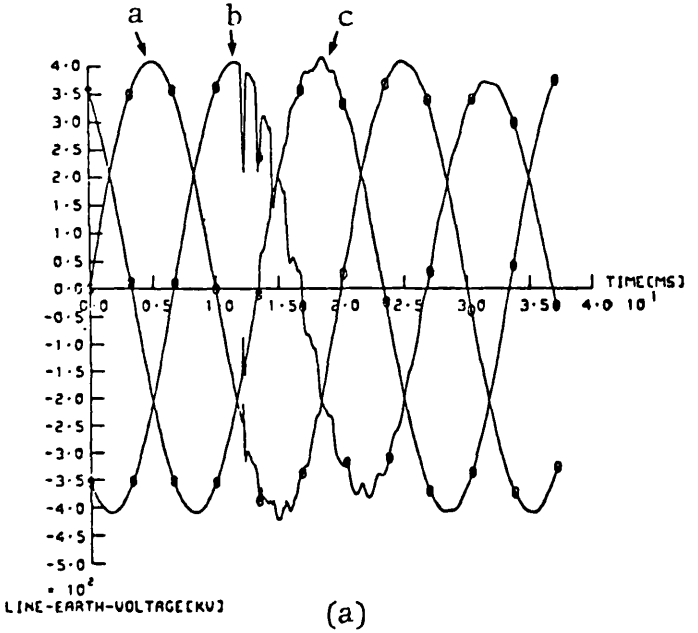

(a)

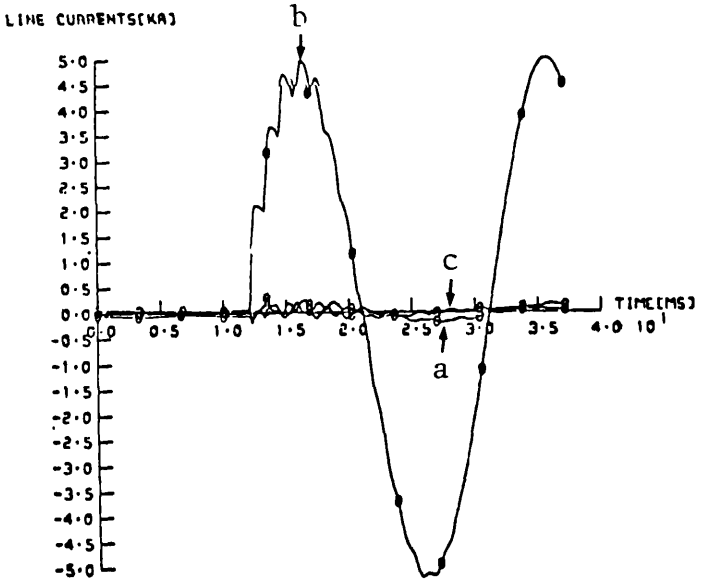

(b)

Fig 6.9

Voltage and current wave-forms at the S.E. of the single-section feeder system examined.

- Solid 'b-E' fault.
- FT = 11.67 ms
- Other fault conditions are similar to that of Fig 6.2.

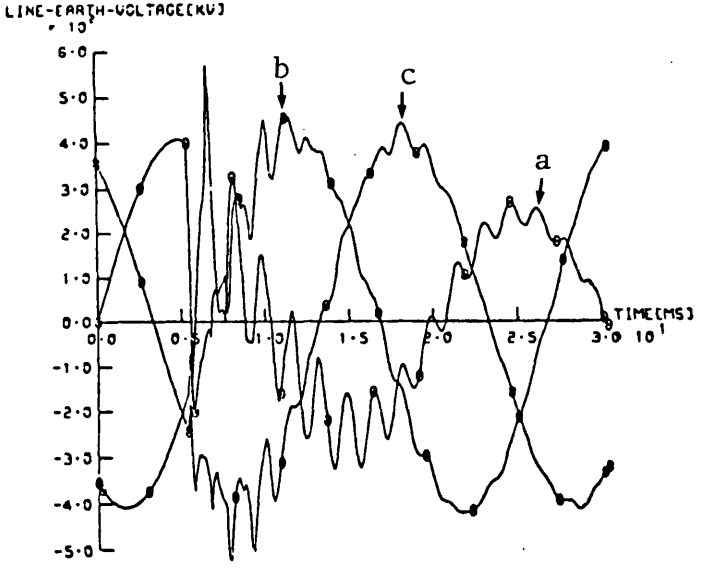

(a)

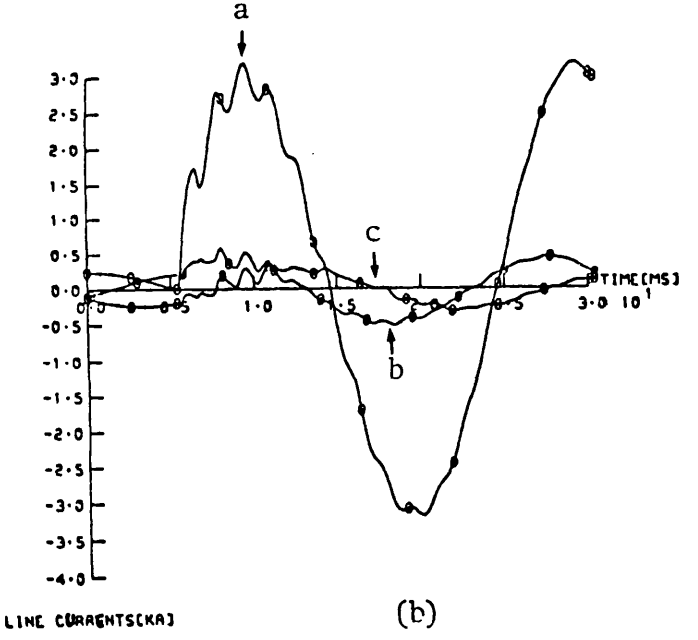

(b)

Fig 6.10

Voltage and current wave-forms at the S.E. of the single-section feeder system examined.

- Solid 'a-E' fault.
- $h_1 = h_0 = 0.0$
- Other fault conditions are similar to that of Fig 6.5.

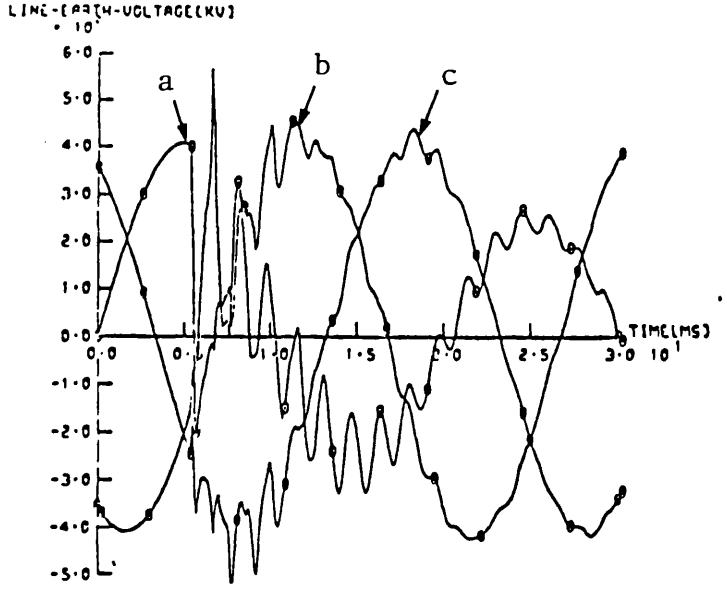

(a)

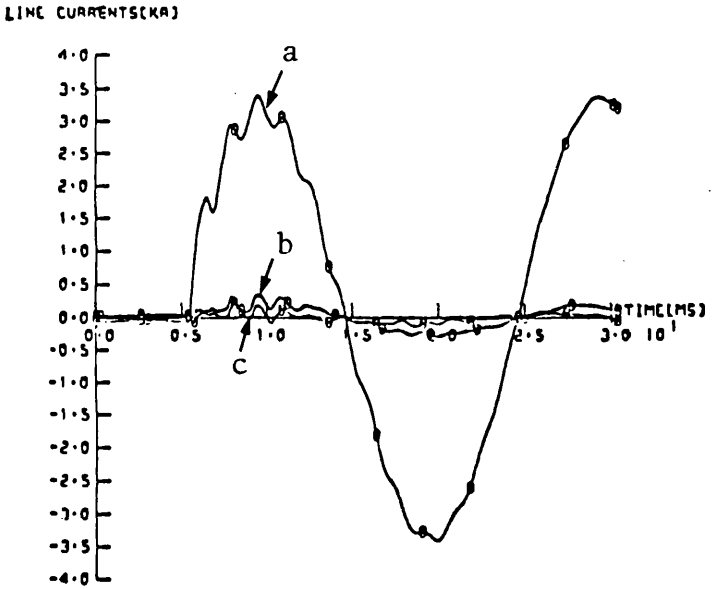

(b)

Fig 6.11

Voltage and current waveforms at the S.E. of the single-section feeder system examined.

- Solid 'a-E' fault.
- $h_1 = 1.25$, $h_0 = 1.4$
- Other fault conditions are similar to that of Fig 6.5.

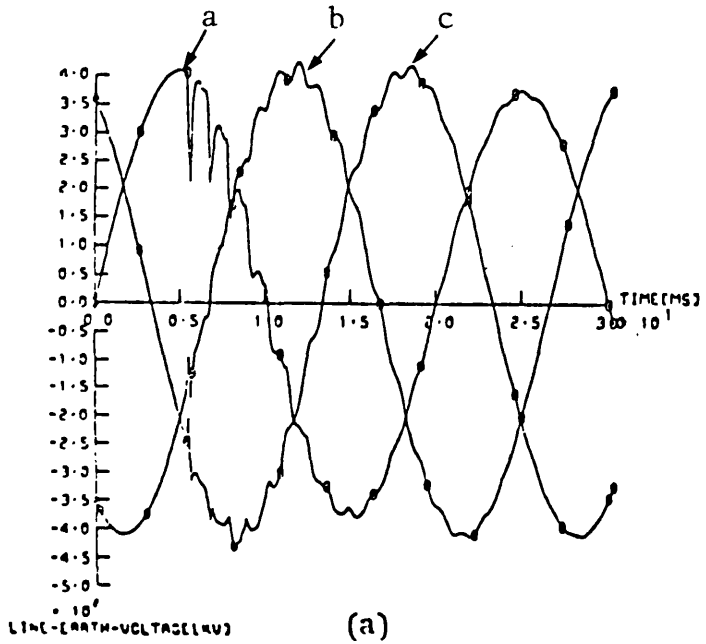

(a)

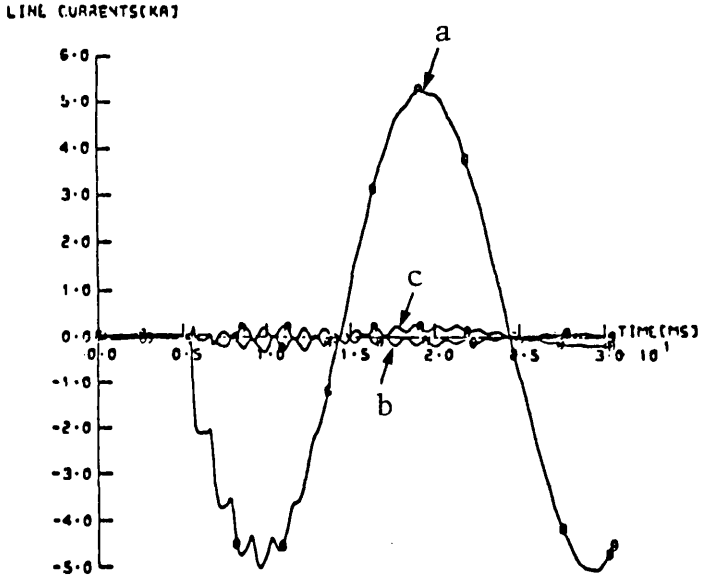

(b)

Fig 6.12

Voltage and current waveforms at the R.E. of the single-section feeder system examined.

- Solid 'a-E' fault under conditions similar to that of Fig 6.2.

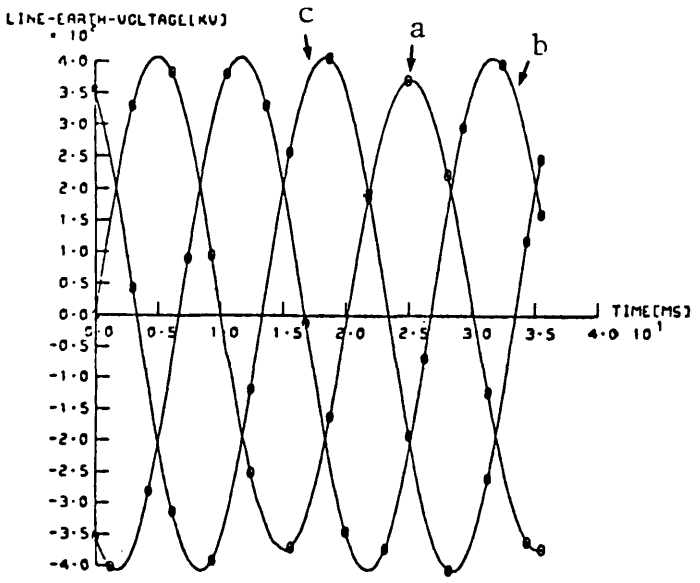

(a)

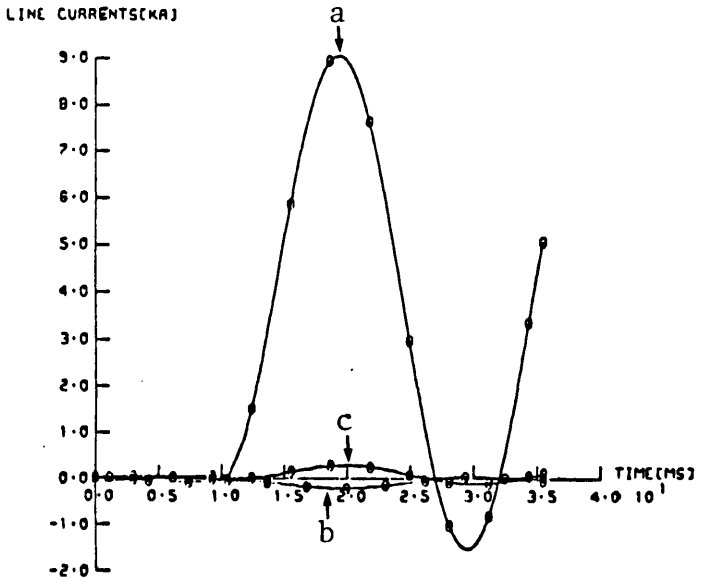

(b)

Fig 6.13

Voltage and current waveforms at the R.E. of the single-section feeder system examined.

- Solid 'a-E' fault under conditions similar to that of Fig 6.4.

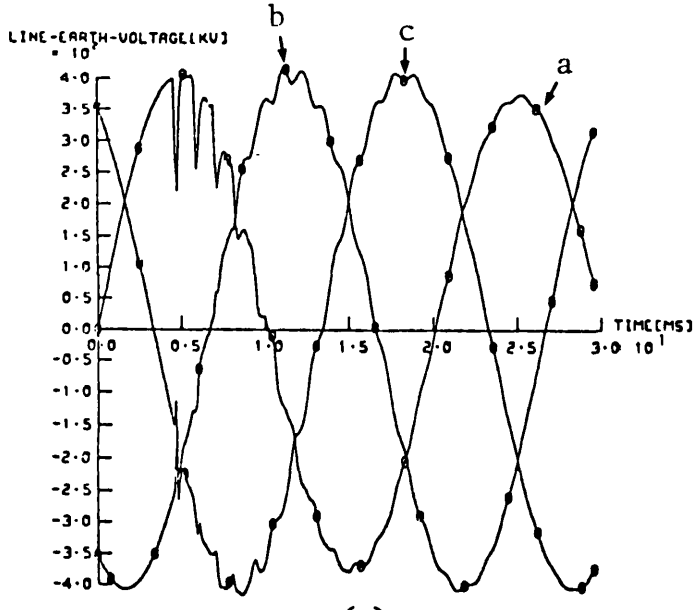

(a)

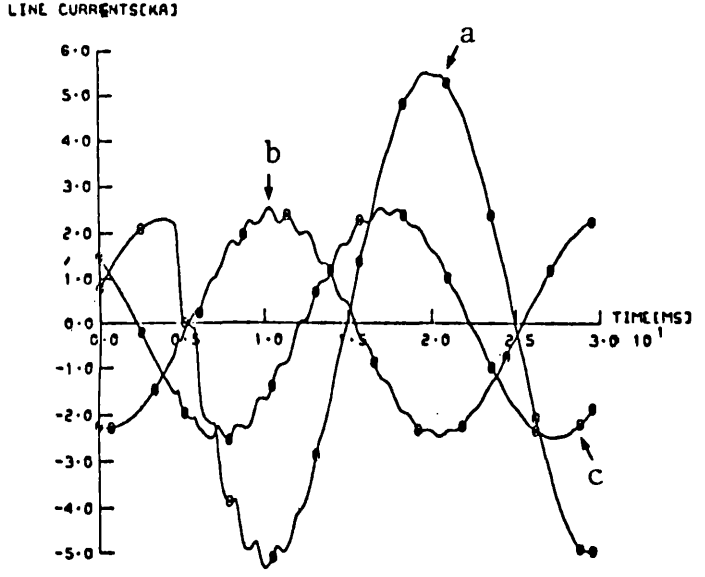

(b)

Fig 6.14

Voltage and current waveforms at the R.E. of the single-section feeder system examined.

- Solid 'a-E' fault under conditions similar to that of Fig 6.6.

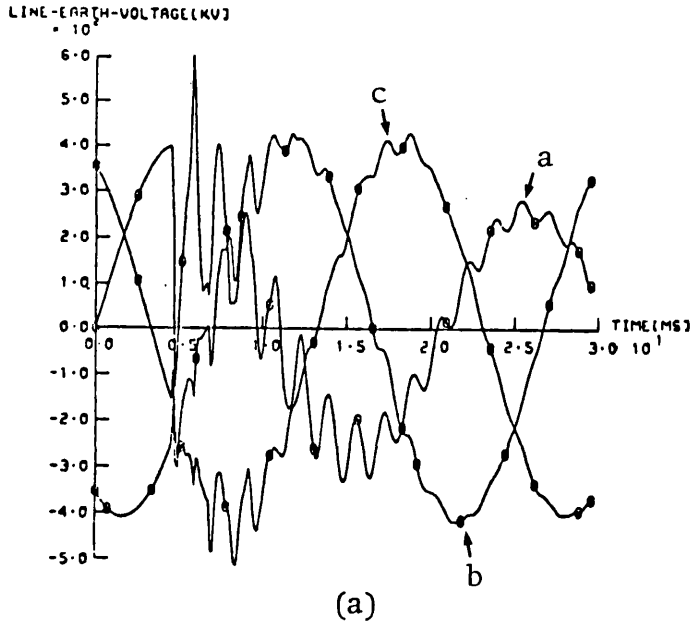

(a)

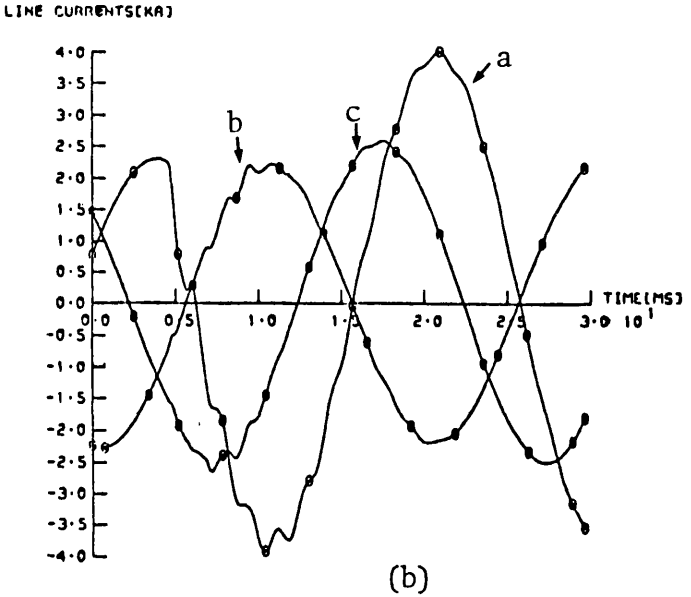

(b)

Fig 6.15

Voltage and current waveforms at the R.E. of the single-section feeder system examined.

- Solid 'a-E' fault.
- R.S.C.L. = 5 GVA
- Other fault conditions are similar to that of Fig 6.6.

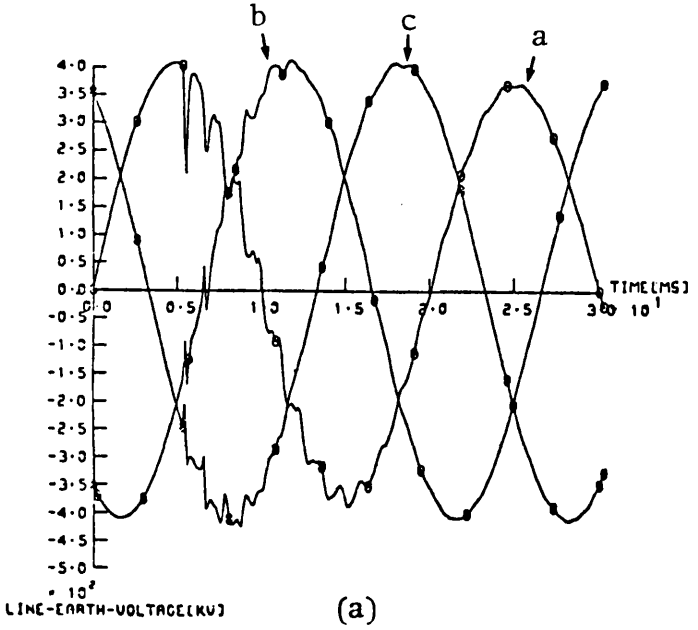

(a)

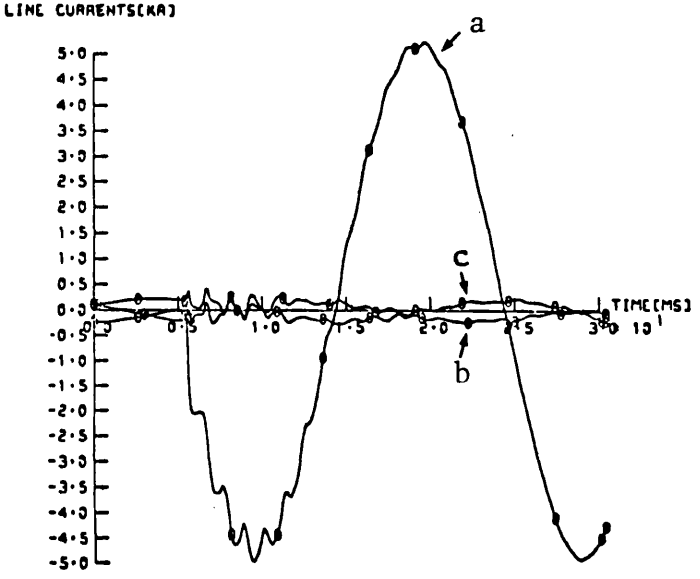

(b)

Fig 6.16

Voltage and current waveforms at the R.E. of the single-section feeder system examined.

- Solid 'a-E' fault under conditions similar to that of Fig 6.10.

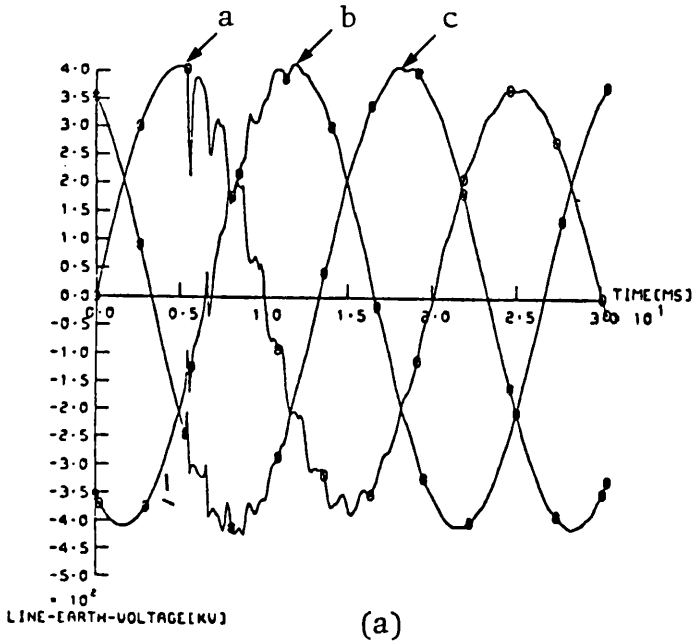

(a)

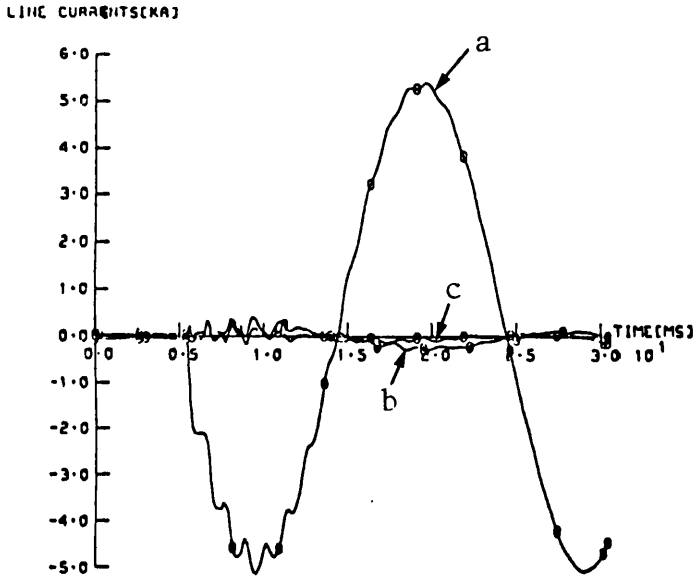

(b)

Fig 6.17

Voltage and current wave-forms at the R.E. of the single-section feeder system examined.

- Solid 'a-E' fault under conditions similar to that of Fig 6.5.

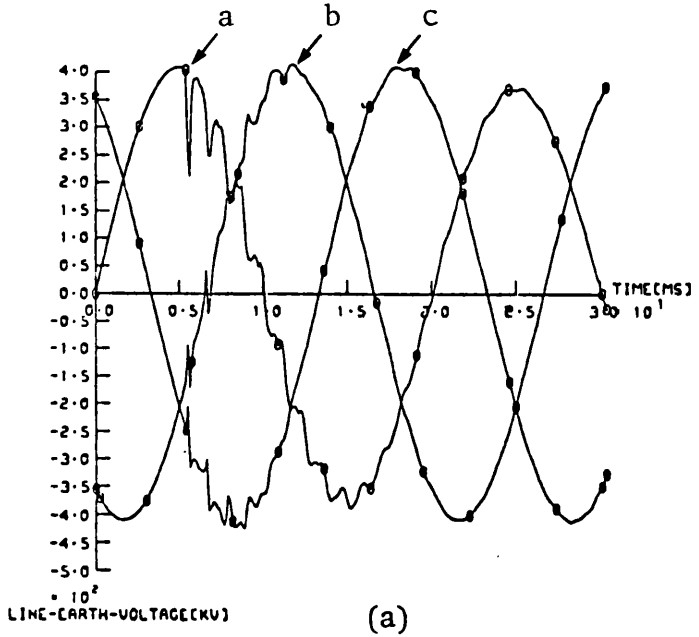

(a)

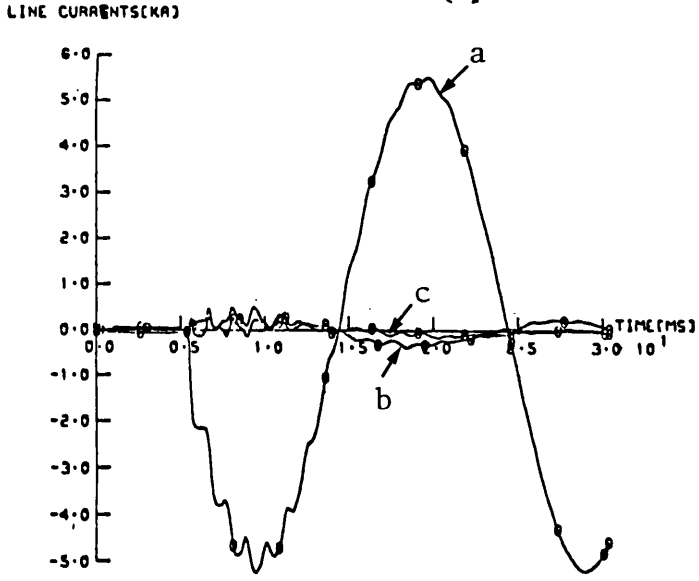

(b)

Fig 6.18

Voltage and current wave-forms at the R.E. of the single-section feeder system examined.

- Solid 'a-E' fault under conditions similar to that of Fig 6.11.

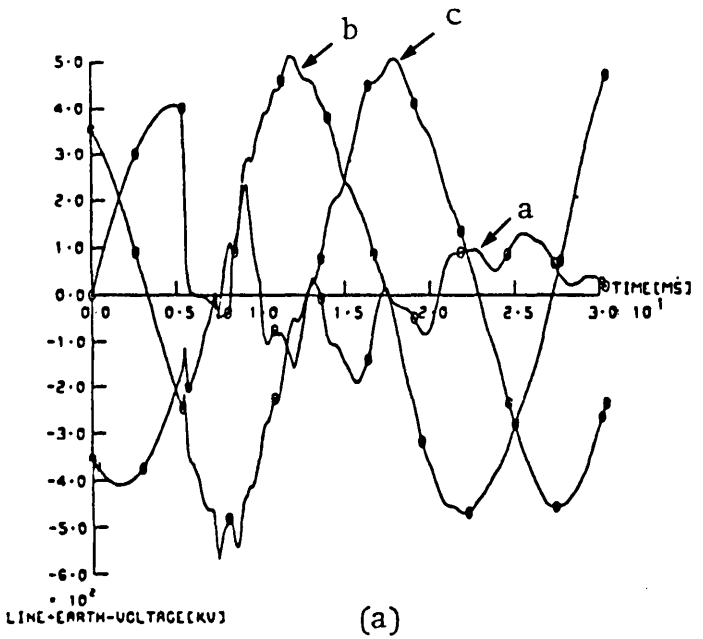

(a)

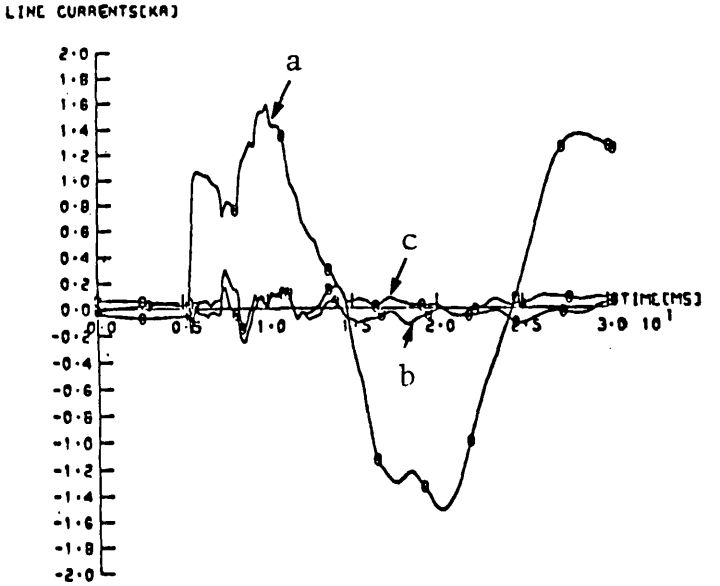

(b)

Fig 6.19

Voltage and current wave-forms at the S.E. of the middle section of the 3-section feeder examined.

- Solid 'a-E' fault under the same conditions as that of Fig 6.2.

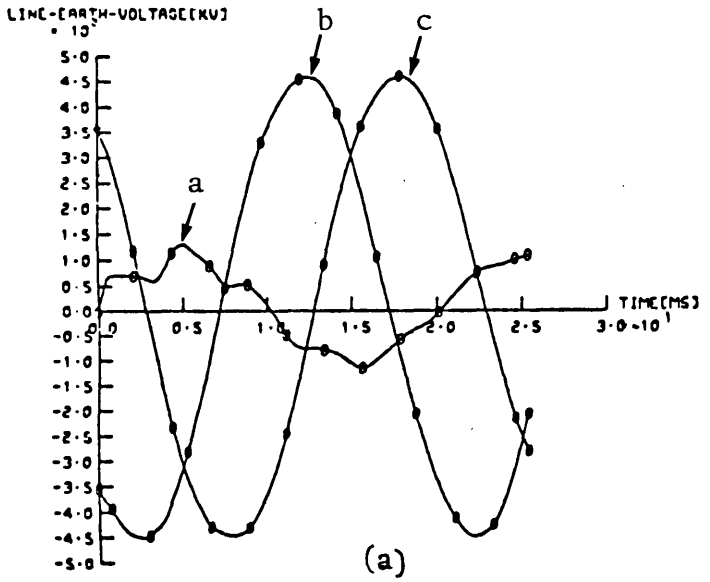

(a)

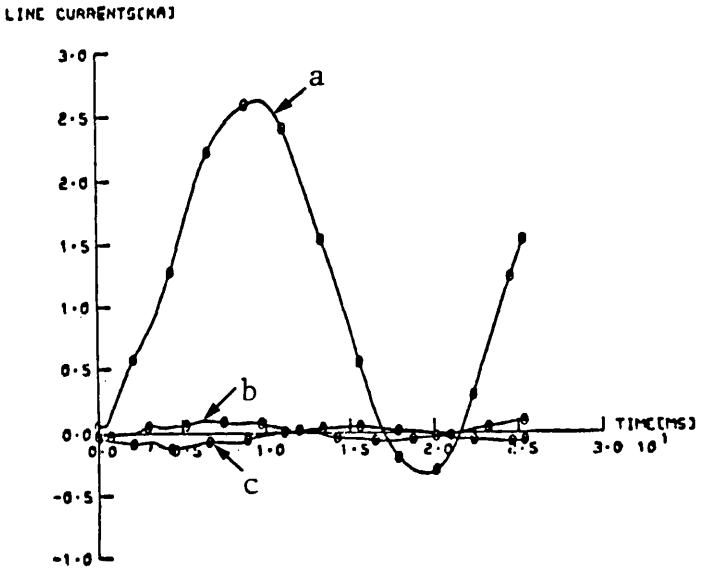

(b)

Fig 6.20

Voltage and current wave-forms at the S.E. of the middle section of the 3-section feeder system examined.

- Solid 'a-E' fault.
- FT = 0.0

- Other fault conditions are similar to that of Fig 6.4.

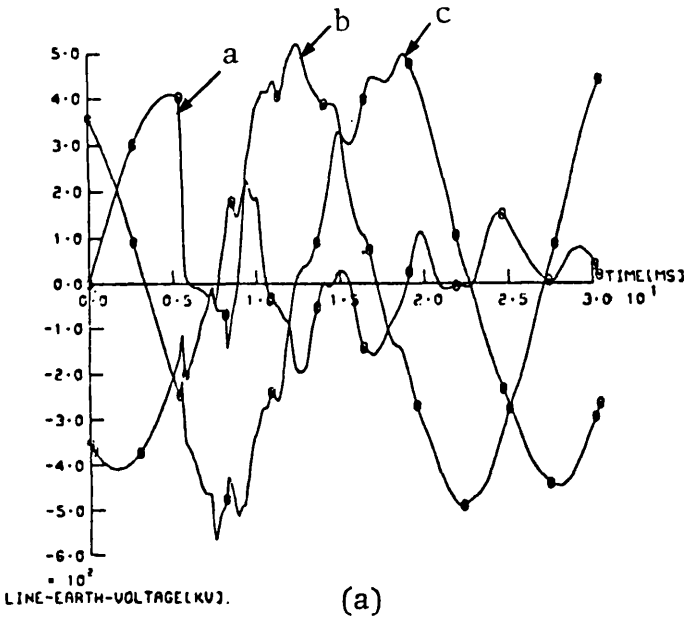

(a)

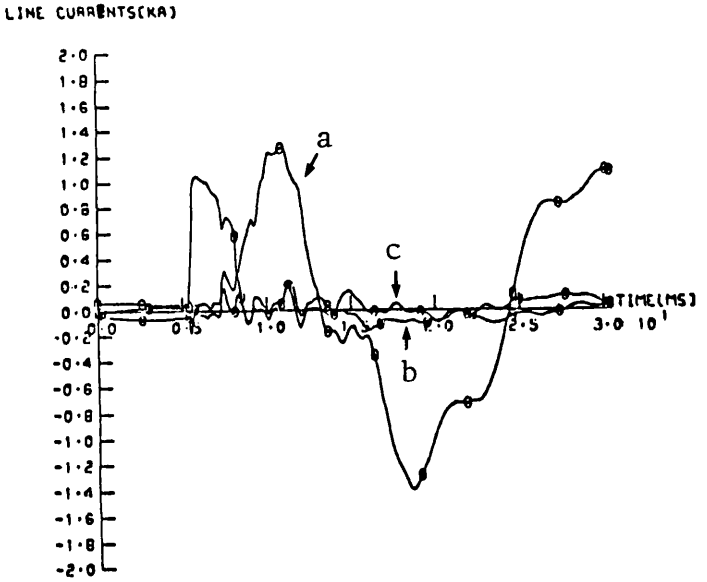

(b)

Fig 6.21

Voltage and current wave-forms at the S.E. of the middle section of the 3-section feeder system examined.

- Solid 'a-E' fault under conditions similar to that of Fig 6.5.

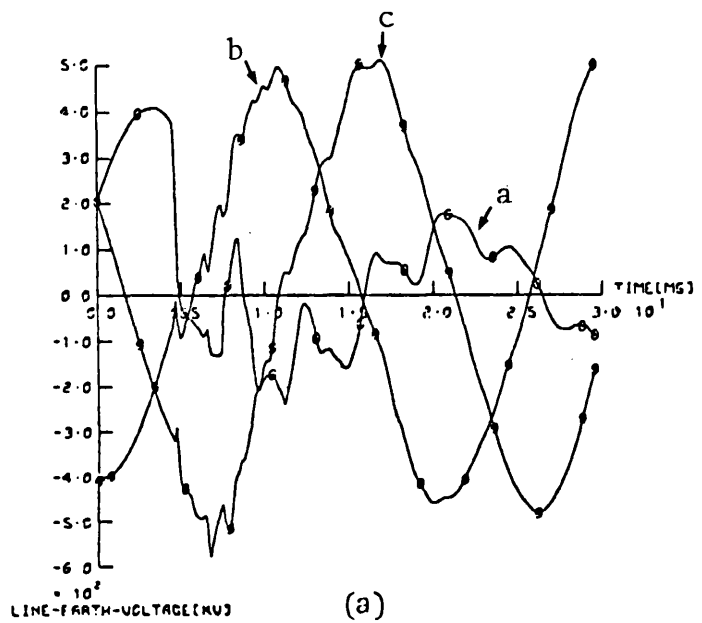

(a)

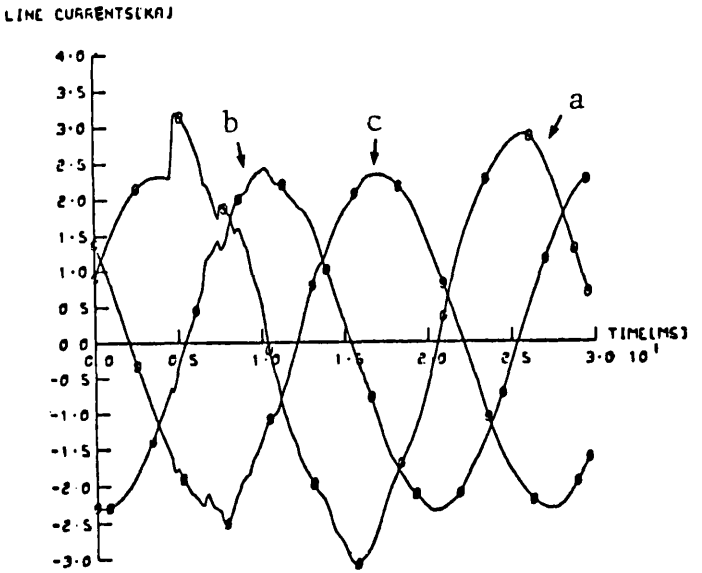

(b)

Fig 6.22

Voltage and current wave-forms at the S.E. of the middle section of the 3-section feeder system examined.

- Solid 'a-E' fault under conditions similar to that of Fig 6.6.

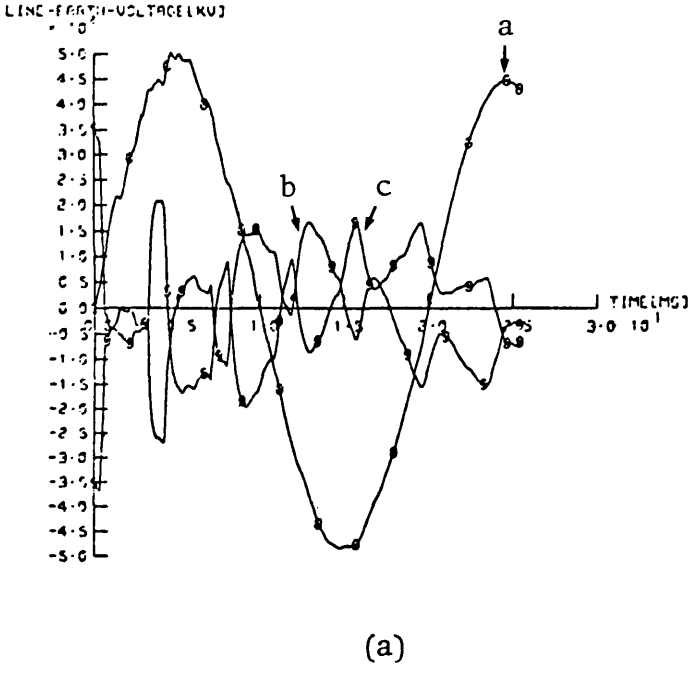

(a)

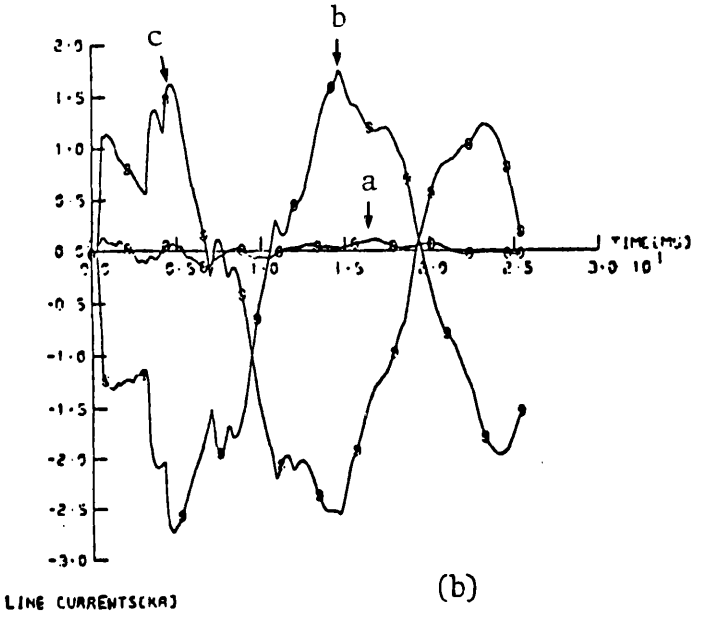

(b)

Fig 6.23

Voltage and current wave-forms at the S.E. of the middle section of the 3-section feeder system examined.

- Solid 'b-c-E' fault.
- $V_S/V_R = \underline{0}^o$
- FT = 0.0
- Other fault conditions are the same as that of Fig 6.19.

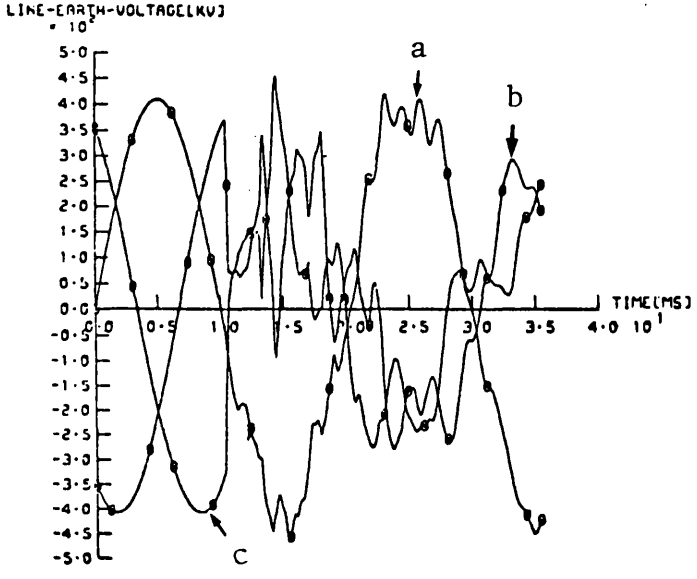

(a)

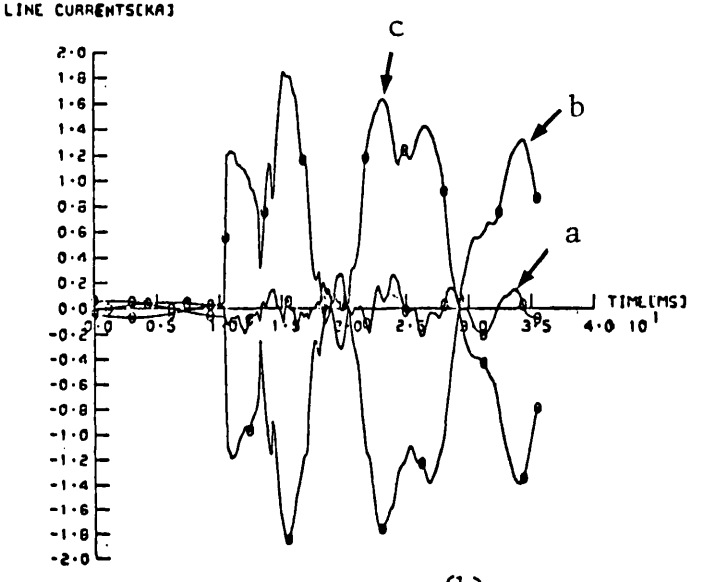

(b)

Fig 6.24

Voltage and current wave-forms at the S.E. of the middle section of the 3-section feeder system examined.

- Solid 'b-c' fault.
- $V_S/V_R = \underline{0}^o$
- FT = 10.0 ms.
- Other fault conditions are similar to that of Fig 6.21.

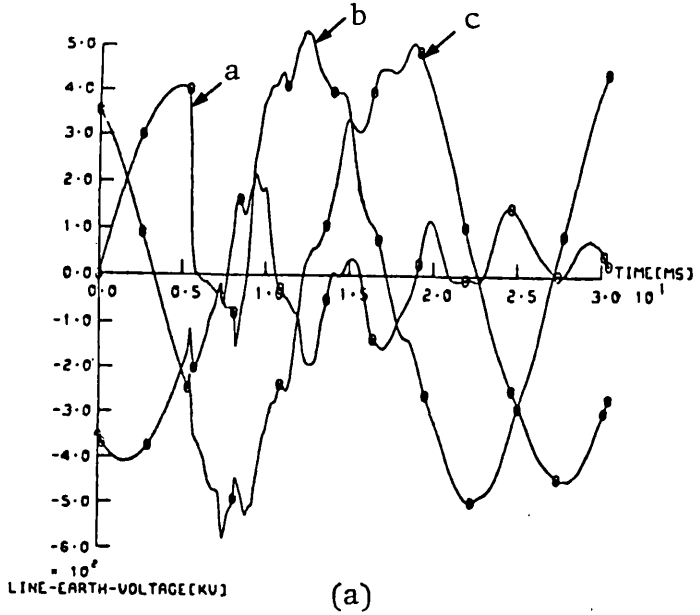

(a)

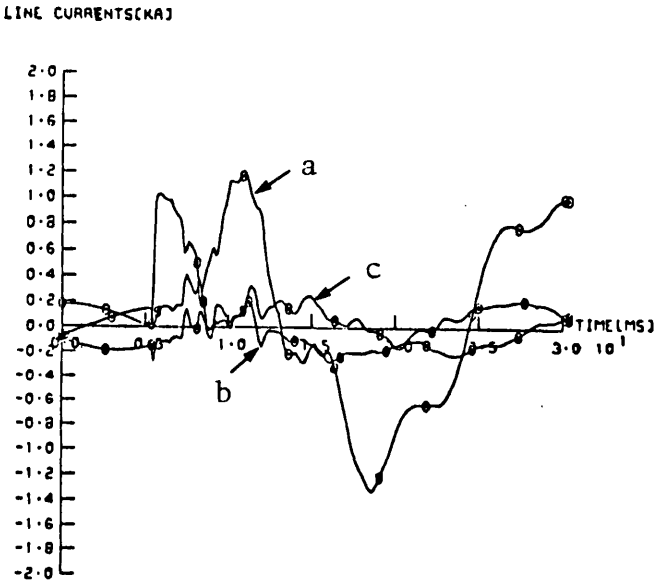

(b)

Fig 6.25

Voltage and current waveforms at the S.E. of the middle section of the 3-section feeder system examined.

- Solid 'a-E' fault.
- $h_1 = 0.25$, $h_0 = -0.19$
- Other fault conditions are similar to that of Fig 6.21.

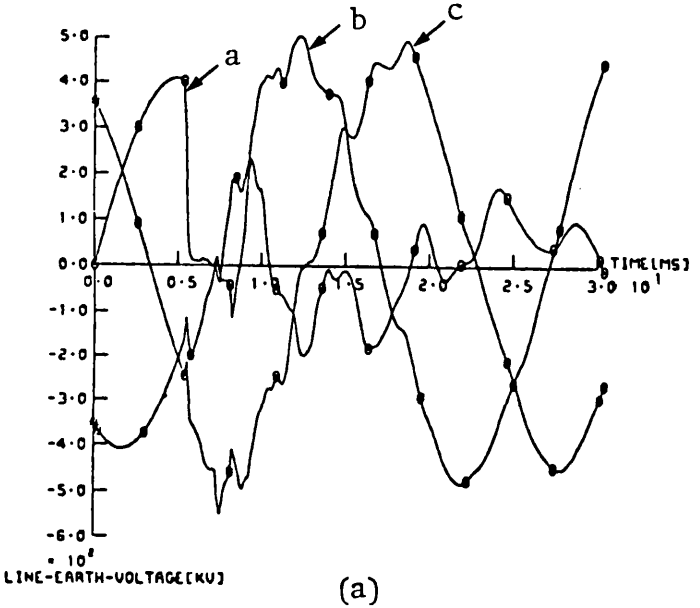

(a)

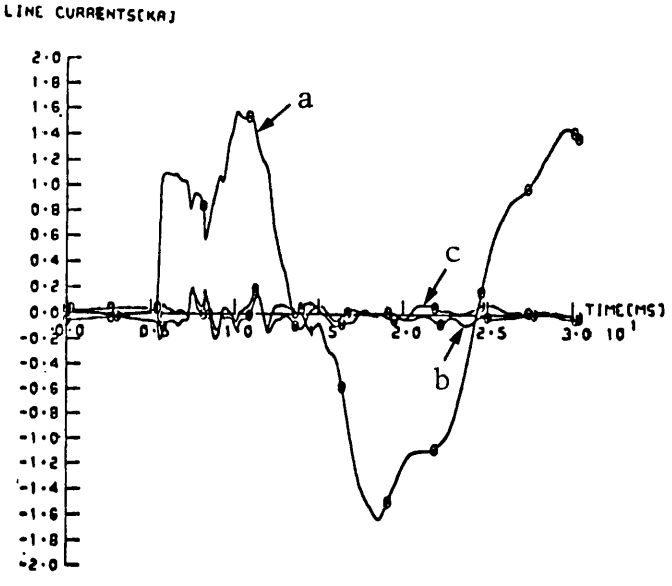

(b)

Fig 6.26

Voltage and current waveforms at the S.E. of the middle section of the 3-section feeder system examined.

- Solid 'a-E' fault.
- $h_1 = 1.25$, $h_0 = 1.4$
- Other fault conditions are similar to that of Fig 6.21.

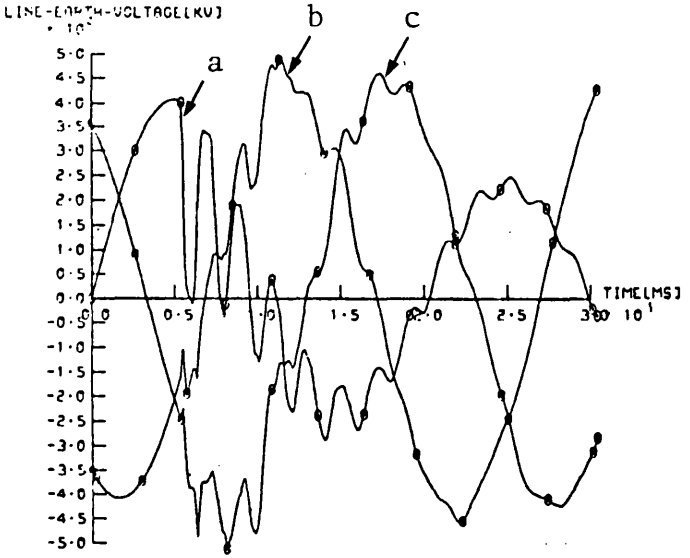

(a)

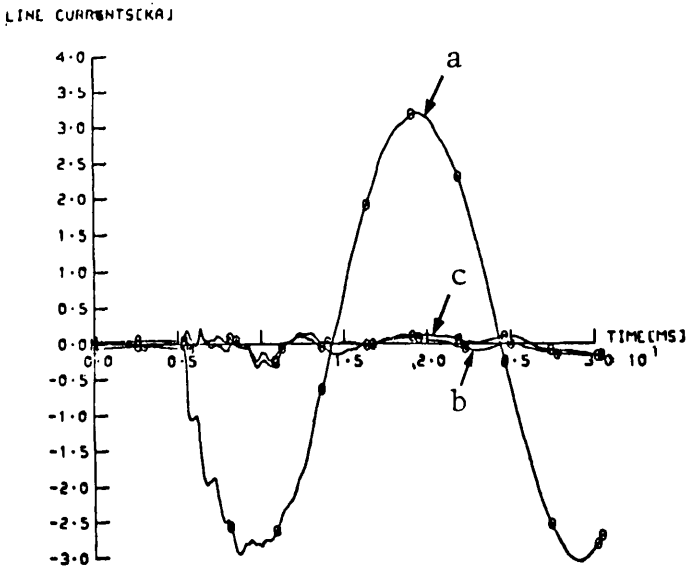

(b)

Fig 6.27

Voltage and current wave-forms at the R.E. of the middle section of the 3-section feeder system examined.

- Solid 'a-E' fault under conditions similar to that of Fig 6.19.

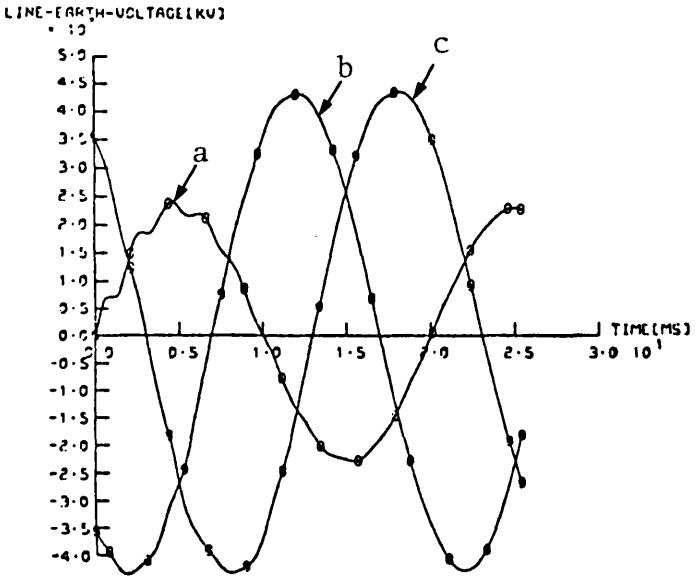

(a)

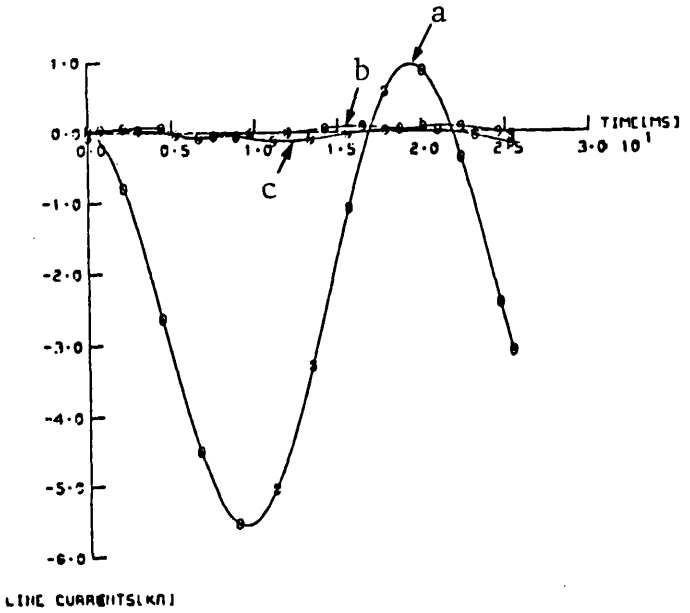

(b)

Fig 6.28

Voltage and current wave-forms at the R.E. of the middle section of the 3-section feeder system examined.

- Solid 'a-E' fault under conditions similar to that of Fig 6.20.

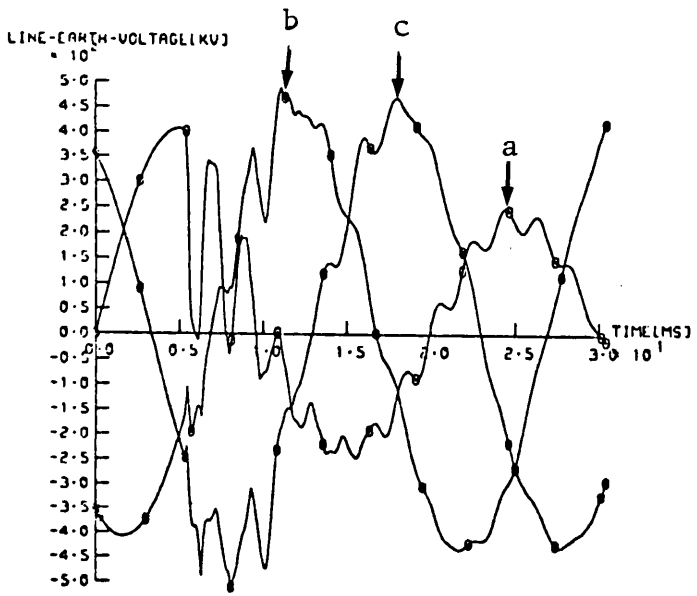

(a)

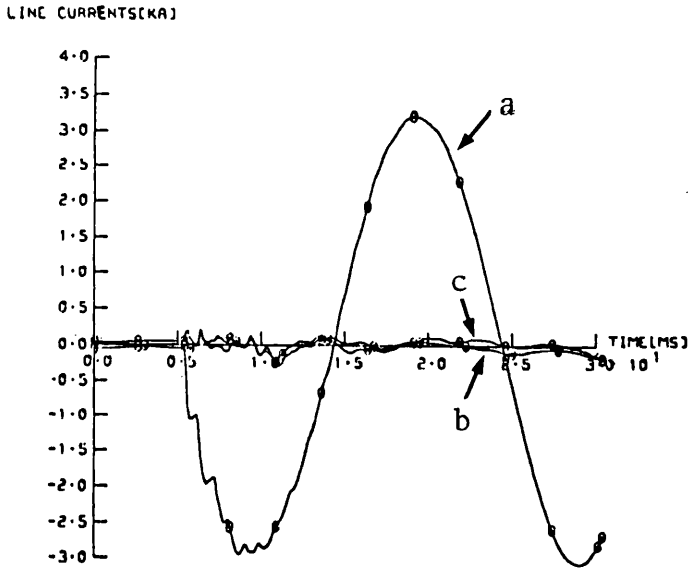

(b)

Fig 6.29

Voltage and current wave-forms at the R.E. of the middle section of the 3-section feeder system examined.

- Solid 'a-E' fault under conditions similar to that of Fig 6.21.

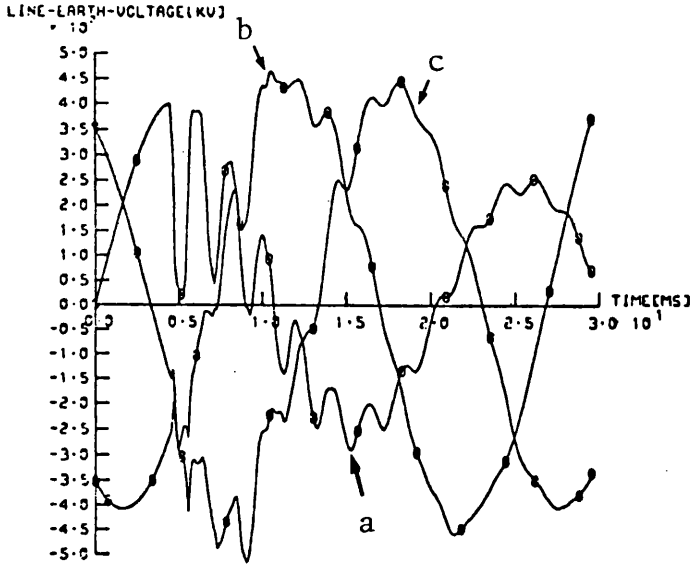

(a)

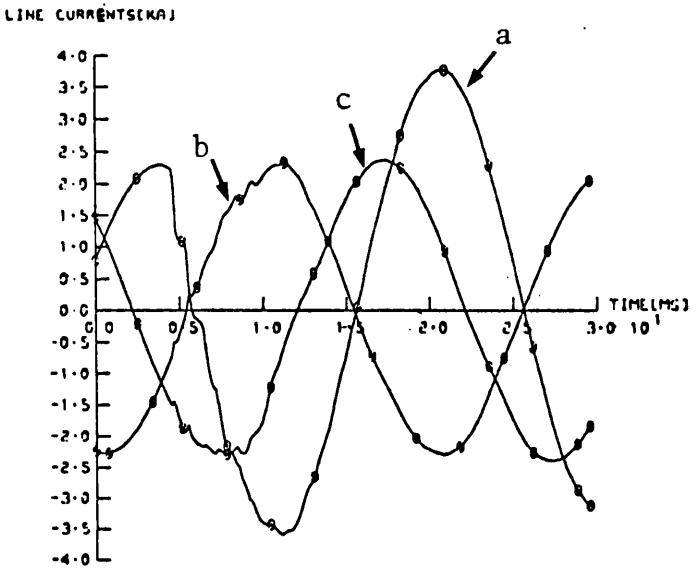

(b)

Fig 6.30

Voltage and current wave-forms at the R.E. of the middle section of the 3-section feeder system examined.

- Solid 'a-E' fault under conditions similar to that of Fig 6.22.

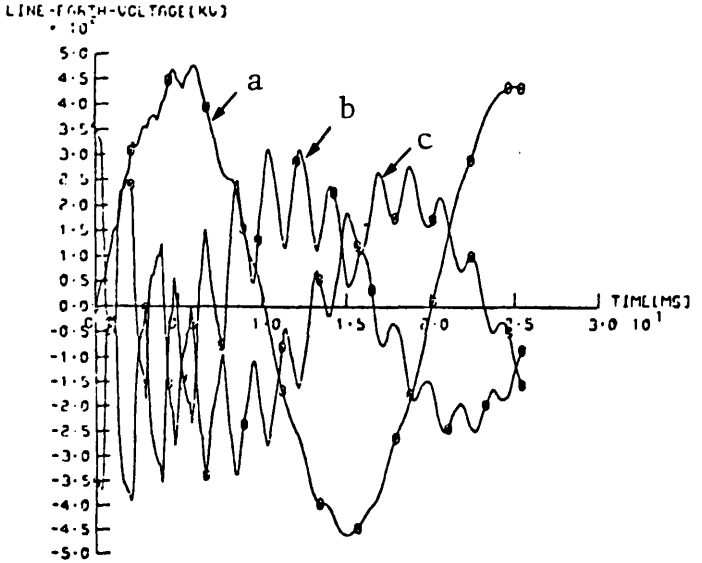

(a)

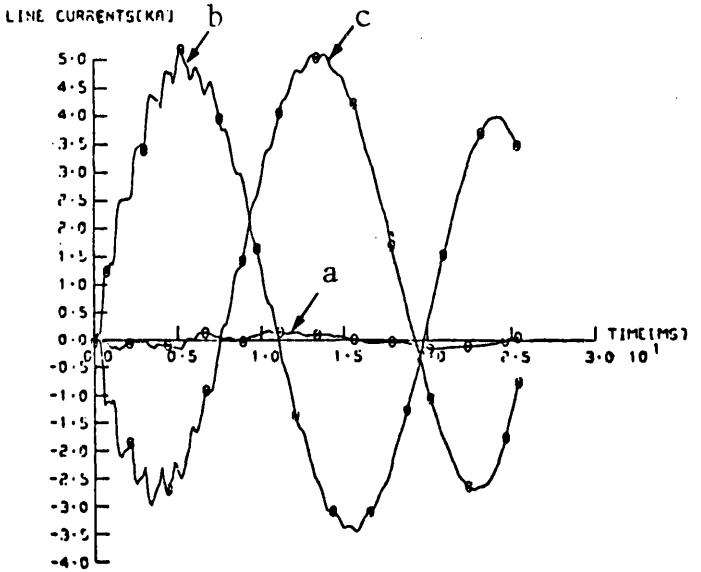

(b)

Fig 6.31

Voltage and current wave-forms at the R.E. of the middle section of the 3-section feeder system examined.

- Solid 'b-c-E' fault under conditions similar to that of Fig 6.23.

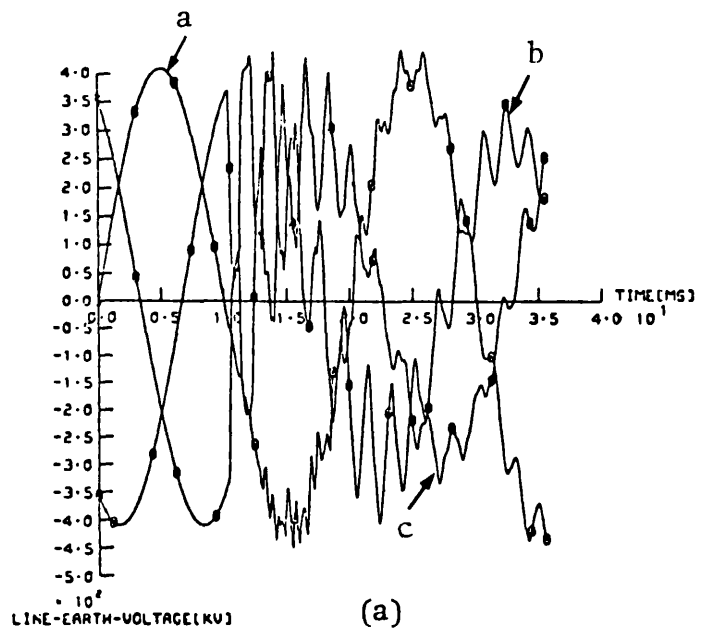

(a)

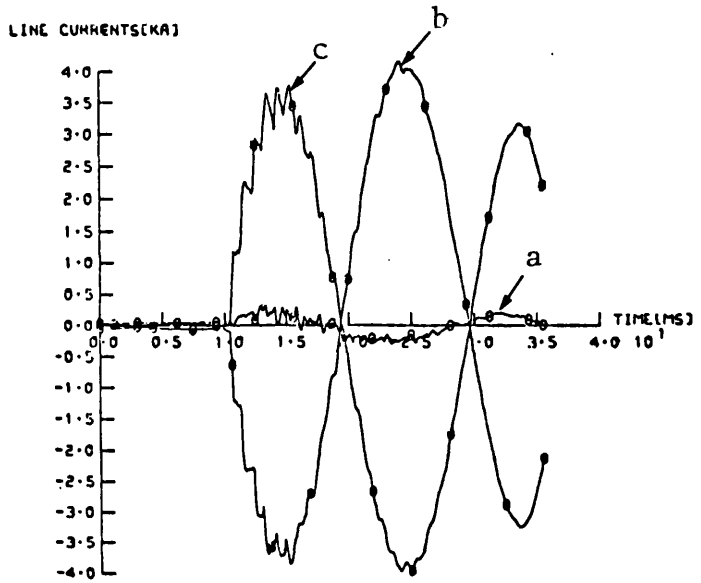

(b)

Fig 6.32

Voltage and current wave-forms at the R.E. of the middle section of the 3-section feeder system examined.

- Solid 'b-c' fault under conditions similar to that of Fig 6.24.

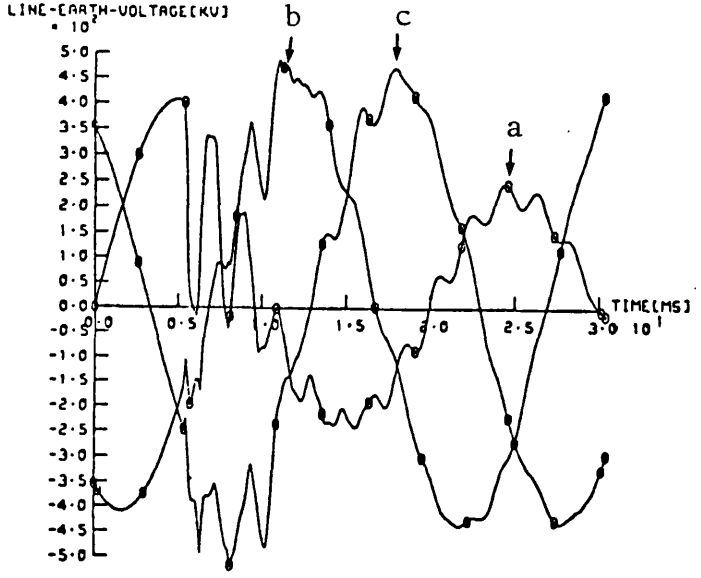

(a)

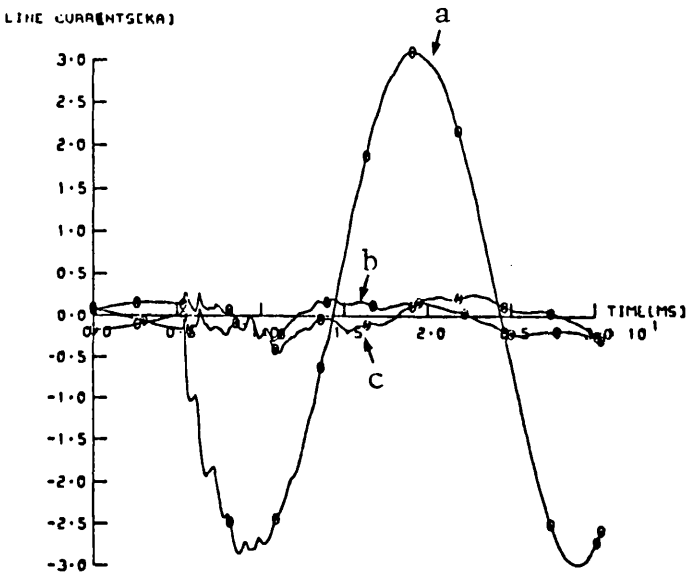

(b)

Fig 6.33

Voltage and current wave-forms at the R.E. of the middle section of the 3-section feeder system examined.

- Solid 'a-E' fault under conditions similar to that of Fig 6.25.

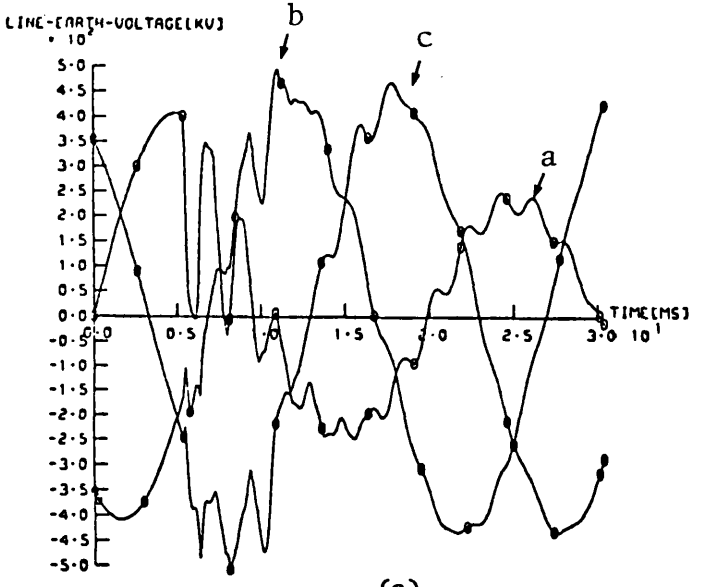

(a)

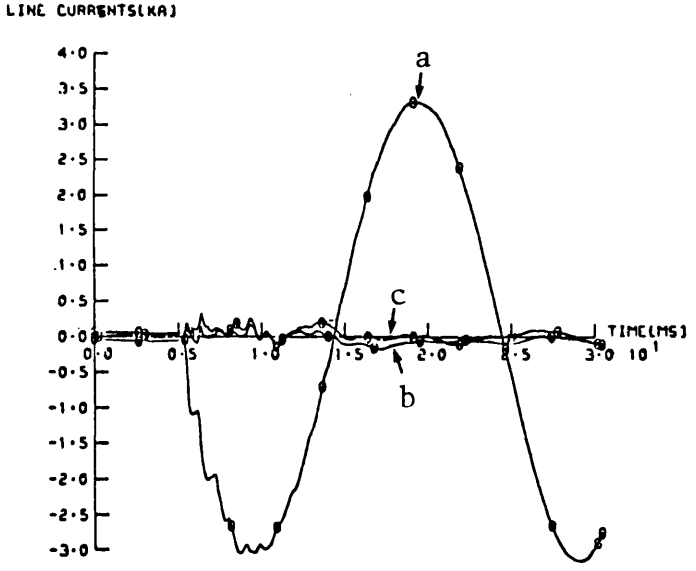

(b)

Fig 6.34

Voltage and current wave-forms at the R.E. of the middle section of the 3-section feeder system examined.

- Solid 'a-E' fault under conditions similar to that of Fig 6.26.

CHAPTER 7 DIGITAL EVALUATION OF FAULT-INDUCED OVER-VOLTAGES

7.1 Introduction

At the designing stages of EHV systems, their insulation levels have usually been determined by the overvoltages produced during line energization. The improvements in EHV circuit breakers, however, indicate that switching-surge over-voltages can be made reasonably low so that fault induced over-voltages become the limiting factor that determines the system insulation levels necessary.[17-22]

This Chapter, therefore is primarily concerned with reporting the results of an extensive study of fault-induced system and shunt-reactor over-voltages. Prediction of over-voltage-levels of the systems considered in this thesis is critically important due to the following factors:-

1. The required system insulation levels are determined so that a single-line-to-earth fault could not develop into double line-to-earth fault, which would be particularly serious in systems employing single-pole autoreclosure.

2. The insulation levels of the 4-reactors can be correctly fixed so that the reactor can function under overvoltage conditions, i.e. reactive power compensation and fault-arc suppression are achieved.

In the digital computer results presented in this Chapter, overvoltages due to single-line-to-earth faults initiated in 3-setion feeder systems are particularly considered under different fault conditions.

7.2 Computational results of system overvoltages

7.2.1 Single-section feeder system overvoltages

The crest value of system line-to-earth voltage is 408.24kV and the maximum crest value of fault-induced overvoltages will be refered to in per unit of that voltage.

The digital studies showed that the worst cases from the point of view of overvoltages are single-line to earth mid-point faults with low capacity source near the observation point. This finding can be seen for the a-E fault of Fig (6.5.a) where the faulted phase overvoltage reaches 1.42 pu while that of phase 'c' is 1.3 pu. The same over-voltages were observed for earth faults involving phases 'b' and 'c' respectively as may be seen from Figs (7.1.a), (7.1.b) respectively.

Under the same fault conditions, other distant faults produced less overvoltages as may be seen for the a-E faults at 210 and 300km from the sending-end respectively - Fig (7.2).

Faults at zero-prefaulted-phase voltage showed no significant over-voltages. The realistic loading of the 300km line corresponds to a load angle of about (12^{o}) and the overvoltages produced by a mid-point a-E fault under conditions similar to that of Fig (7.2) can be seen from Fig (7.3.a) to be 1.32 and 1.27 pu experienced by phases 'a' and 'c' respectively.

Different source capacities were assumed and no overvoltages above 1.42pu were observed. Fig (7.3.b) shows the response for a 'b-c' fault incepted at the mid-point when V_{bc} = positive peak and with source capacities of 5 and 35 GVA at the sending and receiving ends

respectively. Other fault conditions are similar to that of Fig (7.2). The Fig. shows that the overvoltages experienced by both the faulted phases (b,c) and the healthy phase (a) are about 1.49 pu which, in fact, exceed that for the 'b-E' and the 'c-E' faults of Figs (7.1).

No overvoltages over 1.49 pu were observed for any other type af fault under different fault conditions.

7.2.2 3-Section feeder system-overvoltages

In 3-section feeder systems, overvoltages increased significantly. For example, Fig (7.4.a) shows the voltages at the sending-end of the 300km middle line-section for a solid, close-up-a-E-fault. The fault occurs when V_a = positive maximum and the sources at both ends have 35 GVA capacity, each. The wave forms show that the overvoltage experienced by phase 'c' reaches about 1.7 pu. Here, it has to be mentioned that although the fault occurs at the sending-end of the middle line section, the point of fault is physically mid-way in the three section (400, 300 and 100km) feeder system. The same fault, under the same fault conditions, on the single-section feeder produced nearly no overvoltages as shown in Fig (6.2). Again, no overvoltages were observed for single-line-to earth faults that occur at zero voltages.

Fig (6.19.a) shows that the 'c-E' voltage reaches about 1.4 pu for a mid-point fault under the same conditions as that of Fig (7.4.a), and other distant faults produced less severe overvoltages. Fig (7.4.b) shows that the over-voltage of phase 'b' is about the same value (1.7pu) when a solid 'c-E' close-up fault occurs under the same conditions as that of Fig (7.4.a). Other distant a-E faults under the same conditions as that of Fig (7.4.a) produced less severe overvoltages. For example,

Fig (7.5.a ,b) shows that phase 'c' overvoltage reaches about 1.5 pu and 1.44 pu for faults at 40 km and 150 km respectively from the sending-end. For lower sending-end source capacity (5 GVA), Fig (7.6.a) shows that lower overvoltage (V_c = 1.52 pu) are produced under exactly the same fault conditions as that of Fig (7.4.a). Nearly the same over-voltage level resulted in the same phase (c) when source capacities are 35 and 5 GVA at the sending and receiving ends respectively Fig (7.6.b).

Higher sending-end source impedance ratios (Z_{S0}/Z_{S1}) have been found to increase system overvoltages while lower ratios reduced them. This can be seen from Fig (7.7.a) and (7.7.b), for (Z_{S0}/Z_{S1}) = 2.5 and 0.25 respectively, for a-E mid-point faults similar to that of Fig (7.5.b). The Fig. shows that with $|Z_{S0}/Z_{S1}|$ = 2.5 the phase 'c' overvoltage increased from 1.44 pu (Z_{S0}/Z_{S1}=1.0) to 1.49 pu while reduced to about 1.35 pu with $|Z_{S0}/Z_{S1}|$ = 0.25.(the impedance ratio changes by changing Z_{s0})

Overvoltages induced in phase (c) were found to be slightly increased with line loading as shown in Fig (7.8). Fig (7.8.a) shows that V_c = 1.72 pu (compared to the 1.7 pu of Fig (7.4.a)) while Fig (7.8.b) shows that under loading conditions, ($\delta = 30^o$), the overvoltage of Fig (7.5.b) increased from 1.44 pu to about 1.49 pu. Other types of faults have been shown to produce less severe overvoltages as may be seen from the wave, forms . presented in Chapter (6).

Therefore, from Figs (7.1)-(7.5), it can be concluded that the worst cases from the point of view of overvoltages experienced by the healthy phases are single-line-to-ground faults that occur at the mid-point of the system

when the faulted phase voltage is at its positive peak. These overvoltages show complete agreement with other published results concerning uncompensated transmission systems. For example, Kimbark etal[18] predicted in their analysis using the T.N.A. and the lattice diagram that a single line to ground fault can produce an overvoltage on an unfaulted phase as high as 2.1 pu in a 3-phase system. Their predicted worst fault location is the mid-point which also agrees with the results presented in this section.

Similar conclusions regarding overvoltages due to fault initiation have been reached.[19-22] Clerici etal,[19] using the T N A, have found that, due to faults, overvoltages up to 1.7 pu are experienced by their 735KV system. In their assessment of overvoltages due to faults, the authors[22] emphasized that such overvoltages stress the insulation of healthy phases and therefore may fix the minimum acceptable values for air clearences in overhead lines.

Using digital techniques, Boonyubol etal,[20] examined the problem on a transposed 3-phase system. Their predictions agree with Kimbark,[18] and hence with the results presented in this section. Using the Fourier transform overvoltage levels predicted by Johns and Aggarwal[21] are 1.98 and 1.78 pu for single and double circuit systems respectively. It has also been shown[21] that in the case of lines fed from similar capacity sources, the worst case of overvoltages occurs at the mid-point. These findings agree completely with the results presented in Figs (7.1 - 7.8).

It has to be added that high frequency voltage components up to only 4kHz are covered in the digital computer results presented in Figs (7.1 - 7.8) and it follows that if higher frequency components (above 4 kHz) are considered, higher system overvoltages may be produced.

7.3 Computational Results of Reactor Overvoltages

EHV reactors are usually protected against severe overvoltages by surge arrestors.[34,41] Lightning arrestor switching-surge spark-over voltages, as published, are generally[41] 1.35 to 1.55 pu of arrestor crest rating. The lowest arrestor crest rating that has been used with 500kV systems to date is 396kV.[34]

On practical 500 kV systems with line connected shunt reactors, however, an arrestor rating greater than 396kV has been used and in this case the minimum arrestor switching surge spark over voltage would range from 1.85 to 2.13 pu based on 408 kV phase-to-earth crest voltage.[34]

From continuous discussions with some Kennedy and Donkin engineers,[34] it was understood that in a similar work they found out that the above rating is adequate for the phase-reactors and a nominal voltage of 155kV (r.m.s.) across the neutral reactor is reasonable enough to select the neutral reactor break down insulation level.

The objective of this section is, therefore, to examine any severe overvoltages experienced by phase and neutral reactors, in single and 3-section feeder systems under different fault conditions.

7.3.1 Single-section Feeder Reactor Overvoltages

From the computational results of system overvoltages, it has been shown that higher overvoltage levels are produced in case of single-line-to-ground faults that occur at maximum prefault voltage with source capacities of 5, 35 GVA at the sending-end and receiving-end respectively. Therefore, reactor overvoltages will be shown only under these conditions. Figs (7.9) show the reactor voltages for a solid, mid-point earth fault

involving phases 'a' and 'b' respectively under the same fault conditions as that of Fig (7.1.a). Fig (7.9.a) shows that the faulted phase voltage 'V_a' reaches about 1.31 pu while that of phase 'c' is about 1.2 pu. Nearly the same overvoltage levels are produced in phases 'b' and 'a' for the b-E fault of Fig (7.9.b). In the two cases of Fig (7.9), the overvoltage experienced by the neutral reactor does not exceed 100kV, i.e. about 0.46 of the designed neutral crest voltage (219.2 kV).

Fig (6.10.a) shows that the increase of shunt compensation slightly increases reactor overvoltage. Under the same fault conditions as that of Fig (7.9.a) but with $h_1 = 1.25$, overvoltage levels are 1.35 pu and 1.25 pu in the faulted and healthy phases respectively. Neutral voltage is shown to be nearly unchanged. Fig (7.10.b) shows that, under the same fault conditions as that of Fig (7.9.a) but with prefault loading ($\delta = +12^{o}$), reactor overvoltages are slightly reduced.

The effect of fault position on reactor overvoltages is shown in Fig (7.11.a) and (7.11.b) for an a-E fault at distances 210 km and 300 km from the sending-end respectively. Apparantly the reactor overvoltage levels are less than that for the mid-point fault of Fig (7.9.a).

Through the extensive studies of reactor overvoltages, no other fault, under different fault conditions, has produced overvoltage levels higher than 1.35 pu (for phase reactors) and 0.46 pu (for the neutral reactor).

7.3.2 3-Section Feeder Reactor Overvoltages

In this section, the computational results of the thorough investigation of overvoltages experienced by shunt reactors compensating 3-section feeder systems are reported. Particular consideration is given to single

line-to ground faults that occur at the mid-point of the network when the prefault voltage of the faulted phase is at its positive peak.

Fig (7.12.a) and (7.12.b) show the reactor voltages for an a-E and c-E faults respectively, that occur at the sending-end of the middle line section (mid-point of the system) when 'V_a' & 'V_c' respectively are at their positive peak. The Fig. shows that, in both cases, healthy phases experienced an overvoltage of about 1.37 pu, while the neutral reactor overvoltage reached about 0.58 pu. Other distance earth faults under the same conditions as that of Fig (7.12) produced lower overvoltage levels as shown in Fig (7.13.a) and (7.13.b) for an a-E fault at 40km and 150km from the sending-end respectively.

Lower capacity sources at the sending and receiving ends respectively, also resulted in lower overvoltage levels for a close-up a-E fault under the same fault conditions as that of Fig (7.12.a). This can be seen from Figs (7.14.a) and (7.14.b) respectively. The Figs. show that sound phase overvoltagees are 1.25 and 1.23 pu respectively while, in both cases, the neutral reactor voltage reached about 0.45 pu.

Under the same fault conditions as that of Fig (7.12.a), higher sending-end source impedance ratio (Z_{S0}/Z_{S1} = 2.5) has increased the phase and neutral reactor overvoltages to 1.42 and 0.61 pu respectively.

For a solid a-E fault at the sending-end busbar, it has been found that with prefault loading ($\delta = +30^{0}$) and under the same fault conditions as that of Fig (7.12.a), both phase and neutral reactor overvoltages have insignificantly increased as shown in Fig (7.15.a). Fig (7.15.b), however, shows that with a ratio $|V_S/V_R|$ = 1.1, the same fault significantly increased overvoltage levels. The Fig. shows that phase reactor voltage increased from 1.37 to 1.51 pu while that of the neutral reactor increased

from 0.58 to about 0.64 pu. It has to be mentioned, however, that shunt reactor is supposed to stabilize the voltage along the line and the 1.1 $|V_S/V_R|$ ratio may not be reached in practice.

The effect of degrees of shunt compensation on reactor overvoltage is shown in Fig (7.16) for a close-up, solid a-E fault under the same conditions as that of Fig (7.12.a) but with h_1 = .5 and 1.25 respectively. Fig (7.16.a) shows that the neutral reactor overvoltage has drastically increased to 0.89pu, while that of the phase reactor is about 1.23 pu. With an extreme limit of shunt compensation, the phase reactor voltage reached about 1.5 pu (an increase of 0.13 pu compared to Fig (7.12.a) with h_1 = .75), while that of the neutral reactor is reduced to about 0.32 pu.

From the computational results, therefore, Figs (7.9) - (7.16) show that, in general, higher reactor overvoltages are produced in case of 3-section feeder systems, Fig (7.11) - (7.16), than the case with single-section feeder systems. These overvoltages are produced due to single line-to ground faults that occur at the mid-point of the system when the prefault voltage is at its positive peak.

The results show that the worst overvoltage levels experienced by both the phase and the neutral reactors are far below the spark-over ratings of the arrestors protecting them (as mentioned earlier in this section). However, it has to be emphasized that extra care has to be taken when protecting the neutral reactor, in particular, so that the probability of losing it is minimised and secondary arc extinction can be achieved. Also, it has to be mentioned that if higher frequency component voltages are considered in the computational process, overvoltage levels higher than that shown in Figs (7.9) - (7.16) might be expected.

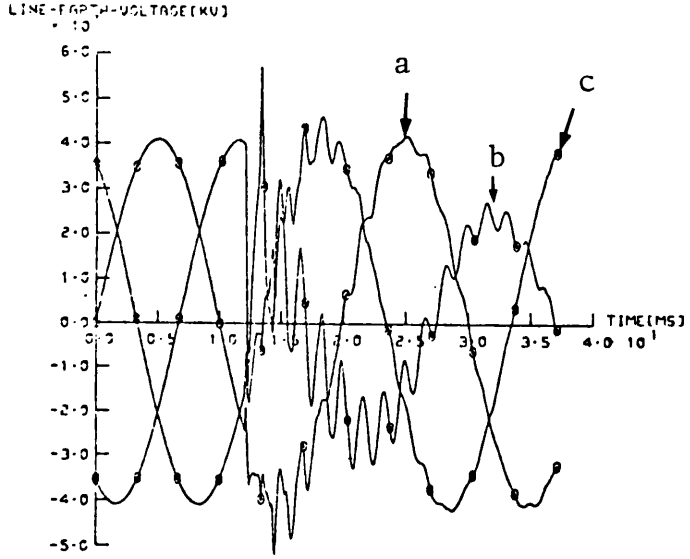

(a)

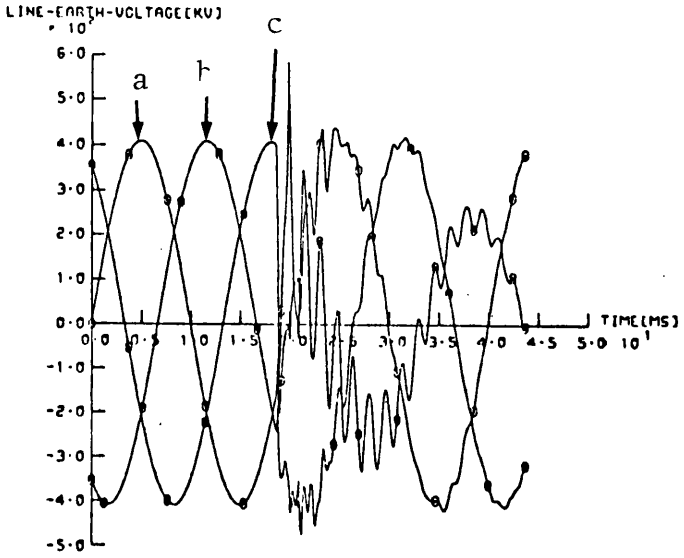

(b)

Fig 7.1

System overvoltages at the S.E. of the single-section feeder system examined.

$X = \ell/2$ (150 km), $V_S/V_R = 0^\circ$

S.S.C.L.=5GVA, R.S.C.L.=35GVA

$Q_S = Q_R = 100.0, h_1 = 0.75,$
$h_0 = 0.6$

$Z_{SSO}/Z_{SS1} = Z_{RSO}/Z_{RS1} = 1.0$

a- Solid 'b-E' fault
FT = 11.67 ms

b- Solid 'c-E' fault
FT = 18.33 ms.

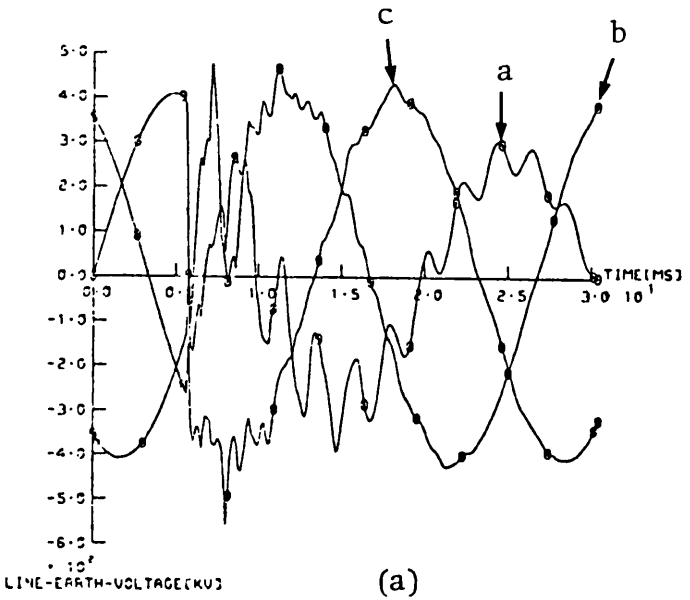

(a)

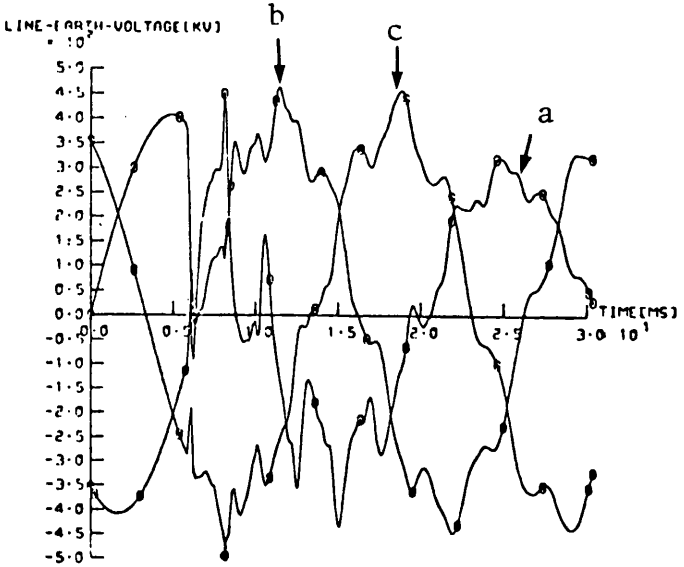

(b)

Fig 7.2

System overvoltages at the S.E. of the single-section feeder system examined.

- Solid 'a-E' fault at max. 'V_a', FT = 5 ms.

a- X = 210 km.

b- X = ℓ (300 km).

- Other fault conditions are similar to that of Fig 7.1.

⊙ Voltage or current of phase 'a'
o Voltage or current of phase 'b'
o Voltage or current of phase 'c'

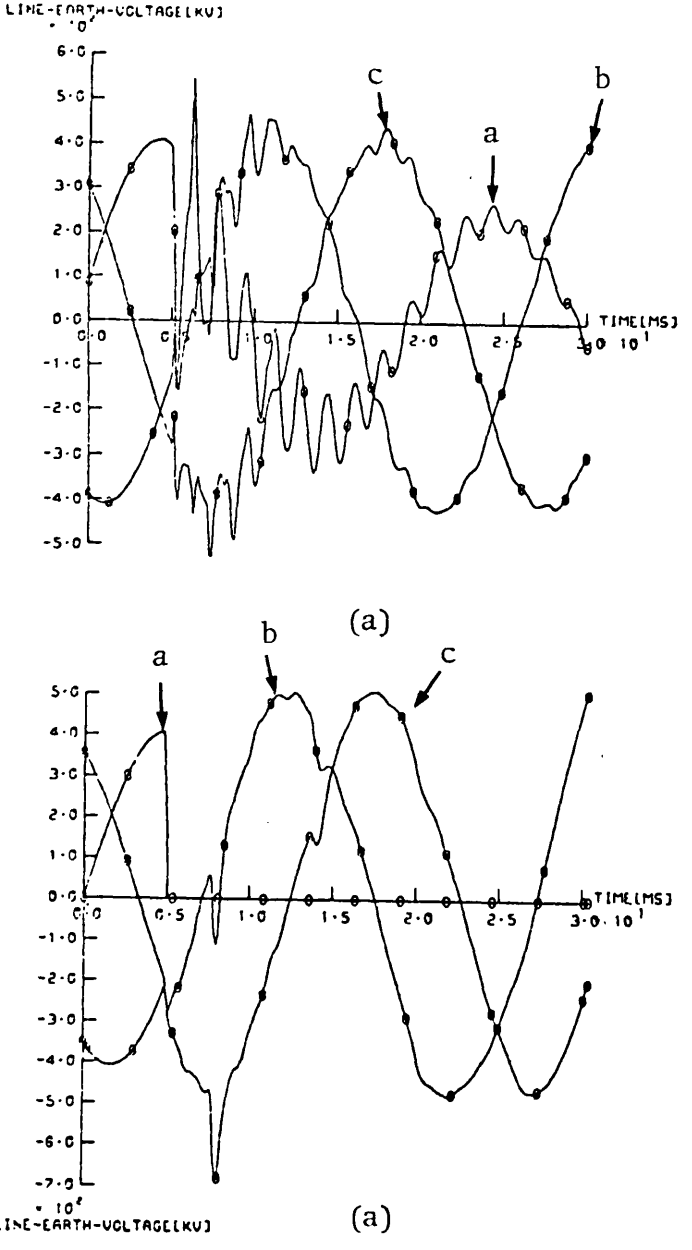

Fig 7.3

System overvoltages at the S.E. of the single-section feeder system examined.

a- Solid 'a-E' fault.

$V_S/V_R = 12^o$, FT = 4.67 ms.

b- Solid 'b-c' fault.

$V_S/V_R = 0^o$, FT = 10.0 ms.

- Other fault conditions are similar to that of Fig 7.1.

Fig 7.4

System overvoltages at the S.E. of the middle section of the 3-section feeder system examined.

- X = 0
- S.S.C.L.=R.S.C.L. = 35GVA

a- Solid 'a-E' fault.
FT = 5 ms.

b- Solid 'c-E' fault.
FT = 18.33 ms.

- Other fault conditions are similar to that of Fig 7.1.

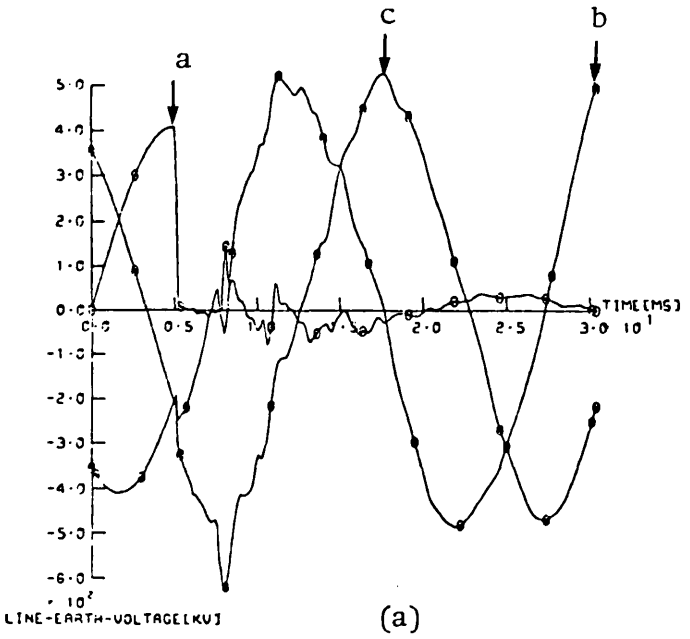

(a)

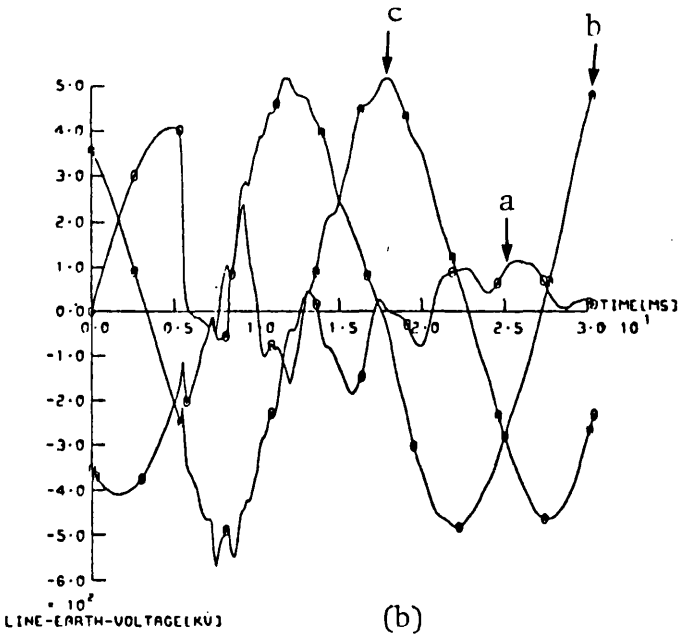

(b)

Fig 7.5

System overvoltages at the S.E. of the middle section of the 3-section feeder system examined.

- Solid 'a-E' faults.

a- X = 40 km

b- X = ℓ/2 (150 km).

- Other fault conditions are similar to that of Fig 7.4.

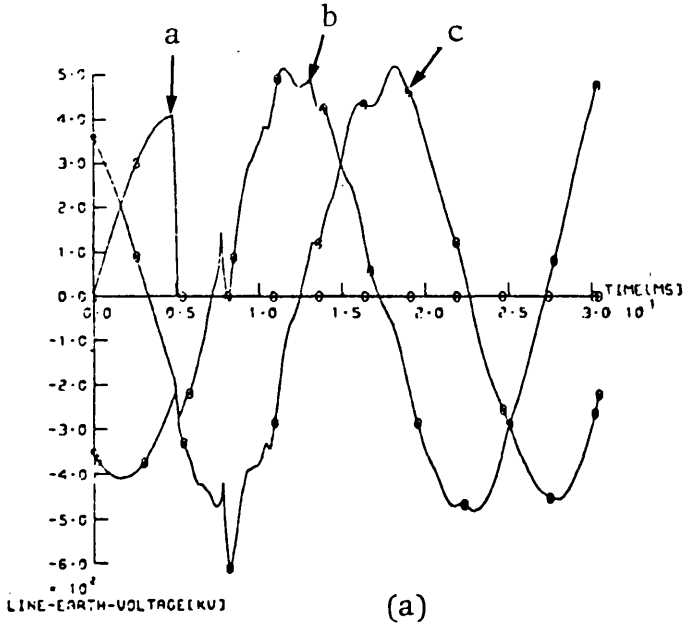

(a)

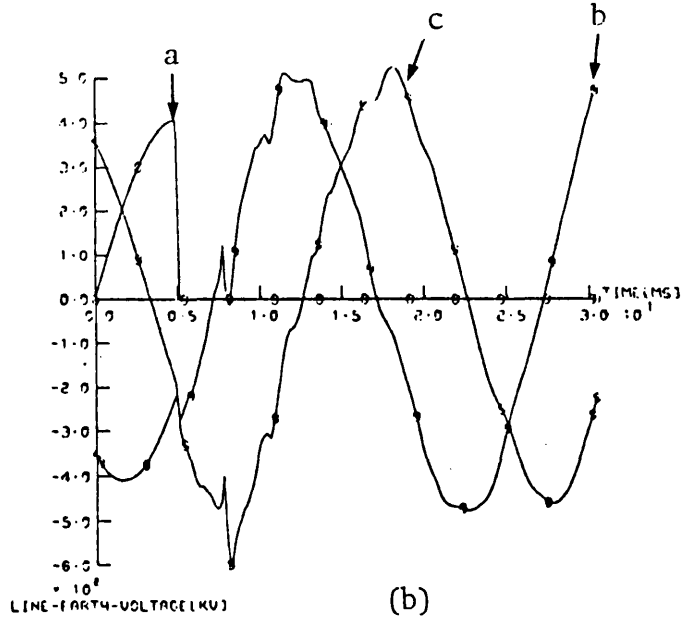

(b)

Fig 7.6

System overvoltages at the S.E. of the middle section of the 3-section feeder system examined.

- Solid 'a-E' fault.

a- S.S.C.L. = 5 GVA
R.S.C.L. = 35 GVA

b- S.S.C.L. = 35 GVA
R.S.C.L. = 5 GVA

- Other fault conditions are similar to that of Fig 7.5.

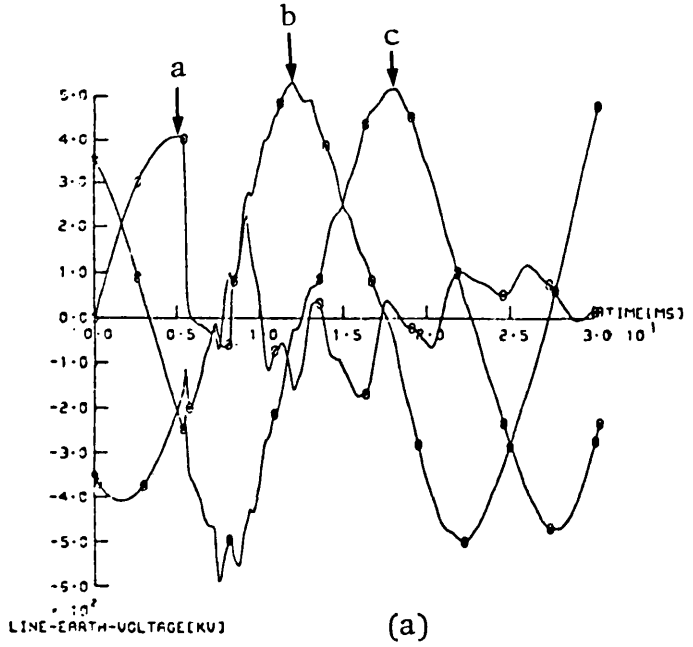

(a)

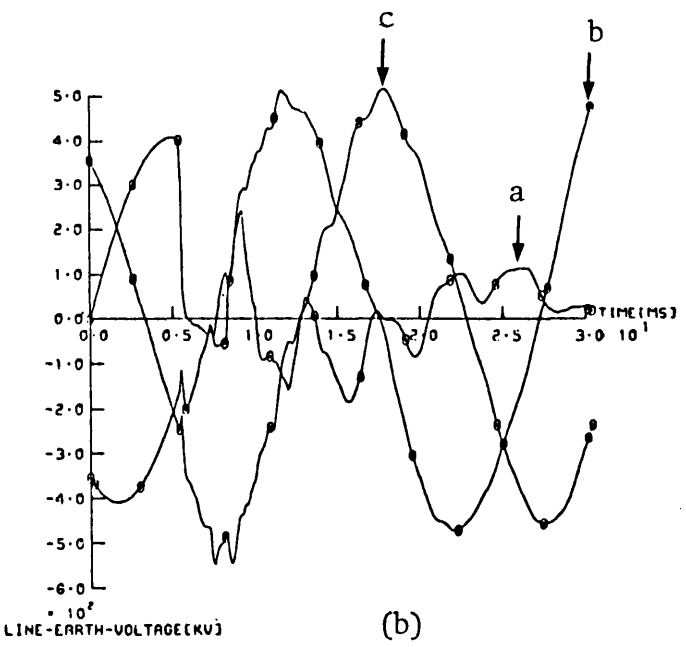

(b)

Fig 7.7

System overvoltages at the S.E. of the middle section of the 3-section feeder system examined.

- Solid 'a-E' mid-point faults.

a- $Z_{SSO}/Z_{SS1} = Z_{RSO}/Z_{RS1} = 2.5$.

b- $Z_{SSO}/Z_{SS1} = Z_{RSO}/Z_{RS1} = 0.25$.

- Other fault conditions are similar to that of Fig 7.5.

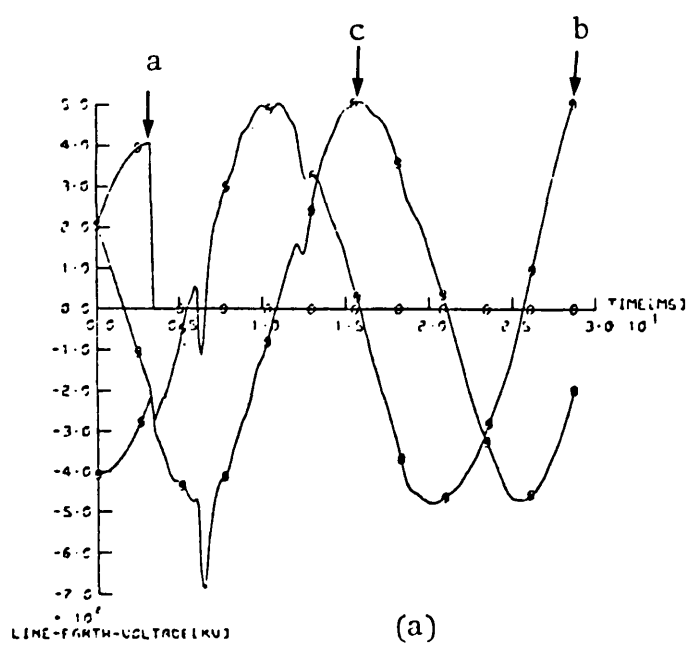

(a)

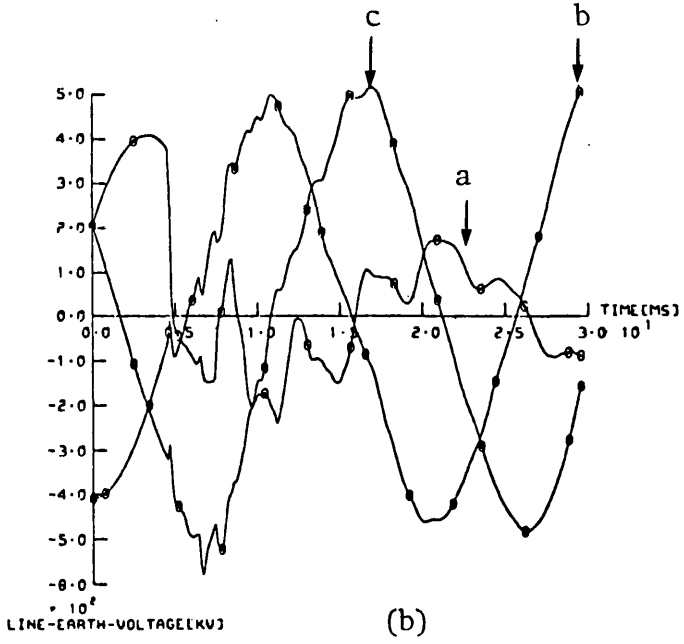

(b)

Fig 7.8

System overvoltages at the S.E. of the middle section of the 3-section feeder system examined.

- Solid 'a-E' faults.

- $V_S/V_R = \underline{|30^o}$

a- X = 0, FT = 3.33 ms.

b- X = 150 km, FT = 4.16 ms.

- Other fault conditions are similar to that of Fig 7.5.

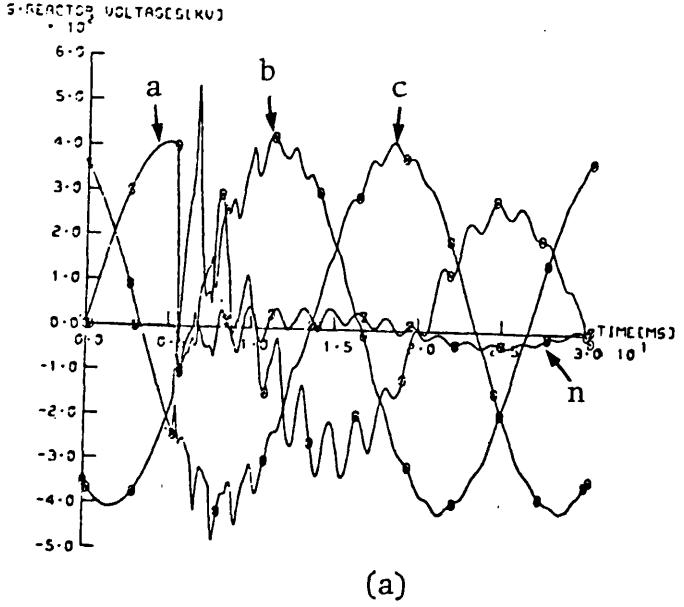

(a)

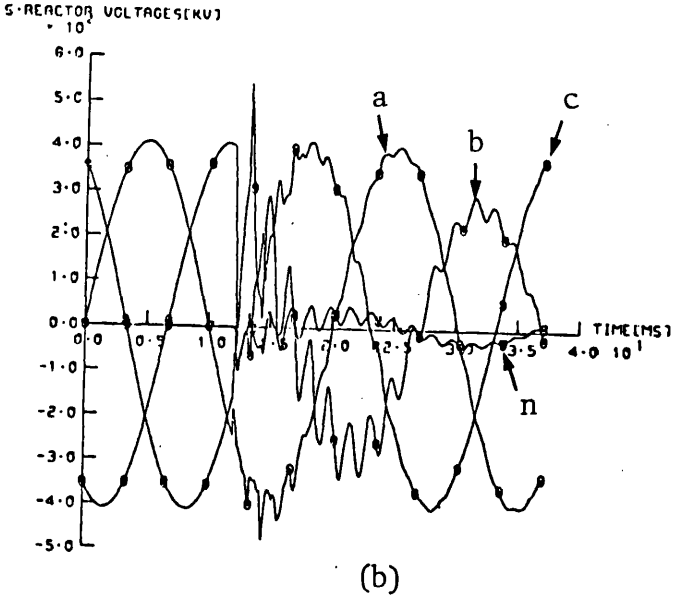

(b)

Fig 7.9

Overvoltages of reactors at the S.E. of the single-section feeder system examined.

- Single-line to earth mid-point faults.

a- Solid 'a-E' fault, FT= 5 ms.

b- Solid 'b-E' fault, FT=11.67ms

- Other fault conditions are similar to that of Fig 7.1.

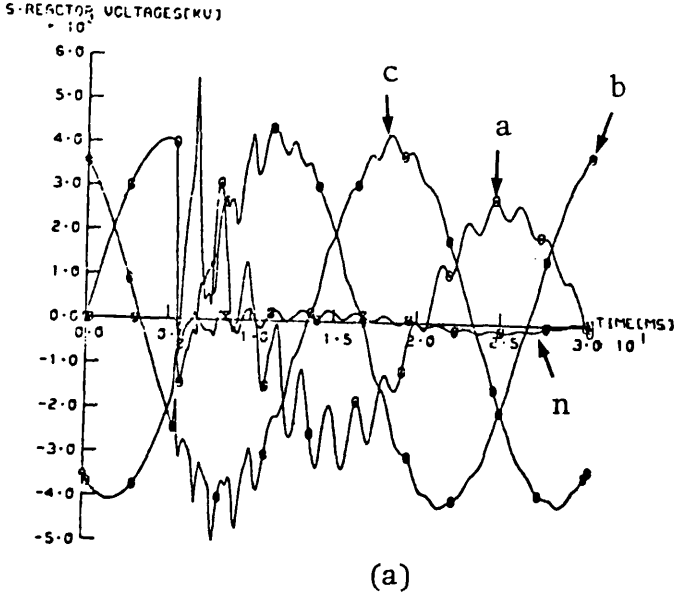

(a)

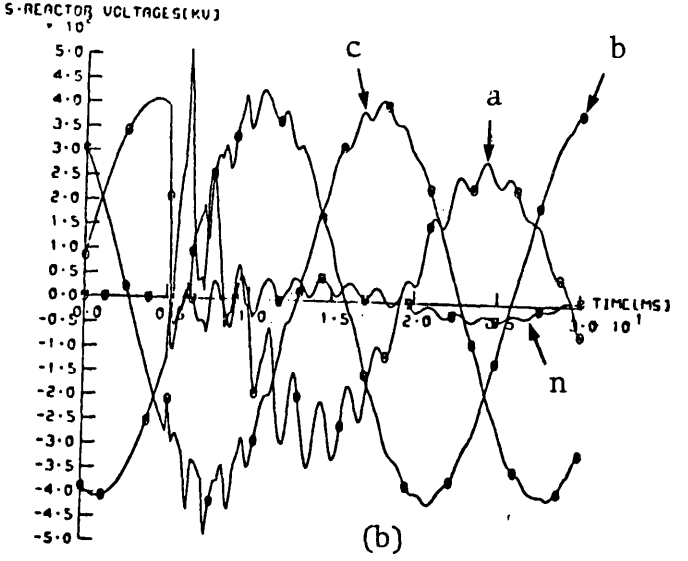

(b)

Fig 7.10

Overvoltages of reactors at the S.E. of the single-section feeder system examined.

- Solid 'a-E' mid-point faults.

a- h_1 = 1.25, h_0 = 1.4, FT = 5 ms.

b- $V_S/V_R = \underline{12}^{\circ}$, FT = 4.67 ms.

- Other fault conditions are similar to that of Fig 7.9.

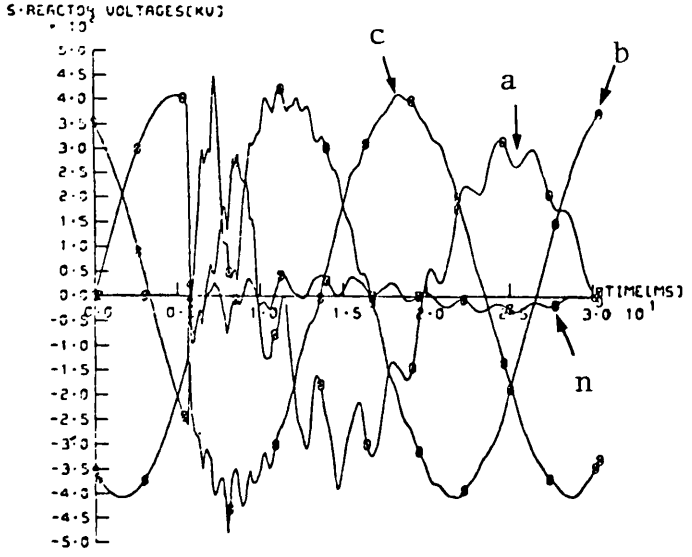

(a)

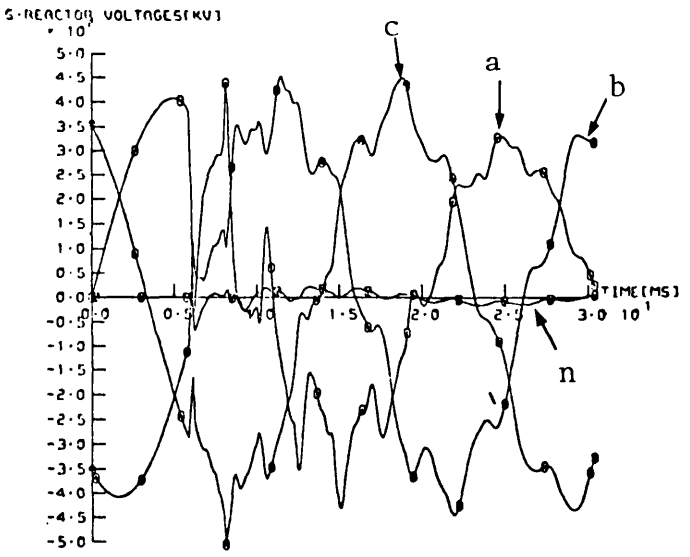

(b)

Fig 7.11

Overvoltages of reactors at the S.E. of the single-section feeder system examined.

- Solid 'a-E' faults.

a- X = 210 km.

b- X = ℓ (300 km).

- Other fault conditions are similar to that of Fig 7.2.

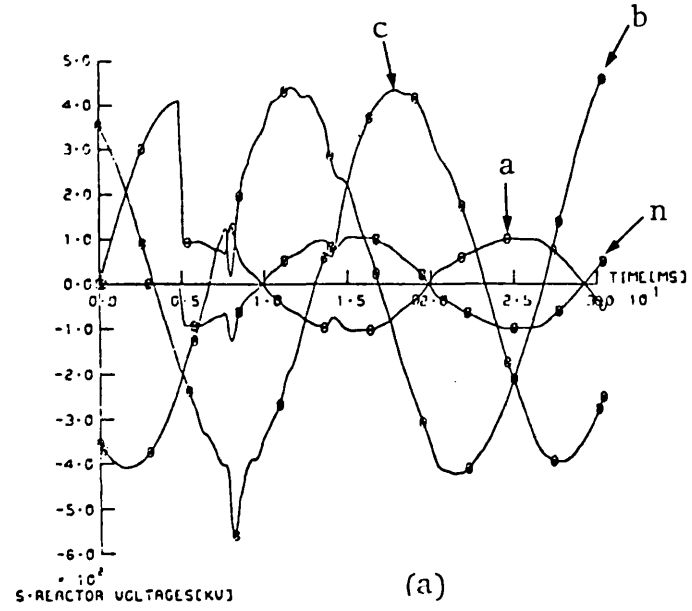

(a)

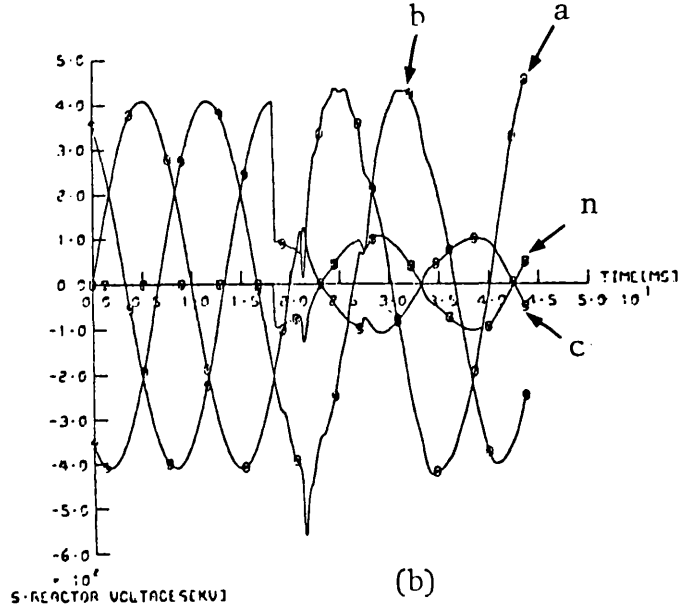

(b)

Fig 7.12

Overvoltages of reactors at the S.E. of the middle section of the 3-section feeder system examined.

- Solid single-line to earth close-up faults.

a- 'a-E' fault.

b- 'c-E' fault.

- Fault conditions are similar to that of Fig 7.4.

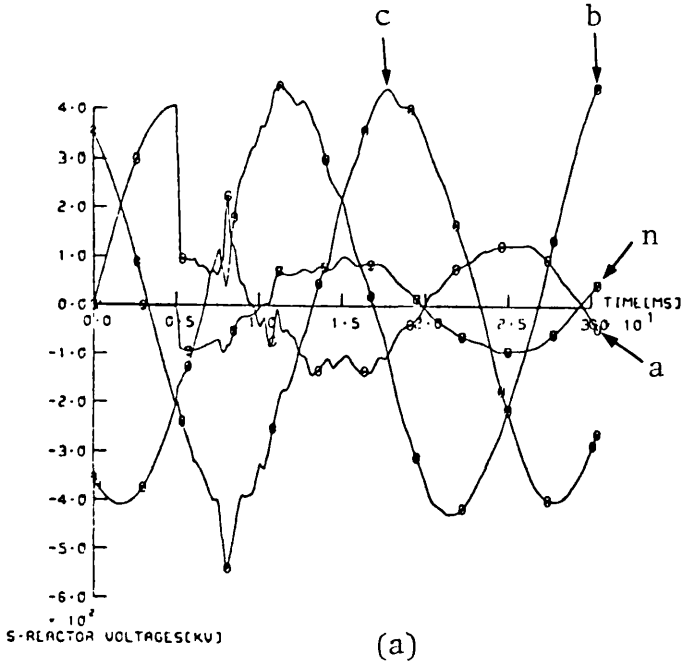

(a)

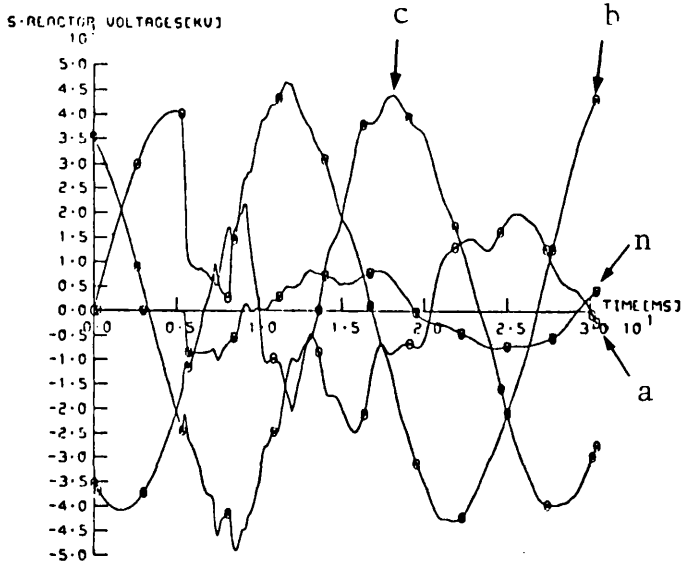

(b)

Fig 7.13

Overvoltages of reactors at the S.E. of the middle section of the 3-section feeder system examined.

- Solid 'a-E' faults.

a- X = 40 km.

b- X = ℓ/2 (150 km).

- Fault conditions are similar to that of Fig 7.5.

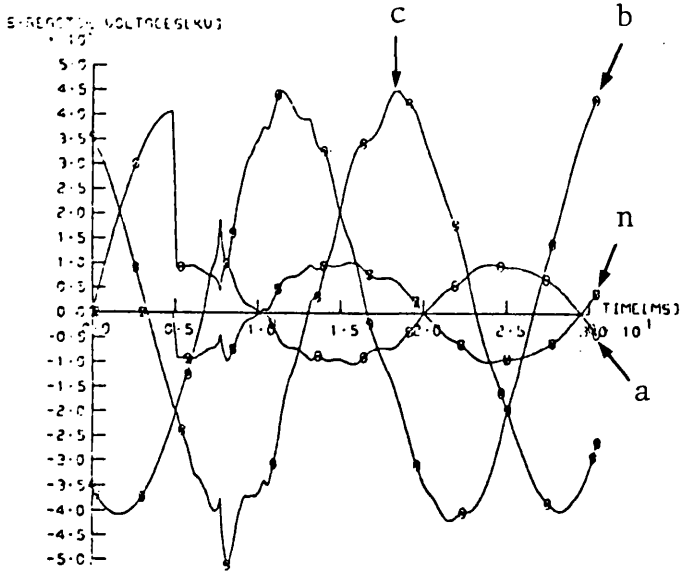

(a)

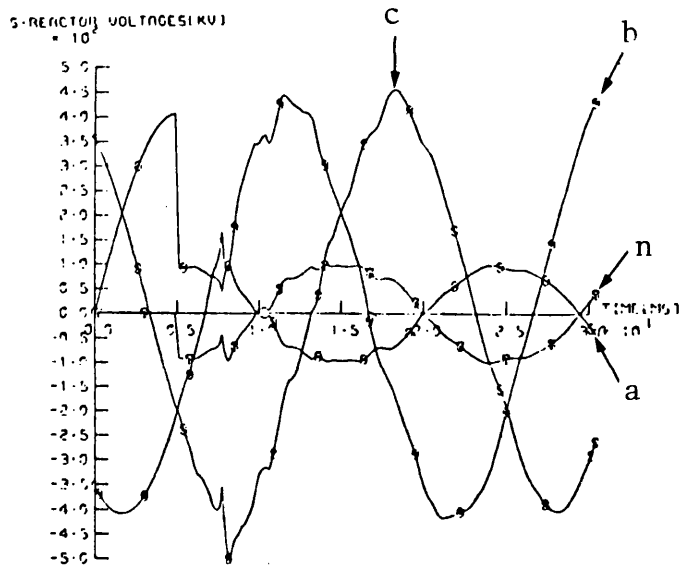

(b)

Fig 7.14

Overvoltages of reactors at the S.E. of the middle section of the 3-section feeder system examined.

- Solid 'a-E' close-up faults.

a- S.S.C.L. = 5 GVA
R.S.C.L. = 35 GVA

b- S.S.C.L. = 35 GVA
R.S.C.L. = 5 GVA

- Fault conditions are similar to that of Fig 7.6.

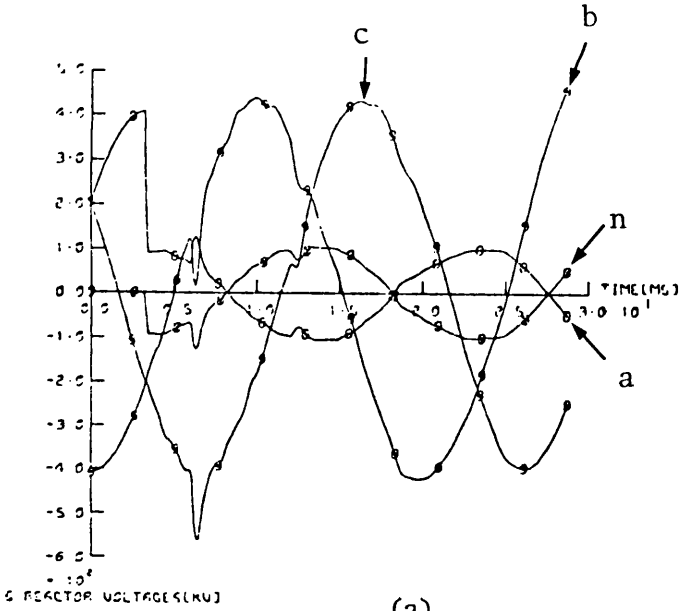

(a)

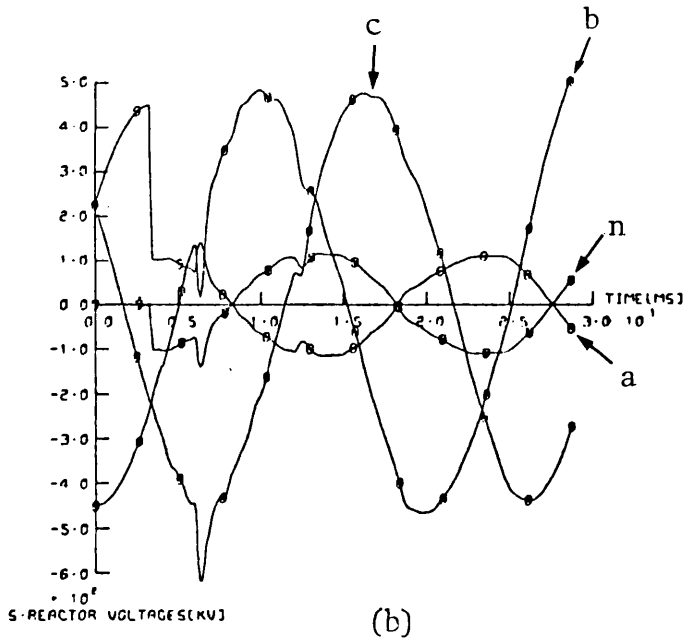

(b)

Fig 7.15

Overvoltages of reactors at the S.E. of the middle section of the 3-section feeder system examined.

- Solid 'a-E' close-up faults.

a- $V_S/V_R = 1.0 \angle 30^o$

b- $V_S/V_R = 1.1 \angle 30^o$

- Fault conditions are similar to that of Fig 9.8.a.

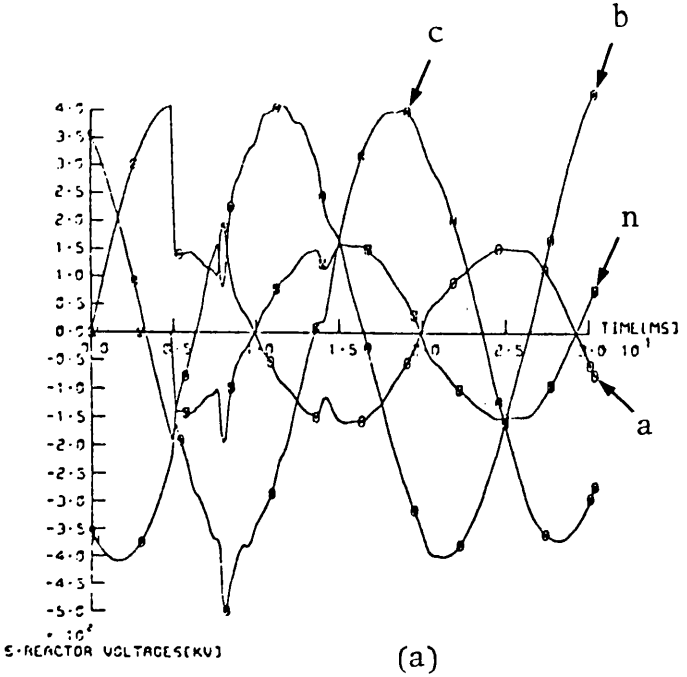

(a)

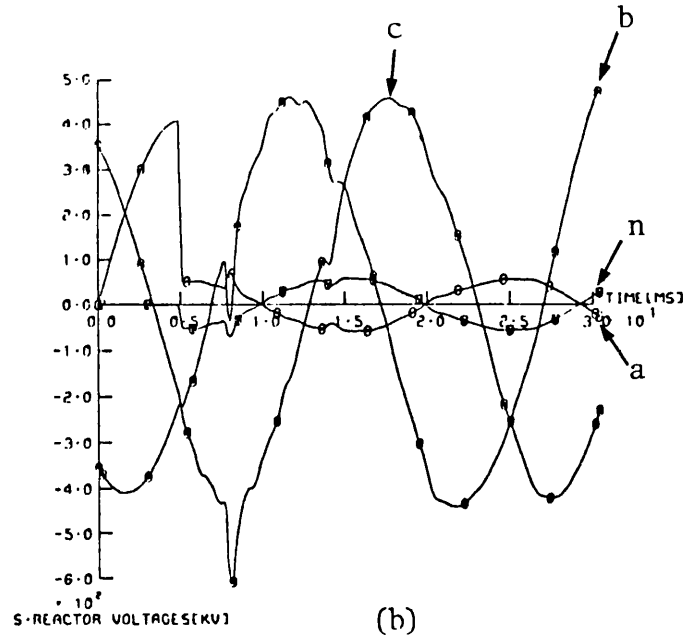

(b)

Fig 7.16

Overvoltages of reactors at the S.E. of the middle section of the 3-section feeder system examined.

- Solid 'a-E' close-up faults.

a- $h_1 = 0.5$, $h_0 = 0.21$

b- $h_1 = 1.25$, $h_0 = 1.4$

- Other fault conditions are similar to that of Fig 7.12.a.

CHAPTER 8 DIGITAL SIMULATION OF SATURATION EFFECTS IN 4-REACTOR COMPENSATED SYSTEMS

8.1 Introduction

The lower value of saturation voltage of non-linear shunt reactors (main reactors) that might be designed for use on EHV systems has been reported[23] to be 1.25 times the rated r.m.s. reactor voltage. However, it is generally felt that saturation effects for a linear reactor would probably begin to occur at higher voltages and a figure around 1.8 times the reactor rated peak voltage has been considered in a realistic system.[34] In addition, the knee-point voltage of the neutral reactor has been assumed to be 155 kV (rms), i.e. 219.2 kV (peak). The knowledge of the knee-point voltages[34] of phase and neutral reactors has enabled the calculation of their saturation currents and flux linkages as tabulated in Table (5.3). According to these saturation levels, a thorough investigation of the likelihood of saturation of any of the 4-reactor limbs has been carried out for the 3-section feeder system.

Faults have been initiated in the middle line-section (300 km) and the possibility of saturation of its sending-end reactors, in particular, under different fault conditions, is reported in section (2) of this Chapter.

As will be seen from section (8.2), the only reactor limb that has reached or exceeded the saturation levels (of Table (5.3)) is the sending-end neutral reactor. This finding is extremely important since, due to saturation, the sending-end neutral reactor can not, as it should do, help in neutralising line inter-phase capacitances and hence, secondary arc extinction will become more difficult.

Saturation of sending-end neutral reactor has been digitally simulated using the methods developed in Chapter (4) and the computer-results showing the effect of the phenomena on primary system response are presented in section (8.3).

8.2 Probability of Saturation of the 4-legged Reactor Scheme

Some of the computer results showing the peak voltage, current, and flux linkage swings of the main and neutral sending-end reactors under different fault conditions are summarised in Table (8.1). The table clearly shows that saturation of any of the phase reactors is very unlikely. From saturation view point, the worst cases for the phase-reactors are obviously cases (1) and (11-16).

For case (1), the Table shows that the reactor flux linkage swing (0.62) is far below its saturation level (equation 5.9). For cases (11-16), the absolute $|V_S/V_R|$ ratio is assumed = 1.1. Inspite of the fact that the shunt reactor is supposed to stabilise the voltage along the line so that the ratio $|V_S/V_R|$ is kept nearly unity, again, the Table shows that the phase-reactor flux linkage swing reaches a maximum value of 0.66 pu (case-11) which is far below unity. It can therefore be concluded that no saturation of any of the phase-reactors is, if ever, possible under different fault conditions.

On the contrary, the Table shows that saturation of the neutral reactor is most likely. From saturation view point, it is evident that the worst cases are, in general, single-line-to-ground faults that occur at an instant of time that corresponds to zero faulted-phase-ground voltage (prior to the fault). At such fault instant, line currents and, hence, reactor currents, are highly offset and it follows that neutral current and flux linkage, in this case, can reach or exceed its saturation levels.

Case Study	Type of Fault	X	V_S/V_R	FT (S)	Sources Z_{SO} / Z_{S1}		Source cap. (GVA)		Sources 'Q' Factor		Shunt compensation		Main Reactor			Neutral Reactor		
					$\frac{Z_{SSO}}{Z_{SS1}}$	$\frac{Z_{RSO}}{Z_{RS1}}$	S.SCL	R.SCL	Q_S	Q_R	h_1	h_0	$V_{m_{(kv)}}$	$I_{m_{(A)}}$	$\psi_{m_{(pu)}}$	$V_{n_{(kv)}}$	I_{n} (A)	ψ_{n} (pu)
1	a-E	0	$\underline{\vert 0^\circ}$	0.005	1	1	35	35	100	100	.75	.6	559	192	0.62	128	149	0.51
2	"	$\ell/2$	"	"	"	"	"	"	"	"	"	"	490	175	0.56	103	112	0.39
3	"	ℓ	"	"	"	"	"	"	"	"	"	"	485	175	0.56	93.5	102	0.350
4	a-E	0	$\underline{\vert 0^\circ}$	0.0	1	1	35	35	100	100	.75	.6	424	185	0.59	109	287	0.991
5	"	$\ell/2$	$\underline{\vert 30^\circ}$	.19166	1	1	35	35	100	100	.75	.6	415	181	0.58	80.7	203	0.70
6	"	ℓ	$\underline{\vert 30^\circ}$	0.0	1	1	35	35	100	100	.75	.6	426	180	0.58	74.5	157	0.54
7	"	0	$\underline{\vert 30^\circ}$	.01833	1	1	35	35	100	100	.75	.6	424	185	0.59	109	287	0.991
8	"	ℓ	$\underline{\vert 30^\circ}$	.005	1	1	35	35	100	100	.75	.6	460	179	0.57	93.5	102	0.350
9	"	$\ell/2$	$\underline{\vert 30^\circ}$	.004166	1	1	35	35	100	100	.75	.6	473	175	0.56	101	111	0.38
10	"	0	$\underline{\vert 30^\circ}$	.00333	"	"	"	"	"	"	"	"	560	179	0.57	128	150	0.52
11	"	0	$1.1\underline{\vert 30^\circ}$	.01833	"	"	"	"	"	"	"	"	467	204	0.66	120	316	1.09
12	a-E	$\ell/2$	$1.1\underline{\vert 30^\circ}$	0.01912	1	1	35	35	100	100	.75	"	456	199	0.64	84.8	213	0.74

Table 8.1

V_m , I_m = peak voltage and current of main reactor

$\psi_m = (\psi_{mp}) / \psi_{mS}$

ψ_{mp} , ψ_{mS} = main reactor peak and saturation flux linkages respectively.

V_n , I_n = peak voltage and current of neutral reactor respectively.

$\psi_n = (\psi_{np}) / \psi_{nS}$

ψ_{np} , ψ_{nS} = neutral reactor peak and saturation flux linkages respectively.

ψ_{mS} , ψ_{nS} are given by equation (5.9).

Case Study	Type of Fault	X	V_S/V_R	FT (S)	Sources Z_{SO} / Z_{S1}		Source cap (GVA)		Sources Q Factor		Shunt compensation		Main Reactor			Neutral Reactor		
					Z_{SSO} Z_{SS1}	Z_{RSO} Z_{RS1}	S.SCL	R.SCL	Q_S	Q_R	h_1	h_0	$V_{m(kv)}$	$I_{m(A)}$	$\psi_{m(pu)}$	$V_{n(kv)}$	$I_{n(A)}$	$\psi_{n(pu)}$
13	a-E	$\ell/2$	$1.1\angle 30^\circ$	0.0	1	1	35	35	100	100	.75	.6	462	196	0.63	74.5	154	0.54
14	"	0	"	.0033	"	"	"	"	"	"	"	"	615	196	0.63	141	165	0.57
15	"	$\ell/2$	"	.004126	"	"	"	"	"	"	"	"	517	192	0.62	90.6	116	0.40
16	"	ℓ	"	0.005	"	"	"	"	"	"	"	"	500	196	0.63	93.5	102	0.35
17	"	0	$\angle 0^\circ$	.005	"	"	"	"	"	"	1.25	1.4	611	315	0.61	71.1	343	0.30
18	"	$\ell/2$	"	"	"	"	"	"	"	"	"	"	501	304	0.59	56.3	253	0.22
19	"	ℓ	"	"	"	"	"	"	"	"	"	"	419	321	0.62	46.4	320	0.28
20	"	0	"	0.0	"	"	"	"	"	"	0.5	0.21	398	125	0.60	167	101	0.50
21	"	$\ell/2$	"	"	"	"	"	"	"	"	"	"	396	122	0.59	127	73.4	0.36
22	"	ℓ	"	"	"	"	"	"	"	"	"	"	403	120	0.58	101	56.2	0.28
23	"	0	"	0.005	"	"	"	"	"	"	"	"	497	112	0.54	195	52.8	0.26
24	a-E	$\ell/2$	$\angle 0^\circ$	0.0	1	1	35	35	100	100	0.5	0.21	469	115	0.55	158	40.1	0.20
25	"	ℓ	"	"	"	"	"	"	"	"	"	"	463	115	0.55	143	36.7	0.18
26	"	0	"	.005	"	"	5	35	"	"	.75	.60	491	177	0.57	98.7	145	0.50
27	"	$\ell/2$	"	.005	"	"	5	35	"	"	.75	.60	471	175	0.56	108	119	0.41
28	"	ℓ	"	"	"	"	"	"	"	"	"	"	409	177	0.57	80.4	162	0.56

Table 8.1 continued

Case Study	Type of Fault	X	V_S/V_R	FT (S)	Sources Z_{SO} / Z_{S1}		Source cap (GVA)		Sources 'Q' Factor		Shunt compensation		Main Reactor			Neutral Reactor		
					Z_{SSO} Z_{SS1}	Z_{RSO} Z_{RS1}	S.SCL	R.SCL	Q_S	Q_R	h_1	h_0	$V_{m(kv)}$	$I_{m(A)}$	$\psi_{m(pu)}$	$V_{n(kv)}$	I_{n} (A)	ψ_{n} (pu)
29	a-E	0	$\underline{\lfloor 0^\circ}$	0.0	1	1	5	35	100	100	.75	.60	421	182	0.58	105	280	0.967
30	"	$\ell/2$	"	"	"	"	"	"	"	"	"	"	416	181	0.58	86.5	212	0.73
31	"	ℓ	"	"	"	"	"	"	"	"	"	"	409	177	0.57	80.4	162	0.56
32	"	0	"	0.005	"	"	35	5	"	"	"	"	500	177	0.57	99.8	144	0.50
33	"	$\ell/2$	"	"	"	"	"	"	"	"	"	"	482	173	0.56	92.4	106	0.37
34	"	ℓ	"	"	"	"	"	"	"	"	"	"	462	172	0.55	81.2	88.8	0.31
35	"	0	"	0.0	"	"	"	"	"	"	"	"	420	182	0.58	105	280	0.967
36	"	$\ell/2$	"	"	"	"	"	"	"	"	"	"	411	179	0.57	77.4	196	0.68
37	"	ℓ	"	"	"	"	"	"	"	"	"	"	405	177	0.57	64.6	141	0.49
38	"	0	$\underline{0^\circ}$	0.005	2.5	2.5	35	35	100	100	.75	.6	581	179	0.57	133	154	0.53
39	"	$\ell/2$	"	"	"	"	"	"	"	"	"	"	496	175	0.56	107	118	0.41
40	"	ℓ	"	"	"	"	"	"	"	"	"	"	492	175	0.56	104	110	0.38
41	"	0	"	0.0	"	"	"	"	"	"	"	"	426	172	0.55	116	289	0.998
42	"	$\ell/2$	"	"	"	"	"	"	"	"	"	"	416	186	0.60	86.1	211	0.73
43	"	ℓ	"	"	"	"	"	"	"	"	"	"	415	182	0.58	80.0	165	0.57
44	"	0	"	.005	1.0	1.0	"	"	300	300	"	"	560	179	0.57	128	150	0.52

Table 8.1 continued

Case Study	Type of Fault	X	V_S/V_R	FT (S)	Sources Z_{SO} / Z_{S1}		Source cap (GVA)		Sources 'Q' Factor		Shunt compensation		Main Reactor			Neutral Reactor		
					Z_{SSO} Z_{SS1}	Z_{RSO} Z_{RS1}	S.SCL	R.SCL	Q_S	Q_R	h_1	h_0	$V_{m(kv)}$	$I_{m(A)}$	$\psi_{m(pu)}$	$V_{n(kv)}$	$I_{n(A)}$	$\psi_{n(pu)}$
45	a-E	$\ell/2$	$\underline{0}^o$	.005	1.0	1.0	35	35	300	300	.75	.6	490	173	0.56	103	112	0.39
46	"	ℓ	"	"	"	"	"	"	"	"	"	"	485	175	0.56	93.5	102	0.35
47	"	0	"	0.0	"	"	"	"	"	"	"	"	425	185	0.59	109	288	0.994
48	"	$\ell/2$	"	"	"	"	"	"	"	"	"	"	416	179	0.57	82	206	0.71
49	"	ℓ	"	"	"	"	"	"	"	"	"	"	416	179	0.57	74.5	157	0.54
50	a-E	0	"	.005	.25	.25	"	"	100	100	0.75	0.60	552	179	0.57	124	148	.408
51	"	$\ell/2$	"	"	"	"	"	"	"	"	"	"	487	175	0.56	87.5	109	0.38
52	"	ℓ	"	"	"	"	"	"	"	"	"	"	483	175	0.56	87.7	97.3	0.34
53	"	0	"	0.0	"	"	"	"	"	"	"	"	420	185	0.59	109	285	0.984
54	"	$\ell/2$	"	"	"	"	"	"	"	"	"	"	416	182	0.58	79.2	203	0.70
55	"	ℓ	"	"	"	"	"	"	"	"	"	"	416	177	0.57	70.8	152	0.52
56	b-c-E	0	$\underline{0}$	0.0	1	1	"	"	"	"	"	"	433	184	0.59	82.4	220	0.76
57	"	"	"	.005	"	"	"	"	"	"	"	"	429	183	0.59	81.5	111	0.38
58	"	$\ell/2$	"	"	"	"	"	"	"	"	"	"	429	179	0.57	67.9	87.1	0.30
59	"	"	"	0.0	"	"	"	"	"	"	"	"	447	179	0.57	62.7	158	0.55
60	"	ℓ	"	"	"	"	"	"	"	"	"	"	424	174	0.56	57.0	122	0.42

Table 8.1 continued

According to Table (8.1), the worst cases are cases 4, 7, 11, 29, 35, 41, 47 and 53. Again, case study (11) may be excluded in view of the fact that shunt reactors are used to stabilise line voltage and an absolute $|V_S/V_R|$ ratio is unlikely to reach 1.1 pu.

Figs (8.1) - (8.3) show the 4-reactor voltage and current wave forms for study cases 4, 7 and 29 (of Table 8.1) respectively. The Figs. clearly show the offset nature of reactor currents, particularly that of the reactor phase connected to the faulted conductor (a) and the neutral. Also the absolute peak voltages and currents reported in Table (8.1) can be seen for the respective cases of Figs (8.1) - (8.3) and reactor flux linkage swings can be roughly calculated using Tables (5.3), (8.1) and equations (5.9).

Relatively high neutral reactor currents and flux linkage swings can also be produced for distant faults as may be seen from study cases 5, 12, 30, 36, 42, 48 and 54, of Table (8.1). Again, excluding case study (12), the reactor voltage and current wave forms for some of the above cases (5, 30, 36) are shown in Figs (8.4) - (8.6) respectively.

A similar series of studies have been carried out to examine the possibility of saturation of receiving-end reactors, and the conclusion is that none of the 4-reactors was found likely to saturate.

8.3 Effect of Reactor Saturation on Primary System Response

From the analysis presented in section (8.2), (Table (8.1) and Figs 8.1 - 8.6), it is very obvious that the neutral reactor would saturate. Accordingly, it has been decided to simulate the phenomena in order to examine its effect on primary system wave forms and hence, on system protective relays. Using the techniques developed in Chapter (4), a

computer program has been developed to simulate neutral reactor saturation in a 3-section feeder system. Computational results are presented in this section.

Fig (8.7) shows the sending-end wave forms under saturation. Fault conditions are analogous to case study (4) of Table (8.1) and saturation is assumed to occur after 5 ms.

Inspite of the fact that the techniques developed in Chapter (4) suggest that saturation time 'T_s' has to be specified, it has to be emphasised that, practically, saturation occurs only when reactor current and flux linkage exceed its saturation levels. The assumption, however, simplifies the investigation process and is highly justified particularly if reactor saturation is proven to have no or insignificant effects on primary system wave forms. Furthermore, it has to be mentioned that the voltage source that simulates saturation is switched into the circuit at the time the fault occurs. Therefore, it follows that due to this voltage source, superimposed voltage and current components are produced at the points of interest before the specified saturation time is reached.

Saturation has been found to have relatively insignificant effects on the sending-end voltage and current wave forms. This remark can be observed by comparing the individual voltage and current components of Fig (8.7) due to 'fault' and 'saturation' as may be seen from Fig (8.8). The Fig shows that the voltage component due to saturation is about 5.2 kV peak (for the healthy phases b,c), reduced to a nearly steady-state peak value of about 0.5 kV (Fig 8.8.b). On the other hand, fault-transient component voltage (Fig 8.8.a), reaches about 130 kV peak for the same phases. Therefore, a saturation voltage component which is about 4% of transient component is not expected to cause any significant change

in the overall voltage wave forms. Figs (8.8.c), (8.8.d) show that saturation component current is a very insignificant fraction of transient component, about 0.35% of its peak.

The effect of saturation time 'T_s' on saturation voltage and current components has also been examined. For example, Fig (8.9) shows the individual components under the same conditions as that of Fig (8.8) except that, in the former case, saturation occurs after 15 ms. A comparison of the two Figs. reveals that saturation time may affect the shape of saturation voltage and current wave forms but their magnitudes are still insignificant compared to the respective transient components.

Although case study (1) of Table (8.1) shows that saturation of the neutral reactor is unlikely for an a-E fault that occurs at maximum prefault a-E voltage, Fig (8.10) examines the effect of saturation, if it ever happens, on system wave forms. Saturation time 'T_s' is assumed to be 15 ms as may be seen from its source voltage wave forms of Fig (8.11.a). The individual transient and saturation voltage and current components of the wave forms of Fig (8.10) are shown in Fig (8.11.b) - (8.11.e). Again, the Figs show that saturation component voltages and currents are very negligible compared to that due to fault.

The effect of reactor saturation on sending-end wave forms in case of distance faults is shown in Fig (8.12) for a mid-point, solid a-E fault. Other fault conditions are similar to that of Fig (8.10).

Figs (8.12.b), (8.12.c) show that sound phase saturation component voltages are about 4% of that due to fault. Figs (8.12.d) and (8.12.e), again show that saturation component currents are very small compared to that due to fault.

Figs(8.13) - (8.14) show both transient and saturation voltage and current components respectively for a mid-point solid a-E fault under the same conditions as that of Fig (8.12) except that in the former cases, the reactor characteristic slope ratio (L_2/L_1 of Fig. 4.2) is assumed to be 0.5 and 0.01 respectively (rather than 0.1 as the case with Fig (8.12)). A comparison of the three Figs. indicates that the profile of saturation component voltage and current wave forms is not significantly affected by different slope ratios. Figs (8.12) - (8.14) show, however, that as the slope ratio increases, the absolute value of these components is reduced.

The effect of sending-end neutral reactor saturation on sending-end primary response under other fault conditions has been examined and the same basic findings were observed. A similar series of studies have been carried out for the receiving-end primary response and the same conclusions, i.e. that saturation does insignificantly affect the primary system wave forms, were reached.

Therefore, in view of these findings, it can be said that due to the fact that primary system response is hardly affected by saturation, system protective relays should be expected to function normally, as is the case with linear shunt reactors.

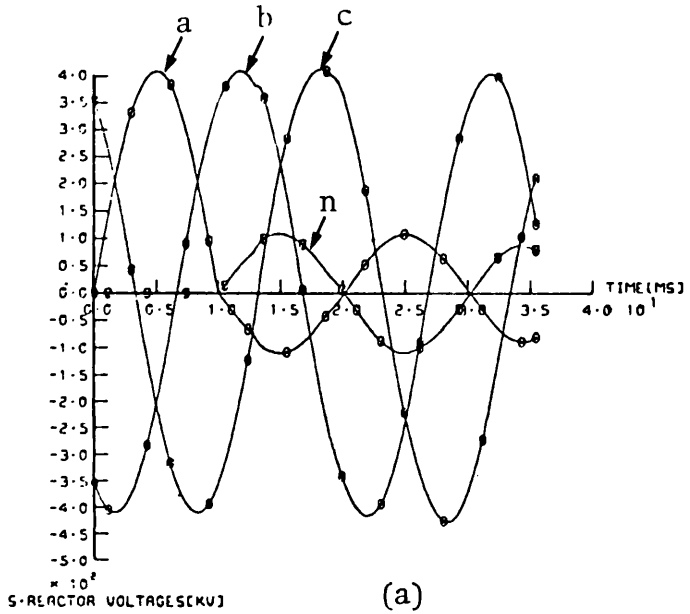

(a)

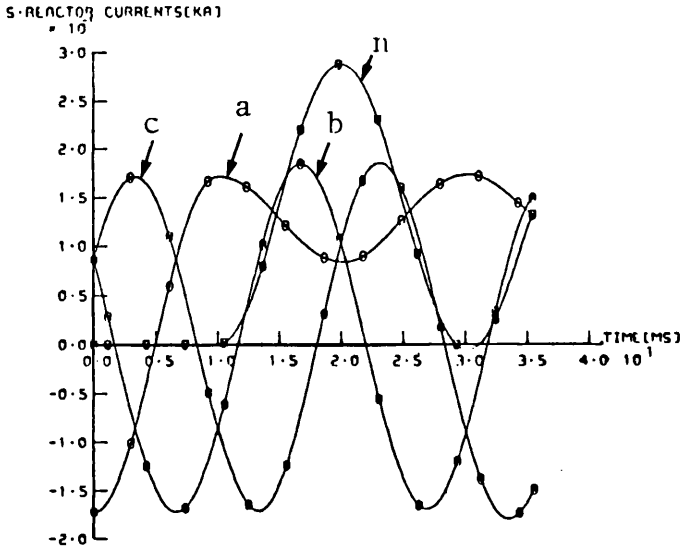

(b)

Fig 8.1

Voltage and current wave-forms of reactors at the S.E. of the middle section of the 3-section feeder system examined.

- Solid 'a-E', close-up fault.
- $V_S/V_R = \underline{0^o}$. FT = 10 ms.
- S.S.C.L. = R.S.C.L. = 35 GVA
- $Z_{SSO}/Z_{SS1} = Z_{RSO}/Z_{RS1} = 1.0$
- $Q_S = Q_R = 1.0$, $h_1 = 0.75$, $h_O = 0.6$

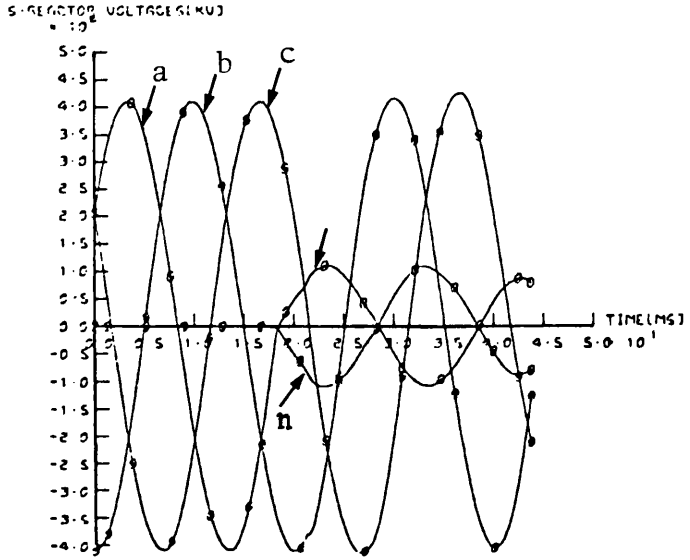

(a)

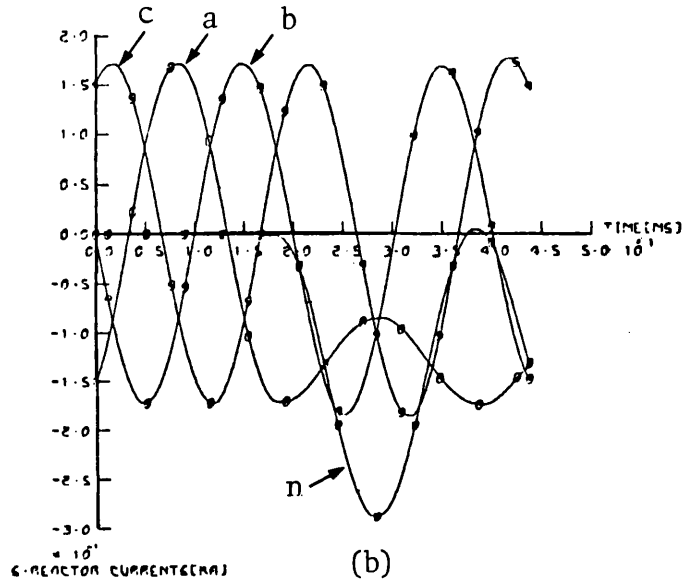

(b)

Fig 8.2

Voltage and current wave-forms of reactors at the S.E. of the middle section of the 3-section feeder system examined.

- Solid 'a-E' close-up fault.
- $V_S/V_R = \underline{30^o}$, FT = 18.33 ms.
- Other fault conditions are similar to that of Fig 8.1.

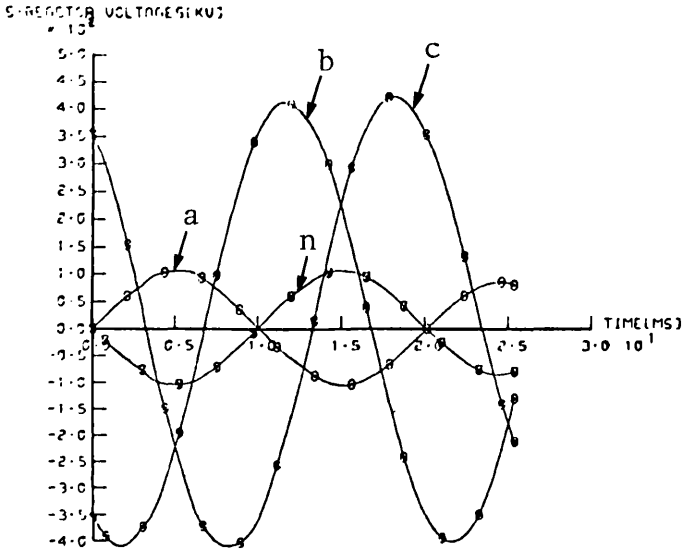

(a)

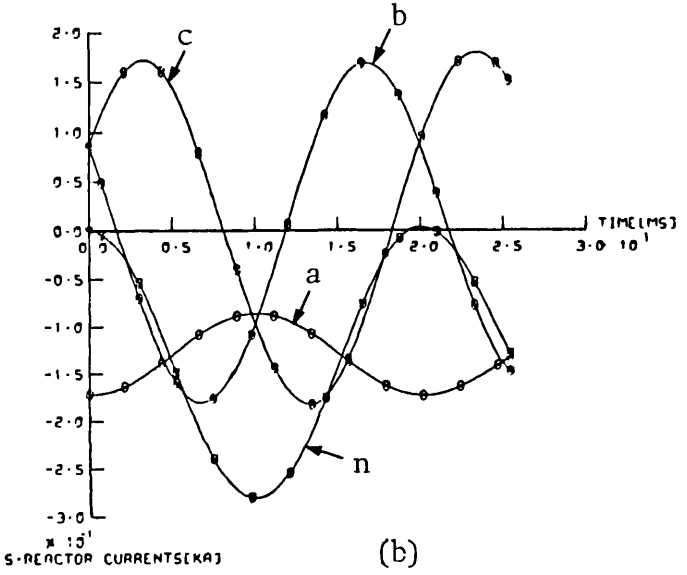

(b)

Fig 8.3

Voltage and current wave-forms of reactors at the S.E. of the middle section of the 3-section feeder system examined.

- Solid 'a-E' close-up fault.
- S.S.C.L. = 5 GVA, FT = 0.
- Other fault conditions are similar to that of Fig 8.1.

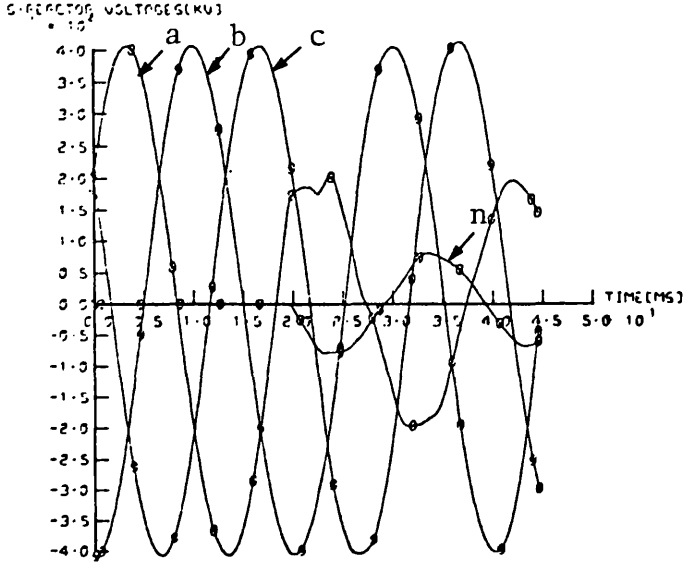

(a)

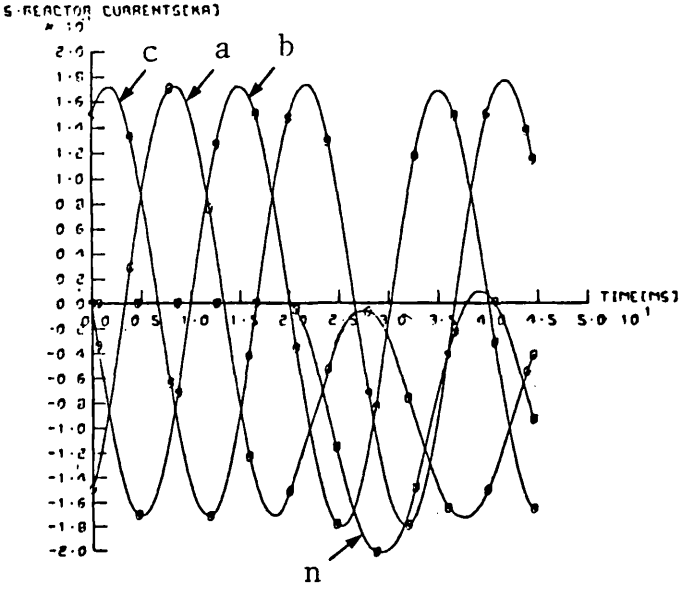

(b)

Fig 8.4

Voltage and current wave-forms of reactors at the S.E. of the middle section of the 3-section feeder system examined.

- Solid 'a-E' mid-point fault.
- $V_S/V_R = \underline{|30^o}$, FT = 19.67 ms.
- Fault conditions are similar to that of Fig 8.2.

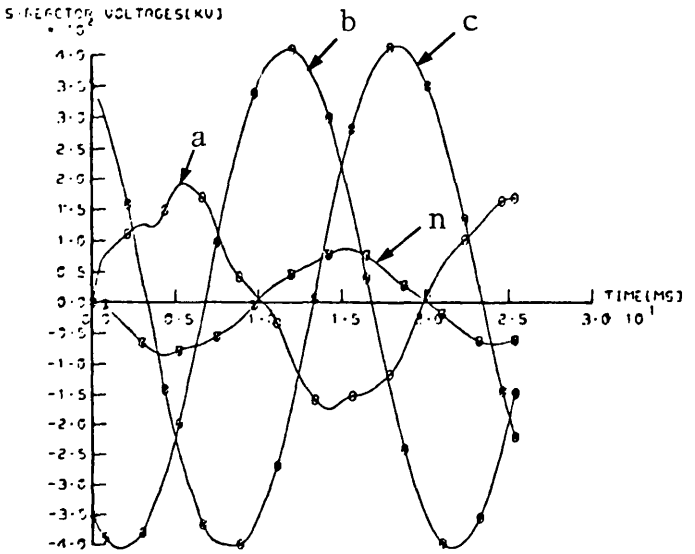

(a)

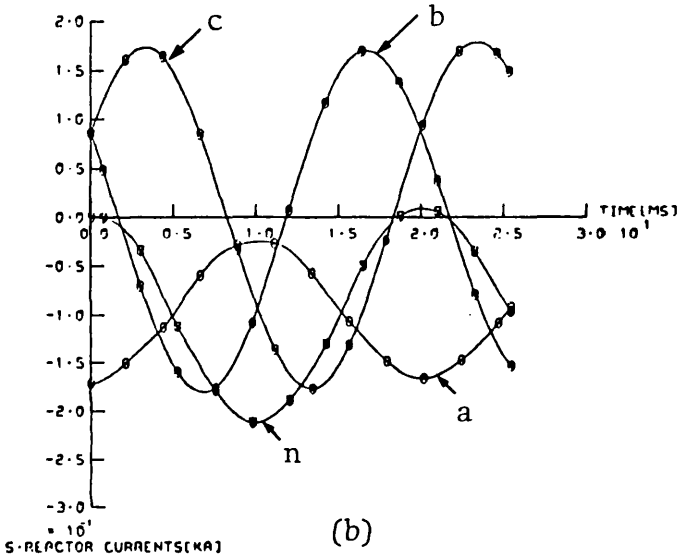

(b)

Fig 8.5

Voltage and current wave-forms of reactors at the S.E. of the middle section of the 3-section feeder system examined.

- Solid 'a-E' mid-point fault.
- Fault conditions are similar to that of Fig 8.3.

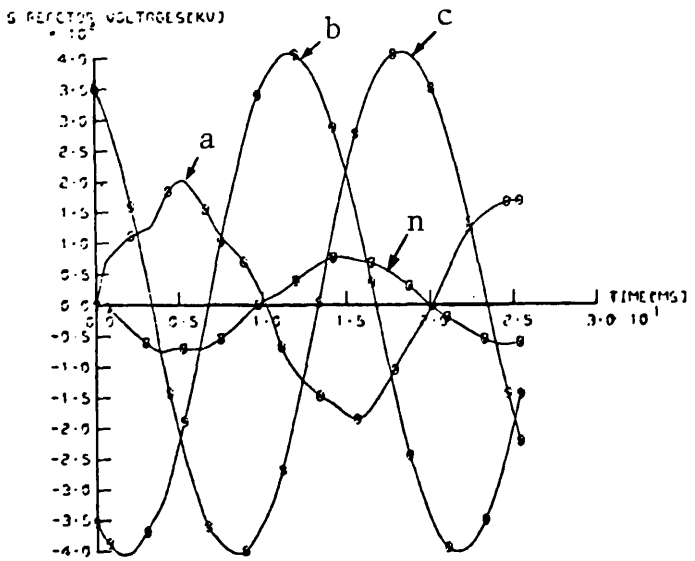

(a)

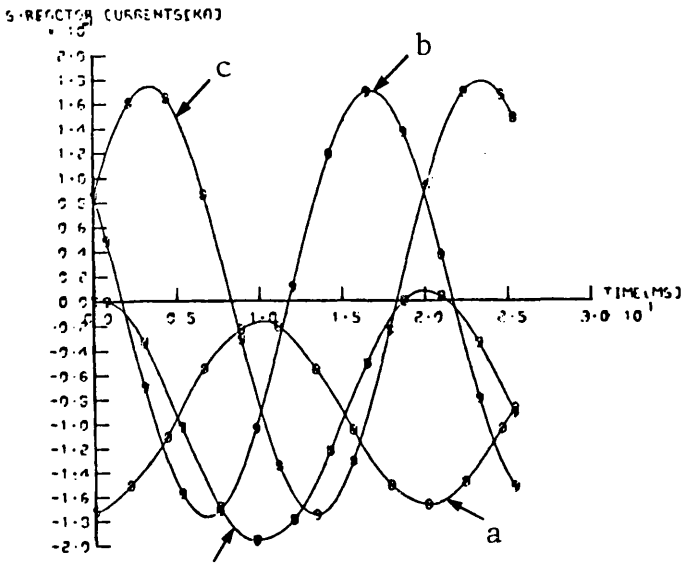

(b)

Fig 8.6

Voltage and current wave-forms of reactors at the S.E. of the middle section of the 3-section feeder system examined.

- Solid 'a-E' mid-point fault.
- S.S.C.L. = 35 GVA
  R.S.C.L. = 5 GVA
- Other fault conditions are similar to that of Fig 8.5.

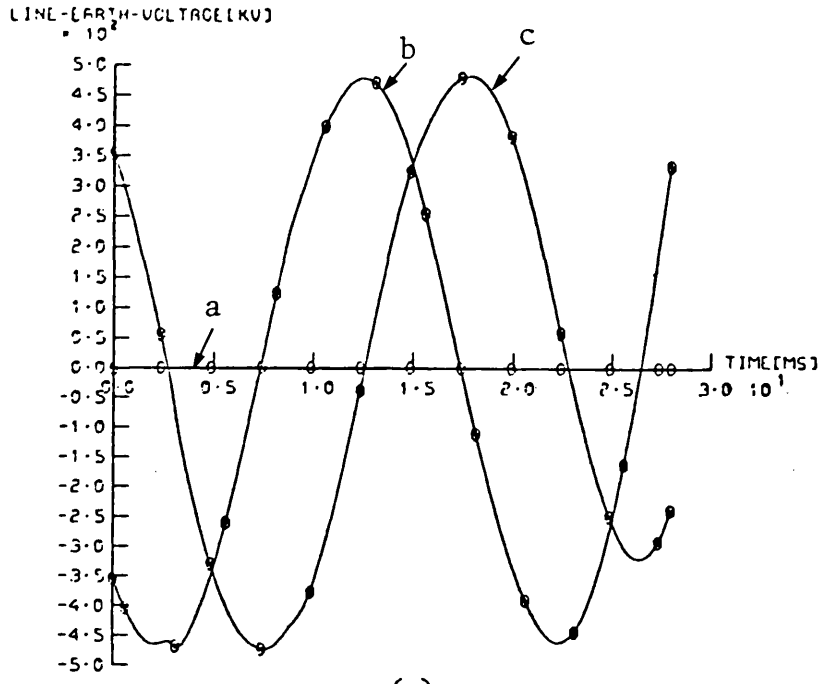

(a)

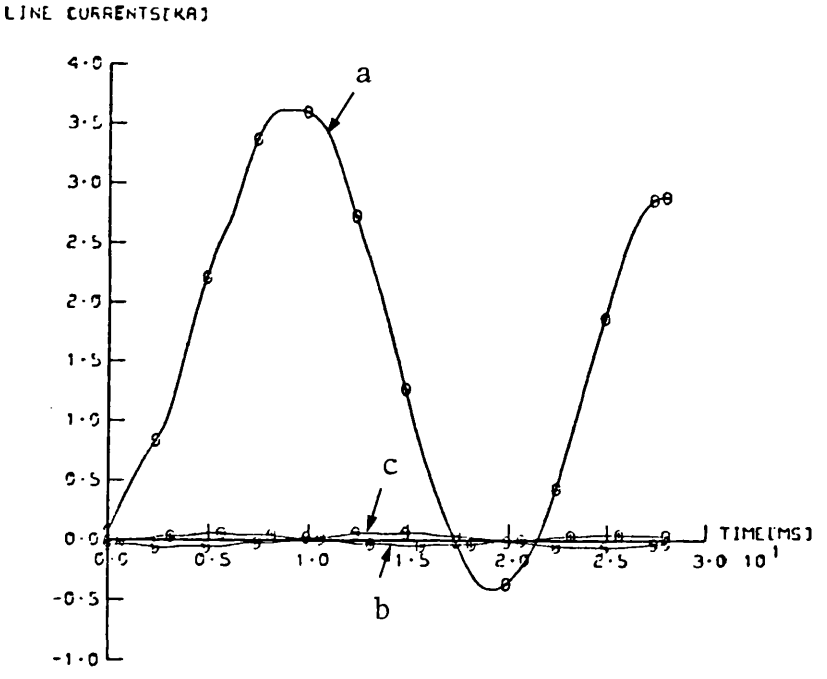

(b)

Fig 8.7

Voltage and current wave forms at the S.E. of the middle section of the 3-section feeder system examined.

- Solid 'a-E' close-up fault, FT = 0
- Neutral reactor is saturated, T_S = 5 ms.
- Fault conditions are similar to that of Fig 8.1.

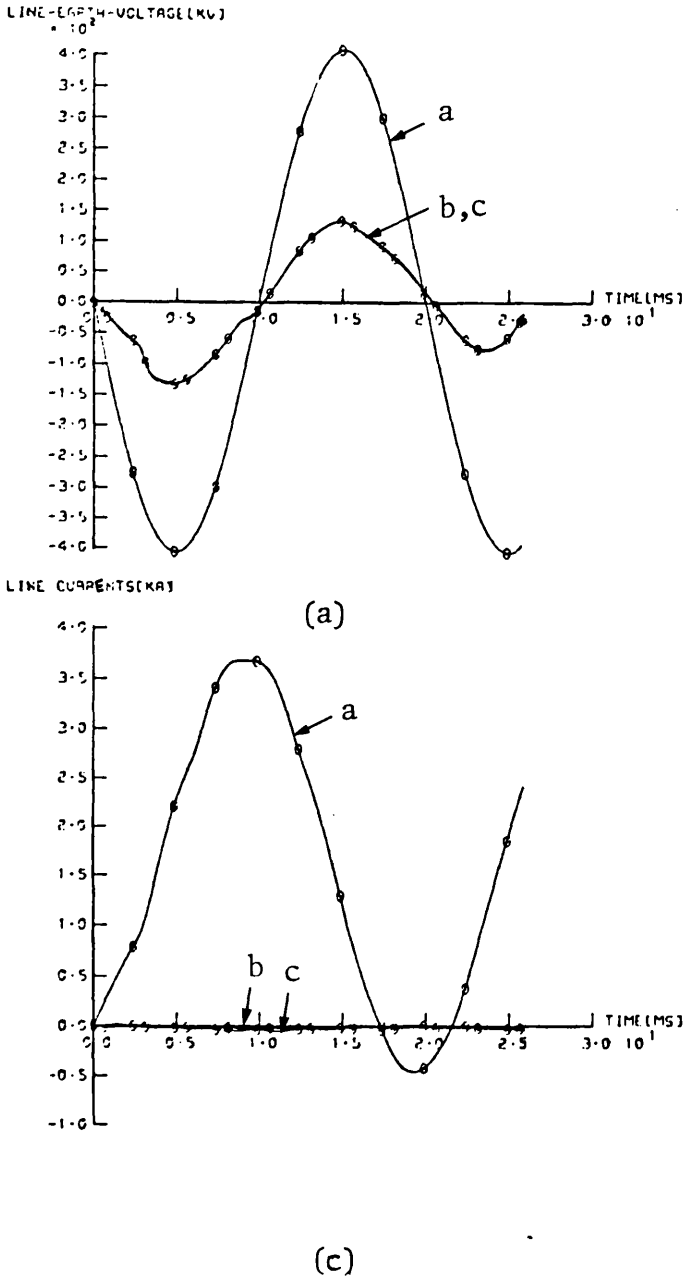

Fig 8.8

Individual components of the voltage and current wave-forms of Fig 8.7.

a- Voltage component due to fault.

b- Voltage component due to saturation.

c- Current component due to fault.

d- Current component due to saturation.

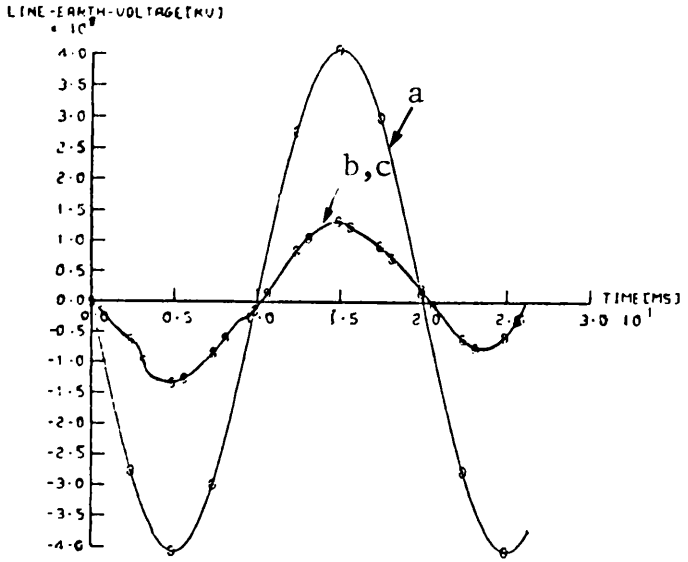

(a)

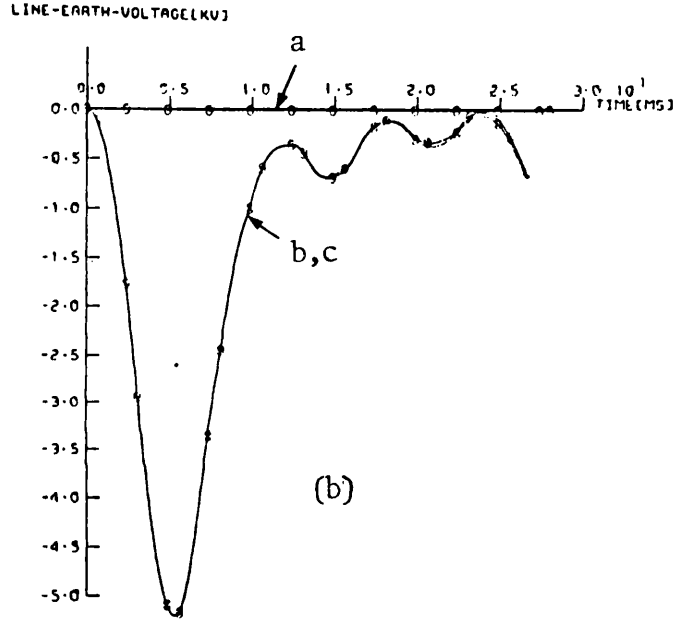

(b)

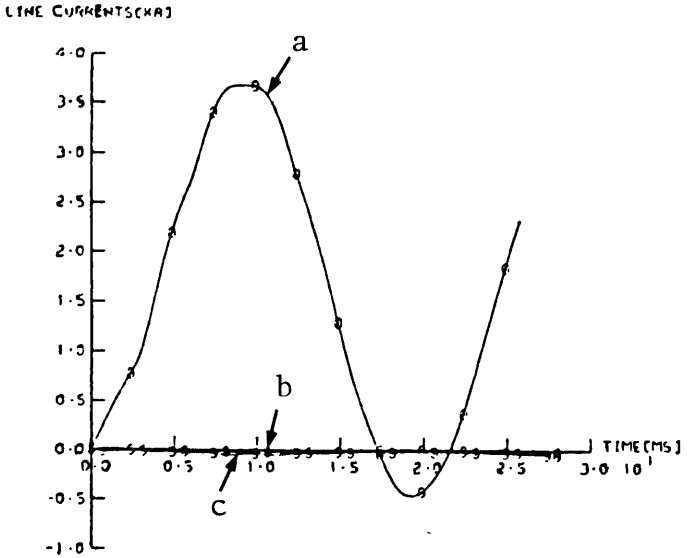

(c)

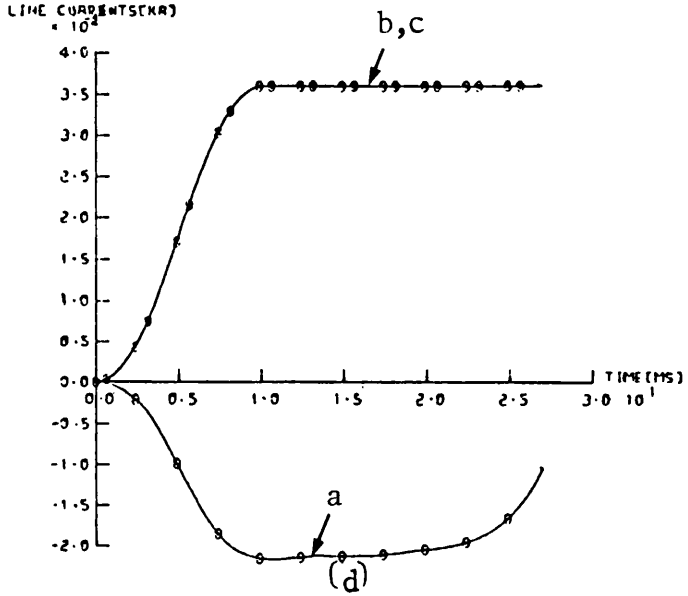

(d)

Fig 8.9

Individual voltage and current components due to fault and saturation.

- Fault conditions are similar to that of Fig 8.7 with 'T_S' = 10 ms.

a- Voltage component due to fault.

b- Voltage component due to saturation.

c- Current component due to fault.

d- Current component due to saturation.

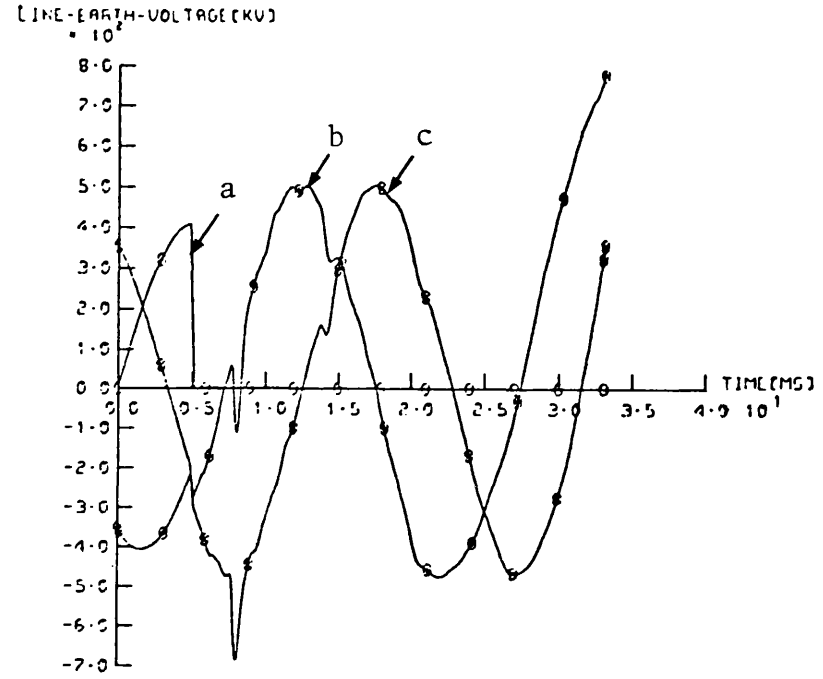

(a)

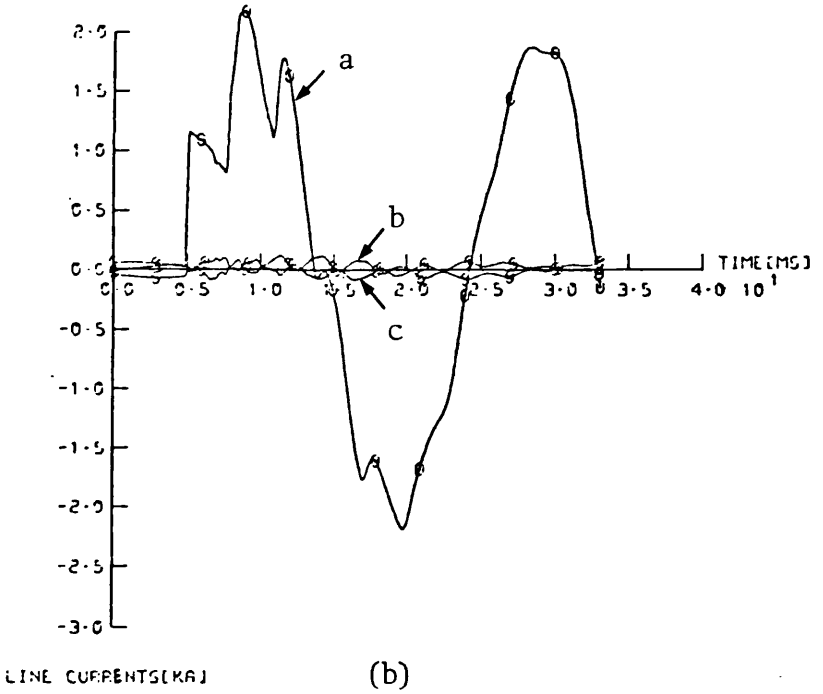

(b)

Fig 8.10

Voltage and current wave-forms at the S.E. of the middle section of the 3-section feeder system examined.

- Solid 'a-E' close-up fault, FT=5ms.
- Neutral reactor is saturated, T_S=10 ms.
- Other fault conditions are similar to that of Fig 8.1.

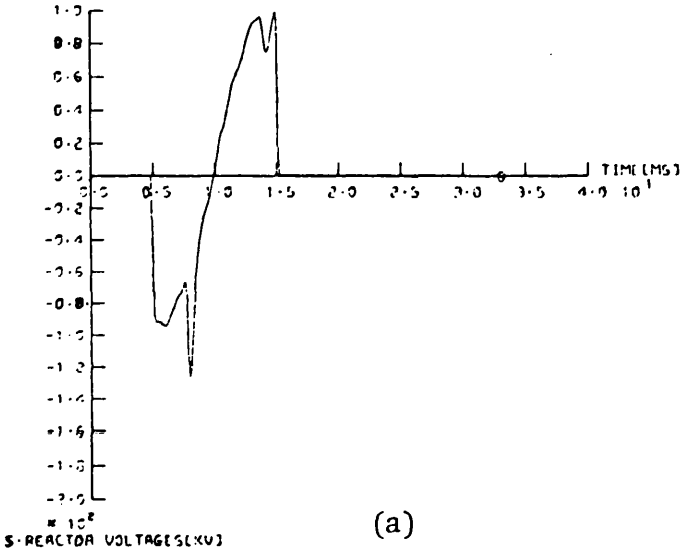

(a)

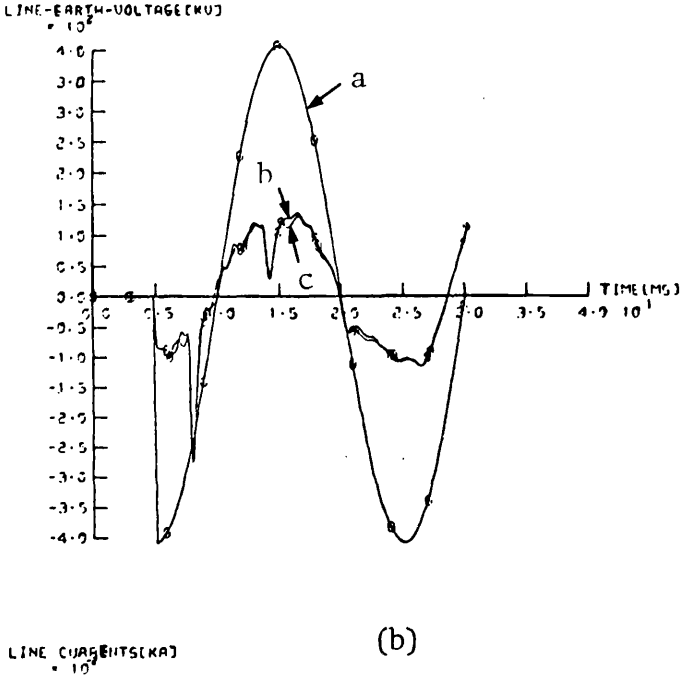

(b)

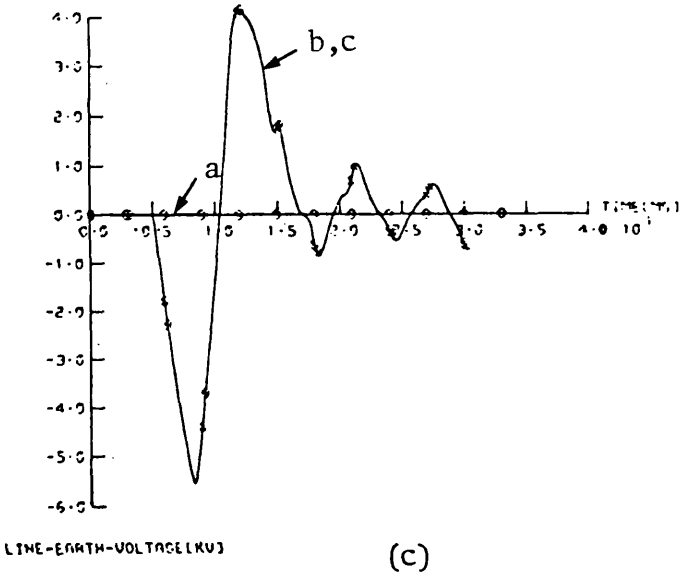

(c)

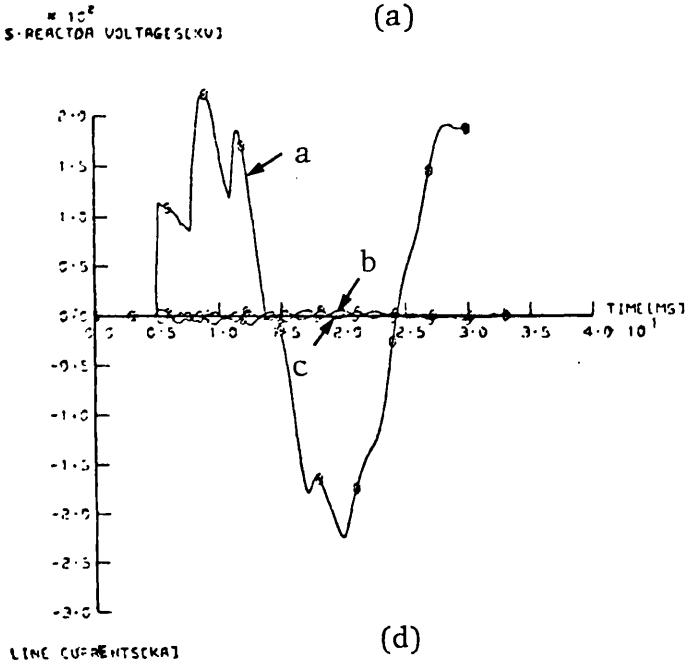

(d)

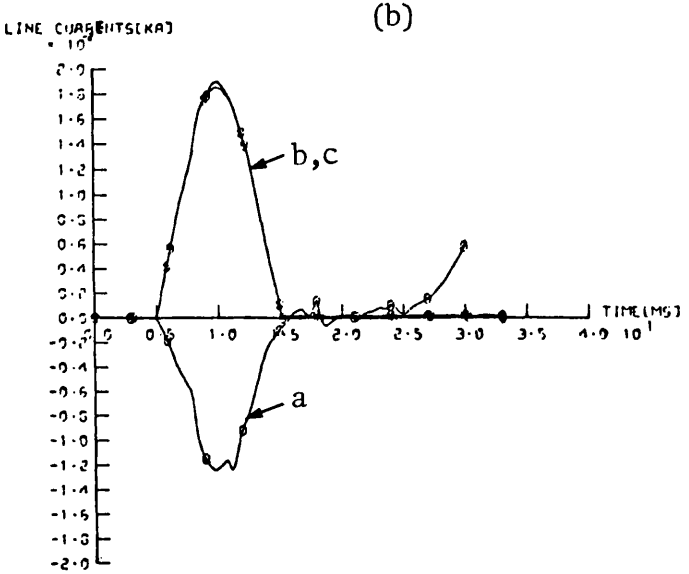

(e)

Fig 8.11

Individual components of the voltage and current wave-forms of Fig 8.10.

a- Saturation voltage source.

b- Voltage component due to fault.

c- Voltage component due to saturation.

d- Current component due to fault.

e- Current component due to saturation.

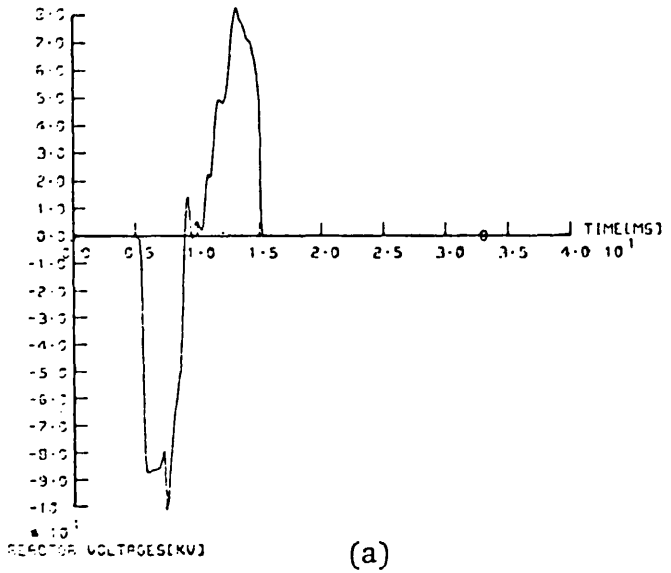

(a)

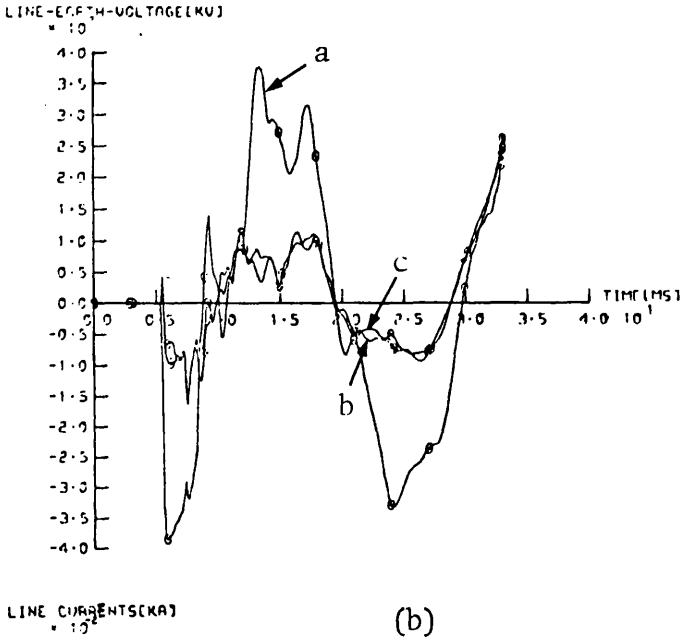

(b)

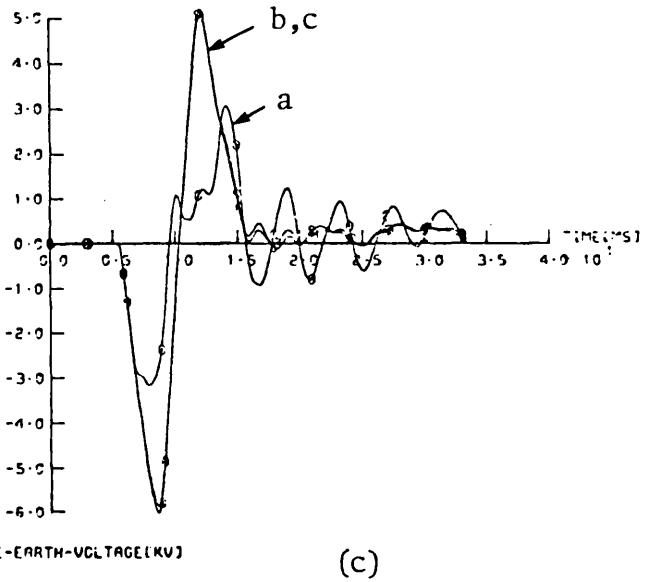

(c)

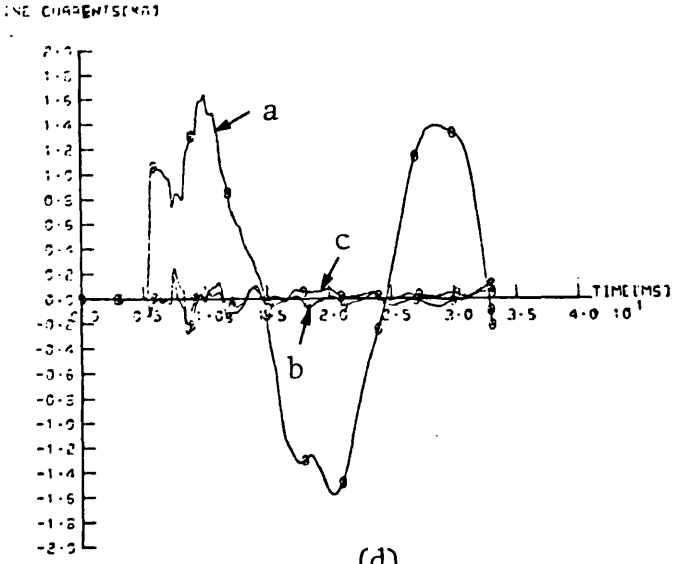

(d)

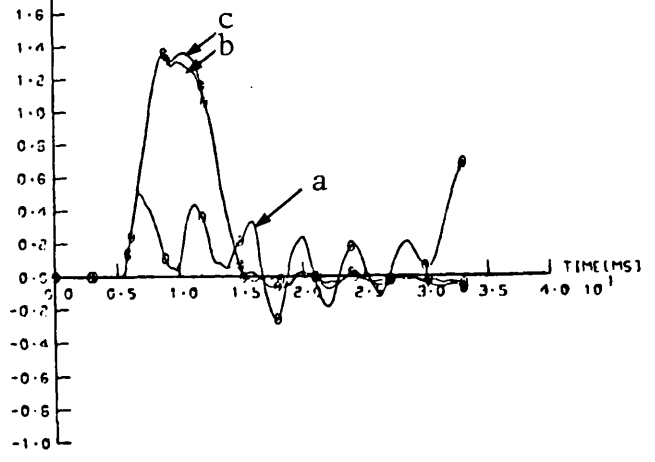

(e)

Fig 8.12

Individual components of voltage and current wave forms at the S.E. of the middle-section of the 3-section feeder system examined.

- Fault conditions are similar to that of Fig 8.10 with 'X' = ℓ/2 (150 km).

a- Saturation voltage source.

b- Voltage component due to fault.

c- Voltage compontnt due to saturation.

d- Current component due to fault.

e- Current component due to saturation.

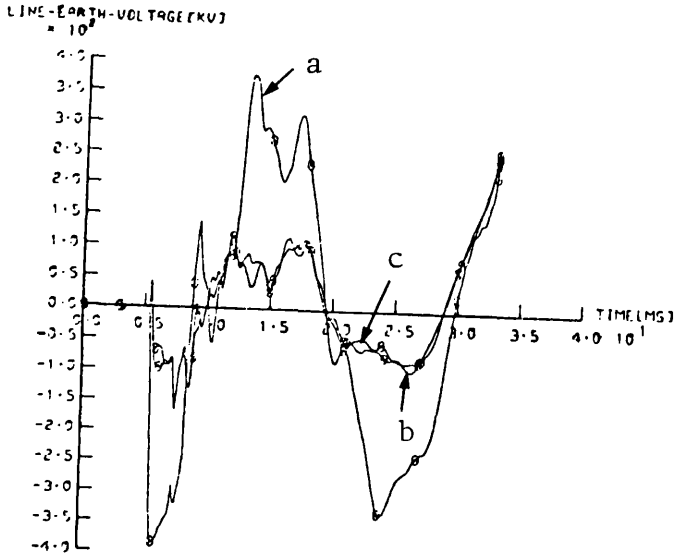

(a)

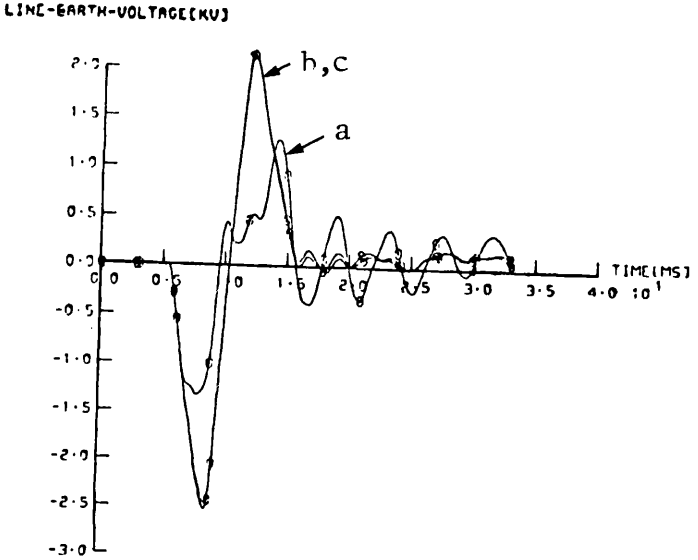

(b)

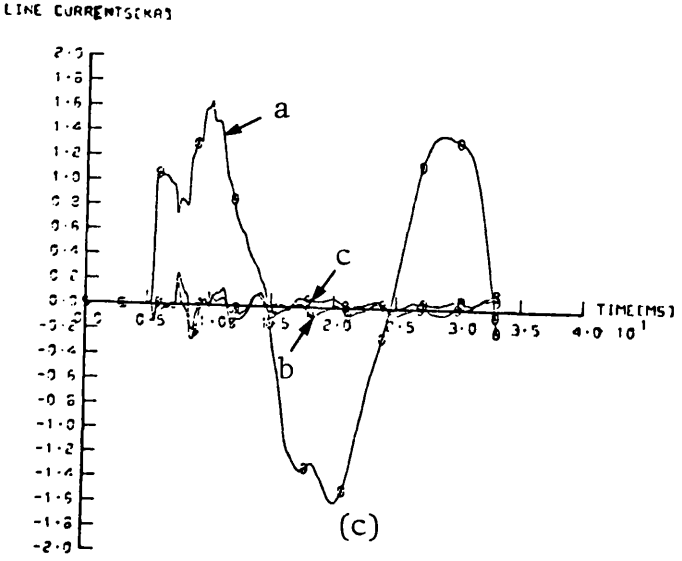

(c)

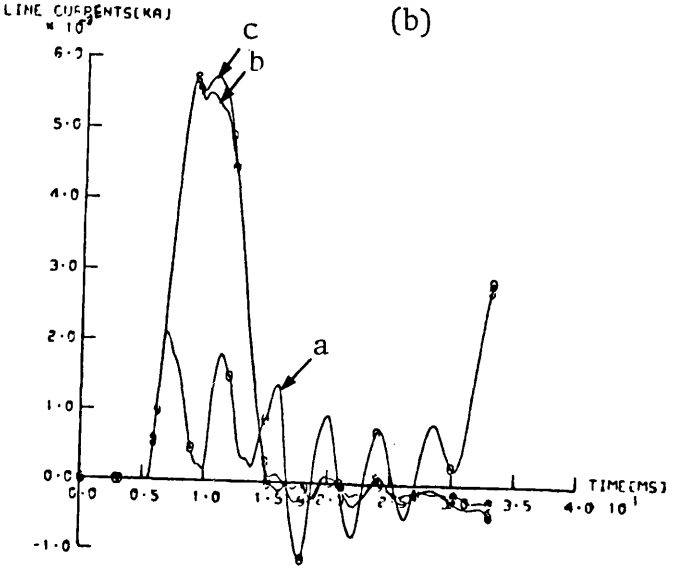

(d)

Fig 8.13

Individual components of voltage and current waveforms at the S.E. of the middle section of the 3-section feeder system examined.

- 'a-E' mid-point fault under the same conditions as that of Fig 8.10 with $L_2/L_1 = 0.5$.

a- Voltage component due to fault.
b- Voltage component due to saturation.
c- Current component due to fault.
d- Current component due to saturation.

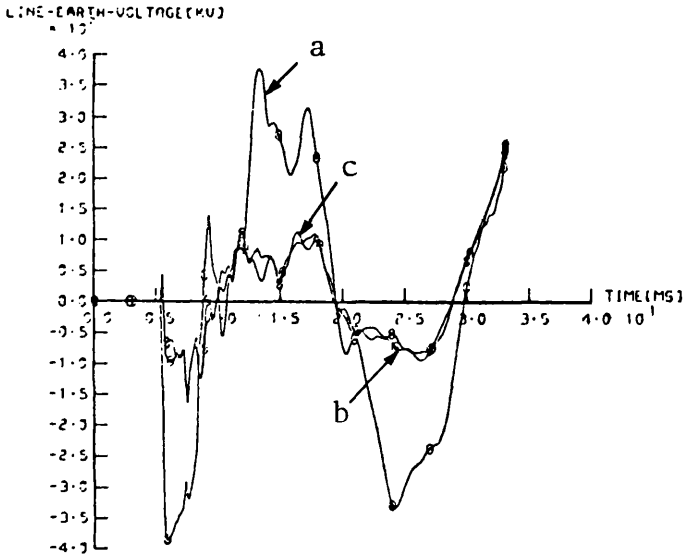

(a)

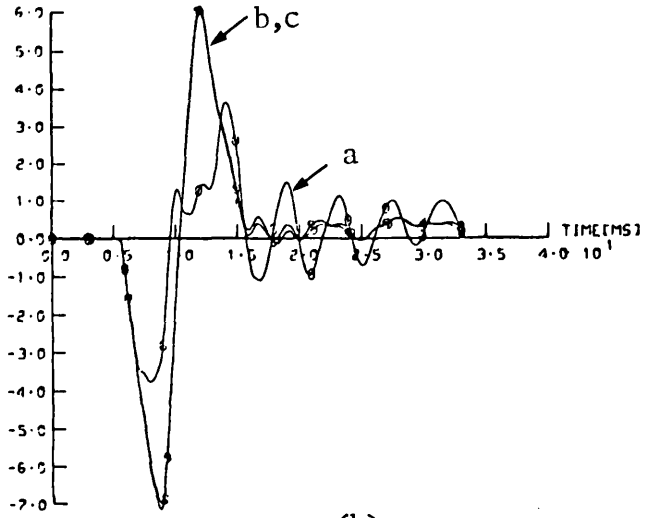

(b)

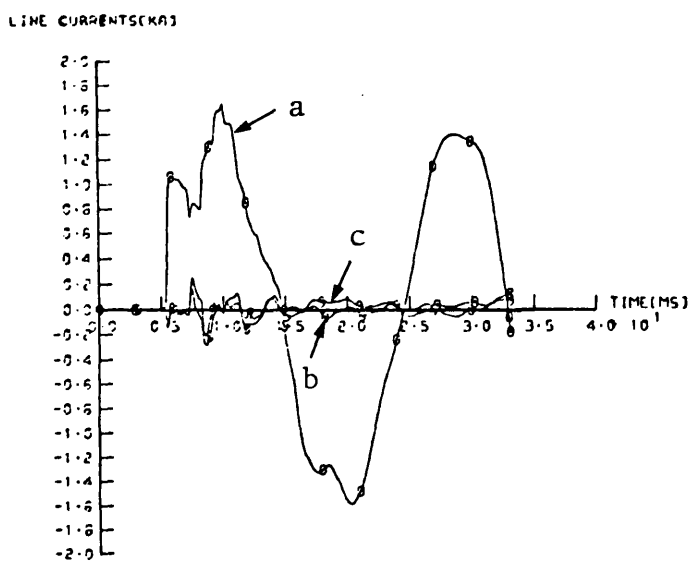

(c)

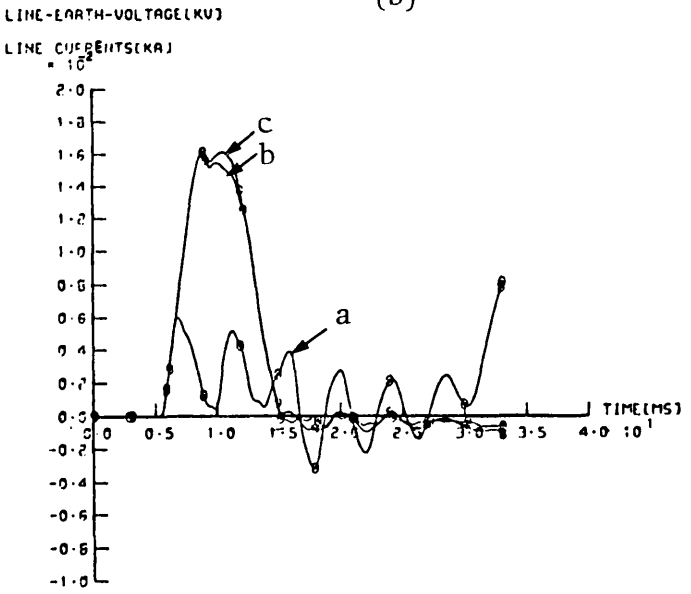

(d)

Fig 8.14

Individual components of voltage and current at the S.E. of the middle section of the 3-section feeder system examined.

- 'a-E' mid-point fault under the same conditions as that of Fig 8.10 with L_2/L_1=0.01.

a- Voltage component due to fault.

b- Voltage component due to saturation.

c- Current component due to fault.

d- Current component due to saturation.

CHAPTER 9 DIGITAL EVALUATION OF DISTANCE RELAY PERFORMANCE

9.1 Introduction

It has always been recoginsed that accurate simulation of EHV power systems under fault-transient conditions provides a true picture of the primary system wave forms and hence a realistic prediction of the performance of protective relays. Furthermore, an improvement of relay performance to meet future demands can be achieved.

The relaying point primary wave forms, evaluated-using frequency domain techniques-and presented in Chapters (6) and (7), showed that considerable travelling wave distortion can often be produced and hence relaying signals are expected to be highly distorted.

Relatively little work, however, has been done on the effect of travelling waves on distance-relay performance. Based on Fourier transform techniques,[53,54] the problem has been examined [57] using cross polarised mho-relays applied to short and long-uncompensated transmission systems. The authors[57] have given particular consideration to travelling wave effects.

Neglecting the frequency variance[55] of line parameters, a similar investigation has been reported.[96] Hughes[97] has examined in detail the performance of a high-speed static distance relay based on the well known block-average principle.[92] Again, test results presented in this paper[97] are not expected to provide a realistic performance of distance relays, since only series impedance of the line has been modelled.

It is one of the primary objectives of this work, therefore, to examine the effect of travelling-wave phenomena on the performance of cross polarised mho relays[93] based on the block-average principle.[92] The work has

been particularly carried out to reveal the effect on relay performance, if any, of shunt compensating the line using a 4-reactor scheme.

Relay performance on uncompensated systems has also been considered and hence a comparison of relay responses on uncompensated and 4-reactor compensated systems is possible.

Digital simulation of relay mixing circuits and the basis of the step-by-step techniques used to derive the relaying signals are presented in Appendix (A5). The calculations necessary to simulate both the transactor and the polarising circuits were presented in Chapter (5) and Appendix (A6). Digital Computer results of relay responses on single and 3-section feeder systems are reported in sections (9.2) and (9.3) respectively.

Response of relays protecting a specific 3-section feeder system under practical loading conditions has also been considered and the computational results are presented in section (9.4).

9.2 Performance Of Relays Applied to Single-Section Feeder Systems

The computational results reported in Chapters (6) and (7) showed that, various factors such as fault instant, fault position, source capacities, type of fault,.....etc., considerably affect the content and duration of travelling wave components in primary system wave forms. In view of the fact that the majority of faults that occur on EHV systems are single-line-to-ground,[37,49,50] transitory in nature, the performance of protective relays for such faults are particularly considered and the effect of the above mentioned factors are examined.

Faults on both compensated and uncompensated systems are initiated and relay performance in terms of speed of operation and measurement accuracy is obtained. The computer results are presented below.

9.2.1 Response of Relays on Uncompensated Systems

Fig (9.1.a) shows the relaying voltage wave forms for a solid a-E, close-up fault. The fault instant is at maximum prefault a-E voltage and source capacities are 35 GVA at both ends.

It can be seen from the Fig. that neither relaying voltage is significantly distorted, the sound-phase wave forms being mainly responsible for that which does occur.

The studies show that for close-up faults, detection time is always a minimum, about 11.4 ms as may be observed from Fig (9.1.c). The output of the coincidence detector is shown in Fig (9.1.b) from which coincident and anti-coincident periods can be observed.

Fig (9.2) shows the corresponding signals for a fault at zero, prefault, a-E voltage and the same general remarks apply. The effect of the transactor on filtering the exponential component is clearly evident from Fig (9.2.a) and the trip-time is about 11.7 ms as may be seen from the integrator output of Fig (9.2.c).

For distance faults, travelling wave distortion is more remarkable as may be seen from the input signals and integrator output of Fig (9.3) for a solid a-E mid-point fault under the same conditions as that of Fig (9.1).

The corresponding signals and integrator output for a mid-point a-E fault at zero voltage are shown in Fig (9.4). Travelling wave distortion produced in signals s_1 and s_2 (of Fig 9.3), for fault at peak voltage, tends to increase relay operating time to about 14.6 ms compared to about 12.5 ms for a zero-voltage fault as may be seen from Figs (9.3.c) and (9.4.c) respectively.

The effect of having low capacity source at the observation point on relay performance is shown, for a mid-point a-E fault, in Fig (9.5). Fault conditions are typically the same as that of Fig (9.3) but with sending-end source capacity of 5 GVA. In view of the fact that this is the worst case from the point of view of travelling wave distortion, Fig (9.5.b) shows that no appreciable build up towards tripping occurs until about 7.8 ms after fault inception. Relay operating time is about 20.8 ms which is rather high compared to that of Fig (9.3.c), 14.6 ms. Here, it has to be emphasized that this delay in relay operation would not be revealed by conventional dynamic testing methods in which the line is represented by a simple resistance-inductance combination.

As may be observed from Table (9.1), relay operating time is relatively low (12.6 ms) for zero-voltage fault analogous to that of Fig (9.5). This finding merits special attention, due to the fact that it has always been recognised that faults at maximum voltage are favourable from the point of view of relay operating time.

Table (9.1) also shows that under fault conditions such as that of Fig (9.5), but with source capacities of 35 and 5 GVA at the sending and receiving ends respectively, travelling wave distortion is less and hence relay operating time is reduced (14.3 ms).

Details of the studies considered for the purpose of examining the effect of source capacities and fault inception time on the performance of sending-end a-earth fault relay are summarised in Table 9.1, where relay trip time and relay reach are shown. The Table clearly shows that,

S.S.C.L (GVA)	35		5		35	
R.S.C.L (GVA)	35		35		5	
Fault Distance X (km)	Relay operating Time (ms)		Relay operating Time (ms)		Relay operating Time (ms)	
	Faults at V_a = max.	Faults at V_a = 0	Faults at V_a = max.	Faults at V_a = 0	Faults at V_a = max.	Faults at V_a = 0
0	11.4	11.7	10.8	11.3	10.3	11.5
40	11.0	10.0	14.3	10.4	11.0	10.0
80	11.7	10.8	16.6	10.5	11.3	10.8
120	12.4	11.7	17.7	11.2	12.2	11.5
150	14.6	12.5	20.8	12.6	14.3	12.4
200	22.5	17.2	31.1	17.0	22.3	16.9
210	27.3	19.8	35.0	23.3	28.7	19.9
220	32.8	27.7	43.5	29.0	32.9	27.9
223.25	-	-	-	-	-	-
230	43.75	38.25	55.0	39.75	43.5	37.75
235	85.0	79.75	95.5	100.75	104.75	80.25
236	No trip	No trip	No trip	No trip	No trip	No trip
237	"	"	"	"	"	"
238	"	"	"	"	"	"
239	"	"	"	"	"	"
240	"	"	"	"	"	"

Table (9.1)

Effect of source capacities on the performance of block average comporator relays applied to single-section uncompensated 500 kv system.

$V_S/V_R = \angle 0^o$, $Q_S = Q_R = 100.0$

$R_f = 0$, $Z_{SSO}/Z_{SS1} = Z_{RSO}/Z_{RS1} = 1.0$

generally, the relay operates much faster for faults at zero faulted phase voltage and in all cases it underreaches, the amount of underreach being about 5 km, i.e. 2.1%. Also it is obvious that the worst case from the point of view of relay operating times is that when a small source capacity (5 GVA) and a large source capacity (35 GVA) are assumed for the sending and receiving-ends respectively.

Travelling wave distortion of the primary wave forms and hence of the relay input signals is the main obvious reason for larger operating times in this case.

Relay response for 5 GVA source capacity at each end has not been examined in detail but relay reach has been found to be also about 235 km for faults at both maximum and zero faulted phase voltage. Also the response of other earth-fault relays has been considered. For example, the reach of the phases 'b' and 'c' relays have been found to be 234 and 235 km for a solid b-E and c-E faults at maximum 'V_b' and 'V_c' respectively and for source capacities of 35,35 and 5,35 at the sending-end and receiving-end respectively.

So far, relay performance has been considered under the assumption of no prefault power transfer. However, the response of the phase 'a' relay has been examined under prefault line loading corresponding to a load angle $\delta = +30^{o}$, power export at the sending-end. Only relay reach has been considered for faults at maximum 'V_a' and different source capacities have been considered. For example, Fig (9.6) shows the relaying signals and integrator outputs for a solid a-E mid-point fault at maximum 'V_a' with source capacities of 35 GVA at each end.

Generally, it can be said that relay operating time increases with prefault loading, particularly for faults within the first half of the protected line. This can be observed by comparing Fig (9.6) ($\delta=30^{o}$) with Fig (9.3) ($\delta=0^{o}$) where the operating time increases from 14.6 to 15.13 ms respectively.

As far as relay reach is concerned, it is shown in Table (9.2) that the relay does overreach when exporting power at the sending-end while the amount of underreach increases when power is imported at the same end.

The maximum amount of overreach is 5% and the amount of underreach is about 6.6% for 5,35 GVA sending-end and receiving-end source capacities. It has been observed from the digital computer results presented in Chapters (6), (7) that due to the dominant aerial mode components in the primary wave forms, travelling waves persist for considerably longer time in case of phase-faults. Therefore it is necessary to examine the performance of phase-relays under such conditions. Figs (9.7) and (9.8) show the relaying signals and the integrator outputs for a mid-point solid b-c fault at maximum and zero 'V_{bc}' respectively. Source capacities are 5,35 GVA at the sending and receiving-ends respectively.

Other fault conditions are similar to that of Table (9.3). Fig (9.7.a) shows the effect of the extremely high travelling wave distortion on the relaying signals and Fig (9.7.b) clearly indicates a delay of measurement until approximately 17 ms after fault inception occurs. From Fig (9.8), considerably more noise is observed in the relaying signals than is the case for the corresponding a-earth fault, Fig (9.5.a). This, however, does not cause a significant delay as indicated by the prominently coincident nature of the relaying signals.

From Figs (9.7) , (9.8), relay operating times are about 24.5 and 12.7 ms compared respectively to 20.8 and 12.6 ms for an a-E fault under the same fault conditions. Table 9.3 shows the effect of a solid b-c fault on relay speed of operation and relay reach. A comparison of Table (9.3) with the corresponding a-E fault of Table (9.1) will clearly show that generally for phase faults (b-c), relay reach decreases and relay operating times increase particularly for faults at maximum 'V_{bc}'.

The detailed studies of the performance of the block-average comporator relays shown in Tables (9.1) - (9.3) can be best substituted by the fault position / operating time characteristics of Fig (9.9), from which the effect of source capacities, fault inception time and type of fault on relay speed of operation and measurement accuracy can be observed. The same remarks applied to Figs (9.1 - 9.8) and Tables (9.1 - 9.3), also apply to Fig (9.9).

Fault	V_S/V_R	Fault instant	S.S.C.L (GVA)	R.S.C.L (GVA)	Relay Reach (km)
a-E	$\lfloor 30^o$	V_a=max	35	35	237
"	"	"	5	35	252
"	"	"	35	5	245
"	"	"	5	5	250
"	"	V_a= 0	35	35	246
"	$\vdash 30^o$	V_a=max	5	35	224
"	$\vdash 30^o$	V_a= 0	5	35	225

Table (9.2)

Effect of prefault line loading on the measurement accuracy of relays applied to uncompensated single-section feeder 500 kV system.

'a-E' fault , $Q_S = Q_R = 100$

$R_f = 0$, $Z_{SSO}/Z_{SS1} = Z_{RSO}/Z_{RS1} = 1.0$

X (km)	Relay operating Time (ms)	
	Fault at V_{bc} = maximum	Fault at V_{bc} = 0
0	11.3	11.6
40	19.3	10.4
80	20.7	10.6
120	21.7	12.7
150	24.7	12.7
200	52.4	19.8
210	62.75	-
220	74.85	-
225	94.25	79.5
226	-	79.6
228	-	80.5
229	-	80.7
230	175.25	Trips
231	178.4	Trips
232	No Trip	No Trip

Table (9.3)

Performance of the 'b-c' relay applied to uncompensated single-section feeder 500 kV system.

$V_S/V_R = \underline{0}^o$

$Z_{SS0}/Z_{SS1} = Z_{RS0}/Z_{RS1} = 1.0$

$Q_s = Q_R = 100.0$

$R_f = 0.0$

S.S.C.L = 5 GVA

R.S.C.L = 35 GVA

9.2.2 Response of Relays on 4-reactor Shunt Compensated Systems

In this section, the performance of block-average comparator relays protecting single-section, double-end-fed, shunt compensated feeder systems is obtained. The effect of degrees of shunt compensation, together with the various factors considered in section (9.2.1), on relaying signals and hence on relay speed of operation and measurement accuracy is examined. Only relays located at the sending-end of the line are considered.

The results presented in Table (9.1) showed that source capacities considerably affect relay performance, particularly their speed of operation in case of distance faults. This may be observed for the compensated system from Figs (9.10) and (9.11) for a solid, mid-point a-E fault with source capacities at line ends of 35,35 and 5,35 GVA respectively. Other fault conditions are similar to the respective uncompensated cases of Figs (9.3) and (9.5).

A comparison of the two Figs shows that due to the low capacity source at the observation point, relaying signals of Fig (9.11.a) are relatively more distorted compared to that of Fig (9.10.a). It is therefore expected that such distortion will cause a delay in relay operation. This can be seen from Figs (9.10.c) and (9.11.c) where trip time increased from 14.1 to 20.5 ms respectively.

A comparison of the uncompensated cases of Figs (9.3) and (9.5) to the respective compensated cases of Figs (9.10) and (9.11) reveals that for the uncompensated cases, relays operate relatively slower, 14.6 and 20.8 ms for Figs (9.3) and (9.5) respectively.

An extensive series of studies has been carried out to examine the effect of different source capacities on relay performance. The results of those

studies are shown in Table (9.4), from which it is seen that, in general, relays tend to overreach when used with shunt compensated systems, the amount of overreach being about 2-3 km, i.e. about 1%. The Table also shows that for faults at maximum voltage, relays take longer time to operate and the worst case is, again, a maximum voltage-fault with source capacities 5,35 GVA at the sending and receiving-ends respectively.

From relay speed of operation point of view, Tables (9.1) and (9.4) show that under the same fault conditions, earth-fault relays, generally, operate faster with compensated systems than is the case with uncompensated systems.

Relay reach with low source capacities at both ends has also been considered and was found to be 242 and 241 km for faults at maximum and zero a-E voltages respectively. Also, the response of other earth-fault relays has been considered. For example, Figs (9.12), (9.13) show the relaying signals and integrator outputs for mid-point 'b-E' and 'c-E' faults respectively. Other fault conditions are analogous to that of Fig (9.11). It is clear from the Figs. that the amount of distortion in the input signals is nearly the same as that of Fig (9.11.a). The relays operate after about 20.83 and 19.2 ms (Figs (9.12.b) and (9.13.b) respectively) compared to 20.5 ms operating time in case of the a-E fault of Fig (9.11).

As far as measurement accuracy is concerned, the reach of phases 'b' and 'c' relays was found to be 241 and 242 km respectively which, again, is nearly the same as that of phase 'a' relay (242 km).

The effect of source capacities and fault inception time on phase (a) relay speed of operation and measurement accuracy is shown in Fig (9.14).

The computational results presented in Chapter (6) showed that primary system wave forms and hence relay input signals are affected by line

S.S.C.L GVA	35		5		35	
S.S.C.L GVA	35		35		5	
Fault Distance X (km)	Relay Operating Time (ms)		Relay Operating Time (ms)		Relay Operating Time (ms)	
	Fault at V_a = max	Fault at V_a = 0	Fault at V_a = max	Fault at V_a = 0	Fault at V_a = max	Fault at V_a = 0
0	10.7	11.7	10.8	11.3	10.3	11.5
40	11.1	10.0	14.0	10.3	11.0	10.0
80	11.7	10.8	15.3	10.5	11.4	10.8
120	12.3	11.9	17.5	11.2	12.2	11.9
150	14.1	12.5	20.5	12.3	13.9	12.7
200	21.3	16.7	29.9	16.5	21.5	16.5
210	23.8	18.1	32.5	19.1	27.1	18.2
220	29.4	25.5	40.5	27.5	29.7	26.6
230	33.75	-	45.25	36.25	32.5	-
235	34.75	37.25	64.25	37.25	42.75	37.75
240	54.5	39.5	85.5	60.25	75.2	39.75
241	54.75	59.5	105.0	80.75	75.25	-
242	74.75	99.5	105.5	139.0	95.25	110.0
243	No Trip	118.5	No Trip	No Trip	No Trip	110.25
244	"	No Trip	"	"	"	No Trip
245	"	"	"	"	"	"

Table 9.4

Effect of source capacities on the performance of block average comparator relays applied to single-section shunt compensated 500 kV system.

$V_S/V_R = \angle 0^o$ $\quad Q_S = Q_R = 100.0$

$R_f = 0$ $\quad Z_{SSO}/Z_{SS1} = Z_{RSO}/Z_{RS1} = 1.0$

$h_1 = 0.75$, $h_O = 0.60$

prefault loading. Fig (9.15) shows the relaying signals and integrator output for a mid-point, solid a-E fault at maximum voltage. The line prefault loading corresponds to load angle ($\delta = 30^{o}$), i.e. power is exported at the relaying-end. Other fault conditions are similar to that of Table (9.5.a). The Fig shows that relay operating time is about 19.13 ms compared to 20.5 ms in case of zero prefault loading.

From the detailed study of the effect of prefault loading on relay performance, it has been found that, compared to the zero prefault loading case (Table (9.4)) operating timesincrease for faults near the relaying point while decrease remarkably for faults near the boundary. This effect may be seen from Table (9.5.a) and Fig (9.16.a) which show that relay reach is 260 km, i.e. the amount of overreach is about 8.33%. Relay trip times under the same fault conditions but with source capacities of (35,35),(35,5) and (5,5) GVA at the sending and receiving-ends, were found to be 14.1, 14.13 and 16.73 ms for the three cases respectively. Apparently, those times are considerably lower than the corresponding operating time of Table (9.5.a) (19.13 ms).

Relay reach with different prefault loadings and different source capacities is presented in Table (9.5.b), which clearly shows a maximum over-reach of 20 km (8.33%) when exporting power at the relaying end. The Table also shows a maximum underreach of 9 km, i.e. just below 4% when the amount of power imported at the relaying end corresponds to a load angle ($\delta = -30^{o}$).

The significantly distorted nature of the wave forms in case of pure phase faults results in an increase in measurement delay. Fig (9.16.b) shows the relay characteristics for solid a-E and b-c faults at maximum 'V_a' and 'V_{bc}' respectively. The characteristics are derived from the detailed studies of relay performance under a-E fault as previously described and for pure b-c faults, some of the results of which are presented here in below.

Fault Distance X (km)	0	40	80	120	150	200	210	250	255	257	260	261
Relay Operating Time (ms)	11.97	13.65	16.53	17.4	19.13	27.25	27.48	52.0	73.35	94.1	104.35	No Trip

Table 9.5.a

Effect of prefault loading on the operating times of 'a-E' block average comporator relay protecting shunt compensated single-section feeder 500 kV system.

$V_S/V_R = \angle 30^o$

a-E fault at V_a = max

S.S.C.L = 5 GVA

R.S.C.L = 35 GVA

$Q_S = Q_R = 100.0$

$Z_{SSO}/Z_{SS1} = Z_{RSO}/Z_{RS1} = 1.0$

$R_f = 0.0$

$h_1 = 0.75$, $h_0 = 0.6$

V_S / V_R	$\angle 30^o$	$\angle 30^o$	$\angle 30^o$	$\angle 30^o$	$\angle 30$	$\angle 30$	$\angle 30$	$\angle 30$	$\angle -30^o$	$\angle -30^o$
S.S.C.L (GVA)	35	5	35	5	35	5	35	5	5	5
R.S.C.L (GVA)	35	35	5	5	35	35	5	5	35	35
Fault at	V_a = max	V_a = max	V_a = max	V_a = max	V_a = 0	V_a = 0	V_a = 0	V_a = 0	V_a = max	V_a = max
Relay Reach (km)	253	260	253	257	253	260	254	258	231	232

Table 9.5.b

Effect of prefault loading on the reach of 'a-E' block average comporator relay protecting shunt compensated single-section feeder 500 kV system.

$Q_S = Q_R = 100.0$

$Z_{SS0}/Z_{SS1} = Z_{RS0}/Z_{RS1} = 1.0$

$R_f = 0.0$

$h_1 = 0.75$, $h_0 = 0.6$

Fault Distance - X (km)		0	40	80	120	150	200	210	220	225	230	232	235	236	237	238
Relay operating time (ms)	Faults at $V_{bc\ max}$	11.5	19.5	20.5	21.2	24.1	50.25	52.25	69.25	-	-	-	95.5	105.85	126.15	135.25
	Faults at $V_{bc} = 0$	11.5	10.4	10.7	12.7	12.8	18.36	-	-	37.25	40.25	60.25	80.5	98.75	No Trip	No Trip

Table 9.5.c

Relay operating time for a solid 'b-c' fault on shunt compensated single-section-feeder 500 kV system.

S S C L = 5 GVA $\quad V_S/V_R = \angle 0^o$

R S C L = 35 GVA $\quad Q_S = Q_R = 100.0$

$Z_{SSO}/Z_{SS1} = Z_{RSO}/Z_{RS1} = 1.0$

$R_f = 0.0 \quad h_1 = .75, \quad h_0 = .60$

Fig (9.17) shows the relay response for a mid-point, solid 'b-c' fault which occurs at maximum V_{bc}. The Fig. clearly shows the considerably distorted relaying signals (Fig 9.17.a) which would in turn result in a larger relay operating time (Fig 9.17.b). The comparison of Fig (9.17) with the corresponding a-E case of Fig (9.11) reveals that for b-c fault, relay operating time is about 26.0 ms compared to 20.5 ms in case of a-E fault.

Relaying signals for 'b-c' faults at zero voltage were found to be relatively more distorted than that for the corresponding a-E faults. This, however, did not show any significant increase in relay operating time (typically, 12.3 and 12.6 ms for the a-E and the b-c relays under the same fault conditions).

The detailed studies showing the 'b-c' relay response are summarised in Table (9.5.c).

Under prefault loading conditions ($\delta = \pm 30^{o}$), relay reach was found to be 246 and 232 km respectively for solid b-c faults that occur at maximum 'V_{bc}' under the same fault conditions as that of Table (9.5.c). The performance of other pure-phase fault relays has also been considered. For example, the reach of the 'a-b' and 'c-a' relays was found to be 238 and 244 km respectively for 'a-b' and 'c-a' solid faults under exactly the same fault conditions as that of Table (9.5.c).

From the results presented in this Chapter, so far, it is clearly shown that generally, relays protecting shunt compensated systems operate faster than those protecting uncompensated systems and the reach of the former is more than that of the latter. This conclusion can be easily derived by a direct comparison of the corresponding results presented in sections (9.2.1) and (9.2.2). However it has been reported[95] that

using a 3-legged reactor arrangement tends to cause an under-reach of 6% for phase-phase faults and 8% for phase-earth faults. To compare the results presented in this Chapter to that given by Fielding[95] etal, the following differences between the systems simulated and simulation techniques have to be taken into account:

1 - The line model is not discretely transposed.
2 - The line parameters are not distributed in nature and they did not take the frequency variance of the parameters into account.
3 - A 3-legged reactor scheme has been used.
4 - The sources are not wholly realistic.
5 - Relay performances have been examined only when exporting power at the relaying-end, i.e. the effect of prefault loading is not clearly established.
6 - An ideal V.T. was used.

In spite of the differences mentioned above, it is shown in Appendix (A7) that, similar to the 4-reactor compensated systems, the tendency of relays applied to 3-reactor compensated systems should be to overreach.

The 3-reactor scheme was digitally simulated with the single-section feeder system considered and the relay performance has been examined. The results obtained are summarised in Table (9.6.a). The Table shows that the reach of the 'a-E' relay is generally in complete agreement with that obtained with 4-reactor compensated systems, i.e., the relay tends to over-reach, the amount of overreach being very insignificent (about 1%).

The effect of shunt compensation on the performance of relays applied to 4-reactor compensated systems is shown in Fig (9.18.a,b). Fault conditions are similar to that of Table (9.4). The overreach and the fast operation (near the boundary) of the relay protecting the compensated system are obvious.

F T (ms)	S.S.C.L (GVA)	R.S.C.L (GVA)	Relay Reach (km)	operating time (ms)
5	35	35	242	85.0
10	35	35	242	100.5
5	5	35	240	105.0
10	5	35	241	-
5	35	5	242	95.0
10	35	5	242	-

Table 9.6.a

Performance of a block average comparator 'a-E' relay applied to a 3-legged reactor compensated single-section feeder 500 kV system. a-E fault.

$Q_S = Q_R = 100.0$

$Z_{SSO}/Z_{SS1} = Z_{RSO}/Z_{RS1} = 1.0$

$R_f = 0.0$

$h_1 = 0.75$

$V_S/V_R = \underline{0}^o$

SSCL (GVA)		35		5		35	
RSCL (GVA)		35		35		5	
Degrees of shunt compens.		Relay Reach (km)		Relay Reach (km)		Relay Reach (km)	
h_1	h_o	Fault at V_a = max	Fault at V_a = 0	Fault at V_a = max	Fault at V_a = 0	Fault at V_a = max	Fault at V_a = 0
0	0	235	235	235	235	235	235
0.5	0.21	240	240	240	240	240	240
0.75	0.6	242	243	242	242	242	243
1.0	1.0	244-45	245	243-44	244	244	245
1.25	1.4	247	247	245	246	246-47	247

Table 9.6.b

Effect of degrees of shunt compensation on the performance of a block-average comparator relay applied to 4-reactor shunt compensated single-section feeder 500 kV system.

- Fault conditions are similar to that of Table (9.6.a).

Equation (A7-1) shows that as the PPS degree of shunt compensation (h_1) increases, j_{x1} decreases and hence the impedance seen by the relay decreases. Therefore it is to be expected that relay reach increases with the PPS degree of shunt compensation (h_1). This finding is confirmed by the computational results summerised in Table (9.6.b) and Fig (9.19).

9.3 Performance of Relays applied to 3-section Feeder Systems

In this section, the performance of block average comparator relays applied to uncompensated and 4-reactor compensated 3-section feeder systems is obtained. Only relays at the sending-end of the middle-line-section are considered.

The results presented in section (9.2) have given a clear indication of the trend of different relays applied to uncompensated and 4-reactor compensated single-section feeder systems, under different fault conditions. Therefore, it would not be practical to present all the results of the detailed studies of the performance of relays on 3-section feeder systems and the presentation of some examples showing relay trends would be justified.

9.3.1 Response of Relays on Uncompensated Systems

Figs (9.20) and (9.21) show relay responses for solid a-E close-up and mid-point faults respectively. The faults occur at maximum 'V_a' and source capacities are 35 GVA at each end. It can be generally said that for faults at maximum 'V_a', relay operating times are much more in case of 3-section systems particularly for faults adjacent to relay location. This may by observed from Figs (9.20), (9.21) and the corresponding cases of single-section feeder systems, Figs (9.1), (9.3) respectively.

In the former cases, relay operating times are 18.7 and 29.1 ms compared to

11.7 and 14.6 ms in the latter cases respectively. The reason for the delay in 3-section feeder relay operation can be explained to be due to the relatively high levels of travelling wave distortion (in the relaying point wave forms) caused by successive propagation (from the point of fault up and down the 3-sections) and reflection (at source discontinuities) of travelling wave components.

For faults at zero voltage, there is little difference between the responses in the alternative system configurations. This can be seen from Fig (9.22) for a mid-point a-E fault. Other fault conditions are similar to that of Fig (9.21). The Fig. shows an operating time of about 13.4 ms compared to 12.5 ms in case of single-section feeder system, Fig (9.4). In fact, it was found that relay response for zero voltage faults differs little from that of relays applied to much shorter uncompensated lines.[57]

As far as relay measurement accuracy is concerned, it was found that relay reach is about 239 and 241 km for maximum and zero voltage faults respectively. This might be considered a better accuracy compared to the 5 km underreach for the corresponding single-section feeder cases of Table (9.1). The performance of other earth-fault relays was found to be nearly the same as that of phase-a and the pure phase-fault relays behaved in a similar manner as that of phase-a, i.e., its performance has deteriorated in a 3-section feeder system compared to that in a single section feeder system.

The detailed study of the performance of phase-a relay in 3-section feeder system is summarised in Table (9.7.a).

Fault Distance X (km)	Relay operating time (ms) Faults at V_a = max		Relay operating time (ms) Faults at V_a = 0	
	No shunt compensation	With shunt compensation	No shunt compensation	With shunt compensation
0	18.7	17.4	12.0	11.6
40	17.2	16.7	12.1	11.1
80	16.3	13.5	10.9	9.9
120	20.9	19.7	11.9	10.9
142.5	28.9	-	-	-
150	29.1	23.5	13.4	11.8
190	-	28.6	-	-
200	-	32.0	23.5	20.6
210	-	-	25.1	22.4
220	-	-	-	26.9
225	50.75	50.25	37.25	35.25
230	54.25	53.25	39.25	36.75
235	64.25	63.25	57.25	38.75
236	-	-	-	-
237	83.25	63.5	58.25	38.80
238	-	-	-	-
239	113.75	73.25	59.25	38.85
240	No trip	73.5	79.2	-
241	"	74.5	98.0	38.9
242	"	84.75	No trip	-
243	"	94.5	"	39.80
244	"	94.6	"	-
245	"	No trip	"	98.25
246	"	"	"	99.25
247	"	"	"	No trip

Table (9.7.a)

Operating time of block average comparator 'phase-a' relay applied to the 500 kV, 3-section feeder 4-reactor compensated system studied.

$V_S/V_R = \underline{|0^o}$, S.S.C.L. = R.S.C.L. = 35 GVA

$Q_S = Q_R = 100.0$ $Z_{SSO}/Z_{SS1} = Z_{RSO}/Z_{RS1} = 1$

$R_f = 0.0$ $h_1 = .75$, $h_0 = .60$

9.3.2 Response of Relays on 4-Reactor Compensated Systems

Figs (9.23), (9.24) show relay responses for close-up and mid-point solid a-E faults respectively. The faults occur at maximum 'V_a' and source capacities are 35 GVA at each end. The primary wave forms from which the signals of Fig (9.24.a) are derived are shown in Figs (6.19). The detailed performance of the phase-a relay is shown in Table (9.7.a)

A comparison of Tables (9.4) and (9.7.a) reveals that relay operation is considerably delayed in case of 3-section feeder compared to single-section feeder particularly for faults adjacent to the relaying point. This feature can also be observed from Figs (9.23), (9.24), which show relay operating times of 17.4 and 23.5 ms compared to 10.7 and 14.1 ms for the corresponding cases in single-section feeder (see Table 9.4).

The conclusion to be drawn from this comparison is that relays applied to 3-section feeder systems are about 7.9 ms slower in operation than those applied to single-section feeder systems for a-E faults at maximum voltage.

Fig (9.25) shows relay response for an a-E mid-point fault at zero voltage under fault conditions similar to that of Fig (9.24). Obviously, the response is not very much different from that in case of single-section feeder system (Table 9.4). Both relay reach and operating time are insignificantly affected due to the nearly travelling wave free primary wave forms (see Table 9.7.a).

The effect of low source capacity at the relaying-end on relay performance is shown in Fig (9.26) for a solid a-E mid-point fault at maximum voltage. Source capacities are 5,35 GVA at the sending and receiving-ends respectively. Other fault conditions are similar to that

of Fig (9.24). The primary wave forms from which the signals of Fig (9.26.a) are derived are shown in Fig (6.21).

As expected, due to the low source capacity at the relaying-end, travelling-wave distortion is further increased and hence relay performance is further deteriorated. Relay operating time reaches about 30.3 ms compared to 23.5 ms with 35 GVA source capacity at each end. The detailed relay response with source capacities of 5,35 GVA is summarised in Table (9.7.b).

The reach of the 'phase-a' relay was examined under prefault loading conditions. Exporting power corresponding to ($\delta = 30^{o}$) at the sending-end, resulted in overreach of about 30 km, i.e., about 12% while importing the same amount of power at the same end produced under reach of about 9 km, i.e. about 3.7%. Fault conditions in the two cases are similar to that of Table (9.7.b).

The realistic loading of the 300 km line-section considered corresponds to a load angle $\delta = 12^{o}$ and the relay reach when exporting this power at the sending-end, under the above fault conditions was found to be about 257 km, i.e. an overreach of about 7.1%.

Relay response for a close-up, solid b-c fault at maximum 'V_{bc}' is shown in Fig (9.27). Source capacities are 5,35 GVA at the sending and receiving-ends respectively and other fault conditions are similar to that of Fig (6.24) from which the relaying signals are derived. The detailed relay response is shown in Table (9.7.b).

Fault detection time reaches about 18.9 ms and 40.0 ms for a close-up and a mid-point fault compared to 11.5 and 24.1 ms for the corresponding b-c faults in single-section feeder systems (Table 8.5.c).

Type of fault	a-E	b-c
Distance of Fault X (km)	Relay operating time (ms)	Relay operating time (ms)
0	18.5	18.9
40	14.2	22.9
80	19.9	25.76
120	27.3	-
150	30.3	40.0
200	42.2	53.75
210	48.75	55.75
220	52.75	64.75
230	64.5	85.5
231	-	94.5
232	-	No trip
235	72.75	"
240	74.75	"
241	84.85	"
242	109.0	"
243	No trip	"

Table (9.7.b)

Performance of block-average comparator relays applied to 500 kV 3-section feeder 4-reactor compensated systems.

$V_S/V_R = \angle 0^o$, $Q_S = Q_R = 100{\cdot}0$, $Z_{SSO}/Z_{SS1} = Z_{RSO}/Z_{RS1} = 1.0$

S S C L = 5 GVA $\quad R_f = 0.0$

R S C L = 35 GVA $\quad h_1 = .75, \quad h_0 = .60$

Exporting power corresponding to $\delta = 30^{o}$ at the sending-end showed that the b-c-relay reach is about 245 km, i.e. 2% overreach , while importing the same power at the same end produced relay reach of about 230 km, i.e. about 4% underreach (fault conditions are similar to that of Fig (9.27)).

Fig (9.28) shows the operating characteristics of both the 'b-c' and the 'a'-relays under the worst conditions from the point of view of travelling wave distortion. The Fig. clearly indicates the relative deterioration in relay performance for the two types of faults applied to 3-section feeder systems.

9.4 Response of Relays applied to a practical 4-reactor Compensated System

In this section a practical 3-section, double-end fed, 4-reactor compensated system analogous to that given in reference (34) is examined. The 3-line sections are of the horizontal configuration described in Chapter (5) of this thesis and are regularly transposed through three equal subsections using the transposition scheme developed in Chapter (3). Each line-section is compensated using the 4-legged reactor scheme described in Chapter (2). The lengths of the 3-line sections are 250, 100 and 200 km from the sending-end to the receiving-end respectively. No local generation at the intermediate points was assumed and the parameters of sources at the remote ends are as follows:

sending-end source capacity (S.S.C.L) = 1.5 GVA

Receiving-end source capacity (R.S.C.L) = 5 GVA

$Z_{SSO}/Z_{SS1} = Z_{RSO}/Z_{RS1} = 0.5$

$Q_S = Q_R = 30.0$

where Q_S, Q_R = quality factors of sending-end and receiving-end sources respectively.

According to the configuration of the three line sections considered, a realistic loading has been found to correspond to a load angle of 2^{o}/50km with the voltage along the line maintained constant. Therefore the realistic prefault loadings of the respective 3-line sections correspond to load angles of 10^{o}, 4^{o}, and 8^{o} respectively. Only shunt compensated systems have been examined under the above prefault loadings.

The block-average comparator relays used throughout this section have the same characteristics as that used in sections (2) and (3) of this chapter from which it follows that the boundary of operation of each couple of relays protecting the 3-respective line sections is 200,80 and 160 km respectively. Only solid a-E and b-c faults have been considered to occur on any of the 3-line sections and the performance of the relays under consideration has been examined.

9.4.1 a-E Faults

Fig (9.29) shows the relaying signals and integrator outputs of the relays protecting the middle line-section when a solid close-up a-E fault occurs at maximum 'V_a' on this section. The performance of the sending-end relay is shown in Fig (9.29.a) from which it is obvious that the pure voltage derived signal 'S_2' contains a relatively low level of high frequency distortion. This is due to the fact that voltage wave fronts are attenuated over the long transmission distances involved. On the other hand the primary current wave forms which occur following faults on long lines are often subject to more rapid change than are observed for very short lines. [53,57] This feature hase also been observed from the primary wave forms presented in Chapters (6), (7). In this respect, it has to be noted that transformer-reactor arrangements have an output voltage which, to a first approximation, is proportional to the rate of change of input current, and it follows that in long lines a significantly higher level of high frequency

distortion is often associated with signal S_1, as seen in Fig (9.29.a). The Fig. shows that due to the distortion of S_1, a time delay, about (8 ms) is taken before a real build up towards tripping occurs. It is also shown that relay operating time is as long as 25.5 ms. Fig (9.29.b) shows that the two input signals to the receiving-end relay are almost anti-coincident due to the fact that the fault is 20 km out of its reach and hence, as required, a complete restraint, as seen from the integrator output, occurs.

As the fault point becomes distant from the relaying point, travelling waves become more pronounced and both signals become more distorted as may be seen for a solid-mid-point a-E fault, from Fig (9.30). Other fault conditions are analogous to that of Fig (9.29). A more delay in the operation of the S.E relay is expected where relay operating time reaches about 36.8 ms as shown in Fig (9.30.a).

The corresponding wave forms for the R.E relay are shown in Fig (9.30.b) where a relay operating time of 28.0 ms can be observed. The relatively higher receiving-end source capacity (5 GVA) results in less travelling wave reflection and hence the R.E relay takes shorter time (28 ms) to operate for a mid-point fault in the middle-line-section. Fig (9.31) shows the corresponding wave forms for an 'a-E' fault at the far end of the middle section. The Fig. shows that a complete restraint for the S.E relay occurs, Fig (9.31.a), and the operating time is about 18.0 ms for the R.E relay. Again it is obvious that due to the relatively higher source capicity at the receiving-end, the R.E relay takes much lower time (18 ms) to operate for a close-up fault, than that taken by the S.E relay (25.5 ms). The detailed performance of the two relays protecting the middle line-section is shown in Table (9.8).

Fig (9.32) shows the relaying signals and integrator outputs for a mid-point a-E fault under the same conditions as that of Fig (9.30) except that the

Fault Distance X (km)	Faults on first line section						Faults on middle line section							
	Relays operating time (ms)						Relay operating time (ms)				Relay operating time (ms)			
	a-E fault at		b-c fault at				a-E fault at				b-c fault at			
	V_a = max		V_{bc} = max		V_{bc} = 0		V_a = max		V_a = 0		V_{bc} = max		V_{bc} = 0	
	SE Relay	RE Relay	SE Relay	RE Relay	SE Relay	RE Relay	SE Relay	RE Relay	SE Relay	RE Relay	SE Relay	RE Relay	SE Relay	RE Relay
0	18	Rest	22.96	Rest	17.76	Rest	25.52	Rest	23.76	Rest	32.24	Rest	21.2	Rest
25	-	-	-	-	-	-	26.0	59.04	23.44	61.04	38.24	67.44	18.72	-
50	22.0	-	32.8	68.82	17.28	-	36.8	28.0	23.20	23.92	43.76	45.04	19.76	19.76
75	-	-	-	-	-	-	58.32	55.52	36.96	21.20	62.0	32.1	41.76	17.76
100	26.24	38.96	31.6	51.76	16.72	24.24	Rest	18.0	Rest	21.8	Rest	22.96	Rest	16.72
150	35.76	28.72	55.28	28.77	21.76	19.52	-	-	-	-	-	-	-	-
200	60.08	22.0	65.2	30.0	-	17.52	-	-	-	-	-	-	-	-
250	Rest	19.92	Rest	24.96	Rest	14.96	-	-	-	-	-	-	-	-

Table (9.8)

Performance of block-average comparator relays applied to 500 kV practical 3-section feeder system.

For section (1) $V_S/V_R = 1.0 \angle 10^o$ S.S.C.L = 1.5 GVA $Q_S = Q_R = 30.0$

For section (2) $V_S/V_R = 1.0 \angle 4^o$ R.S.C.L = 5 GVA $Z_{SSO}/Z_{SS1} = Z_{RSO}/Z_{RS1} = 0.5$

For section (3) $V_S/V_R = 1.0 \angle 8^o$ $R_f = 0.0$ $h_1 = .75$, $h_0 = .60$

fault occurs at zero a-E voltage. The Fig shows that relays signals are less noisy and the offset nature of primary currents has been filtered by the transactor circuits. Due to the nearly zero travelling wave distortion, the two relays take nearly the same time (23.2, 23.92 ms for S.E and R.E relays respectively) to operate.

Figs (9.33), (9.34) show the relaying signals and comparator outputs for solid a-E faults at a distance of 50 km from the relaying points of the first line section respectively. Faults occur at maximum 'V_a' and other fault conditions are similar to that mentioned above. Due to the relatively longer distances involved (compared to faults in the middle-section), travelling wave components are more attenuated and hence a better performance of the relays protecting that section is expected. The fault is detected by the S.E relay after about 22.0 ms (Fig 9.33.a) compared to 36.8 ms taken by the S.E relay to detect a similar fault in the middle section (Fig 9.30.a). It may appear from the signals of the R.E relay of (Fig 9.33.b) that no tripping will occur. However, from the experience gained from the studies presented earlier, if the observation time is extended to say 128 ms, a build up towards tripping will be observed. This prediction may be justified by the S.E relay response of Fig (9.34.a). However, due to the complexity of the R.E source when a fault occurs at 50 km from the S.E of the first line-section, it would take longer time for the R.E relay to operate (Fig 9.33.b).

Fig (9.34.a) shows that sending-end relay operates after about 60 ms and the response of the R.E relay of Fig (9.34.b) shows that it nearly behaves in the same way as the S.E relay of Fig (9.33.a). The fault is detected after the same time 22.0 ms.

The response of relays protecting the first line section for faults at zero a-E voltage has been found to be similar to that of the middle line. For example, a close-up fault is detected after about 20.24 ms by the S.E

relay while a complete restraint of the R.E relay occurs.

Also, a-E faults under the above fault conditions have been assumed to occur in the third line-section and the performance of the relays showed a tendency to behave in the same way as that protecting the first line-section. For example, a solid a-E close-up fault has been detected after about 27.38 ms by the S.E relay and a complete restraint of the R.E relay has occured.

9.4.2 b-c Faults

It is now well recognised that the primary wave forms for pure phase-faults are, in general, significantly more distorted in nature (Chapters (6), (7)) and hence the input signals to the pure phase-fault-relays will result in an increase in measurement delay.

Consider first, a pure 'b-c' solid fault on the middle-section of the system examined.

Figs (9.35-9.37) show solid 'b-c' faults near the S.E busbar, at the mid-point and near the R.E busbar of the middle line-section respectively. The faults occur at maximum 'V_{bc}' and other fault conditions are similar to that for a-E faults. Figs (9.35.a) clearly show a considerable delay in the operation of the 'b-c' relay which is about 32.24 ms compared to 23.76 ms in case of 'a-E' fault relay. Fig (9.35.b) shows that almost complete anticoincidence of the input signals to the R.E relay exists and hence a restraint of that relay should be expected. Fig (9.36.a) shows that both relays will operate after nearly the same time, 43.76 and 45.0 ms for the S.E and R.E relays respectively. Again, for the corresponding earth faults, the delay experienced by the 'b-c' relays is considerable.

Fig (9.37.a) shows that the response of the S.E relay is nearly the same as

that of the R.E relay of Fig (9.35.b) where its complete restraint is obvious. On the other hand, the response of the R.E relay of Fig (9.37.b) seems to be even better than that of the S.E relay of Fig (9.35.a). Fault detection time is about 22.96 ms as seen from Fig (9.37.b), and this faster operation of the R.E relay could be due to the relatively simple R.E source when a fault at the R.E busbar of the middle line section occurs.

Fig (9.38) shows the response of the two relays for a solid 'b-c', mid-point fault when the voltage between the faulted phases is zero. Other fault conditions are the same as that of Fig (9.36). The Fig. clearly shows that the input signals to the two relays are less noisy and due to the nearly zero travelling wave distortion, the two relays seem to operate at the same time (19.76 ms).

Figs (9.39), (9.40) show the response of the S.E and R.E relays when a solid 'b-c' fault occurs at equal distances from the relay locations (in the first section) respectively. Other fault conditions are similar to that of Figs (9.36).

A comparison of Fig (9.39.a) with Fig (9.33.a) reveals that the distortion of the input signals to the 'b-c' relay persists for longer time than the case with the phase-a relay. However, the operating time in the former case (32.8 ms) is not significantly higher than that in the latter (32.0 ms). Again, due to the relatively longer travelling distances involved (compared to 'b-c' faults in the middle section) travelling wave components are more attenuated for faults on the first section as may be seen from Table (9.8). Fig (9.39.b) shows that the R.E relay takes a very long time, about 69.0 ms to operate for the 'b-c' fault at its boundary.

The behaviour of the S.E and R.E relays of Fig (9.40) is nearly the same as that of the R.E and S.E relays of Fig (9.39) respectively. For a fault 50 km

away from the R.E relay, the fault is detected after about 30.0 ms Fig (9.40.b) compared to 32.8 ms taken by the S.E relay for a fault 50 km away from it. Also the same fault is detected by the S.E relay after about 65.2 ms Fig (9.40.a) which corresponds to about 68.8 ms taken by the R.E relay to detect the same fault, 50 km away from the S.E of the first line section. Table (9.8) obviously shows that the performance of 'phase-a' relay is much better than that of the 'b-c' relays from the point of view of speed of operation.

Figs (9.41), (9.42) show the input signals and comparator outputs for the cases corresponding to Figs (9.39), (9.40) but for faults at zero 'V_{bc}'. The better performance of the relays in both cases compared to maximum 'V_{bc}' faults is obvious and it is shown that the S.E and R.E relays operate after 17.52 ms respectively to detect a fault 50 km away from their respective relay locations.

Although, a detailed study to examine the measurement accuracy of different relays has not been carried out, the results presented here in this section may show that the reach of the relays can not be that different from that examined in sections 9.2 and 9.3 above.

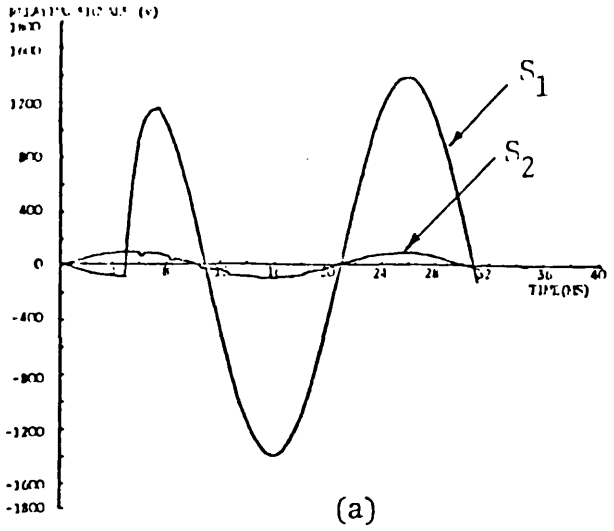

(a)

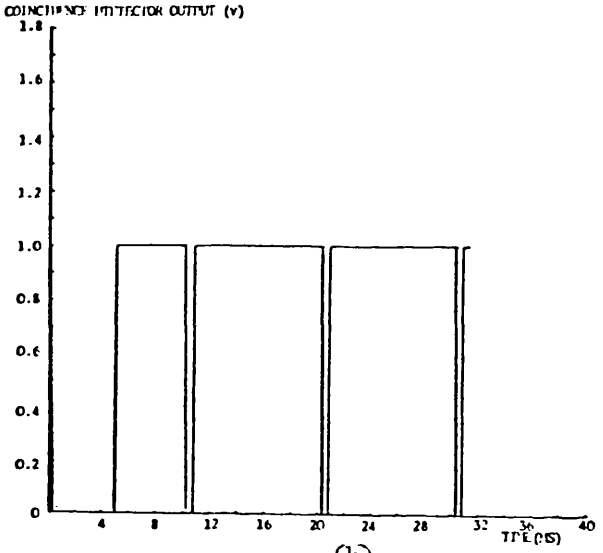

(b)

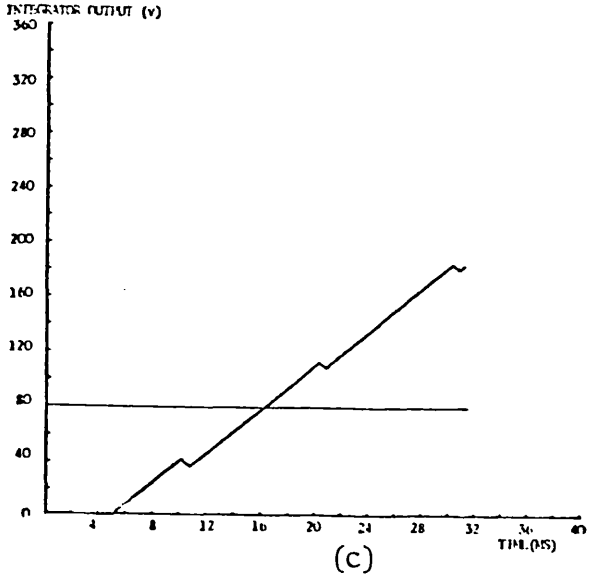

(c)

Fig 9.1

Relay response for an 'a-E' close-up fault on the single-section feeder system examined.

- $V_S/V_R = \underline{|0^o}$, FT = 5 ms
- S.S.C.L. = R.S.C.L. = 35 GVA.
- $Q_S = Q_R = 100.0$. $h_1 = h_0 = 0.0$.

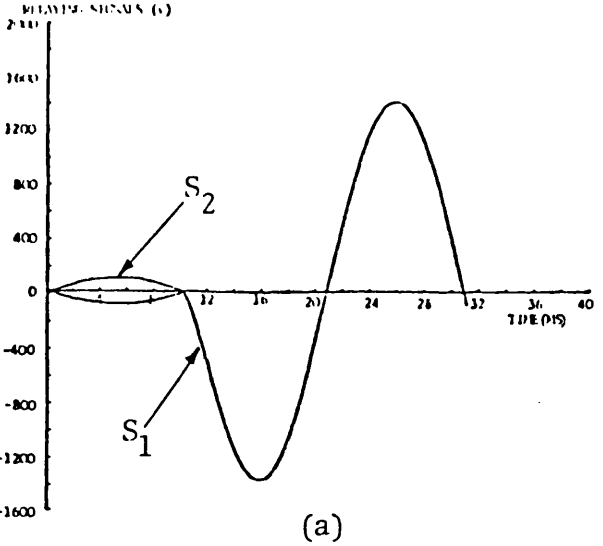

(a)

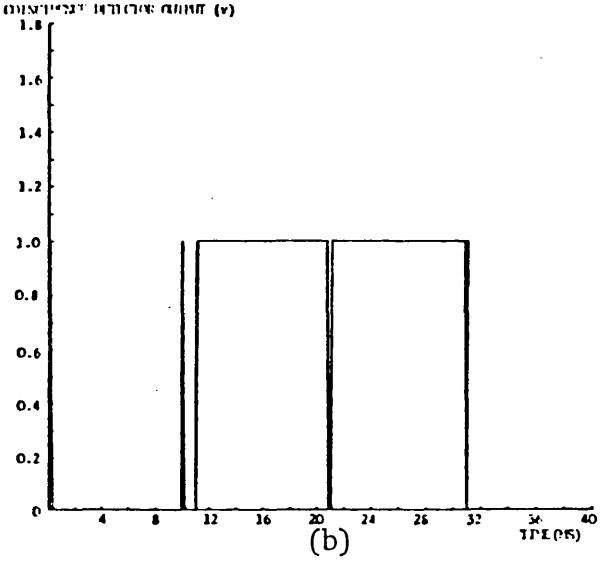

(b)

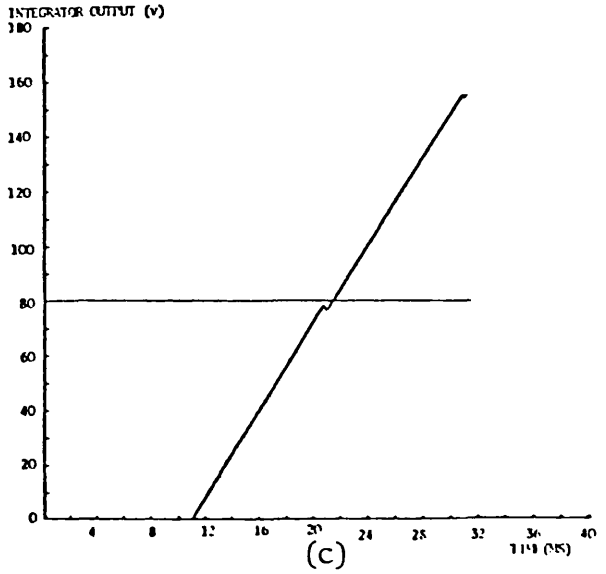

(c)

Fig 9.2

Relay response for an 'a-E' close-up fault on the single-section feeder system examined.

- FT = 10.0 ms
- Other fault conditions are similar to that of Fig (9.1).

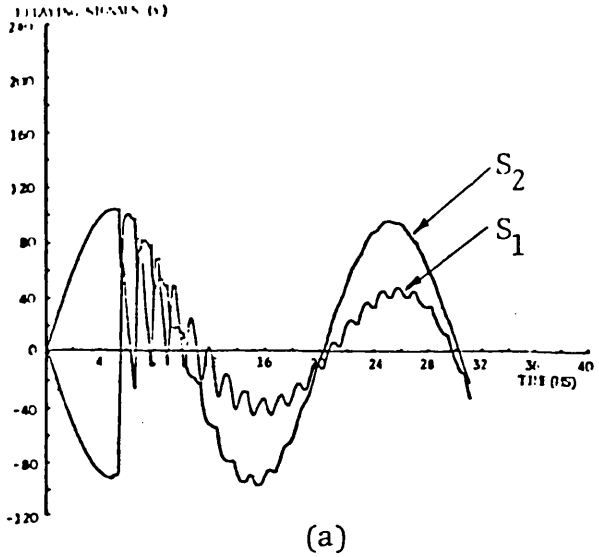

(a)

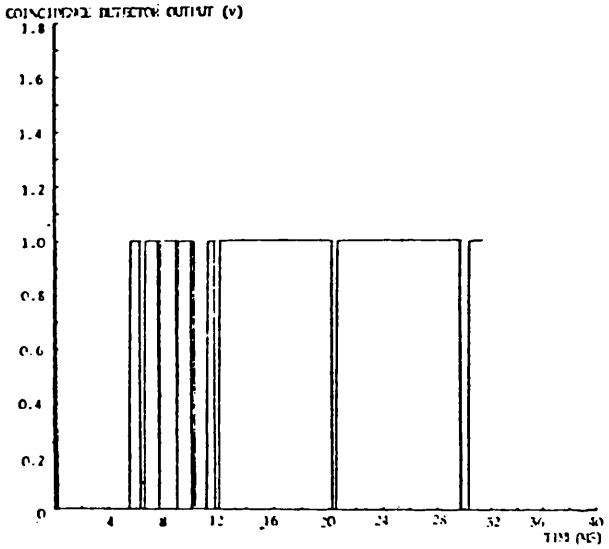

(b)

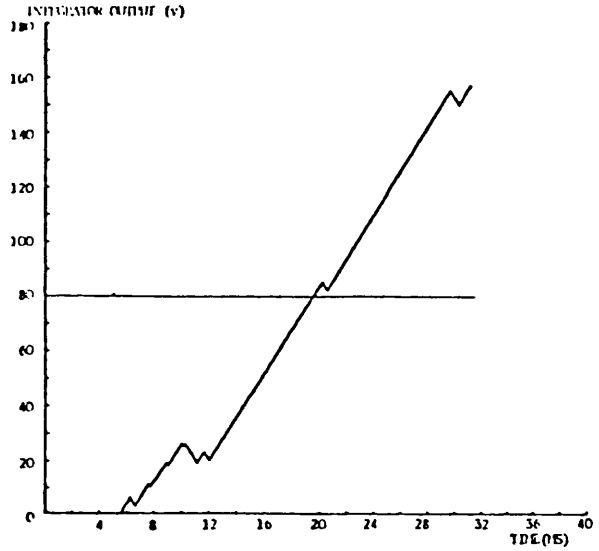

(c)

Fig 9.3

Relay response for an 'a-E' mid-point fault on the single-section feeder system examined.

- Fault conditions are similar to that of Fig 9.1.

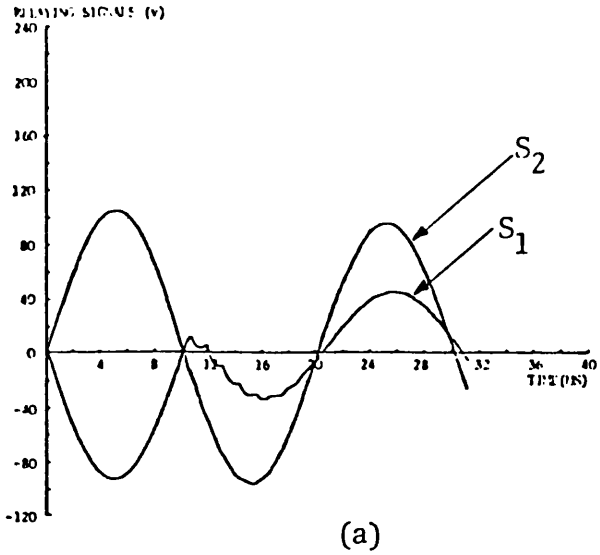

(a)

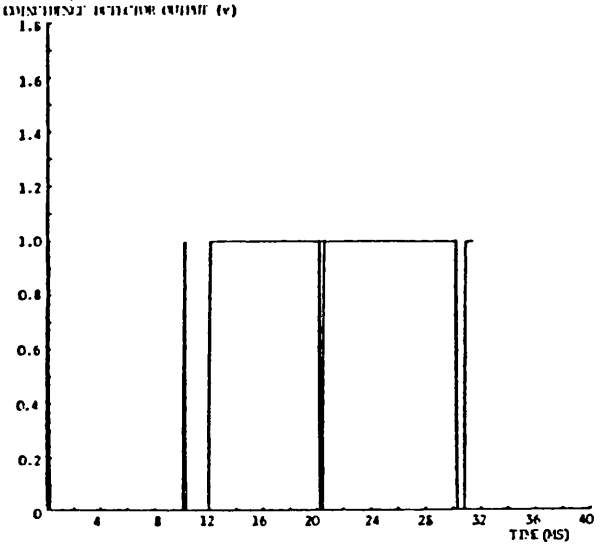

(b)

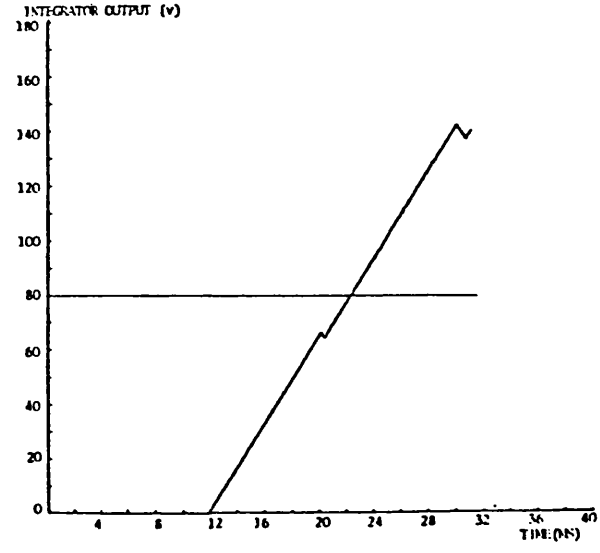

(c)

Fig 9.4

Relay response for an 'a-E' mid-point fault on the single-section feeder system examined.

- Fault conditions are similar to that of Fig 9.2.

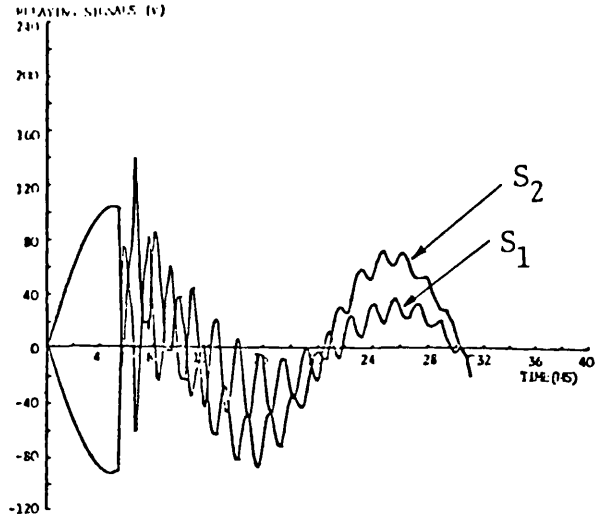

(a)

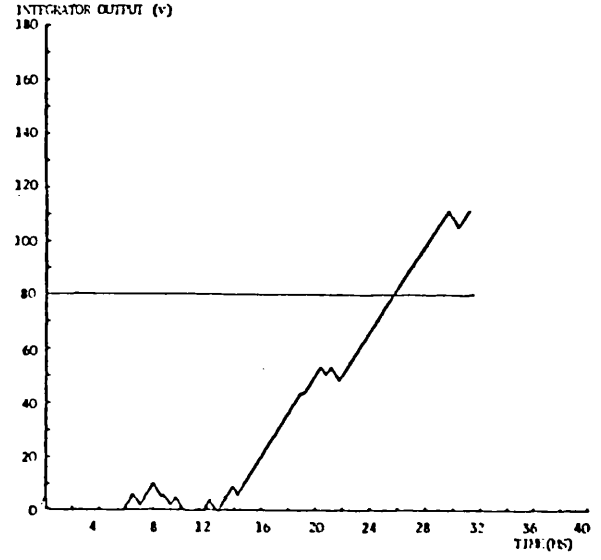

(b)

Fig 9.5

Relay response for an 'a-E' mid-point fault on the single-section feeder system examined.

- S.S.C.L. = 5 GVA, R.S.C.L. = 35 GVA.
- Other fault conditions are similar to that of Fig 9.3.

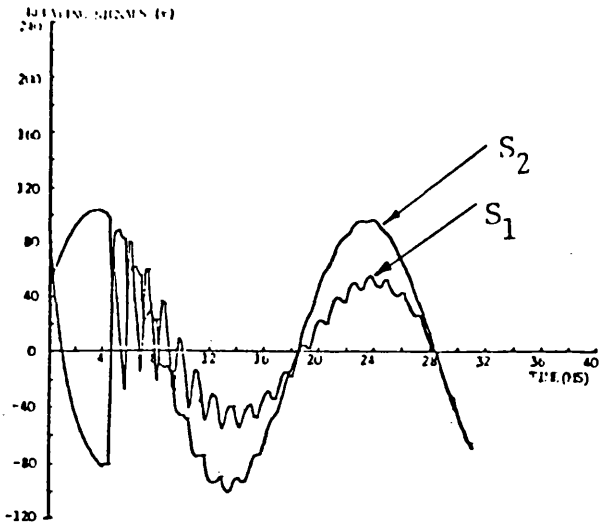

(a)

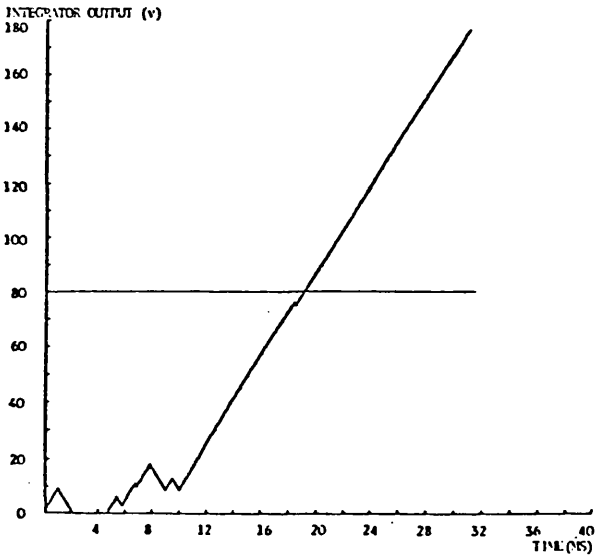

(b)

Fig 9.6

Relay response for an 'a-E' mid-point fault on the single-section feeder system examined.

- $V_S/V_R = \underline{30^o}$, FT = 4.17 ms.
- Other fault conditions are similar to that of Fig 9.3.

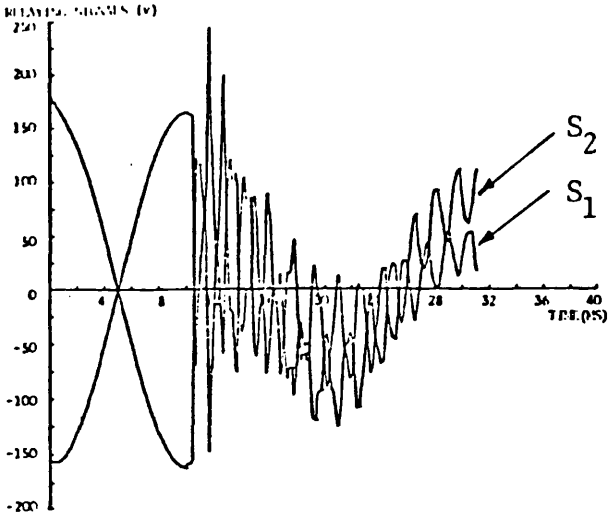

(a)

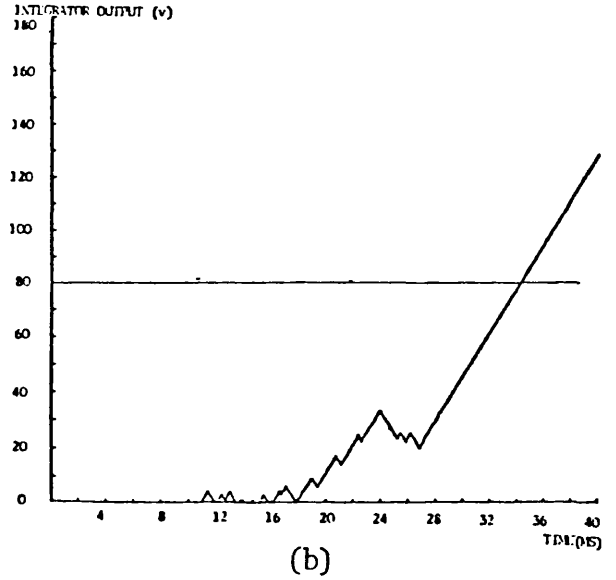

(b)

Fig 9.7

Relay response for a 'b-c' mid-point fault on the single-section feeder system examined.

- $V_S/V_R = \underline{0}^o$, FT = 10 ms.
- Other fault conditions are similar to that of Fig 9.5.

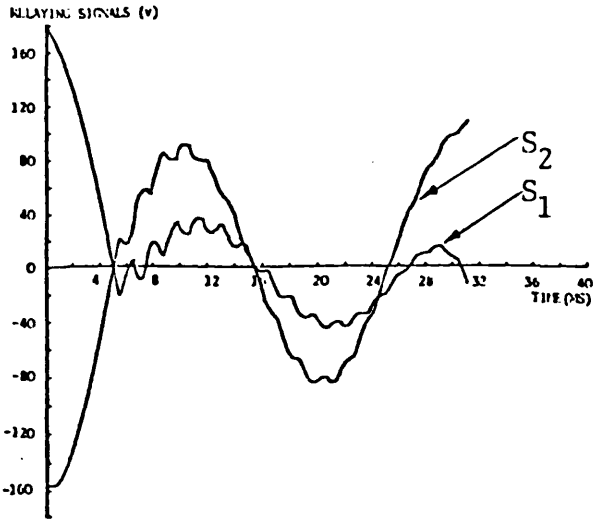

(a)

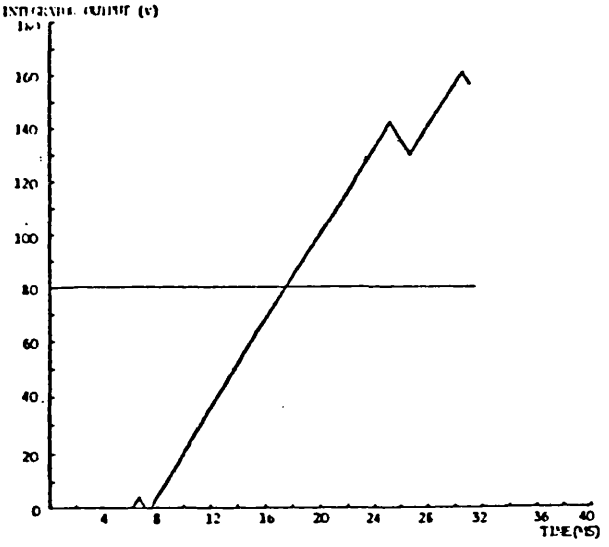

(b)

Fig 9.8

Relay response for a 'b-c' mid-point fault on the single-section feeder system examined.

- FT = 5 ms.
- Other fault conditions are similar to that of Fig 9.7.

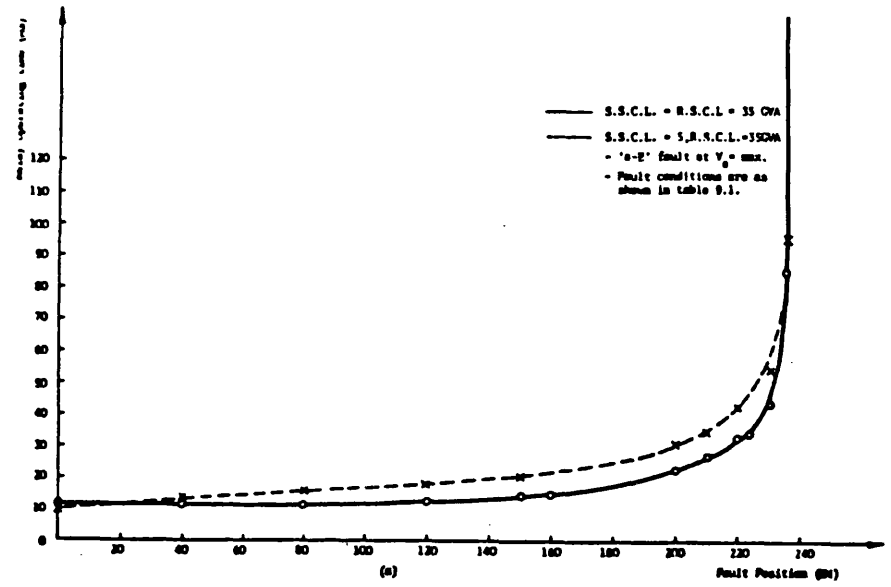

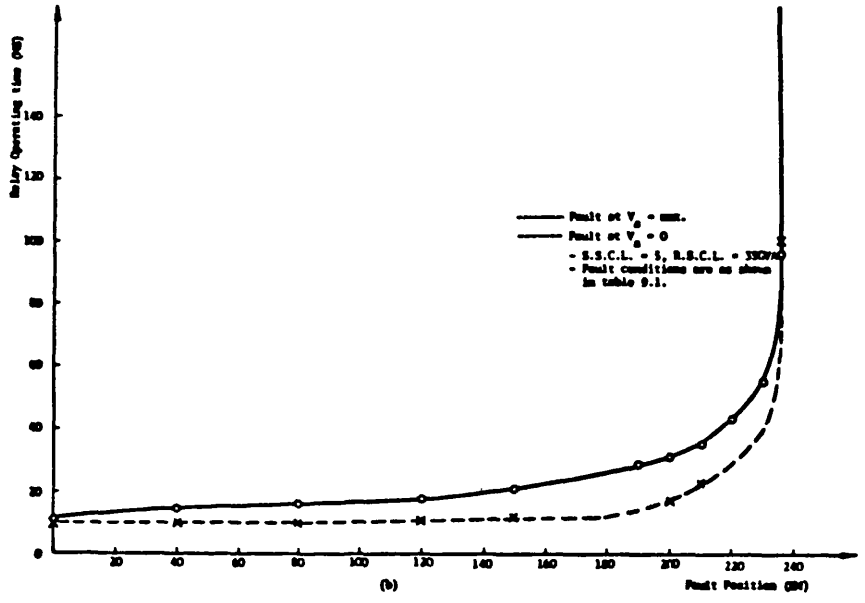

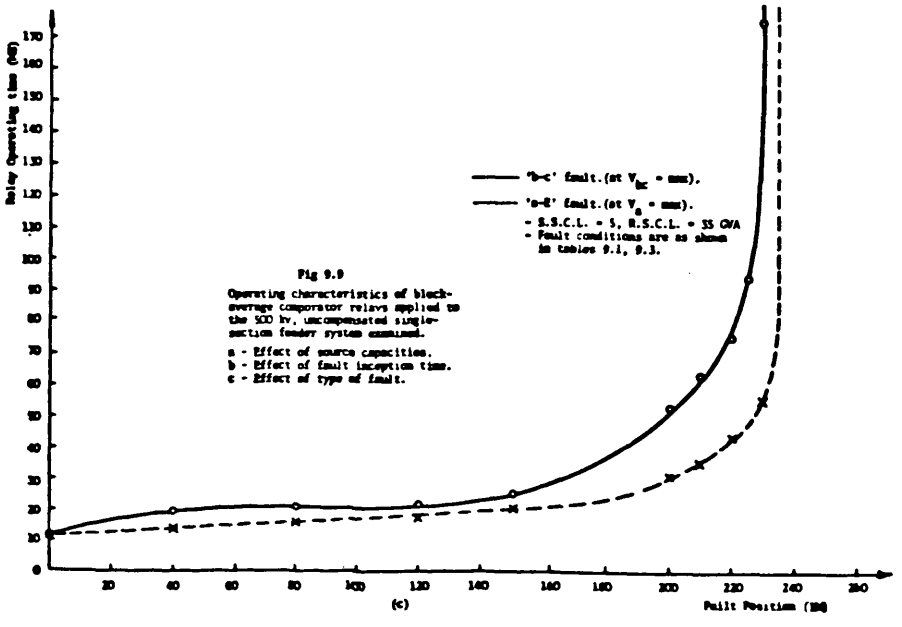

Fig 9.9

Operating characteristics of block-average comparator relays applied to the 500 kv, uncompensated single-section feeder system examined.

a - Effect of source capacitive.
b - Effect of fault inception time.
c - Effect of type of fault.

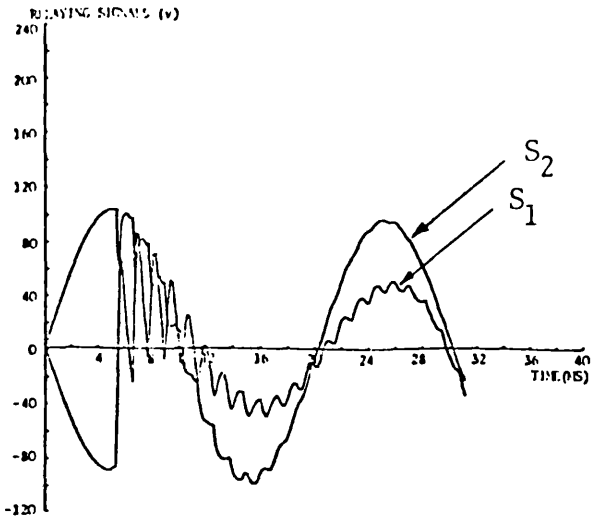

(a)

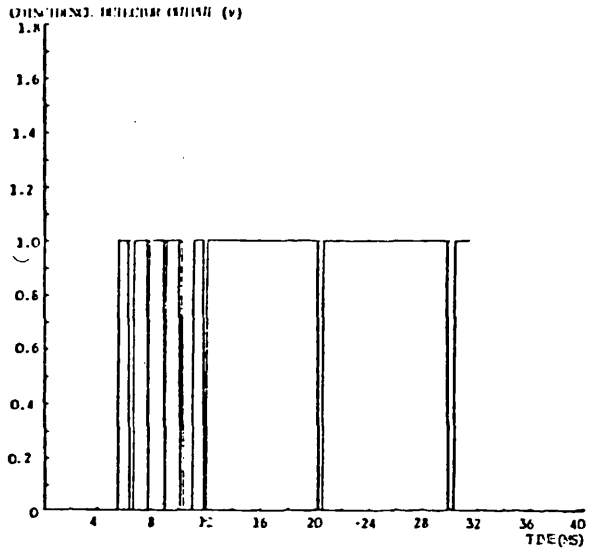

(b)

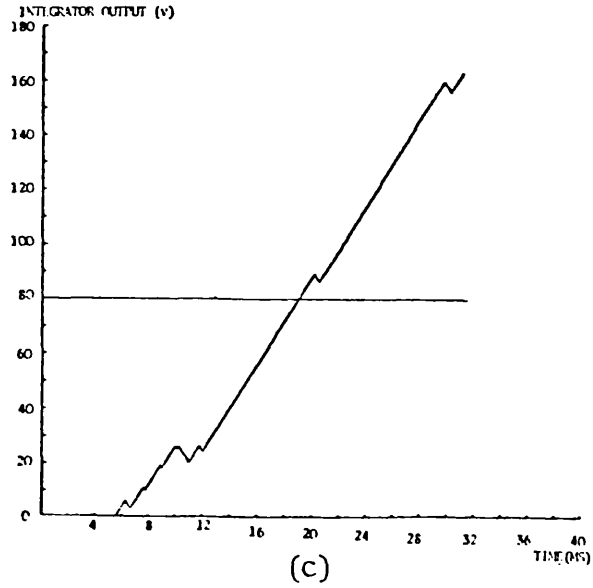

(c)

Fig 9.10

Relay response for an 'a-E' mid-point fault on the single-section feeder system examined.

- h_1 = 0.75, h_0 = 0.6.
- Other fault conditions are similar to that of Fig 9.3.

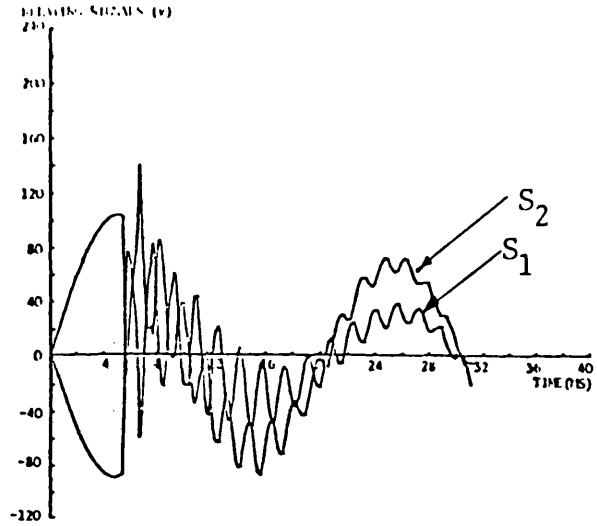

(a)

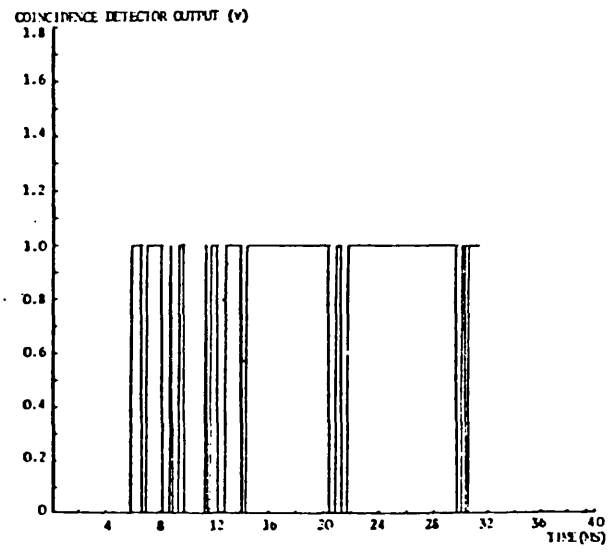

(b)

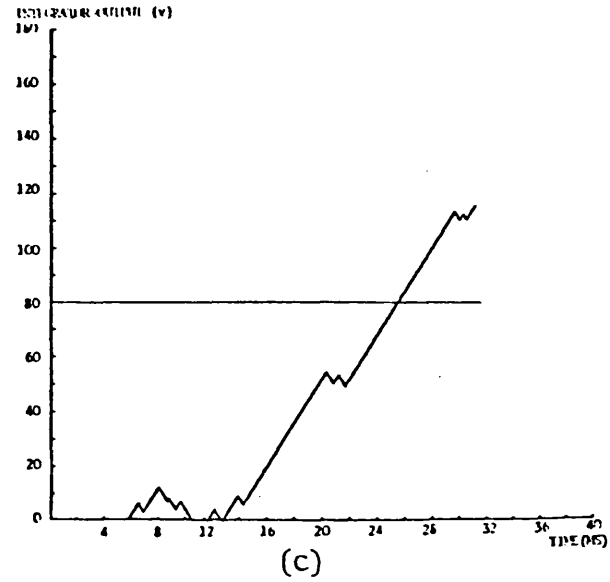

(c)

Fig 9.11

Relay response for an 'a-E' mid-point fault on the single-section feeder system examined.

- h_1 = 0.75 , h_0 = 0.6.
- Other fault conditions are similar to that of Fig 9.5.

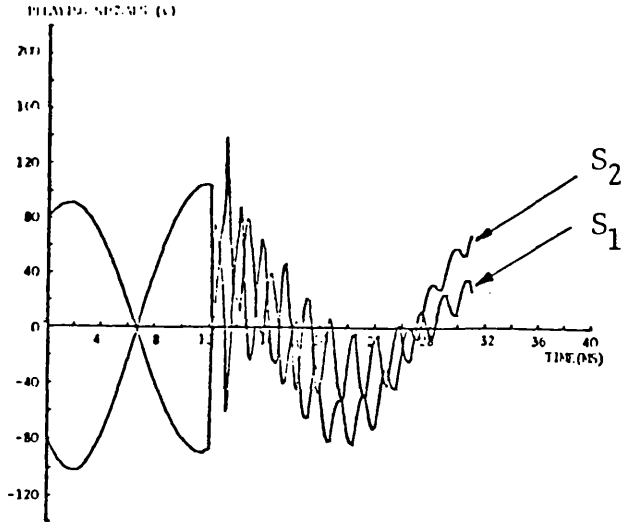

(a)

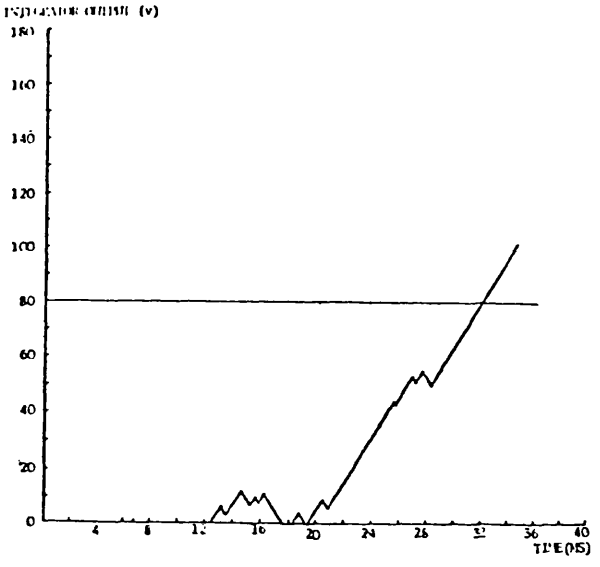

(b)

Fig 9.12

Relay response for 'b-E' mid-point fault on the single-section feeder system examined.

- FT = 11.67 ms.
- Other fault conditions are similar to that of Fig 9.11.

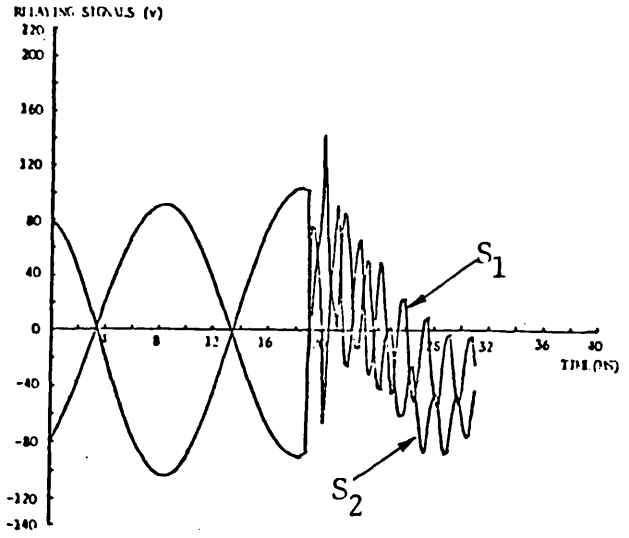

(a)

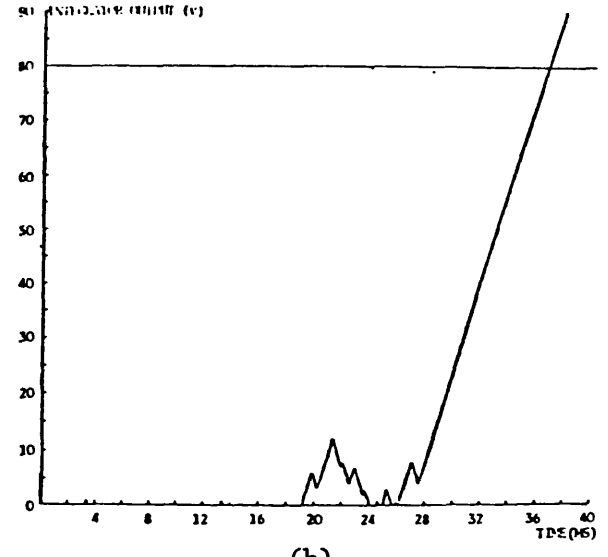

(b)

Fig 9.13

Relay response for a 'c-E' mid-point fault on the single-section feeder system examined.

- FT = 18.33 ms.
- Other fault conditions are similar to that of Fig 9.11.

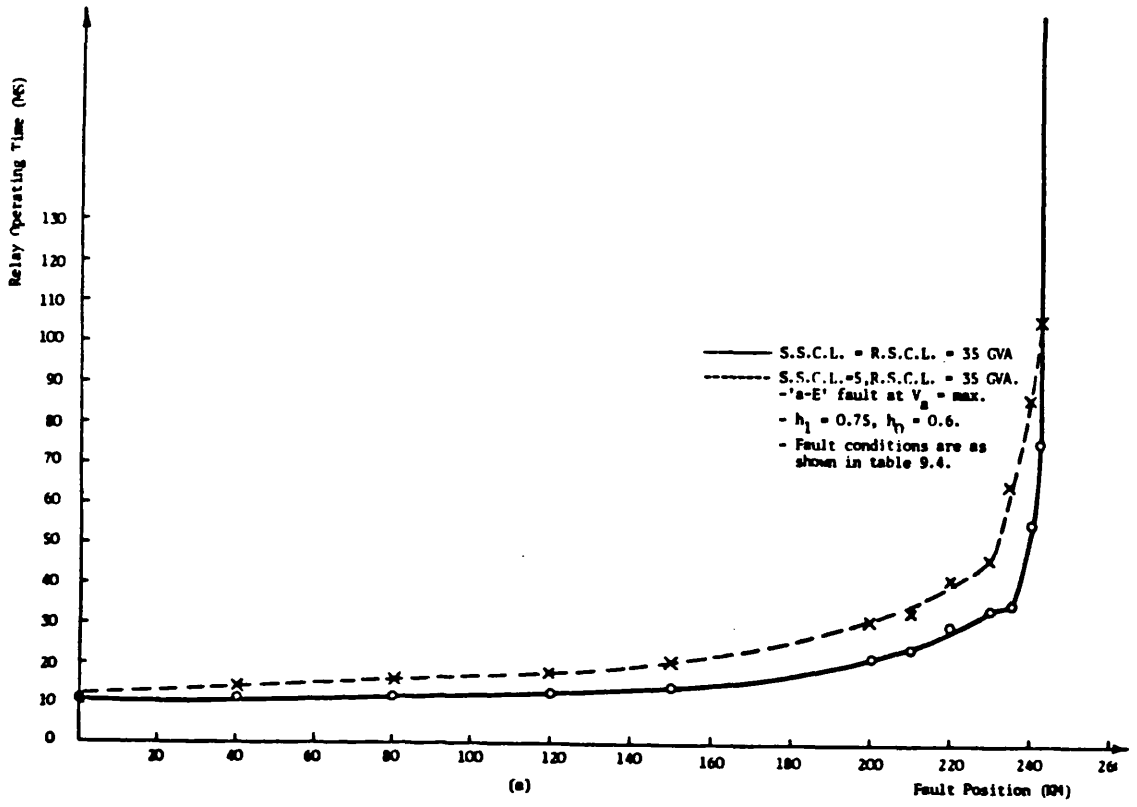

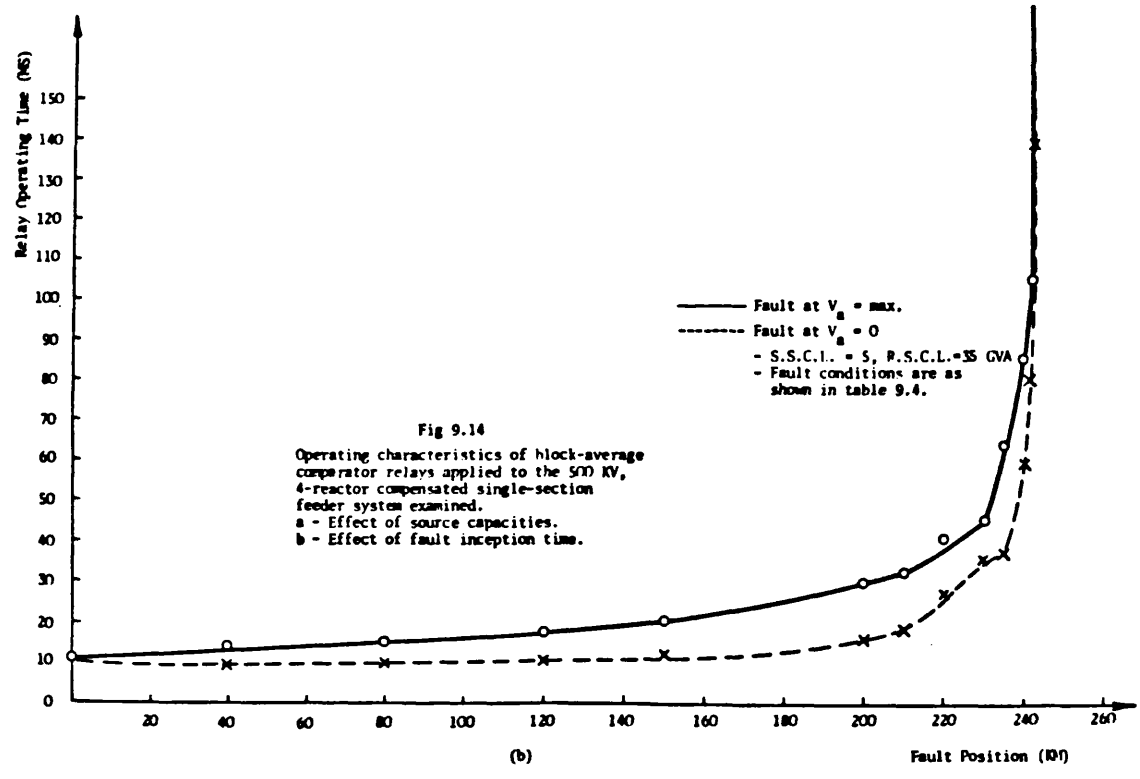

Fig 9.14

Operating characteristics of block-average comparator relays applied to the 500 KV, 4-reactor compensated single-section feeder system examined.
a - Effect of source capacities.
b - Effect of fault inception time.

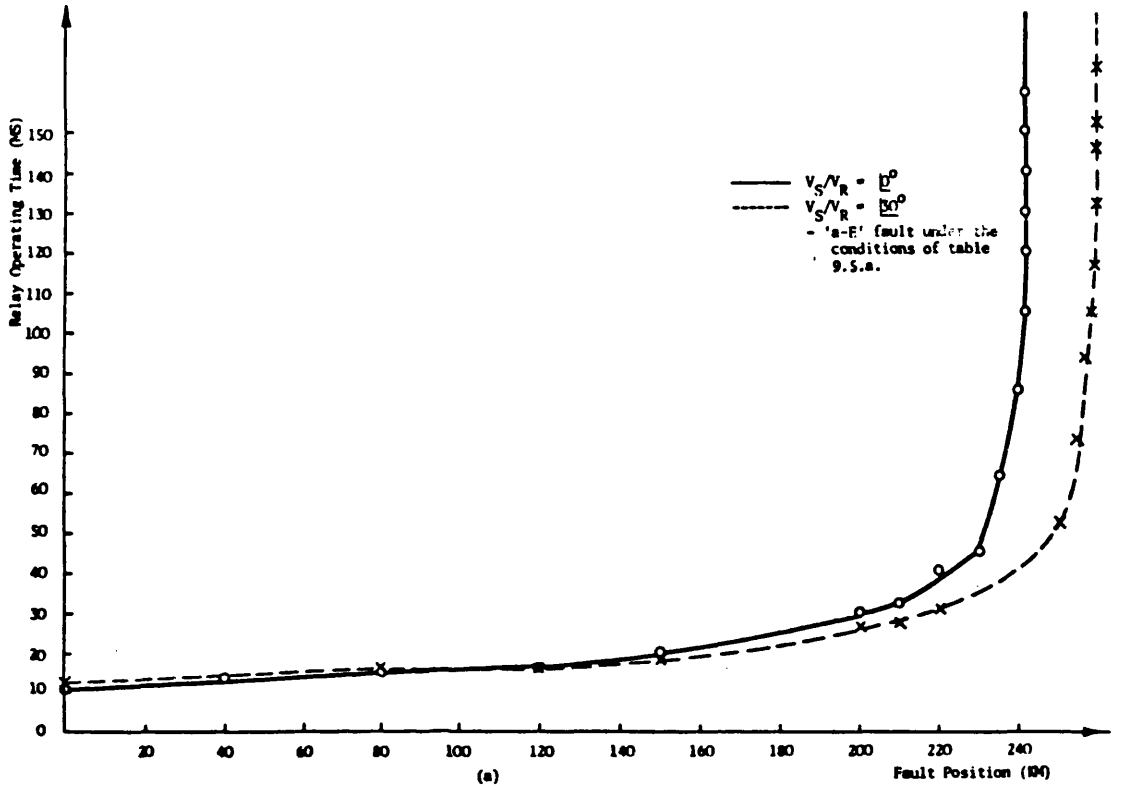

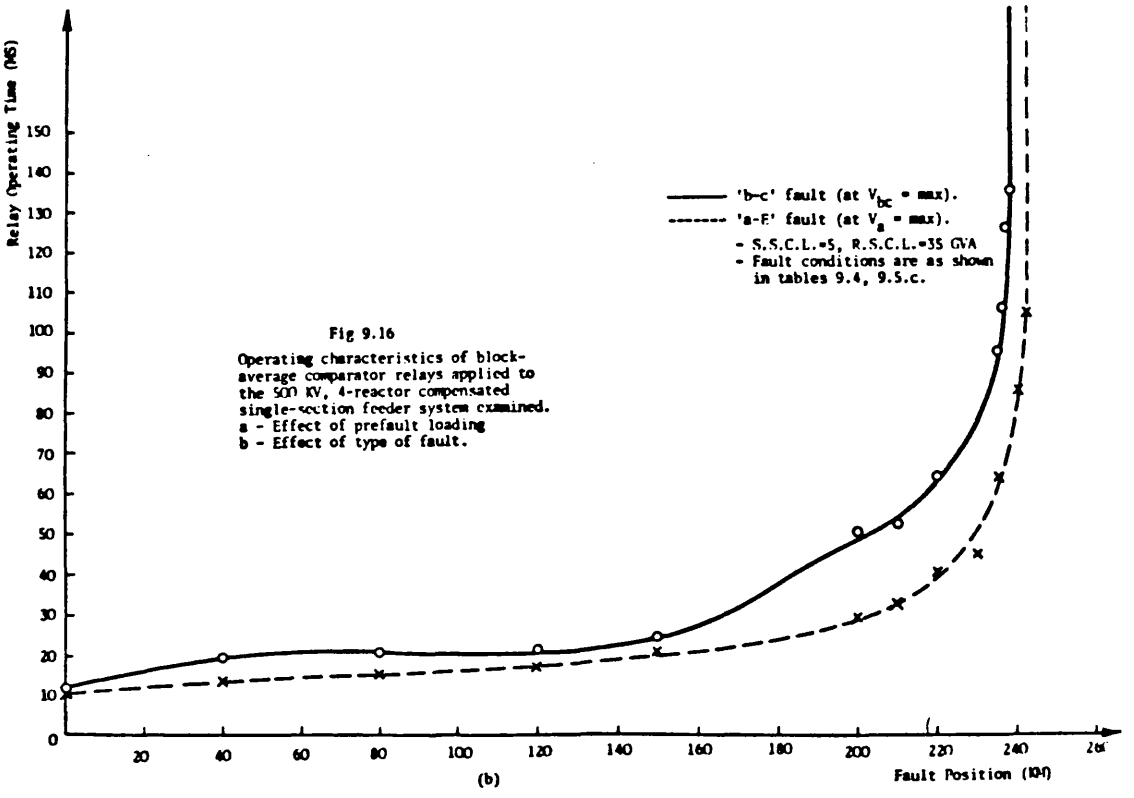

Fig 9.16

Operating characteristics of block-average comparator relays applied to the 500 KV, 4-reactor compensated single-section feeder system examined.
a - Effect of prefault loading
b - Effect of type of fault.

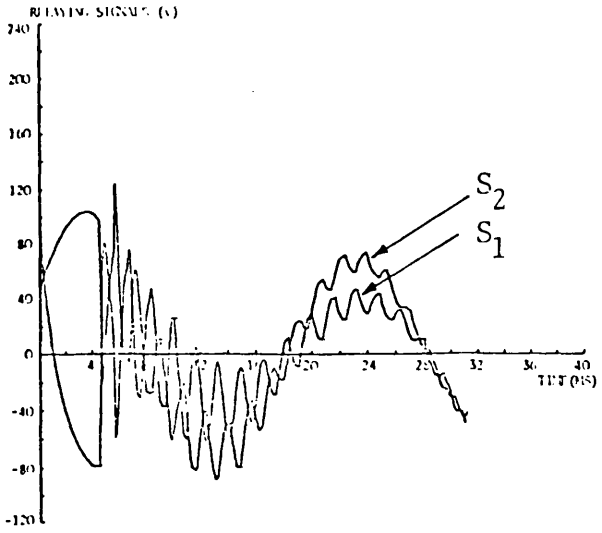

(a)

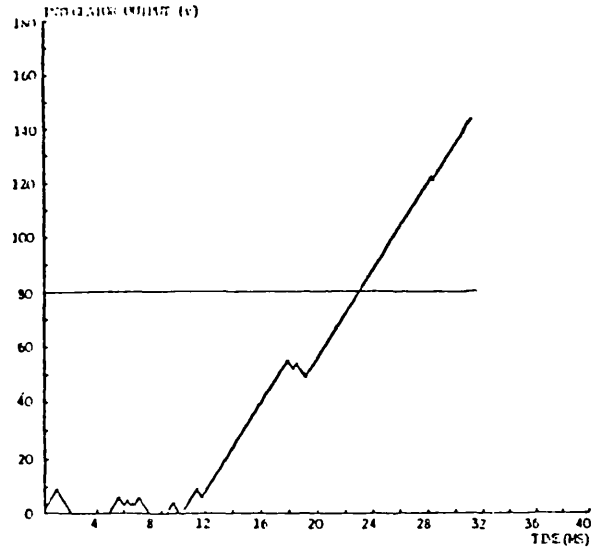

(b)

Fig 9.15

Relay response for an 'a-E' mid-point fault on the single-section feeder system examined.

- $V_S/V_R = \underline{30^o}$, $h_1 = 0.75$, $h_0 = 0.6$.
- FT = 4.17 ms.
- Other fault conditions are similar to that of Fig 9.5.

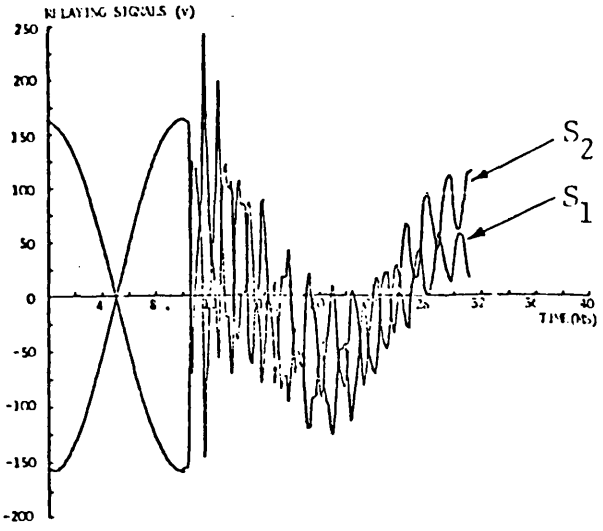

(a)

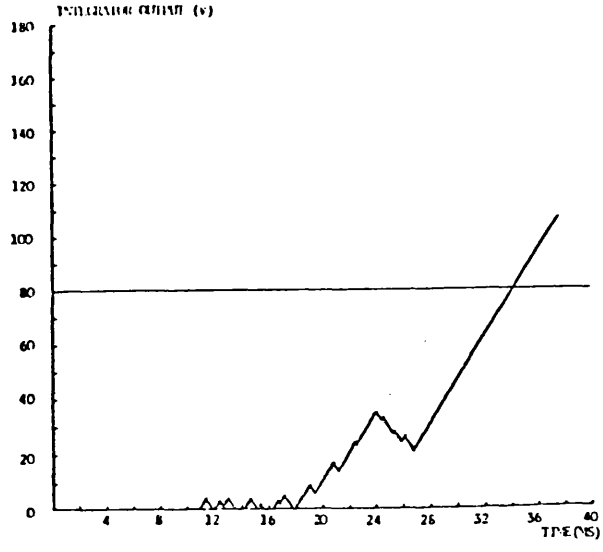

(b)

Fig 9.17

Relay response for a mid-point 'b-c' fault on the single-section feeder system examined.

- $h_1 = 0.75$, $h_0 = 0.6$
- Other fault conditions are similar to that of Fig 9.7.

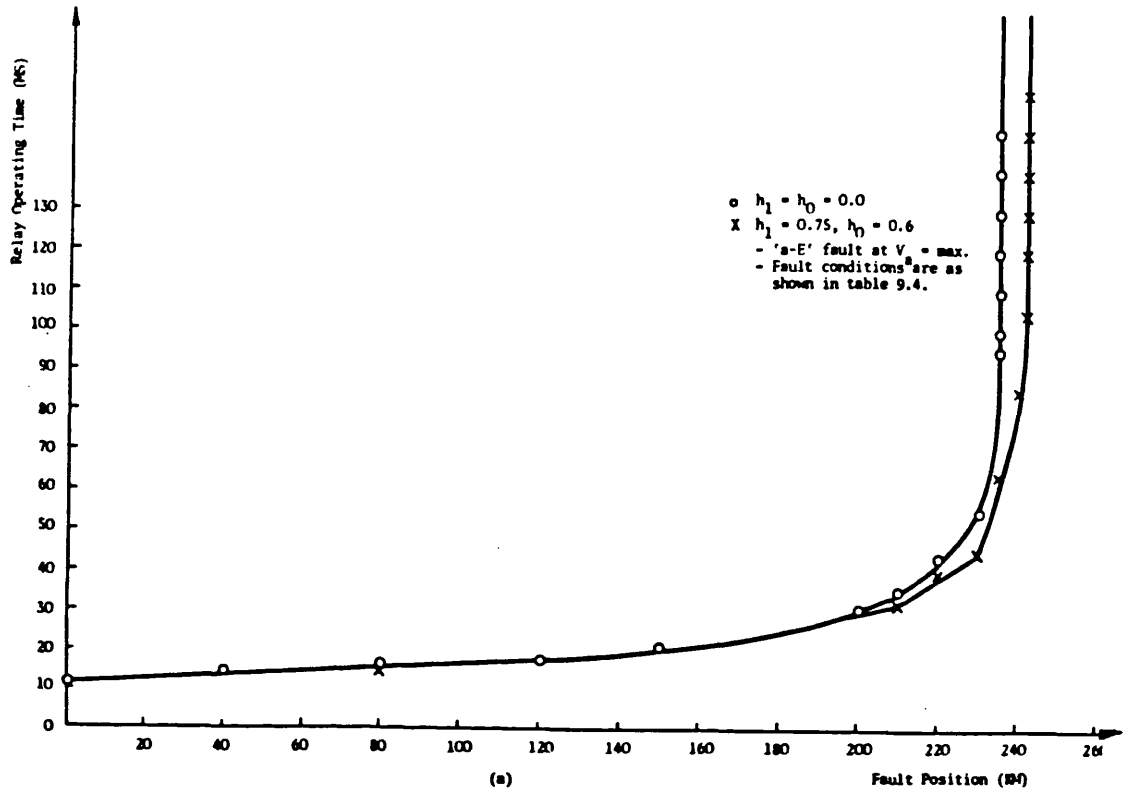

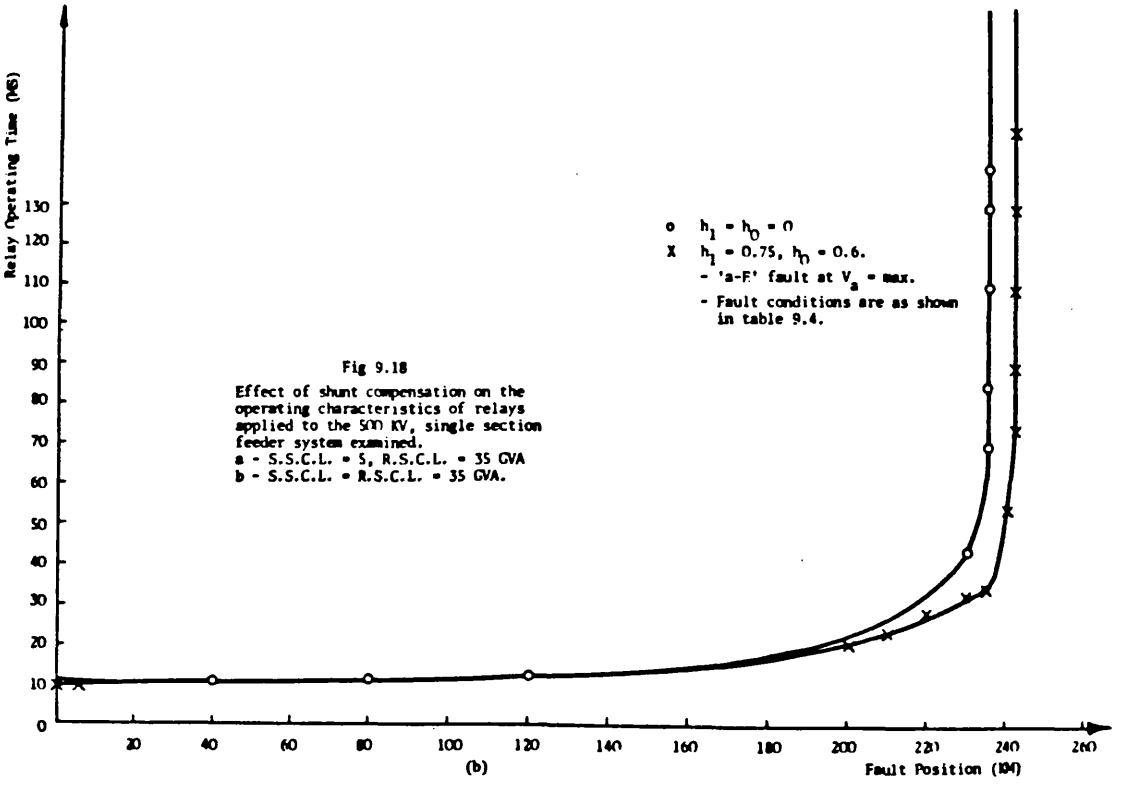

Fig 9.18

Effect of shunt compensation on the operating characteristics of relays applied to the 500 KV, single section feeder system examined.
a - S.S.C.L. = S, R.S.C.L. = 35 GVA
b - S.S.C.L. = R.S.C.L. = 35 GVA.

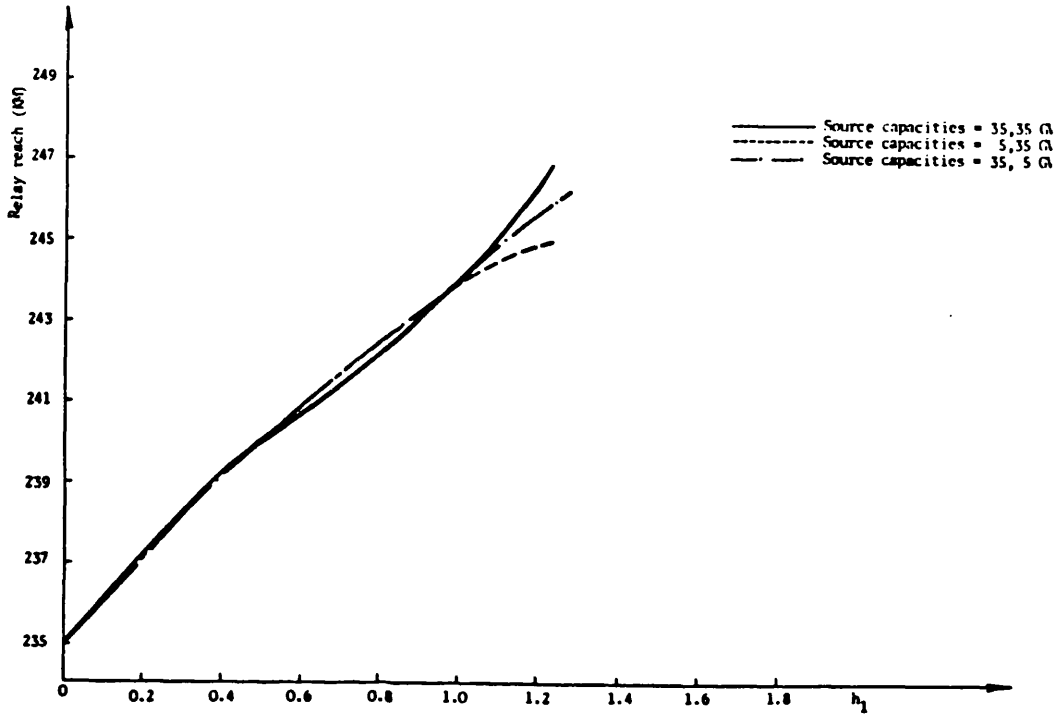

(a)

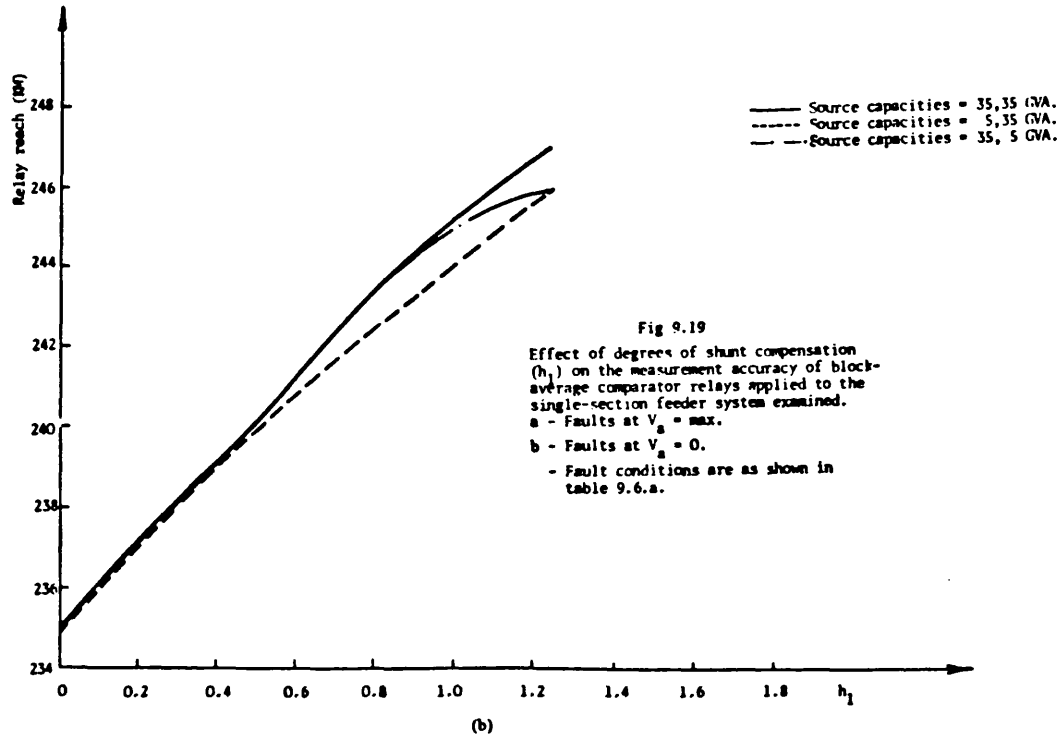

(b)

Fig 9.19

Effect of degrees of shunt compensation (h_1) on the measurement accuracy of block-average comparator relays applied to the single-section feeder system examined.

a - Faults at V_a = max.

b - Faults at V_a = 0.

- Fault conditions are as shown in table 9.6.a.

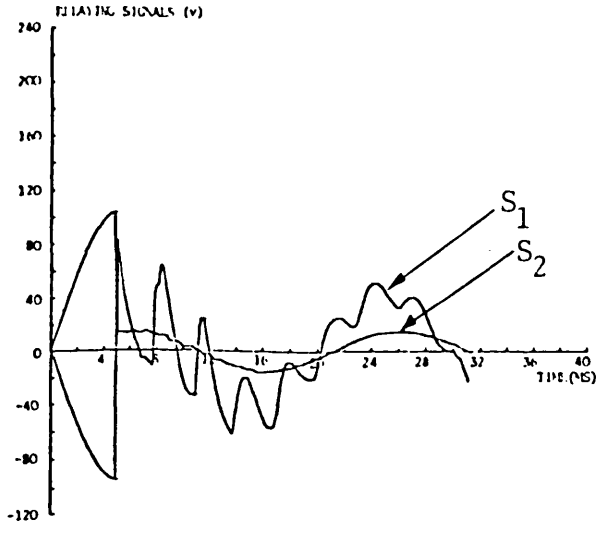

(a)

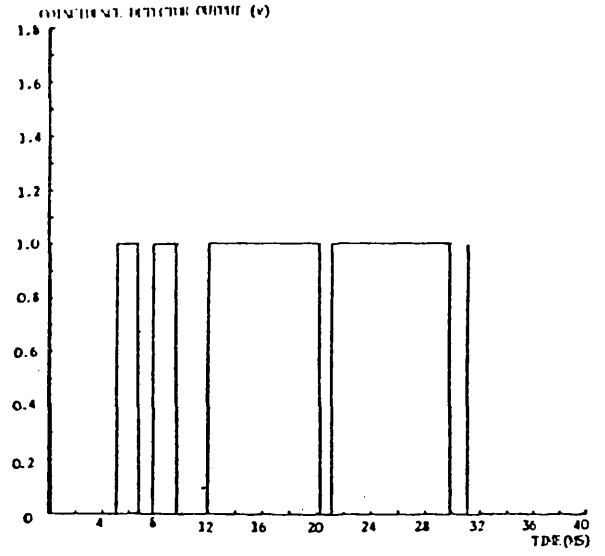

(b)

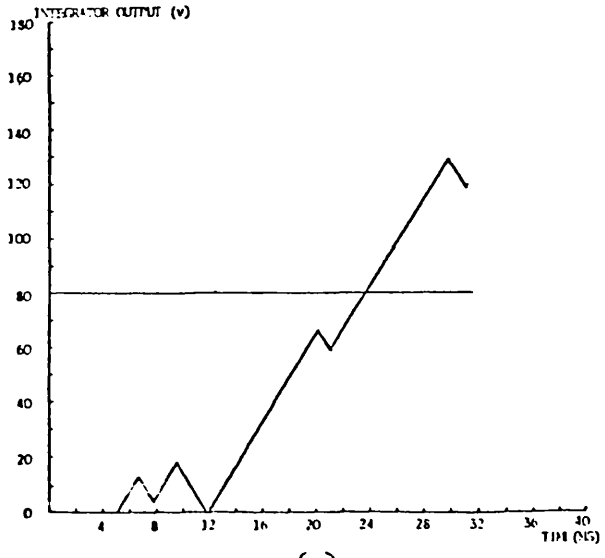

(c)

Fig 9.20

Relay response for an 'a-E' close-up fault on the middle section of the 3-section feeder system examined.

- Fault conditions are similar to that of Fig 9.1.

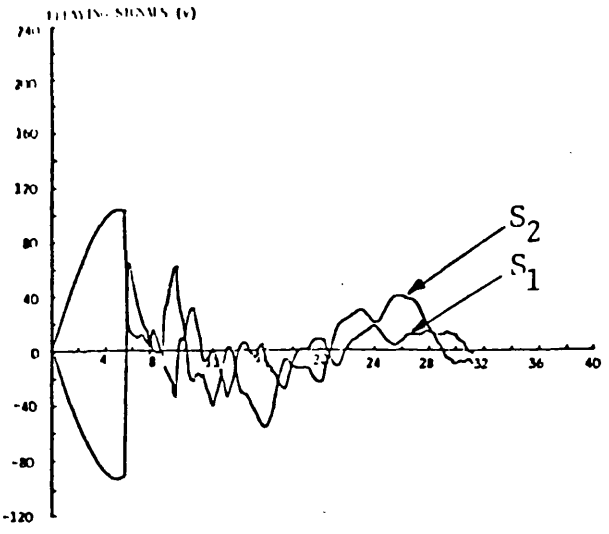

(a)

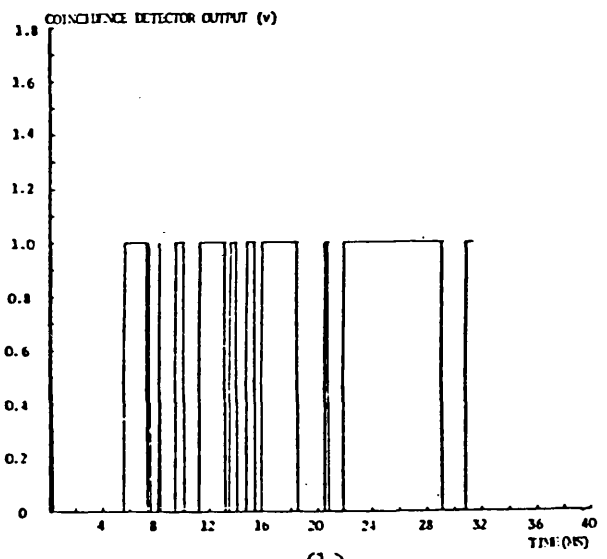

(b)

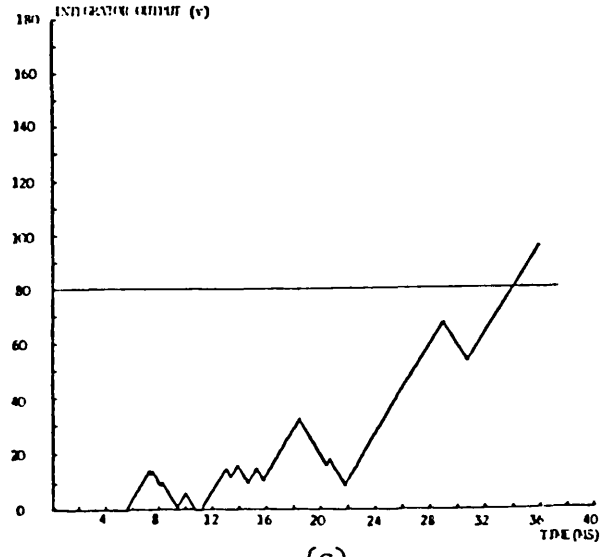

(c)

Fig 9.21

Relay response for an 'a-E' mid-point fault on the middle section of the 3-section feeder system examined.

- Fault conditions are similar to that of Fig 9.3.

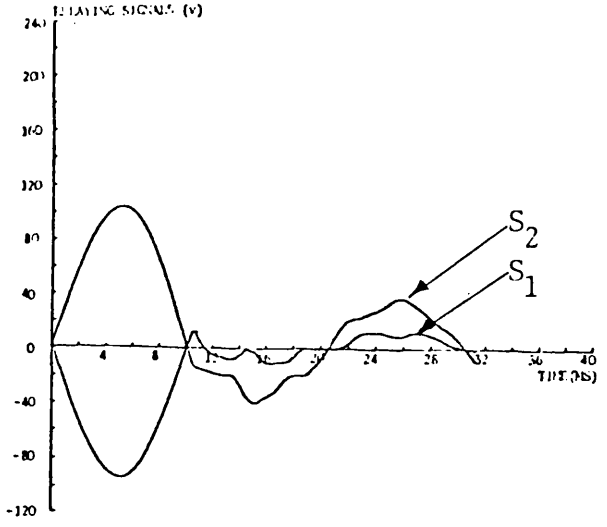

(a)

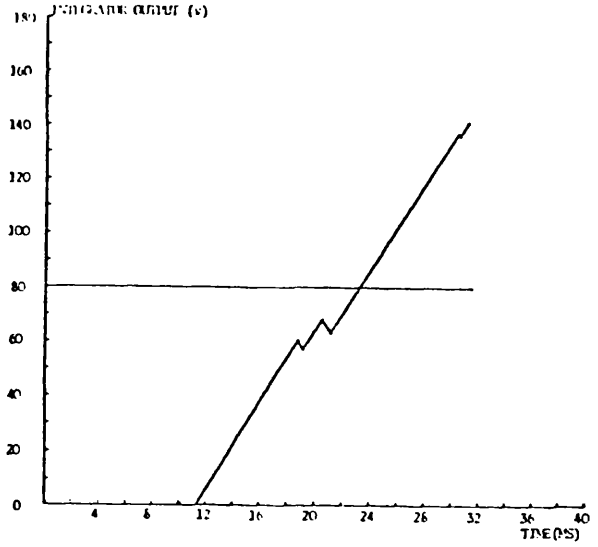

(b)

Fig 9.22

Relay response for an 'a-E' mid-point fault on the middle section of the 3-section feeder system examined.

- Fault conditions are similar to that of Fig 9.4.

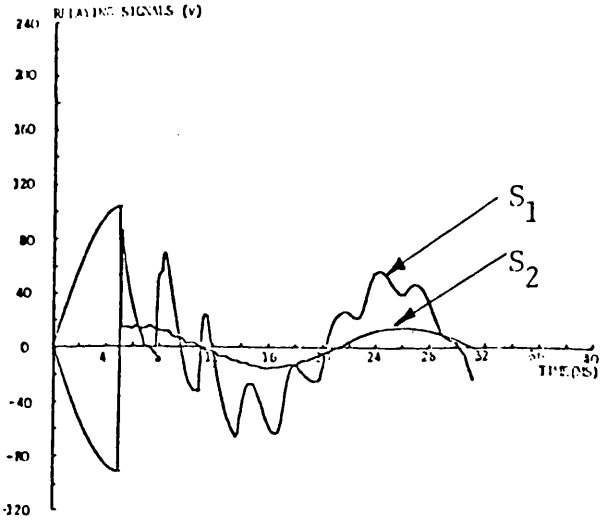

(a)

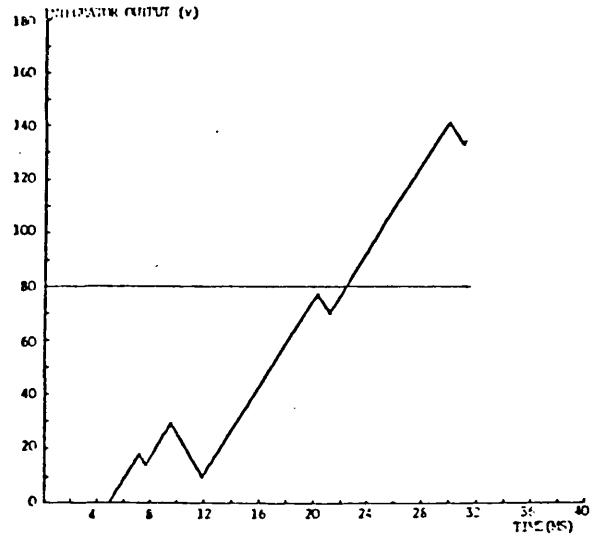

(b)

Fig 9.23

Relay response for a close-up 'a-E' fault on the middle section of the 3-section feeder system examined.

- $h_1 = 0.75$, $h_0 = 0.6$.
- Other fault conditions are similar to that of Fig 9.20.

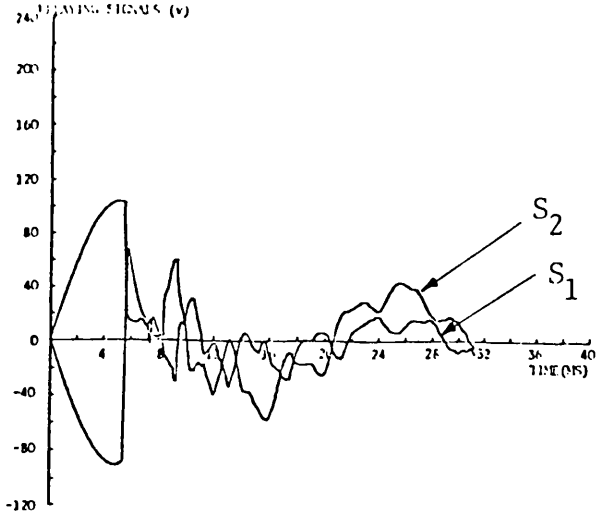

(a)

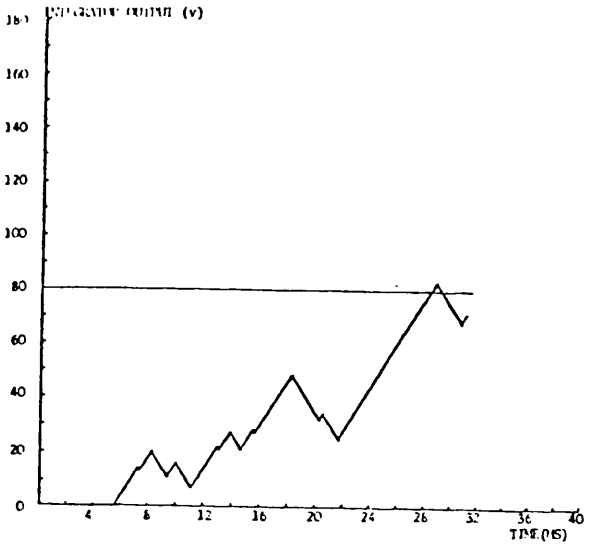

(b)

Fig 9.24

Relay response for a mid-point 'a-E' fault on the middle section of the 3-section feeder system examined.

- Fault conditions are similar to that of Fig 9.10.

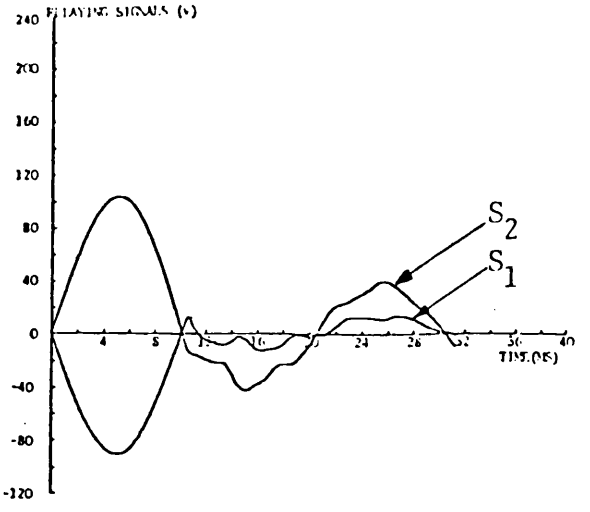

(a)

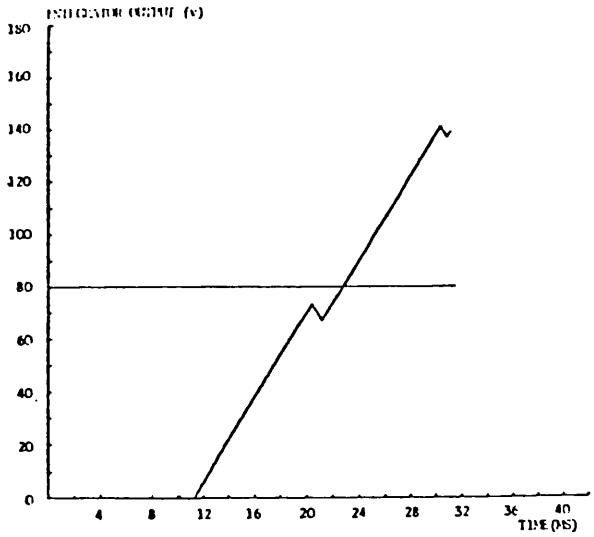

(b)

Fig 9.25

Relay response for a mid-point 'a-E' fault on the middle section of the 3-section feeder system examined.

- FT = 10 ms.
- Other fault conditions are similar to that of Fig 9.10.

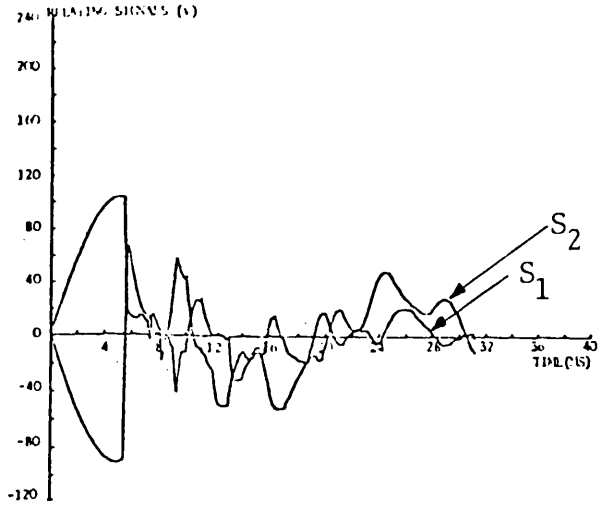

(a)

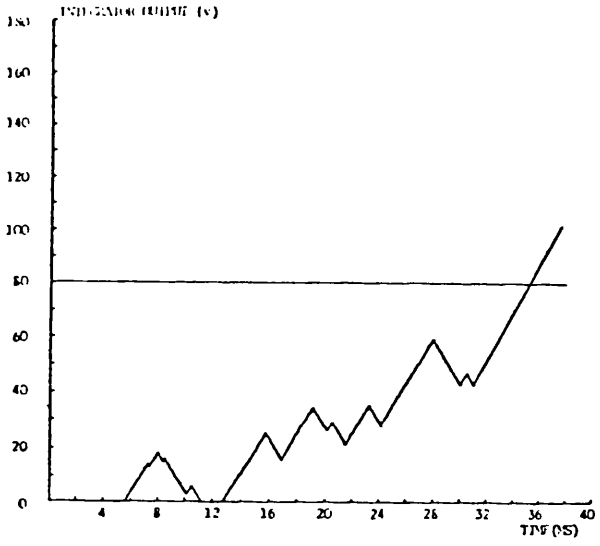

(b)

Fig 9.26

Relay response for a mid-point 'a-E' fault on the middle section of the 3-section feeder system examined.

- Fault conditions are similar to that of Fig 9.11.

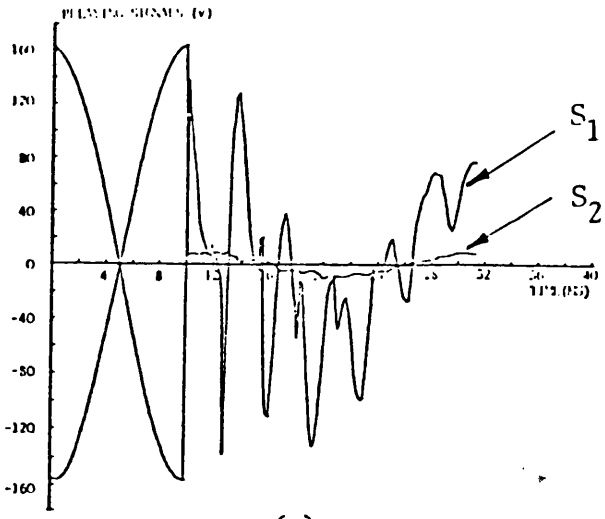

(a)

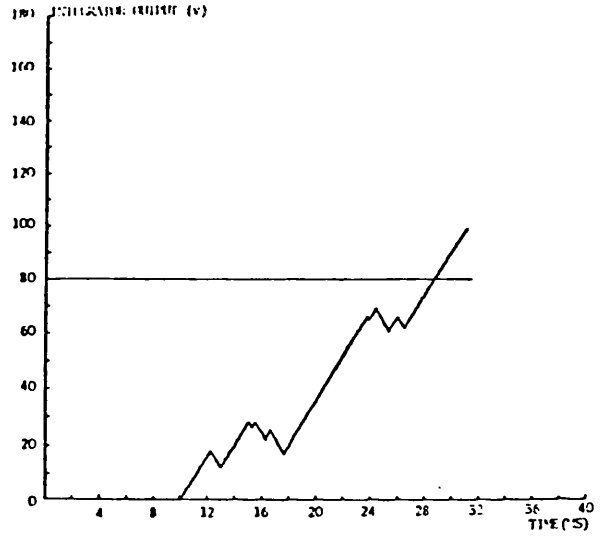

(b)

Fig 9.27

Relay response for a close-up 'b-c' fault on the middle section of the 3-section feeder system examined.

- Fault conditions are similar to that of Fig 9.17.

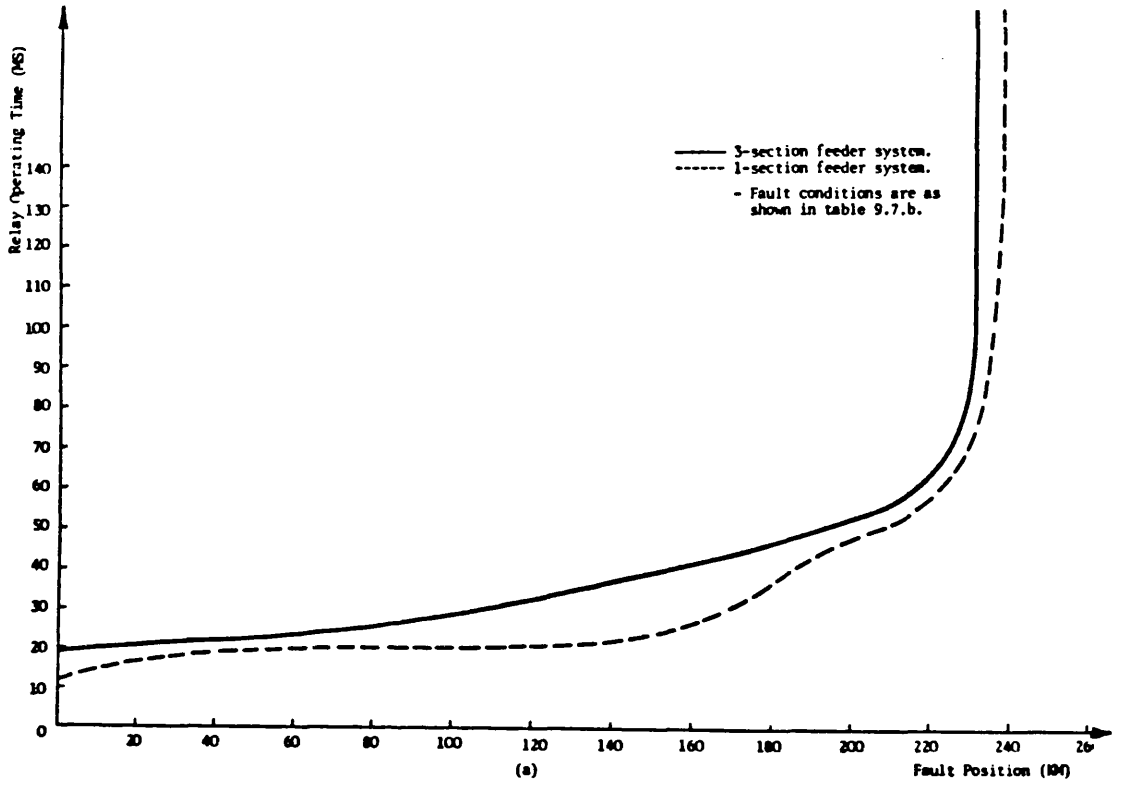

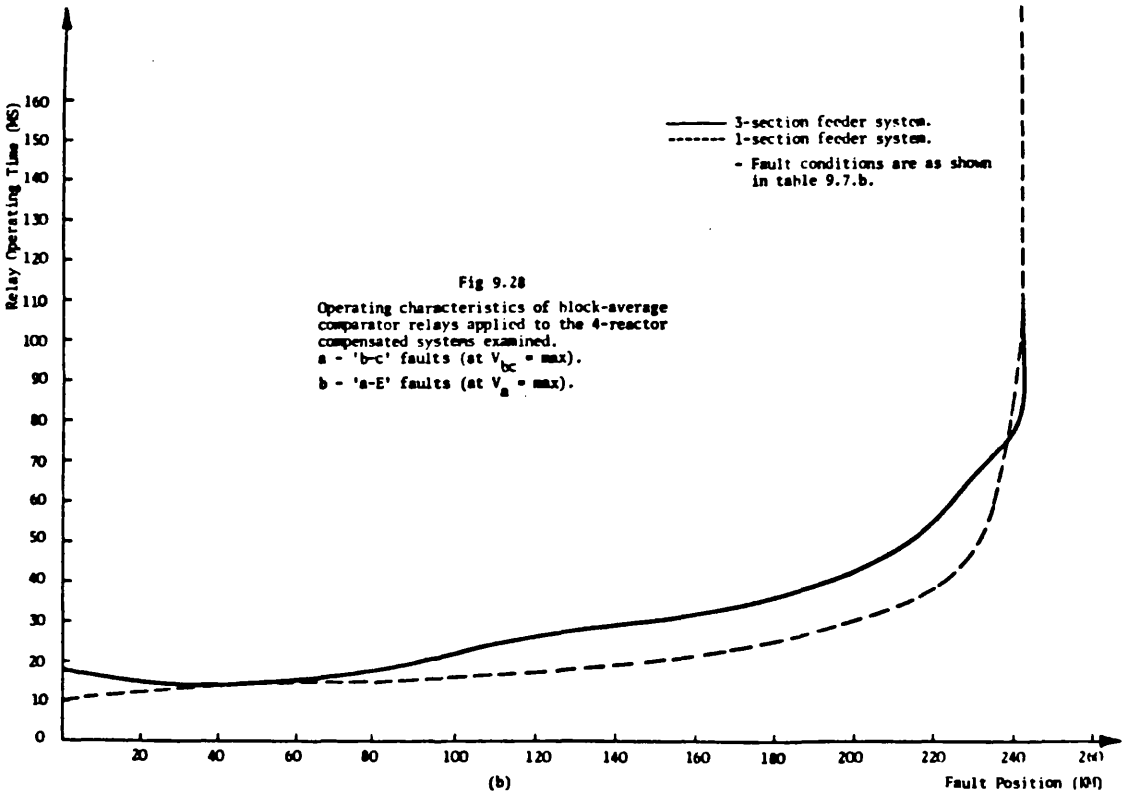

Fig 9.28

Operating characteristics of block-average comparator relays applied to the 4-reactor compensated systems examined.
a - 'b-c' faults (at V_{bc} = max).
b - 'a-E' faults (at V_a = max).

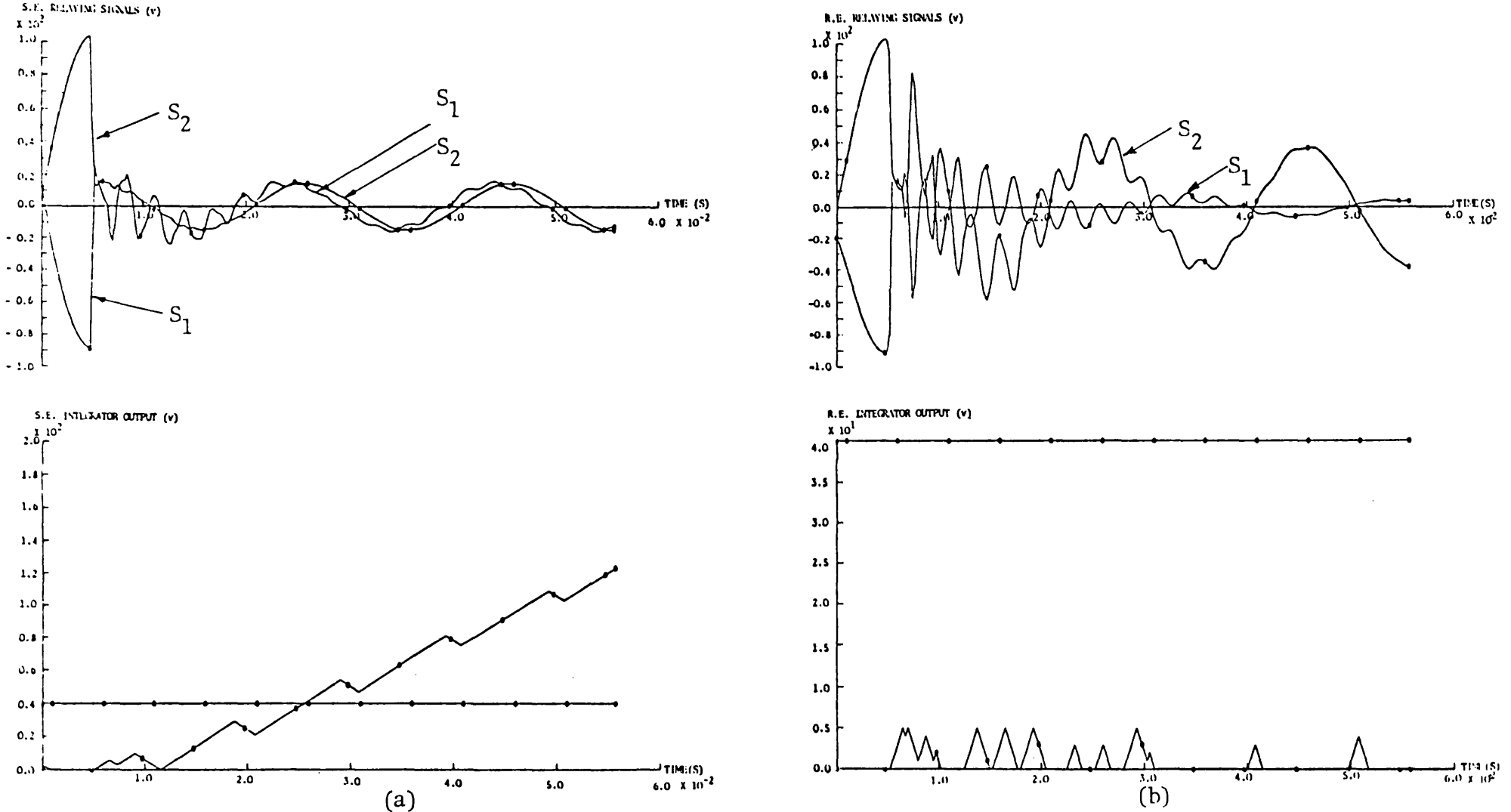

Fig 9.29
Response of relays applied to the middle section of the practical 3-section feeder system examined.

- 'a-E' fault at V_a = max
- X = 0.0

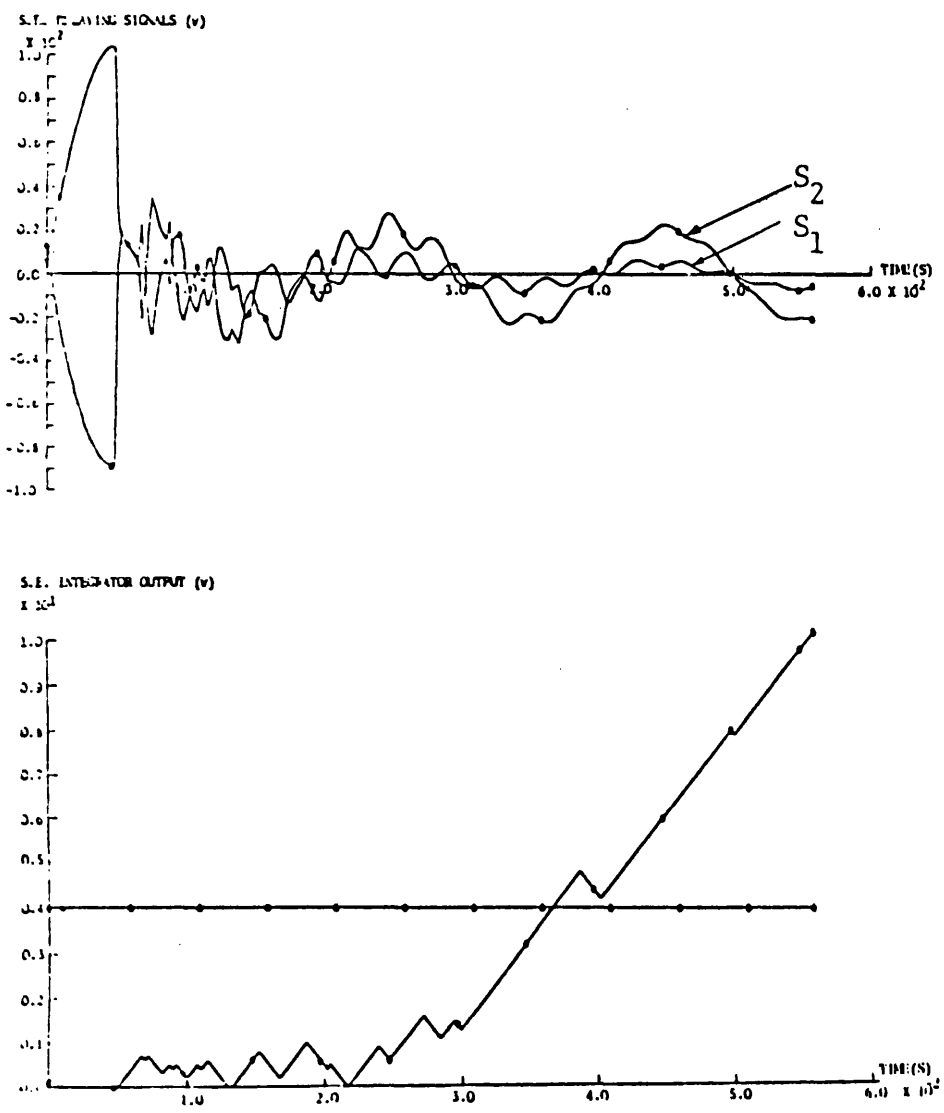

(a)

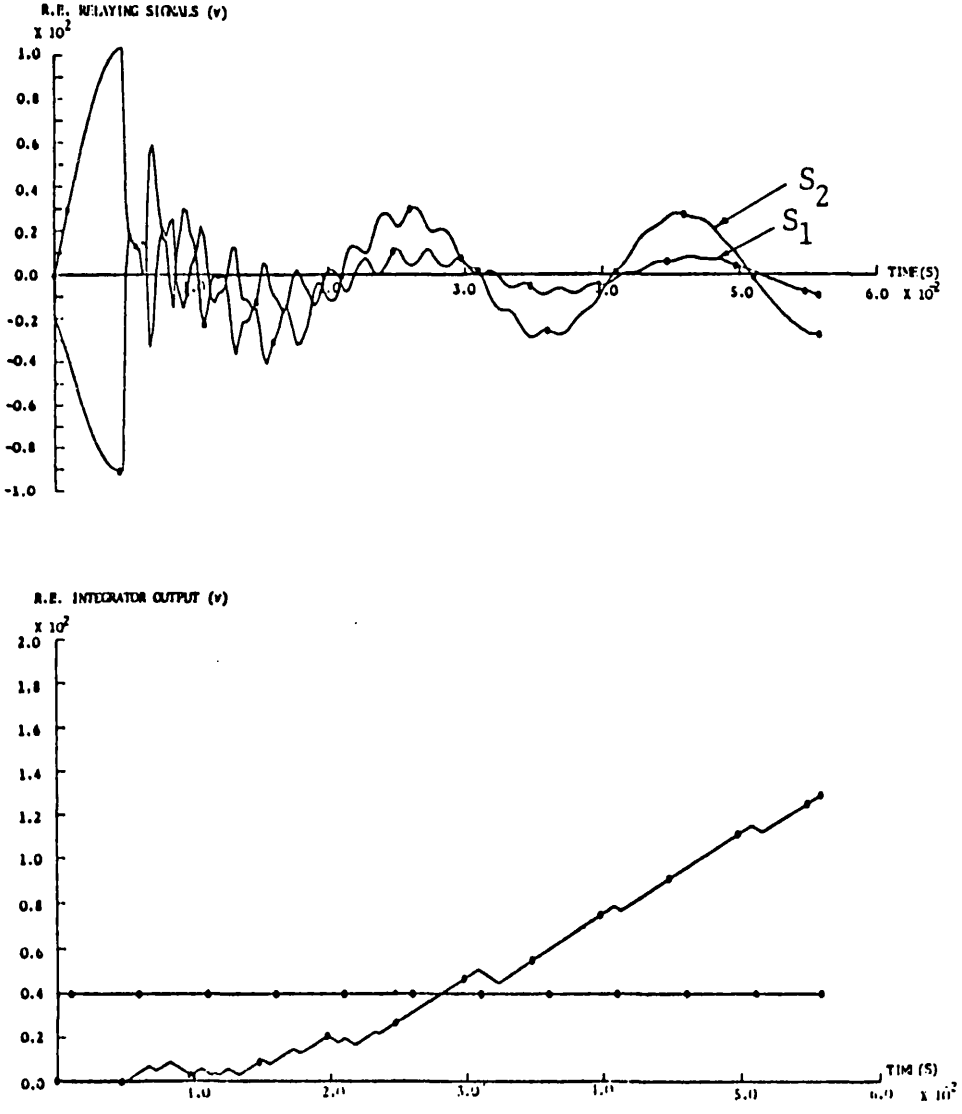

(b)

Fig 9.30

Response of relays applied to the middle section of the practical 3-section feeder system examined.

- 'a-E' fault at V_a = max
- X = 50.0 km.

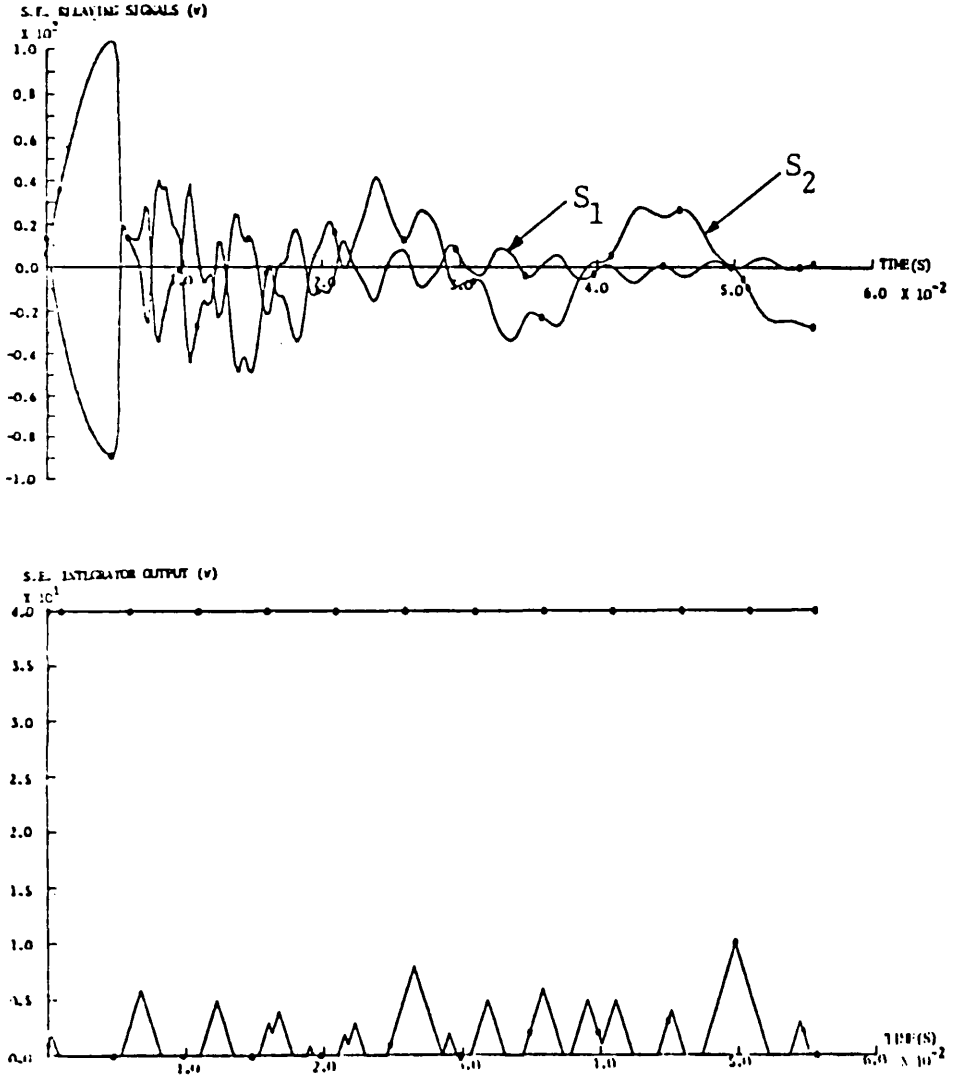

(a)

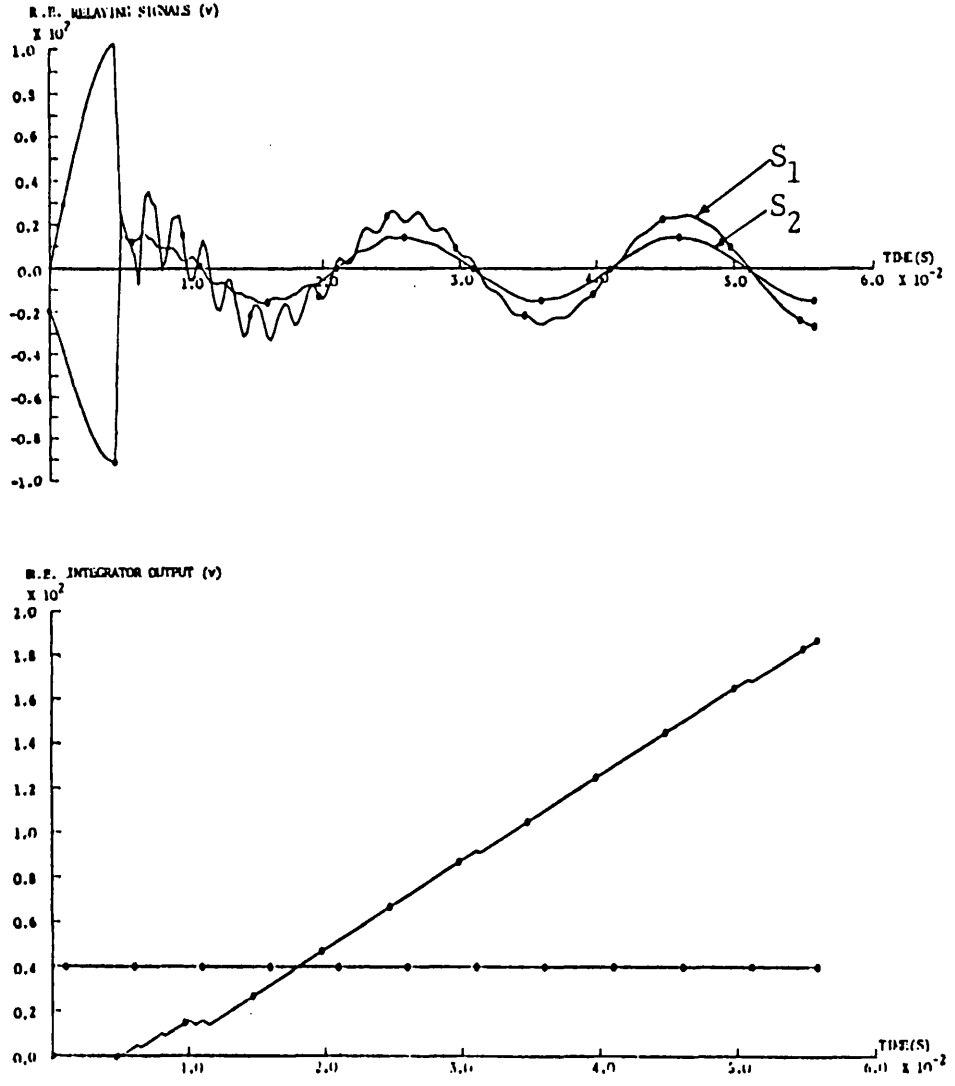

(b)

Fig 9.31

Response of relays applied to the middle section of the practical 3-section feeder system examined.

- 'a-E' fault at V_a = max
- X = 100.0 km.

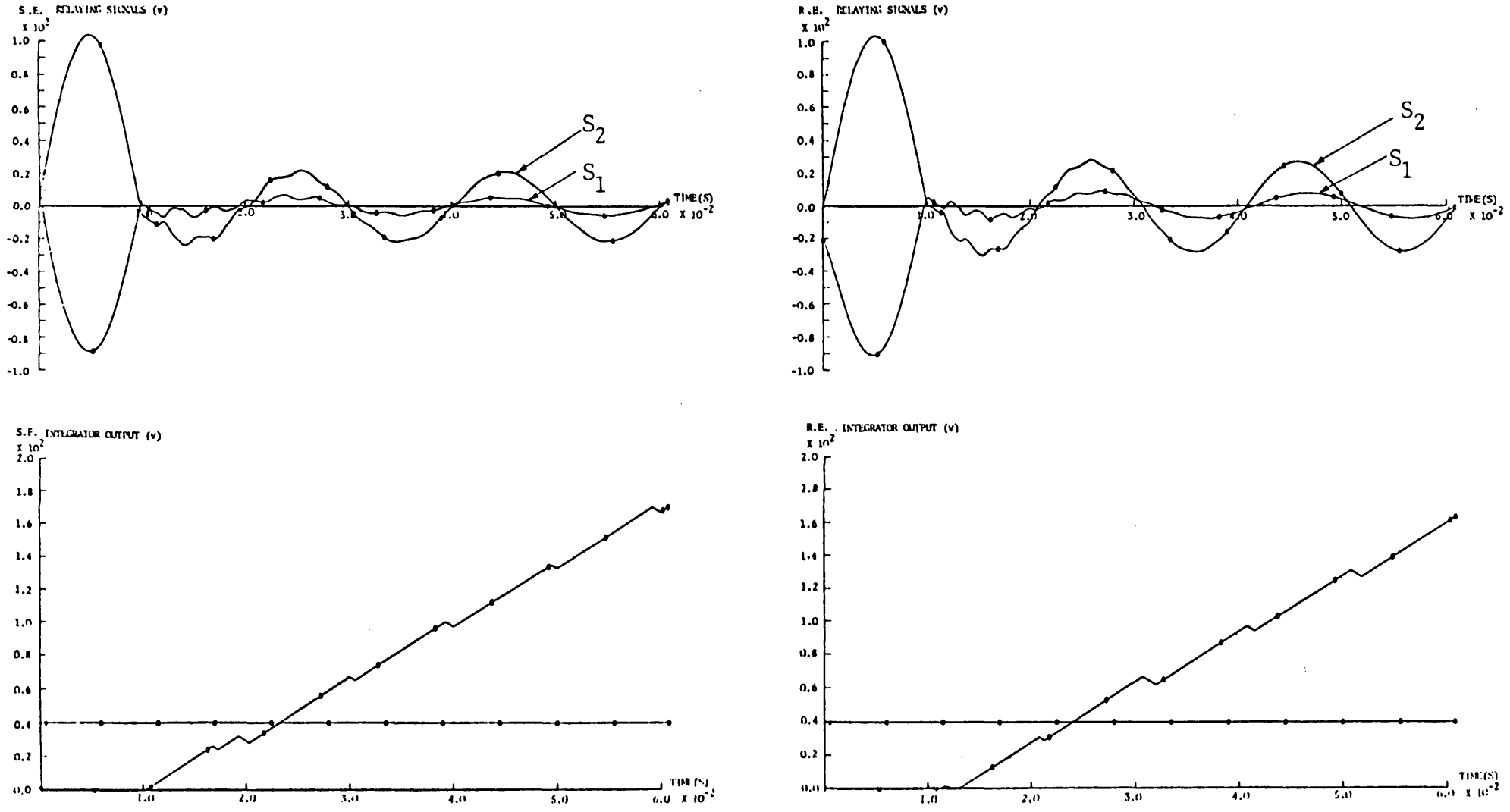

Fig 9.32

Response of relays applied to the middle section of the practical 3-section feeder system examined.

- 'a-E' fault at $V_a = 0.0$
- X = 50.0 km.

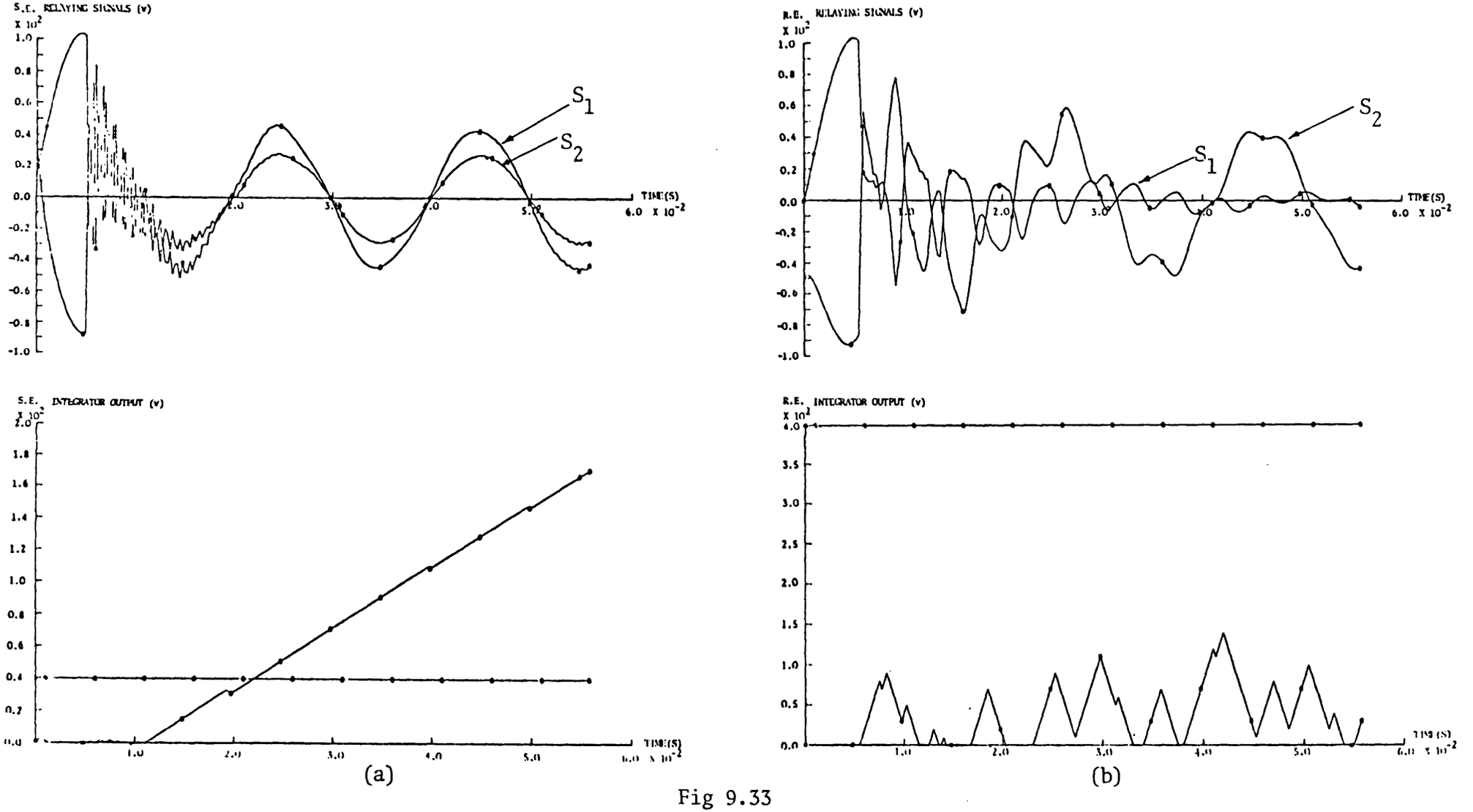

(a) (b)

Fig 9.33

Response of relays applied to the first section of the practical 3-section feeder system examined.

- 'a-E' fault at V_a = max.
- X = 50.0 km.

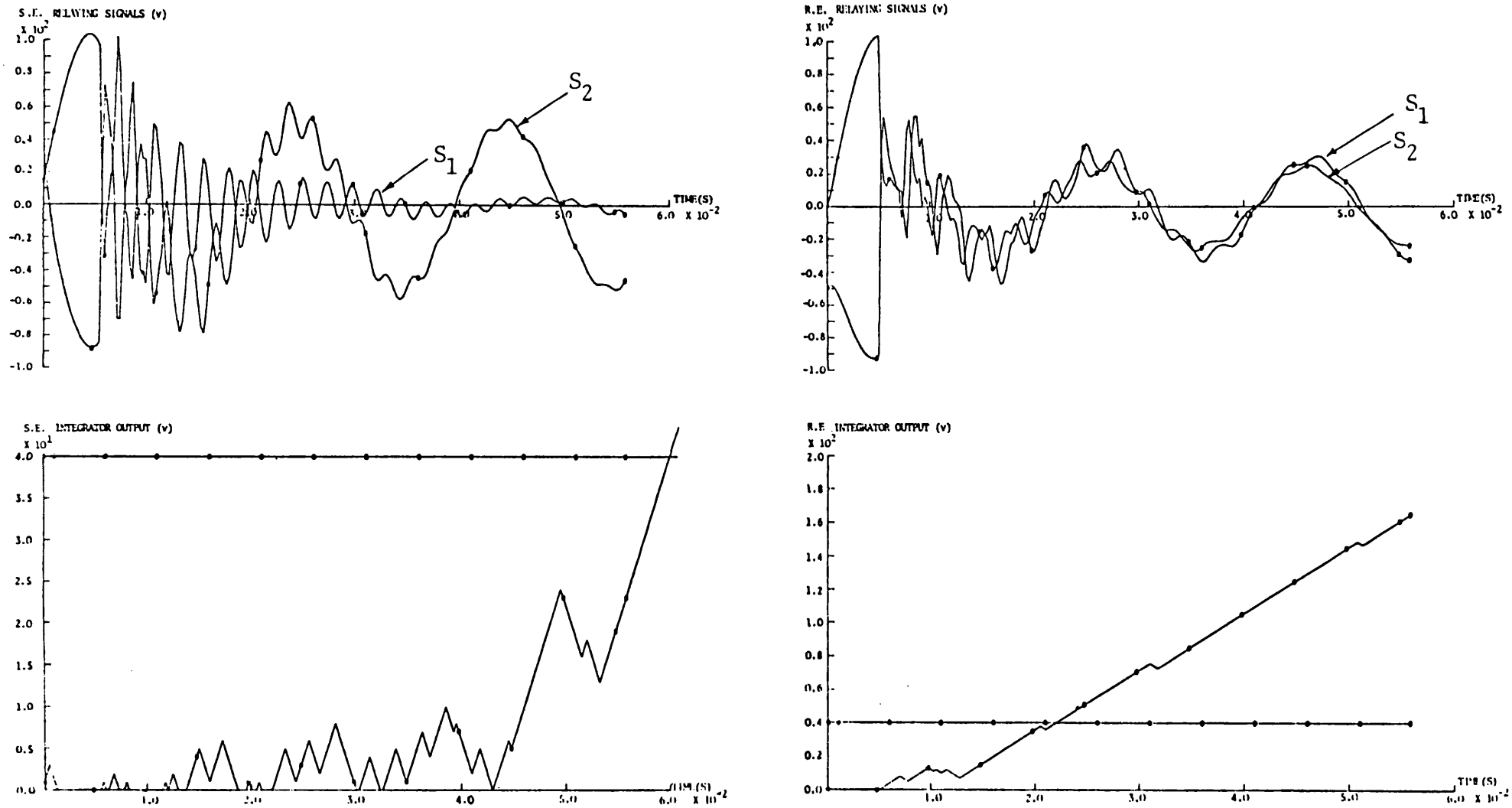

Fig 9.34

Response of relays applied to the first section of the practical 3-section feeder system examined.

- 'a-E' fault at V_a = max
- X = 200.0 km.

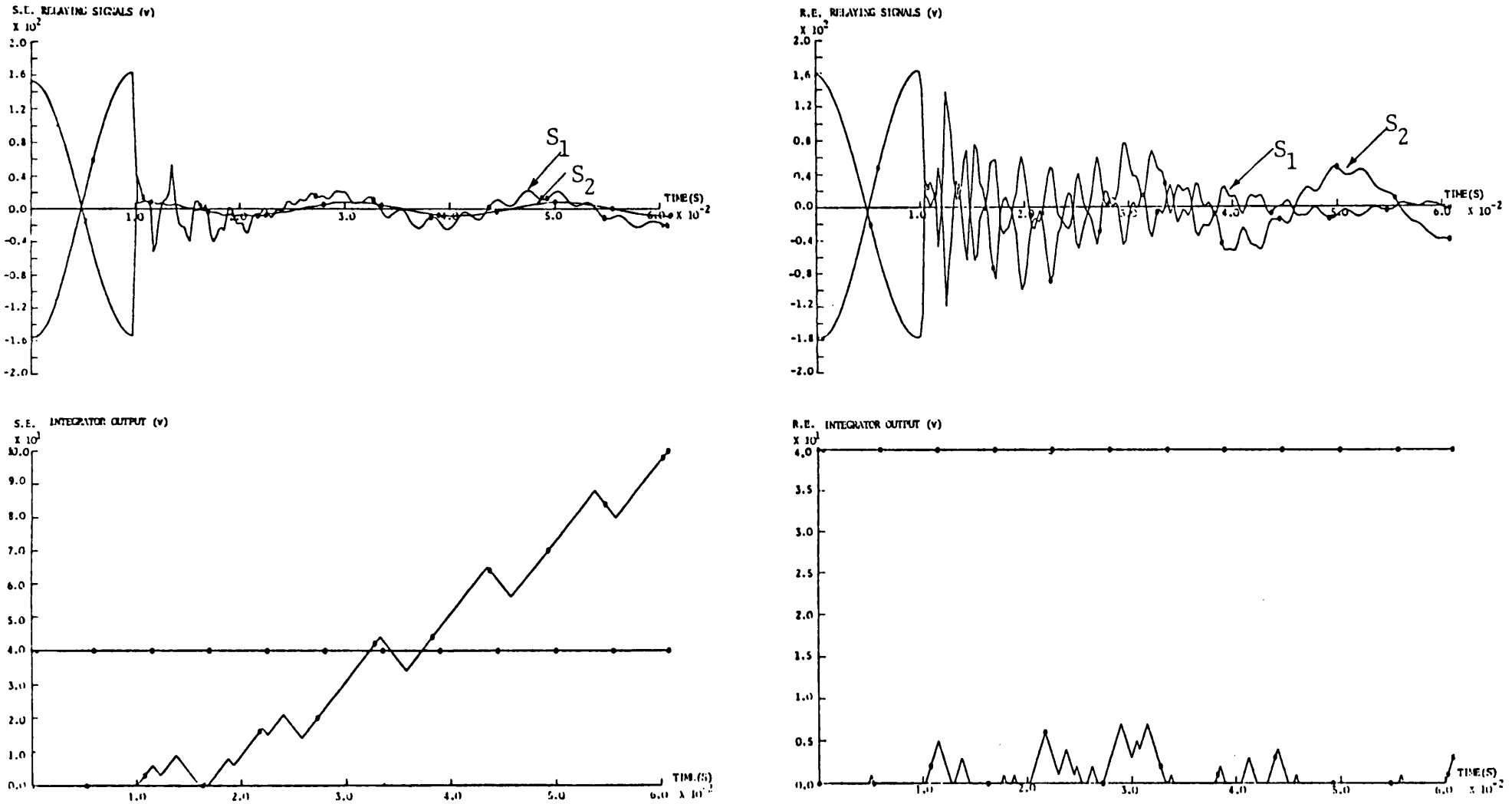

Fig 9.35

Response of relays applied to the middle section of the practical 3-section feeder system examined.

- 'b-c' fault at V_{bc} = max
- X = 0.0

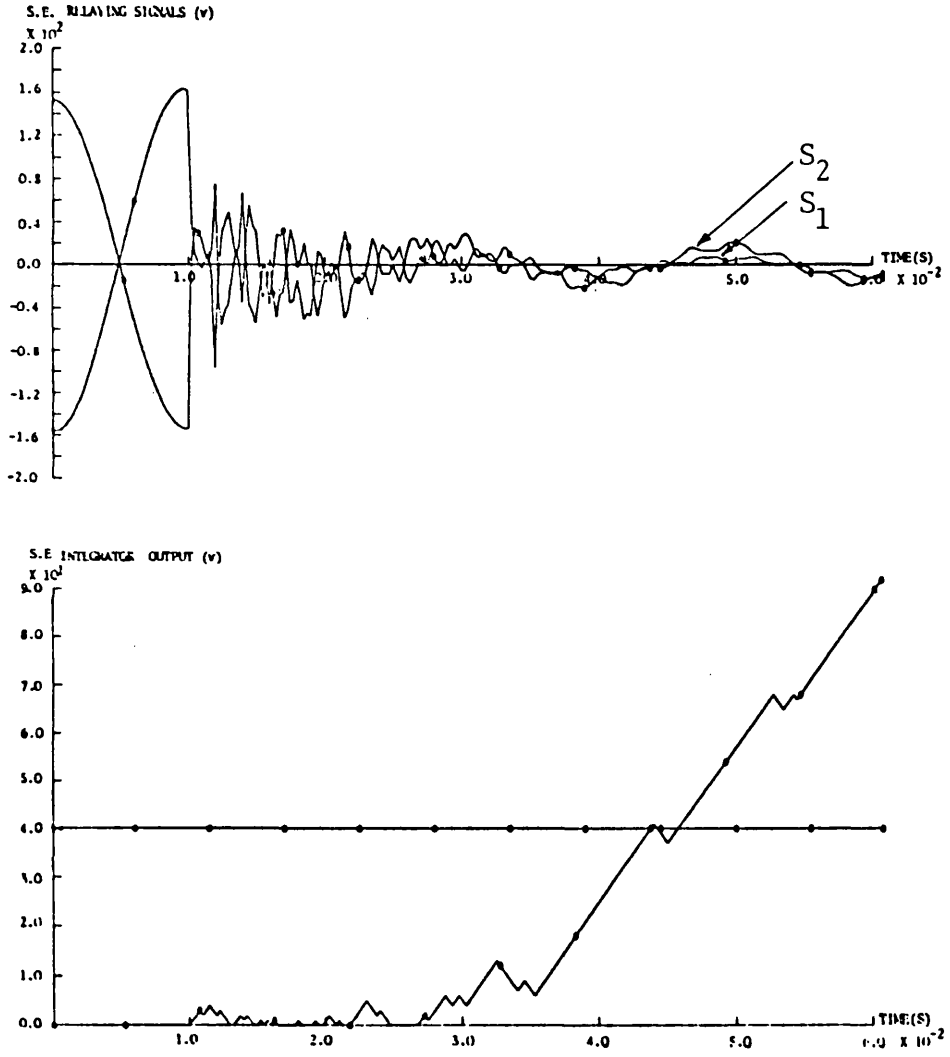

(a)

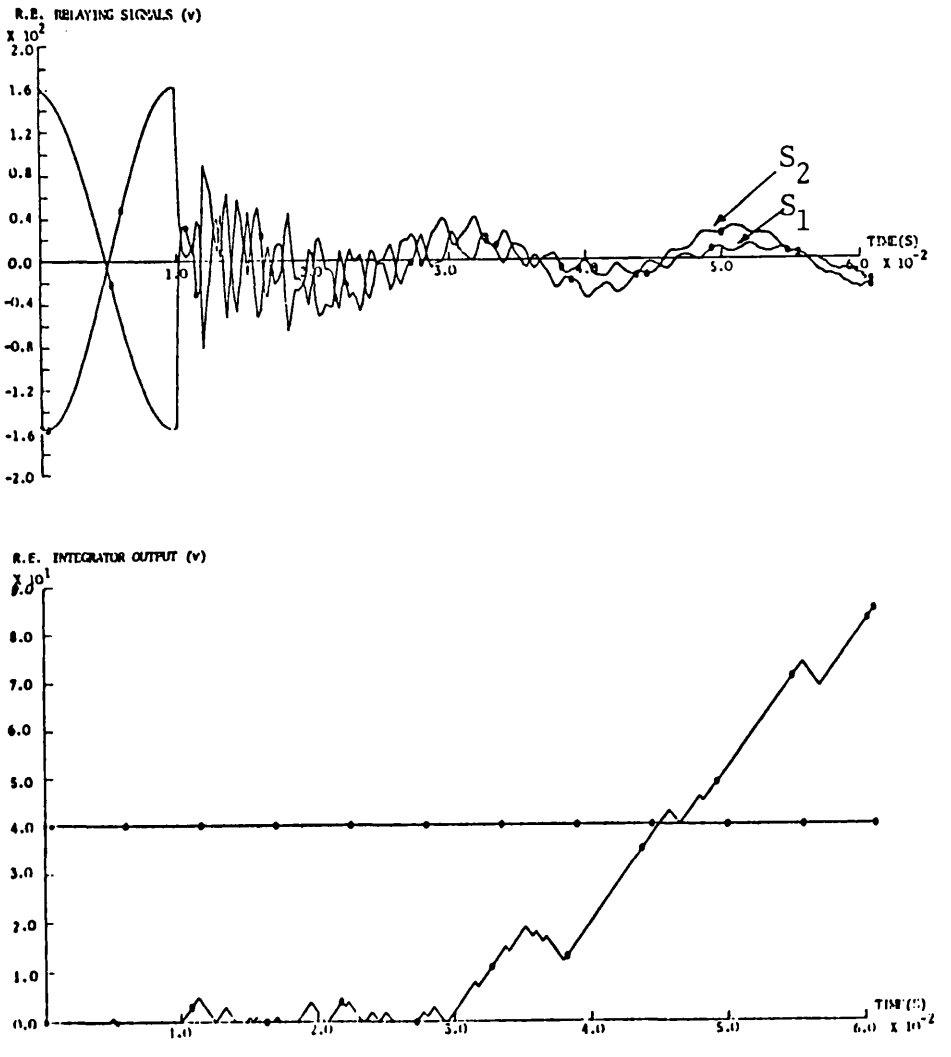

(b)

Fig 9.36

Response of relays applied to the middle section of the practical 3-section feeder system examined.

- 'b-c' fault at V_{bc} = max.
- X = 50.0 km.

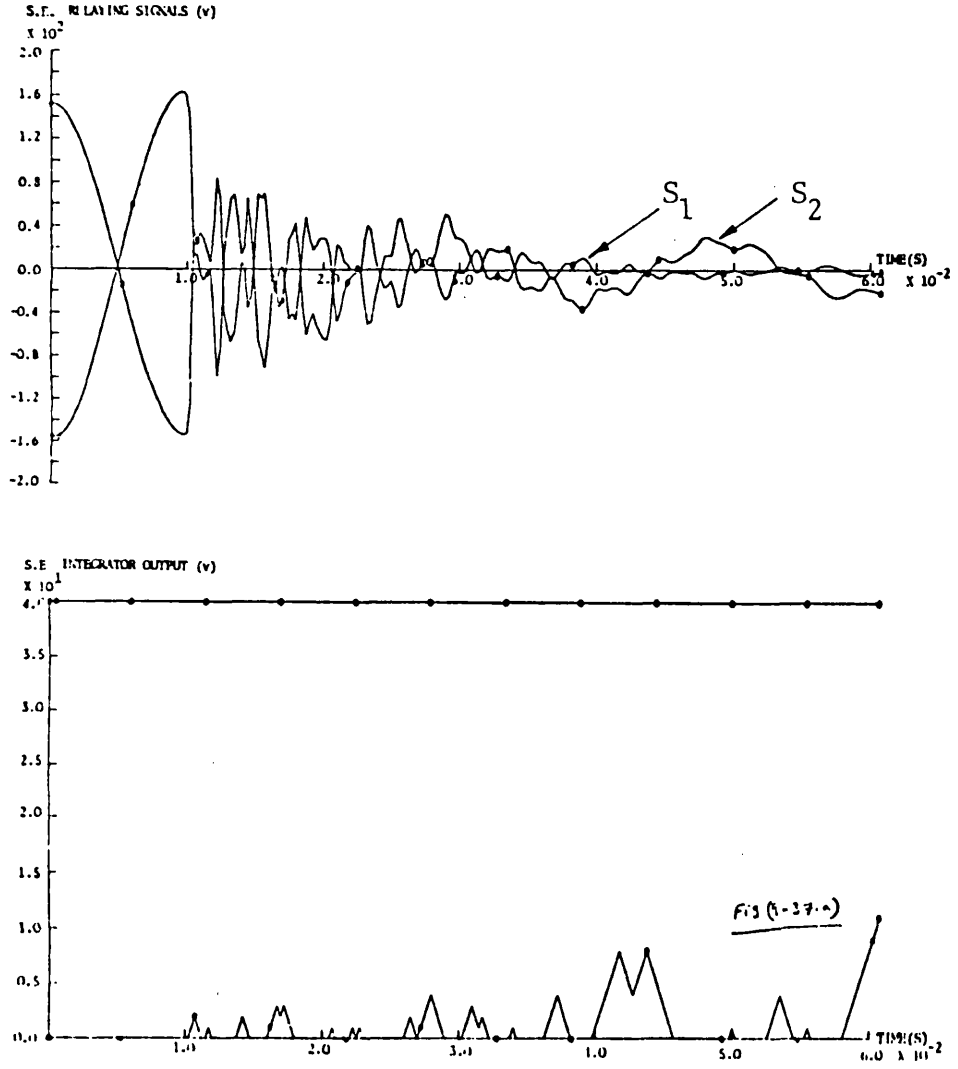

(a)

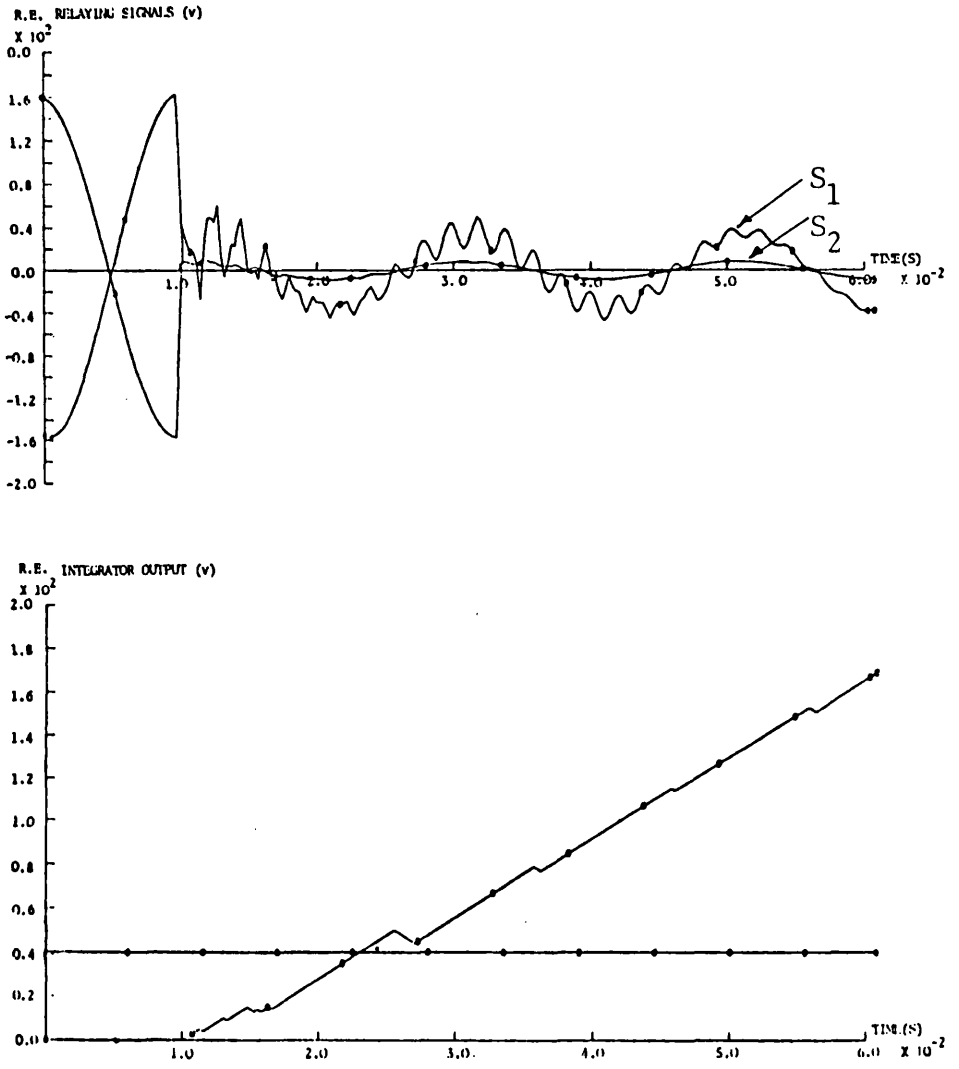

(b)

Fig 9.37

Response of relays applied to the middle section of the practical 3-section feeder system examined.

- 'b-c' fault at V_{bc} = max.
- X = 100.0 km.

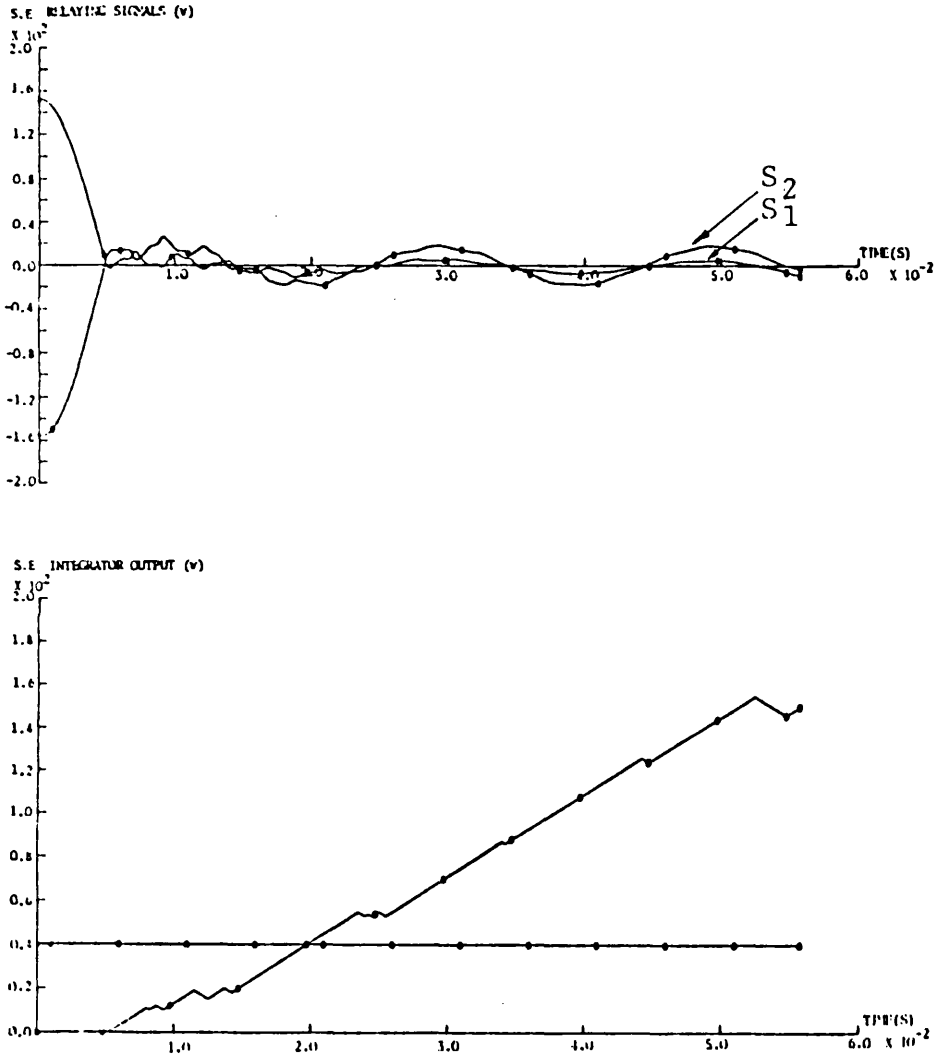

(a)

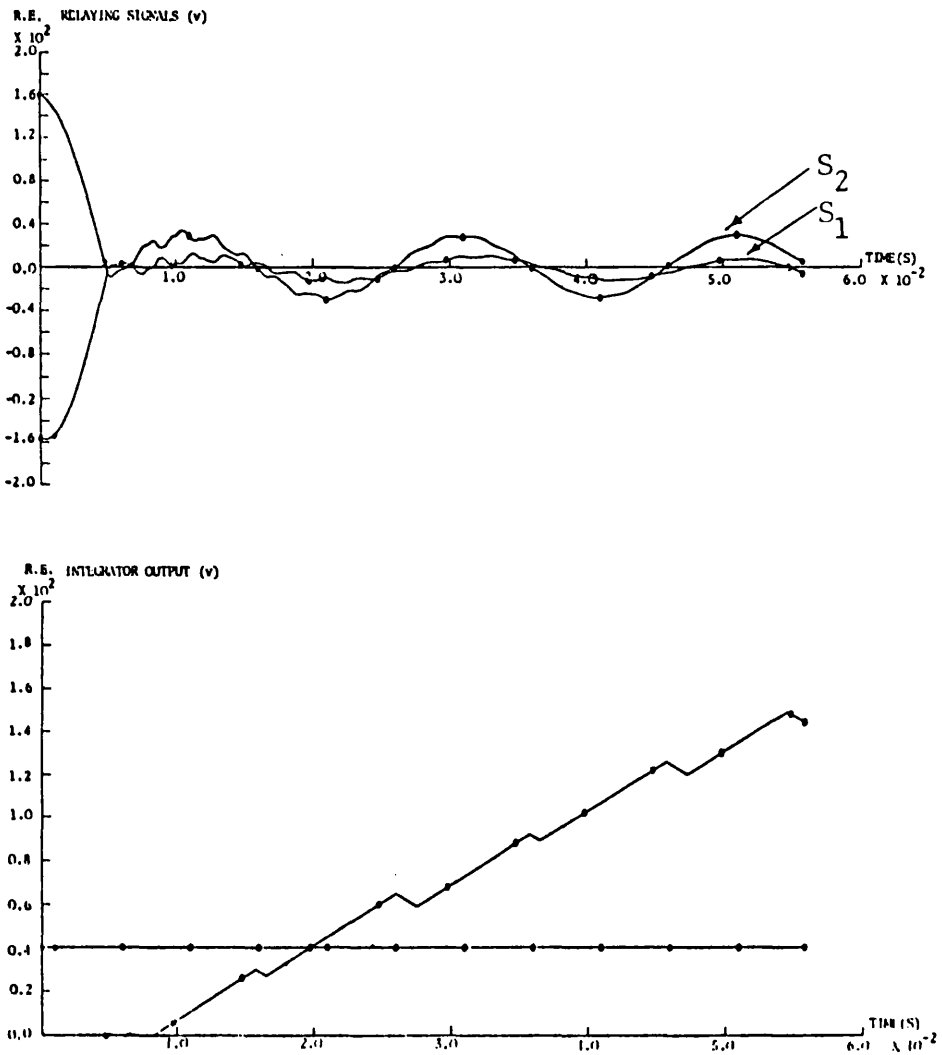

(b)

Fig 9.38

Response of relays applied to the middle section of the practical 3-section feeder system examined.

- 'b-c' fault at $V_{bc} = 0.0$
- X = 50.0 km.

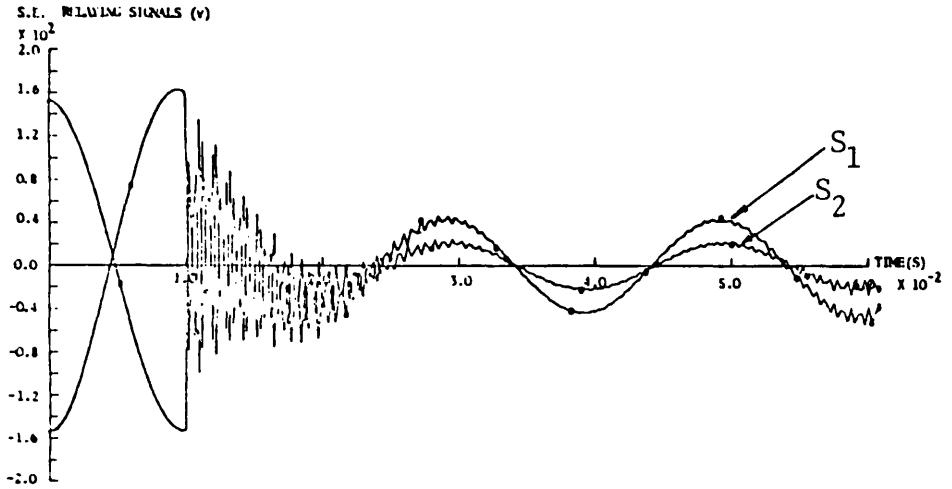

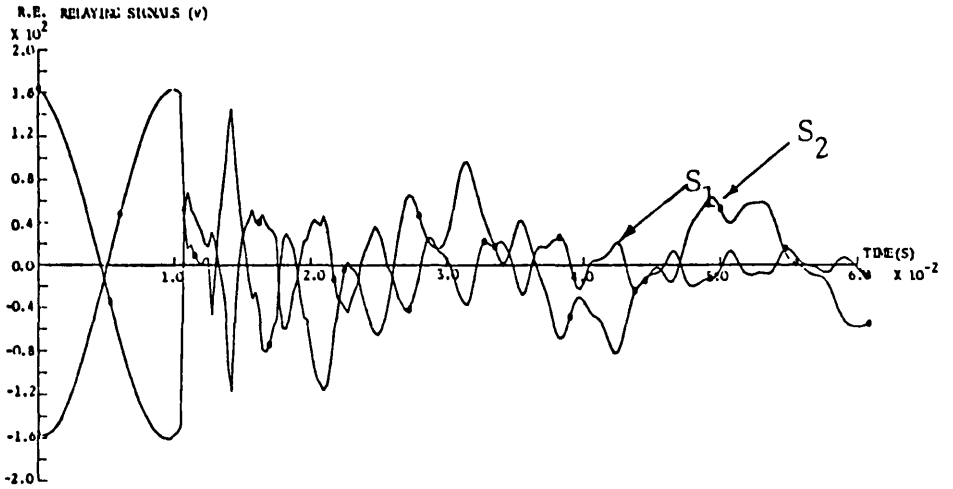

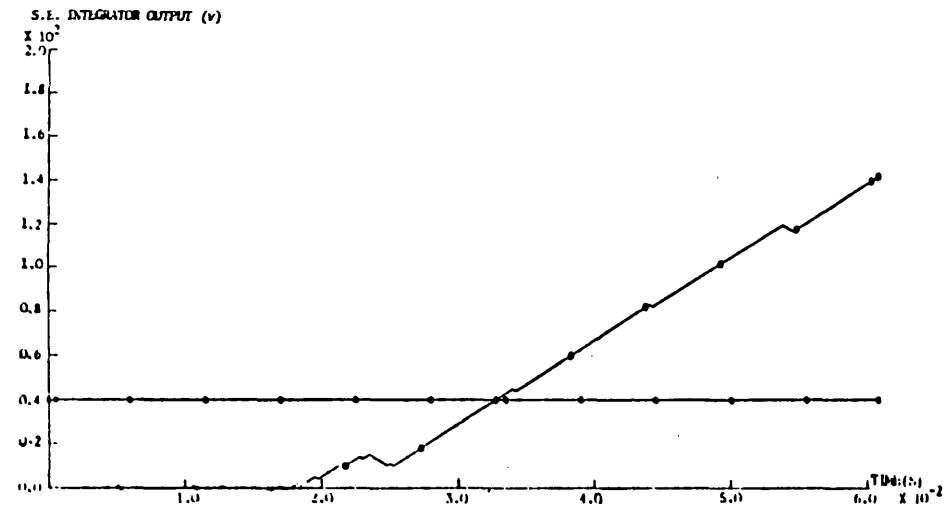

(a)

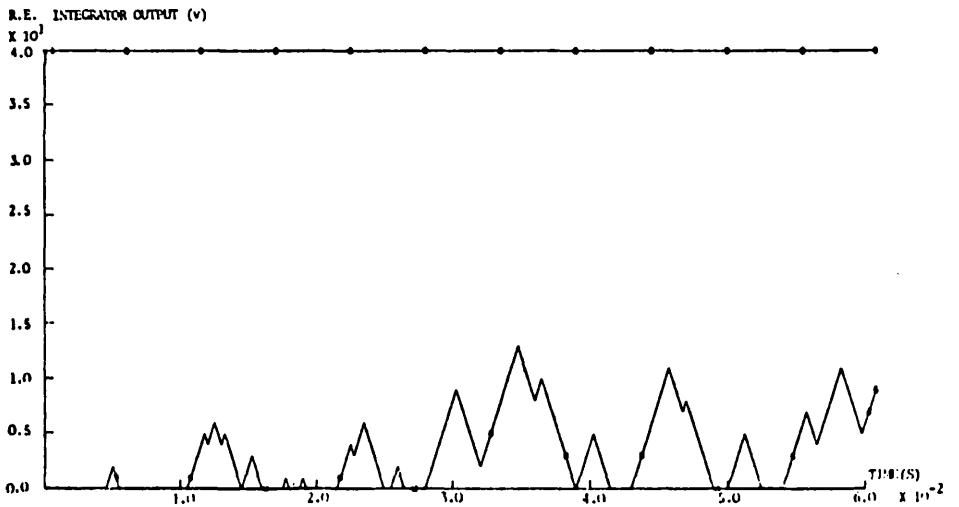

(b)

Fig 9.39

Response of relays applied to the first section of the practical 3-section feeder system examined.

- 'b-c' fault at V_{bc} = max
- X = 50.0 km.

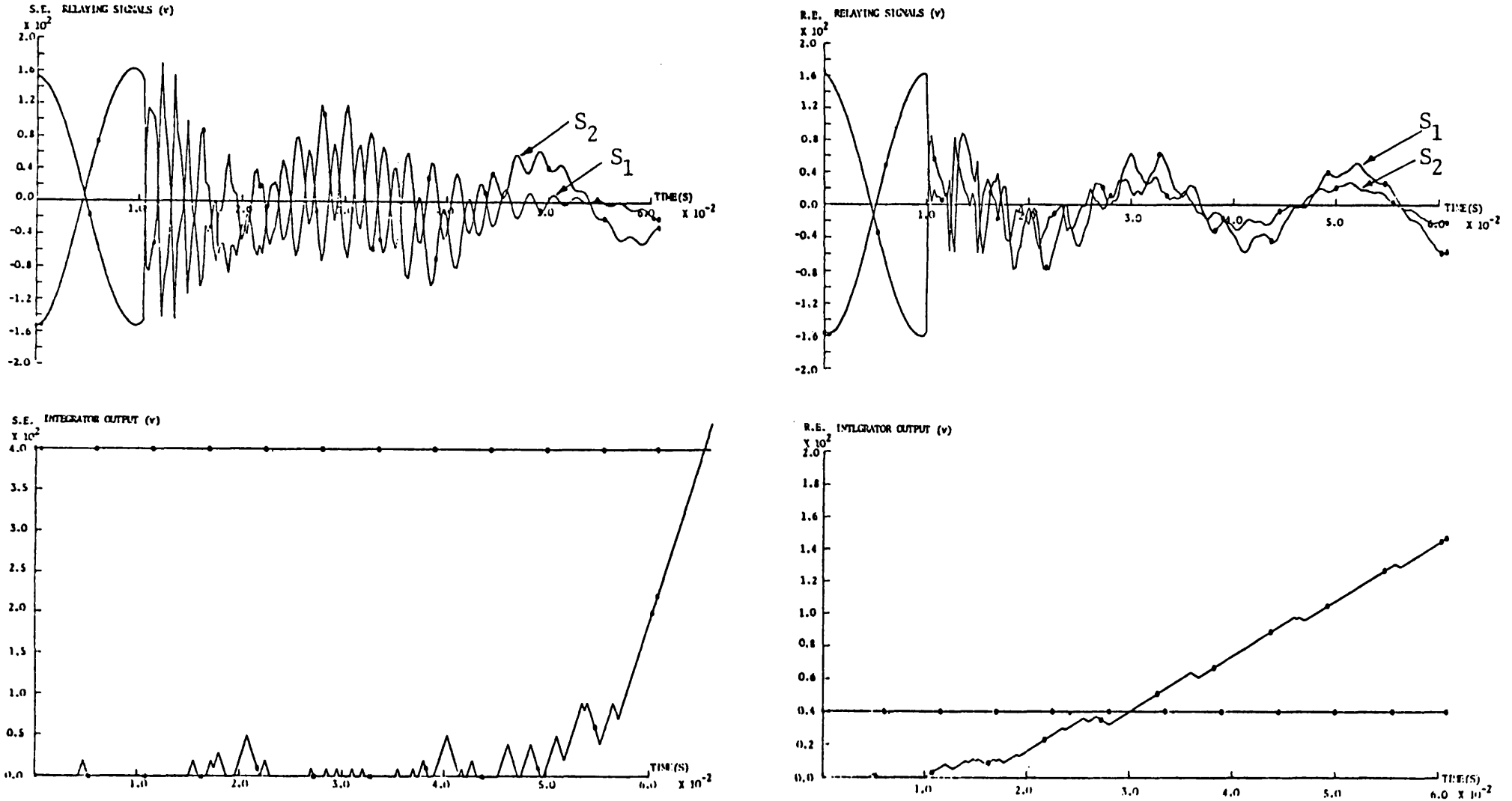

(a) (b)

Fig 9.40

Response of relays applied to the first section of the practical 3-section feeder system examined.

- 'b-c' fault at V_{bc} = max.
- X = 200.0 km.

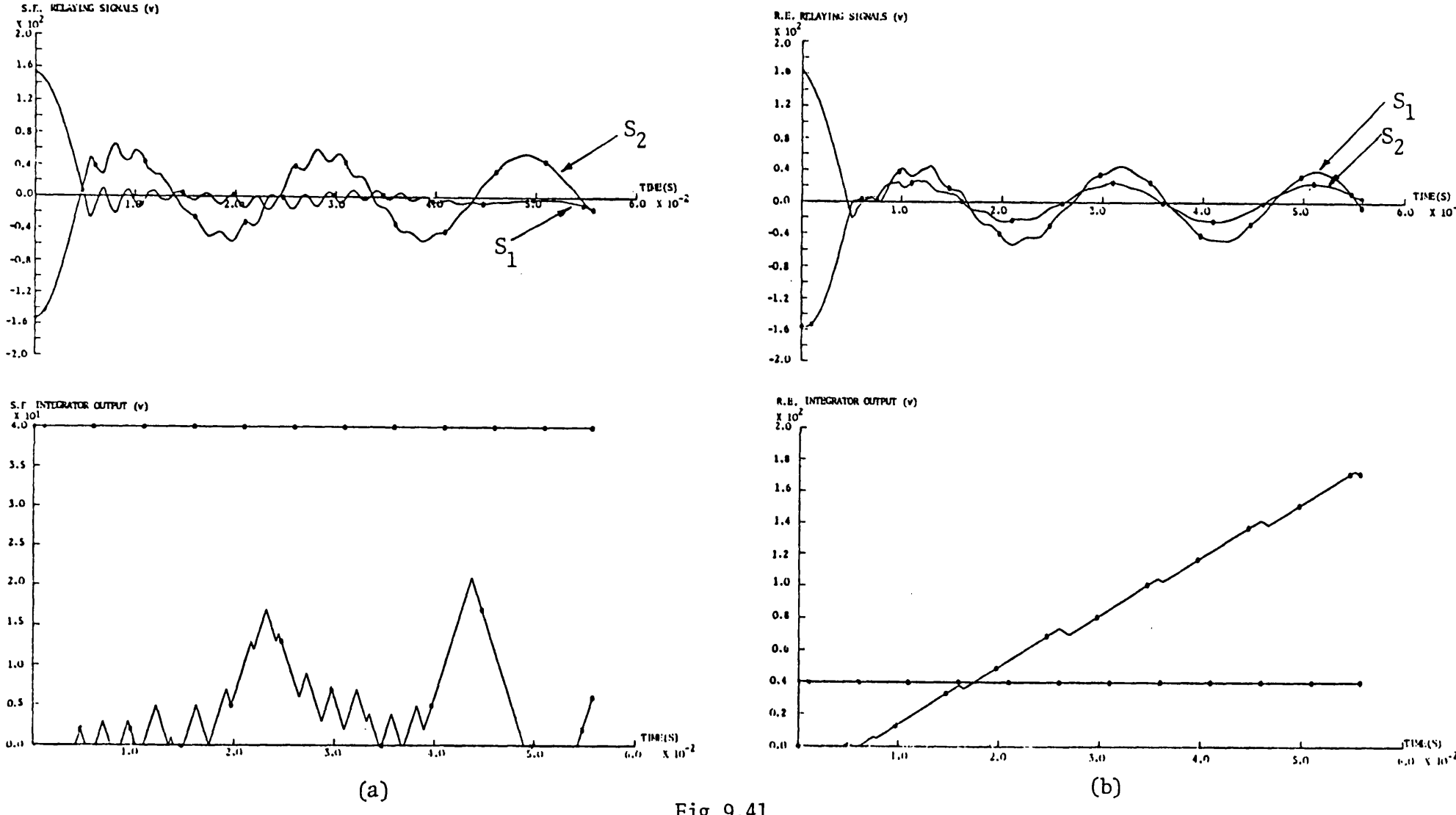

Fig 9.41

Response of relays applied to the first section of the practical 3-section feeder system examined.

- 'b-c' fault at V_{bc} = 0.0
- X = 200.0 km.

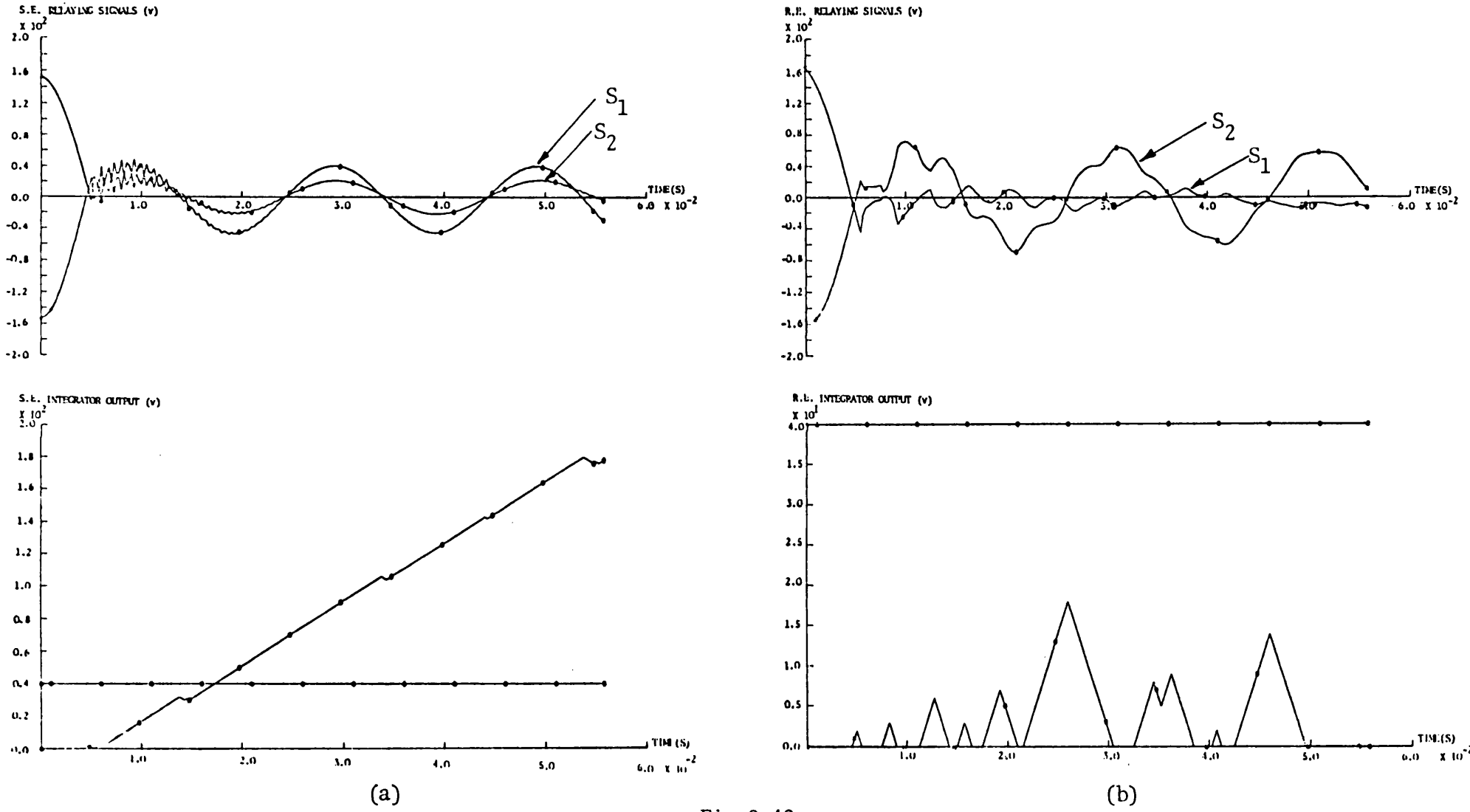

(a) (b)

Fig 9.42

Response of relays applied to the first section of the practical 3-section feeder system examined.

- 'b-c' fault at V_{bc} = 0.0
- X = 50.0 km.

CHAPTER 10 CONCLUSIONS AND FUTURE WORK

10.1 Conclusions

In power transmission systems employing single-pole autoreclosure, 4-reactor schemes are usually adopted for reactive power compensation and fault-arc suppression. In this thesis, therefore, a thorough investigation of 4-reactor compensated systems under unbalanced fault-transient conditions has been carried out.

Using the simulation methods developed in this thesis, a realistic prediction of the system post-fault behaviour can be achieved. Such prediction is extremely important in ascertaining the performance of protective schemes and as a development aid in any case where they prove inadequate. They are also important for determining economical system and reactor insulation levels.

Mathematical models for incorporating 4-reactor compensators into single section feeder systems under fault-transient conditions are developed in Chapter (2). The high frequency dependence of line parameters[54,55] as influencing system transient behaviour is taken into account. Evaluation of these parameters over a wide range of frequencies is described in Appendix (A1).

Using matrix function theory, the methods developed in Chapter (2) are based on the theory of natural modes as developed [12] for application to multi-conductor lines, as outlined in Appendix (A2). Faults are simulated by a suddenly[53,54,56] applied voltage of appropriate magnitude and polarity, at the point of fault. Applying the principle of superposition, the overall system response is obtained in frequency domain and the time variation of the voltages

and currents of interest is obtained using the inverse Fourier[88-91] transform. Simulation of different types of unsymmetrical shunt faults is considered in Appendix (A3).

Also in Chapter (2), a brief review of existing shunt-compensation schemes together with possible reactor arrangements[37] used in EHV systems for the purpose of reactive power compensation and secondary arc extinction are described. The 4-reactor scheme, used throughout the present investigation, is considered in detail.

A very generalised simulation methods for studying multi-section feeder systems are developed in Chapter (3). The methods efficiently enable considering systems of any number of feeders where different types of faults can be initiated and system response at any point of interest obtained.

In addition, a very general and accurate transposition scheme, suitable for frequency-domain digital techniques is developed. In the same Chapter, analysis of the main source network models (based on arbitrarily defined short-circuit levels at the terminating busbars) is presented.

The methods developed for dealing with reactor saturation are described in Chapter (4). Being very general, the methods enable the evaluation of superimposed voltage and current components due to saturation and hence the overall system response at the point of interest. Saturation of any of the 4-reactor limbs can be simulated.

In Chapter (5) parameters of systems studied are described. These include line and main source parameters,[54] shunt-reactor parameters,[37] Fourier transform parameters[88-91] and protective relay parameters.[57] Also transmission line charts developed for the line configuration examined are described.

The simulation methods developed in Chapters (2) - (4), together with system parameters presented in Chapter (5) have been used to develop digital computer programs to study the following:

1 - Effect of shunt compensation on primary system response for both single and 3-section feeder systems.

2 - System and reactor-limb overvoltages

3 - The probability of reactor saturation and its likely effect on:

   a. Primary system response.

   b. The performance of system protective relays.

4 - Effect of shunt-compensation on the performance of distance protection applied to single and 3-section feeder systems.

The computational results presented in Chapters (6) - (9) cover in detail the above mentioned effects and the conclusions to be drawn are given here in below.

The effect of shunt compensation on primary system response is examined in Chapter (6). From the computational results presented in this Chapter, the following general conclusions may be drawn:

1 - For uncompensated systems, the results confirmed, in general, a complete agreement with that presented by references (53,54,56).

2 - For shunt compensated systems, the results clearly showed that shunt compensation has nearly no, but little effect on the profile of primary system wave forms. The only difference observed is naturally the reduction of the prefault and post-fault steady-state current components with the increase of the PPS degree of shunt compensation (h_1).

3 - The primary wave forms of both single and 3-section feeder systems are influenced in the same way by the following factors:

a - Fault position

b - Fault inception time

c - Source parameters; particularly their capacities

d - Prefault loading

e - Type of fault

f - Degrees of shunt compensation

The influence of factors (a-f) above is, again, in excellent agreement with the reported results for uncompensated systems. [53,54,56]

4 - under the same fault conditions, the wave forms associated with the fault on 3-section feeder systems are very considerably more distorted than is the case for the single-section arrangement. This finding is mainly due to the fact that, for faults on 3-feeder systems, travelling waves successively propagate through different line sections towards the terminating networks and are partially reflected from source discontinuities back to the fault point producing relatively high levels of travelling-wave distortion. Compared to single-feeder systems, travelling waves take relatively high transit time between any point of fault and source discontinuities and it follows that in case of 3-feeder systems, the apparent frequency of travelling wave components is relatively low.

Due to the fact that system damping is much higher at high frequencies, the relatively low frequency components take rather longer to disappear for faults on 3-feeder systems than is the case with single-feeder systems.

5 - Findings (1-4) above apply to system response at any desired observation point.

6 - Findings (1-5) above, confirm the validity and the generality of the simulation methods developed in Chapters (2) and (3).

System and reactor-limbs overvoltages are digitally evaluated in Chapter (7). The results presented in this Chapter showed that:

1 - In the two configurations considered, the worst case from over-voltage point of view is single-line-to-ground mid-point faults that occur at maximum, prefault, faulted-phase voltage.

2 - System and reactor overvoltages are relatively low in case of single-section feeder systems than is the case with 3-section feeder systems.

3 - The maximum system overvoltage observed is about 1.72 pu experienced by phase 'c' for a solid a-E fault that occurs at the sending end busbar of the middle line-section of the 3-feeder system. Bearing in mind that fault location is at the middle of the network, this finding is in excellent agreement with fault induced overvoltages predicted by other authors. [17-22]

4 - Maximum overvoltage levels experienced by phase reactors are far below the spark-over rating of their arrestors. [34]

5 - Although the maximum neutral-reactor overvoltage observed is also below its arrestor spark-over rating,[34] it has to be emphasised that special care has to be taken to protect the neutral reactor against any possible severe overvoltages if successful single-pole autoreclosure is to be acheived.

Digital evaluation of reactor saturation is presented in Chapter (8). The computational results presented in this Chapter showed that, in 3-section feeder systems only the currents and flux linkages of the neutral reactor at the sending-end of the middle line section, exceeded its saturation level.[23,34] Due to the offset nature of current wave forms, the results showed that the worst case from saturation point of view is single line to ground faults that occur at zero voltage.

The effect of neutral reactor saturation on system response has also been digitally evaluated in Chapter (8). The digital computer results presented in this chapter have revealed two main important findings:

1 - The effect of saturation on primary system wave forms is very insignificant.

2 - System protective schemes would function normally under neutral-reactor saturation conditions.

The response of cross-polarised mho relays utilising the well known block-average comparators is digitally evaluated in Chapter (9). Digital simulation of relay mixing circuits is described in Appendix (A5) and protective relay parameters for the systems considered are presented in Appendix (A6).

The computational results presented in Chapter (9) examine the performance of relays applied to uncompensated and 4-reactor shunt compensated single and 3-section feeder systems.

Relay performance in terms of measurement accuracy and speed of operation under different fault conditions is described.

In general, the results showed that, for the relays protecting shunt compensated systems, there is always a tendency to overreach while that used with uncompensated systems tend to underreach. For example, with zero prefault loading of the single-section feeder, the maximum amounts of underreach and overreach were found to be about 2.1% and 1.0% respectively. Exporting power at the relaying point ($\delta=30^{o}$) increased the reach in both uncompensated and compensated systems, to reach, about 5% and 8% respectively. Importing power at the same end ($\delta=-30^{o}$) however, reduced the reach by about 6.6% and 3.3% for uncompensated and

shunt compensated systems respectively. The amounts of relay reach mentioned above have been observed for solid a-E faults under different fault conditions. For pure phase-faults, and zero prefault loading, relays on uncompensated and shunt compensated systems have been found to further underreach, the amounts of underreach being about 4% and 1% respectively. In case of shunt compensated systems, the amount of overreach has been found to increase with the PPS degree of shunt compensation (h_1) ranging from 2.1% underreach to 3.3% overreach with zero and 1.25 PPS degrees of compensation respectively.

The results showing the response of the 'phase-a' relay on a 3-legged reactor compensated single section feeder system showed that, generally, the relay tends to overreach, a fact that has been proved mathematically in Appendix (A7) and which is in contrast with some published results.[95]

As far as relay speed of operation is concerned, relays protecting shunt compensated systems have been found to generally operate faster than that used with uncompensated systems. The speed of relays used with both compensated and uncompensated systems have been found to be influenced equally in the same way by factors such as source capacities, prefault loading, fault instant and type of fault, and this is shown by the time contours for both systems presented in Chapter (9) of this thesis.

For faults on 3-section feeder systems, measurement accuracy of relays used with both uncompensated and 4-reactor compensated systems was found to be nearly the same as that used with single-section feeder systems. However, a remarkable deterioration in relays speed of operation has been observed, particularly for faults at maximum faulted-phase voltage. For example, a solid a-E close-up fault on the single-section feeder system, is detected 8 ms faster than the same fault on the 3-section feeder system.

No significant difference between the two systems from the point of view of relay speed of operation has been found for faults at zero faulted-phase (s) voltage.

Performance of relays protecting the practical system examined in Chapter (9) has shown little difference from that protecting the 3-section feeder system examined throughout this thesis.

To conclude, it has been found, that for practical loading and compensation levels, both relay measurement accuracy and speed of operation are reasonably maintained, the total measurement error being $\pm$ 8%. It can therefore be said that, for practical purposes, there is no significant deterioration in the measuring accuracy of such relays when applied to linear, 4-legged reactor, shunt compensated, 500 kV systems.

10.2 Future Work

The work presented in this thesis may form the basis for future investigation of shunt and series compensated EHV and UHV transmission systems for the purpose of attaining economical system insulation level and developing the present protective schemes if they prove inadequate for such applications.

Future work therefore may be carried out along the following lines:

1 - The simulation techniques developed in Chapters (2) - (4), together with the findings presented in Chapters (6) - (9) may be used as a reference to other future work in the same field.

2 - In the present work, only a single-circuit 3-phase system has been considered. However, the fault simulation technique presented,

particularily for shunt-compensated systems, is very general and its application to double-circuit systems is a future possibility.

3 - Only shunt unsymmetrical faults have been simulated in this thesis. Future work can therefore consider balanced and unbalanced series faults on shunt-compensated systems.

4 - A SLG fault may lead to faults involving more than one phase and hence the simulation of simultaneous faults could be considered. In this case, for the multi-phase faults, the prefault conditions are no longer steady-state but a SLG fault which has to be simulated.

5 - A time invariant fault arc resistance has been assumed throughout this work. However, for more realistic simulation of secondary arc on a 4-legged reactor compensated system, the non-linear nature of the arc resistance has to be simulated. The present work therefore may be used as a basis for future studies concerning fault-arc phenomena in 4-reactor compensated systems.

6 - In this work, saturation of the simple 4-legged reactor arrangement has been considered. Future work, however, may consider the simulation of that phenomena associated with self-saturated reactors.[68,75] The simulation may make use of a combination of the Fourier technique and Duhamel's integral.

7 - For very long EHV lines, shunt reactors and series capacitors are usually adopted. Series capacitors are used to neutralise part of the line inductance and hence the line transmission capability is improved. The computer programs developed in this thesis can be used as a basis for the simulation of series-shunt-compensated systems.

8 - This thesis considered only one type of realistic source configuration. In practice, however, source complexities can be unlimited and the simulation of these sources can reflect a realistic picture of the relaying point wave forms and hence the performance of protective relays can be obtained under realistic fault conditions.

9 - The simulation of realistic sources, under realistic fault conditions can also help in predicting system overvoltages and hence system insulation level can be determined.

10 -Future work, based on the results presented in this thesis, may be directed towards the development of high performance, wider-bandwidth transducers. At the same time this work may be extended for the evaluation of system response at the secondaries of transducers in common use these days. However, this last aspect may require the simulation of transducers in frequency domain.

11 -Only fault initiation has been considered in this thesis. After the occurence of faults, however, circuit-breaker opening and reclosing take place and has to be considered in future work.

12 -If circuit-breaker opening is simulated, higher system and reactor overvoltages may be produced. Therefore, in such a case in order to determine system and reactor economical insulation levels, the overvoltage phenomena has to be thoroughly investigated. It may happen that due to severe overvoltages, protective gap flash-over may occur on the main or neutral reactor and the simulation of the phenomena may form an interesting field for future research.

13 -In predicting system and reactor overvoltages, high frequency voltage components up to only 4kHz were covered in the present work. In future

work, therefore, more efficient computer programs can be developed (using the more advanced computers) to cover higher frequency voltage components and hence more accurate prediction of overvoltages is achieved.

APPENDIX (A1.1) TRANSMISSION LINE PARAMETERS FOR FAULT-TRANSIENT STUDIES

Since the recent trend in protecting EHV systems is to limit[54] relay operating time to a 3/4 of a cycle or even less, the traditional method of calculating system transient using symmetrical[48] component methods and lumped parameter representation is no longer valid in the present work. This is because themethod gives the values of fault voltages and currents after the transient phenomena due to wave propagation have died down.

The basic line parameters are the series impedance and the shunt admittance which are uniformly distributed along its length. For a multi-conductor line, basic line parameter matrices have been formulated[55] for realistic transient studies, and are presented in this Appendix.

Other line parameters such as surge impedance, surge admittance, and propagation constant matrices are derived from these basic parameters.

A1.1.1 Series Impedance Matrix

The series impedance matrix (Z), consists of three main componants:

1. The impedance due to the physical geometry of the conductors (Z_g). This component takes into account the electro-magnetic coupling between the conductors of a practical system.
2. The self impedance of line conductors (Z_c)
3. The impedance which accounts for the earth return path (Z_e)

Thus the series impedance matrix of a multi-conductor line is of the form:

$$Z = R_c + R_e + J (X_g + X_c + X_e) \quad \ldots\ldots \text{A1.1}$$

The series impedance matrix (Z) and each of its component matrices are of the order 3P +q where:

P = number of circuits

q = number of earth wires.

The components of the series impedance matrix (Z) are evaluated as follows:

A1.1.1.1 Impedance due to physical geometry (Z_g)

The impedance matrix due to the physical geometry of the line conductors shown in Fig (A1.1) is of the form:

$$Z_g = JX_g = \frac{J\,W\mu}{2\pi}.B \qquad \text{..... A1.2}$$

B is known as the charge-coefficient matrix and its elements are defined as:

$$B_{ij} = \log_e (D_{ij} / d_{ij}) \qquad \text{..... A1.3}$$

where :

D_{ij} = distance between the ith conductor and the image of the jth conductor

d_{ij} = distance between the ith conductor and the jth conductor (for $i \neq J$)

= radius of ith conductor for (i = j)

A1.1.1.2 The Self Impedance of the Conductors (Z_c)

Considering a single-circuit EHV line with two earth wires, the self impedance matrix of the conductors is one where diagonal elements represent the self impedances of the phase conductors and earth wires and whose off-diagonal terms are zero as given by equation A1.4.

$$[Z_c] = [Z_{sc} \quad Z_{sc} \quad Z_{sc} \quad Z_{se} \quad Z_{se}]_{diag.} \qquad \text{..... A1.4}$$

Since it is a common practice to bundle the conductors of EHV lines, the self impedance of the bundled conductors is:

$$Z_{Sc} = \frac{Z_{SSc}}{NSC} \qquad \text{..... A1.5}$$

where:

Z_{SSc} = self impedance of a sub-conductor of the bundle

NSC = number of sub-conductors constituting the bundle.

The calculation of the self impedance of the conductors is complicated mainly due to the fact that it depends on too many factors such as stranding of the conductors, presence of steel core (in ACSR conductors), non uniform current density (due to skin effect), frequency and other disign features.

In practice, two equations are commonly used to evaluate the self impedance matrix of the conductors. One is used for the low frequency range, less than or equal to 500 Hz, and theother for high frequency range, greater than 500 Hz.

For low frequencies, (Z_c) can be calculated by assuming a uniform current distribution in the conductors, (and also the influence of stranding and the steel core of the conductor can be neglected).[56] In this case, the elements of the matrix given by equation A1.4 are:

$$Z_c = R_{dc} + \frac{JW\mu}{2\pi} \log_e (r/r_{gm}) \qquad \text{..... A1.6}$$

where

R_{dc} = d.c. resistance

r = phase conductor or earth wire redius

r_{gm} = phase conductors or earth wire mean rad.,which is given by the cable manufacturer.

$$R_{dc} = \frac{\rho}{n.\pi . r_s^2} \qquad \text{..... A1.7}$$

where

n = number of conducting strands.

r_s = radius of each strand.

As the frequency increases, the skin effects become more and more important. Due to the skin effect, the current density is not uniform throughout the overall radius of the conductors. The self impedance of the conductors is very much affected by the non-uniformity of current distribution. The conductor resistance increases with frequency where its inductance decreases as the frequency increases. Fig (A1.2) shows a typical variation of self inductance and resistance with frequency, which for computational efficiency, is stored in piece wise linearised form.[53]

The self impedance of the conductors at higher frequencies (above 2.5 kHz) may be calculated by the method suggested by Galloway et al [55] as follows: For phase conductors (the same thing applies to earth wires):

$$Z_c = R_c + JX_c$$

where

$$R_c = X_c = \frac{K.\rho.m}{\sqrt{2.r_o(n_o + 2)\pi}} \qquad \text{..... A1.8}$$

and

$$m = \sqrt{W\mu/\rho}$$

r_o = radius of each outer strand

n_o = number of strands in the outer layer

K = factor accounts for conductor stranding $\simeq$ 2.25

In the present work, the standard conductor is substituted by a solid aluminium conductor of the same overall radius, and the self impedance is evaluated on the basis of non-uniform current density due to skin effect. This method is commonly used for design purposes for evaluating the self impedance of ACSR conductors.[56]

The self impedance of a solid conductor with non-uniform current distribution is given by[80]:

$$Z_c = \frac{\rho \cdot m}{2\pi r} \quad \frac{BER\ mr + J\ BEI\ mr}{BEI'\ mr - J\ BER'\ mr} \qquad \text{..... A1.9}$$

The terms BER and BEI are the abbreviations for 'Bessel real' and 'Bessel imaginary'. The functions BER mr and BEI mr are the Bessel functions and BER' mr and BEI' mr are respectively the derivatives of these functiobs with respect to mr. These functions are evaluated for any argument (mr) by solving their infinite series expansion and sets of tables are available giving the values of BER and BEI for various arguments (mr).[80]

A1.1.1.3 Impedance due to the earth-return path (Z_e)

The contribution to the line series impedance of resistance and reactance R_e and X_e, due to the earth-return path, is calculated by using the infinite series developed by Carson.[81] Carson's equations have been expressed in a form suitable for digital simulation by Galloway et al[55] and they are:

$$R_e = 2\ P\ W\ \mu / 2\ \pi \qquad \text{..... A1.10}$$

$$X_e = 2\ Q\ W\ \mu / 2\ \pi \qquad \text{..... A1.11}$$

P and Q are real and imaginary correction component matrices. Their elements are calculated as a function of the elements of the matrices r and θ such that:

$$r_{ij} = \sqrt{\frac{W\ \mu}{\rho}\ D_{ij}} \qquad \text{..... A1.12}$$

where

θ_{ij} = the angle subtended at the ith conductor by the image of the ith and jth conductors as shown in Fig (A1.1).

For $r_{ij} \leq 5$

$$P_{ij} = \frac{\pi}{8}(1-S_4) + \tfrac{1}{2}\log\left(\frac{2}{\gamma r_{ij}}\ S_2\right) + \tfrac{1}{2}\theta_{ij} S_2' - \sigma 1 + \sigma 1 + \sigma 3 \qquad \text{..... A1.13}$$

and

$$Q_{ij} = \frac{1}{4} + \frac{\log(\frac{2}{\gamma r_{ij}})(1 - S_4)}{2} - \frac{Q_{ij}\, S_4'}{2} + \frac{\sigma_1}{\sqrt{2}} - \frac{\pi S_2}{8} + \frac{\sigma_3}{\sqrt{2}} - \frac{\sigma_4}{2} \quad \ldots\ldots \text{A1.14}$$

for $r_{ij} > 5$

$$P_{ij} = \frac{\cos\theta_{ij}}{\sqrt{2}\cdot r_{ij}} - \frac{\cos 2\theta_{ij}}{r_{ij}^2} + \frac{\cos 3\theta_{ij}}{\sqrt{2}\, r_{ij}^3} + \frac{3\cos 5\theta_{ij}}{\sqrt{2}\, r_{ij}^5} \quad \ldots\ldots \text{A1.15}$$

and

$$Q_{ij} = \frac{\cos\theta_{ij}}{\sqrt{2}\, r_{ij}} - \frac{\cos 3\theta_{ij}}{\sqrt{2}\, r_{ij}^3} + \frac{3\cos 5\theta_{ij}}{\sqrt{2}\, r_{ij}^5} \quad \ldots\ldots \text{A1.16}$$

where, γ = Euller's constant = 1.7811

S_2 , S_2' , S_4 , S_4' , σ_1 , σ_2 , σ_3 and σ_4 are the infinite[81] series expressed in terms of r_{ij} and θ_{ij}.

It is quite clear from equations A1.12 - A1.16 that the matrices P and Q are functions of frequency and hence the impedance due to the earth-return path given by equations A1.10, A1.11 is frequency dependant. Carson's formulas for the impedance due to the earth-return path are based on the assumption that the earth is homogeneous with constant resistivity and with unity permeability and permittivity. The earth, however, is not homogeneous and its resistivity varies along the depth of the earth layer.

A more rigorous and general solution[82-84] for the earth-return impedance has been reported. In particular the solution permits the earth-return path to be considered as three layers of different resistivities,permeabilities and permittivities. It is therefore important to take into account the stratified earth effects when calculating the impedance due to earth-return path, if

sufficient data concerning earth layers is available. In the absence of such data, Carson's equations may be used for design purposes.

A1.1.2 Transmission Line Shunt Admittance Matrix

On the assumption that the conductance of free space is negligable, the shunt admittance matrix of the transmission line contains only imaginary terms which correspond to the capacitive coupling between the conductors and the conductors and the earth. It is a matrix of the order $3P+q$, where P is the number of circuits and q is the number of earth wires. It is defined as:

$$Y = J2\pi W \varepsilon B^{-1} \qquad \ldots\ldots \text{A1.17}$$

where

B^{-1} is the inverse of the charge co-efficient matrix B given by equation A1.2.

Let

$$C = 2\pi\varepsilon B^{-1}$$

$\therefore$ the elements of the matrix (C) define the various capacitances as follows:

$$C_{ij} = -c_{ij} \quad \text{for } (i \neq j)$$

$$C_{ij} = \sum_{J=1}^{J=3P+q} c_{ij} \quad (\text{for } i=j)$$

where

c_{ij} = capacitance between conductors i and j for $i \neq j$

c_{ij} = capacitance between conductor i and the earth for $i = j$.

The effect of earth return path on line capacitance is very insignificant over a very wide range of frequencies[56] (up to 1 Mc/s), and hence it was considered to be frequency invariant through-out the present investigation.

Elimination of Earth Wires

Since the voltages and currents in the earth wires are not important, it is necessary to eliminate elements in rows and coulomns corresponding to them in

both series impedance and shunt admittance matrices. Thus the performance of the phase conductors, which is of interest, remains unchanged and the system analysis is very much simplified.[55-56]

Earth wires are normally earthed at regular intervals, hence, they can be assumed to have zero (or near zero) potentials if standing voltages between towers are neglected.

Under the above assumption, earth wire elements in matrices (Z) and (Y) are eliminated.

In the computer programs developed throughout this work, the steps for formulating the basic line matrices (Z, Y) suggested by Galloway etal[55] have been followed since they are considered to be computationally efficient.

APPENDIX (A1.2) EVALUATION OF PHASE AND NEUTRAL REACTANCES OF THE 4-REACTER SCHEME

As previously shown in section (2.3.1) the positive and zero phase sequance impedances of Figs (2.1.a) and (2.1.c) can be calculated by applying a set of positive and zero phase sequence voltages respectively to the two circuits.

Therefore it follows that;

For the circuit of Fig (2.1.c); we have,

$$\begin{aligned} X_1 &= XP \\ X_0 &= XP + 3X_n \end{aligned} \qquad \ldots\ldots \text{A1.18}$$

similarly for Fig (2.1.a)

$$\begin{aligned} X_1 &= (X_{\ell g} \cdot X_{\ell h}) \,/\, (X_{\ell h} + 3X_{\ell g}) \\ X_0 &= X_{\ell g} \end{aligned} \qquad \ldots\ldots \text{A1.19}$$

For the two circuits of Fig (2.1.a,c) to be equal, the corresponding quantities of equation A1.18 and A1.19 should be equal.

i.e. $X_1 + 3X_n = X_{\ell g}$ A1.20.a

and $X_1 = (X_{\ell g} \cdot X_{\ell h}) \,/\, (X_{\ell h} + 3X_{\ell g})$ A1.20.b

substituting from A1.20.a into A1.20.b

$$\therefore \quad X_1 = \frac{(X_1 + 3X_n)\, X_{\ell h}}{X_{\ell h} + 3(X_1 + 3X_n)}$$

from which

$$X_{\ell h} = X_1 (X_1 + 3X_n) \,/\, X_n \qquad \ldots\ldots \text{A1.20.c}$$

Therefore, the parameters of the two circuits of Fig (2.1.a,c) are related to each other by equations (A1.20.a) and (A1.20.c).

Now, for reactive power compensation,

$$B_{L1} = h_1 \cdot B_{c1} \quad \text{..... A1.21}$$

And for total elimination of interphase capacitances,

$$B_{\ell h} = B_{ch} \quad \text{..... A1.22}$$

But from equations 2.2 and 2.3

$$B_{ch} = (B_{c1} - B_{c0}) / 3$$

and from equations A1.20

$$X_{\ell h} = X_1 (X_1 + 3X_n) / X_n$$

i.e.

$$B_{\ell h} = \frac{X_n}{X_1 (X_1 + 3X_n)}$$

$\therefore$ Applying equation A1.22

$$\therefore (B_{c1} - B_{c0}) / 3 = \frac{X_n}{X_1 (X_1 + 3X_n)} = \frac{X_n}{\frac{1}{B_{L1}} \left(\frac{1}{B_{L1}} + 3X_n \right)}$$

$$\text{or} \quad X_n = \frac{B_{c1} - B_{c0}}{3h_1 B_{c1}} \left(\frac{1}{h_1 B_{c1}} + 3X_n \right)$$

$$\text{or} \quad X_n \left(1 - \frac{(B_{c1} - B_{c0})}{h_1 \cdot B_{c1}}\right) = \frac{B_{c1} - B_{c0}}{3h_1^2 \cdot B_{c1}^2}$$

$$\text{or} \quad X_n = \frac{B_{c1} - B_{c0}}{(3h_1^2 \cdot B_{c1}^2)} \cdot \frac{h_1 B_{c1}}{(h_1 B_{c1} - B_{c1} + B_{c0})}$$

$$\text{or} \quad X_n = \frac{B_{c1} - B_{c0}}{3h_1 B_{c1} (B_{c1} (h_1^{-1}) + B_{c0})} \quad \text{..... A1.23}$$

Equation A1.23 is not a general one and an alternative way of putting X_n in a more general form is as follows:

From Fig (2.1.c) the PPS and ZPS impedances are:

$$X_1 = XP \quad , \quad B_{L1} = 1/XP$$

$$X_0 = XP + 3X_n \quad , \quad B_{L0} = \frac{1}{X_1 + 3X_n}$$

From Fig (2.2.a) we have

$$B_{c1} = B_{cg} + 3B_{ch}$$

$$B_{\ell} = B$$

But for the second purpose, i.e. ground fault suppression,

$$B_{LO} = h_0 \cdot B_{cO} \qquad \text{..... A1.24}$$

$$\therefore \quad h_0 = \frac{B_{LO}}{B_{cO}} = \frac{1}{(X_1 + 3X_n)\, B_{cg}}$$

i.e. $h_0 \cdot B_{cg} (X_1 + 3X_n) = 1$

or $h_0 \cdot B_{cg} \cdot X_1 + 3h_0 \cdot B_{cg} \cdot X_n = 1$

or $$X_n = \frac{1 - h_0 B_{cg} X_1}{3 h_0 B_{cg}}$$

$$X_n = \frac{1}{3} \left(\frac{1}{h_0 B_{cg}} - X_1 \right)$$

But from equations 2.3

$$B_{cg} = B_{cO}$$

and from equation A1.21,

$$B_{L1} = \frac{1}{X_1} = h_1 B_{c1}$$

$$\therefore \quad X_n = \frac{1}{3} \left(\frac{1}{h_0 B_{cO}} - \frac{1}{h_1 B_{c1}} \right)$$

or finally:

$$X_n = \frac{h_1 B_{c1} - h_0 \cdot B_{cO}}{3 . h_1 B_{c1} h_0 B_{cO}} \qquad \text{..... A1.25}$$

$$X_1 = \frac{1}{h_1 \cdot B_{c1}} \qquad \text{..... A1.26}$$

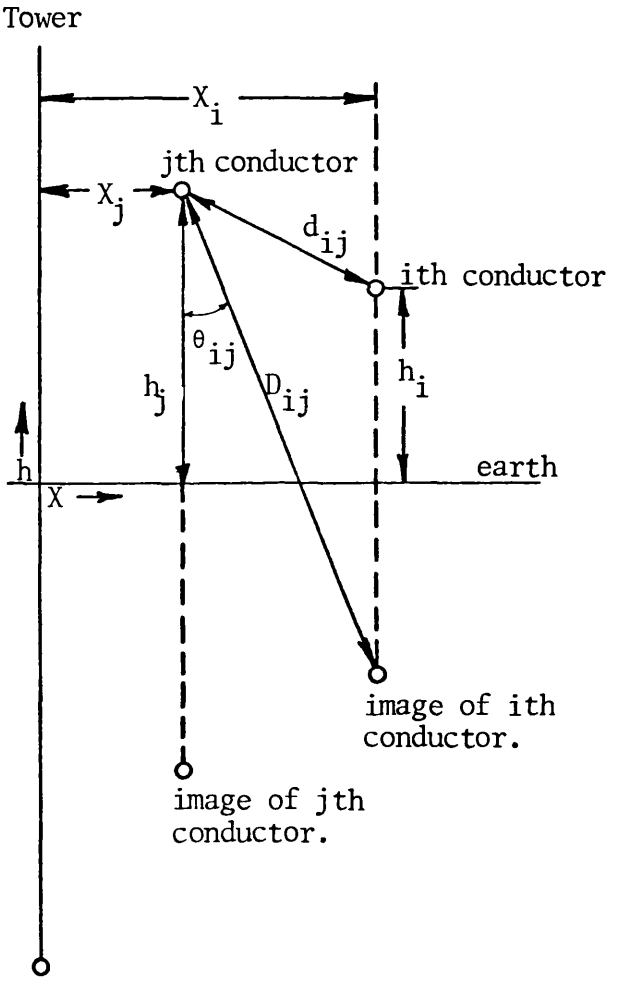

Fig A1.1

Schematic diagram of conductor positions with respect to axis of symmetry.

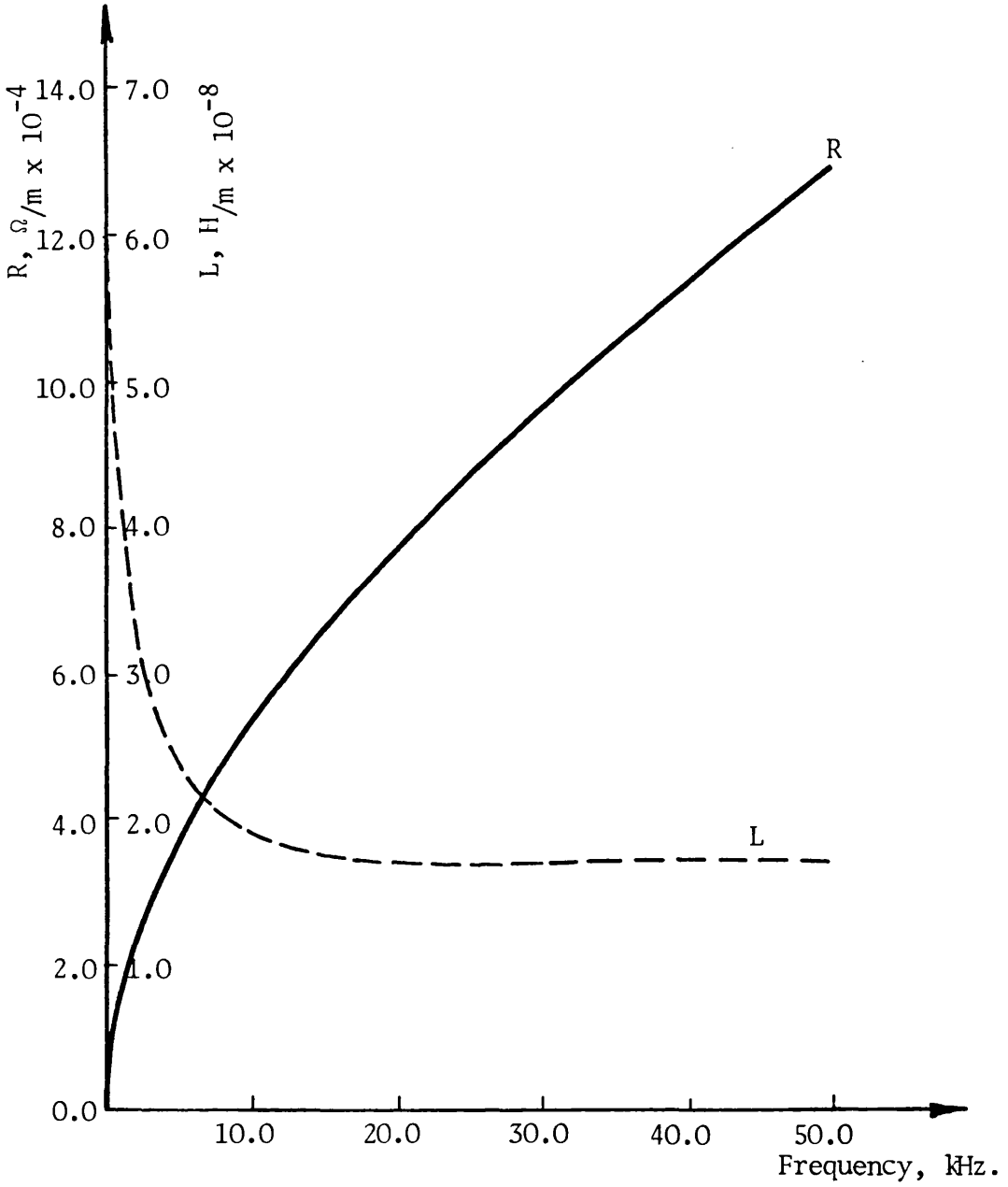

Fig A1.2

Variation of line inductance and resistance with frequency.

APPENDIX A2 SOLUTION OF TRAVELLING WAVE PHENOMENA IN POLYPHASE SYSTEMS.[12,13,86,87]

Fig A2.1 shows conductor (1) of a practical n - conductor transmission line where the effect of electromagnetic and electrostatic coupling is shown. Consider a very small element; Δx in the line. The voltage drop ΔV_1 across the element at a certain frequency is:

$$\Delta V_1 = -(Z_{11} I_1 + Z_{12} I_2 + ... + Z_{1n} I_n) \Delta x$$

$$\therefore \frac{\Delta V_1}{\Delta x} = -(Z_{11} I_1 + Z_{12} I_2 + ... + Z_{1n} I_n)$$

or

$$\frac{dV_1}{dx} = -(Z_{11}.I_1 + Z_{12} I_2 + ... + Z_{1n} I_n)$$

For conductors 2, 3, ..., n the rate of change of voltages $\frac{dV_2}{dx}$, $\frac{dV_3}{dx}$ ..... $\frac{dV_n}{dx}$ are similarly evaluated so that:

$$\frac{dV_1}{dx} = -(Z_{11} I_1 + Z_{12} I_2 + Z_{13} I_3 + ... + Z_{1n} I_n)$$

$$\frac{dV_2}{dx} = -(Z_{21} I_1 + Z_{22} I_2 + Z_{23} I_3 + ... + Z_{2n} I_n)$$

$$\frac{dV_3}{dx} = -(Z_{31} I_1 + Z_{32} I_2 + Z_{33} I_3 + ... + Z_{3n} I_n)$$

$$\vdots$$

$$\frac{dV_n}{dx} = -(Z_{n1}.I_1 + Z_{n2} I_2 + Z_{n3} I_3 + ... + Z_{nn} I_n)$$

or in matrix form

$$\left[\frac{dV}{dx}\right] = -\left[Z\right]\left[I\right] \qquad ..... \text{A2.1}$$

Going back to Fig (A2.1), and apply the same thing to currents. The difference in the current between the ends of the element Δx of conductor (1) is given by:

$$\Delta I_1 = \Delta I_{11} + \Delta I_{21} + \Delta I_{31} + \ldots\ldots + \Delta I_{n1}$$

where

$$\Delta I_{11} = -(V_1 + \Delta V_1)\, Y_{11}.\Delta x \simeq -V_1\, Y_{11}.\Delta x$$

$$\Delta I_{21} = -(V_1 - V_2)\, Y_{12}\, \Delta x$$

$$\Delta I_{31} = -(V_1 - V_3)\, Y_{13}\, \Delta x$$

$$\vdots$$

$$\Delta I_{n1} = -V_1\,(Y_{11}\,\Delta x + Y_{12}\,\Delta x + Y_{13}\,\Delta x + \ldots\ldots + Y_{1n}\,\Delta x) + V_2\, Y_{12}\,\Delta x + \ldots\ldots + V_n\, Y_{1n}\,\Delta x.$$

$$\therefore \frac{\Delta I_1}{\Delta x} = -(Y_{11} + Y_{12} + \ldots\ldots + Y_{1n})\, V_1 + Y_{12}\, V_2 \ldots\ldots + Y_{1n}\, V_n$$

or

$$\frac{dI_1}{dx} = -(Y_{11} + Y_{12} + \ldots\ldots + Y_{1n})\, V_1 + Y_{12}\, V_2 \ldots\ldots + Y_{1n}\, V_n$$

Applying the same principle to conductors 2,3, 4 ..... , n, the rate of change of currents with respect to x is given by:

$$\begin{bmatrix} \frac{dI_1}{dx} \\ \frac{dI_2}{dx} \\ \vdots \\ \frac{dI_n}{dx} \end{bmatrix} = - \begin{bmatrix} Y_{11}+Y_{12}+\ldots+Y_{1n} & -Y_{12} & \ldots\ldots & -Y_{1n} \\ -Y_{21} & Y_{21}+Y_{22}+\ldots+Y_{2n} & \ldots\ldots & -Y_{2n} \\ \vdots & \vdots & \vdots & \vdots \\ -Y_{n1} & -Y_{n2} & \ldots\ldots & Y_{n1}+Y_{n2}+\ldots+Y_{nn} \end{bmatrix} \begin{bmatrix} V_1 \\ V_2 \\ V_3 \\ \vdots \\ V_n \end{bmatrix}$$

or in a more general form

$$\left[\frac{dI}{dx} \right] = - [Y]\,[V] \qquad \ldots\ldots \text{A2.2}$$

Differentiating equations A2.1 , A2.2 with respect to x and for simplicity matrices (Z),(Y),(V),(I),$\left(\frac{dV}{dx}\right)$ and $\left(\frac{dI}{dx}\right)$ will be written from now onward without the matrix notation.

$$\therefore \frac{d^2V}{dx^2} = - Z.\frac{dI}{dx}$$

and

$$\frac{dI^2}{dx^2} = - Y.\frac{dV}{dx}$$

or

$$\frac{d^2V}{dx^2} = - Z\ Y\ V \qquad \text{..... A2.3}$$

$$\frac{d^2I}{dx^2} = - Y.Z.I$$

The solution of equation A2.3 is very difficult due to the fact that the second orders rate of change of voltage and current in each phase are a function of the voltages and currents in all phases. However, the solution is obtained if the phase voltages and currents are related to the component voltages and currents by the linear transformations[12]:

$$V = S.V_c \qquad \text{..... A2.4}$$

$$I = Q.I_c$$

where the (n x n) square matrices S and Q are so that the second order differential equations involve diagonal matrices only. Mutual effects are thus eliminated, making a direct solution component for component possible.

V_c = Coulomn vector matrix of the order (n x 1) of the n component voltages V_{c1}, V_{c2}, V_{c3}, ... V_{cn} respectively.

I_c = Coulomn vector matrix of the order (n x 1) of the n component currents I_{c1}, I_{c2}, I_{c3}, ... I_{cn} respectively.

Substituting equation A2.4 into A2.3 we get:

$$\frac{dV^2}{dx^2} = S\ \frac{d^2V_c}{dx^2}$$

or

$$\frac{d^2V_c}{dx^2} = S^{-1}\ Z\ Y\ V$$

$$= S^{-1}\ Z\ Y\ S\ V_c$$

$$\therefore \quad \frac{d^2V_c}{dx^2} = S^{-1}.Z\ Y\ S\ V_c$$

To simplify the analysis, let:

where $ZY = P$

$$P_{ij} = \sum_{k=1}^{n} Z_{ik} \cdot Y_{kj} \qquad \text{..... A2.5}$$

$$\therefore \quad \frac{d^2V_c}{dx^2} = S^{-1}\ P\ S.V_c \qquad \text{..... A2.6}$$

The product $S^{-1}\ P\ S$ is diagonalised to become

$$[\ S^{-1}\ P\ S\ ] = [\ \gamma_1^2 \quad \gamma_2^2 \quad \gamma_3^2 \ldots\ldots \gamma_n^2\ ]\ \text{diag} \qquad \text{..... A2.7}$$

Substitute in equation 4.2.3

$$\therefore \begin{bmatrix} \frac{d^2V_{c1}}{dx^2} \\ \frac{d^2V_{c2}}{dx^2} \\ \vdots \\ \frac{d^2V_{cn}}{dx^2} \end{bmatrix} = [\ \gamma_1^2 \quad \gamma_2^2 \quad \gamma_3^2 \ldots\ldots \gamma_n^2\ ]\ \text{diag.} \begin{bmatrix} V_{c1} \\ V_{c2} \\ \vdots \\ V_{cn} \end{bmatrix} \qquad \text{..... A2.8}$$

From equation A2.8 we have:

$$\begin{aligned} \frac{d^2V_{c1}}{dx^2} &= \gamma_1^2\ V_{c1} \\ \frac{d^2V_{c2}}{dx^2} &= \gamma_2^2\ V_{c2} \\ &\vdots \\ \frac{d^2V_{cn}}{dx^2} &= \gamma_n^2\ V_{cn} \end{aligned} \qquad \text{..... A2.9}$$

Solving equation A2.9 will give:

$$
\begin{aligned}
V_{c1} &= V_{c1}^{+}\, e^{-\gamma_1 x} + V_{c1}^{-}\, e^{\gamma_1 x} \\
V_{c2} &= V_{c2}^{+}\, e^{-\gamma_2 x} + V_{c2}^{-}\, e^{\gamma_2 x} \\
&\vdots \\
V_{cn} &= V_{cn}^{+}\, e^{-\gamma_n x} + V_{cn}^{-}\, e^{\gamma_n x}
\end{aligned}
\qquad \ldots\ldots \text{A2.10}
$$

or in general:

$$V_c = V_c^{+}\, e^{-\gamma x} + V_c^{-}\, e^{\gamma x} \qquad \ldots\ldots \text{A2.11}$$

where: V_{c1}, V_{c2}, ... V_{cn} in equations A2.9 - A2.11 are the modal voltages which are related to the phase voltages by the square matrix S of equation A2.4

S = voltage eigen vector matrix.

= eigen vectors of Z.Y.

γ^2 = eign values of Z.Y.

Now considering the solution for the currents using equations A2.3 and A2.4:

$$\frac{d^2 I}{dx^2} = Y\, Z\, I$$

$$I = Q\, I_c$$

From equation A2.5, $P = Z\, Y$.

Since the network considered is passive (transmission line), it can be said that:

$$Z = Z_t\,, \quad Y = Y_t\,,$$

and hence:

$$\frac{d^2 I}{dx^2} = (Y_t \cdot Z_t)\, I$$

$$= (Y\, Z)_t \cdot I$$

or $$\frac{d^2 I}{dx^2} = P_t\, I \qquad \ldots\ldots \text{A2.12}$$

Substituting from equation A2.4 into equation A2.3, to get the currents:

$$\frac{d^2 I}{dx^2} = Q\, \frac{d^2 I_c}{dx^2}$$

$$\therefore \quad \frac{d^2 I_c}{dx^2} = Q^{-1} \frac{d^2 I}{dx^2} = Q^{-1} P_t Q I_c$$

$$\therefore \quad \frac{d^2 I_c}{dx^2} = Q^{-1} P_t Q I_c \qquad \text{..... A2.13}$$

where Q (of equations A2.4, A2.13) = current eigen vector matrix,

$Q^{-1} P_t Q$ = current eigenvalues matrix which is diagonalised to be of the form:

$$Q^{-1} P_t Q = \left[\acute{\gamma}_1^2 \quad \acute{\gamma}_2^2 \quad \acute{\gamma}_3^2 \ldots\ldots \acute{\gamma}_n^2 \right] \text{diag.} \qquad \text{..... A2.14}$$

Now, for the diagonalisation of equations A2.7, A2.14 the determinats (D) and $(\acute{D})$ of $(P - \gamma_i^2)$ and $(P_t - \acute{\gamma}_i^2)$ respectively must yield to zero,[12]

i.e. $$D (P - \gamma_i^2) = 0$$
$$\acute{D} (P_t - \acute{\gamma}_i^2) = 0 \qquad \text{..... A2.15}$$

However, $P_t - \acute{\gamma}_i^2 = (P - \acute{\gamma}_i^2)_t$, because $\acute{\gamma}_i^2$ is diagonal (contains only diagonal elements).

Where γ_i^2 , $\acute{\gamma}_i^2$ are $\gamma_1^2, \gamma_2^2 \ldots\ldots, \gamma_n^2$ and $\acute{\gamma}_1^2, \acute{\gamma}_2^2 \ldots\ldots \acute{\gamma}_n^2$ respectively.

Then,

$D (P - \acute{\gamma}_i^2) = \acute{D} (P - \acute{\gamma}_i^2)_t = 0$,

and because the determinant of any matrix = the determinant of the transposed matrix, i.e. $\acute{D} (P - \acute{\gamma}_i^2)_t = \acute{D} (P - \acute{\gamma}_i^2)$

and $$D (P - \gamma_i^2) = \acute{D} (P - \acute{\gamma}_i^2)$$

or $$\gamma_i = \acute{\gamma}_i$$

i.e. the voltage and current modal propagation coefficients are identical.

It is sometimes usefull to deal in terms of the components Z_c matrix and, from equations A2.1, A2.4 we have:

$$\frac{d_V}{dx} = -Z I \quad , \quad V = S V^c \quad , \quad I = Q I^c$$

$$\therefore \quad S \frac{dV^c}{dx} = -Z Q I^c$$

or $\frac{dV^c}{dx} = - S^{-1} Z Q I^c$ A2.16.a

and from equation A2.11 we have:

$$V_c = V_c^+ . e^{-\gamma x} + V_c^- . e^{\gamma x}$$

where γ, V_c^+ and V_c^- are determined from equations A2.7, and A2.11 respectively.

Differentiating equations A2.11 we get:

$$\frac{dV_c}{dx} = -\gamma e^{-\gamma x} . V_c^+ + \gamma e^{\gamma x} . V_c^- \quad \text{..... A2.16.b}$$

where

$$e^{-\gamma x} = \left[e^{-\gamma_1 x} \quad e^{-\gamma_2 x} \quad e^{-\gamma_3 x} \ldots\ldots \quad e^{-\gamma_n x} \right] \text{diag.} \quad \text{..... A2.16.c}$$

equating equations A2.16 (a,b) we get:

$$\frac{dV_c}{dx} = -\gamma V_c^+ e^{-\gamma x} + \gamma V_c^- e^{\gamma x} = -S^{-1} Z Q I_c$$

or

$$V_c^+ e^{-\gamma x} - V_c^- e^{+\gamma x} = \gamma^{-1} S^{-1} Z Q I_c \quad \text{..... A2.17.a}$$

The product $(\gamma^{-1} S^{-1} Z Q)$ can be chosen to be diagonal. Indeed, because γ^{-1} is diagonal, so too is $S^{-1} Z Q$.

Thus replacing $\gamma^{-1} S^{-1} Z Q$ by Z^c we get:

$$V_c^+ e^{-\gamma x} - V_c^- e^{+\gamma x} = Z^c I_c \quad \text{..... A2.17.b}$$

Equation A2.17.b means that modal component of currents are related only to the corresponding modal component of voltages.

I_c of equation A2.17.b is of the form:

$$I_c = I_c^+ e^{-\gamma x} + I_c^- e^{+\gamma x} \quad \text{..... A2.18}$$

where

$$I_c = \begin{bmatrix} I_{c1} \\ I_{c2} \\ \vdots \\ I_{cn} \end{bmatrix}, \quad I_c^+ = \begin{bmatrix} I_{c1}^+ \\ I_{c2}^+ \\ \vdots \\ I_{cn}^+ \end{bmatrix}, \quad I_c^- = \begin{bmatrix} I_{c1}^- \\ I_{c2}^- \\ \vdots \\ I_{cn}^- \end{bmatrix}, \quad Z_c = \begin{bmatrix} Z_{c1} \\ Z_{c2} \\ \vdots \\ Z_{cn} \end{bmatrix} \quad \text{.. A2.19}$$

The component voltages V_c and the component currents I_c given by equations A2.11 and A2.18 may be evaluated by solving for the constents of integration from the defined boundary conditions. Once the component voltages and currents are known, the corresponding phase quantities may be evaluated from equations A2.4.

Voltages And Currents At The Boundaries

Now consider the voltages and currents at the boundaries; From equation A2.17 (a,b), if only one modal component is considered, we have:

$$V_{c1}^{+} e^{-\gamma_1 x} - V_{c1}^{-} e^{\gamma_1 x} = Z_1^c \left(I_{c1}^{+} e^{-\gamma_1 x} + I_{c1}^{-} e^{\gamma_1 x} \right) \quad \text{..... A2.20}$$

Equation A2.20 must be true for all values of x, and this can only be true if the coefficients of the exponentials are the same,

i.e.
$$V_{c1}^{+} = Z_1^c \, I_{c1}^{+}$$
$$V_{c1}^{-} = -Z_1^c \, I_{c1}^{-} \quad \text{..... A2.21}$$

$\therefore$ At the sending end of the line:

$$x = 0, \quad V = V_S$$

$$\therefore V_S = S \, V^c = S \left(V_c^{+} + V_c^{-} \right) \quad \text{..... A2.22.a}$$

$$\text{or } V_S = S \, Z^c \left(I_c^{+} - I_c^{-} \right)$$

and

$$I_S = Q \, . \, I^c = Q \left(I_c^{+} + I_c^{-} \right) \quad \text{..... A2.22.b}$$

At the receiving end of the line:

$$x = \ell, \quad V = V_R$$

$$\therefore V_R = S \, . \left(e^{-\gamma \ell} \, . \, V_c^{+} + e^{\gamma \ell} \, . \, V_c^{-} \right)$$
$$I_R = Q \, . \left(e^{-\gamma \ell} \, . \, I_c^{+} + e^{\gamma \ell} \, . \, I_c^{-} \right) \quad \text{..... A2.22.c}$$

From equation A2.22.a we have:

$$\left(I_c^{+} - I_c^{-} \right) = Z^{c-1} \, . \, S^{-1} \, V_S$$

and from equation A2.22.b we have:

$$\left(I_c^{+} + I_c^{-} \right) = Q^{-1} \, I_S$$

$$\therefore \quad I_c^+ = (Z^{c-1}\ S^{-1}\ V_S + Q^{-1}\ I_S) / 2$$
$$I_c^- = (Q^{-1}\ I_S - Z^{c-1}\ S^{-1}\ V_S) / 2 \qquad \text{..... A2.22.d}$$

Substituting A2.22.d into A2.22.c we get:

$$\therefore \quad Q^{-1}\ I_R = \frac{e^{-\gamma\ell}}{2} (Z^{c-1}\ S^{-1}\ V_S + Q^{-1}\ I_S) + \frac{e^{\gamma\ell}}{2} (Q^{-1}\ I_S - Z^{c-1}\ S^{-1}\ V_S)$$

or

$$Q^{-1}\ I_R = \text{Cosh}\ \gamma\ell\ Q^{-1}\ I_S - \sinh\ \gamma\ell\ Z^{c-1}\ S^{-1}\ V_S.$$

Now if modal quantities are used

$$\therefore \quad I_R^c = \cosh\ \gamma\ell\ .Q^{-1}\ I_S - \sinh\ \gamma\ell\ Z^{c-1}\ S^{-1}\ V_S \qquad \text{..... A2.23}$$

substituting A2.22.d into A2.22.c to get the receiving end voltage;

$$S^{-1}\ V_R = e^{-\gamma\ell}\ V_c^+ + e^{\gamma\ell}\ V_c^-$$
$$= e^{-\gamma\ell}\ Z^c\ I_c^+ - e^{\gamma\ell}\ Z^c\ I_c^-$$
$$= \frac{e^{-\gamma\ell}}{2} \cdot Z^c\ (Z^{c-1}\ S^{-1}\ V_S + Q^{-1}\ I_S) - \frac{e^{\gamma\ell}\ Z^c}{2} (Q^{-1}\ I_S - Z^{c-1}\ S^{-1} V_S)$$
$$= \frac{(e^{\gamma\ell} + e^{-\gamma\ell})}{2} S^{-1}\ V_S - (\frac{e^{\gamma\ell} - e^{-\gamma\ell}}{2})\ Z^c\ Q^{-1}\ I_S$$

$$\therefore \quad S^{-1}\ V_R = \cosh\ \gamma\ell\ S^{-1}\ V_S - \sinh\ \gamma\ell\ Z^c\ Q^{-1}\ I_S \qquad \text{..... A2.24.a}$$

$$\text{or} \quad V_R^c = \cosh\ \gamma\ell\ S^{-1}\ V_S^c - \sinh\ \gamma\ell\ Z^c\ I_S^c \qquad \text{..... A2.24.b}$$

It has to be noted that V_R is sometimes written as:

$$V_R = S \cosh\ \gamma\ell\ S^{-1}\ V_S - S \sinh\ \gamma\ell\ Z^c\ Q^{-1}\ I_S$$

and since both Z^c and $\sinh\ \gamma\ell$ are diagonal

$$\therefore \quad V_R = S \cosh\ \gamma\ell\ S^{-1}\ V_S - S\ Z^c \sinh\ \gamma\ell\ Q^{-1}\ I_S$$
$$= S \cosh\ \gamma\ell\ S^{-1}\ V_S - S\ Z^c\ Q^{-1}\ Q \sinh\ \gamma\ell\ Q^{-1}\ I_S$$
$$= S \cosh\ \gamma\ell\ S^{-1}\ V_S - Z_0\ Q \sinh\ \gamma\ell\ Q^{-1}\ I_S$$

i.e.

$$V_R = S \cosh\ \gamma\ell\ S^{-1}\ V_S - Z_0.Q \sinh\ \gamma\ell\ .\ Q^{-1}\ I_S \qquad \text{..... A2.25}$$

where the polyphase surge impedance is:

$$Z_0 = S\ Z^c\ Q^{-1} \qquad \text{..... A2.26}$$

where

$$Z^c = \gamma^{-1}\ S^{-1}\ Z\ Q$$

$$\therefore \quad Z_0 = S\ \gamma^{-1}\ S^{-1}\ Z \qquad \text{..... A2.27}$$

Now $(Z_0)_t = Q_t^{-1}\ Z_t^c\ S_t$ and since Z^c is diagonal, hence;

$$(Z_0)_t = Q_t^{-1} \cdot Z^c \cdot S_t \qquad \text{..... A2.28.a}$$

It can be shown that $Q_t.S$ is diagonal:

If $Q_t.S = D =$ a diagonal matrix

$$Q_t = S^{-1}.D = D\,S^{-1} \quad \text{..... A2.28.b}$$

$$(Q_t)^{-1} = Q^{-1}{}_t = S\,D^{-1}$$

Also $S_t.Q = D_t = D$

$$\therefore S_t = D\,Q^{-1} \quad \text{..... A2.28.c}$$

Substituting from A2.28.b,c into A2.28.a we get:

$$(Z_0)_t = S.D^{-1} \cdot Z_t^c \cdot D \cdot Q^{-1}$$

or

$$Z_{0t} = S.Z^c.Q^{-1} \quad \text{..... A2.28.d}$$

Equation A2.28 is typically the same as that giving Z_0 in equation A2.26. This means that Z_0 is a symmetrical matrix.

Equations A2.23 and A2.24 describe the modal current and voltage components at the receiving end of the line. Using these two equations, the polyphase network equations could be derived as follows:

From equation A2.24.b we have:

$$\cosh \gamma\ell\, V_S^c - V_R^c = \sinh \gamma\ell\; Z^c\, I_S^c$$

$$\therefore I_S^c = (\sinh \gamma\ell)^{-1} \cdot Z^{c-1} (\cosh \gamma\ell\, V_S^c - V_R^c)$$

$$\therefore I_S^c = \sinh^{-1}\gamma\ell\; Z^{c-1} \cdot \cosh \gamma\ell\, V_S^c - \sinh^{-1}\gamma\ell \cdot Z^{c-1} \cdot V_R^c$$

But $\coth \gamma\ell = \dfrac{\cosh \gamma\ell}{\sinh \gamma\ell}$ and $\operatorname{cosech}\gamma\ell = \dfrac{1}{\sinh \gamma\ell}$

$$\therefore I_S^c = \coth \gamma\ell\, Z^{c-1} \cdot V_S^c - \operatorname{cosech} \gamma\ell\, Z^{c-1} \cdot V_R^c \quad \text{..... A2.29}$$

Also $I_S = Q\, I_S^c$ (form equation A2.4)

$$\therefore I_S = Q\, Z^{c-1} \coth \gamma\ell\, V_S^c - Q\, Z^{c-1}\, S^{-1} \operatorname{cosech} \gamma\ell\, Z^{c-1} \cdot V_R^c$$

$$\text{or } I_S = Q\, Z^{c-1}\, S^{-1}\, S \coth \gamma\ell\, S^{-1} V_S - Q\, Z^{c-1}\, S^{-1}\, S \operatorname{cosech} \gamma\ell\, S^{-1} V_R$$

But equation A2.26 gives Z_0 as $= S\, Z^c\, Q^{-1}$

$$\text{or } Z_0^{-1} = Y_0 = Q\, Z^{c-1}\, S^{-1}$$

Substituting in the equation of I_S above:

$$\therefore \quad I_S = Z_0^{-1} \cdot S \coth \gamma\ell \, S^{-1} V_S - Z_0^{-1} S \operatorname{cosech} \gamma\ell \, S^{-1} V_R$$

$$\text{or} \quad I_S = Y_0 \cdot S \coth \gamma\ell \, S^{-1} V_S - Y_0 S \operatorname{cosech} \gamma\ell \, S^{-1} V_R \qquad \ldots\ldots \text{A2.30}$$

Now, from equations A2.24 we have:

$$I_S^c = \sinh^{-1} \gamma\ell \, Z^{c-1} (\cosh \gamma\ell \, V_S^c - V_R^c)$$

Substituting the value of I_S^c in equation A2.23

$$\therefore \quad I_R^c = \cosh \gamma\ell \sinh^{-1} \gamma\ell \, Z^{c-1} (\cosh \gamma\ell \, V_S^c - V_R^c) - \sinh \gamma\ell \, Z^{c-1} V_S^c$$

$$I_R^c = Z^{c-1} (\cosh^2 \gamma\ell \sinh^{-1} \gamma\ell - \sinh \gamma\ell) V_S^c - Z^{c-1} \coth \gamma\ell \cdot V_R^c$$

$$\text{But} \quad \frac{\cosh^2 \gamma\ell}{\sinh \gamma\ell} - \sinh \gamma\ell = \frac{\cosh^2 \gamma\ell - \sinh^2 \gamma\ell}{\sinh \gamma\ell} = \frac{1}{\sinh \gamma\ell} = \operatorname{cosech} \gamma\ell$$

substituting to get I_R^c

$$\therefore \quad I_R^c = Z^{c-1} \cdot \operatorname{cosech} \gamma\ell \cdot V_S^c - Z^{c-1} \coth \gamma\ell \cdot V_R^c$$

$$\text{or} \quad I_R^c = Y^c \operatorname{cosech} \gamma\ell \cdot V_S^c - Y^c \cdot \coth \gamma\ell \cdot V_R^c \qquad \ldots\ldots \text{A2.31}$$

Again from equation A2.4, $I_R = Q I_R^c$

substituting in A2.31 we get:

$$\therefore \quad I_R = Q Z^{c-1} \operatorname{cosech} \gamma\ell \, S^{-1} V_S - Q Z^{c-1} \coth \gamma\ell \, S^{-1} V_R$$

$$\text{or} \quad I_R = Q Z^{c-1} S^{-1} S \operatorname{cosech} \gamma\ell \, S^{-1} V_S - Q Z^{c-1} S^{-1} S \coth \gamma\ell \, S^{-1} V_R$$

$Y_0 = Q Z^{c-1} S^{-1}$, substitute to get I_R

$$\therefore \quad I_R = Y_0 \cdot S \cdot \operatorname{cosech} \gamma\ell \, S^{-1} V_S - Y_0 S \coth \gamma\ell \, S^{-1} V_R \qquad \ldots\ldots \text{A2.32}$$

Equations A2.30 and A2.32 can be rewritten in matrix form as:

$$\begin{bmatrix} I_S \\ \hline I_R \end{bmatrix} = \left[\begin{array}{c|c} Y_0 S \coth \gamma\ell \, S^{-1} & -Y_0 S \operatorname{cosech} \gamma\ell \, S^{-1} \\ \hline Y_0 S \operatorname{cosech} \gamma\ell \, S^{-1} & -Y_0 S \coth \gamma\ell \, S^{-1} \end{array}\right] \begin{bmatrix} V_S \\ \hline V_R \end{bmatrix}$$

$\ldots\ldots$ A2.33

or

$$\begin{bmatrix} V_S \\ \hline V_R \end{bmatrix} = \left[\begin{array}{c|c} S \coth \gamma\ell \, S^{-1} Z_0 & -S \operatorname{cosech} \gamma\ell \, S^{-1} Z_0 \\ \hline S \operatorname{cosech} \gamma\ell \, S^{-1} Z_0 & -S \coth \gamma\ell \, S^{-1} Z_0 \end{array}\right] \begin{bmatrix} I_S \\ \hline I_R \end{bmatrix}$$

$\ldots\ldots$ A2.34

Sometimes equation A2.33 is required in terms of the modal voltages and currents. Using equations A2.28.d and A2.33 yield the required relation as:

$$\begin{bmatrix} I_S^c \\ \hline I_R^c \end{bmatrix} = \left[\begin{array}{c|c} Y_c \cdot \coth \gamma\ell & -Y_c \operatorname{cosech} \gamma\ell \\ \hline Y_c \operatorname{cosech} \gamma\ell & -Y_c \cdot \coth \gamma\ell \end{array}\right] \begin{bmatrix} V_S^c \\ \hline V_R^c \end{bmatrix} \qquad \ldots\ldots \text{A2.35}$$

Usually it is more adaquate to write the transmission network equations so that sending end quantities are related to receiving end quantities by a two-port transfer matrix. This can be acheived as follows:

From equations A2.29 and A2.31 and by using equation A2.28.d we can get:

$$\begin{bmatrix} V_S \\ \hline I_S \end{bmatrix} = \left[\begin{array}{c|c} S \cosh \gamma\ell\, S^{-1} & S \sinh \gamma\ell\, S^{-1} Z_0 \\ \hline Y_0.S.\sinh \gamma\ell.S^{-1} & Y_0.S \cosh \gamma\ell\, S^{-1} Z_0 \end{array}\right] \begin{bmatrix} V_R \\ \hline I_R \end{bmatrix} \quad \ldots\ldots \text{A2.36}$$

It can be seen that equation A2.36 gives the transmission network equations in terms of the well known 'A B C D' constant matrices,

where:

$$\begin{aligned} A &= \cosh(\psi\ell) \\ B &= \sinh(\psi\ell).Z_0 \\ C &= Y_0.\sinh(\psi\ell) \\ D &= Y_0.\cosh(\psi\ell).Z_0 \end{aligned} \quad \ldots\ldots \text{A2.37}$$

$$\cosh(\psi\ell) = S.\cosh(\gamma\ell)\, S^{-1}$$

$$\sinh(\psi\ell) = S.\sinh(\gamma\ell)\, S^{-1}$$

For a single-circuit, 2-conductor line, the dimention of any of the matrices given in equation A2.37 is (3 x 3).

In modal form, equation A2.36 becomes:

$$\begin{bmatrix} V_S^c \\ \hline I_S^c \end{bmatrix} = \left[\begin{array}{c|c} \cosh \gamma\ell & -Z_c \cdot \sinh \gamma\ell \\ \hline Y_c \sinh \gamma\ell & -\cosh \gamma\ell \end{array}\right] \begin{bmatrix} V_R^c \\ \hline I_R^c \end{bmatrix} \quad \ldots\ldots \text{A2.38}$$

Equations A2.36, A2.38 are the basic equations used in the analythical and digital analysis presented in this thesis.

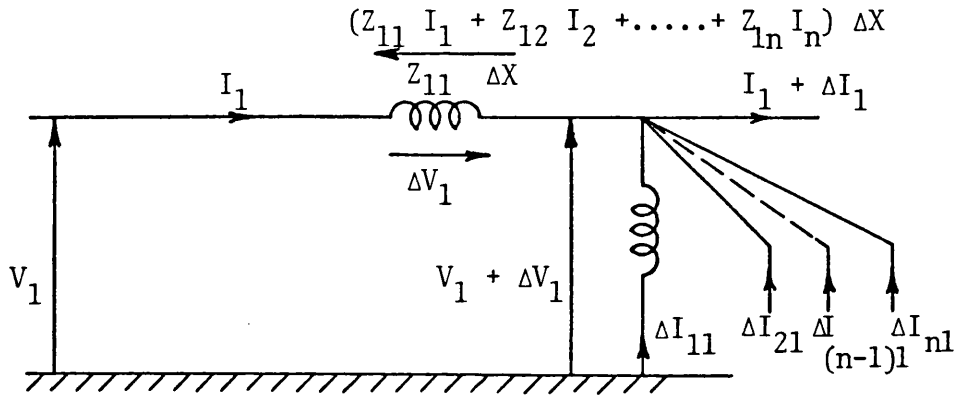

Fig A2.1

Shunt and series coupling between the conductors of an n-conductor system.

APPENDIX (A3)

FAULT SIMULATION FOR A MULTI-CONDUCTOR 3-PHASE SYSTEM

In general, faults on transmission systems may be catagorised under two headings; series faults and shunt faults.

Series faults may involve single-pole switching and one or more conductor opening. These conductors may be at one busbar or at different busbars. They may occur either due to the breaking of the ocnductors or through the action of the circuit breakers and other devices which may not result in the opening of all the three phases simultaneously. Series faults form some sort of unbalance in the system impedances and does not involve either the earth or any interconnection between phases.

Shunt faults such as single-phase-to ground, two-phase-to-ground, phase-to-phase, three-phase faults with or without connection to ground, and their combination, again form some sort of unbalance between phases or between phases and ground. These faults may occur either through impedances or direct short circuits.

When any of the above two types of faults, i.e. shunt faults and series faults, occur on a power system, they may produce balanced or unbalanced currents and hence they may be classified accordingly to balanced or unbalanced faults. However, in practice, most of the faults that occur[80] on power systems are unsymmetrical shunt faults. The frequency of occurance of unsymmetrical faults has been shown [56] to be 10%, 15% and 70% for 2L-G, L-L, and SLG faults respectively. Kimbark,[37,49] however, has indicated that SLG faults represent more than 90% of faults that may occur on power systems.

Since any unsymmetrical fault causes unbalanced currents to flow in the system, it has been well recognised that symmetrical component method is a useful tool of analysis to determine system voltages and currents in all parts of a system after the occurance of the fault.[80] It has been used

for the steady-state analysis of unsymetrical faults and by some researchers for transient analysis.[40] The practical application of this method, however, has been limited to balanced systems with limumped parameters. It may also be used for analysis of distributed parameters balanced or unbalanced systems but the solution in such cases may be extremely difficult.

Symmetrical 3-phase faults on 3-phase systems are usually analysed classically by assuming a single-phase model and the solution is extended to the other two-phases. The solution assumes symmetry and neglects both series and shunt coupling between conductors and therefore the method is not suitable if the line under consideration is untransposed and if an accurate fault analysis is required.

In this Appendix, therefore, the method of simulating shunt unsymmetrical faults is presented. Only the principle of the technique used is given since fault simulation is considered in detail for the system studied in terms of the system two-port transfer matrices throughout this thesis. The technique described below is based on phase co-ordinates[56] and is readily applicable for both steady-state and transient sustained fault analysis.

A3.1 Basic Principle of fault Simulation technique

When a fault occurs on one of the conductors of a 3-phase circuit, voltage at the fault point drops and current is fed to the fault from different parts of the circuit. The potential difference across the fault is equal to the voltage drop in the fault impedance, and if the fault impedance is zero, then the faulted-phase voltage drops to zero at the location of the fault. Therefore, the behaviour of the faulted conductor can simply be simulated by applying a hypothetical voltage source with a series impedance at the instant of fault inception. The e.m.f of this hypothetical source at any instant of time is equal and opposite to the prefault voltage at the point of fault and the series impedance of the

voltage source is equal to the fault impedance. Assuming that the circuit is under steady-state condition before the occurance of the fault the application of a fault can be better understood by considering Fig (A3.1). It can be seen from the Figure that two sources $+V_f$ and $+V_{ff}$ are connected in series with the fault impedance Z_f. The first hypothetical source ($+V_f$) is equal in magnitude and of the same polarity as the voltage at the location of the fault before the fault occurs. The connection of this source does not change the prefault circuit conditions. Before the occurance of fault, switch S_1 is closed (V_{ff} is short circuited). Under this condition no current flows into or out of the hypothetical branch, because the voltages balance at its terminals at any instant of time.

The application of fault is acheived by opening switch S_1 (switching V_{ff} into the circuit). The fault is therefore simulated by the hypothetical source (V_{ff}) in series with the fault impedance Z_f. Under such condition, V_{ff} balances $+V_f$ at every instant of time so that the voltage across the fault is equal to the product of the fault current multiplied by the fault impedance.

Voltages and currents at any point of the faulted circuit are obtained by solving the circuit of Fig (A3.1) by the principle of superposition [80] which is well recognised as a powerful tool for solving such problems. First, V_{ff} is short circuited by closing switch S_1, voltages and currents at any point of the circuit are obtained as if the hypothetical branch is opened. These voltages and currents are the prefault steady-state values since the connection of ($+V_f$) does not alter the assumed prefault steady-state conditions.

The second part of the solution is to obtain voltages and currents at any point in the circuit due to the fault, i.e. switch S_1 open. This is achieved by short circuiting all the sources in the circuit leaving their respective

impedances and the required voltages and currents are obtained when $+V_{ff}$ is the only e.m.f source present in the circuit.

The overall solution is therefore the sum of the above two mentioned solutions. In other words, under fault conditions, voltages and currents at any point in the circuit are the sum of voltage and current steady-state components plus voltage and current components due to the fault. It has to be emphasised that before the fault occurs, no current flows in the hypothetical branch and hence the current into the fault is due only to the application of the e.m.f source (V_{ff}). Voltages and currents at any point in the circuit after the occurance of the fault are called transient voltages and currents respectively. They are measured from the time of fault inception.

An alternative solution to the faulted circuit, under balanced or unbalanced faults, at the point of fault,may be acheived by replacing each hypothetical voltage source with its series impedance by its Thevenin-Norton's equivelant current source with its shunt admittance. The current source replacing an e.m.f source with infinite series impedance produces zero current and the total injected current to the line at the point of fault is the sum of all individual currents produced by the current sources connected to it.

The current source method may be advantageous over the e.m.f source method in case of faults involving fault impedances, otherwise the e.m.f source method is generally used.[56]

A3.2 Simulation of Unsymmetrical Faults

According to the simulation technique presented in section A3.1 simulation of unbalanced shunt faults are presented. For unbalanced faults, the

faulted phase or phases are represented by fictitious voltage source (s) in series with finite series impedance (s). The unfaulted phase or phases are represented by fictitious voltage source (s) in series with infinite impedance (s). For earth faults, the e.m.f of the hypothetical source (s) is equal and opposite to the prefault voltage to earth of the faulted phase(s) at the point of fault and the series impedance is the fault impedance connected between the conductor and earth. For phase faults, the hypothetical source e.m.f is equal and opposite to the line to line voltage between the faulted pair of phases before the fault occurs and its series impedance is the fault impedance between the pair of lines under consideration. It can be seen from the above that only the affected lines are fed from the hypothetical sources and therefore unbalanced energisation of the system is expected at the location of the fault.

A3.2.1 Single-line-to-earth faults

For single line-to-ground-faults, only the faulted phase fault impedance is finite and is replaced by a hypothetical voltage source (V_{ff}) in series with a series impedance = Z_{fa} as shown for an a-E fault in Fig (A3.2.b). The fault impedance between each unfaulted phase and the earth and each pair of unfaulted phases is infinite. This is shown in Fig (A3.2.b) by the open circuited hypothetical voltage sources.

The circuit of Fig (A3.2.b) for an a-E fault can be replaced according to Thevenin-Norton's theorem to the circuit of Fig (A3.2.c), in which the source current of all sources except the faulted phase source is zero. Accordingly, the following relations apply:

$$I_a = Y_{fa} \cdot V_{ffa}$$
$$I_b = 0 \times V_{ffb}$$
$$I_c = 0 \times V_{ffc}$$

in matrix form

$$\begin{bmatrix} I_a \\ I_b \\ I_c \end{bmatrix} = \begin{bmatrix} Y_{fa} & 0 & 0 \\ 0 & 0 & 0 \\ 0 & 0 & 0 \end{bmatrix} \begin{bmatrix} V_{ffa} \\ V_{ffb} \\ V_{ffc} \end{bmatrix} \quad \ldots\ldots \text{A3.1}$$

where

I_a, I_b, I_c = total injected currents due to the fictitious current sources to phases a, b, c respectively.

V_{ffa}, V_{ffb}, V_{ffc} = the e.m.f's of the fictitious sources connected between the earth and phases a, b, c respectively.

$Y_{fa} = 1/Z_{fa}$, where Z_{fa} = series impedance of the fictitious voltage source.

and for the a-E fault

$V_{ffa} = -V_{fa}$, $I_b = I_c = 0$

V_{fa} = prefault voltage to earth of phase a.

For general single-earth faults, the admittance matrix given in equation A3.1 is diagonal having only one element corresponds to the reciprocal value of the fault impedance to earth.[54,86]

A3.2.2 Double line-to-earth faults

Similar to the simulation of SLG faults, two line-to-earth faults (2LG) are simulated in Fig A3.3. Again, the fault impedances between the faulted pair of phases and between the unfaulted phase and earth are replaced by open circuited voltage sources. As the Figure shows a-b-E fault, all voltage sources involving phases a and b are switched on to the circuit i.e. V_{ffa}, V_{ffb}, V_{ffab} in series with Z_{fa}, Z_{fb}, Z_{fab} respectively as shown in Fig (A3.3.b). Similarly all current sources produce zero currents except that involving phases a and b, i.e. current sources I_{aO}, I_{bO} and I_{ab} in parallel with Y_{fa}, Y_{fb} and Y_{fab} respectively are switched on to the circuit.

From Fig (A3.3.c), at the point of fault:

$$I_a = I_{a0} + I_{ab}$$

$$= Y_{fa} \cdot V_{ffa} + Y_{fab} (V_{ffa} - V_{ffb})$$

$$I_a = V_{ffa} (Y_{fa} + Y_{fab}) - Y_{fab} \cdot V_{ffb}$$

similarly

$$I_b = I_{b0} - I_{ab}$$

$$I_b = Y_{fb} \cdot V_{ffb} - (V_{ffa} - V_{ffb}) Y_{fab}$$

$$= -Y_{fab} \cdot V_{ffa} + (Y_{fb} + Y_{fab}) V_{ffb}$$

$$I_c = 0$$

in matrix form

$$\begin{bmatrix} I_a \\ I_b \\ I_c \end{bmatrix} = \begin{bmatrix} (Y_{fa} + Y_{fab}) & -Y_{fab} & 0 \\ -Y_{fab} & (Y_{fb}+Y_{fab}) & 0 \\ 0 & 0 & 0 \end{bmatrix} \begin{bmatrix} V_{ffa} \\ V_{ffb} \\ V_{ffc} \end{bmatrix} \quad \ldots\ldots \text{A3.2}$$

Again equation A3.2 may represent a general 2 line-ground fault where the off-diagonal terms of the fault admittance matrix corresponds to the faulted conductors concerned take the values of the negated (phase-phase) impedance reciprocals, while the diagonal terms take the values of the sum of the reciprocal of the phase-earth and phase-phase impedances.

A3.2.3 Line-to-line faults

For line-line faults, the fault impedance between each line-to-earth and impedance between phases are infinite, except for the faulted phases. An a-b fault is shwon in Fig (A3.4). The fictitious e.m.f source V_{ffab} in series with its impedance Z_{fab} and the current source I_{ab} in parallel with the admittance Y_{fab} are the only sources that inject current to the line as shown from Fig (A3.4.b,c) respectively.

From Fig (A3.4.c), the following relations apply at the fault point:

$$I_a = I_{ab}$$

$$= Y_{ab} \ (V_{ffab}) \quad \text{and} \quad V_{ffab} = V_{ffa} - V_{ffb}$$

$$I_a = Y_{ab} \ (V_{ffa} - V_{ffb})$$

similarly

$$I_b = -I_{ab}$$

$$I_b = -Y_{ab} \ (V_{ffa} - V_{ffb})$$

and $I_c = 0$

In matrix form

$$\begin{bmatrix} I_a \\ I_b \\ I_c \end{bmatrix} = \begin{bmatrix} Y_{ab} & -Y_{ab} & 0 \\ -Y_{ab} & Y_{ab} & 0 \\ 0 & 0 & 0 \end{bmatrix} \begin{bmatrix} V_{ffa} \\ V_{ffb} \\ V_{ffc} \end{bmatrix} \qquad \ldots\ldots \text{A3.3}$$

From equation A3.3 it can be said that for general isolated faults, the off-diagonal terms of the fault admittance matrix corresponding to the faulted phases concerned take the values of the negated impedance reciprocals (phase-phase), while their diagonal terms take reciprocal values of the phase-phase fault impedances.[86]

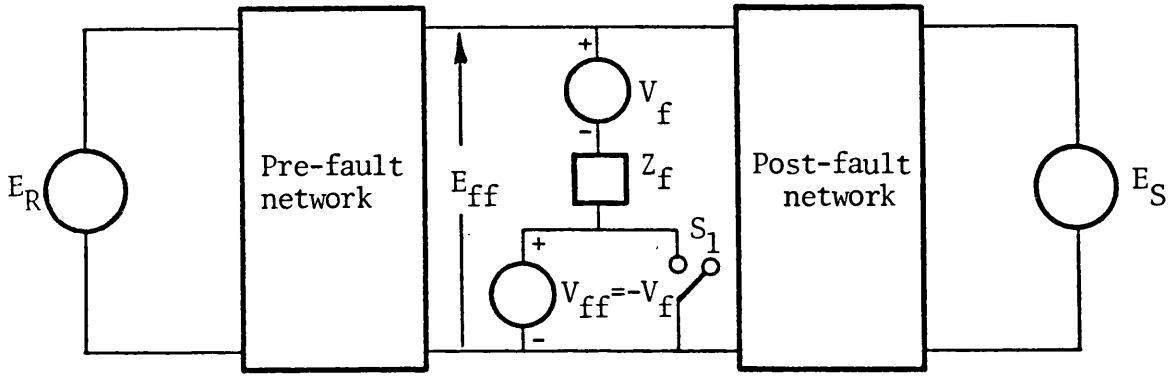

Fig A3.1

Fault simulation technique.

- S_1 close : system under steady-state conditions.
- S_1 open : system under fault conditions.

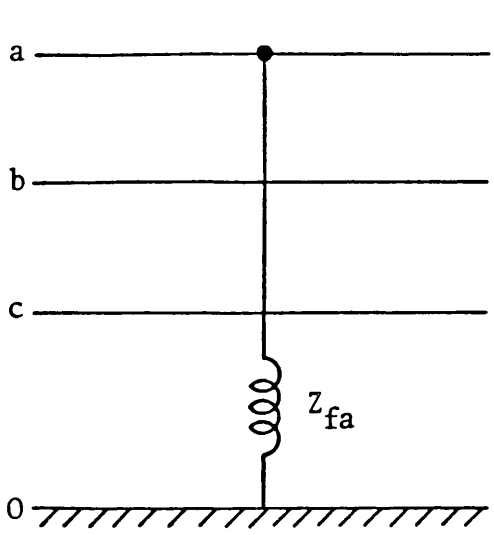

a - 'a-E' fault.

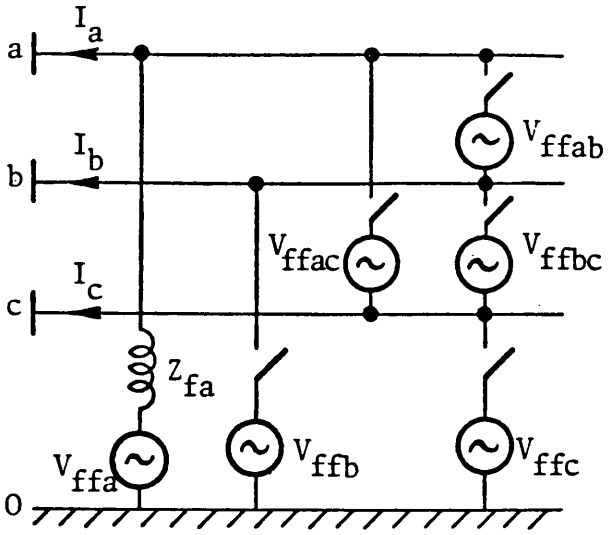

b - voltage sources in series with fault impedances.

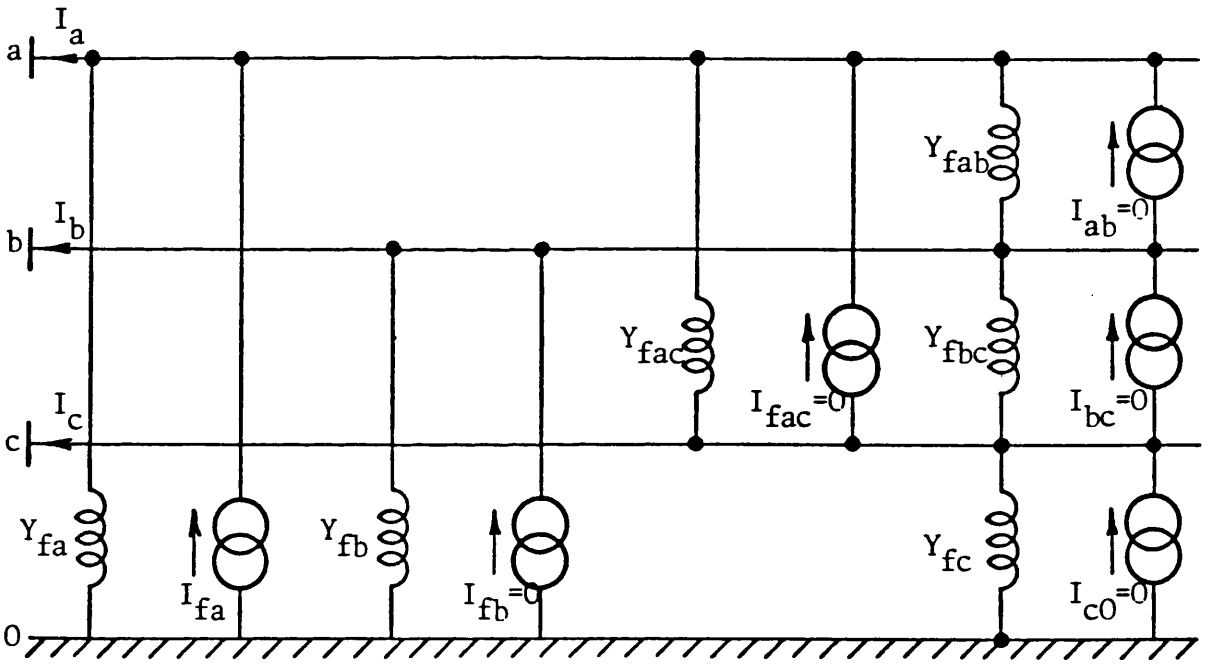

c - current sources in parallel with fault admittances.

Fig A3.2

Simulation of single line-to-ground faults (a-E).

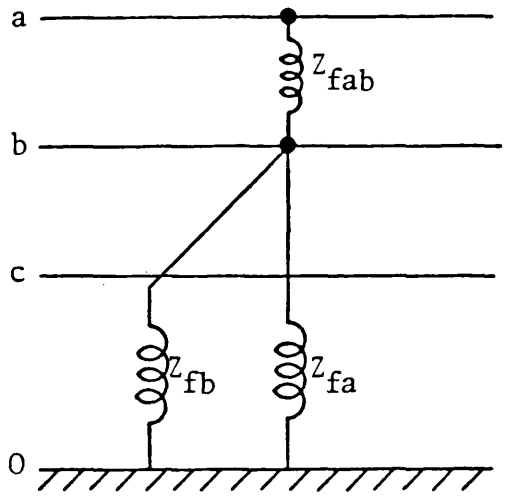

a - 'a-b-E' fault.

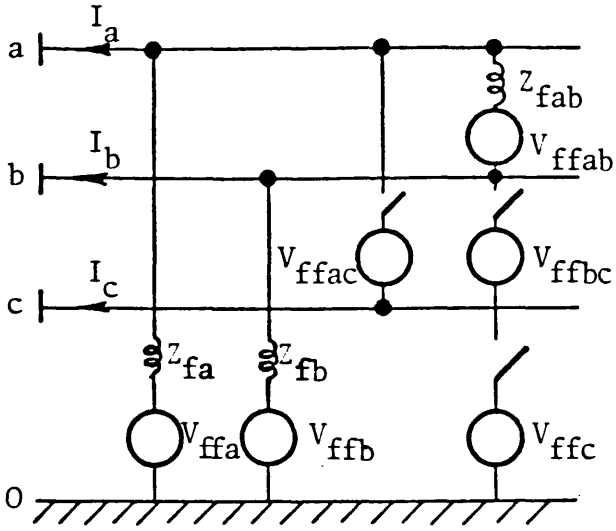

b - Voltage sources in series with fault impedances.

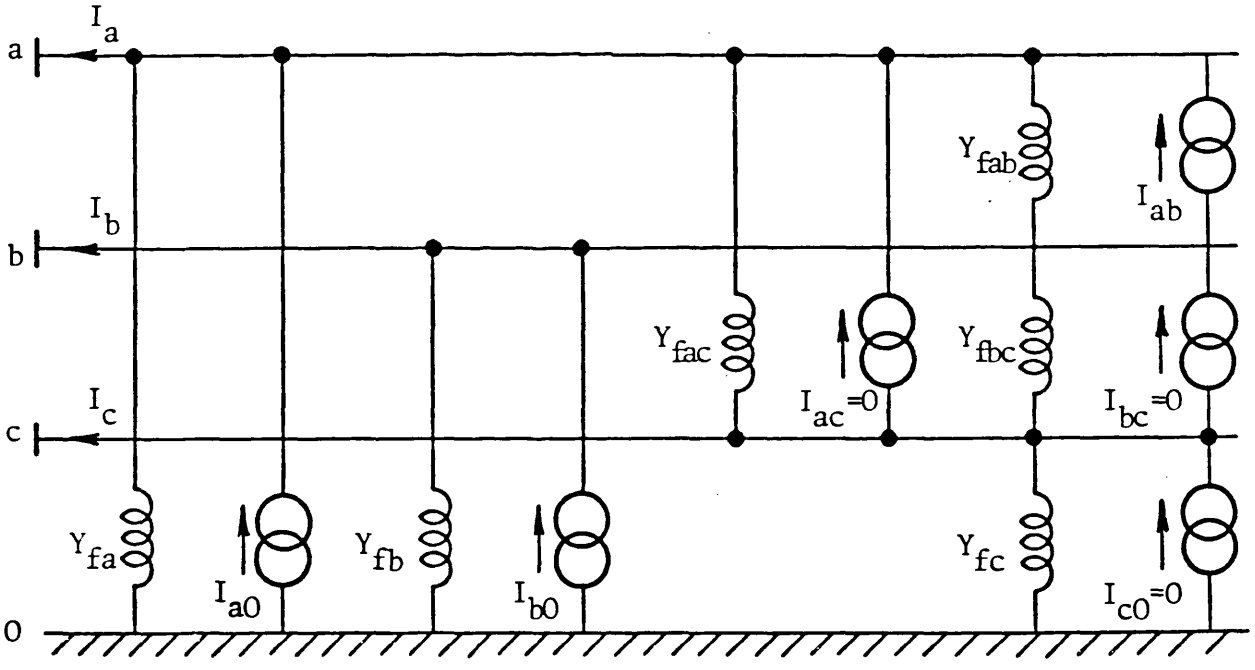

c - Current sources in parallel with fault admittances.

Fig A3.3

Simulation of double line-ground faults (a-b)

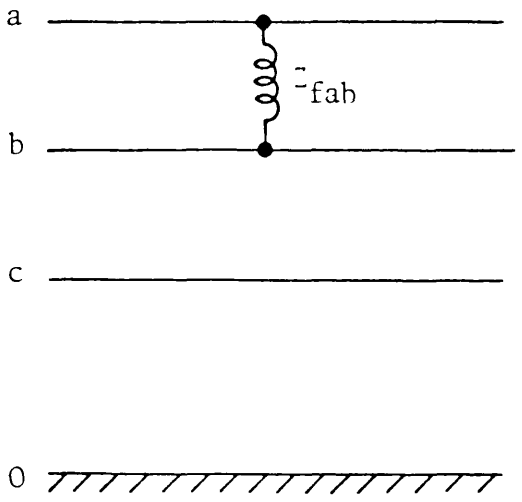

a - 'a-b' fault.

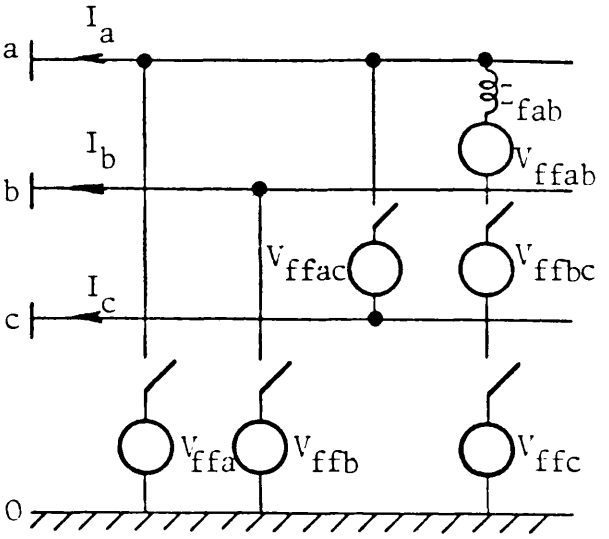

b - Voltage sources in series with fault impedances.

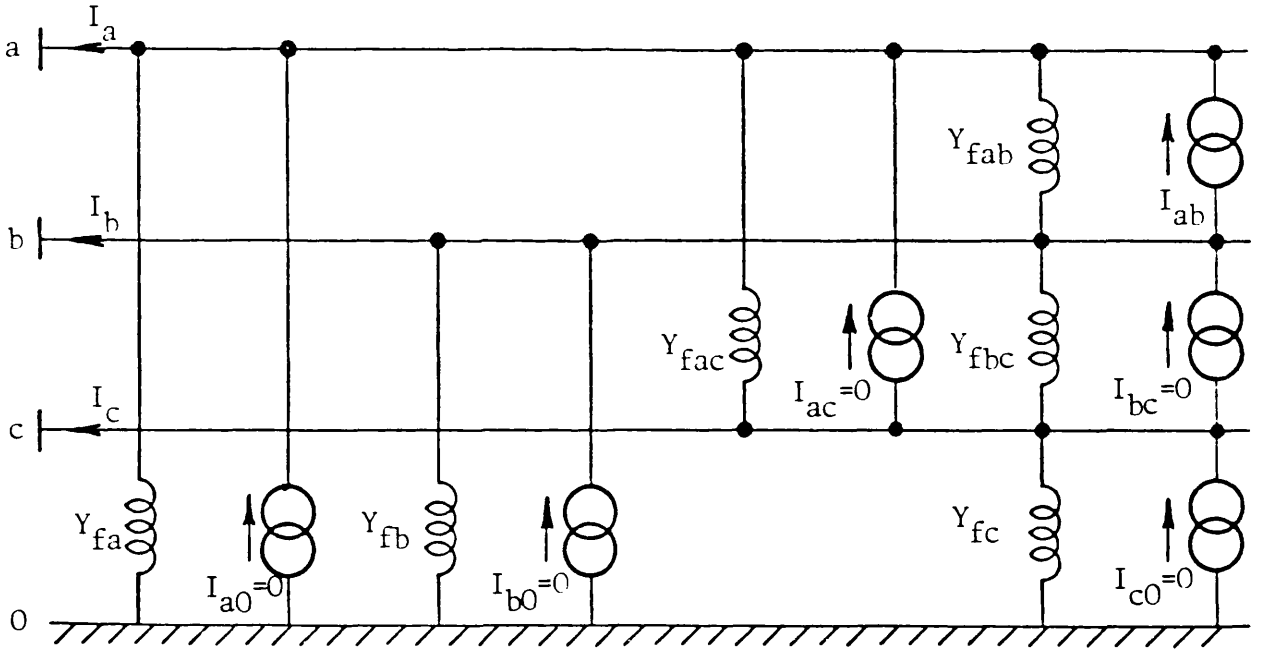

c - Current sources in parallel with fault admittances.

Fig A3.4

Simulation of line-to-line faults (a-b).

APPENDIX (A4)

EVALUATION OF TRANSMISSION LINE CHARTS [49]

A4.1 Steady-state Recovery Voltage Chart

For both charts, a factor 'k', named, capacitance ratio is required.

$$k = C_0/C_1$$

where: $C_0 = C_g$ A4.1

$C_1 = C_g + 3C_h$

as previously described in Chapter (2).

For the line construction considered, this ratio was shown to be (0.63), which is in complete agreement with that given by Kimbark[49] for a horizontal construction, 2 bundle/conductor line with 2-earth wires.

In recovery voltage chart, loci of constant values of 'V_{rpu}' plotted in rectangular co-ordinates of degrees of compensation (h_0, h_1) are straight lines. The points of Fig (5.2) and able (5.1) are evaluated as follows:

$$H_1 = (k.\ H_0) \ /\ f\ (V_{rpu}) \qquad \text{..... A4.2}$$

and

$$f(V_{rpu}) = \frac{1 + 2.\ V_{rpu}}{1 - V_{rpu}} \qquad \text{..... A4.3}$$

where :

$H_1 = 1 - h_1$, $H_0 = 1 - h_0$

V_{rpu} = per unit value of steady-state recovery voltage.

As may be seen from Fig (5.2), another set of straight lines appear. These lines are of constant reactor (X_0/X_1) ratio. For example, for unearthed reactor banks, $X_0 = \infty$, and the corresponding locus is the horizontal axis according to equation A4.4.

$$h_1 = kh_0 \, (X_0/X_1)$$

and $$dh_0/dh_1 = 1/k(X_0/X_1) \qquad \text{..... A4.4}$$

where:

$\frac{dh_0}{dh_1}$ = slope of any constent reactance ratio lines in Fig (5.2).

For Y connected reactors with solidly earthed neutral, $X_0 = X_1$, i.e. $X_0/X_1 = 1.0$. In this case the slope of this line is equal to (1/k), and is shown by the dotted line BE of Fig (5.2). If the neutral is earthed through an inductance X_n, its working region will be between $X_0/X_1 = \infty$ and $X_0/X_1 = 1$, i.e. between the horizontal axis and line BE. In some cases the lines compensated may require a capacitance[49] (c_n) in the neutral instead of (X_n). These lines occupy the area below the horizontal axis. It might be also seen from Fig (5.2), that point 'B' ($h_1 = h_0 = 0$) represents the uncompensated line. It has also to be noticed that any point along line 'ACD' represents a completely neutralized line inter-phase capacitance, i.e. no recovery voltage nor secondary arc current as will be shown in section A4.2. However, degrees of shunt compensation may be chosen some where along this line but away from point 'A'. This is because taking $h_1 = h_0 = 1$, may lead to some sort of series resonance which ultimately may result in a very high voltage between the faulted phase and the earth. Similar resonance conditions may arise any where along the line marked ($V_{rpu} = \infty$). Line 'BE' is the locus for a 3-reactor scheme (the neutral is solidly earthed). It is parallel to 'AC'. As may be seen from Fig (5.2) the recovery voltage increases as one proceeds along the line. Its value is always higher than it would be if the correct neutral reactor is used. Point 'E' represents a resonance case which occurs at $h_1 = (2+k)/3$. For the line under consideration this occurs at $h_1 \tilde{=} .876$.

A4.2 Secondary Arc Current Chart

The second family of straight lines, representing residual fault current, are parallel and have positive slope. Loci of constant values of current as a function of degrees of shunt compensation (h_1, h_0) were plotted as shown in Fig (5.3).

Each number of points constituting one of the straight lines of Fig (5.3) are calculated as follows:[49]

$$H_1 = k H_0 - 3 I_{rpu} \quad \text{..... A4.5}$$

where :

I_{rpu} = the permit value of the secondary arc current based on the PPS charging current of the line.

The slope dh_1/dh_0 is

$$\frac{dh_1}{dh_0} = 1/k \quad \text{..... A4.6}$$

The family of straight lines intercept the horizontal axis at $(1 - k + 3 I_{rpu})$ and their interception with the vertical axis is $(K - 1 - 3 I_{rpu})/k$.

Equation A4.5 was used to get the family of straight lines of Fig (5.3).

Refering to Fig (5.3), positive signs of 'I_{rpu}' means that the residual current is in phase with the line charging current. The same thing applies to Fig (5.2), i.e. positive signs of V_{rpu} means that the recovery voltage is in phase with the normal phase-to-earth voltage.

Transmission line charts are dealt with in more detail in reference (49), where all the equations presented are derived.

APPENDIX (A5) DIGITAL SIMULATION OF RELAY MIXING CIRCUITS

A5.1 Basic Considerations

The performance of distance relays is affected by the response of the auxiliary circuits used in deriving the necessary relaying signals. Therefore, adequate simulation of the transient response of the mixing circuits is essential in an investigation of this nature.

The relaying signals that are compared in a static phase-angle comparator to produce the polarised mho characteristics are of the well known form:[57,92]

$$S_1 = I_L Z_r - V_L$$
$$S_2 = V_L + VP \qquad \text{..... A5.1}$$

The current derived component of equation A5.1 is usually derived by passing the compensated current through a transformer reactor[92] (transactor), while the polarising voltage component (VP) is derived from healthy phase or phases. A better understanding of how the two voltage components are derived may be achieved from the following examples:[53,93]

1- For a residually compensated a-E relay, equation A5.1 becomes:

$$S_1 = (I_a + kI_{res.}) Z_r - V_a$$
$$S_2 = V_a + kP_{e.} V_{bc} \qquad \text{..... A5.2}$$

where:

k = residual compensating factor

$= \frac{1}{3} (|ZL_0/ZL_1| - 1)$

ZL_0, ZL_1 = ZPS and PPS line impedances respectively.

$KP_e = |K_p| \angle 90^o$ = sound phase polarising voltage constant.

$I_{res.}$ = residual current at current transformer secondaries.

I_a, I_b, I_c = currents in phases a, b and c at the current transfprmer secondaries respectively.

V_a, V_b, V_c = voltage of phases a, b, c respectively at the secondaries of voltage transformers.

Z_r = current replica impedance.

2 - For a pure b-c phase fault, equation A5.1 becomes

$$S_1 = (I_b - I_c)\, Z_r - V_{bc}$$
$$S_2 = V_{bc} + KP_p .\, V_a \qquad \text{..... A5.3}$$

where

$$KP_p = |KP_p| \angle -90^o$$

Equations A5.2, A5.3 are a commonly used method for deriving the polarised voltage component and is the one used in the course of this work. A two-stage 90^o phase-shift circuit necessary to ensure co-phasal relaying and polarising components during healthy conditions has been used and is examined in detail together with the transformer reactor circuit in the following sections.

When considering transient characteristics of distance protection, it is necessary to examine the time variation of signals S_1 and S_2 of equation A5.1. For an a-E fault, the general form of the two signals is:

$$S_1 = f_1 [i_a(t) + k\, i_{res}(t)] - V_a(t)$$
$$S_2 = V_a(t) + f_2 [V_{bc}(t)] \qquad \text{..... A5.4}$$

Apparently equation A5.4 shows that the function of the current derived component in signal S_1, i.e. $f_1 [i_a(t) + ki_{res}(t)]$ is dependent on the method used to realise the replica impedance 'Z_r'.For example an arrangement in which the compensated current is passed through a series combination of resistance and inductance has a different transient response from that of a parallel resistance-inductance-transformer reactor arrangement.[57,92] Also equation A5.4 shows that the function $f_2 [V_{bc}(t)]$ is dependent on the method used to phase-shift the sound-phase voltage.

Signals S_1 and S_2 are compared in a coincidence circuit[92] producing

standard output pulses which are positive unity when S_1 and S_2 are of the same polarity and zero when they are of opposite polarity. The pulses are applied to an integrating circuit whose output increases linearly during the time when the pulse is positive unity and falls at the same rate when the pulse is zero. The final element in the relay is a level detector which switches when the integrator output exceeds some preset value and resets when the output falls below some second value. A ratio of set to reset voltage of two for the level detector has been taken, and so the absolute minimum operating time of each of the six principle fault-type relays is one half cycle of power frequency.

The basis of the method of digitally simulating the transient response of the relays hings upon sampling the simulated relay signals at regular intervals (which has been oftenly 0.125 ms, throughout this work), to determine when the signals are simultaneously of like polarity and exceed the pick up or setting voltage level.

A5.2 Responses of Voltage and Current Transformers

Primary system wave forms presented in Chapters (6), (7) show that under some fault conditions low frequency current components are produced. It is the duty of modern high-speed static comparators that saturation effects can be avoided and hence exponential and other low frequency components that appear in the primary current are faithfully reproduced as scaled values in the current transformer secondaries.[57] Also under some fault conditions, particularly fault inception time, it was observed that high frequency current components are produced in the system primary current. However, WRIGHT[94] has shown that any high-frequency components present in the primary current of a transformer will be satisfactorily transformed. Furthermore, the author indicated that the accuracy of reproduction of high frequency components is higher than that obtained at the nominal power-system frequency

particularly for predominantly resistive burdens. In this respect, it has to be mentioned that in modern schemes of distance protection, transformer-reactor arrangement is usually employed. Since the latter has an equivalent circuir of a parallel resistor-inductor arrangement, the majority of high frequency current components pass effectively through the resistive branch, and the resulting current transformer burden for high frequency components is therefore mainly resistive. Therefore, in order to correctly simulate the current transformer secondary currents, it is necessary when evaluating sysrem currents to include components in the spectrum up to 10 kHz.[57] This frequency is obviously much higher than the truncation frequency encountered in the primary system response presented in Chapters (6), (7) and thus the current transformer secondary currents are realistically simulated.

As far as the voltage transformers are concerned, all significant frequencies in the spectrum of the voltages appear at their secondary terminals and, again, a truncation frequency of 10 kHz, when computing primary system voltages, is sufficient for a true indication of the performance. In the course of present work, however, when simulating the primary system voltages, only frequencies up to the c.v.t high frequency cutoff-point (3dB) examined have been included when the time variation of voltages were evaluated using the inverse Fourier transform. Scalling down the voltage wave forms obtained (according to the nominal V.T. turns ratio) yields the voltages that would appear at the secondary of the high-fidelity c.v.t., with a frequency response of the idealised low pass type.[57]

A5.3 Simulation of Transformer-Reactor Arrangement

Due to the non-periodic nature of the current-transformer secondary current, it is necessary to adopt a step-by-step approach to evaluate the two input signals. In order to simulate the voltages developed by the transformer-reactor replica impedance circuits, the following procedure is followed:

According to the equivalent circuit of the transformer-reactor referred to the primary shown in Fig (A5.1.a), and by neglecting the burden of the comparator and mixing circuits we have:

$$\frac{V_0(t)}{N} = i_p(t).R_T = L_T \cdot \frac{di_q}{dt}(t) \qquad \text{..... A5.5.a}$$

and

$$i_L(t) = i_p(t) + i_q(t) \qquad \text{..... A5.5.b}$$

where

L_T, R_T = referred magnetising inductance and resistance of transformer reactor.

Differentiating equation A5.5.b we get:

$$Pi_L(t) = Pi_p(t) + Pi_q(t) \qquad \text{..... A5.5.c}$$

where

$$P = \frac{d}{dt}$$

$\therefore$ From equation A5.5.a

$$V_0(t) = N \cdot i_p(t).R_T = N.L_T.Pi_q(t)$$

or

$$P.V_0(t) = N.Pi_p(t).R_T$$

substituting the value of $Pi_p(t)$ from equation A5.5.c

$$\therefore \quad PV_0(t) = N.R_T.(Pi_p(t) - Pi_q(t))$$

But from A5.5.a, $Pi_q(t) = \frac{V_0(t)}{N.L_T}$, substituting in the above equation

$$\therefore \quad PV_0(t) = N.R_T\left(Pi_L(t) - \frac{V_0(t)}{N.L_T}\right)$$

$$\therefore \quad PV_0(t) = N.R_T\, Pi_L(t) - \frac{R_T}{L_T} \cdot V_0(t)$$

$$\therefore \quad V_0(t) = N.L_T\, Pi_L(t) - \frac{L_T}{R_T} \cdot PV_0(t)$$

or

$$V_0(t) + \frac{L_T}{R_T} \cdot \frac{dV_0(t)}{dt} = N.L_T.\frac{di_L(t)}{dt} \quad \text{..... A5.6}$$

where

N = Ratio of secondary to primary turns on transformer reactor.

V_L = Relaying voltage at voltage transformer secondaries.

I_L = Relaying current - at current transformer secondaries.

V_0 = Output voltage of transformer-reactor.

Equation A5.6 can be evaluated using step-by-step techniques in which the compensated current input is sampled at a rate of $1/\Delta T$, where ΔT is the time interval between current or voltage samples.

In terms of sampled values taken at times $t_n = n\Delta T$, $t_{n-1} = (n-1)\Delta T$, after the process is commenced, the output voltage and input current at time $t_x = (n - \frac{1}{2})\,\Delta T$ may be written as:

$$V_0(t_x) = [V_0(t_n) + V_0(t_{n-1})]/2$$

$$\therefore \frac{dV_0(t_x)}{dt} = [V_0(t_n) - V_0(t_{n-1})]/\Delta T \quad \text{..... A5.7}$$

and

$$\frac{di_L(t_x)}{dt} = [i_L(t_n) - i_L(t_{n-1})]/\Delta T \quad \text{..... A5.8}$$

Substituting equations A5.7 and A5.8 into equation A5.6, the output voltage of the transformer reactor at a time t_n is:

$$V_0(t_n) = \frac{\left[\frac{N.L_T}{\Delta T}\,[i_L(t_n) - i_L(t_{n-1})] - V_0(t_{n-1})\left[\frac{1}{2} - \frac{L_T}{R_T.\Delta T}\right]\right]}{\left(\frac{1}{2} + \frac{L_T}{R_T.\Delta T}\right)} \quad \text{..... A5.9}$$

At power frequency, the replica impedance Z_r is given as the output voltage divided by the input current as:

$$Z_r = \frac{V_O}{i_L} = \frac{V_O}{\dfrac{(V_{O/N}) \cdot R_T + JW_O L_T}{R_T \cdot JW_O \cdot L_T}}$$

or A5.10

$$Z_r = \frac{J N W_O L_T . R_T}{R_T + JW_O . L_T}$$

From equation A5.10

$$|Z_r| = \frac{N W_O L_T . R_T}{\sqrt{R_T^2 + W_O^2 L_T^2}} = \frac{N . R_T}{\sqrt{1 + \tan^2 \angle Z_r}} \quad \text{..... A5.11}$$

and $\angle Z_r = \tan^{-1} R_T / W_O L_T$ A5.11

Substituting equation A5.11 into equation A5.9, the output voltage can be written in an alternative form as:

$$V_O(t_n) = \left[2 |Z_r| \sec \angle Z_r \left[i_L (t_n) - i_L (t_{n-1}) \right] - V_O(t_{n-1}) \left[W_O \Delta T - \text{Cot} \angle Z_r \right] \right] / (W_O . \Delta T + \text{Cot} \angle Z_r)$$

..... A5.12

A5.4 Simulation of Polarising phase-shift circuits

From the polarising phase-shift circuit of Fig A5.1.b, we have:

$$V_S(t) = V_{C2}(t) + V_{C1}(t) + V_O(t) \quad \text{..... A5.13.a}$$

Double-differentiating equation A5.13.a w.r.t time

$$\therefore \frac{d^2}{dt^2} V_S(t) = \frac{d^2 V_{C2}(t)}{dt^2} + \frac{d^2 V_{C1}(t)}{dt^2} + \frac{d^2 V_O(t)}{dt^2} \quad \text{..... A5.13.b}$$

But from Fig A5.1.b

$$i_1(t) = C_P \frac{d V_{C1}(t)}{dt}, \quad i_2(t) = C_P \frac{d V_{C2}(t)}{dt} \quad \text{..... A5.13.c}$$

and the voltage drop across $R_P = V_{RP}(t) = R_P (i_1(t) - i_2(t))$

multiplying equation A5.13.b by C_P and substituting the values of $i_1(t)$ and $i_2(t)$ given in equation A5.13.c:

$$\therefore C_P \frac{d^2 V_S(t)}{dt^2} = \frac{di_1(t)}{dt} + \frac{di_2(t)}{dt} + C_P \frac{d^2 V_O(t)}{dt^2} \quad \text{..... A5.14.a}$$

Also from equation A5.13.c and Fig A5.1.b we have:

$$V_{RP} = (i_1 - i_2)\ R_P = V_{C2}(t) + V_O(t)$$

Differentiating the above equation we get:

$$\frac{di_1(t)}{dt} = \frac{1}{R_P}\left[\frac{dV_{C2}(t)}{dt} + \frac{dV_O(t)}{dt}\right] + \frac{di_2(t)}{dt} \qquad \text{..... A5.14.b}$$

and

$$V_O(t) = i_2(t).R_P \qquad \text{..... A5.14.c}$$

substituting equation A5.14.c into A5.14.b

$$\therefore \frac{di_1(t)}{dt} = \frac{1}{R_P}\left[\frac{dV_{C2}(t)}{dt} + R_P\ \frac{di_2(t)}{dt}\right] + \frac{di_2(t)}{dt}$$

$$= \frac{1}{R_P}\left[\frac{i_2(t)}{C_P} + R_P \cdot \frac{di_2(t)}{dt}\right] + \frac{di_2(t)}{dt}$$

$$= \frac{1}{R_P}\left[\frac{V_O(t)}{R_P.C_P} + \frac{dV_O(t)}{dt}\right] + \frac{dV_O(t)}{R_P.dt}$$

$$\therefore \frac{di_1(t)}{dt} = \frac{V_O(t)}{R_P^2.C_P} + 2 \cdot \frac{dV_O(t)}{dt.R_P} \qquad \text{..... A5.15}$$

Substituting equation A5.15 into equation A5.14.a, and substitute $dV_O(t) = R_P.\ di_2(t)$

$$\therefore C_P \frac{dV_S^2}{dt^2} = \frac{V_O(t)}{R_P^2.C_P} + 2\ \frac{dV_O(t)}{R_P.dt} + \frac{dV_O(t)}{R_P.dt} + CP.\ \frac{d^2V_O(t)}{dt^2}$$

or

$$C_P \cdot \frac{dV_S^2}{dt^2} = \frac{V_O(t)}{C_P.R_P^2} + 3\ \frac{dV_O(t)}{R_P.dt} + CP \cdot \frac{d^2V_O(t)}{dt^2} \qquad \text{..... A5.16}$$

Intograting equation A5.16, we get:

$$C_P.\ \frac{dV_S(t)}{dt} = \frac{1}{C_P.R_P^2} \int V_O(t)\ dt + \frac{3}{R_P} \cdot V_O(t) + C_P.\ \frac{dV_O(t)}{dt} + K$$

..... A5.17

where K = constant of integration.

Solving equation A5.17 at two instants of time, i.e. $t_x = (n - \frac{1}{2})\Delta T$ and $t_y = (n + \frac{1}{2})\Delta T$, respectively, so that on substitution, the constant of integration K is eliminated

$$\therefore \; C_P \left[\frac{dV_S(t_y)}{dt} - \frac{dV_S(t_x)}{dt} \right] = \frac{1}{C_P.R_P^2} \int_{t_x}^{t_y} V_O(t)\, dt + \frac{3}{R_P} \left[V_O(t_y) - V_O(t_x) \right] + C_P \left[\frac{dV_O(t_y)}{dt} - \frac{dV_O(t_x)}{dt} \right] \quad \ldots\ldots \text{A5.18}$$

Assuming piecewise linearisation between samples of the input voltage, the following relationships are obtained:

$$\frac{dV_S(t_y)}{dt} = \left[V_S(t_{n+1}) - V_S(t_n) \right] / \Delta T$$

$$\frac{dV_S(t_x)}{dt} = \left[V_S(t_n) - V_S(t_{n-1}) \right] / \Delta T$$

$$V_O(t_y) = \left[V_O(t_{n+1}) + V_O(t_n) \right] / 2 \quad \ldots\ldots \text{A5.19.a}$$

$$V_O(t_x) = \left[V_O(t_n) + V_O(t_{n-1}) \right] / 2$$

$$\frac{dV_O(t_y)}{dt} = \left[V_O(t_{n+1}) - V_O(t_n) \right] / \Delta T$$

$$\frac{dV_O(t_x)}{dt} = \left[V_O(t_n) - V_O(t_{n-1}) \right] / \Delta T$$

and

$$\int_{t_x}^{t_y} V_O(t)dt = \int_{(n-1)\Delta T}^{(n+1)\Delta T} V_O(t)dt$$

$$\therefore \int_{t_x}^{t_y} V_O(t)dt = \left[\frac{V_O(t_{n-1})}{2} + 3\, V_O(t_n) + \frac{V_O(t_{n+1})}{2} \right] \cdot \frac{\Delta T}{4} \quad \ldots\ldots \text{A5.19.b}$$

substituting equation A5.19 into equation A5.18, yields the step-by-step solution for the polarising circuit output voltage of the form:

$$V_O(t_{n+1}) = V_O(t_{n-1}) + \left[\frac{C_P}{\Delta T} \left[V_S(t_{n-1}) - 2\, V_S(t_n) + V_S(t_{n+1}) \right] \right] - \left[\frac{3\Delta T}{4.C_P.R_P^2} + 2\, \frac{C_P}{\Delta T} \cdot V_O(t_n) \right] / \left[\frac{3}{2R_P} + \frac{\Delta T}{8C_P R_P^2} + \frac{C_P}{\Delta T} \right] \quad \ldots\ldots \text{A5.20}$$

Equation A5.20 can be simplified by taking into account that in order to obtain the required phase shift (90^{o}) at power frequency, the circuit parameters must be such that $R_P = \frac{1}{W_O \cdot C_P}$, substituting into equation A5.20

$$\therefore \quad V_O(t_{n+1}) = V_O(t_{n-1}) + \left[V_S(t_{n-1}) - 2\ V_S(t_n) + V_S(t_{n+1}) - \left[\frac{3\ W_O^2 \cdot \Delta T^2}{4} + 2 \right] V_O(t_n) \right] \Big/ \left[1 + \frac{3.W_O\ \Delta T}{2} + \frac{W_O^2\ \Delta T^2}{8} \right]$$

..... A5.21

It can be seen from equations A5.12 and A5.21 that in order to start the step-by-step process, a value for the initial output voltage in both cases must be available. This was achieved by starting computation during the prefault period, during which time an initial value can be calculated from the steady-state sinusoidal system response. It has to be noticed that when phase-fault-relays are simulated, where the healthy-phase voltage is to be shifted by (-90^{o}), the derived component is subtracted from the relaying voltage and the precise level of polarisation required is obtained by utilising the approximate proportion of the total output of the phase-shift circuit.

The algorithms given by equations A5.12 and A5.21 have been tested for accuracy purposes by comparing the outputs obtained when the input is subjected to a variety of analythical wave forms such as a wave form with exponential, power frequency, and high frequency components. In all cases, it was found that, practically, there is no difference between the output voltages obtained using the analythical expressions and those obtained using the step-by-step techniques developed, using a sampling interval

ΔT = 0.125 ms.

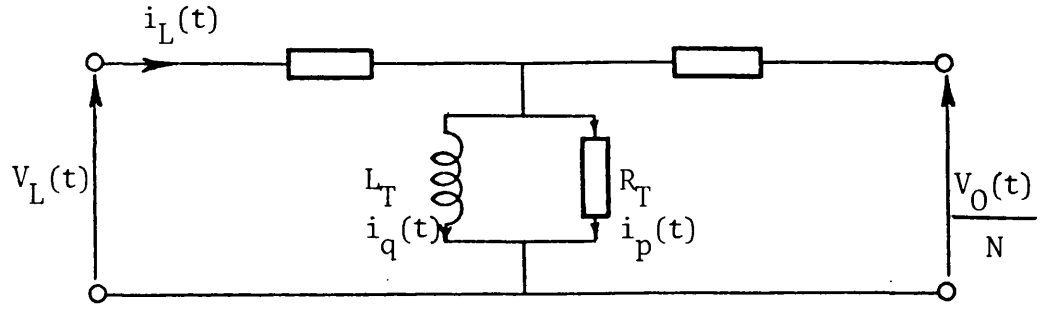

(a)

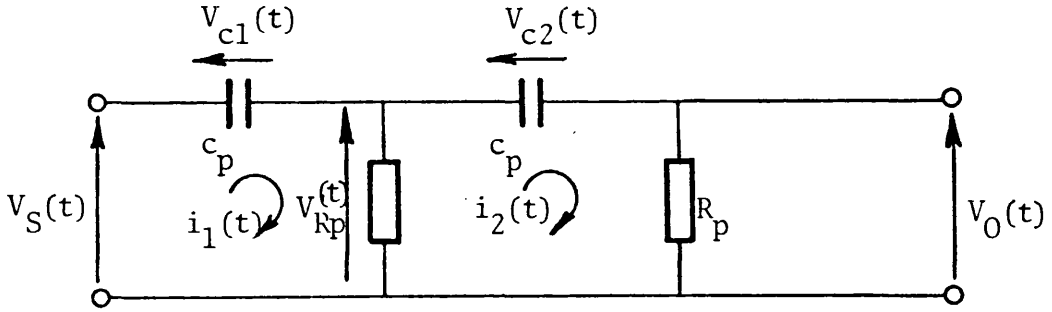

(b)

Fig A5.1

Transformer-reactor and phase shift circuits.

a - transformer reactor arrangement (referred to the primary).

b - Polarising phase-shift circuit.

APPENDIX (A6) EVALUATION OF PROTECTIVE RELAY PARAMETERS

It has been shown that it is commonly necessary to place replica impedances in the secondary of the current transformers in order to develop the relaying signal S_1 given by equation A5.1. The best form of replica impedance, which is often used, is the transformer reactor[57] whose modified circuit is given in Fig (A5.1.a). It is essentially an air gap transformer whose circuit originally is as shown in Fig (A6.1.a). R_b is a burdning resistance so that neglecting the secondary winding reactance (which is relatively low because of the air gap), yields the equivalent circuit of Fig (a6.1.b), from which,

$$\acute{R}_b = \frac{R_b}{N^2}$$

$$\frac{V_O}{\acute{V}_O} = N \;,\; V_O = N \times \acute{V}_O$$

But $$\frac{\acute{V}_O}{I} = \acute{Z}_r = \frac{JX_m.R_b/N^2}{JX_m + R_b/N^2}$$

or $$\acute{Z}_r = \frac{JR_b.X_m}{R_b + JX_m.N^2}$$

$$\therefore \quad \acute{Z}_r = \frac{JX_m \cdot R_b}{N^2(JX_m + R_b/N^2)} \qquad \text{..... A6.1.a}$$

where $\acute{Z}_r$ is the replica impedance referred to the primary,

and $$\angle\acute{Z}_r = \tan^{-1} R_b/N^2.X_m \qquad \text{..... A6.1.b}$$

$$|\acute{Z}_r| = \frac{R_b \cdot X_m}{\sqrt{R_b^2 + X_m^2 N^4}} = \frac{X_m}{\sqrt{1 + N^4.X_m^2/R_b^2}}$$

$$\therefore \; \acute{Z}_r = \frac{X_m}{\sqrt{1 + \frac{X_m^2}{(R_b/N^2)^2}}} = \frac{X_m}{\sqrt{1 + \text{Cot}^2\phi T}}$$

where $\tan \phi T = R_b/N^2 X_m$, $\text{Cot}\ \phi T = \dfrac{N^2 \cdot X_m}{R_b}$

$$\therefore \quad \text{Cot}^2\ \phi T = \frac{N^4\ X_m^{\ 2}}{R_b^{\ 2}} = \frac{X_m^{\ 2}}{(R_b/N^2)^2}$$

$$\therefore \quad |\acute{Z}_r| = \frac{X_m}{\sqrt{1 + \text{Cot}^2\ \phi T}} \qquad \text{..... A6.1.c}$$

But $$\frac{Z_r}{Z_r'} = \frac{N^2}{1}$$

$$\therefore \quad |Z_r| = N^2\ |\acute{Z}_r|$$

substituting $\acute{Z}_r$ from equation (A6.1.c)

$$\therefore \quad |Z_r| = N^2 \cdot \frac{X_m}{\sqrt{1 + \text{Cot}^2\ \phi T}} \qquad \text{..... A6.2.a}$$

where:

Z_r is the replica impedance at the secondary of the transactor.

The relaying signal produced by the transactor is therefore:

$$S_1 = IZ_r - V_a$$

or in its transduced form

$$S_1 = N_c \cdot IZ_r - N_v \cdot V_a \qquad \text{..... A6.2.b}$$

where:

N_c , N_v are the turns ratio of C.T and V.T respectively.

In terms of $\acute{Z}_r$, S_1 becomes

$$S_1 = N_c . I\ N^2\ \acute{Z}_r - N_v\ V_a$$

$$\text{or} \quad \frac{S_1}{I.N_v} = \frac{N_c.N^2}{N_v} \cdot \acute{Z}_r - \frac{V_a}{I}$$

$$\text{or} \quad \acute{S_1} = \frac{N_c.N^2}{N_v} \cdot \acute{Z}_r - \frac{V_a}{I}$$

If S_1 is zero, $\acute{S_1}$ also yields to zero, and

$$Z_r = \frac{N_c}{N_v} \cdot N^2 \cdot Z_r' \qquad \text{..... A6.2.c}$$

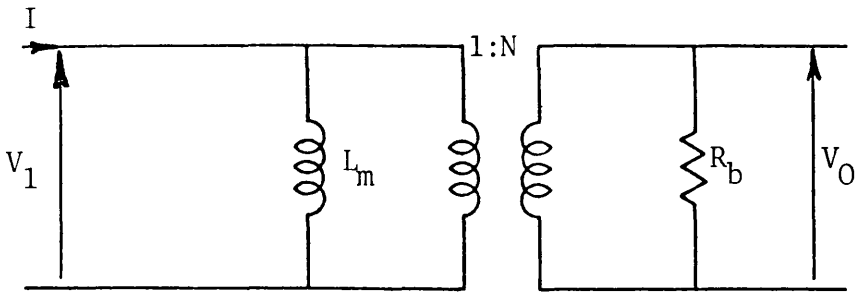

(a)

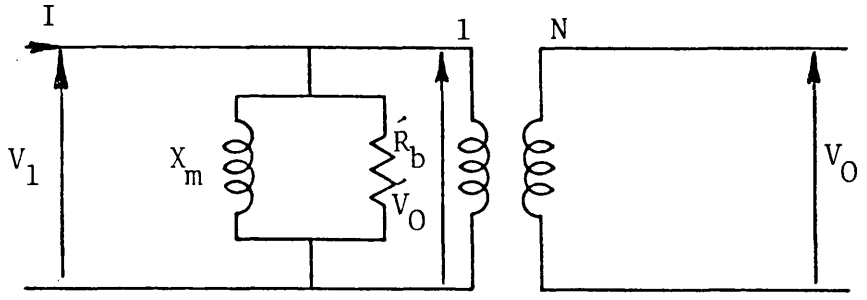

(b)

Fig A6.1

Simple transformer-reactor equivalent circuit.

a - Original circuit.

b - equivalent circuit referred to the primary.

APPENDIX (A7) EVALUATION OF MEASUREMENT ACCURACY OF RELAYS APPLIED TO 3-REACTOR COMPENSATED SYSTEMS

From Fig (A7.1), a solid a-E fault occurs at the far end of the line, and,

$$i_{a2} = \frac{V_a}{Z_{L1}+Z_m} = V_a/Z_S$$

$$\because \quad I_a = i_{a1} + i_{a2} = \frac{V_a}{jX_1} + \frac{V_a}{Z_S} = \frac{V_a(Z_S + jX_1)}{jX_1 \cdot Z_S}$$

The impedance seen by the sending end relay is:

$$Z_r = V_a/(I_a + k\, I_{res.})$$

$$= \frac{V_a}{V_a \left[(Z_S + jX_1)/(Z_S.jX_1) \right] + k.I_{res.}}$$

But, $I_{res.} = I_a+I_b+I_c = \frac{V_a}{Z_S} + \frac{V_a+V_b+V_c}{jX_1}$

or $I_{res.} \simeq \frac{V_a}{Z_S}$

$$\therefore \quad Z_r = \frac{V_a}{V_a\,(Z_S + jX_1)/(Z_S.jX_1) + k.V_a/Z_S}$$

substituting $k = \frac{1}{3} \left[(Z_{LO}/Z_{L1}) - 1 \right]$

$$\therefore \quad Z_r = \frac{1}{\left[(Z_S+jX_1)/(Z_S.jX_1) \right] + \frac{1}{3.Z_S}\left(\frac{Z_{LO}}{Z_{L1}} - 1\right)}$$

Where $Z_{LO} = Z_S + 2\,Z_m$, $Z_{L1} = Z_S - Z_m$

Substituting in the above equation yields;

$$Z_r = \frac{3.Z_{L1}}{(Z_{L1}/jX_1) + 3} \qquad \text{..... A7.1}$$

$\therefore$ For a non compensated system $jX_1 = \infty$ and the impedance Z_r yields the

line PPS impedance Z_{L1}.

For any degree of shunt compensation (h_1), X_1 will have a certain value and therefore 'Z_r' in this case will be definitely less than the PPS impedance 'Z_{L1}'. Thus the impedance seen by the relay is less than 'Z_{L1}' and the relay tends to overreach. The computational results presented in Chapter (9) also confirm this finding, see Table (9.6.a).

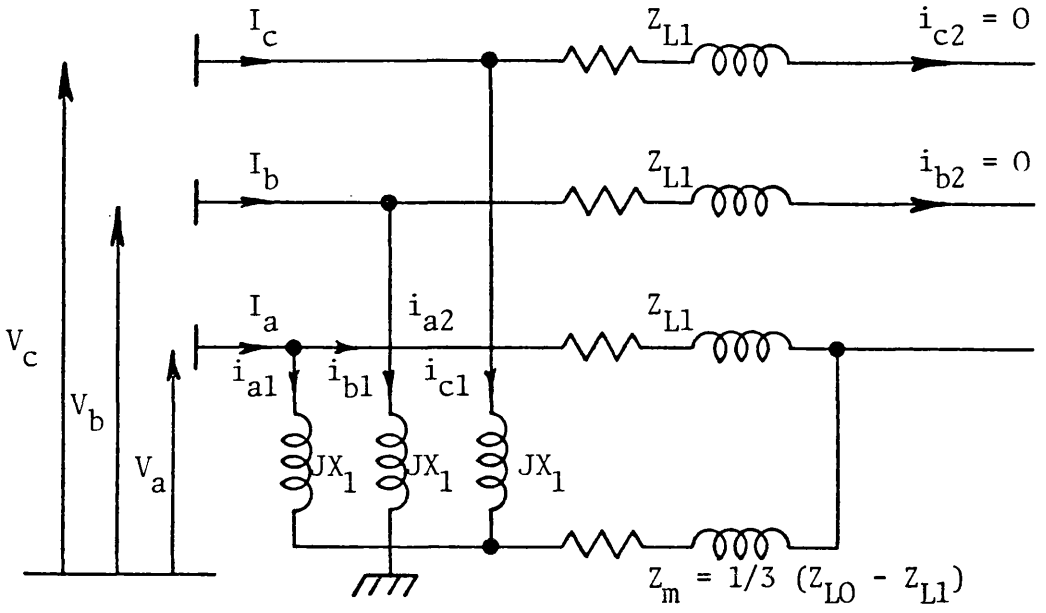

Fig A7.1

Solid 'a-E' fault at the far end of a 3-reactor compensated system.

APPENDIX (A8) PUBLISHED WORK

Some of the work developed in this thesis has been published and is presented in this appendix.

Performance of distance protection of e.h.v. feeders utilising shunt-reactor arrangements for arc suppression and voltage control

A.T. Johns., B.Sc., Ph.D., C.Eng., M.I.E.E., M. El-Nour., M.Sc., and R.K. Aggarwal, B.Eng., Ph.D., C.Eng., M.I.E.E.

Indexing terms: *Transmission-line theory, Relays, Waves*

Abstract: Digital techniques for modelling the faulted response of any arbitrary linear shunt-reactor compensated e.h.v. transmission-line system are described. The methods are specifically developed to meet the requirements of offline or programmable test-equipment-based feeder-protection studies. The essential differences in the faulted response of single and 3-section feeders are established by reference to 500 kV interconnections involving 4-reactor linear shunt compensators. An extensive study of modern distance protection applied to various feeder configurations is reported and the paper concludes with an evaluation of protection performance in a typical sectionalised interconnector of length 550 km.

List of principal symbols

$l_1, l_2, .. l_n$ = line lengths of feeder having n sections
L = length of faulted line section
x = distance to fault
$l_{S1}, l_{S2} .. l_{S(n-1)}$ = line lengths of sending-end composite source
$l_{R1}, l_{R2} .. l_{R(n-1)}$ = line lengths of receiving-end composite source
C_1, C_0 = p.p.s. and z.p.s. shunt capacitance per unit length of assumed ideally transposed line
h_1, h_0 = degree of p.p.s. and z.p.s. shunt compensation
B_{L1}, B_{L0} = magnitude of p.p.s. and z.p.s. inductive susceptance of shunt reactor bank at nominal system frequency $(1/\omega_0 L_1, 1/\omega_0 L_0)$
B_{C1}, B_{C0} = magnitude of p.p.s. and z.p.s. capacitive susceptance of any line section at nominal system frequency, assuming ideal transposition $(\omega_0 C_1 l, \omega_0 C_0 l)$
Z_p, Z_n = phase and neutral impedances of shunt reactor bank
L_1, L_0 = p.p.s. and z.p.s. inductance of shunt reactor bank
ω_0 = nominal system angular frequency
ω = angular freqnecy
l = any line length l_1, l_2, etc.
$\bar{V}, \bar{I}$ = voltage and current transforms
U = unit matrix
Q = voltage eigenvector matrix
γ = modal propagation constant matrix
ψ = $Q\gamma Q^{-1}$
Z_0 = $Y_0^{-1} = Q\gamma^{-1}Q^{-1}Z$ = polyphase surge impedance metrix
Z = series-impedance matrix per unit length of line
Y = shunt-admittance matrix per unit length of line
$\bar{V}_i, \bar{V}_r$ = incident and reflected voltage transforms
Z_S, Z_R = sending- and receiving-end main-source impedance matrices
Z_{SS}, Z_{SR} = sending- and receiving-end composite-source impedance matrices
s.c.l. = short-circuit level
S_1, S_2 = general form of relaying signals
V_L = relaying voltage at voltage transformer (v.t.) secondaries
I_L = relaying current at current transformer (c.t.) secondaries
Z_r = current replica impedance
V_P = sound-phase polarising voltage
Z_{S0}/Z_{S1} = ratio of z.p.s. to p.p.s. impedance of main source
0 = null matrix

Subscripts

a, b, c = phases a, b, c
t = transpose of matrix

1 Introduction

The use of shunt compensation for voltage control in long distance a.c. transmission feeders is a long established technique[1] and recent years have seen increasing worldwide interest in the use of various static shunt reactor devices[2] as an alternative to rotating synchronous compensators. In the case of static reactors, it is common to use an essentially balanced 3-phase set of reactors which are directly connected to the transmission line or are connected to the system via transformers situated at various points along a complete interconnection.[3] Until quite recently, very little had been reported on the performance of distance protection applied in such situations. However, a study by Fielding *et al.*[4] revealed that the performance of a distance relay incorporating the extensively used block-average comparator arrangement,[5] although satisfactory, was nevertheless modified somewhat when applied to a relatively

Paper 906C, first received 22nd February and in revised form 7th July 1980

The authors are with the Power Systems Laboratory, School of Electrical Engineering, University of Bath, Claverton Down, Bath BA2 7AY, England

0143-7046/80/05304 + 13 $01·50/0

simple single-section shunt compensated lumped parameter laboratory model system.[6]

The work reported in Reference 4 was confirmed to a consideration of distance relay performances in a system utilising 3-phase static shunt-reactor compensation of the linear and saturable types. However, where single-pole autoreclosure is involved, it is commonly necessary to employ essentially linear 4-reactor arrangements in order to aid the rapid extinction of secondary arcs and thereby permit satisfactory reclosure following transient faults.[7,8] In such arrangements, the main reactors are usually connected in star with the common points connected to earth through a neutral reactor, the parameters of which are dependent on arc extinction times sought, the line parameters and the degree of steady-state positive sequence reactive compensation effected by the three main reactors.[9] Despite the fact that single-pole autoreclosure is being increasingly applied globally, the state of knowledge of typical modern high-speed distance protection, even during the initial measuring prefault clearance period, is even more limited than that relating to applications involving 3-reactor shunt compensation. This paper therefore represents an attempt to rectify the latter deficiency.

It is important to note that, quite apart from any effect the alternative reactor arrangements may have on relay performances, the transmission-system configuration itself can significantly affect distance relay performances.[10] In particular, the lower apparent frequencies of the travelling-wave induced components which arise in long line applications are generally more troublesome because they can fall within the bandwidth of the protective relays and signal transducers and thereby more significantly affect performance.[11] Furthermore, long distance shunt-compensated feeders are often sectionalised with protection connected at the termination of each section, so that, even for faults close to a particular relay, the travelling-wave components may still possess a relatively low apparent frequency. In general, it is therefore to be expected that, irrespective of the precise nature of the protective relays used, the variation of distance protection performance with system configuration is likely to be very marked in long shunt compensated sectionalised arrangements. The first objective of this paper is therefore to outline the basis of primary-system digital-simulation techniques which have been developed with the foregoing considerations in mind and which have been designed to be sufficiently flexible to enable a larger variety of protection gear application studies to be performed using offline or real-time programmable test facilities than has hitherto been possible. In order to obtain maximum realism, the frequency variance of all line and earth parameters is simulated,[12] together with the effect of discrete conductor transpositions as commonly used in long distance transmission systems.

The second main objective is to report the salient features of an extensive offline study of the performance of typical crosspolarised mho relays utilising the block-average principle[5,14] when applied to interconnectors involving the use of horizontally constructed 500 kV lines. The results of a general study involving single-section and 3-section arrangements are presented and the effect of the degrees of compensation and feeder configurations on both speed and accuracy of the relays is established. The paper concludes with a consideration of the performance of distance relays connected at the various locations along a typical 3-section feeder arrangement operating at specific loading and compensation levels.

2 Basic system model

As mentioned previously, long shunt-compensated feeders are often sectionalised with protection and reactor banks situated at either end of each section. From a protection point of view, it is particularly important to be able to simulate faults on any feeder section and to determine the primary system faulted responses at the points to which protective gear is connected. Earlier digital-simulation methods developed for studying distance relay performances on relatively simple essentially homogeneous uncompensated feeders[12] are clearly not directly applicable in such cases, but they nevertheless form a very useful basis for the methods reported in this paper.

Particular emphasis has been placed on providing a simulation which is sufficiently flexible for determining the response of a feeder consisting of an arbitrary number of sections n. Fig. 1 shows the basic arrangement considered and it is evident that a simulation of faults on the first section will involve a solution of an entirely different set of mathematical functions to those involved when simulating faults on one of the other sections. The mathematical procedures and associated digital computer programs necessary to provide a realistic simulation of faults on single feeder sections[12] are in themselves somewhat lengthy and

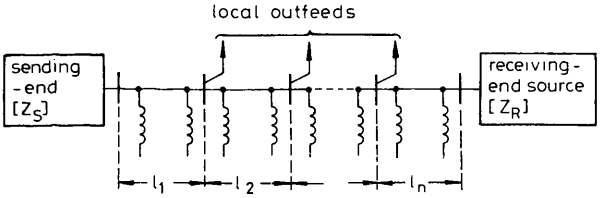

Fig. 1 *Basic system model*

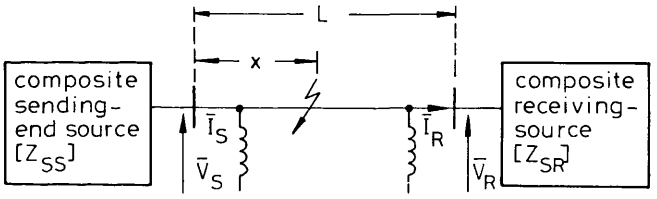

Fig. 2 *Equivalent system model*

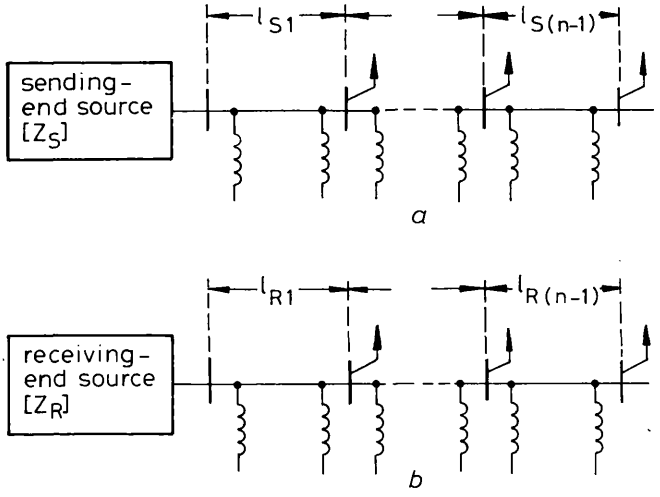

Fig. 3 *Composite source networks*

a Sending end
b Receiving end

involved, and it has been necessary to ensure that such problems are not compounded to the extent that, in computing terms, a rather intractable solution results. With this very important factor in mind, the complete arrangement of Fig. 1 is first reduced to the equivalent circuit shown in Fig. 2. A composite equivalent source is connected at each end of the line section on which it is desired to simulate a fault, the schematic arrangements of the latter being shown in Figs. 3*a* and *b* for the sending and receiving ends, respectively.

It is easily verified that, in order to simulate faults anywhere on an n-section system, each composite source must possess at least $(n-1)$ line sections. The line-length data can then be specified in accordance with the requirements of a given study so as to fix the section on which it is desired to simulate a fault. For example, a fault on the midsection of a three-section feeder ($n = 3$) is simulated by specifying the line-length data such that

$$l_1 = l_{S1}, \quad l_2 = L, \quad l_3 = l_{R1}, \quad l_{S2} = l_{R2} = 0$$

Alternatively, a fault on the line adjacent to the sending-end source of the same basic system would be simulated by putting $l_{S1} = l_{S2} = 0, l_1 = L, l_2 = l_{R1}, l_3 = l_{R2}$.

3 Fundamental relationships

3.1 Simulation of shunt-reactor banks

Fig. 4 shows the circuit of the four-reactor arrangement considered. Although the line sections to which such reactors are connected are not in practice ideally transposed, it is nevertheless common to assume ideal transposition when determining the inductive parameters of the reactors. This is the approach followed here so that, in terms of the positive-phase-sequence (p.p.s.) and zero-phase-sequence (z.p.s.) values of the line shunt capacitance (C_1, C_0), the parameters of the shunt-reactor bank when arranged to compensate one half of any line section of length l are as given in eqn. 1:

$$\left.\begin{aligned} h_1 &= B_{L1}/B_{C1} = 2/(\omega_0^2 L_1 C_1 l) \\ h_0 &= B_{L0}/B_{C0} = 2/(\omega_0^2 L_0 C_0 l) \end{aligned}\right\} \quad (1)$$

There are a number of factors which determine the degrees of shunt compensation (h_0, h_1), and for a typical line

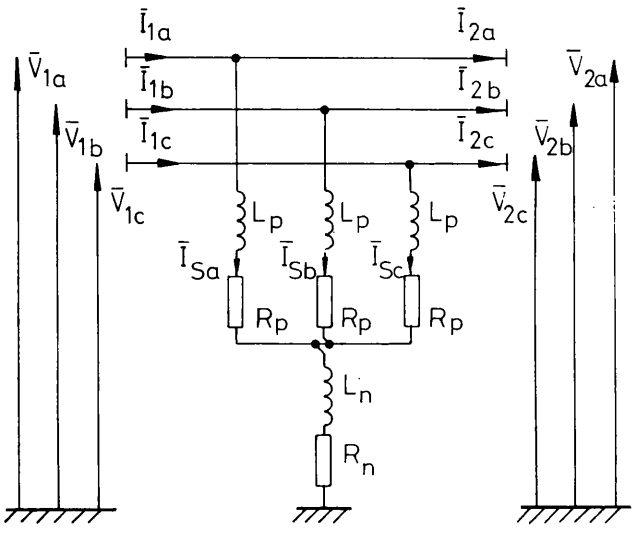

Fig. 4 *Shunt reactor arrangement*

they generally lie between extremes of zero and 1·2.[7-9] The line shunt capacitances (C_1, C_0) are evaluated in the usual manner from an average sum of all the conductor self and mutual capacitances per unit length of the line section under consideration. It is evident from Fig. 4 that the p.p.s. inductance of the reactor bank L_1 is equal to the inductance per phase and that the z.p.s. inductance $L_0 = (L_p + 3L_n)$. It follows from eqn. 1 that the phase and neutral parameters of the reactor bank are as given in eqn. 2.

$$\left.\begin{aligned} L_p &= L_1 = 2/(\omega_0^2 h_1 C_1 l) \\ L_n &= 2(h_1 C_1 - h_0 C_0)/(3\omega_0^2 h_0 h_1 C_0 C_1 l) \end{aligned}\right\} \quad (2)$$

The resistances R_P and R_n are relatively very low, a typical Q factor of each limb at nominal system frequency (power frequency) being 250. If suitable test data were acquired, it would be possible to include any significant frequency variance of the shunt-reactor parameters. However, resort to this degree of complexity is of somewhat questionable value in view of the fact that, for distance protective gear evaluation, it is only the components in the spectrum of a disturbance up to about 2 kHz which are of greatest relevance.[10] Reactor impedances consistent with constant values of R_p, R_n, L_p and L_n, as defined in eqn. 3 were therefore used in the course of this work.

$$\left.\begin{aligned} Z_p &= R_p + j\omega L_p = \frac{2}{\omega_0 h_1 C_1 l}\left\{\frac{1}{250} + j\frac{\omega}{\omega_0}\right\} \\ Z_n &= R_n + j\omega L_n = \frac{2(h_1 C_1 - h_0 C_0)}{3\omega_0 h_0 h_1 C_0 C_1 l}\left\{\frac{1}{250} + j\frac{\omega}{\omega_0}\right\} \end{aligned}\right\} \quad (3)$$

It is convenient ultimately to combine the shunt-reactor arrangements with the line sections involved and for this purpose the canonical form of the two port or transfer matrix function defining the arrangement of Fig. 4 (eqn. 4) is particularly useful.

$$\begin{bmatrix} \bar{V}_1 \\ \bar{I}_1 \end{bmatrix} = \begin{bmatrix} U & 0 \\ Y_s & U \end{bmatrix} \begin{bmatrix} \bar{V}_2 \\ \bar{I}_2 \end{bmatrix} \quad (4)$$

The difference of the current vectors $[\bar{I}_1 - \bar{I}_2]$ defines the current which flows in the reactor $[I_S]$ and the latter is seen to be simply related to the impedance matrix $[Z_s] = [Y_s]^{-1}$ of the shunt reactor by eqn. 5.

$$\begin{bmatrix} \bar{V}_{2a} \\ \bar{V}_{2b} \\ \bar{V}_{2c} \end{bmatrix} = [Z_s]\,[I_s]$$

$$= \begin{bmatrix} Z_p + Z_n & Z_n & Z_n \\ Z_n & Z_p + Z_n & Z_n \\ Z_n & Z_n & Z_p + Z_n \end{bmatrix} \begin{bmatrix} \bar{I}_{Sa} \\ \bar{I}_{Sb} \\ \bar{I}_{Sc} \end{bmatrix} \quad (5)$$

The submatrix $Y_s = [Z_s]^{-1}$ which is used in the transfer matrix representation of the reactor is thus as given in eqn. 6.

$$[Y_S] = [Z_S]^{-1} = \frac{1}{Z_p(Z_p + 3Z_n)} \times$$

$$\begin{bmatrix} Z_p + 2Z_n & -Z_n & -Z_n \\ -Z_n & Z_p + 2Z_n & -Z_n \\ -Z_n & -Z_n & Z_p + 2Z_n \end{bmatrix} \tag{6}$$

3.2 Simulation of discretely transposed line sections

In long distance transmission systems, discrete transposition of the line conductors is often performed at the termination of each section or at intermediate points thereon. It is particularly important to simulate the effect of such transpositions, because they represent an abrupt point of discontinuity from which incident wave components are partially reflected. In consequence, it is to be expected that the transient components in distance relaying measurands will be affected. Fig. 5 shows a very common transposition arrangement which has been simulated in the course of this work. Although this has been drawn only for the faulted section of the source and line model of Fig. 2, the same transposition arrangements have been used to describe the unfaulted lines within each composite source of Fig. 3.

It has been found useful initially to compute the matrices describing each homogenous length of line so that they are uniquely ordered in accordance with the conductor positions (a, b, c) on the homogeneous section adjacent to the sending end S. For a midsection fault as shown, the transfer matrices describing the section between the fault point F and the receiving end R are given by matrix equations 7.[12]

$$\begin{bmatrix} \bar{V}_f \\ \bar{I}_{fR} \end{bmatrix} = \begin{bmatrix} A_{2f} & B_{2f} \\ C_{2f} & D_{2f} \end{bmatrix} \begin{bmatrix} \bar{V}_{R2} \\ \bar{I}_{R2} \end{bmatrix}, \begin{bmatrix} V_{S3} \\ \bar{I}_{S3} \end{bmatrix} \times \begin{bmatrix} A & B \\ C & D \end{bmatrix} \begin{bmatrix} \bar{V}_{R3} \\ \bar{I}_{R3} \end{bmatrix} \tag{7}$$

where

$$A_{2f} = \cosh\{\psi(2L/3 - x)\}, \quad B_{2f} = \sinh\{\psi(2L/3 - x)\}Z_0,$$
$$C_{2f} = Y_0 B_{2f} Y_0, \quad D_{2f} = Y_0 A_{2f} Z_0$$

and

$$A = \cosh\{\psi L/3\}, \quad B = \sinh\{\psi L/3\}Z_0,$$
$$C = Y_0 B Y_0, \quad D = Y_0 A Z_0$$

The polyphase propagation constant matrix ψ is obtained by using the voltage eigenvector matrix Q to transform the system steady-state voltage differential eqn. 8 into a series of uncoupled differential equations of the form of eqn. 9.[12, 13]

Now the products $Q^{-1} \exp(\pm \psi x) Q$ define exponents involving the modal propagation constant $\gamma(\exp(\pm \gamma x))$, and it follows from matrix function theory that ψ is computed at all frequencies in the spectrum of interest as the product $Q \gamma Q^{-1}$.

$$\frac{d^2 \bar{V}}{dx^2} = ZY\bar{V} \tag{8}$$

$$Q^{-1}\bar{V} = Q^{-1} \exp(-\psi x) Q Q^{-1} \bar{V}_i + Q^{-1} \exp(\psi x) Q Q^{-1} \bar{V}_r \tag{9}$$

Combination of eqns. 7 to form a total line transfer matrix between points F and R can be achieved by introducing a transposing matrix M which effects the necessary transpositions by relating the vectors $[\bar{V}_{R2}\ \bar{I}_{R2}]^t$, $[\bar{V}_{S3}\ \bar{I}_{S3}]^t$. The transposing matrix is simply deduced by noting the previously mentioned manner in which the vectors in eqns. 7 have been ordered, i.e.

$$\begin{bmatrix} \bar{V}_{R2} \\ \bar{I}_{R2} \end{bmatrix} = [\bar{V}_{R2c}\bar{V}_{R2a}\bar{V}_{R2b}\bar{I}_{R2c}\bar{I}_{R2a}\bar{I}_{R2b}]^t$$

$$\begin{bmatrix} \bar{V}_{S3} \\ \bar{I}_{S3} \end{bmatrix} = [\bar{V}_{S3b}\bar{V}_{S3c}\bar{V}_{S3a}\bar{I}_{S3b}\bar{I}_{S3c}\bar{I}_{S3a}]^t$$

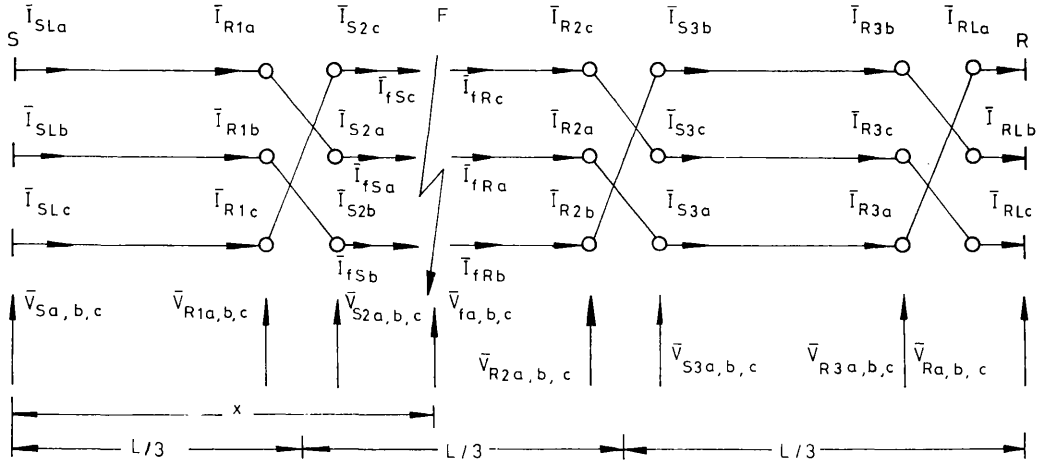

Fig. 5 *Discretely transposed line model*

Matrix $[M]$ is therefore as given in eqn. 10, so that the overall line transfer matrix between points F and R is given by eqn. 11.

$$\begin{bmatrix} \bar{V}_{R2} \\ \bar{I}_{R2} \end{bmatrix} = [M] \begin{bmatrix} \bar{V}_{S3} \\ \bar{I}_{S3} \end{bmatrix} \tag{10}$$

$$\begin{bmatrix} \bar{V}_f \\ \bar{I}_{fR} \end{bmatrix} = \begin{bmatrix} A_{2f} & B_{2f} \\ C_{2f} & D_{2f} \end{bmatrix} [M] \begin{bmatrix} A & B \\ C & D \end{bmatrix} [M] \begin{bmatrix} \bar{V}_R \\ \bar{I}_{RL} \end{bmatrix}$$

$$= \begin{bmatrix} A_{L2} & B_{L2} \\ C_{L2} & D_{L2} \end{bmatrix} \begin{bmatrix} \bar{V}_R \\ \bar{I}_{RL} \end{bmatrix} \tag{11}$$

where $[M] = \begin{bmatrix} T & 0 \\ 0 & T \end{bmatrix}$ and $[T] = \begin{bmatrix} 0 & 1 & 0 \\ 0 & 0 & 1 \\ 1 & 0 & 0 \end{bmatrix}$

By a similar approach, the line-transfer matrix linking points F and S is obtained from eqn. 12.

$$\begin{bmatrix} \bar{V}_f \\ -\bar{I}_{fS} \end{bmatrix} = \begin{bmatrix} A_{1f} & B_{1f} \\ C_{1f} & D_{1f} \end{bmatrix} [M]^{-1} \begin{bmatrix} A & B \\ C & D \end{bmatrix} \begin{bmatrix} \bar{V}_S \\ -\bar{I}_{SL} \end{bmatrix}$$

$$= \begin{bmatrix} A_{L1} & B_{L1} \\ C_{L1} & D_{L1} \end{bmatrix} \begin{bmatrix} \bar{V}_S \\ -\bar{I}_{SL} \end{bmatrix} \tag{12}$$

where

$$A_{1f} = \cosh\{\psi(x - L/3)\},$$
$$B_{1f} = \sinh\{\psi(x - L/3)\}Z_0,$$
$$C_{1f} = Y_0 B_{1f} Y_0,$$
$$D_{1f} = Y_0 A_{1f} Z_0$$

Exactly similar methods are likewise used to describe the overall transfer matrices between the fault point and the sending and receiving ends for faults on the first or third homogeneous sections of the discretely transposed line model of Fig. 5. Furthermore, in the case of an unfaulted section of any length l within the composite sources, the line transfer matrix between ends will be given by eqn. 13.

$$\begin{bmatrix} \bar{V}_S \\ \bar{I}_{SL} \end{bmatrix} = \left[\begin{bmatrix} A_l & B_l \\ C_l & D_l \end{bmatrix} [M] \right]^3 \begin{bmatrix} \bar{V}_R \\ \bar{I}_{RL} \end{bmatrix} \tag{13}$$

where

$$A_l = \cosh\{\psi l/3\},$$
$$B_l = \sinh\{\psi l/3\}Z_0,$$
$$C_l = Y_0 B_l Y_0,$$
$$D_l = Y_0 A_l Z_0$$

3.3 Combination of line and shunt reactor banks

For computational purposes, it is convenient to combine the line sections with the shunt reactors in the manner illustrated in Fig. 6 to form a line/reactor equivalent circuit. The situation at the receiving end is seen to be such that the vectors $\bar{I}_{RL} = \bar{I}_1$ and $\bar{I}_2 = \bar{I}_R$. It follows directly from the previously developed relationships of eqns. 4 and 11 that

$$\begin{bmatrix} \bar{V}_f \\ \bar{I}_{fR} \end{bmatrix} = \begin{bmatrix} A_{L2} & B_{L2} \\ C_{L2} & D_{L2} \end{bmatrix} \begin{bmatrix} \bar{V}_R = \bar{V}_1 \\ \bar{I}_{RL} = \bar{I}_1 \end{bmatrix}$$

$$= \begin{bmatrix} A_{L2} + B_{L2} Y_s & B_{L2} \\ C_{L2} + D_{L2} Y_s & D_{L2} \end{bmatrix} \begin{bmatrix} \bar{V}_2 = \bar{V}_R \\ \bar{I}_2 = \bar{I}_R \end{bmatrix}$$

$$= \begin{bmatrix} A_2 & B_2 \\ C_2 & D_2 \end{bmatrix} \begin{bmatrix} \bar{V}_R \\ \bar{I}_R \end{bmatrix} \tag{14}$$

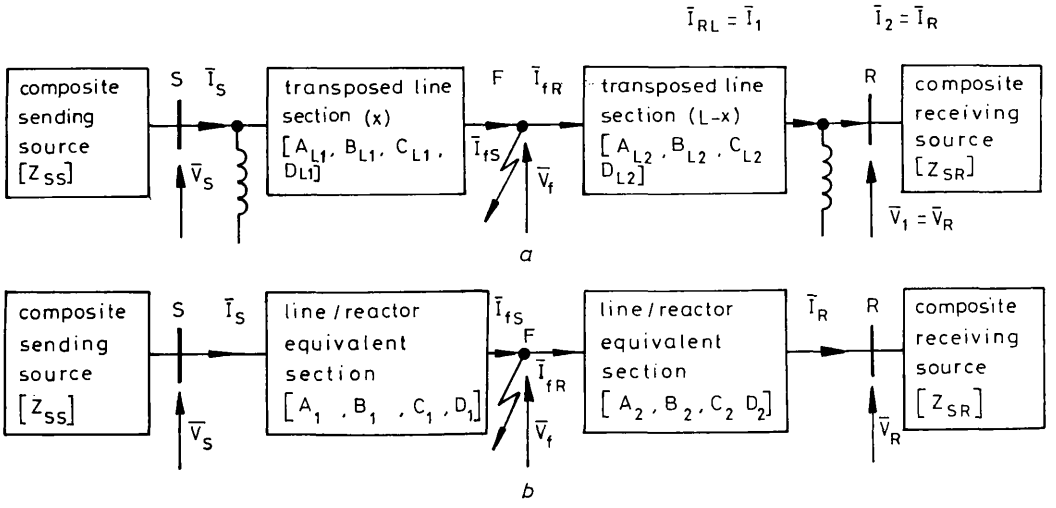

Fig. 6 *Combination of line and shunt-reactor banks*

a Actual arrangement
b Equivalent arrangement

The transfer matrix eqn. 13 which describes the equivalent line/reactor section linking points F and S is likewise derived from eqns. 4 and 12.

$$\begin{bmatrix} \bar{V}_f \\ -\bar{I}_{fS} \end{bmatrix} = \begin{bmatrix} A_{L1} + B_{L1} Y_s & B_{L1} \\ C_{L1} + D_{L1} Y_s & D_{L1} \end{bmatrix} \begin{bmatrix} \bar{V}_S \\ -\bar{I}_S \end{bmatrix}$$

$$= \begin{bmatrix} A_1 & B_1 \\ C_1 & D_1 \end{bmatrix} \begin{bmatrix} \bar{V}_S \\ -\bar{I}_S \end{bmatrix} \quad (15)$$

It is likewise possible to obtain an equivalent line/reactor representation for the unfaulted sections within each composite source. In this case, however, the transfer matrix describing the transposed line section (eqn. 13) has to be pre- and post-multiplied by the transfer matrix describing the shunt reactors (eqn. 4) to give the overall equivalent defined in eqn. 16.

$$\begin{bmatrix} \bar{V}_S \\ \bar{I}_S \end{bmatrix} = \begin{bmatrix} U & 0 \\ Y_s & U \end{bmatrix} \left[\begin{bmatrix} A_l & B_l \\ C_l & D_l \end{bmatrix} [M] \right]^3 \begin{bmatrix} U & 0 \\ Y_s & U \end{bmatrix} \begin{bmatrix} \bar{V}_R \\ \bar{I}_R \end{bmatrix} \quad (16)$$

3.4 Computation of composite source impedances

It will be recalled from Section 2 that each composite source consists of a cascade of $(n-1)$ compensated line sections as shown in Fig. 3. The effective impedances of the composite sources have to be precomputed over a range of frequencies consistent with the bandwidths of the protection and transducer arrangements under study[10] and Fig. 7 is useful for illustrating the methods which have been developed for so doing. Each line and its associated terminating shunt reactors is represented by the transfer matrix equivalent in the manner outlined in Section 3.3 (eqn. 16). In the course of this work, the impedance matrix of each local infeed/outfeed (Z_{n-2}, Z_{n-1}, etc.) has been estimated from a knowledge of the power frequency short-circuit levels and the ratio of zero-phase-sequence to positive-phase-sequence impedance of the source in question. It is, of course, possible to compute the source matrices corresponding to more complex local source network models, but, in many applications, the local infeed during fault conditions is relatively small and the considerable extra computational effort required can be avoided without serious loss of realism.

With reference to Fig. 7, the transfer-matrix equation 17 defines the response of the line/reactor combination of the first source section.

$$\begin{bmatrix} \bar{V}_{n-1} \\ \bar{I}_{n-1} \end{bmatrix} = \begin{bmatrix} A_{n-1} & B_{n-1} \\ C_{n-1} & D_{n-1} \end{bmatrix} \begin{bmatrix} \bar{V}_{n-2} \\ \bar{I}_{n-2} \end{bmatrix} \quad (17)$$

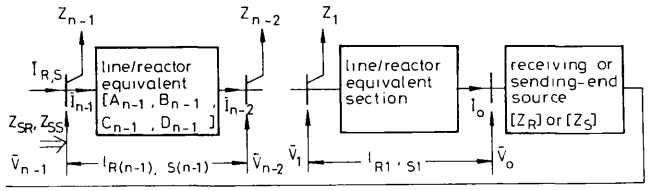

Fig. 7 *Composite source equivalent*

Now the total current entering the first section at, say, the receiving end is given by $\bar{I}_R = \bar{I}_{n-1} + [Z_{n-1}]^{-1} \bar{V}_{n-1}$ and it follows that the overall transfer matrix of the first section, including the local infeeding source of impedance $[Z_{n-1}]$, is as given in eqn. 18.

$$\begin{bmatrix} \bar{V}_{n-1} = \bar{V}_R \\ \bar{I}_R \end{bmatrix} =$$

$$\begin{bmatrix} A_{n-1} & B_{n-1} \\ C_{n-1} + [Z_{n-1}]^{-1} A_{n-1} & D_{n-1} + [Z_{n-1}]^{-1} B_{n-1} \end{bmatrix} \times \begin{bmatrix} \bar{V}_{n-2} \\ \bar{I}_{n-2} \end{bmatrix} \quad (18)$$

Similar relationships are likewise computed to describe the remaining $(n-2)$ source sections and their respective local infeeds. The requisite number of transfer matrices required to describe a given composite source are then multiplied in the usual canonical manner to finally provide a matrix relationship of the form of eqn. 19.

$$\begin{bmatrix} \bar{V}_R \\ \bar{I}_R \end{bmatrix} = \begin{bmatrix} A_R & B_R \\ C_R & D_R \end{bmatrix} \begin{bmatrix} \bar{V}_0 \\ \bar{I}_0 \end{bmatrix} \quad (19)$$

At the main source, the current and voltage vectors are related to the impedance matrix $[Z_R]$ by $\bar{V}_0 = [Z_R]\bar{I}_0$ and substitution into eqns. 19 yields $\bar{V}_R = [A_R Z_R + B_R]\bar{I}_0$ and $\bar{I}_R = [C_R Z_R + D_R]\bar{I}_0$. The total composite source-impedance matrix at the receiving end $[Z_{SR}]$ is then finally computed from eqn. 20.

$$Z_{SR} = [A_R Z_R + B_R][C_R Z_R + D_R]^{-1} \quad (20)$$

Similar procedures are likewise performed to define the total composite source impedance $[Z_{SS}]$ at the sending end.

4 Fault simulation

The fundamental relationships developed in Section 3 have been deliberately formulated in such a way as to effectively enable any compensated feeder arrangement to be reduced to the faulted circuit model shown in Fig. 6*b*. Details of the methods of digitally simulating faults on such a model by using matrix functions and numerically evaluated Fourier transforms are reported in Reference 12. It is worthwhile noting that the latter methods, which were developed for studying very much simpler uncompensated single-section homogeneous feeders, were validated by comparison with fault throwing tests on an actual system.[15] No corresponding field test data have been acquired for the case of long shunt-compensated feeders, and similar direct validation of the techniques here developed has not therefore been possible. However, by deliberately formulating the fundamental relationships to reduce the present problem to a previously validated simulation form, it has been possible to press closer to actual field test validation than would otherwise be the case.

4.1 Parameters of systems studied

4.1.1 Line construction: Fig. 8 shows the typical quad. conductor 500 kV line configuration considered. The positions of the conductors illustrated correspond to

the positions over the first one third of the line section from the sending end of any discretely transposed section (see Fig. 5). The data for the line are:

(*a*) phase conductors are 4 x 477 MCM Al alloy, 21·5 mm overall equivalent, 242 mm^2 Al equivalent, 19/4·3 mm stranding

(*b*) earth wires are 7/35 mm Alumoweld

(*c*) earth resistivity is 100 Ω m.

The frequency variation of all earth and conductor parameters is simulated.

4.1.2 Source and reactor parameters: The Q-factor at the nominal power frequency of 50 Hz was taken as 30 for all p.p.s. and z.p.s. source impedances. In practice, the normal service loading levels on long compensated feeders are typically between one half to two thirds of the surge-impedance power level, and the corresponding level of p.p.s. shunt compensation required (h_1) is approximately 0·75. For the line in question, the sequence capacitance ratio C_0/C_1 is approximately equal to 0·572, and the associated level of zero-sequence compensation h_0 required to theoretically minimise both secondary arc current and residual voltages is approximately 0·563.[9] The majority of the studies were therefore performed with the two latter degrees of compensation but, in studies involving different levels of p.p.s. compensation, both h_1 and h_0 were chosen so as to minimise the secondary arcing currents.

4.1.3 System configurations: The number of possible system configuration encountered in practice is, of course, very large, but feeders with more than three sections between main sources are relatively rare. In order to gain a general assessment of both primary-system responses and the associated distance relay responses, together with the effects of system configuration and source conditions, etc., a general study has been performed for the two configurations shown in Fig. 9. In the case of the 3-section feeder (Fig. 9*b*), the local source infeeds were assumed negligible and faults were simulated on the 300 km midsection. A comparison of the performance of distance relays protecting an identical line of length 300 km in both single and 3-section compensated feeders was thereby possible. The main sources were modelled by the normal lumped parameter source networks based upon the short-circuit levels and sequence-impedance ratios at power frequency. Shunt capacitance at the terminating busbars was deliberately not included in order to enable the performance of the relays to be obtained under conditions of worst case travelling-wave distortion.[11,12]

The general study is usefully complemented by a specific study of the response of distance protection applied to a typical feeder arrangement operating at specific system loading conditions. Fig. 10 gives details of the specific system studied in which the first-zone operating time characteristics of distance relays connected at all line section terminations ($S_1R_1S_2R_2S_3R_3$) is examined. The ratio of zero sequence to positive sequence impedance of each main and local source was taken as 0·5 and, in this case also, the main sources feeding busbars S_1 and R_3 were represented by simple lumped parameter source models.

4.2 *Main features of primary system responses*

4.2.1 Effect of feeder configuration: Studies of the alternative feeder arrangements illustrated in Fig. 9 show that for given faults and main source conditions, there is a very marked difference between the response of single-section and 3-section feeders. Fig. 11 shows a comparison of the responses observed at the relaying point S following a solid 'a'-earth fault adjacent to S ($x = 0$). Both voltage and current waveforms are seen to differ significantly in the two cases but the most important feature of the response is that the current waveforms associated with the fault on the 3-section feeder are very considerably more distorted than is the case for the single-section arrangement. In this respect, it will be evident from Fig. 9 that, in the case of the 3-section feeder, the travelling-waves of current set up following fault inception successively propagate through

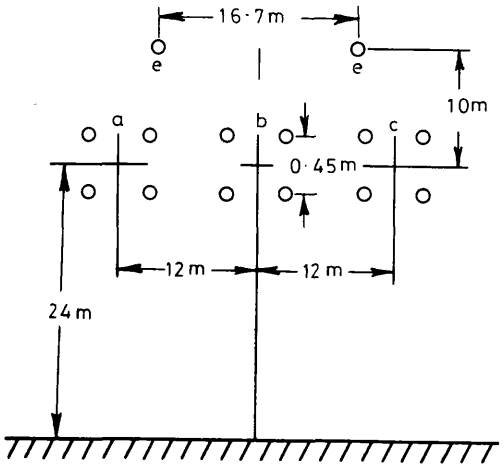

Fig. 8 *500 kV line construction simulated*

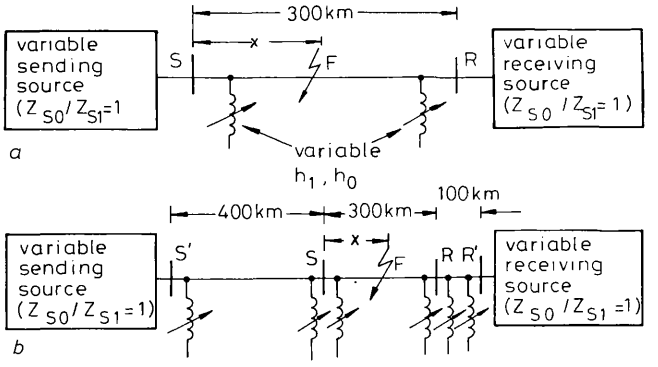

Fig. 9 *General system configuration*

a Single-section arrangement
b 3-section arrangement

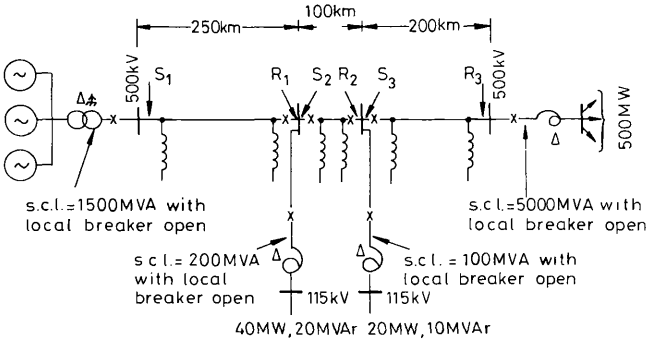

Fig. 10 *Specific system configuration*

$h_1 = 0{\cdot}75, h_0 = 0{\cdot}56$ for each section

point S towards S' and are partially reflected from the latter back through S to produce the relatively high levels of travelling-wave current distortion observed.

Fig. 12 typifies the differences in the faulted phase voltage waveforms observed following identical earth and phase fault conditions on single and 3-section feeders. In both cases, the fault is midway between the relaying points S and R on the 300 km section ($x = 150$ km). In the case of the single-section feeder, the frequencies of the travelling-wave components are largely governed by the wave transit times between the point of fault and the source discontinuity S of Fig. 9*a*. They are consequently of relatively high frequency by comparison with those produced on the 3-section arrangement where the wave transit time between the points of major discontinuity (F and S') is longer (see Fig. 9*b*).

The differences in the transient response of the alternative feeder arrangements of Fig. 9 is less marked when considering faults at or near zero voltage point-on-wave.

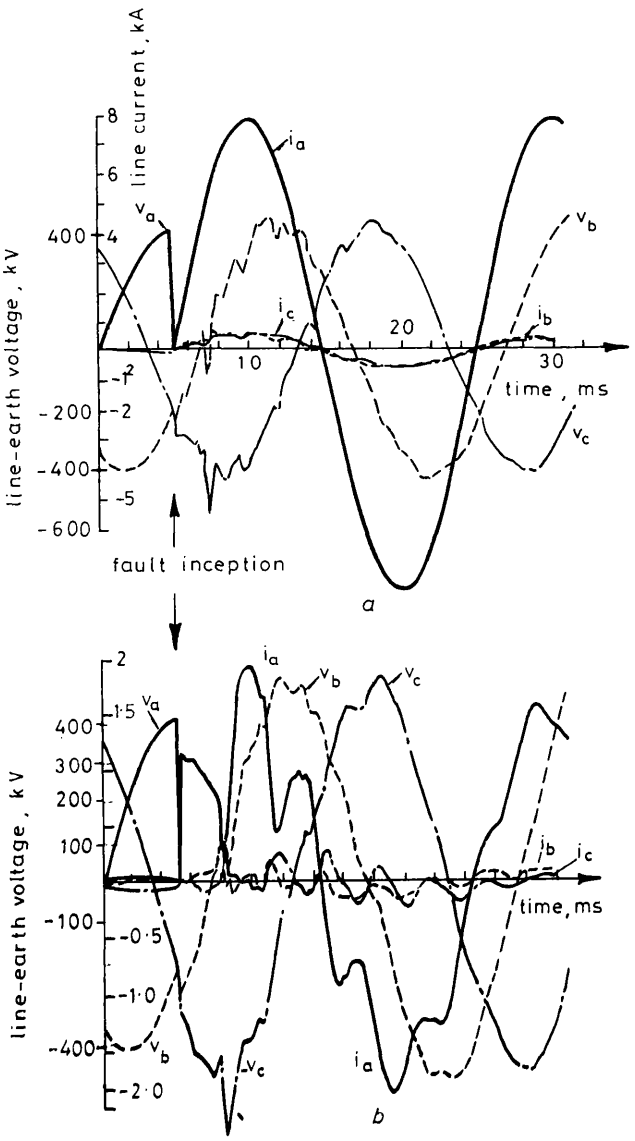

Fig. 11 *Faulted response of general configuration for close-up earth fault*

'a'-earth solid fault at $x = 0$; waveforms observed at S (Fig. 9); sending s.c.1. = 5 GVA. receiving s.c.1. = 35 GVA; $h_1 = 0{\cdot}75$
a Single-section feeder (Fig. 9*a*)
b 3-section feeder (Fig. 9*b*)

However, it is important to observe that in the case of faults near peak voltage, the frequency of the travelling-wave distortion in both current and voltage waves associated with single-section feeders is relatively high. On the other hand, maximum voltage faults at a corresponding position on the 3-section feeder produce relatively low frequency distortion which in turn will increase the relay measuring time by an amount which is dependent on the bandwidth of the transducers and protective relay circuits.[10,11]

4.2.2 Effect of compensation levels: An extensive study of the arrangement of Fig. 9 has shown that the fault transient components caused following faults on both multi- and single-section feeders are largely independent of the level of shunt compensation used. This is somewhat as expected because even for values of h_1 as high as 1·2, which represents a near maximum practicable upper limit, each limb of the main reactor banks has an inductance L_p typically in excess of 4H. It follows that the shunt reactors present what, for practical purposes, can be regarded as an open circuit to any travelling wave (essentially high-frequency) phenomena. Indeed, it is only the lower-frequency phenomena such as exponential components of current associated with faults near zero voltage point-on-wave which are affected by the reactors and, even in this case, the difference between the faulted response waveforms obtained with and without shunt reactors connected has been found to be small. It is therefore to be expected that the transient accuracy of distance relays applied to 4-reactor compensated lines of a given length will be comparable

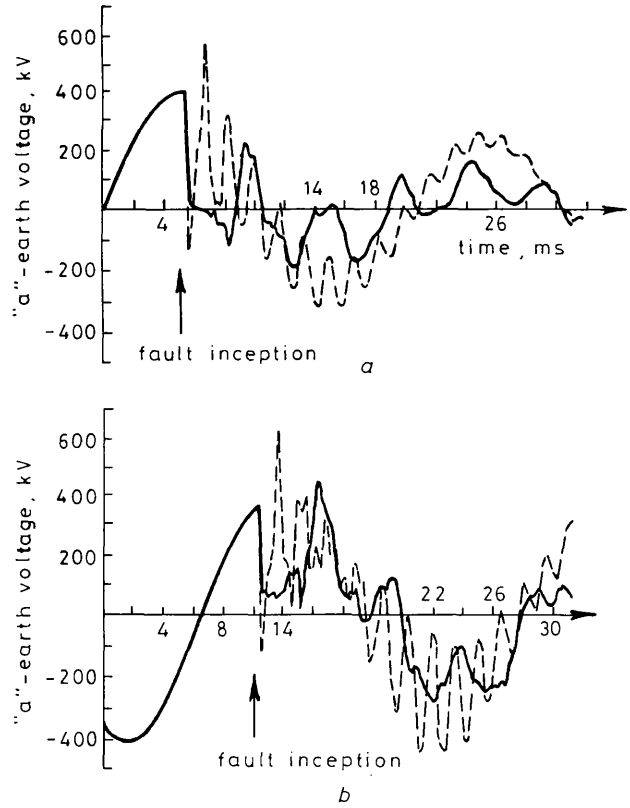

Fig. 12 *Faulted response of general configuration for midpoint earth-fault*

Sending s.c.1. = 5 GVA; receiving s.c.1. = 35 GVA; waveforms observed at S (Fig. 9); $h_1 = 0{\cdot}75$;
——— = 3-section feeder;
– – – – = single-section feeder
a 'a'-earth solid midpoint fault ($x = 150$ km)
b 'a'-'b' solid midpoint fault ($x = 150$ km)

with that of similar relays connected to an uncompensated feeder of the same construction and length. This latter finding is largely in line with some of the results presented by Fielding *et al.* which showed that there was no serious degradation in the transient accuracy of a block-average distance relay applied to a single-section linear 3-reactor compensated feeder.[4]

From a protection point of view, the main effect of the reactors is to increase the steady-state components of the postfault current levels. This is, of course, due to the fact that, in the compensated case, the reactor bank appears in parallel with the fault loop impedance, thus reducing the impedance presented to distance relays and thereby causing a slight overreaching tendency. Fig. 13 illustrates the foregoing point with reference to the faulty phase currents and voltages associated with an 'a'-earth fault on the general 3-section model of Fig. 9*b*. It can be seen that the peak value of the voltage waveform observed at S changes very slightly as the degree of compensation is increased. On the other hand, the peak of the current waveform at a compensation $h_1 = 1{\cdot}25$ exceeds that at the lower level of compensation ($h_1 = 0{\cdot}5$) by approximately 150 A.

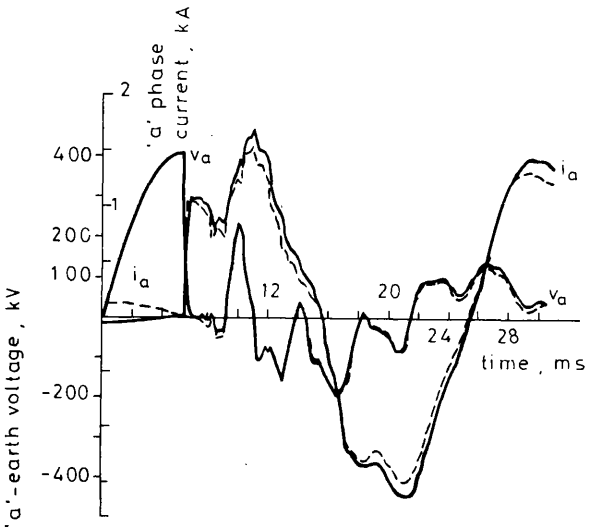

Fig. 13 *Typical effect of degree of compensation on primary system waveforms for 3-section feeder*

Sending s.c.1. = 5 GVA; receiving s.c.1. = 35 GVA; waveforms observed at *S* (Fig. 9*b*); 'a'-earth solid fault at $x = 150$ km
——— $h_1 = 1{\cdot}25$,
– – – – $h_1 = 0{\cdot}5$

5 Distance protection performance evaluation

The relays investigated are of the crosspolarised mho type and utilise signals of the familiar phasor form given in eqn. 21.[14]

$$S_1 = I_L Z_r - V_L$$
$$S_2 = V_L + V_P \qquad (21)$$

The foregoing signals are compared in the well known block-average comparator arrangement,[5] details of the methods for simulating the response of the mixing and relaying circuits being given in Reference 10. Each relay is arranged to have a ratio of set to reset voltage of 2 and thereby possesses an absolute minimum operating time of 10 ms on the nominally 50 Hz system.

The response of first zone relays having a nominal setting of 80% of the line section in question is considered, and the level of polarisation is 10% of the relevant sound-phase voltage(s). Each comparator has a setting voltage of 0·1 V and, in the case of the general application study configuration shown in Fig. 9, the majority of the responses were performed for source short-circuit levels of 5 GVA and 35 GVA at the sending and receiving ends, respectively. The latter conditions give relatively high levels of travelling-wave distortion[12] and consequently enable a near worst case indication of the performance of the relays connected at point S to be obtained.

The nominal transducer ratios were taken as 500/0·11 and 1200/1 for the vts and cts respectively. The frequency response of the vts was of the lowpass high-fidelity type and, in order to indicate the near optimal response from the

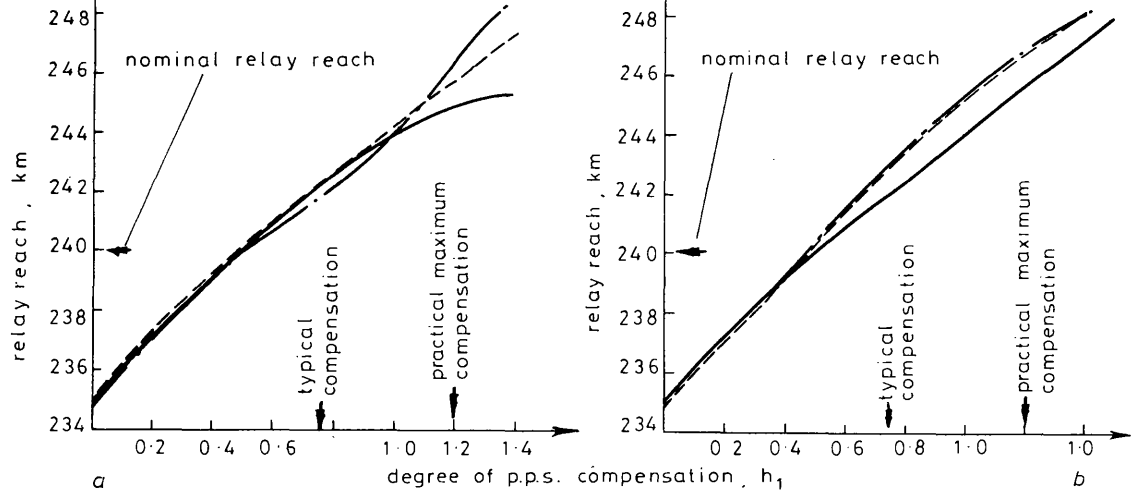

Fig. 14 *Variation of reach of earth fault relay with p.p.s. shunt compensation*

'a'-earth solid faults, 'a'-earth relay located at end *S* of single-section feeder (Fig. 9*a*)
——— sending s.c.1. = 5 GVA, receiving s.c.1. = 35 GVA
– – – – sending s.c.1. = 35 GVA, receiving s.c.1. = 5 GVA
— · — sending s.c.1. = 35 GVA, receiving s.c.1. = 35 GVA

a faults at peak of prefault 'a'-earth voltage
b faults at zero of prefault 'a'-earth voltage

point of view of minimising relay operating times and ensuring reverse fault stability, a cvt high-frequency cutoff (−3 dB point) of 1 kHz was used.[10]

5.1 General application study

5.1.1 Measurement accuracy: Fig. 14 illustrates how the degree of compensation affects the reach of the 'a'-earth relay at point S in Fig. 9*a* and, in accordance with the observations made in Section 4.2.2, the reach is seen to increase with the degree of compensation. However, even at an extreme level of compensation corresponding to $h_1 = 1{\cdot}2$, the reach does not exceed 247 km which in turn represents an overreach of less than 3%. On the other hand, with no compensation ($h_1 = 0$) the relays have been found to operate for faults up to approximately 235 km, which in turn corresponds to about 2% of underreach.

It should be noted that the responses obtained include also all the errors which are unavoidably encountered in practice, i.e. residual compensation errors and errors caused by assuming ideal transposition when setting the relays. It follows that not all the error observed is attributable to the presence of shunt compensation. In this respect, it is evident from Fig. 14 that the measurement error solely attributable to compensation does not exceed approximately 5%, a finding which has been found also to apply to the response of phase-fault relays.

The foregoing findings apply equally to the three-section arrangement and to the relays connected at end *R* in Fig. 9. For practical loading and compensation levels, no case involving a total error in excess of ± 6% has been observed. It can thus be concluded that there is, for practical purposes, no significant deterioration in the measuring accuracy of block-average type relays applied to linear 4-reactor shunt compensated feeders.

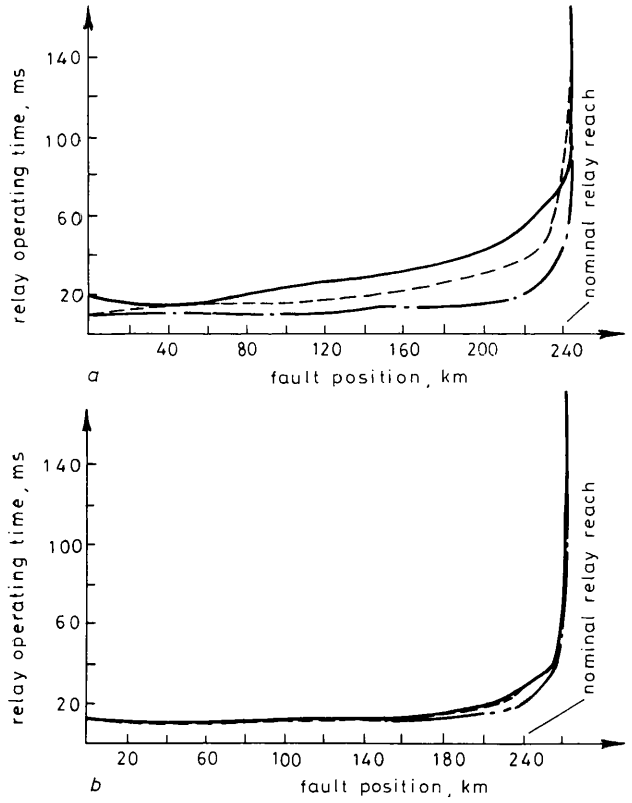

Fig. 15 *Time-response of earth-fault relay applied to 300 km compensated line*

'a'-earth solid fault; 'a'-earth relay at end *S* (Fig. 9); sending s.c.1. = 5 GVA; receiving s.c.1. = 35 GVA; $h_1 = 0{\cdot}75$

——— = relay applied to 3-section feeder (Fig. 9*b*) (digitally simulated)

– – – – = relay applied to single-section feeder (Fig. 9*a*) (digitally simulated)

— · — = relay applied to single-section feeder (relay tested on analogue test-bench facility)

a faults at peak of pre-fault 'a'-earth voltage

b faults at zero of pre-fault 'a'-earth voltage

5.1.2 Relay operating times: Fig. 15 shows the time response of the 'a'-earth relay at *S* for both single and 3-section arrangements which are typically compensated at a level of $h_1 = 0{\cdot}75$. In the case of faults which occur near zero voltage point-on-wave (Fig. 15*b*), the responses are almost identical and there is, for practical purposes, no significant difference between the performances in the alternative configurations. Also shown in Fig. 15*b* is the time response revealed from a series of tests on the block-average relay when using a signals derived from a lumped parameter single-end fed dynamic test bench in which only the series impedance of the line was modelled. The model shunt reactors used had an unrealistically low *Q*-factor of approximately 7 and, because only the series impedance of the line could be modelled, travelling-wave components were not reproduced. Although faults near zero voltage produce relatively very low levels of travelling-wave distortion, they are nevertheless responsible for the slight difference in the responses obtained near the boundary of operation. Despite the fact that the test bench simulation is not wholly realistic in terms of simulating the primary system, the results obtained for zero voltage faults do correlate sufficiently well with the digitally simulated responses to provide a useful independent means of confirming the latter.

The much higher level of h.f. distortion produced following faults at voltage maximum produces a slowing of relay responses and reference to Fig. 15*a* shows that, unlike zero voltage faults, there is a marked difference between the relay response in the two alternative applications considered. For example, a fault at the midpoint of the line gives relay operating times of 20 ms and 30 ms for the single and 3-section feeders, respectively. Furthermore, in the case of relay applied to the 3-section feeder, the response for a close-up fault deteriorates to the extent of being approximately 8 ms slower than that for an identical fault at maximum voltage on the single-section feeder. As mentioned previously, the lower apparent frequencies of the travelling-waves observed in the case of sectionalised feeders undoubtedly accounts for the slower response observed in the 3-section arrangement. The precise level of travelling-wave distortion present is quite clearly the main factor which determines the time response. This is particularly evident from a comparison of the single-section feeder responses obtained by using the test-bench facility and the digital simulation (Fig. 15*a*). As mentioned previously, the bench testing programme included only the line series impedances and high-frequency components of relaying voltage and current were not therefore produced. The latter limitation largely accounts for the difference in the responses obtained from the bench testing and digital simulation programmes and it further illustrates the important part which high-frequency distortion plays in determining relay responses.

A simplified computer simulation in which only the line series impedance was modelled has been performed as part of a partial validation exercise involving a comparison between the relay responses as obtained by dynamic bench

testing and digital simulation. For practical purposes, the responses thereby obtained were identical with the bench test results shown in Figs. 15*a* and *b*, thus providing evidence of the realism with which the low-frequency response of the relaying circuit has been digitally modelled. Due to the limitations of the bench test method, similar direct evidence of the adequacy of the digital simulation in respect of modelling the high-frequency response of the relaying circuits was not possible. However, as part of the process of validating earlier work on the block-average relays,[10] some secondary injection tests involving discrete high-frequency components of voltage and current were performed. These tests included injecting realistic levels of discrete high-frequency currents into the transformer-reactor circuit,[11] and a comparison with the corresponding comparator responses as obtained by digital modelling revealed no significant inadequacies in the modelling of the relay circuits. Similar block-average relays were considered during the course of the work here presented and it has therefore been concluded that the digital modelling of the relay circuits themselves is adequate for a realistic indication of performance under field operating conditions.

The time response of the 'b'–'c' phase-fault relay illustrated in Fig. 16 again shows that there is a marked difference between the operating time for faults at maximum voltage on the single and 3-section compensated feeder arrangements. For example, for a midpoint fault (approximately 62·5% of the relay reach), the operating times are approximately 40 ms and 24 ms for faults on the 3-section and single-section feeders, respectively. On the other hand, a corresponding fault at the zero of the prefault voltage gives an operating time of approximately 12 ms for both feeder arrangements. A comparison of Figs. 15 and 16 shows that, irrespective of the configuration involved, the time response for pure phase faults is inferior to that for single phase-to-earth faults.

The previously mentioned extent to which the degree of compensation affects relay responses is also evident from Fig. 16. It can be seen that, although the phase-fault relay does not actually overreach its nominal setting in any application, a relative overreaching tendency occurs to the extent that, for the single-section feeder, the reach is approximately 8 km larger (approximately 3% of the relay reach) with a compensation level of $h_1 \simeq 0{\cdot}75$ than that obtained for zero compensation. Although not illustrated, a similar margin of relative overreaching tendency has been observed for the 3-section feeder.

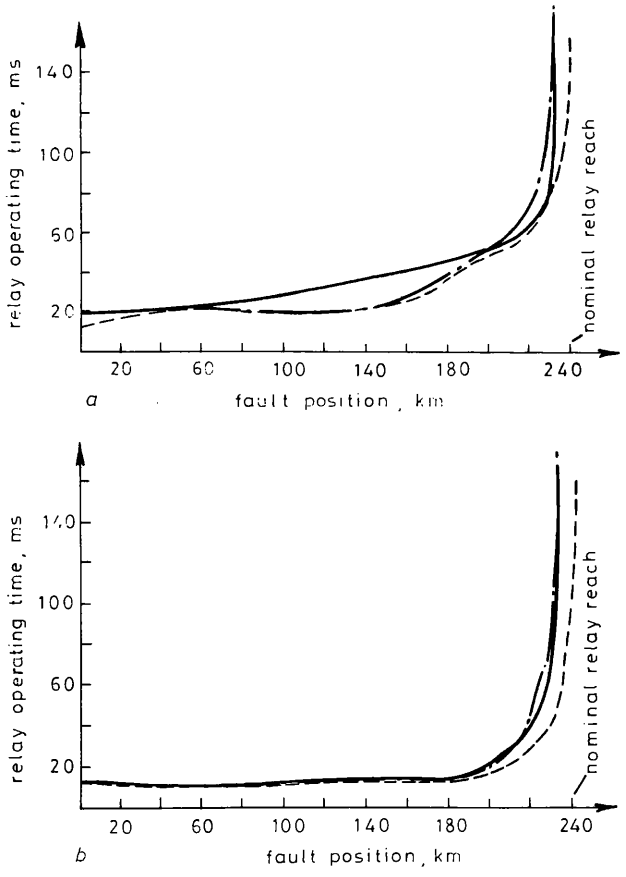

Fig. 16 *Time response of phase-fault relay applied to 300 km line*

'b'-'c' solid faults; 'b'-'c' relay at end *S* (Fig. 9); sending s.c.1. = 5 GVA; receiving s.c.1. = 35 GVA
——— = relay applied to 3-section feeder (Fig. 9*b*), $h_1 = 0{\cdot}75$
– – – – = relay applied to single-section feeder (Fig. 9*a*), $h_1 = 0{\cdot}75$
—·—·— = relay applied to single-section feeder (Fig. 9*a*), $h_1 = 0{\cdot}75$
a faults at peak of 'b'-'c' voltage
b faults at zero of 'b'-'c' voltage

5.2 *Specific application study*

The performance of zone-1 distance relays protecting each section of the specific application considered (Fig. 10) is shown in Fig. 17. Both earth-fault and phase-fault relay responses shown in Figs. 17*a* and *b* respectively, indicate that there is a marked difference in the performance of the relays protecting each section. This is particularly so for faults at peak voltage point-on-wave, there being just under one half-cycle of power frequency difference between the close-up fault operating time of the earth fault relays connected at points *S*1 and *S*3. The corresponding difference in the case of phase faults is approximately three-quarters of a cycle of power frequency.

It is important to note that the relay time responses for peak voltage faults in particular are generally more inverse in nature over the whole range of possible fault positions than has previously been found to be the case for simpler single-section uncompensated feeders.[10] For example, it can be seen from Fig. 17*b* that, in the case of the phase fault relay protecting section $S3 - R3$, the operating

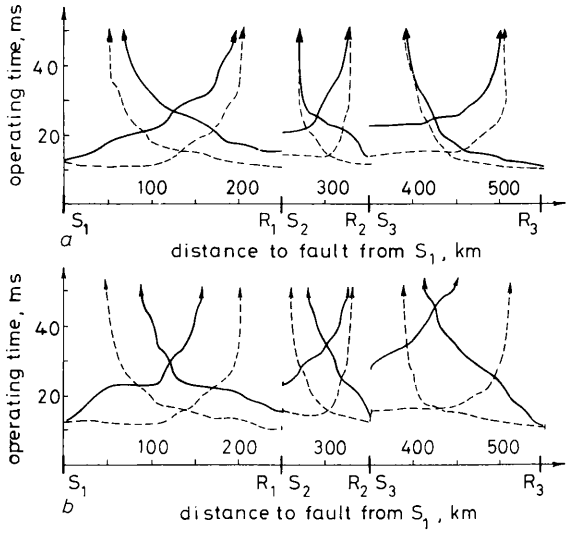

Fig. 17 *Response of relays applied to specific system configuration*

System details given in Fig. 10
——— = faults at peak of prefault voltage
– – – – = faults at zero of prefault voltage
a 'a'-earth solid faults
b 'b'-'c' solid faults

time for a fault 75 km distant from end $S3$ reaches approximately 2·5 cycles of power frequency.

The relative differences in the response of the relays are conveniently illustrated by reference to Fig. 18 which shows the relative responses of the sending-end relays following faults at voltage peak. It can be seen that the difference in responses is much more marked in the case of phase faults, there being a difference of approximately 25 ms between the operating times of the relays at $S1$ and $S3$ following faults at half the respective relay reaches.

The response illustrated in Fig. 18*a* for the earth fault relay at $S2$ (protecting the 100 km midsection feeder) is useful for indicating the extent to which the performance of modern distance relays can be modified in practical multisection shunt compensated schemes. It can be seen that the operating time of this relay always exceeds 20 ms and reaches approximately 30 ms for an earth fault at 60% of the relay reach. On the other hand, earlier work concerned with identical block-average relays applied to a single-section uncompensated 400 kV feeder of comparable length (128 km) indicated a relay operating time of approximately 12 ms for single phase-to-earth faults over the whole of the range 0–60% of the relay reach.[10]

6 Conclusions

In this paper, methods are presented for realistically modelling practical 4-reactor shunt compensated e.h.v. systems and techniques whereby the models may be used to determine responses for arbitrary loading, source and compensation conditions have been described. The complexity of typical shunt-compensated systems has hitherto represented a particularly difficult problem from a computational point of view, but the importance of employing very realistic primary-system simulation techniques which adequately model the system under consideration has clearly emerged. The results of this work thus indirectly confirm the desirability of recent trends towards the use of programmable test equipment as an alternative to simpler more conventional approximate analogue testing techniques, and the digital methods of simulation described in this paper are of obvious importance in this context.

The majority of the primary-system simulation studies utilised an IBM 360/195 computer linked to a Prime 400 interactive computer facility which in turn was used for modelling the transducers and relay circuits. In computing terms, almost all the total requirement relates to a simulation of the primary system, and typical c.p.u. times of approximately 25 s and 40 s for single-section and 3-section studies, respectively, have been required. The latter times are those required to produce the time variation of the voltages and currents at both ends of a faulted line section for a postfault observation time of approximately 250 ms. Work is now in progress to reduce the computing time by optimally structuring the software and by pre-evaluating and storing more of those matrix functions which are independent of both system configuration and fault position, etc., Preliminary assessments indicate that, by so doing, the c.p.u. time required will be less than approximately one half of present requirements.

Broadly, it has been found that it is the system configuration, rather than the precise levels of shunt compensation, which is the principal factor which determines the performance of modern distance protection applied to shunt compensated feeders. For example, it has been found that following faults at peak voltage point-on-wave, there is a marked difference between the time responses in single-section and 3-section configurations. In particular, the relay operating time for close-up faults at maximum voltage is generally larger in multisection feeders than in otherwise similar single-section arrangements.

It is important to note that the time responses in respect of faults at or near zero voltage point-on-wave have been found not to vary significantly with application and furthermore they are, for practical purposes, almost identical with those obtained in similar uncompensated feeders.

The main effect of the shunt reactors is to cause an increase in the relay reach of typically 5% over a p.p.s. compensation range of 0–1·2. Such increases are largely configuration independent, and it is concluded that the maximum reach which is likely to occur in a given application will be some 5% in excess of the reach as obtained in a similar uncompensated application study. Furthermore, the studies have revealed that the overall error is such that the zone-1 reach does not deviate from the nominal reach setting by more than ± 6%. On this basis, it can safely be further concluded that there is no serious likelihood of indiscrimination occurring in schemes employing a nominal 80% zone-1 setting.

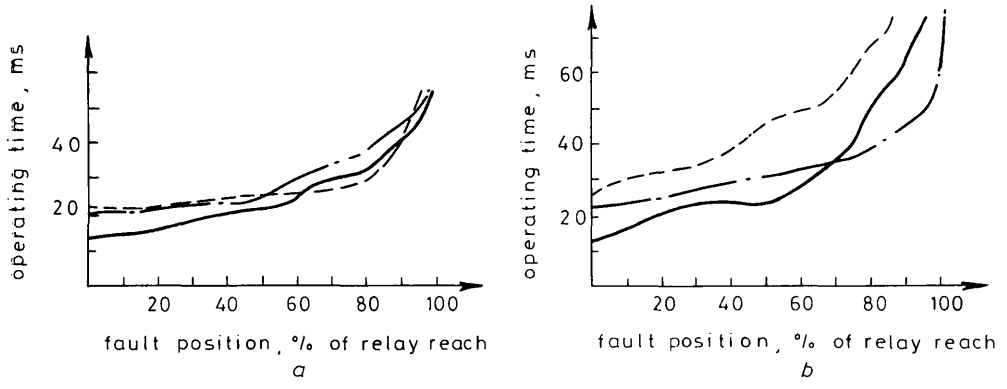

Fig. 18 *Normalised time-response of sending end relays in specific system configuration*

Faults applied at peak of prefault voltage
——— = relay connected at point S_1
—·— = relay connected at point S_2
– – – – = relay connected at point S_3
a Response of 'a'-earth relays
b Response of 'b'-'c' relays

The specific application study reported in this paper shows that there is a significant difference between the time response of the relays protecting each line section. This is particularly so for faults at maximum voltage point-on-wave, where it has been found that a difference in close-up fault operating times of typically one half-cycle of power frequency can occur. Furthermore, it has been found that even for block-average relays with a theoretically minimum operating time of one-cycle of power frequency, operating times in excess of one cycle over the whole range of fault coverage can occur for some of the relays applied to the specific feeder application studied. In so far as it is possible to generalise, it can be said that such responses are likely to meet the requirements of the majority of applications but the system configuration dependent nature of the problem nevertheless tends to indicate the necessity for individual application studies in cases where some doubt exists. No serious problem relating to the use of block-average based comparator distance relaying schemes has been found, but it could be unsafe to extrapolate the findings to existing or proposed distance protection schemes utilising other comparison circuits.

7 Acknowledgments

The authors are grateful for the provision of facilities at the University of Bath and would like to thank Professor J. F. Eastham for his encouragement. They also acknowledge many interesting discussions with engineers in industry, particularly at GEC and Kennedy & Donkin Consulting Engineers. Especial thanks are due to W. H. Parrington of Kennedy & Donkin for his continued help in the provision of system data. Finally, the authors are grateful to the UK Science Research Council for financial assistance in the provision of interactive computing facilities at the Rutherford Computing Laboratories.

8 References

1 FRIEDLANDER, E., and GARRARD, C.J.O.: 'Long distance power transmission by alternating current', *Engineering*, 1942, **1**, pp. 2–16
2 BARTHOLD, L.O. BECKER, H., DALZELL, J., COOPER, C.B., NORMAN, H.B., PEIZOTO, C.A., REICHERT, K., ROY, J.C., and THOREM, B.: 'Static shunt devices for reactive power control': CIGRÉ, Paris, paper 31–80 1974
3 AINSWORTH, J.D., COOPER, C.B., FRIEDLANDER, E., and THANAWALA, H.L.: 'Long distance a.c. transmission using static voltage stabilisiers and switched linear reactors': *ibid.*, paper 31–09, 1974
4 FIELDING, G., CHEETHAM, W.J., THANAWALA, H.L., and WILLIAMS, W.P.: 'The performance of a distance relay applied to a long distance e.h.v. line with static shunt compensation': *ibid.*, paper 34–02, 1978
5 JACKSON, L., PATRICKSON, J.B., and WEDEPOHL, L.M.: 'Distance protection: optimum dynamic design of static relay comparators', *Proc. IEE*, 1968, **115**, (2), pp. 280–287
6 THANAWALA, H.L., KELHAM, W.O. and WILLIAMS, W.P.: 'The application of static shunt reactive compensators in conjunction with line series capacitors to increase the transmission capabilities of long lines': CIGRÉ, Paris, paper 31–09, 1976
7 KIMBARK, E.W.: 'Suppression of ground-fault arcs on single-pole-swtiched e.h.v. lines by shunt reactors', *IEEE Trans*, 1964, **PAS-83**, pp. 285–290
8 HAUBRICH, H.J., HOSEMANN, G., and THOMAS, R.: 'Single-phase auto-reclosing in e.h.v. systems': CIGRÉ, Paris, paper 31–09 1974
9 KIMBARK, E.W.: 'Charts of three quantities associated with single-pole switching', *IEEE Trans.*, 1975, **PAS-94**, pp. 383–394
10 JOHNS, A.T., and AGGARWAL, R.K.: 'Performance of high-speed distance relays with particular reference to travelling-wave effects', *Proc. IEE*, 1977, **124**, (7), pp. 639–646
11 JOHNS, A.T., and AGGARWAL, R.K.: 'Discussion on performance of high-speed distance relays with particular reference to travelling-wave effects', *ibid.*, 1978, **125**, (8), pp. 761–765
12 JOHNS, A.T., and AGGARWAL, R.K.: 'Digital simulation of faulted e.h.v. transmission lines with particular reference to very-high-speed protection', *ibid.*, 1976, **123**, (4), pp. 353–359
13 WEDEPOHL, L.M.: 'Application of matrix methods to the solution of travelling-wave phenomena in polyphase systems', *ibid.*, 1963, **110**, (12), pp. 2200–2212
14 WEDEPOHL, L.M.: 'Polarised mho distance relay', *ibid.*, 1965, **112**, (3), pp. 525–535
15 STALEWSKI, A.: 'System tests, Sundon-Cowley 400 kV circuit, Sundon 400 kV substation'. CEGB Transmission Division Design Department Report No. 63, 1975

PERFORMANCE OF HIGH SPEED DISTANCE PROTECTION APPLIED TO 4-REACTOR STATIC SHUNT COMPENSATED SYSTEMS

A T Johns, M A H Abuelnour and R K Aggarwal

School of Electrical Engineering, University of Bath, UK

1. Introduction

Until very recently, little had been reported on the performance of modern distance protection applied to long static shunt compensated feeders. A study by Fielding et al [1] has however shown that distance protection performance is modified somewhat when applied to simple single-section shunt compensated feeders but the latter work was confined to three reactor arrangements.

Where single-pole autoreclosure is involved, 4-reactor shunt compensators are necessary in order to provide rapid extinction of secondary arcs [2]. The state of knowledge of distance protection performance in long shunt compensated feeders using 4-reactor arrangements is however even more limited than that relating to 3-reactor schemes and, in view of the increasing world-wide use of single-pole autoreclosure, this paper is primarily concerned with reporting some recently developed primary system simulation techniques together with the salient features of an extensive response evaluation of distance protective relays utilising the well-known block-average technique.

2. Basic shunt compensated system models

Shunt compensated feeders are rarely sectionalised into more than three compensated sections and, in order to obtain an assessment of the primary system responses and associated distance relaying performances, the two basic configurations shown in Fig 1 have been studied. For the 3-section feeder (Fig 1b) the intermediate source infeeds were assumed to be negligible and faults were simulated on the 300km mid-section. A comparison of the performance of distance relays protecting an identical length of line in both single and 3-section feeders was thereby possible.

3. Primary system simulation

Fig 2 shows the circuit of a typical 4-reactor arrangement. In terms of the p.p.s. and z.p.s. values of the shunt capacitance of the line (C_1,C_o) the parameters of any shunt reactor bank compensating a line section of length ℓ is as given in eqn (1).

$$\begin{aligned} h_1 &= 2/\omega_o^2 L_1 C_1 \ell \\ h_o &= 2/\omega_o^2 L_o C_o \ell \end{aligned} \qquad (1)$$

The factors which determine the degrees of shunt compensation (h_o,h_1) are well documented in the literature [2] and will not be considered in detail. In practice h_1,h_o lie between extremes of 0 and 1.2 and it is possible to determine the reactor impedances from eqn (2).

$$\begin{aligned} Z_p &= R_p + j2\omega/\omega_o^2 h_1 C_1 \ell \\ Z_n &= R_n + j2\omega(h_1 C_1 - h_o C_o)/3\omega_o^2 h_o h_1 C_o C_1 \ell \end{aligned} \qquad (2)$$

Combination of the shunt reactor arrangements with the various line sections is conveniently achieved by use of the canonical relationship of eqn (3). In terms of the basic reactor parameters (Z_p,Z_n), the sub-matrix $[Y_S]$ used in so describing each reactor is given by eqn (4).

$$\begin{bmatrix} \bar{V}_1 \\ \bar{I}_1 \end{bmatrix} = \begin{bmatrix} U & 0 \\ Y_S & U \end{bmatrix} \begin{bmatrix} \bar{V}_2 \\ \bar{I}_2 \end{bmatrix} \qquad (3)$$

$$[Y_S] = [Z_S]^{-1} = \frac{1}{Z_p(Z_p+3Z_n)} \begin{bmatrix} Z_p+3Z_n & -Z_n & -Z_n \\ -Z_n & Z_p+3Z_n & -Z_n \\ -Z_n & -Z_n & Z_p+3Z_n \end{bmatrix} \qquad (4)$$

Fig 3 shows the method used to reduce the actual compensated feeder model (Fig 3a) to an equivalent model (Fig 3b) in which the line sections up to and beyond the fault point are combined with the terminating reactors. With reference to Figs 2 and 3, the situation at the receiving end is such that $\bar{I}_{RL} = \bar{I}_1$ and $\bar{I}_2 = \bar{I}_R$. Furthermore, it is possible to describe the line section between the point of fault and the receiving end using the two-port polyphase relationship of eqn (5)[3].

$$\begin{bmatrix} \bar{V}_f \\ \bar{I}_{fR} \end{bmatrix} = \begin{bmatrix} A_{L2} & B_{L2} \\ C_{L2} & D_{L2} \end{bmatrix} \begin{bmatrix} \bar{V}_R \\ \bar{I}_R \end{bmatrix} \qquad (5)$$

where $A_{L2} = \cosh \psi(\ell-x)$, $B_{L2} = \sinh \psi(\ell-x)Z_o$, $C_{L2} = Y_o B_{L2} Y_o$, $D_{L2} = Y_o A_{L2} Z_o$, $\psi = Q\gamma Q^{-1}$, Q = voltage eigenvector matrix, γ = propagation constant matrix, $Z_o = Y_o^{-1}$ = polyphase surge impedance matrix.

Combination of eqns (3) and (5) is performed to obtain the relationships of eqn (6) which in turn describes the line/reactor equivalent section shown in Fig 3b.

$$\begin{bmatrix} \bar{V}_f \\ \bar{I}_{fR} \end{bmatrix} = \begin{bmatrix} A_{L2} & B_{L2} \\ C_{L2} & D_{L2} \end{bmatrix} \begin{bmatrix} \bar{V}_R = \bar{V}_1 \\ \bar{I}_{RL} = \bar{I}_1 \end{bmatrix} = \begin{bmatrix} A_{L2}+B_{L2}Y_S & B_{L2} \\ C_{L2}+D_{L2}Y_S & D_{L2} \end{bmatrix} \begin{bmatrix} \bar{V}_2 = \bar{V}_R \\ \bar{I}_2 = \bar{I}_R \end{bmatrix} = \begin{bmatrix} A_2 & B_2 \\ C_2 & D_2 \end{bmatrix} \begin{bmatrix} \bar{V}_R \\ \bar{I}_R \end{bmatrix} \qquad (6)$$

It is likewise possible to obtain an overall two-port matrix describing the line and reactor section between the sending-end and fault point. In the equivalent circuit of Fig 3, each source terminating the faulted section RS comprises the main source and, where present, the infeeding compensated sections. The basis of the frequency domain based digital methods of simulating faults on a circuit model of the equivalent form of Fig 3b are given in reference 3.

3.1 Line configuration

A typical 500 kV quad conductor line model has been studied. Frequency variance of all line and earth plane parameters has been included and the data are: (a) phase conductors are 4x477MCM Al, Alloy, 21.5m overall equivalent, 242 sq mm Al equivalent, 19/4.33 stranding; (b) earth wires are 71.35mm Alumoweld; (c) earth resistivity is 100Ωm. Each line section has the usual discrete transpositions at intervals of one-third of the total line length involved.

3.2 Source and Reactor Parameters

Each limb of the shunt reactors was arranged to have a Q factor of 250 at 50Hz and the corresponding Q factor for each main source was equal to 30. Normal service loading on long-compensated feeders is typically between one half to two thirds of surge impedance power loading and the corresponding level of p.p.s. shunt compensation required (h_1) is approximately 0.75. For the line construction considered the associated level of z.p.s. compensation required to

- neutralise secondary arc currents and residual voltages (h_o) is approximately 0.57. The majority of the studies were performed for the latter two degrees of compensation but in studies involving other levels, both h_1 and h_o were chosen so as to minimise secondary arcing currents.

4. Salient Features of Primary System Responses

An extensive series of studies have shown that there is a very marked difference between the response of single section and 3-section feeders. For example, Fig 4 shows a comparison of the responses observed at the relaying point S following a solid "a"-earth fault at S (x=0). The voltage waveforms are seen to differ significantly and, most importantly, the waveforms associated with the fault on the 3-section feeder are very considerably more distorted than is the case for the single section arrangement. The reason for this is that the travelling waves of current set up in the 3-section feeder of Fig 1 successively propagate through point S towards point S' and are partially reflected from S' back through S to produce relatively high levels of travelling wave distortion. In the case of the single section feeder (Fig 1a) the transit time between any point of fault and the point at which the relays are connected is relatively small and much higher frequency more rapidly attenuated travelling wave distortion is produced. Similar findings have been found to apply to pure interphase faults clear of earth.

5. Performance of Distance Protection

The relays investigated are of the cross-polarised mho type and utilise signals of the form $S_1 = I_L Z_r - V_L$, $S_2 = V_L + V_p$. The signals are compared in the block-average comparator arrangement and details of the methods of simulating the response of the relaying circuits and transducers are given in reference 4. The response of zone-1 relays having a nominal setting of 80% of the 300km line section are considered, and 10% of sound phase polarisation voltage is used. Nominal transducer ratios of 500/0.11 for the v.t.'s and 1200/11 for the c.t.'s were taken, and a c.v.t. high frequency cut-off (-3dB point) of 1kHz was used.

5.1 Measurement Accuracy

Fig 5 shows how the degree of compensation affects the reach of the "a"-earth relay, and it can be seen that the latter tends to increase with the degree of compensation. However, even at an extreme level of $h_1 = 1.2$, the overreach is less than 3%. With no compensation, the relays are found to possess about 2% of underreach. To summarise, it has been found that for practical loading and compensation levels the total measurement error is within ±6% of the nominal value and it can be concluded that, for practical purposes, there is no significant deterioration in the measuring accuracy of such relays when applied to linear 4-reactor shunt compensated feeders.

5.2 Speed of Operation

The time response of an "a"-earth relay at S on the alternative configurations of Fig 1 (h_1=0.7) is shown in Fig 6. It can be seen from Fig 6 that there is a very marked difference between the responses in the alternative configurations. For example, a fault at the midpoint of the line gives relay operating times of 20ms and 30ms for the single and 3-section feeders respectively. In the case of a relay applied to the 3-section feeder, the response for a close-up fault deteriorates to the extent of being approximately 8ms slower than that for an

identical fault at maximum voltage on the single section feeder. For faults at or near voltage zero point-on-wave there is little difference between the responses in the two alternative configurations. Indeed, it has been found that the performance for zero voltage faults differs little from that of relays applied to much shorter uncompensated feeders. [4]

6. Conclusions

The performance of modern high speed distance protection utilising typical block-average comparator devices is significantly affected by the system configuration, ie, the sectional arrangements involved. Measurement accuracy has not, for practical purposes, been found to vary significantly with the degree of compensation employed. In the case of faults near peak voltage point-on-wave there is however a significant difference in the relay operating times for an identical relay protecting the single or 3-section feeders. This is primarily due to the larger transit times involved in the latter arrangement, with the result that the higher frequency components are of relatively low frequency. Consequently, there is some increase in relay operating times in 3-section feeders and, in some applications where faster fault clearance times are sought, it may be necessary to reappraise the situation in relation to the pre-filtering of relaying signals prior to processing in block-average comparators.

7. References

1. Fielding G, Cheetham W J, Thanawala H L and Williams W P: 'The performance of a distance relay applied to a long distance ehv line with static shunt compensation', CIGRE, Paris paper 34-02, 1978.

2. Kimbark E W: 'Suppression of ground-fault arcs on single-pole-switched ehv lines by shunt reactors', IEEE Trans, 1964, PAS-83, pp 285-290.

3. Johns A T & Aggarwal R K: 'Digital simulation of faulted ehv transmission lines with particular reference to very-high-speed protection', Proc IEE, 1976, 123, (4), pp 353-359.

4. Johns A T & Aggarwal R K: 'Performance of high speed distance relays with particular reference to travelling-wave effects', Proc IEE, 1977, 124, (7), pp 639-646.

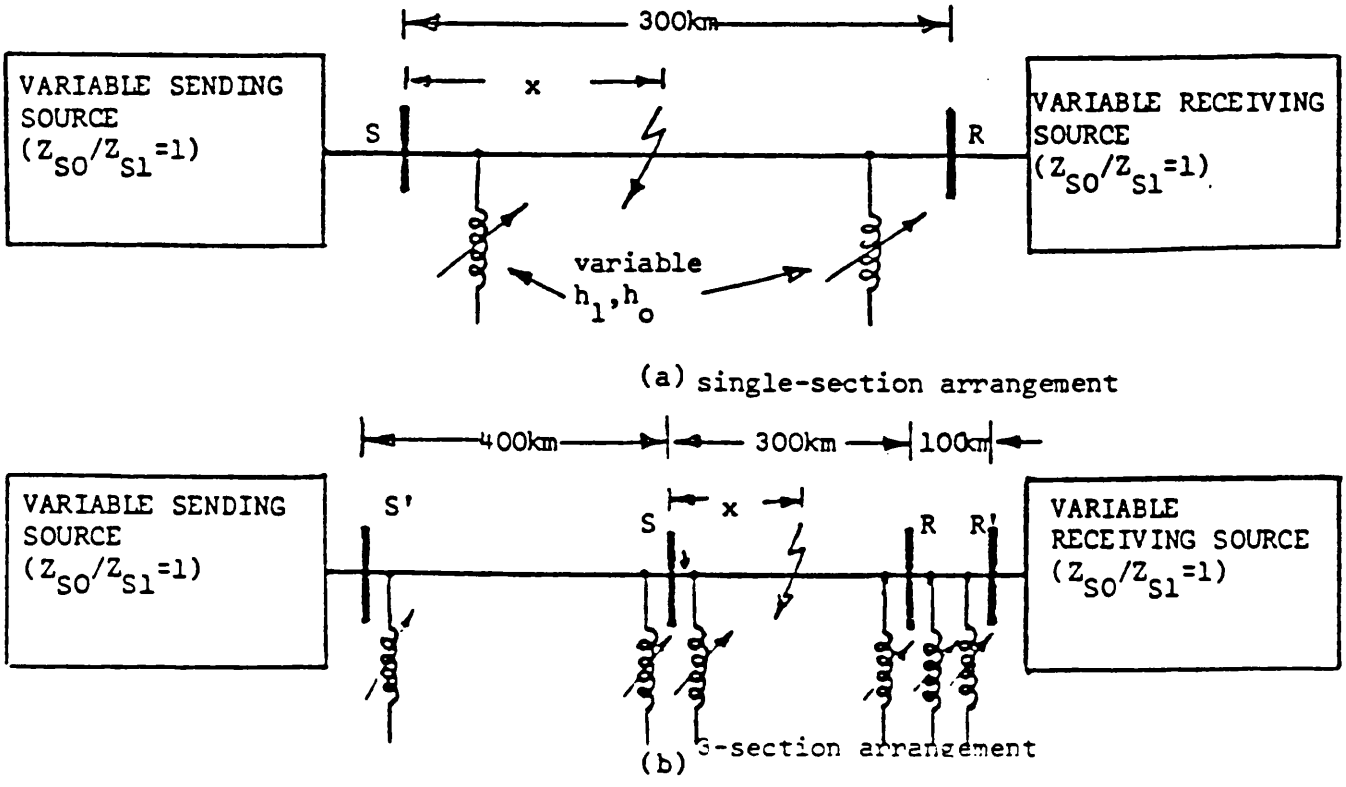

Fig 1 Basic shunt compensated systems studied

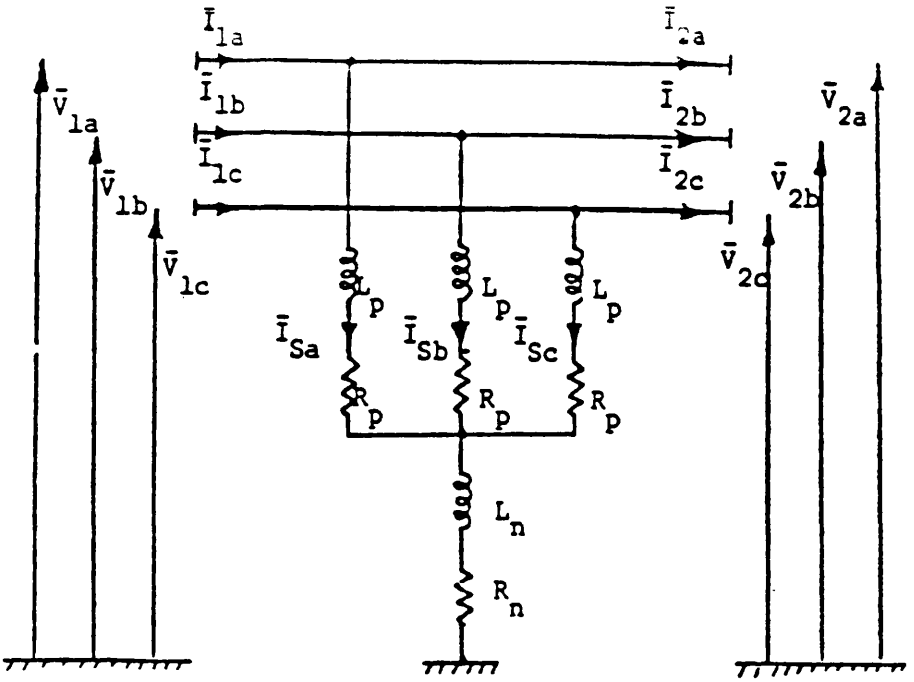

Fig 2 Typical 4-limb shunt reactor arrangement

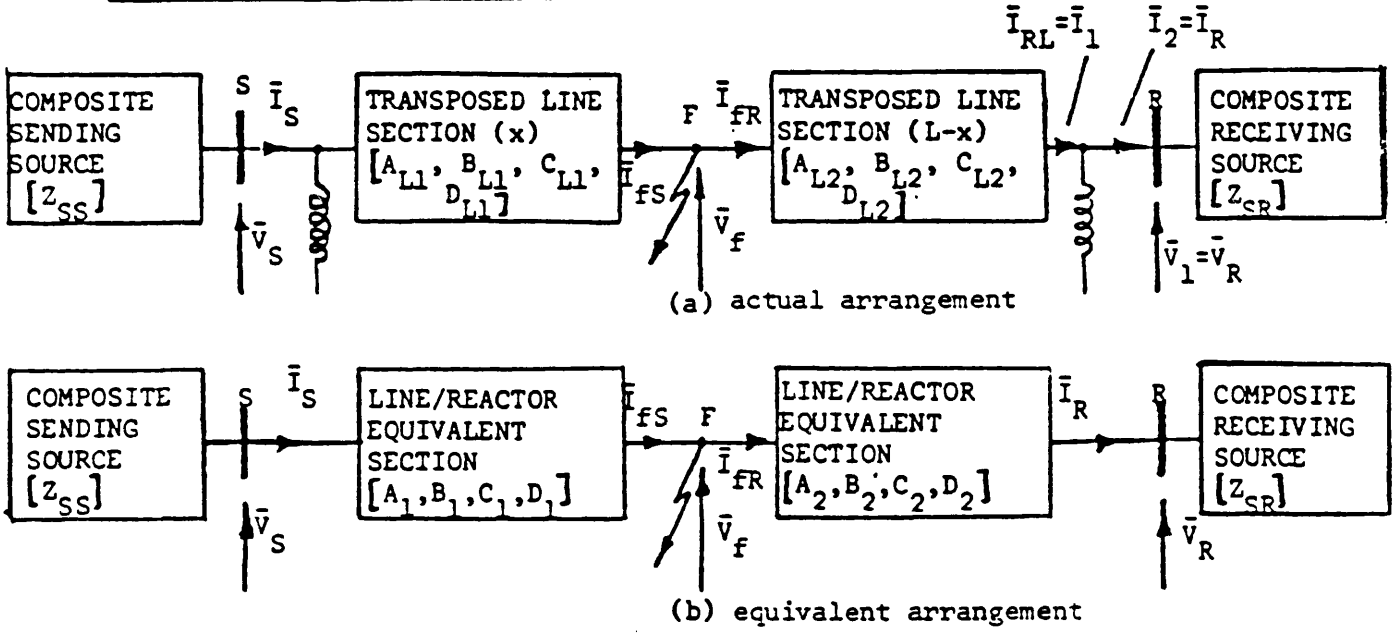

Fig 3 Line and shunt reactor combination

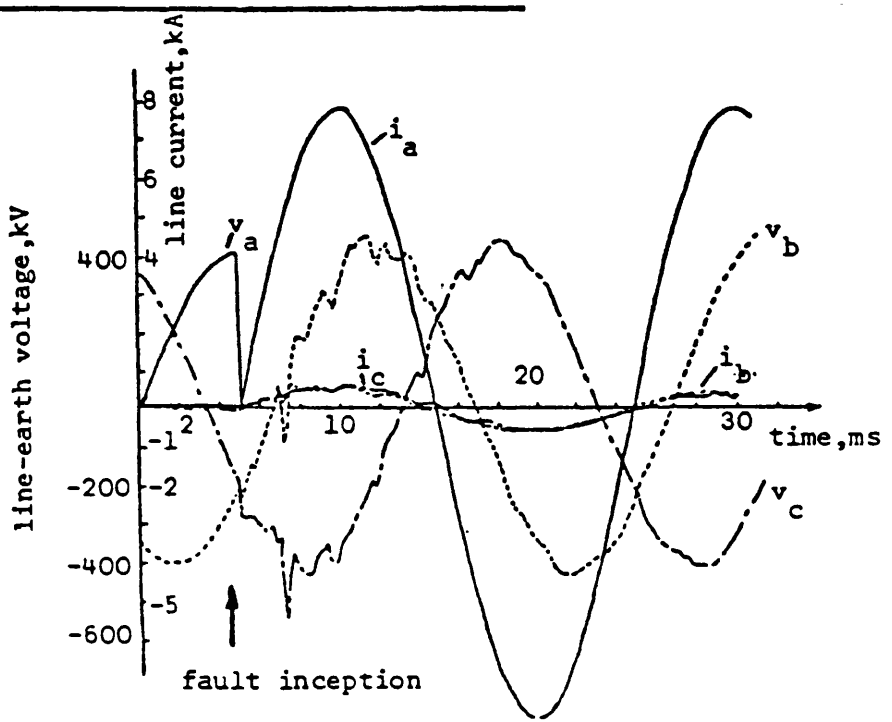

4(a) response of single section feeder (Fig 1a)

REFERENCES

1. GERT, R.
'Temporary overvoltages. Thier classification, magnitude, duration shape and frequency of occurance.'
CIGRE Report 33-12 , 1972.

2. CARROLL, D.P.
'Computer simulation of electrical transients in power systems.'
Proc. of the 1973 IEEE international symposium on circuit theory.

3. BICKFORD, J.P. and DOEPEL, P.S.
'Calculation of switching transients with particular reference to line energisation.'
Proc. IEE, Vol. 114, No. 4, April 1967.

4. BATTISSON, M.J. et al.
'British investigations on the switching of long EHV transmission lines.'
CIGRE Report 13-02, 1970.

5. HAUSPURG, A. et al.
'Overvoltages on the AEP 765 kv-system.'
IEEE Trans. on power apparatus and systems.
Vol. PAS -88, No. 9, September 1969.

6. URAM, R. and MILLER, R.W.
'Mathematical analysis and solution of transmission line transients- part I - Theory.'
IEEE Trans. on power apparatus and systems, Vol. PAS-83, November 1964.

7. URAM, R. and FEERO, W.E.
'Mathematical analysis and solution of transmission line transients-part II - Applications.'
IEEE Trans. on power apparatus and systems, Vol. PAS - 83, November 1964.

8. DOMMEL, H.W.
'Digital computer solution of electromagnetic transients in single and multi-phase networks.'
IEEE Trans. on power apperatus and systems, April 1969.

9. BEWLEY, L.V.
'Travelling waves on transmission systems.'
New York : Wiley, 1951.

10. BARTHOLD, L.O. and CARTER, G.K.
'Digital travelling wave solutions.'
AIEE Trans. PAS, December 1961.

11. TRAN, D.K.
'Laplace analysis and computer simulation of transient current in power transmission lines.'
pt 1 - single line with lossy earth return.
pt 2 - polyphase systems with lossy earth return.
Proc. IEE, Vol. 124, No. 2, February 1977.

12. WEDEPOHL, L.M.
'Application of matrix methods to the solution of travelling-wave phenomena in polyphase systems.'
Proc. IEE, Vol. 110, No. 12, December 1963.

13. WEDEPOHL, L.M. and MOHAMED, S.E.T.
'Multi conductor transmission lines. Theory of natural modes and fourier integral applied to transient analysis.'
Proc. IEE, Vol. 116, No. 9, September 1969.

14. HEDMAN, D.E.
'Propagation on overhead transmission lines - I - Theory of modal analysis.
IEEE Trans. on power apparatus and systems, March 1965.

15. BATTISSON, M.J. et al.
'Calculation of switching phenomena in power systems.'
Proc. IEE, Vol. 114, No. 4, April 1967.

16. BATTISSON, M.J. et al.
'Some effects of the frequency dependence of transmission line parameters.'
Proc. IEE, Vol. 116, No. 7, July 1969.

17. BALASUBRAMANIAN, R. and GUPTA, S.
'Calculation of transient due to fault initiation on a double-circuit transmission line.'
Proc. IEE Vol. 123, No. 6, June 1976.

18. KIMBARK, E.W. and LEGATE, A.C.
'Fault surge versus switching surges - a study of transient overvoltages caused by line-to-ground-faults.'
IEEE Trans. on power apparatus and systems, Vol. PAS-87, September 1968.

19. CLERICI, A. and TASCHINI. A.
'Overvoltages due to line energisation and re-energisation versus overvoltages caused by faults and fault clearing in ehv systems.'
IEEE Trans. on power apparatus and systems, Vol. PAS-89, 1970.

20. BOONYUBOL, C. et al.
'A mathematical analysis of transmission-line transients related to fault surges.'
IEEE Trans. on power apparatus and systems, Vol. PAS-89, 1970.

21. JOHNS, A.T. and AGGARWAL, R.K.
'Fault induced overvoltages on double-circuit ehv transmission lines.'
IEEE winter meeting , N.Y, February 1978.

22. CLERICI, A. et al.
'Overvoltages due to fault initiation and fault clearing and their influence on the design of UHV lines.'
CIGRE report 33-17 - 1974.

23. MERRY, S.M. and TAYLOR, E.R.
'Overvoltages and Harmonics on EHV systems.'
IEEE Trans., PAS - 1972, PP 2537 - 2544.

24. BICKFORD, J.P. and EL - DEWIENY, R.M.K.
'Energisation of transmission lines from inductive sources. Effects of nonsimultaneous closure also investigated.'
Proc. IEE, Vol. 120, No. 8, August 1973.

25. GLAVITSCH, H.
'Problems associated with switching surges in EHV Networks.'
Brown Boveri review, Vol. 33, No. 415, 1966.

26. GLAVITSCH, J.
'Power-frequency overvoltages in EHV systems.'
The Brown Boveri Review Vol. 51, No. 1/2, 1964.

27. BALTENSPERGER, P. and RUOSS, E.
'Switching overvoltages in EHV and UHV networks.'
CIGRE Report 13-14, 1970.

28. BARNES, H.C. et al.
'Long-line 765 kv test result and analysis.'
CIGRE report 31 - 09, 1974.

29. BARNES, H.C. and CALECA, V.
'Initial experience on the 765 kv system of the American Electric Power Company (U.S.A.).' CIGRE report 31 - 06, 1970.

30. DILLARD, J.K. et al.
'Controlling of switching surges on 1100 kv transmission system.'
IEEE Trans., Vol. PAS-89, No. 8, November 1970.

31. NORTON, E.T.
'Use of EHV shunt reactors to control overvoltages calls for more know-how.'
Electrical World, September 1965.

32. TRUAX, C.J. et al.
'The study of reclosing transients on a 765 kv shunt compensated transmission line.'
IEEE Trans., Vol. PAS-97, No. 4, July/August 1978.

33. BARIL, G.A.
'Overvoltages and insulation co-ordination analysis and application for 735 kv.'
CIGRE report 33-09, 1970.

34. Kennedy and Donkin Consulting Engineers.
'500 kv interconnection between the central system and the atlantic coast of Colombia.'
Report No. 10, June 1976.

35. SHIPLEY, R.B.
'Digital analysis of single-pole switching on EHV lines.'
IEEE Trans., Vol. PAS-87, No. 8, August 1968.

36. KNUDSEN, N.
'Single phase switching of transmission lines using reactors for extinction of the secondary arc.'
CIGRE report 310, 1962.

37. KIMBARK, E.W.
'Suppression of ground-fault arcs on single-pole-switched EHV lines by shunt reactors.'
IEEE Trans. on power apparatus and systems, March 1964.

38. EDWARDS, L.
'Single-pole switching on TVA's paradise-division 500 kv line. Design concepts and staged fault test results.'
Paper 71 TP 147 - PWR, recommended and approved by the transmission and distribution committee of the IEEE Power Engineering Society for presentations at the IEEE winter power meeting, New York 31-1-71 to 5-2-71.

39. PETERSON, H.A. and DRAVID, N.V.
'A method for reducing dead time for single-phase reclosing in EHV transmission.'
IEEE Trans. Vol. PAS-88, No. 4, April 1969.

40. RIZK, A.M.
'Single-phase auto-reclosure of extra-high-voltage transmission lines.'
Proc. IEE, Vol. 116, No. 1, January 1969.

41. CARLSSON, L. et al.
'Single-pole reclosing on EHV lines.'
CIGRE report 31-03 1974.

42. HAUBRICH, H.J.
'Single-phase auto-reclosing on EHV systems.'
CIGRE report 31-09 1974.

43. HAUN, R.K.
'13-years experience with single-phase reclosing at 345 kv.'
IEEE Trans, Vol. PAS-97, No. 2, March/April 1978.

44. CHADWICK, J.W., JR and GOFF, L.E., JR.
'Development of a static single-pole relaying scheme for the TVA 500 kv system.'
Proc. of the American Power Conference, Vol. 33, 1971.

45. EDWARDS, L.
'Single-pole switching studied on 500 kv line.'
Electrical world, August 22 1966.

46. HOBSON, J.E. and MULLER, H.N., JR.
'Single-pole fault clearing for greater stability.'
Westinghouse Engineer, February 1942.

47. MAIKOPAR, A.S.
'Prospects of single-phase automatic reclosure on 500 kv long distance lines 500 km in length when using shunting reactors.'
Electric technology in USSR, 1964, pp 348-355.

48. BALSER, S.J. et al.
'Single-pole switching. A comparison of computer studies with field test results.'
Paper T73 406-6 presented at the IEEE PES summer meeting and EHV/UHV conference, Vancouver, B.C., Canada, July 15 - 20 1973.

49. KIMBARK, E.W.
'Charts of three quantities associated with single-pole switching.'
IEEE Trans., Vol. PAS-94, No. 2, March/April 1975.

50. KIMBARK, E.W.
'Selective-pole-switching of long double-circuit EHV line.'
IEEE Trans., Vol. PAS-95, No. 1, January/February 1976.

51. LAMBERT, S.R. et al.
'Long line single-phase switching transients and their effect on station equipment.'
IEEE Trans. Vol. PAS-97, No. 3, May/June 1978.

52. SHPERLING, B.R. and FAKHERI, A.
'Single-phase switching parameters for untransposed EHV transmission lines.'
IEEE Trans. Vol. PAS-98, No. 2, March/April 1979.

53. JOHNS, A.T. and AGGARWAL, R.K.
'Digital simulation of faulted e.h.v. transmission lines with particular reference to very-high speed protection.'
Proc. IEE., Vol. 123, No. 4, April 1976.

54. JOHNS, A.T.
'Computer simulation studies of new methods of distance protection for e.h.v. lines.'
Report on Science Research Council Research, University of Bath, 1975.

55. GALLOWAY, R.H. et al.
'Calculation of electrical parameters for short and long polyphase transmission lines.'
Proc. IEE., Vol. 111, No. 12, 1964, pp 2051 - 2059.

56. BANERJEE, A.R.
'Fault transient analysis of power transmission line.'
Ph.D. Thesis, University of Bath, 1976.

57. JOHNS, A.T. and AGGARWAL, R.K.
'Performance of high-speed distance relays with particular reference to travelling-wave effects.'
Proc. IEE., Vol. 124, No 7, July 1977.

58. JOHNS, A.T. and EL-KATEB, M.M.T.
'Developments in techniques for simulating faults in e.h.v. transmission systems.'
Proc. IEE., Vol. 125, No. 3, March 1978.

59. HUBER, F.
'Shunt reactors for the 765 kv system in the U.S.A.'
Brown Boveri Review, 1969.

60. FELDMAN , J.M. and WILSON, D.D.
'Shunt reactor compensation on present and future transmission systems.'
Proc. American Power Conference,1969.

61. DOBSA, J. and HUBER, F.
'Shunt reactors with and without loadable secondary windings.'
Brown Boveri Review, No. 8, 1972.

62. BARTHOLD, L.O. et al.
'Static shunt devices for reactive power control.'
CIGRE report 31 - 08, 1974.

63. FRIEDLANDER, E.
'High voltage a.c. power transmission development.'
Philos. Trans. A(GB), Vol. 275, No. 1248, pp 189 - 192, 1973.

64. The Control of system voltage using A.C. saturated reactors.
G.E.C. publication No. TD-6301T-1068.

65. YOUNG, D.J.
'Voltage fluctuations and their suppressions.'
ERA distribution conference, Edinburgh, October 1967.

66. BECKER, H. et al.
'Three phase shunt reactors with continuously controlled reactive current.'
CIGRE report 31 - 13, 1972.

66.a 'First static compensator in service.'
G.E.C. Journal, Vol. 35, No. 1, 1968.

67. ENGBERG, K. et al.
'Reactors and capacitors controlled by thyristors for optimum power system VAR control.'
Technical Seminar on reactive power compensation in power systems at the University of Birmingham, 11 - 12 September 1979.

68. PACHECO, E.J.P
'System voltage control using saturated iron cored reactors.'
Ph.D. Thesis, UMIST, U.K., 1977.

69. REICHERT, K. et al.
'Controllable reactor compensator for more extensive utilisation of high voltage transmission systems.'
CIGRE report 31 - 04, 1974.

70. FRIEDLANDER, E.
'Static network stabilisation - recent progress in reactive power control.'
GEC Journal, Vol. 33, No. 2, 1966.

71. AINSWORTH, J.D. et al.
'Recent developments towards long distance a.c. transmission using saturated reactors.'
International conference on HVDC and/or A.C. power transmission, London U.K., 19 - 23 November 1973,
IEE, p 242 - 7.

72. FRIEDLANDER, E. and YOUNG, D.J.
'The Quin-reactor for voltage stabilisation.'
Electrical review, 22 July 1966.

73. FRIEDLANDER, E.
'The development of saturated reactors for network stabilisation as applicable to magnet power supplies.'
Second International Conference on magnet technology, Oxford, U.K. 1967.

74. AINSWORTH, J.D. et al.
'Application of saturated reactors to a.c. voltage stabilisations for HVDC transmission and other large convertors.'
A paper recommended by IEEE PES summer meeting and EHV/UHV conference, Vancouver, Canada, July 15 - 20 1973.

75. ABU ELNOUR, M.
'Saturable reactors in electrical power systems.'
M.Sc. Thesis, University of Bradford, U.K., 1976.

76. PARTON, J.E. et al.
'Three phase iron-cored-hormonic-free reactor.'
10th Universities power engineering conference, January 1975,
Aston University, Birmingham, U.K.

77. EDLINGER, A. et al.
'The use of high voltage reactors for the compensation of extra high voltage transmission lines.'
CIGRE report 402, 1964.

78. FRIEDLANDER, E. and JONES, K.M.
'Saturated reactors for long distance bulk power lines.'
Electrical review, 27 June 1969.

79. CLERICI, A. et al.
'Influence of shunt reactors on switching surges.'
IEEE Trans., Vol. PAS-89, No. 8, November/December 1970.

80. STEVENSON, W.D. , JR.
'Elements of power system analysis.'
McGrow - Hill book company, second edition, 1962.

81. CARSON, JR.
'Wave propagation in overhead wires with ground return.'
Bell system technology journal, 1926,5, p. 539.

82. WEDEPHOL, L.M.
'Wave propagation in multi-conductor overhead lines - calculation of series impedance for multilayer earth.'
Proc. IEE, Vol. 113, No. 4, April 1966.

83. AMETANI, A.
'Stratified earth effects on wave propagation - frequency - dependent parameters.'
Paper T74 081-6, presented at the IEEE PES winter meeting, New York, N.Y., January 27 - February 1 1974.

84. NAKAGAWA, M. et al.
'Further studies on wave propagation in overhead lines with earth return: Importance of stratified earth.'
Proc. IEE, Vol. 120, No. 12, December 1973.

85. DABULEANU, A. and SEMLYEN, A.
'Modelling of transpositions and double circuit transmission lines in switching surge calculations.'
IEEE Trans. (PAS), Vol.-PAS-94, No. 2, March/April 1975.

86. WEDEPOHL, L.M. and MOHAMED, S.E.T.
'Apparant impedances of very long multi-conductor transmission lines.'
Proc. IEE, Vol. 117, No. 7, July 1970.

87. WEDEPHOL, L.M.
'Electrical characteristics of polyphase transmission systems with special reference to boundary-value calculations at power-line carrier frequencies.'
Proc. IEE, Vol. 112, No. 11, November 1965.

88. AMETANI, A.
'The application of the fast fourier transform to electrical transient phenomena.'
Int. J. Elec. Eng. Educ., Vol. 10, pp 277 - 287, 1973.

89. WILCOX, D.J.
'Numerical laplace transformation and inversion.'
Int. J. Elec. Eng. Educ., Vol. 15, pp 247 - 265, 1978.

90. DAY, S. et al.
'Developments in obtaining transient response using Fourier transforms. Part I: Gibbs phenomena and Fourier integrals.'
Int. J. Elec. Eng. Educ., Vol. 3, pp 501 - 506, 1965.

91. DAY, S. et al.
'Developments in obtaining transient response using Fourier transforms. Part II: use of the modified Fourier transform.'
Int. J. Elec. Eng. Edu., Vol. 4, pp 31 - 40, 1966.

92. JACKSON, L. et al.
'Distance protection: Optimum dynamic design of static relay comparators.'
Proc. IEE, Vol. 155, No. 2, February 1968.

93. WEDEPOHL, L.M.
'Polarised mho distance relay; new approach to the analysis of practical characteristics.'
Proc. IEE, Vol. 112, No. 3, 1965.

94. WRIGHT, A.
'Current transformers - their transient and steady-state performance.'
Chapman and Hall Ltd., 1968.

95. FIELDING, G. et al.
'The performance of distance protection relay applied to a long distance EHV line with static shunt compensation.'
CIGRE report 34 - 02, 1978.

96. COTHARI, G.C. et al.
'Computer-aided analysis of high speed protective relays.'
Proc. IEE, Vol. 121, No. 7, July 1974.

97. HUGHES, M.A.
'Distance relay performance as affected by capacitor voltage transformers.'
Proc. IEE, Vol. 121, No. 12, December 1974.